ICENS
INTERNATIONAL CONFERENCE ON ENGINEERING AND NATURAL SCIENCES
24-28 May 2016 /Sarajevo

Investigation of Surface Roughness in Turning of Co-based Super Alloy Haynes 25 under Cryogenic Cooling

Murat Sarıkaya[1], Sener Karabulut[2,], Abdulkadir Gullu[3]*

Abstract

This study focuses on an experimental investigation for determining surface roughness during turning of cobalt based super alloy Haynes 25. Tests were carried out under two cutting conditions such as cryogenic cooling and dry cutting. For cryogenic cooling, liquid nitrogen (LN_2) was used. Cutting speed and feed rate were considered as cutting parameters. In turning tests, uncoated carbide insert was employed. After experiments, average surface roughness (Ra) were measured for process performance indicator. Regression analysis was performed to obtain the surface roughness result under different cutting parameters and conditions. It was seen that cryogenic machining increased significantly surface quality of machined surfaces during turning of Co-based metal Haynes 25.

Keywords: *Co-based super alloy; cryogenic machining; surface roughness, statistical analysis*

1. INTRODUCTION

Super alloy metals (also known as high-performance alloys) have been used for a lot of applications involving aerospace industry, defense industry, chemical industry, medical industry, nuclear reactors, submarines et al. because of their excellent properties such as low thermal conductivity, high strength, wear resistance, heat and corrosion resistance [1]. Some of such alloys are Hastelloy, Inconel, Hastelloy, Waspaloy, Incoloy and Haynes alloys. Cobalt based Haynes 25 super alloy has important properties including high-temperature strength and oxidation resistance. It has been used in many engineering applications. [2], [3]. However, machinability of super alloy metals is quite difficult compared with carbon steels. Therefore, they are usually called as difficult-to-machine alloy. Cobalt, nickel, chromium, titanium which are located in these metals, allows high strength, wear and corrosion resistance. During metal cutting processes, two main issues occur and these are poor surface quality of the machined surface and the short tool life of the cutting insert [4]. There are some cooling/lubrication ways for increasing the surface quality and tool life. Some of these methods are cryogenic cooling, solid coolants/lubricants, wet cooling (traditional cooling), minimum quantity lubrication, high pressure coolants, and compressed air/gases [5]. When they are effectively used, cooling methods and cutting fluids can improve the tool life and surface quality [6]. In spite of some significant benefits of these cooling/lubrication methods, there are some unfavorable impacts such as environmental pollution and worker health. Also, the recycling of used cutting fluids is very difficult and expensive [7]. In chip removal operations, in so as to remove the negative effects of the cutting fluids, cryogenic cooling and high pressure air cooling can be used. When literature has been examined, it has been seen that there are several works on the use of cryogenic cooling. For instance, Sarikaya [8] studied the effect of cooling/lubrications methods involving dry, conventional and cryogenic machining in turning of AISI 316Ti stainless steel. It was determined that cryogenic cooling is an alternative method for increasing the surface quality of machined parts. Ahmed et al. [9] explored the influence of cryogenic cutting with help of modified tool holder on flank wear, tool life and surface roughness during turning of AISI 4340 steel. Wang et al. [10] performed an experimental investigation about cryogenic machining. They expressed that cryogenic cooling is more effective than dry cutting in term of cutting insert temperature and tool wear. Dhananchezian and Kumar [11] made an experimental work so as to identify the influence of liquid nitrogen when it was delivered to cutting insert surfaces through micro-holes on the tool insert during the cutting of the Ti–6Al–4V alloy. They determined that cryogenic machining combined with a modified cutting insert showed better output than conventional cooling. Venugopal et al. [12] explored the influence of cooling/lubrication methods involving dry, wet and cryogenic on tool wear during the cutting of Ti–6Al–4V alloy. According to their results, when it was compared with other methods, cryogenic cooling provided an important effect in terms of tool life. Umbrello et al. [13] made an experimental study in order to see the influence of cryogenic and dry machining on the surface integrity. They was point out that cryogenic cutting showed better result than other methods. In addition, the use of cryogenic cooling provided an important improvement on tool life, surface quality and dimensional accuracy [14] - [16]. It has been seen that from literature review, there are some works dealing with cryogenic machining. However, in turning of cobalt based super alloy Haynes 25 with several cooling methods such as dry, wet and cryogenic, surface roughness was not studied. Therefore, present work investigated the influence of cryogenic machining on surface roughness in turning of Co-based super alloy Haynes 25.

2. EXPERIMENTAL PROCEDURE

2.1 Material, CNC machine, cutting tool and measurement

In tests, cobalt-based super alloy Haynes 25 was used for workpiece material. The chemical composition of material is listed in Table 1.

Table 1. Chemical composition of material

% Weight								
C	Co	Cr	Fe	Ni	P	S	Si	W
0.10	Balance	20.3	1.58	10.20	<0.005	0.0008	0.01	14.7

Tests were carried on a Falco Fl-8 model (Taiwan) CNC lathe machine. It has a maximum spindle speed of 4800 rpm and a 15 kW drive motor. An uncoated carbide insert that its ISO code is SNMG 12 04 08-QM and a tool holder that its ISO code is PSBNR 2020K-12 produced by Sandvik were used. Experimental set-up is seen in Fig. 1. Surface roughness measurement samples were taken from the machined surface, at three separate circumferential points along the direction of tool motion, and the arithmetic average of the measurements was calculated. The surface profile measuring method was employed in measuring surface roughness, using a Time brand TR100 portable surface roughness tester (profilometer), capable of determining profile changes as Ra (average surface roughness) values.

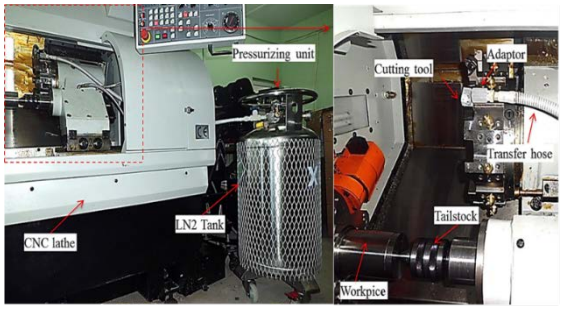

Figure 1. The experimental setup

2.2 Cutting parameters

In this study, cutting parameters were cutting speed (Vc) and feed rate (f). The levels of cutting parameters were selected through plot tests and the manufacturer's handbook. In turning experiments, depth of cut (ap = 1 mm) were fixed and cutting speed, feed rate and their values are listed in Table 2. Experiments were performed with dry and cryogenic cutting from tool inside with help of liquid nitrogen (LN_2). For cryogenic cooling, liquid nitrogen was directly delivered from liquid nitrogen pressure tank to tool holder at a pressure of 1.5 bars. Three holes were drilled on tool holder. The diameter of the first hole on tool holder was made at 6 mm dimension and it provided a connection between tool holder and liquid nitrogen container with the help of hose and adaptor. Liquid nitrogen accumulated inside of the tool holder has been released towards environment as gas vapor with help of the other two holes by taking the heat from insert. Diameter of the gas exit holes was made at 1.5 mm dimension. Experimental setup for cryogenic cooling is seen in Fig. 1.

Table 2. Experimental parameters

Item	Description
Cutting speed	30; 45 and 60 m/min
Feed rate	0.08; 0.12 and 0.16 mm/rev
Cutting insert	Uncoated carbide - SNMG 120408
Tool holder	PSBNR 2020K12
Depth of cut	1 mm
Cutting condition	Dry and cryogenic

3 RESULT AND DISCUSSION

3.1 Experimental Results

Surface quality of the machined workpiece is one of the most important quality indicator in manufacturing industry. In machining processes, the surface quality can be improved with the cutting parameters and conditions. In this study, an attempt was made to improve the surface quality through cutting parameters and cutting conditions. Figure 2 and Figure 3 shows surface roughness results depending on machining parameters. According to these figures, an important increase in surface

roughness was observed with the increasing of feed rate. From the literature, there is a direct relationship between feed rate and surface roughness, and that increased surface roughness in response to increased feed rate is within expectations [17]. Therefore, this result is expected and is parallel with the literature. Increasing in surface roughness depending on feed rate can be explained that increasing the feed rate accelerates a vibration and occurs high heat between tool-chip interface and so higher surface roughness on machined workpiece surface exists [8, 18].

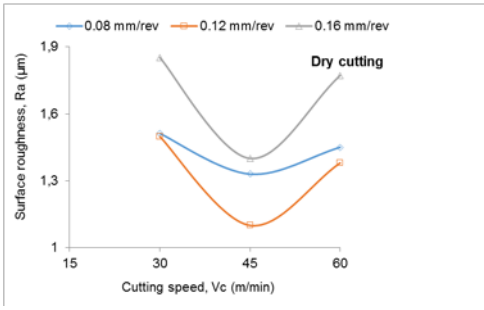

Figure. 2. Surface roughness result under dry cutting

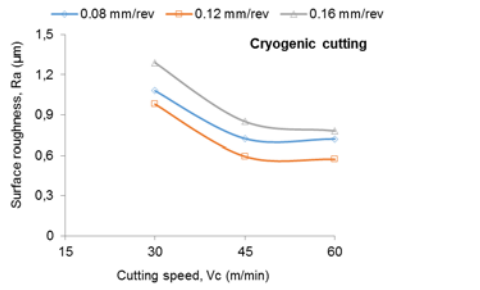

Figure 3. Surface roughness result under cutting

When Figure 2 and Figure 3 was examined, it was seen that surface roughness exhibited a decrease trend with increasing of cutting speed. It is known that in order to improve surface quality, the cutting speed can be increased within reasonable limits [17]. This situation can be explained that increasing temperature in the machining process created the plastic deformation and the chip flow easier [8, 18]. In addition, it was estimated that due to a decreasing with built-up edge (BUE) and built-up layer (BUL) formations cutting tool wear was influenced positively, and hence this condition provides rise to an improvement in the surface quality [19]. However, in dry cutting process, when cutting speed was reached at level of 60 m/min level, surface roughness was observed in an increase tendency. This may be due to accelerating the cutting tool wear. In machining operations, when coolants and cutting lubricants are employed as efficiently, higher dimensional accuracy and a lower surface roughness may be obtained occur; further, a lower cutting tool wear may be occurred [8]. According to Figure 3, an important decrease was observed in turning of workpiece under cryogenic cooling condition. The reason of this result can be expressed with a lower the cutting temperature, adhesion on cutting tool and tool wear when cryogenic cooling was applied to cutting tool [20].

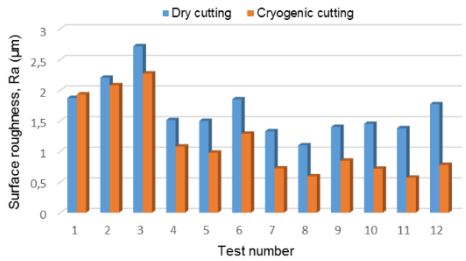

Figure. 4. Comprassion of surface roughness result

3.2 Regression Analysis

A regression analysis was applied to identify the relationship between the input parameters and test outputs. In this investigation, input parameters are cutting speed (Vc), the feed rate (f) and the cooling condition (C) and the surface roughness (Ra) is the output. A mathematical equation based on first order model was written for predicting Ra. The first-order model can be written as following with Equation (1):

$$y = \beta_0 + \beta_1 . i_1 + \beta_2 . i_2 + \beta_3 . i_3 \quad (1)$$

where, y is output, and i_1, i_2, and i_3 are the values of the input parameters. The term β is the regression coefficient. The first-order model can be expressed as a function of the cooling condition (C), the feed rate (f) and the cutting speed (Vc). The relationship between the output and the machining parameters from Equation (1) was adapted as given in following Equation (2):

$$Ra_{pre} = \beta_0 + \beta_1 . C + \beta_2 . f + \beta_3 . V_c \quad (2)$$

According to Eq. (2) a regression equation for surface roughness can be expressed as following Eq. (3).

$$Ra_{pre} = 2.213 - 0.6340xC + 2.35xf - 0.0854 * Vc \quad (3)$$

Where cooling condition was taken as 1 and 2 for dry and cryogenic cooling, respectively.

A graphical analysis method was made so as to assess the contents of the residual of the model. The sufficiency of the models was studied by examining the residuals. The normal-probability plot of the residuals for the surface roughness is seen in Figure 4. It is seen that the residual rather appropriately tend towards a straight line, meaning that errors are normally delivered. This demonstrates that the predictive model is satisfactory.

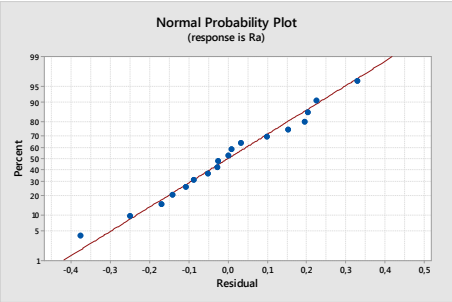

Figure.5 Normal probability plot

4 CONCLUSION

The results obtained from this study can be summarized as follows:

- A cryogenic cooling using liquid nitrogen from tool inside was applied successfully in turning of Co-based super alloy Haynes 25.
- While surface quality decreased with an increase in the feed rate, it showed an improvement tendency with an increase in the cutting speed and with the use of the cryogenic cooling.
- Surface roughness was influenced negatively when cutting speed was increased to reach the level of 60 m/min under dry cutting condition.
- According to normal probability plot, in order to predict the surface roughness under different cutting parameters and conditions the written regression equation can be used.

ACKNOWLEDGMENT

This research was supported by the Scientific and Technological Research Council of Turkey (TUBITAK), Project no 112M029. Thanks TUBITAK for financial support.

ICENS
INTERNATIONAL CONFERENCE ON ENGINEERING AND NATURAL SCIENCES
24-28 May 2016 /Sarajevo

Strength properties of Çatalağzı class F fly ash geopolymer mortar activated with different NaOH amount

Okan Karahan[1]*, I. Isa Atabey[2]

Abstract

In this study, compressive strength and flexural tensile strength of alkali activated fly ash geopolymer mortars were presented. Class F Çatalağzı fly ash was used in this study. NaOH concentration amount as the main influencing factors on the compressive strength and flexural tensile strength were investigated. Mortar mixture parameters were 3 and 0.35 for sand-binder ratio, and water-binder ratio, respectively. Na concentrations in mortar mixture were chosen as 6%, 9%, 12%, 15% and 18% in weight basis. Heat curing temperature and heat curing duration were chosen as 100°C and 24 hours respectively. For each NaOH concentration, three prismatic specimens with 40×40×160 mm dimensions were prepared using a three-cell mortar cast. After heat curing period in a laboratory oven, the samples were left to cool down to room temperature, then the compressive and flexural strengths were measured according to TS EN 1015-11. High compressive strength and flexural tensile strength, as high as 80 MPa and 10 MPa respectively, were obtained from the geopolymer mortar made with the current fly ash.

Keywords: *Fly Ash, Geopolymer, Alkali-activated*

1 INTRODUCTION

The most famous waste that can be used in concrete is fly ash. Fly ash can be replaced cement content up to 30%. The current European standard EN 197 (2000) allows a replacement level up to 55% cement by fly ash in cement mixture CEM IV. By this way 10% of cement production can be saved which is not enough to solve the environmental impact. [1]. Alkali activated materials have become the focus of an increasing scientific interest, offering a competitive ‘‘green’’ alternative to traditional building materials [2].

Fly ash based geopolymers are one branch of the geopolymer family and have attracted more attention since the 1990s [3]. The alkali-activation technology of coal fly ash is one of several potential solutions to minimize the harmful disposal of fly ash [4]. The use of fly ash in the alkali-activation process (geopolymerization) also contributes to the reduction of the exploitation of natural raw materials, and at the same time complies with the more complicated demands of the construction industry in terms of characteristics and the quality of the construction materials [5].

Class F fly ash is a good source for geopolymers and that NaOH is better than other activators for the activation of the fly ash in the production of geopolymers [6]. Alkali activator solutions play an important role in the dissolution of Si and Al oxides. Hence, geopolymers are synthesized by mixing the most common alkaline activators that are strong alkaline solutions such as sodium hydroxide with aluminosilicate reactive materials [7]. Several studies show that curing temperature plays an important role in the geopolymerization process of fly ash-based geopolymer and that an increase in the curing temperature accelerated the activation of fly ash with an alkali activator [8], [9], [10].

[1] *Corresponding author: Erciyes University, Department of Civil Engineering, 38039, Kayseri, Turkey.* okarahan@erciyes.edu.tr
[2] *Cumhuriyet University, Sivas Vocational High School, 58140, Sivas, Turkey.* iatabey@cumhuriyet.edu.tr

Literature was shown that heat-cured geopolymer concrete possesses high compressive strength. Joseph and Mathew [11] reported 58 MPa compressive strength obtained from the mixture that cured at 100 °C curing temperature for 24 hours, tested at 28 days. Olivia and Nikraz [12] achieved 60 MPa compressive strength with 14 Molar NaOH solution for 24 hours heat curing at 75°C degree. Gorhan and Kurklu [7], obtained 22 MPa and 8 MPa, compressive and flexural tensile strength respectively, from the fly ash geopolymer mortar made with 9 molar NaOH solutions, at temperature of 85°C, for 24 hours heat curing. Ryu et al. [13] reported the highest compressive strength was 45 MPa of concrete made with alkali activated fly ash with NaOH for 24 hours at 60°C. Vora and Dave [14] reported highest compressive strength is in the order of 40 MPa for geopolymer concrete made with Class F fly ash mixture of NaOH and water glass. Atiş et al. [15] reported 120 MPa compressive strength and 15 MPa flexural tensile strength are obtained from fly ash geopolymer mixture activated with 14% NaOH, and cured at 115°C for 24 h.

The aim of this research is to study the effects of different NaOH amount on geopolymer mortar made with fly ash. This is achieved by measuring the unit weight, workability, flexural and compressive strength of fly ash geopolymer mortar studied. This study is a part of preliminary studies of PhD thesis carried out at Erciyes University.

2 PROPERTIES OF MATERIALS

2.1 Fly Ash

Fly ash was supplied from CNR Mining and Transporting Incorporation located in Çatalağzı power station in Zonguldak, which is northern city of Turkey. Its total value of SiO_2+Al_2O_3+Fe_2O_3, is higher than 70% and CaO amount is less than 10%, present fly ash is classified as class F type and low lime fly ash according to ASTM C618 [16] specification. Specific gravity of fly ash was 2.10 and its remaining on 45µm sieve was 29%. 28 - Day Pozzolanic activity index was 87.8%. Chemical compositions of class F fly ash used were presented in Table 1.

Table 1. Chemical compositions of fly ash (%)

Oxide	SiO_2	Al_2O_3	Fe_2O_3	CaO	MgO	SO_3	Total Alkali	TiO_2	Cl^-	Free CaO	LOI
Fly Ash	55.38	25.50	6.14	2.02	2.00	0.14	3.12	1.20	0.0014	0.18	2.74

2.2 Reference sand

The sand used was CEN reference siliceous sand with maximum aggregate size of 2.0 mm. The absorption value of the sand used was 0.57% and its relative density at saturated surface dry (SSD) condition was 2.69. The gradation of sand and limits of TS EN 196-1 [17] were presented in Table 2.

Table 2. Fine aggregate gradations and values of standard limits

	Particle size (mm)					
	0.08	0.16	0.5	1.0	1.6	2.0
Remaining (%)	99.6	87.1	68.9	32.7	3.1	0
Limits (%)	99 ± 1	87 ± 5	67 ± 5	33 ± 5	7 ± 5	0

2.3 Activator

The activator used in this investigation was sodium hydroxide. The chemical composition of sodium hydroxide (obtained from Koruma Klor Alkali) is summarized in Table 3.

Table 3. *Chemical composition of sodium hydroxide and limits*

NaOH (%)	Na_2CO_3 (%)	NaCl (%)	Fe (ppm)
98.27	0.35	0.02	13.17
min. 98.00	max. 0.40	max. 0.10	max.15

2.3 Water

A drinking tap water taken from the city water supply system was used as mixing water.

3 EXPERIMENTAL PROGRAM

Mortar mixtures made with fly ash used as binder were produced using standard reference sand, drinking tap water and NaOH as activator. In the mortar mixture, sand/fly ash ratio and water/fly ash ratio were kept constant as 3 and 0.35 respectively. Sodium concentrations in mortar mixture were chosen as 6%, 9%, 12%, 15% and 18% in weight basis. Sodium concentration is taken into account in this study, therefore, additional water that comes within NaOH is considered and determined; and then, that amount is reduced from mixing water to keep water/fly ash ratio at 0.35. The fly ash geopolymer mixture proportion details are presented in Table 4.

Table 4. Mix design of all mixtures made with different activator concentration

Na (%)	Water Fly Ash Ratio	Fly Ash (g)	Sand (g)	Water (g)	NaOH (g)	Water Content (g)
6	0.35	450	1350	146.93	46.96	10.57
9	0.35	450	1350	141.65	70.43	15.85
12	0.35	450	1350	136.37	93.91	21.13
15	0.35	450	1350	131.09	117.39	26.41
18	0.35	450	1350	125.80	140.87	31.70

The mixing procedures of the mortar involved the following. First, the activator were added to the mix in the mixing water. Water and fly ash were placed in Hobart mixer and mixed in slow mode for 30 sec. Second, the sand was poured for 30 sec. while mixing was in slow mode. Then, third, mixture was mixed in fast mode for 30 sec. Fourth, the mixing was stopped and waited 15 sec. Fifth, the mixture was mixed for 60 sec. in fast mode [17]. Then, flow workability of mortar was conducted to the consistency of mortar mixture determined using mortar flow test having a mini cone with a base diameter of 100 mm. Fresh mortar was placed into mini frustum cone on its vibrating table with a standard manner prescribed in TS EN 1015-3 [18], and the cone was lifted. Then, the fresh mortar was dropped from 12.5 mm height for 15 times in 15 second with vibrating table. In consequent, mortar spreaded, and the maximum spread was measured. The average of two values of spread diameter was recorded.

Last, the freshly mixed mortar was taken from the mixer and fed into specimens mold and jolted 60 times in 1 minute to obtain full compaction. For each NaOH concentration, three prismatic specimens with 40×40×160 mm dimensions were prepared using a three-cell mortar cast. Fresh fly ash geopolymer mixture were prepared using different amount of activator concentration, then, they were subjected to 100°C heat curing temperature for 24 hours heat curing duration. After heat curing period in a laboratory oven, the samples were left to cool down to room temperature, then unit weight, compressive and flexural strengths were measured according to TS EN 1015-11 [19]. For each hardened fly ash geopolymer mixture, flexural tensile strength measurements were carried out using three prismatic specimens by performing a third point loading test. The compressive strength measurements were carried out using six broken pieces of the prismatic specimens obtained from flexure test. Average of three specimens and average of six specimens were used for a data point for flexure test and compressive strength test, respectively.

4 RESULTS AND DISCUSSIONS

4.1 Flow workability and unit weight

The results of measurement of the flow workability and hardened unit weight were presented in Table 5. The sodium hydroxide activated fly ash mortar mix were very strict, having a flow about 101-105 mm. Table 5 shows that sodium hydroxide content decreased the workability and, the increase in content of activator further decreased workability.

Hardened unit weight of alkali activated fly ash mortar was between 1.96-2.08 g/cm^3. Table 5 also shows increase in the sodium concentration causes increase in unit weight. Consequently, inclusion of sodium concentration in fly ash activated mortar reduces flow workability and increases unit weight values.

Table 5. Flow workability and unit weight of all mixtures

Na (%)	Water Fly Ash Ratio	Flow (mm)	Unit Weight (g/cm^3)
6	0.35	105	1.96
9	0.35	103	2.04
12	0.35	104	2.05
15	0.35	102	2.07
18	0.35	101	2.08

4.2 Flexural and compressive strengths

Flexural and compressive strength tests were carried out on prismatic mortar samples with 40x40x160 mm dimensions. The flexural and compressive strength test results, which were average of three and six samples, respectively, were presented in Table 6.

Table 6. Flexural and compressive strength of geopolymer mortar

Na (%)	Water Fly Ash Ratio	Strength (MPa)	
		Flexural	Compressive
6	0.35	4.2	22.2
9	0.35	8.9	42.6
12	0.35	9.1	52.3
15	0.35	9.7	75.1
18	0.35	10.8	79.5

It can be seen from Table 6 that the available lowest flexural strength in the order of 4.2 MPa, the highest flexural strength is in the order of 10.8 MPa. The available lowest flexural strength is obtained from fly ash geopolymer mortar containing 6% of Na content. The highest flexural strength is obtained from fly ash geopolymer mortar containing 18% Na content. Table 6 also shows that as Na content increases flexural strength increased. The presence of Na content, when compared with 6% Na content, increased the average flexural strength by 112%, 117%, 131% and 157% for 9, 12, 15 and 18% Na content, respectively.

Similarly, for compressive strength, an increase in Na content of geopolymer mixtures causes an increase in compressive strength up to 18% content of Na. The fly ash geopolymer mortar containing 6%, 9%, 12%, 15% and 18% Na concentration were 22.2, 42.6, 52.3, 75.1 and 79.5 MPa compressive strength, respectively. The compressive strength of fly ash geopolymer mortar mixtures increased about 92%, 136%, 238% and 258% at Na content of 9%, 12%, 15% and 18%, respectively.

Finally, when Na content increases from 6% to 18%, strength properties of fly ash geopolymer mortar increases in general. Materials with such a wide compressive strength category can be employed in different areas of use. For example building bricks blocks can be produced using alkali activated fly ash geopolymer mortar and concrete, further more paving stone, kerb stone, tiles or similar materials can be produced using alkali activated fly ash geopolymer binder.

5 CONCLUSIONS

From this laboratory work about geopolymer mortar made with class F fly ash the following conclusions were made.

- Inclusion of Na concentration in fly ash geopolymer mortar reduces flow workability and increases unit weight values.
- This experimental study has shown that it is possible to obtain a very high compressive and flexural tensile strength from fly ash geopolymer mortar mixture, up to 80 MPa and 10 MPa for 24 hours at 100°C curing temperature, respectively.

- As the Na concentration increases in the geopolymer mortar mixture, the compressive and flexural tensile strengths increase up for 24 hours at 100°C curing temperature.
- There seem to be a beneficiary potential of using class F fly ash in the production of geopolymeric concrete or mortar as a construction material.

ACKNOWLEDGEMENTS

The authors would like to thank CNR Mining and Transporting Incorporation for the supply of fly ash for their support. They would also like to thank Erciyes University Scientific Research Unit for providing financial support for this research (FDK-2014-5613).

REFERENCES

[1]. Alaa M. Rashad, Sayieda R. Zeedan, The effect of activator concentration on the residual strength of alkali-activated fly ash pastes subjected to thermal load. Construction and Building Materials 25 (2011) 3098–3107.
[2]. Maria Chiara Bignozzi, Stefania Manzi, Maria Elia Natali, William D.A. Rickard, Arie van Riessen, Room temperature alkali activation of fly ash: The effect of Na_2O/SiO_2 ratio, Construction and Building Materials 69 (2014) 262–270.
[3]. M.A.M. Ariffin, M.A.R. Bhutta, M.W. Hussin, M. Mohd Tahir, Nor Aziah, Sulfuric acid resistance of blended ash geopolymer concrete Construction and Building Materials 43 (2013) 80–86
[4]. Jae Eun Oh, Yubin Jun, Yeonung Jeong, Characterization of geopolymers from compositionally and physically different Class F fly ashes, Cement & Concrete Composites 50 (2014) 16–26.
[5]. M. Komljenovi´c∗, Z. Ba˘s˘carevi´c, V. Bradi´c, Mechanical and microstructural properties of alkali-activated fly ash geopolymers, Journal of Hazardous Materials 181 (2010) 35–42.
[6]. Schmucker M, MacKenzie KJD. Microstructure of sodium polysialate siloxo geopolymer. Ceram Int 2005;31:433–7.
[7]. Görhan Gökhan , Kürklü Gökhan ,The influence of the NaOH solution on the properties of the fly ash-based geopolymer mortar cured at different temperatures, Composites: Part B 58 (2014) 371–377
[8]. Palomo A, Grutzeck MW, Blanco MT. Alkali-activated fly ashes – a cement for the future. Cem Concr Res 1999;29(8):1323–9.
[9]. Van Jaarsveld JGS, Van Deventer JSJ, Lukey GC. The effect of composition and temperature on the properties of fly ash- and kaolinite-based geopolymers. Chem Eng J 2002;89(1–3):63–73.
[10]. Hardjito D, Cheak CC, Ing CHL. Strength and setting times of low calcium fly ash based geopolymer mortar. Mod Appl Sci 2008;2(4):3–11.
[11]. Joseph B, Mathew G, Influence of aggregate content on the behavior of fly ash based geopolymer concrete, ScientiaIranica A (2012) 19 (5), 1188–1194.
[12]. Olivia M, Nikraz H., Properties of fly ash geopolymer concrete designed by Taguchi method, Materials and Design 36 (2012) 191–198.
[13]. Ryu GS, Lee YB, Koh KT, Chung, YS, The mechanical properties of fly ash-based geopolymer concrete with alkaline activators, Construction and Building Materials 47 (2013) 409–418.
[14]. Vora PR , Dave UV, Parametric Studies on Compressive Strength of Geopolymer Concrete, Procedia Engineering 51 (2013) 210 – 219.
[15]. C.D. Atiş, E.B. Görür, O. Karahan, C. Bilim, S. İlkentapar, E. Luga, Very high strength (120 MPa) class F fly ash geopolymer mortar activated at different NaOH amount, heat curing temperature and heat curing duration, Construction and Building Materials, 2015 (96) 673-678.
[16]. ASTM C 618, Standard specification for coal fly ash and raw or calcined natural pozzolan for use as a mineral admixture in concrete. Annual Book of ASTM Standards; 2005.
[17]. TS EN 196-1, Method of testing cement, Part 1.Determination of strength, TSE, Ankara, 2002.
[18]. TS EN 1015-3, Methods of test for mortar for masonry – Part 3: Determination of consistence of fresh mortar (by flow table), TSE, Ankara, 2000.
[19]. TS EN 1015-11, Mortar testing method, Part 11.Measurement of compressive and flexural tensile strength of mortar, TSE, Ankara, 2000.

ICENS
INTERNATIONAL CONFERENCE ON ENGINEERING AND NATURAL SCIENCES
24-28 May 2016 /Sarajevo

Observing the Effect of Source Location and Size on Tsunami Amplitudes for Landslide-Sourced Tsunamis

Servet Mert Kutsal[1], Abdul Hayir[2]

Abstract

In this study, the purpose is to determine the effect of the location of submarine mass movement and size of sources on tsunami amplitudes using simple source model. To observe these parameters, the same-size sources are taken into account in different depths ranging from 0.25 km to 2 km and also different source areas are selected as 10x10 km2, 30x30km2, 50x50 km2 and 100x100 km2 in constant depth. The maximum tsunami amplitudes are discussed with different depths and source areas respectively. In the model, the fluid is assumed as incompressible and the flow is irrotational. Laplace-Fourier transform methods are used for mathematical solutions. Results for tsunami peak amplitudes are presented for selected parameters. The results show that there is an inverse proportion between the amplitude value and the depth of the source. The plots of peak amplitude versus source location show that amplitude values decrease when the water depth increases for all source areas. It can be said that a small area source can generate a large amplitude tsunami if the location of landslide source is close to the free surface of the ocean. According to the results, it is possible to claim that the shallower the water, the higher the amplitudes. The interaction of the tsunami wave forms each other are examined for different parameters and illustrated.

Keywords: *Landslide source area,Laplace-Fourier transform, submarine mass movements, tsunami amplitudes,tsunami source model*

1 INTRODUCTION

Tsunamis are believed to be one of the most natural enemies of the humankid as the damage it gives financial and emotional. The official definiton of tsunami is “a wave train, or series of waves, generated in a body water by an impulsive disturbance that vertically displaces the water column” [1]. It can be generally created by the vertical motion of a fault under the sea bottom during the earthquake, submarine volcanic eruption, atmospheric conditions, submarine slides and slumps [2]. There are many studies about tsunamis modeling either analytically or numerically in the literature [3]. Tsunamis are long period gravity water waves, disperse with velocity $cT = \sqrt{gh}$, where h is the ocean depth and g is the gravitational acceleration. According to the equation, there is a direct proportion between water depth and the velocity of tsunami wave. It can be seen that a tsunami wave behaves fundamentally different in the open ocean and close to the coast. Moreover, the previous studies show that the bigger the source area the higher the amplitude [4,5]. In fact, both location of the source and size of the source area are effective parameters on tsunami amplitudes. As well as, this paper aims to compare effects of location and size of the source area, and give the opportunity to observe how the ocean depth and source area effect the tsunami amplitudes. To contribute the understanding the effective parameters, the basic kinematic model is used for different source-areas and ocean depths. The near field tsunami amplitudes values are discussed with different sizes source area and for different ocean depths respectively.

2 METHOD AND THEORY

To define tsunami wave generation, the basic kinematical model is used. The fluid is assumed as incompressible and the flow is irrotational. The solution in this paper constitues in ‘linearized’ solution, which is known as the ‘shallow water solution’. It works well if the water depth is much smaller than the length of water waves. Inclusion of neglected non-linear terms in the boundary conditions would have permitted a solution involving solitary waves [6]. Laplace-Fourier transform methods are used for mathematical solutions.

2.1 Mathematical Model

That is the motion of a fluid domain, D, bounded above by the free surface of the ocean $z= \eta(x,y;t)$ and below by the rigid ocean floor $z= -h(x,y) + \zeta (x,y;t)$, where $\eta(x,y;t)$ is the free surface elevation, $h(x,y)$ is the water depth and $\zeta (x,y;t)$ is the sea

[1] *Corresponding author: Kocaeli University, Department of Civil Engineering, 41000, İzmit/Kocaeli, Turkey.* servetmertt@gmail.com

[2] *Co-author:Istanbul Technical University, Institute of Earthquake Engineering and Disaster Management,34000,Maslak/Istanbul, Turkey.* ahayir@itu.edu.tr

floor displacement function. For simplicity, h(x,y) is assumed to be a constant. Before the vibration, the fluid is assumed to be at rest, thus the free surface and the solid boundary are defined by z=0 and z=-h, respectively.

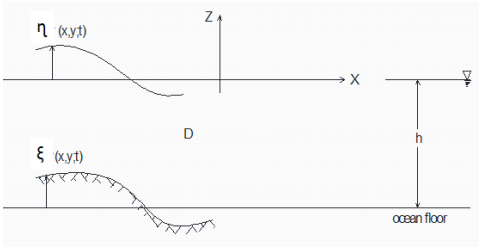

Figure 2. The simple kinematical source model

Actually, it is considered the boundaries of two types: the above-mentioned free surface separating water from the atmosphere, and rigid surfaces including the bottom and surfaces of bodies floating in beneath the free surface.

2.2 Problem Formulations and Equations

If it is assumed that the fluid is incompressible and the flow is irrotational, the motion of fluid layer is such that the fluid velocity potential ϕ(x,y;t) satisfies the Laplace differantial equation [7] , and the potential ϕ(x,y,z;t) must satisfy the following boundary conditions;

$$\nabla^2\phi(x,y,z;t) = 0 \qquad (1)$$

ϕz (x,y,z;t) - ηt (x,y;t) = 0 at z=0 (2a)

ϕt (x,y,z;t) – g η (x,y;t) =0 at z=0 (2b)

ϕz (x,y,z;t) - ξt (x,y;t) = 0 at z=0 (2c)

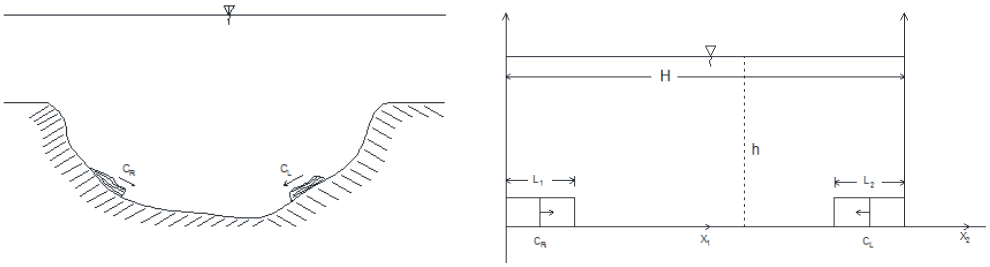

Figure 2. (a) The schematical drawn of original problem *(b) The linearized form of problem*

A linearized shallow water solution (for water depth much smaller than the tsunami wavelength) can be obtained by the Fourier-Laplace transform, defined as;

$$f(k;s) = \int_{-\infty}^{+\infty} e^{-ik2y}\left[\int_{-\infty}^{+\infty} e^{ik1x}\left[\int_0^{\infty} e^{-st} f(x,y;t)dt\right]dx\right]dy \qquad (3)$$

Transformation of the equation of motion and boundary condition, and the assumptions of linearity and shallow-water lead to the following solution for the transform of η , $\bar{\eta}$ (k;s), in terms of the transform of ξ, $\bar{\xi}$ (k;s) [8].

It can be evaluated η(x,y;t) for specified ξ(x,y;t) by computing its transform $\bar{\xi}$ (k;s), substituting it into following equation and inverting $\bar{\eta}$ (k;s) to obtain η(x,y;t),

$$\bar{\eta}(k;s) = \frac{s^2\,\bar{\xi}(k;s)}{s^2+\omega^2}\,\frac{1}{\cosh kh} \qquad (4)$$

Where ω is the circular frequency of the wave motion,

$$\omega^2 = gk\tanh kh$$

To obtain final solution, following steps are calculated in order. Finally, η(x,y;t) is calculated by using inverse FFT method. In this paper, Mathematica programme is used for computing equations. As a result, final equations result as;

$$\xi R = \int_0^{cRt1} e^{ik1x1} \left(\int_{x/cR}^{\infty} \zeta_0 Exp[-st]\, dt \right) dx_1 \quad (5)$$

$$\xi L = \int_{H-cLt2}^{H} e^{ik1x1} \left(\int_{(x-H)/cL}^{\infty} \zeta_1 Exp[-st]\, dt \right) dx_1 \quad (6)$$

ξR represents the uplift of right slide and cR is the velocity of right slide and ξL is for the uplift and cL is velocity of left slide.

3 NUMERICAL RESULTS

To determine the effects of location and source sizes on near field tsunami amplitudes using simple source model, two slides are taken into account in constant depth. The results of scenarious are compared. To observe these parameters, two main scenarious are selected. For the first scenario, sizes of sources are constant under variable ocean depths. L x W = 30 x 30 km^2 (L is length of the source and W is width of source), H=80 km (H is distance between two sources), and ocean depth, h, is variable.

The graph of the peak amplitude $\eta max/\zeta_0$ versus cR/cT is plotted for the ocean depth is ranging from 0.5km to 2km, the results are as follow;

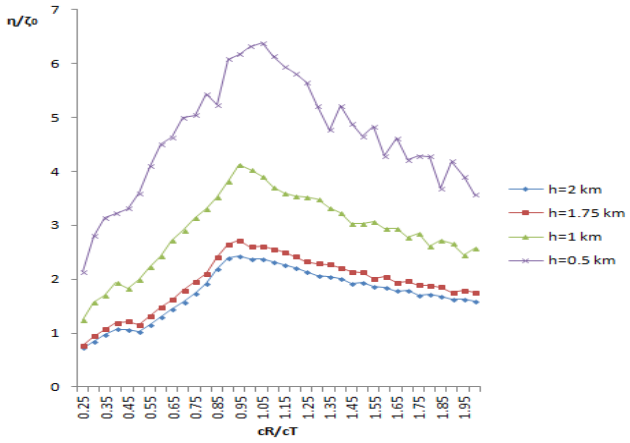

Figure 3. Comparing the peak amplitudes for constant-sized source area and different ocean depths

It is obviously seen from the graphs that the peak amplitudes increases while the ocean depth decreases. The deeper source causes smaller amplitude value. The maximum amplitude values are seen on h=0.5 km, also the shallowest ocean depth.

The other scenario is also for variable-sized source areas under constant ocean depth. To observe the source area effect, distance between slides and ocean depth remain constant. The variable parameter, source sizes, are assumed as LxW = 10x10 km^2, 30x30km^2, 50x50 km^2 and 100x100 km^2 respectively. The obtained graphs are as follow,

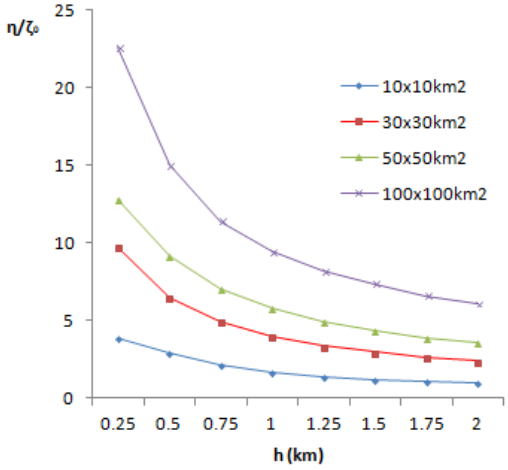

Figure 3. Comparing the peak amplitudes for constant-sized source area and different ocean depths

Each colors in figure belong to four different sizes. It is obviously seen that the amplitude values decrease when the water depth increases for all size of source areas. As gained from the previous result, the amplitude value has a inverse propotion with the water depth. The other important issue is about size of source. When the sizes of sources become bigger, the amplitude values increase. For instance, 100x100 km^2 area has higher amplitude values than 10x10 km^2.

Up to this section, it can be easily said that while tsunami amplitude has an inverse proportion with the ocean depth, it has a direct proportion with the source size. Two main truth are obtained as 'the deeper the ocean, the lower the amplitude' and 'the bigger the source, the higher the amplitude'. Here, an alternative scenario is examined. To compare the differences, two scenarious are combined as the smaller area (30x30 km^2) that is located a shallower depth (h=0.25 km) and a bigger source area (100x100 km^2) located in a deeper side (h=2 km). The 3D forms of tsunami waveforms is shown in Figure 4,

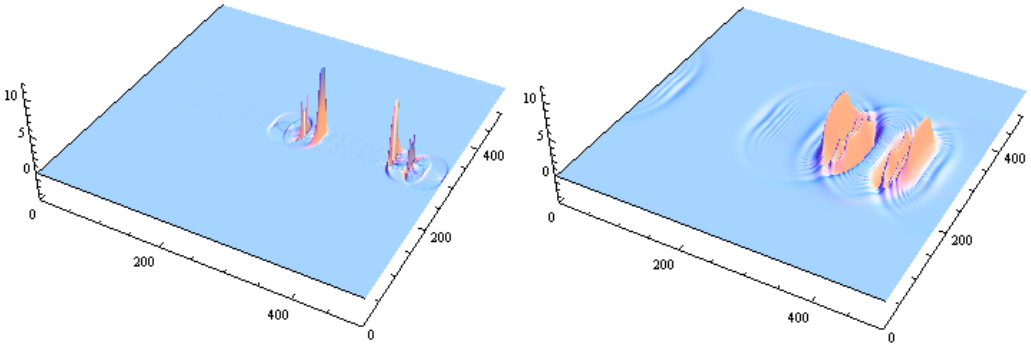

Figure 4. The 3D plots for 30x30 km^2 area in h=0.25 km and 100x100 km^2 area for h=2 km respectively

These figures show that 30x30 km^2 area has higher amplitude than 100x100 km^2 area. Furthermore, to compare the source area size and the location that source occur an other graph is plotted in Figure 5. This figure, 2D and combined form of Figure 4 to see clearly the effect, show that how maximum amplitude values change. As also gained previous outcomes, amplitude values have a peak at cR/cT ~ 1. The essential point is combination of water depth and source size. The bigger source area is assumed as located in h=2 km and the smaller source area is assumed as located in h=0.25 km. Although the 100x100 km2 has higher values than 30x30 km^2 for the same depth, it can be change when the bigger area source proceses in deeper water. As a result from Figure 5, the plot has the peak amplitude at shallower scenario without dealing size of area.

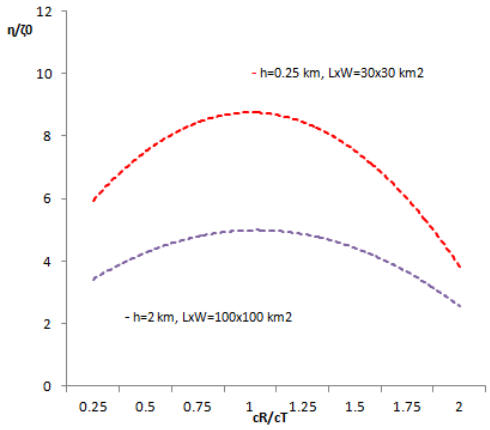

Figure 5. Peak amplitude values versus cR/cT for different depth and different-sized source

4 CONCLUSION

In this paper, the effective parameters on landslide-sourced tsunami amplitudes were investigated. The basic model was taken into account, the selected parameters, size and location of source, were examined on this basic model, and the range of possible tsunami amplitudes was illustrated.

The amplitudes depends on the source sizes of area (LxW). It can be obviously seen that the bigger the slide, the higher the amplitude (e.g. see Figure 3 and Figure 4). This parameter were investigated for different areas, the same result has gained about the size and amplitude relationship. The other scenario shows that tsunami amplitudes are inversely releated to water depth; the shallower the water, the higher the amplitudes. However, another point that attracts the attention is relation between size and water depth. This study emphasizes this combination. The comparison of size and location shows that a small area source can generate a large amplitude tsunami if the water is shallow. The plot of the peak amplitude η/ζR versus cR/cT for both shallower water - smaller area and deeper water - bigger area has a peak at shallower scenario without dealing size of area. The results verify that location of source is more dominant parameter than the size of sources on tsunami amplitude.

REFERENCES

[1]. International Institute for Geo-Information Science and Earth Observation
[2]. Gutenberg, B., *Tsunami and earthquakes*. Bulletein of the Seismological Society of America 29 (4), 517-526,1939
[3]. Trifunac M.D., Hayir A.,Todorovska M.I., *Near-field tsunami wave forms from slumps and submarine slides.* Dept. of Civil Eng. Report No. CE 01-01, Univ. Of Southern California, Los Angeles, California, 2001.
[4]. Hayir, A., *The near-field tsunami amplitudes caused by submarine landslides and slumps spreading in two orthogonal directions.* Ocean Engineering 33 (5–6), 654–664, 2006.
[5]. Mert, S., Hayır, A., *Effects of sunmarine multiple mass movements on near the field tsunami amplitude.* 5th Interational Earthquake Symposium, 2015.
[6]. Hayir, A., *The effects of variable speeds of a submarine block slide on near-field tsunami amplitudes*. Ocean Engineering 30, pp. 2329–2342, 2003.
[7]. Hammack, J., *A note on tsunamis: their generation and propagation in an ocean of uniform depth.* J. Fluid. Mech. 60 (Part 4), 769-799, 1973.
[8]. Todorovska, M.I., Trifunac, M.D., *Generation of Tsunamis by a slowly spreading uplift of the sea floor*. Soil Dynamics and Earthquake Engineering 21, 151-167, 2001.

BIOGRAPHY

Name Surname: Servet MERT KUTSAL

Place and Date of Birth: 12.03.1990/ Gölcük

E-Mail: servetmertt@gmail.com

EDUCATION:

B.Sc.: 2012, Yıldız Technical University, Enviromental Engineering Department

2013, Yıldız Technical University, Civil Engineering Department

M.Sc: 2016, Istanbul Technical University, Institute of Earthquake Engineering and Disaster Management

PROFESSIONAL EXPERIENCE:

2012~2014 : Project Engineer at Derya Engineering Constr. Consult. Industry and Trade Co.

2014: Research Assistant at Kocaeli University

ICENS
INTERNATIONAL CONFERENCE ON ENGINEERING AND NATURAL SCIENCES
24-28 May 2016 /Sarajevo

Prediction of Unconfined Compressive Strength of Weathered Rocks Using P-durability Index and Porosity in Soft Computing Models

Nurcihan Ceryan[1], Samet Berber[2], Sener Ceryan[2]

Abstract

Uniaxial compressive strength (UCS) of intact rocks is an important and pertinent property for characterizing and evaluation of the engineering behaviours of rock mass. Different parameters were used to predict UCS. It is known that the slake durability of a rock is an important property and is closely related to its mineralogical composition. Ultrasonic tests, which are among the most important non-destructive tests. In the early study, considering the advantages of these said indices, P-durability index was defined as the slake durability index multiplied to P-wave velocity in the solid parts of rock materials. Porosity is the index widely used to estimate rock material strength, because it is an important physical property that aids in governing physical attributes of rocks. For this, P-durability index and porosity were used in the soft-computing models for the prediction of UCS of rock materials with different weathering grade from the literature. In this study, the applicability of using P-durability index and porosity for predicting the uniaxial compressive strength were examined. For this, the non-linear multiple regression (NLMR), fuzzy inference system (FIS) and artificial neural network methods (ANN) were used to create the predictive model

Keywords: *Uniaxial compressive strength, P-durability index, porosity, Fuzzy Interface System, Non-Linear Multiple Regression, Artificial Neural Network*

1 INTRODUCTION

Uniaxial compressive strength (UCS) of intact rocks is an important and pertinent property for building stone durability, characterizing rock mass and assessment of engineering behavior of rock mass. This parameter is widely used in rock mechanic engineering. The test requires high-quality core samples with regular geometry. Standard cores cannot always be extracted from weak, highly fractured, thinly bedded, foliated and/or block-in-matrix rocks [1]. In addition, careful execution of this test is difficult, time-consuming, and expensive, as well as involving destructive tests ([1]. To overcome this difficulty, various predictive models based on index tests, including mineralogical-petrographic analyses, physical properties, an elastic wave velocity test and basic mechanical tests have been developed by many researchers [2]. Most investigations involve determining the individual correlation between one index and the UCS, while certain studies have used models that relate the indices simultaneously with the UCS. In addition to these conventional methods, new techniques, soft computing techniques, for estimating the UCS have also garnered considerable attention. Several researchers have recently proposed meaningful relationships using a fuzzy inference system (FIS) to UCS [2]. Many researchers have attempted to estimate the UCS using artificial neural network methods (ANN). This method can be used to solve problems that are not suitable for conventional statistical methods [3].

Considering that the rock materials consist of a solid and porous portion, intrinsic properties that affect the UCS of rock materials can be divided into two groups; one is pore characteristics, and the second is microstructural variables, consisting of the mineralogical composition and rock texture [2]. These cases were considered using soft computing models to estimate the UCS of the volcanic rock materials herein. To represent the mineralogical composition and rock texture, the P-durability index derived from the P-wave velocity in the solid portion of the rock materials, and the slake durability index were suggested by Ceryan [2]. Furthermore, the porosity was used as a characteristic of the porous rock material [2]. In this study, the applicability of using P-durability index and porosity together for predicting the uniaxial compressive strength of the volcanic rock from the literature [4] was examined. For this, the non-linear multiple regression (NLMR), fuzzy inference system (FIS) and artificial neural network methods (ANN) were used to create the predictive model. The performance index (PI) was used to determine the accuracy of the FIS, NLMR, and ANN models developed.

[1] *Corresponding author: Mining and Mineral Extraction Department, Balıkesir University, Balikesir, Turkey , nceryan@balikesir.edu.tr*

[2]*Department of Geological Engineering, Balikesir University, Balikesir, Turkey*

2 METARIAL AND METHODS

2.1 Materials

The porosity (n), P-wave velocity in dried samples (V_p), slake durability index and uniaxial compressive strength of samples were taken from the study performed by Korkmaz and Ceryan [4]. The P-wave velocity in rock samples that lack pores and fissures, V_m, was calculated using Eq. 1 (from [2])

$$\frac{1}{V_p} = \frac{\phi}{V_{fl}} + \frac{1-\phi}{V_m} \qquad (1)$$

Where V_p is the P-wave velocity in the sample, V_{fl} is the velocity in the fluid, ϕ is the ratio of the path length in the fluid to the total path length (i.e., the porosity), and V_m is the P-wave velocity in the rock samples that lack pores and fissures (i.e., the P-wave velocity for the solid portion of the rock. The P-wave velocity in the solid portion of the rock materials given in Eq. 1 and the slake durability index were combined by Ceryan [4] and used to characterize the influence of the microstructural variables on the UCS of rock materials. P-durability index, V_{md} suggested by Ceryan[2] was defined as following equation:

$$V_{md}=V_m x I_d \qquad (2)$$

where V_{md} is P- durability, index V_m is the P-wave velocity in rock samples without pores and fissures (i.e., the P-wave in the solid portion) and the I_d is the slake durability index (%). The index and the strength properties of the samples examined was given at Figure 1.

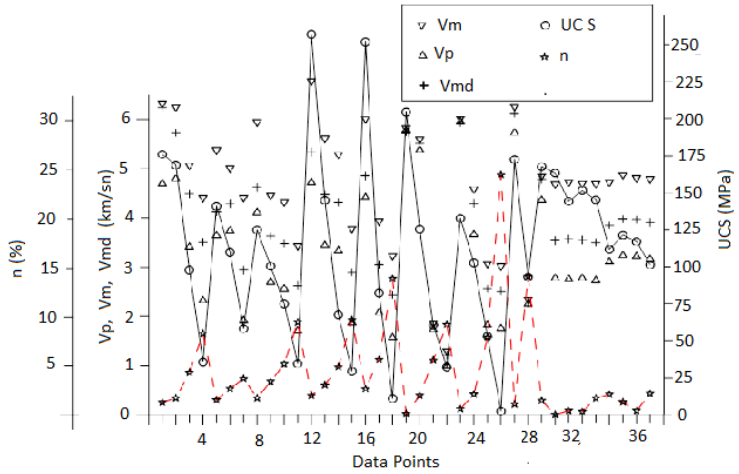

Figure 1.Index and strength properties of the samples examined

The input and output data were normalized to prevent the model from domination by variables with large values, which is common in soft computing models. In this study, the data were normalized using Eq. (3).

$$z_i=x_i/x_{max} \qquad (3)$$

z_i is the scaled value, x_i is the original data, and x_{min} is the minimum of the original data

2.1 Fuzzy Interface System

In classical logic, the membership value of any member is equal to 1 if it is included in the set; if not, that value is equal to 0. On the contrary, the members of a fuzzy set can take the membership values ranging between 0 and 1 in fuzzy logic [5]

$$A = \{x, \mu_A(x)\} \mid x \in X \qquad (3)$$

Here, the fuzzy set "A" is represented by a membership function such as μA(x) in the information universe of X. This membership function μA(x) defines the membership degree of each member in the set. In literature, commonly two different types of fuzzy inference system are used[5]. The Mamdani algorithm to use in a steam machine control is mostly preferred in engineering geology studies ([1],[6]). The notation of the "if-then" rules used in the algorithm is commonly given as follows:

Ri: If xi is Aij and … and xr is Air then y is Bi i=1, 2, …, k (4)

where, k is the number of rules, xi (i=1, 2, …, l) is the input variable, and y is the output variable. Aij and Bij are the linguistic terms and Aij(xj) and Bi are the fuzzy sets defined by the membership functions.. The final output of the Mamdani fuzzy model "B" is also a fuzzy set. There are many defuzzification methods which are briefly defined as the transformation of a fuzzy set into a numerical value (([1],[5],[6.])

In this study, a Mamdani algorithm was also constructed. The parameters of porosity and P-durability index constitute the input variables in the model to define quantitative weathering degree of rock mass. For this purpose, all input and output variables normalized previously, were used. Nine different fuzzy sets such as "UCS1", …,"UCS8" and "UCS9" were constructed for the output variable uniaxial compressive strength of the samples investigated. The output fuzzy set was defined as following; UCS1={0/0,1/0,1/0.1,0/0.2}, UCS2={0/0.1,1/0.2,0/0.3}, UCS3={0/0.2,1/0.3,0/0.4}, UCS4={0/0.3,1/0.4,0/0.5}, UCS5={0/0.4,1/0.5,0/0.6}, UCS6={0/0.5,1/0.6,0/0.7}, UCS7={0/0.6,1/0.7,0/0.8}, UCS8={0/0.7,1/0.8,0/0.9}, and UCS9={0/0.8, 1/0,9, 1/1.0, 0/1.0} (Fig.1). Considering these output fuzzy sets and using the simple regression equations constructed between the input and the output variables previously, Fuzzy sets for the input variable, porosity, were defined as following; ptr1={0/1,1/1,1/0.46577,0/0.29514}, pr2={0/0.46577,1/0.29514,0/0.19533}, pr3={0/0.29514, 1/0.19533,0/0.124516}, pr4={0/0.19533,1/0.124516,0/0.06959}, pr5={0/0.124516,1/0.06959,0/0.024705} pr6={0/0.06959,1/0.024705,0/0.01344}, pr7={0/0.024705,1/0.01344,0/0.006721}, pr8={0/0.01344, 1/0.006721, 0/0.003832} and pr9={0/0.003832,1/0.006721,1/0, 0/1. The fuzzy sets constructed for the input variable "P-durability index" were given as following; Vm1={0/0,1/0,1/0.18561,0/0.412842}, Vm2={0/0.18561, 1/0.412842,0/0.53637},Vm2={0/0.18561,1/0.412842,0/0.53637} Vm3={0/0.412842, 1/0.53637,0/0.624425}, Vm4={0/0.53637,1/0.624425,0/0.69237}, Vm5={0/0.624425,1/0.69237,0/0.748}, Vm6={0/0.69237,1/0.748,0/0.79513,}, Vm7={0/0.748,1/0.79513,0/0.83597}, Vm8={0/0.79513, 1/0.83597, 0/0.87188} and Vm9={/0.83597,1/0.87188,1/1, 1/0} (Fig. 2)

Considering various possible combinations between the input fuzzy sets, total 18 "if-then" rules were constructed considering the data of the sample investigated (Table 1). To determine the resultant membership functions belong to the output parameter UCS, the fuzzy operator "max" was implemented. And, for the defuzzification of these resultant functions, the center of gravity method was used (Fig. 3).

2.2 Non-linear Multiple Regression

The regression analysis is statistical tool that can be applied to examine the relationships between variables [7]. In this technique, the relationship between independent (predictor) variable and dependent (output) variable is systematically determined in the form of a function [7]. By performing linear multiple regression (LMR) technique a linear multiple relationship between input and output parameters can be obtained, while non-linear multiple regression (NLMR) is a technique to achieve a non-linear relationship between these parameters [7]. Non-linear multivariable regression functions are described, and consequently, iterative estimation algorithm is developed to be utilized for the purposes of this study. Different non-linear multiple regression models are developed for estimating the UCS of rock using two input parameters, including porosity (n) and P-durability index (V_{md}). Consequently, the results of developed models were compared to select the most accurate model.

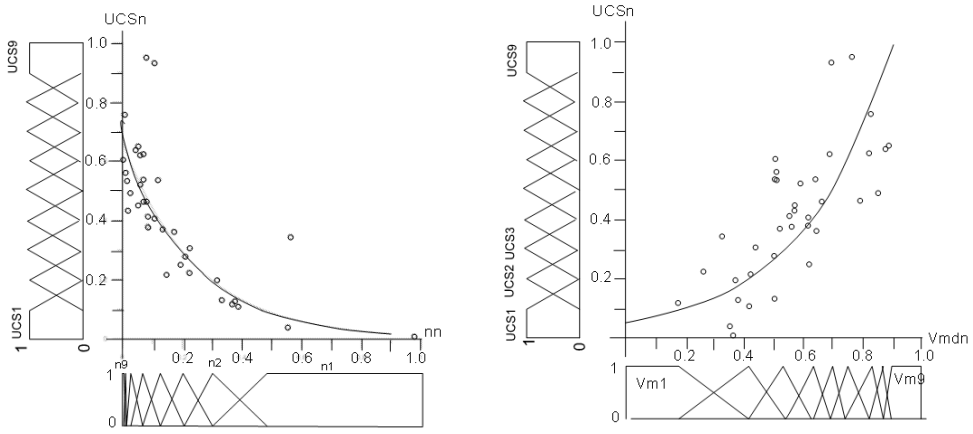

Figure 2. Extraction of input and output fuzzy set for quantitative weathering degree (UCSn; the scaled value of uniaxial compressive strength, prn: the scaled value of porosity, Vmdn: the scaled value P-durability index)

Table 1. if-then rules the fuzzy model to predict quantitative weathering degree

Rules number	*Rules*
1	*If (input1 is pr1) and (input2 is Vmd2) then (output1 is UCS1)*
2	*If (input1 is pr2) and (input2 is Vmd1) then (output1 is UCS1)*
3	*If (input1 is pr2) and (input2 is Vmd2) then (output1 is UCS2)*
4	*If (input1 is pr3) and (input2 is Vmd1) then (output1 is UCS2)*
5	*If (input1 is pr3) and (input2 is Vmd4) then (output1 is UCS3)*
6	*If (input1 is pr4) and (input2 is Vmd3) then (output1 is UCS2)*
7	*If (input1 is pr4) and (input2 is Vmd4) then (output1 is UCS4)*
8	*If (input1 is pr5) and (input2 is Vmd4) then (output1 is UCS5)*
9	*If (input1 is pr5) and (input2 is Vmd3) then (output1 is UCS5)*
10	*If (input1 is pr5) and (input2 is Vmd7) then (output1 is UCS5)*
11	*If (input1 is pr5) and (input2 is Vm6) then (output1 is UCS7)*
12	*If (input1 is pr6) and (input2 is Vmd3) then (output1 is UCS5)*
13	*If (input1 is pr6) and (input2 is Vm4) then (output1 is UCS5)*
14	*If (input1 is pr6) and (input2 is Vmd9) then (output1 is UCS6)*
15	*If (input1 is pr7) and (input2 is Vmd8) then (output1 is UCS5)*
16	*If (input1 is pr8) and (input2 is Vmd3) then (output1 is UCS5)*
17	*If (input1 is pr9) and (input2 is Vmd8) then (output1 is UCS8)*
18	*If (input1 is pr9) and (input2 is Vmd3) then (output1 is mf6)*

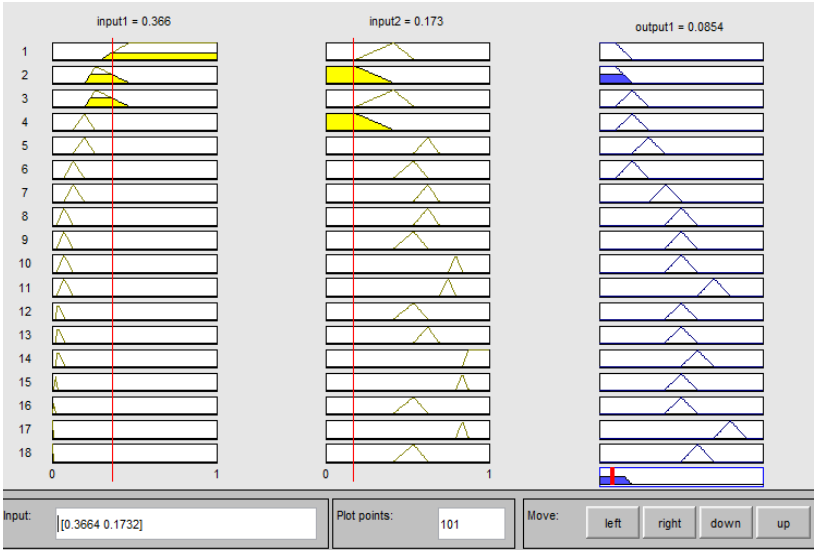

Figure 3. An example calculation of the constructed fuzzy model

Considering performance index, the model giving best performance was obtained as following equation

$$Y=62.5694\ 0.9043^{n}\ V_{md}^{\ 0.65723} \qquad (9)$$

2.3 Artificial Neural Networks (ANN)

Many papers and books provide a detailed description of the ANN (f2]). In this study, a feed forward neural network structure was used, and a brief description of the method is provided herein.

The running procedure typically involves two phases: forward computing and backward computing. In forward computing, each layer uses a weight matrix associated with each connection from the previous layer to the next layer (from [2]). The hidden layer has the weight matrix W_{ij} and the activation function $f^{(1)}$; the output layer has the weight matrix W_{jm} and the activation function $f^{(2)}$. Given the network input vector $x \in R^{nx1}$, the output from the output layer, which is the response (output) of the network $y \in R^{mx1}$, can be written as follows .

$$y_m = f^{(2)}\left\{\sum_{j=1}^{m}\left[f^{(1)}\left(\sum_{i=1}^{n} x_i W_{ij} + b_j\right)\right] W_{jm} + b_m\right\} \qquad (8)$$

The ANN structure was given following figure (Fig. 4). In this study, three widely used transfer functions, namely tangent sigmoid, linear, and log-sigmoid, were evaluated in trial experiments. After the forward computing phase, backward computing, which depends on the algorithms to adjust the weights, was performed. The process of adjusting these weights to minimize the differences between the actual and desired output values is referred to as network training or learning. If the differences (errors)

are greater than the desired values, the errors are passed backwards through the weights in the network. In ANN terminology, this phase is also referred to as the back-propagation algorithm (from [2]).

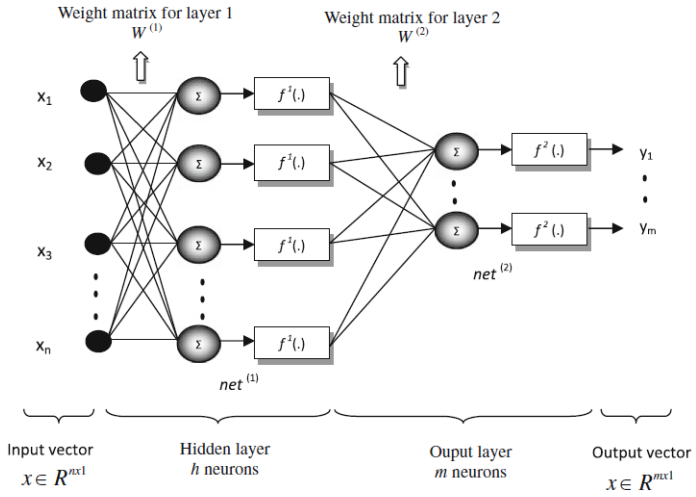

Figure 4. ANN structure ([8])

Depending on the techniques used to train the feed-forward neural network models, different back-propagation algorithms have been developed. In this study, the Levenberg-Marquardt back-propagation algorithm ([2]) was used for training. The Levenberg-Marquardt back-propagation algorithm is a second-order nonlinear optimization technique that is usually faster and more reliable than other back-propagation techniques ([2]). The Levenberg-Marquardt optimization algorithm represents a simplified version of the Newton method and was applied to the training ([2]).

The training process can be perceived as determined a set of weights that minimize the error (ep) for all samples in the training set (T). In the back-propagation phase, the performance index E(W) to be minimized was defined as the sum of the squared errors between the target and network output, namely,

$$\mathrm{E(W)} = e^T e \tag{9}$$

where W consists of all weights in the network, and e is the error vector comprising the errors for all the training examples.

When training with the Levenberg-Marquardt algorithm, the changing weights ΔW can be computed as follows.

$$\Delta \mathrm{W_k} = -\left[J_k^T J_k + \mu_k I\right]^{-1} J_k^T e_k \tag{10}$$

Then, the update of the weights can be adjusted as follows:

$$\mathrm{W_{k+1}} = \mathrm{W_k} + \Delta \mathrm{W_k} \tag{11}$$

where J is the Jacobian matrix, I is the identify matrix, and μ is the Marquardt parameter to be updated using the decay rate β depending on the outcome. In particular, μ is multiplied by the decay rate β ($0<\beta<1$) when E(W) decreases, while μ is divided by β when E(W) increases in a new k.step (from [2]).

3 RESULT AND DISCUSSION

For the ANN application, a three-layered structure was constructed for modeling. The optimal number of neurons in the hidden layer was determined through trial and error by varying the number of neurons from 2 to 10. Various types of activation functions are possible, but the sigmoid function was used for each layer in this study; 15 training epochs were used. The values μ_0 and β used were 0.001 and 0.1, respectively. To justify the FIS, NLMR, and ANN model accuracies, the root mean square error (RMSE), variance account factor (VAF), maximum determination coefficient value (R^2), adjusted determination coefficient (Adj.R^2) and performance index (Eq.12- Eq.14 ([1], [9]) were computed for each model. The performance index (PI) suggested by Yagiz et al. [9] was used examine the accuracy of the said models in this study;

$$PI = R^2 + 0.01VAF - RMSE \quad (12)$$

$$\text{RMSE} = \sqrt{\frac{1}{n}\sum_{t=1}^{n}(d_t - y_t)^2} \quad \text{and} \quad \text{R}^2 = \frac{\sum_{t=1}^{n}(d_t - d_{mean})^2 - \sum_{t=1}^{n}(d_t - y_t)^2}{\sum_{t=1}^{n}(d_t - d_{mean})^2} \quad 13)$$

$$VAF = 1 - (var(d_t - y_t)/var d_t) \quad \text{and} \quad AdjR^2 = 1 - \frac{(n-1)}{(n-p-1)}(1-R^2) \quad (7)$$

where n is the number of training or testing samples, p is the model input quantity, and d_t and y_t are the measured and predicted values, respectively.

In this study, the availability of the P-durability index suggested Ceryan [2] and porosity together to predict UCS was examined. For this the physical properties and P-wave velocity values of the volcanic rock samples were taken from literature, [4]. And the prediction models or UCS were established using FIS, NLRM and ANN methods. In these model, P-durability index suggested and porosity were used as input parameters. For the ANN application, a three-layered structure was constructed for modeling. The optimal number of neurons in the hidden layer was determined through trial and error by varying the number of neurons from 2 to 10. Various types of activation functions are possible, but the sigmoid function was used for each layer in this study; 15 training epochs were used. The values μ0 and β used were 0.001 and 0.1, respectively. The results from this study using ANN and FIS were compared to the NLRM model results (Fig 5).

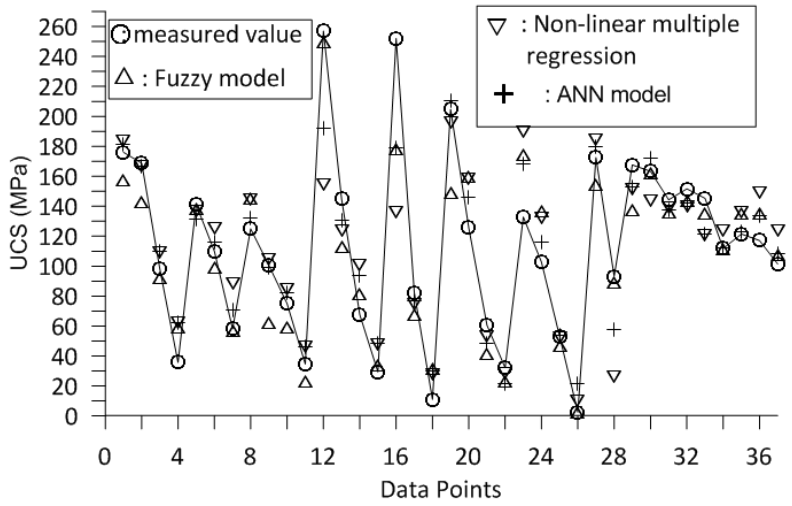

Figure 5. The FIS, NLRM and ANN model performance

The predictions and measured UCS values for the training and testing portions were compared with the desired UCS values using graphical presentations and considering the relationships between the data points and UCS (Fig. 6). In addition, the RMSE, VAF, R^2, Adj.R^2 and PI values obtained for the model suggest in this study were compared (Table 2). The RMSE was calculated from the normalized data.

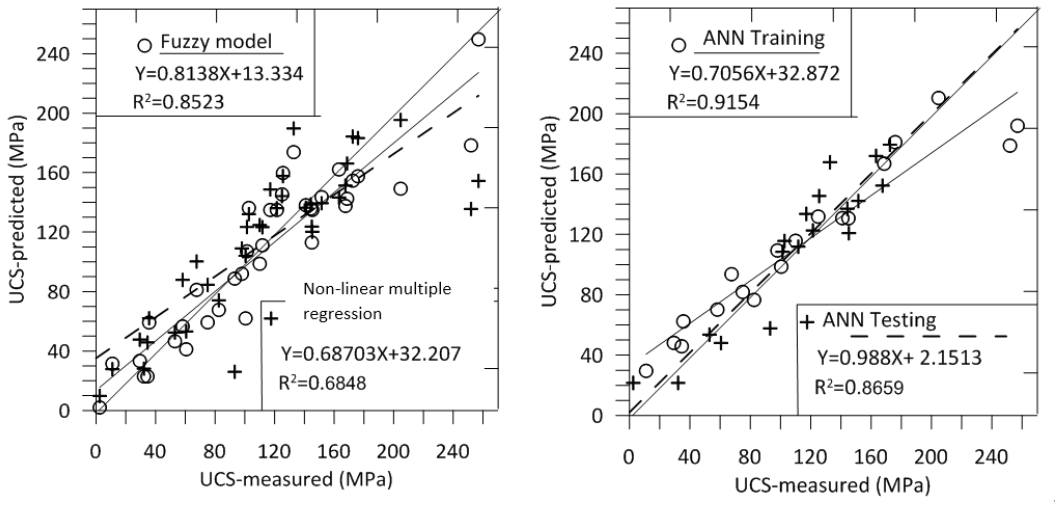

(a) (b)

Figure 6. The cross -correlation graphs of the unia

Maximum and minimum values of UCS measured were 257 and 2.5 MPA while the values obtained from FIS model were and 2.15 and 249.8 MPa, respectively. The said values of the UCS measured using in ANN training period were 11 and 257 MPa while the values in testing period were 2.5 and 172.5 MPa, respectively.

The difference between the training and testing performances of these models is marginal. For performance of these models, the best R^2, Adj.R^2, VAF and RMSE and P, WMAPE and NS values were generated from the ANN model, while the worst statistical values were generated using NLRM (Table 2). Otherwise, the differences between the training and testing performance of ANN model were not significant. The PI values from the training and testing period for the ANN model are 1.720349 and 1.655273, while the PI value is e 1.590704 for FIS model. The values for NLRM modes is 1.22944 (Table 2). It can be said that the FIS and ANN models generally performance well.

Table 2 Prediction performance measures of the models developed

RMSE	R^2	Adj. R^2	Min (MPa)	Max (MPa)	VAF(%)	PI
			Non-Linear Multiple Regression (NLRM)			
0.125031	0.684757	0.666213	9.85890	195.4947	66.97131	1.22944
			Fuzzy Interface System (FIS)			
0.088051	0.852306	0.843619	2.1492	249.75	82.64483	1.590704
			Artificial Neural Network training period			
0.062383	0.915412	0.904838	29.70925231	210.5291	86.732	1.720349
			Artificial Neural Network testing period			
0,095339	0.881721	0.86595	21.69472141	179.571	86.88905	1.655273

4 CONCLUSION

In this study, the availability of the P-durability index suggested Ceryan [2] and porosity together to predict UCS was examined. For this the physical properties and P-wave velocity values of the volcanic rock samples were taken from literature, [4]. And the prediction models or UCS were established using FIS, NLRM and ANN methods. In these model, P-durability index suggested and porosity were used as input parameters.

As a result of this study, it concluded that, P-wave durability index can be used to characterize the influence of the microstructural variables on the UCS of the samples investigated and using a combination of the index and porosity as input parameters can be estimate engineering behaviors of rock materials. In addition, the authors suggest that the proposed ANN and FIS model can be used to predict UCS of rock materials.

REFERENCES

[1]. Gokceoglu C. and Zorlu K. "A fuzzy model to predict the uniaxial compressive strength and the modulus of elasticity of a problematic rock". *Engineering Applications of Artificial Intelligence*, 2004, 17, 61–72

[2]. Ceryan, N. "Application of support vector machines and relevance vector machines in predicting uniaxial compressive strength of volcanic rocks", *Journal of African Earth Sciences* 100, 634–644, 2014

[3]. Aqil, M., Kita, I., Yano, A. and Nishiyama, S."A comparative study of artificial neural networks and neuro-fuzzy in continuous modeling of the daily and hourly behavior of runoff". *Journal of Hydrology*, 2007, 337, 22-34

[4]. Korkmaz, N. and Ceryan, N. "An Example for The Prediction of the Uniaxial Compressive Strength of Weathered Rocks Using The Weathering Indices based on P-Wave Velocity". *11th International Multidisciplinary Scientific Geoonference 20-25 June 2011, SGEM 2011, Bulgaria*, Volume I, 347-354, 2011

[5]. Zadeh, L."Fuzzy sets." *Information and Control"*, 1965, 8, 338–353

[6]. Sonmez, H., Gokceoglu, C., Nefeslioglu, H.A and Kayabasi, A. Estimation of rock modulus: for intact rocks with an artificial neural network and for rock masses with a new empirical equation", *International Journal of Rock Mechanics and Mining Sciences.*2006. 43 (2) ,224–235

[7]. Armaghani, D.J., Amin, M. M., Yagiz, S. Faradonbeh, R.S. and Abdullah, R.A. "Prediction of the uniaxial compressive strength of sandstone using various modeling techniques" *International Journal of Rock Mechanics & Mining Science*s, 2016, 85, 174–186

[8]. Ham, F. and Kostanic, I. *Principles of Neurocomputing for Science and Engineering* 2001, Macgraw-Hill. USA

[9]. Yagiz, S, Sezer E.A, and Gokceoglu ,C. ".Artificial neural networks and nonlinear regression techniques to assess the influence of slake durability cycles on the prediction of uniaxial compressive strength and modulus of elasticity for carbonate rocks". *International Journal for Numerical and Analytical Methods in Geomechanics*. 2012, 36, 1636–1650.

ICENS
INTERNATIONAL CONFERENCE ON ENGINEERING AND NATURAL SCIENCES
24-28 May 2016 /Sarajevo

Investigating the Effects of Obstructive Sleep Apnea on EEG Signals by Using Bispectral Analysis

Necmettin Sezgin[1]

Abstract

This paper describes a new technique to analyze the EEG signal and recognize the EEG signal characteristics of obstructive sleep apnea (OSA) by using bispectral estimation before, during and after an OSA. The polysomnograms of 44 OSA patients were analysed. Identified 9000 OSA signal samples were used for the experiment. Bispectral analysis is an advanced signal processing technique that quantifies quadratic nonlinearities (phase – coupling) among the components of a signal. Results show that after an OSA the delta, theta, alpha, beta and gamma waves of EEG exhibit higher degree of phase coupling phenomena than during and before OSA. The results could be useful in detecting OSA events or OSA related arousals to characterize sleep fragmentation from EEG signals.

Keywords: Bispectral analysis, quadratic phase coupling, EEG signals, obstructive sleep apnea.

1. INTRODUCTION

Humans spend nearly one-third of their lives sleeping. Good sleep is an essential precondition to the maintenance of mental and physical health. As people enter middle age and beyond, the upper respiratory tracts of some individuals shrink, which may lead to obstruction of the nasal passages and snoring during sleep. This apnea may affect the quality of sleep and health when it occurs frequently, and may even cause death in severe cases. Sleep Apnea Syndrome (SAS) is a very common sleep disorder. Breathing often stops for more than ten seconds each instance in a case of SAS, after which the patient must struggle to return to a normal state of breathing. This continues in cyclic fashion. A patient is considered to suffer from SAS if he or she suffers breathing stoppages an average of five times per hour for more than ten seconds each time. However, after a patient awakens because of SAS, the resumption of breathing must occur continuously for more than 3 seconds [1]. SAS is usually diagnosed by analysis of clinical polysomnography (PSG) signals, which measure the chest and abdominal breathing effort, nasal and oral airflow, and blood-oxygen (SpO2) saturation, electroencephalogram (EEG) and by electrocardiogram (ECG).

The EEG signal indicates the electrical activity of the brain. They are highly random in nature and may contain useful information about the brain state. However, it is very difficult to get useful information from these signals directly in the time domain just by observing them. They are basically non-linear and nonstationary in nature. Hence, important features can be extracted for the diagnosis of different diseases using advanced signal processing techniques. EEG signals are quite useful since they give off no radiation, are noninvasive, and are suitable for monitoring over long periods of time. In addition, useful EEG reference values are available for studying SAS. EEG signals are neither stationary nor arbitrarily shifted in frequency range, and can be classified as five types of basis waves, namely as delta (δ), theta (θ), alpha (α), beta (β), and gamma (γ) waves. There is an abrupt frequency shift in the EEG signal when sleep apnea starts and especially ends: Sleep EEG activity shifts from a delta wave to theta and alpha waves in the range of 4~13 Hz. This phenomenon is used as a criterion for identifying SAS [2]. SAS may occur for 10 seconds or more when a patient falls asleep during non-rapid eye movement (NREM) sleep. When breathing becomes normal, brain waves tend to shift to a relatively continuous frequency signal above delta, namely in the theta and alpha wave frequency bands [3,4]. If we compare EEG signals with nasal and oral airflow signals when symptoms of OSA, we see that the nasal and oral airflow signals are clearly reduced, and the EEG signal shifts above the delta frequency band, when an episode of OSA occurs.

Bispectral analysis is an advanced signal processing technique that quantifies quadratic nonlinearities (phase-coupling) among the components of a signal. There are only a few reports concerning the bispectrum of EEG. Barnett et al. [5] first reported the Bispectral analysis of EEG in 1971. Sigl and Chamoun [6] introduced the detailed principle and concept of bispectral analysis in 1994. Ning and Bmnzino [7] have studied the bispectral estimates of hippocampal EEGs under various stages of sleep such **as** quiet waking, rapid eye movement (REM)and slow wave sleep and have reported successin distinguishing betweenthe different vigilant states. Muthuswamy et al. [8] reported the bispectral analysis of burst patterns in EEG. This analytic technique is also known as a core technology of the Bispectral Index System (BIS) monitor (Aspect Medical Systems, Natick, MA). Minfen et al. [9] analysed the parametric **bispectral estimation of EEG signals in different functional states of brain. Hongy et al. [10]**proposed a model of EEG signals according to the parameter model stimulated by nonGaussian white noise

[1]*Corresponding author: Batman University, Department of Electrical and Electronics Engineering, Batman, Turkey.*
necmettinsezgin@gmail.com

to estimate the bispectrum of EEG in order to obtain a sensitive parameter to discriminate the different stages of epilepsy. Wang et al. [11] extracted the features from single sleeping EEG signal of rats using approximate entropy (ApEn) combined with bispectrumanalysis. Ye et al. [12] observed a distribute characteristics on the bispectral coupling of EEG according to depth of anesthesia using bispectrumanalysis method in a type of nonlinear signal processing and Zhang et al. [13] analysed the bispectrum of focal ischemic cerebral EEG signal and indicate that the EEG bispectrum analysis may be useful to distinguish the ischemic region from the normal one and to estimate the ischemic extent. Nonetheless, not much emphasis has been placed on the detection and characterization of nonlinear properties in the EEG signals for OSA patients.

Although bispectral analysis involves complicated mathematics, today's computers are powerful enough for real-time bispectral analysis of EEG data. Bispectral measurements have been carried out for EEG signals monitoring [14]. This paper investigates the presence of nonlinearities in EEG signals before, during and after OSA events by using bispectral analysis.

2. MATERIALS AND METHODS

2.1. Subjects and database preparation

The polysomnograms of 44 OSA patients (mean ±SD) age 35±9 years, body mass index (BMI) 32±6 kg/m^2 were analysed. All subjects were free of any cardiac history. Diagnosis was based on clinical symptoms and polysomnographic (PSG) outcomes. PSG study included EEG (channel C3-A2, sampling frequency=256 Hz), left and right electrooclugram, leg movements, body positions, thoracic and abdominal wall expansion (by respiratory inductive plethysmography), oronasal airflow (by Nasal pressure, Pnasal), arterial oxygen saturation SaO_2 (by pulse oximetry), submental electromyography (EMG) and electrocardiogram (ECG). All of the recordings were performed in accordance with the medical ethical standards [15]. The PSG was scored manually according to standard criteria [16, 17] by two experts with extended experience of interpreting sleep data and rated for OSA. They had identified 9000 OSA signal samples (3000 EEG samples for each of before, during and after OSA) from whole EEG signal data. The duration of each signal sample was 10 seconds (2560 data points) which is the minimum obstruction duration for an OSA.

2.2. Bispectral analysis

Bispectral analysis is a statistical process that measures the degree of phase coupling present in a time domain signal [6, 18]. The Fourier transform of the second-order cumulant, i.e., the autocorrelation function, is the traditional power spectrum. The Fourier transform of third-order cumulant-generating function is called the bispectrum or bispectral density. Applying the convolution theorem allows fast calculation of the bispectrum. They fall in the category of higher-order spectra (HOS), or polyspectra and provide supplementary information to the power spectrum. One of the disadvantages of using power spectrum is that it suppresses phase information in the signal. A third order spectrum or bispectrum preserves phase information.

Bispectral analysis has found success in the area of identifying phase relationship of signals between different frequency bands [19]. In contrast to power spectrum estimation, bispectrum estimation reveals the non-Gaussian and nonlinear information. This allows the detection and characterization of nonlinear mechanisms, the brain activity in this study, which produces time series through phase relations of their harmonic components.

Let x(k) be discrete, stationary, zero-mean random process, and its third-order cumulant sequence $C_{3x}(n_1, n_2)$ will be identical to its third-moment sequence given by [19],

$$\begin{aligned} C_{3x}(n_1,n_2) &= cum\{x(k)x(k+n_1)x(k+n_2)\} \\ &= \langle x(k)x(k+n_1)x(k+n_2)\rangle \\ &\quad -\langle x(k)\rangle\{\langle x(k)x(k+n_1)\rangle+\langle x(k)x(k+n_2)\rangle+\langle x(k+n_1)x(k+n_2)\rangle\} \\ &\quad +2\langle x(k)\rangle^3 \end{aligned} \tag{1}$$

where $\langle . \rangle$ denotes the expectation operation.

Defining the *r*th order moment of function x(k) as,

$$m_{rx}(n_1,n_2,...n_{r-1}) = \langle x(k)x(k+n_1)...x(k+n_{r-1})\rangle \tag{2}$$

Then we can write Equation (1) as,

$$C_{3x}(n_1,n_2) = m_{3x}(n_1,n_2) - \left(m_x(m_{2x}(n_1)+m_{2x}(n_2)+m_{2x}(n_2-n_1)) - 2m_x^3\right) \tag{3}$$

Additionally, the third order cumulant can alternatively be written as,

$$C_{3x}(n_1,n_2) = m_{3x}(n_1,n_2) - m_{3x}^{G}(n_1,n_2) \tag{4}$$

Where $m_{3x}(n_1,n_2)$ is the third order moment function of x(k) and $m_{3x}^{G}(n_1,n_2)$ is the third order moment function of a Gaussian rondom process with the same first and second order characteristics of x(k).

$$m_{3x}^{G}(n_1,n_2) = m_x(m_{2x}(n_1) + m_{2x}(n_2) + m_{2x}(n_2 - n_1)) - 2m_x^3 \tag{5}$$

An important result of Equation (4) is that for a Gaussian process, x(k), the third order cumulant is zero [19, 20].

$$\begin{aligned} &m_{3x}(n_1,n_2) = m_{3x}^{G}(n_1,n_2), \text{ then} \\ &C_{3x}(n_1,n_2) = 0 \end{aligned} \tag{6}$$

In addition, we note that for zero mean process, the third order cumulant and the third order moment operation are equivalent, thus Equation (4) simplifies to,

$$C_{3x}(n_1,n_2) = m_{3x}(n_1,n_2) \tag{7}$$

Wheras the autocorrelation examines the relationship between two points, the third order cumulant examines the relationship between combinations of three points within a time series. The third order cumulant have the following symmetry properties:

$$C_{3x}(n_1,n_2) = C_{3x}(n_2,n_1) = C_{3x}(-n_1,n_2-n_1) = C_{3x}(n_1-n_2,-n_2) \tag{8}$$

Transforming the third-order cumulant into frequency domain yields the bispectrum,

$$B(\omega_1,\omega_2) = \sum_{n_1=-\infty}^{\infty}\sum_{n_2=-\infty}^{\infty} C_{3x}(n_1,n_2)W(n_1,n_2)e^{-j(\omega_1 n_1+\omega_2 n_2)} \quad |\omega_1|,|\omega_2| \le \pi \tag{9}$$

Where $W(n_1, n_2)$represents atwo-dimensional window function which is employed to reduce the variance of the bispectrum estimate. Equation (9) is equivalently expressed as an average over the Fourier transform $X(\omega)$ of x(k),

$$B(\omega_1,\omega_2) = \left\langle X(\omega_1)X(\omega_2)X^{*}(\omega_1+\omega_2)\right\rangle \tag{10}$$

where $B(\omega_1,\omega_2)$ is the bispectrum of x(k). In general $B(\omega_1,\omega_2)$ is complex and a sufficient condition for its existence is that $C_{3x}(n_1,n_2)$ is absolutely summable. Using the properties of $C_{3x}(n_1,n_2)$, the following symmetry properties can be derived for the bispectrum:

$$\begin{aligned} B(\omega_1,\omega_2) &= B(\omega_2,\omega_1) \\ &= B^{*}(-\omega_2,-\omega_1) \\ &= B(-\omega_1-\omega_2,\omega_2) \\ &= B(\omega_1,-\omega_1-\omega_2) \end{aligned} \tag{11}$$

where * denotes complex conjugate. Also $B(\omega_1,\omega_2)$ is periodic in $\omega_1$and$\omega_2$with period 2π. $B(\omega_1,\omega_2)$is a symmetric function, such that a triangular region $0 \le \omega_2 \le \omega_1,\ \omega_1+\omega_2 \le \pi$ could completely describe the whole bispectrum. A peak observed in the triangular region indicates that the energy component at frequency $\omega_1+\omega_2$ is produced, likely due to the quadratic nonlinearity dependence, called quadratic phase coupling (QPC), at the bifrequency (ω_1,ω_2) [21]. On the contrary, a flat bispectrum at the two frequency components ω_1 and ω_2 suggests no such activities. Consequently, phase coupled components contribute extensively to the third-order cumulant sequence of a process. This unique capability of bispectral analysis becomes a useful tool to detect and quantify the possible existence of QPCs in the EEG signals of OSA patient.

The bispectral analysis was performed based on the direct method that uses Fast Fourier Transform algorithm to reduce the computation time for estimating the bispectrum [22].

There is a main frequency component of signal at frequency (f_1, f_2) where $f_1 = f_2$ and there is a phase coupling at frequency (f_1,f_2) where $f_1 \neq f_2$. There are situations in which the interaction between harmonic components causes contribution to the

power at their sum (or difference) frequencies. Such a phenomenon which gives rise to certain phase relations of the same type as the frequency relations is called quadratic phase coupling [19].

To quantify the non-Gaussianity of a random process, the sum of the magnitudes of the estimated bispectrum was adopted as a measure [7], i.e.,

$$D = \sum_{(\omega_1,\omega_2)} |B(\omega_1,\omega_2)|, \quad 0 \le \omega_2 \le \omega_1 \text{ and } \omega_1 + \omega_2 \le \pi \tag{12}$$

While, the frequency range for subband of EEGs are as follows;

Delta(δ) 0.5-4 Hz, i.e., 0.5 Hz < (f_1, f_2) < 4 Hz
Theta(θ) 4-8 Hz, i.e., 4 Hz < (f_1, f_2) < 8 Hz
Alpha(α) 8-13 Hz, i.e., 8 Hz < (f_1, f_2) < 13 Hz
Beta(β) 13-32 Hz, i.e., 13 Hz < (f_1, f_2) < 32 Hz
Gamma(γ) 32-64 Hz, i.e., 32 Hz < (f_1, f_2) < 64 Hz

The quantity of phase coupling for each subband can be calculated using Equation (12) for triangular region $0 \le \omega_2 \le \omega_1$ and $\omega_1 + \omega_2 \le \pi$ since this completely describe the whole bispectrum.A detailed description about the methods and applications of higher order spectral analysis can be obtained from [19].

3. RESULTS AND DISCUSSION

3.1. Bispectral analysis of EEG signals for OSA patients

In Figure 1, Figure 2 and Figure 3 for one patient (45-year-old male), it is shown the EEGs, power spectrum, bispectrum and bispectrum in positive frequency for before, during and after an OSA respectively. The power spectrum and bispectrum in positive frequencies are normalized as having values 0 to 1. For the calculation of bispectrum a Hanning window of 0.05 second width was utilized. From the figures, for the theta and alpha waves, it can be seen that the peak of phase coupling exist more in Figure 2 than in the Figure 1. A high phase coupling after an OSA occured for all waves especially in delta wave. A strong phase coupling present in the signal shows the presence of harmonically related frequency components. Comparing power spectrum to bispectrum in positive frequencies; it can be seen that some peaks present, exist by phase coupling, in the bispectrum while they are not exist in the power spectrum and vice versa. For example, in Figure 1, there is a high peak about frequency f = 19 Hz in bispectrum (Figure 1d) while there is not such peak in the power spectrum (Figure 1b) at this frequency. Furthermore, in Figure 1, there is a peak about frequency f = 26 Hz in the power spektrum (Figure 1b) while there is not such peak in the bispectrum (Figure 1d) at this frequency.

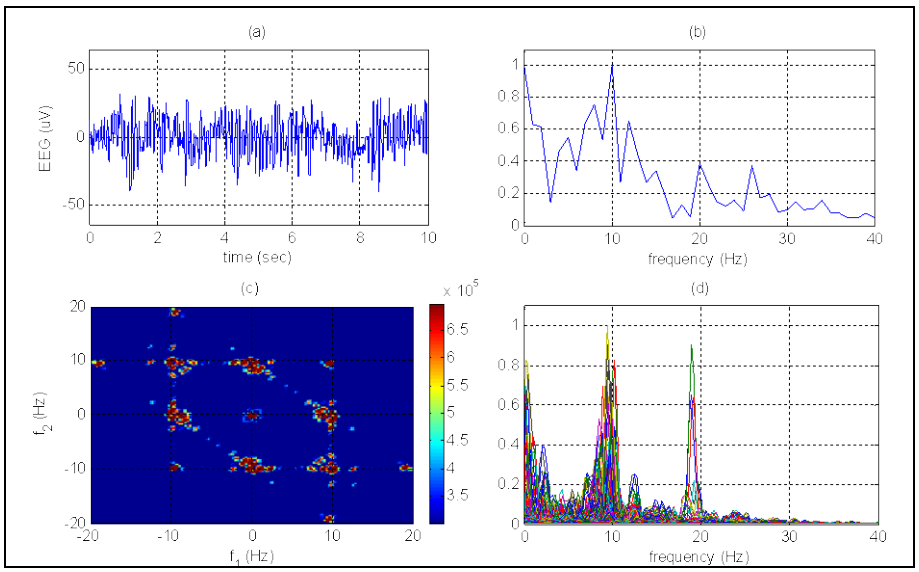

Figure 1. EEG signal before OSA; (a) EEG signal, (b) power spectrum of EEG signal, (c) bispectrum of EEG signal and (d)) bispectrum of EEG signal for positive frequency.

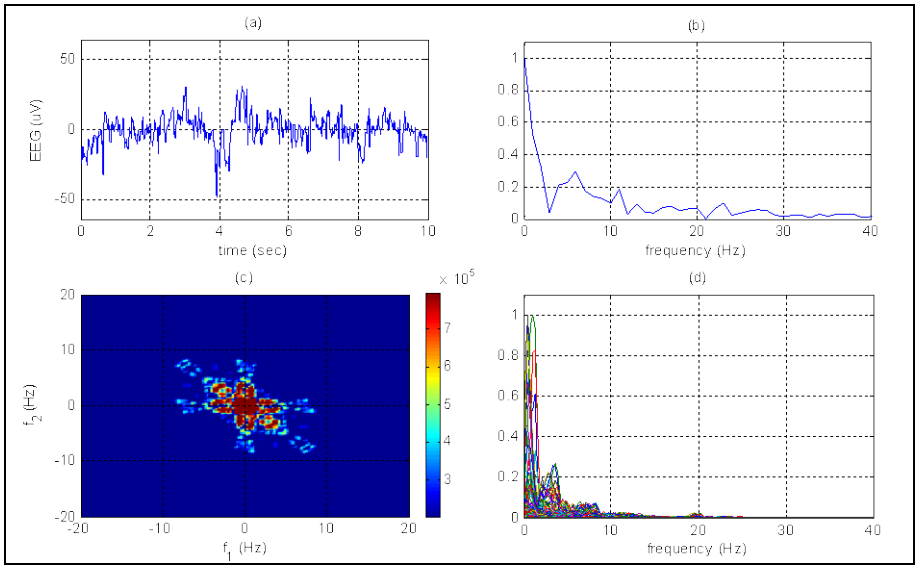

Figure 2. EEG signal during OSA; (a) EEG signal, (b) power spectrum of EEG signal, (c) bispectrum of EEG signal and (d)) bispectrum of EEG signal for positive frequency.

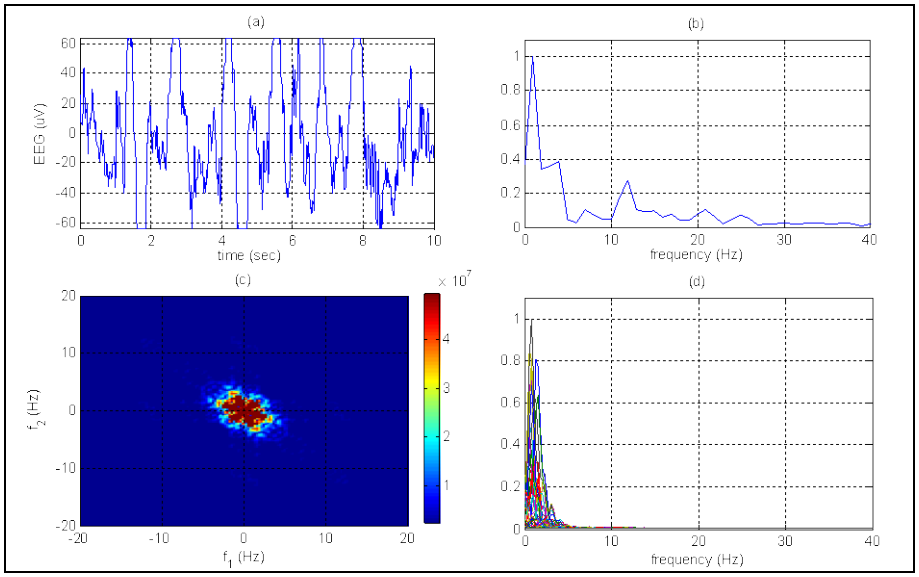

Figure 3. EEG signal after OSA; (a) EEG signal, (b) power spectrum of EEG signal, (c) bispectrum of EEG signal and (d)) bispectrum of EEG signal for positive frequency.

The quantity of phase copling for each event of 9000 was calculated. In Table the mean and standard deviation (SD) results for all 9000 events of 44 patients are shown. From the Table, while the patient enter the OSA the quantity of phase coupling decrease for delta wave while increase for the theta and alpha waves. Because of having arousal just after an OSA, cause a strong phase coupling; the amount of phase coupling for all waves increase especially in delta wave after an OSA event.

Table. The mean and SD value of phase coupling quantity for 5-subband of EEG for 9000 event of 44 patients.

EEG band	Before OSA (mean±SD)	During OSA (mean±SD)	After OSA (mean±SD)
Delta (δ)	255.30 ± 85.10	65.30 ± 22.45	2760.00 ± 451.10
Theta (θ)	4.15 ± 1.25	25.20 ± 9.12	33.55 ± 12.34
Alpha (α)	5.90 ± 2.67	27.15 ± 7.54	24.50 ± 11.00
Beta (β)	9.72 ± 5.15	9.65 ± 4.78	43.10 ± 16.90
Gamma (γ)	0.14 ± 0.03	0.12 ± 0.04	1.50 ± 0.06

4. CONCLUSIONS

An EEG signal just after an OSA have higher bispectral peak amplitude than EEG signal during OSA and before OSA. These findings might imply that EEG signal after OSA have higher degree of phase coupling, due to nonlinearities in the signals, than EEG during OSA and before OSA. Relating this to the pathology of OSA, the EEG signal after OSA has generally more different frequency components (different bands) than the EEG during and before OSA. This means while the patient starts to apnea till end of apnea the nonlinearity in the brain dynamics increase.

There is a high phase coupling present in the peaks, which appear in the bispectrum plot. The magnitude of the bispectrum can be used to estimate the amount of phase coupling present in the sample. A strong phase coupling present in the signal shows the presence of harmonically related frequency components.

Bispectral analysis has not been widely applied to EEG analysis because of being technically more difficult than the conventional power spectral analysis to implement. Also the interpretation of bispectrum is quite difficult. Bispectral analysis extracts more information about a time-varying signal than power spectral analysis, thus offering more potential clinical utility. Acorrelation between inter-frequency phase-coherence of cortical EEG and levels of consciousness may reflect phase coherent synchronization over large spatial regions mediated by deeper brain structures.

In the present study the identification of OSA has been exhibited by using bispectral analysis of EEG signals. The results could be useful in detecting OSA events or OSA related arousals to characterize sleep fragmentation from EEG signals. This study can be improved and an automated system can be designed, and it can be integrated into the present polysomnographs for automatic OSA identification. This can reduce the diagnosis time and improve the medical service efficiency.

REFERENCES

[1] Sugi T, Nakamura M, Shimokawa T, Kawana F. Automatic detection of EEG arousals by use of normalized parameters for different subjects. Biomedical Engineering 2003: 146-147.

[2] Dennis A. Silage: Spectral and coherence analysis applied to sleep apnea. Engineering in Medicine and Biology Magazine 1990; 1 (9): 76-78.

[3] Akin M, Arserim MA, Kiymik MK, Turkoglu İ. A new approach for diagnosing epilepsy by using wavelet transform and neural networks. Proceedingsof the 23rd Annual International Conference of the IEEE; 2001. pp. 25-28.

[4] Fairbanks DNF, Mickelson SA, Woodson BT. Snoring and Obstructive Sleep Apnea. Philadelphia: Lippincott Williams & Wilkins. 2003: 9-15.

[5] Barnett TP, Johnson LC, Naitoh P, Hicks N, Nute C. Bispectrum analysis of electroencephalogram signals during waking and sleeping. Science 1971; 172: 401–2.

[6] Sigl JC, Chamoun NG. An introduction of bispectral analysis for the electroencephalogram.Journal of Clinical Monitoring 1994;10(6): 392-404.

[7] Ning T, Bronzino JD. Bispectral analysis of the rat EEG during various vigilance states. IEEE Trans Biomed Eng 1989; 36: 497–9.

[8] Muthuswamy J, Sherman DL, Thakor NV. Higher-order spectral analysis of burst patterns in EEG. IEEE Trans Biomed Eng 1999; 46: 92–9.

[9] Minfen S, Lisha S, Beadle PJ. Parametric bispectral estimation of EEG signals in different functional states of brain. First International Conference on Advances in Medical Signal and Information Processing; 2000. pp. 66-72.

[10] Hongyi W, Yang X, Yongxiu L, Yansu L, Dezhong Y. Study of epileptic rat's EEG using bispectrum analysis. First International Conference on Neural Interface and Control; 2005. pp. 119-122.

[11] Wang Y, Wang W, Liu Y, Wang D, Liu B, Shi Y, Gao P. Feature Extracting of Weak Signal in Real-Time Sleeping EEG with Approximate Entropy and Bispectrum Analysis. 3rd International Conference on Bioinformatics and Biomedical Engineering; 2009. pp. 1-4.

[12] Ye SY, Jeong DU, Shon JM, Park JD, Choi BC, Jeon GR. Monitoring of the EEG using the bispectrum analysis on the anesthetic depth. 30th Annual Conference of IEEE Industrial Electronics Society; 2004; 3. pp. 3211-3215.

[13] Zhang JW, Zheng CX, Xie A. Bispectrum analysis of focal ischemic cerebral EEG signal using third-order recursion method. IEEE Transactions on Biomedical Engineering 2000; 47(3): 352-359.

[14] Johansen JW, Sebel PS**.** *Development and clinical application of electroencephalographic bispectrum monitoring***.** Anesthesiology 2000; 93: 1336–1344.

[15] Potter VR. Bioethics: Bridge to the Future. Englewood Cliffs, NJ: Prentice-Hall; 1971.

[16] American Academy Of Sleep Medicine (AASM) Task Force. Sleep-related breathing disorders in adults: recommendations for syndrome definition and measurement techniques in clinical research. Sleep; 1999; 22. pp.667–689.

[17] Rechtschaffen A, Kales A. A manual of standardized terminology, techniques and scoring system for sleep stage of human subjects. Washington, D.C.: Public Health Service U. S. Government Printing Office; 1968.

[18] Hinich MJ, Clay CS. The application of the discrete fourier transform in the estimation of power spectra, coherence and bispectra of geophysical data. Reviews of Geophysics 1968;6(3): 347-363.

[19] Nikias CL, Petropulu AP. Higher order spectral analysis: A nonlinear signal processing framework. Engle-wood Cliffs, NJ: Prentice-Hall; 1993.

[20] Nikias CL, Raghuveer MR. Bispectrum Estimation: A digital signal processing framework.Proc. IEEE 1987; 75(7): 867-891.

[21] Raghuveer MR, Nikias CL. Bispectrum estimation: A parametric approach, IEEE Trans. Acoust., Speech, Signal Processing 1985; 33: 1113-1230.

[22] Brillinger DR. An introduction to polyspectra. Ann. Math. Statist 1965; 36: 1351-1374.

ICENS
INTERNATIONAL CONFERENCE ON ENGINEERING AND NATURAL SCIENCES
24-28 May 2016 /Sarajevo

Planning Multiple UAVs to Visit Points of Interest Considering Flight Range and Service Time Constraints

Murat Karakaya[1], Ender Sevinc[2]

Abstract

Unmanned Aerial Vehicles (UAVs) have proved their value in both civilian and military applications in the recent years even though they have their own limitations such as limited flight ranges and high operation costs. In this work, we propose an optimization problem as to minimize the number of used UAVs to service all the given Points of Interest (PoIs) during the agreed service time windows. To solve this optimization problem, we use a greedy approach to reach a reasonable solution in an acceptable time period. The results of extensive simulation tests show the effectiveness of the proposed heuristic for different flight ranges, PoI topologies, and time windows.

Keywords: *Unmanned Aerial Vehicles, Route planning, Genetic Algorithm, Optimization, Simulation*

1. INTRODUCTION

Unmanned Aerial Vehicles (UAVs) have exhibited their value in both civilian and military applications in the recent years even though they have their own limitations such as limited flight ranges and high operation costs. Applications exploit the mobility of UAVs to service many customers located at Points of Interest (PoIs).One of the important Quality of Service requirements of these applications is to visit the determined PoIs during a given service time period. As the number of UAVs owned by the applications is limited due to the expensive price tag on UAVs, in real life applications, we face with an optimization problem.

In this work, we define this optimization problem as to minimize the number of UAVs used to service all the given PoIs during the agreed service time windows (TW). Moreover, we also aim to minimize the total traveled distance by all UAVs. Thus, the main constraints in the problem are UAV flight range (FR) and time windows (TW) of PoIs. We term this problem the Covering All PoI by Multiple UAVs Problem (CAP/MUP).

Since CAP/MUP can be classified as a combinatorial optimization problem, we opt to use a greedy approach to reach a reasonable solution in an acceptable time period. Thus, we design a heuristic solution called Nearest Neighbor for Maximum PoI/ Multiple UAV (NN-MP/MU) based on Nearest Neighbor (NN) heuristic. Searching for the nearest neighbor is an important problem in a variety of applications, including knowledge discovery and data mining, pattern recognition and classification, machine learning, data compression, multimedia databases, document retrieval, and statistics. Though being a deterministic solution, high-dimensional nearest neighbor problems arise naturally when complex objects are represented by vectors of d numeric features [10]. The Nearest Neighborhood (NN) heuristic is known in the literature for its simplicity and effectiveness in searching the given space. Especially for complex problems, the NN heuristic can reach an acceptable result in a reasonable time.

In generic Nearest Neighbor (NN) heuristic, one selects the nearest PoI as the next one unless it cannot return to base due to the diminished flight range (FR). However, in this case, another optimization problem appears which are related with the delays spent among the PoIs. Therefore, we adopted the NN method into the CAP/MUP such that the developed NN-MP/MU heuristic first finds three nearest PoIs and the PoI causing the least delay is picked up within that set. The critical point is that selected PoI might not be the nearest, but the one from the closest three while satisfying all other constraints.

Vehicle Routing Problem with Time Windows (VRPTW) is closely related with the presented work. Both problems consider that the mobile must visit a location during the given time window. There are many solution methods proposed for VRPTW in the literature. These solutions can be classified into two main groups: exact solutions [3, 4, 5, 6, 7] and heuristic-based solutions [8, 9]. Heuristic-based solutions proposed in the literature employ well known meta-heuristics such as Simulated Annealing, Tabu Search, and Genetic algorithms among others.

[1] *Corresponding author: Atılım University, Department of Computer Engineering, 06836, İncek / Ankara, Turkey.* murat.karakaya@atilim.edu.tr

[2] *Mıddle East Technical University, Computer Eng. Dept , Ankara/TURKEY,* ender@ceng.metu.edu.tr

The solutions mentioned above assume that the mobile (vehicle) can wait if it arrives earlier to a given location (depot) compared to the time window and this waiting duration does not have any effects on the traveled distance of the vehicle. This may be an acceptable assumption for the vehicles moving on the ground. However, a flying vehicle (e.g. UAV) has two options for waiting: either UAV can continue fly for passing the time in the air or it can land on, wait, and take off again. Thus, any solution for the UAV routing problem should take into consideration the amount of waiting time due to the limited flight range[2]. In this work, we modify the NN heuristic to generate routes for multiple UAVs considering flight range and waiting times to meet the service time requirement as discussed below.

2. PROPOSED METHOD

The aim of this study is to develop a good adaptation of the NN heuristic for the problem the Covering Maximum PoI by Multiple UAVs Problem (CMP/MUP).

Nearest Neighbor (NN) heuristic is a simple to use, nonetheless effective for specific topology. In generic NN heuristic, one selects the nearest node as the next one. However, in the present study, there is another main constraint which defines when UAV visits each Point of Interest (PoI). As this problem can be classified as a combinatorial optimization problem [6], we use a greedy approach in order to reach a reasonable solution in an acceptable time period.

In generic NN heuristic, route planning begins from the base and continues with the nearest PoI complying with the time window (TW) of the to-be-visited PoI. That is, the NN heuristic eliminates the PoIs whose ready and due times do not fit to the UAV's arrival time to them. As the final step, the NN method selects the nearest PoI to the current one provided that the UAV can have enough remaining flight range (FR) for returning to the base.

We improve the generic NN heuristic noticing that in some cases, the nearest PoI might have a rather late ready time than that of the second or the third closest PoIs. If we select the nearest one as the next PoI, this choice would cause UAV to wait in the air until the ready time expires. Explicitly, doing so decreases the flight range of the UAV without visiting any node. Therefore, we propose to select the next PoI among the three closest PoIs according to their ready time. The one with the earliest ready time is selected as the next PoI. This process increases the flexibility of algorithm for maximizing the path travelled and clearly decreases the possible delay times. We name this improved heuristic as the NN heuristic for Maximum PoI/ Multiple UAV (NN-MP/MU).

In fact, this trade-off between "flight distance" and "waiting in the air" is believed to be a good sample of greedy approach. We may not select the nearest PoI for the sake of having less delay in the air. But we must keep in mind that this selection is limited to the second or the third closest PoI at most. By the help of this 3-closest PoI set, it has been observed in our experiments that UAVs are able to visit more PoI than that of generic NN heuristic.

Figure 1. Generic NN vs. NN-MP/MU Executions

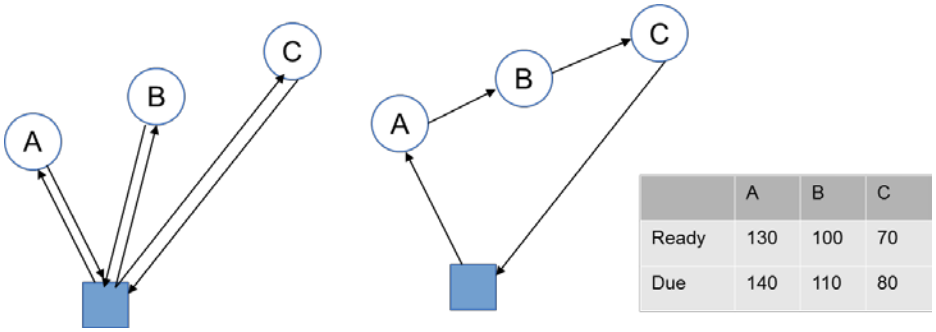

	A	B	C
Ready	130	100	70
Due	140	110	80

If Fig.1 is examined, the strategies of the generic NN and NN-MP/MU are given. Given the ready-due times of the related nodes the generic NN algorithm on the left-hand side, will assign the PoI C since it has the closest ready time. However, after visiting that node it will miss the time windows for PoIs A and B. Because of that reason, other UAVs have to be assigned for the rest. This situation will be the opposite in NN-MP/MU on the right-hang side. In NN-MP/MU, all the PoIs can be visited by only one UAV which puts forward the aim of this study. Though it may result in more travelling distance, fewer UAVs will be assigned and due to the dataset we might have less travelling distances.

3 EXPERIMENT RESULTS

In this section, NN-MP/MU and generic NN solutions are compared using different VRPTW benchmark problem data files [1] along with various UAV flight ranges.

3.1 Simulation Setup and Parameters

All the test results given in the following tables and figures are obtained by taking the mean of the results of 10 independent runs. We have used both R and C data sets described in [1] in order to observe the effect of different typologies and time windows.

In the experiments, R data sets, R101 thru R105, and C data sets, C101 thru C105, are used. The main simulation parameters and their default values are shown in Table 1. All of the PoIs in the datasets, i.e. 100 nodes, have been included.

Table 1. Simulation parameter settings

Parameter	Default Value	Range	Notes
Data Set	R101	R101-R105, C101-C105	10 Different VRPTW benchmark problems
Number of PoIs	101	101	1st PoI is selected as Base, then the rest 100 are assumed to be the PoIs visited

3.2 Results of Experiments

It is declared in [1] that the geographical data are randomly generated in problem sets R, clustered in C datasets. It is known that the geographical data are randomly generated in problem sets R1 and R2, clustered in problem sets C1 and C2.

Table 2. Simulation test results

Data Set	Generic NN		NN-MP/MU	
	# of UAVs	Total Distance travelled	# of UAVs	Total Distance travelled
R101	29	2276,19	16	1902,67
R102	27	2182,38	16	1969,35
R103	20	1690,22	14	1696,85
R104	14	1431,47	12	1761,97
R105	19	1823,34	13	1856,99
C101	46	3579,40	30	3823,09
C102	36	3076,10	26	3207,15
C103	32	2734,65	28	3019,55
C104	30	2759,30	28	3166,37
C105	32	2587,42	23	3475,92

As seen in Table 2, NN-MP/MU uses less number of UAVs compared to the generic NN for all the considered cases in the tests. We compare the improvement of NN-MP/MU over the generic NN as the percentage of used UAV numbers and traveled distance in Table 3. We observe that NN-MP/MU uses considerable less number of UAVs esp. in R datasets. On the other hand, NN-MP/MU uses 40% fewer UAVs than that of NN algorithm considering all datasets.

Table 3. Improvement of NN-MP/MU over the generic NN

Data Set	UAV used	Distance Ratio
R101	81,25%	19,63%
R102	68,75%	10,82%
R103	42,86%	-0,39%
R104	16,67%	-18,76%
R105	46,15%	-1,81%
C101	53,33%	-6,37%
C102	38,46%	-4,09%
C103	14,29%	-9,44%
C104	7,14%	-12,86%
C105	39,13%	-25,56%
Average	**40,80%**	**-4,88%**

For the total distance traveled, in general, NN-MP/MU produce 4.88% less distance. Thus, the NN-MP/MU does decrease the total traveled distance slightly. This could be due to generic NN heuristic's success on clustered topologies. In other words, generic NN heuristic assigns more number of UAVS and they travel among a few of them, even go only for one node in most cases. This results in less travel distance in total. In fact, this also shows that NN-MP/MU might be developed in terms of total travelled distance. This is left as a future work.

As it can be clearly seen in Fig.2, NN-MP/MU has superiority over generic NN algorithm in terms of UAV numbers. Moreover generic NN has drawbacks esp. in R datasets where the PoIs are created and placed due to randomly generated geographical data. The performance results between NN-MP/MU and generic NN are apparent in R datasets especially Even though, we can conclude that with respect to different underlying topologies and various time window settings, NN-MP/MU is robust and successful.

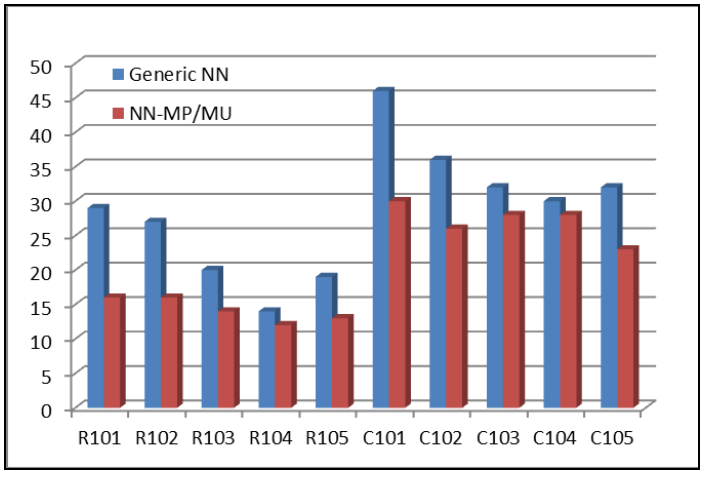

Figure 2. Comparison of number of UAVs used by both solutions for different benchmark data sets

4 CONCLUSION & FUTURE WORK

The aim of this study is to present an optimized NN heuristic which can be applied to especially for large number of nodes. In the results , we observe that the optimized NN heuristic generates UAV paths using considerable fewer number of UAVs compared to generic NN. However, total travel distance seems to be slightly lower on the average. Therefore, as a future work, we would like to develop a sophisticated algorithm in order to minimize the total travel distance as well.

REFERENCES

[1]. *VRPTW benchmark problems, 2005, [WWW document; retrieved January 2016] URL http://w.cba.neu.edu/~msolomon/problems.htm*
[2]. Olli Bräysy and Michel Gendreau, "Vehicle Routing Problem with Time Windows, Part I: Route Construction and Local Search Algorithms.", Transportation science, vol. 39, no. 1, pp. 104-118, 2005.
[3]. Desrochers, M., J. Desrosiers, M. M. Solomon. 1992. A new optimization algorithm for the vehicle routing problem with time windows. Oper. Res. 40 342–354.
[4]. Irnich, S., D. Villeneuve. 2006. The shortest path problem with resource constraints and k-cycle elimination for k ≥ 3. INFORMS J. Comput. 18(3) 391–406.
[5]. Jepsen, M., B. Petersen, S. Spoorendonk, D. Pisinger. 2006. A nonrobust branch-and-cut-and-price algorithm for the vehicle routing problem with time windows. Oper. Res. Forthcoming.
[6]. Guy Desaulniers, François Lessard, Ahmed Hadjar, "Tabu Search, Partial Elementarity, and Generalized k-Path Inequalities for the Vehicle Routing Problem with Time Windows", Transportation Science, Vol. 42, No. 3, August 2008, pp. 387–404
[7]. Kallehauge, B., N. Boland, O. B. G. Madsen. 2007. Path inequalities for the vehicle routing problem with time windows. Networks 49 273–293.
[8]. Cordeau, J-F.; Laporte, G.; Mercier, A., "A unified tabu search heuristic for vehicle routing problems with time windows", Journal of the Operational Research Society, Volume 52, Number 8, 1 August 2001, pp. 928-936(9)
[9]. G.B. Alvarenga, G.R. Mateus, G. de Tomic, A genetic and set partitioning two-phase approach for the vehicle routing problem with time windows, Computers & Operations Research 34 (2007) 1561–1584.
[10]. S. Cost, S.Salzberg, "A Weighted Nearest Neighbor Algorithm for Learning with Symbolic Features", Machine Learning, 10, 57-78 (1993), 1993 Kluwer Academic Publishers, Boston. Manufactured in The Netherlands.
[11]. S.Arya, D.M.Mount, N.S. Netanyahu, R. Silverman, "An Optimal Algorithm for Approximate Nearest Neighbor Searching in Fixed Dimensions", Journal of the ACM, Vol. 45, No. 6, November 1998, pp. 891–923.

ICENS
INTERNATIONAL CONFERENCE ON ENGINEERING AND NATURAL SCIENCES
24-28 May 2016 /Sarajevo

Thermodynamic and Thermoeconomic Analysis of Split Type Air Conditioners Combined with Boiler

Engin Gedik[1*], Bahadir Acar,[1] Metin Kaya[1], Kenan Sarimese[2]

Abstract

Today, cooling systems have been used in so many places. The cooling systems consume high amount of energy. Due to the fact that split type air conditioners are the mostly used devices in all around the world, the energy efficiency of these devices has gained extreme importance. In the present study, it is aimed to investigate system performance of the split type air conditioner (SAC) combined with boiler in point view of energy, exergy and thermoeconomic aspect. For this purpose an experimental test rig designed and built. A constant hot water has been obtained by using a boiler before the condenser unit of the wall type split air conditioner. A series of experimental studies were conducted and obtained data were used to calculate the exergy efficiency, energy consumption and system performance. As a result of the analysis, the cooling performance was computed as 19.6% and 26.2% for the air conditioner without and with boiler respectively. The energy consumption was decreased with the increase of efficiency as expected. When it is compared with and without boiler from the economical point of view the device was consumed 0.0395 EUR/h and 0.0465 EUR/h respectively.

Keywords: Split type air conditioner; boiler; energy-exergy; thermoeconomic

1. INTRODUCTION

Because the modern civilization is intensively based on energy and machinery, energy consumption is accepted as an indicator of development for a country. On the other hand, since the energy resources currently in use are not unlimited, increasing demand of energy and depleting resources of especially fossil fuels have made it necessary to attempt for developing more energy-efficient devices and machinery as well as modifying the currently operating systems to make them more efficient if possible. Energy-efficient refrigeration is of great importance for many industrial sectors and engineering applications which can greatly lower the production or storage costs. [1] On the other hand important point is that consumers require more-efficient and well-designed products for improving their quality of life. As with other household appliances, the demand for high performance split air conditioners (SACs) has increased rapidly. Indoor and outdoor SAC units need to be coherent; however, indoor units require more attention because of the necessity for high performance on a small scale [2]. Fin and tube heat exchanger (FTHE) and cross-flow fan (CFF) are play an important role to increase the efficiency of SACs. A number of experimental and numerical studies focused on the FTHEs and CFF inside air conditioner systems. Performance test of heat exchangers were examined in a wind tunnel by Tuztas and Egrican [3]. Shih et al. [4] numerically studied for 2D geometry of a CFF in a conventional SAC indoor unit.

Energy efficiency of condenser unit of the SAC which was covering with evaporative cooling pads having various thickness was investigated by Martinez et.al [5]. Experimental and numerical analysis were performed by Sumeru [6] et.al. with using ejector as a sudden expansion component in a split type air conditioner.

While in the domestic and commercial air conditioning application, how to reducing the refrigerant charge is still the main problem for the safety use of hydrocarbons [7]. Padalkar et al. [8] has investigated the performance of split type air conditioner for the working fluids HCFC-22 and HC-290. Kumlutaş et al. [2] has introduced a three-dimensional representative thin-section model for modelling SAC indoor units, and also heat transfer and fluid flow analysis was performed to determine the characteristics of the device in their study. They concluded that the difference between the numerical and experimental studies were within acceptable limits and also numerical tool is the way to determine the performance of SAC.

In the present study a novel Split type air conditioner was proposed and investigated experimentally in domestic air conditioner system. The main objective of this paper is to investigate the performance of novel air conditioner integrated water heater (boiler) technology in the application of buildings. For this purpose an experimental test rig was designed and built. Numerous experimental test were conducted on the manufactured experimental apparatus. Thermodynamic and thermoeconomic analysis were made. Obtained data from experimental study were presented tabular and graphical form and discussed in detail.

[1] *Corresponding author: Karabuk University, Faculty of Technology, Department of Energy Systems Engineering, 78050, Karabuk, Turkey. egedik@karabuk.edu.tr , bacar@karabuk.edu.tr, mkaya@karabuk.edu.tr*

2 *Karabuk University, Graduate School of Natural and Applied Sciences, 78050, Karabuk, Turkey, ksarimese@gmail.com*

2. MATERIALS AND METHOD

2.1 Experimental study

In this paper, thermal performance of a split type air conditioner combined with boiler has been examined experimentally. A schematic diagram of the tested air conditioner system in this study, shown in Figure 1. The apparatus consists of the basic components of the refrigeration cycle as compressor, condenser, evaporator, expansion valve, four-way valve. In addition that boiler is combined with the conventional split air conditioner which novelty of the present study.

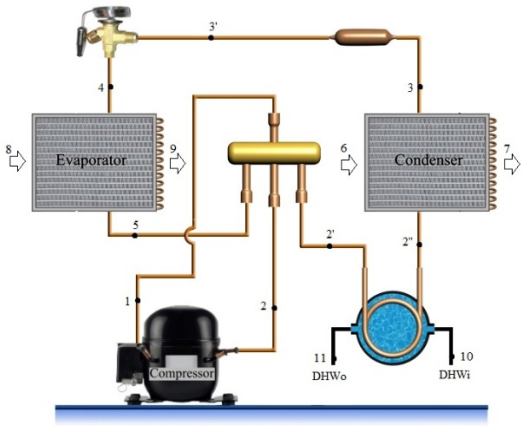

(a) Schematic view

(b) Experiments

c) Outdoor unit, valve and boiler

Figure 1. Schematic diagram and experimental test rig.

Manufactured device works with the basic vapour compression refrigeration cycle. In common use, an air conditioner is a device that lowers the air temperature. The cooling is typically achieved through a refrigeration cycle, but sometimes evaporation or free cooling is used. To work the produced device by-pass valve on the outdoor unit must be opened and boiler return valve must be closed. In the operation condition with boiler, extracted heat from the outdoor condenser to the ambient is directed to boiler, so that the heat extracted to water placed in boiler instead of outdoor environment. By this way a great amount of energy saving is obtained and also coefficient of efficiency of the system is increased. Initially, the device was worked with cooling mode and then it was worked with heating mode. In the experiments pressure and temperatures values were measured and recorded to a personnel computer. Obtained data experiments for the SAC with and without boiler were summarized in Table.1 and Table 2 respectively.

2.2 Exergy Analysis of System

When a substance is under heating T and pressure P, having special entropy s and special enthalpy h, reduced to T_0 environmental temperature, special exergy owned or availability, it can be calculated as follows;

$$E_x = (h - h_0) - T_0(s - s_0) \quad (1)$$

By calculating the exergy values of inlet and outlet points for every device shown in the Fig. 1, the difference between exergy inlet and outlet, and exergy destruction can be calculated as follows:

$$ED = (\sum Ex_{inlet} - \sum Ex_{outlet}) \quad (2)$$

Exergetic efficiency, an indicator of irreversibility (second law efficiency), is required [11]. Second law efficiency is as general;

$$\eta_{II} = \frac{\text{Useful work output}}{\text{Maximum possible (reversible) work output}} \quad (3)$$

Eq. 3 is expressed as follows for exergy at inlet and outlet of all device

$$\eta_{II} = \frac{Ex_o}{Ex_i} \tag{4}$$

Exergy destructions and efficiencies in evaporator, compressor, condenser, expansion valve and boiler unit in split air conditioner can be calculated following equations;

Exergy destruction in compressor;

$$\dot{ED}_{comp} = \dot{E}_{X2'} - \dot{E}_{X1} + \dot{W}_{comp,el} \tag{5}$$

$$\dot{W}_{comp,el} = \frac{W_{comp}}{\eta_{el} * \eta_{mec}} \tag{6}$$

Exergy destruction in condenser;

$$\dot{ED}_{con} = \left(\dot{E}_{X2} - \dot{E}_{X6} \right) - \left(\dot{E}_{X3} - \dot{E}_{X7} \right) \tag{7}$$

Exergy destruction in expension valve;

$$\dot{ED}_{ev} = \dot{E}_{X4'} - \dot{E}_{X3} \tag{8}$$

Exergy destruction in evaporator;

$$\dot{ED}_{evap} = \left(\dot{E}_{X4} + \dot{E}_{X8} \right) - \left(\dot{E}_{X5} + \dot{E}_{X9} \right) \tag{9}$$

Exergy destruction in boiler;

$$\dot{ED}_{boiler} = \left(\dot{E}_{X2} + \dot{E}_{X9} \right) - \left(\dot{E}_{X3} + \dot{E}_{X10} \right) \tag{10}$$

Exergy efficiency is also calculated by the following Equation

Exergy efficiency of compressor;

$$\eta_{Ex,comp} = \frac{Ex_2 - Ex_1}{W_{comp,el}} \tag{11}$$

Exergy efficiency of condenser;

$$\eta_{Ex,cond} = \frac{Ex_3 + Ex_7}{Ex_2 + Ex_6} \tag{12}$$

Exergy efficiency of expansion Valve;

$$\eta_{Ex,\exp} = \frac{Ex_3}{Ex_4} \tag{13}$$

Exergy efficiency of evaporator;

$$\dot{\eta}_{ex,cond} = \frac{Ex_5 + Ex_9}{Ex_4 + Ex_8} \tag{14}$$

Exergy efficiency of boiler;

$$\dot{\eta}_{ex,boiler} = \frac{Ex_3 + Ex_{10}}{Ex_2 + Ex_9} \tag{15}$$

Exergetic efficiency of system can be calculated as follows ;

$$\eta_{ex,system} = \frac{ED_{evap}}{W_{comp,el}} \quad (16)$$

2.3 Thermoeconomic Analysis

Thermoeconomic analysis is the process that make the analysis thermal sytsyems with respect to termodynamic and economic point of view. It is used in order to minimize production costs. Total cost has two component as investment and operating cost as given;

$$C_T = C_{inv} + C_{op} \quad (17)$$

Total invesment cost is need to convert annual capital cost to calculate the unit cost of cooling. In the present study fixed annual capital cost method was used.

$$C_{inv} = \frac{CRF \times C}{Q_c \times 2280} \quad (18)$$

Where C is the installation costs, Qc cooling power and CRF is the capital payback factor. CRF is calculated with the following equation:

$$CRF = \frac{i \times (1+i)^n}{(1+i)^n - 1} \quad (19)$$

Where, i and n defined as the annual rate and the operating time of the system (annual) respectively. In this sytem annual rate and operating time is considered as 10% and 10 years respectively.

Cost of the electrical energy is the consumed electrical energy price per cooling power and it is callculated as:

$$C_{op} = \frac{C_{el} \times P_{inp}}{Q_c} = \frac{C_{el}}{COP} \quad (20)$$

Where C_{el} is electrical price, P_{inp} is consumed power, Q_c is cooling power and COP is coefficient of performance. Consumed power is calculated as:

$$P = U \times I \quad (21)$$

Where U is voltage and I is defined as current. These values were measured with boiler and without boiler situation and measured data were used to calculate thermoeconomic analysis.

3 RESULTS AND DISCUSSION

In the present work, SAC combined with and without boiler were performed for thermodynamic and thermoeconomic analysis. Results obtained from experimental works are transferred to tabular forms as change in inlet and outlet temperatures of the components, inlet and outlet pressure changes of the components, entalphy and entropy values and calculated exergy values as can be seen from Table.1 and Table 2. Table.1 summarize the exergy values of the conventional SAC without boiler.

Table.1 Basic thermodynamic properties of the measured points and exergy values for the SAC without boiler

Conventional SAC (without boiler)								
Point	**Equipment**	**Fluid**	**T**	**P**	**m**	**h**	**s**	**Ex**
1	Compressor inlet	R22	14	4,8	0,03171	415,777	1,792	1,37906
2	Compressor outlet	R22	98	22	0,03171	459,992	1,798	2,72439
2'	Condenser inlet	R22	95	22	0,03171	457,26	1,791	2,70394
3	Condenser outlet	R22	43	21	0,03171	253,682	1,178	2,04399
3'	Expansion valve inlet	R22	43	21	0,03171	253,682	1,178	2,04399
4	Expansion valve outlet	R22	6	4,5	0,03171	253,682	0,803	5,58936
4'	Evaporator inlet	R22	6	4,5	0,03171	207,092	1,0253	2,0103
5	Evaporator outlet	R22	12	4,5	0,03171	414,913	1,794	1,33275
6	Condenser inlet	Air	35	1	0,76	308,23	1,727	0
7	Condenser outlet	Air	45	1	0,76	318,282	1,7606	0,47825
8	Evaporator inlet	Air	22	1	0,2486	295,17	1,685	0,01427
9	Evaporator outlet	Air	8	1	0,2486	281,2823	1,6369	0,12697

Table.2 Basic thermodynamic properties of the measured points and exergy values for the SAC combined with boiler

SAC combined with Boiler								
Point	**Equipment**	**Fluid**	**T**	**P**	**m**	**h**	**s**	**Ex**
1	Compressor inlet	R22	12	4,5	0,03878	414,913	1,794	1,62977
2	Compressor outlet	R22	90	22	0,03878	452,289	1,778	3,26407
2'	Boiler inlet	R22	90	22	0,03878	452,289	1,778	3,26407
2"	Boiler outlet	R22	43	21	0,03878	405,618	1,643	3,0151
2"	Condenser inlet	R22	43	21	0,03878	405,618	1,643	3,0151
3	Condenser outlet	R22	35	19	0,03878	243,101	1,145	2,47074
3'	Expansion valve inlet	R22	35	19	0,03878	243,101	1,145	2,47074
4	Expansion valve outlet	R22	4	6	0,03878	243,101	1,153	2,37824
4	Evaporator inlet	R22	4	6	0,03878	243,101	1,153	2,37824
5	Evaporator outlet	R22	8	4	0,03878	413,048	1,798	1,51121
6	Condenser inlet	Air	35	1	0,76	308,23	1,727	0
7	Condenser outlet	Air	45	1	0,76	318,282	1,7606	0,47825
8	Evaporator inlet	Air	22	1	0,2486	295,17	1,685	0,01427
9	Evaporator outlet	Air	8	1	0,2486	281,2823	1,6369	0,12697
10	Boiler inlet	Water	10	5	0,33	42,508	0,15104	0,68181
11	Boiler outlet	Water	40	5	0,33	167,97	0,57221	0,64557

Exergy destruction of basic components of the split air conditioner with and without boiler is shown in Figure.2. As can be seen from the figure exergy destruction of the components for the with boiler case much higher than without boiler case. Maximum exergy destruction value was found in compressor equipment as 4.5 for the with boiler case while minimum exergy destruction value was found as 0.06 in condenser of the SAC.

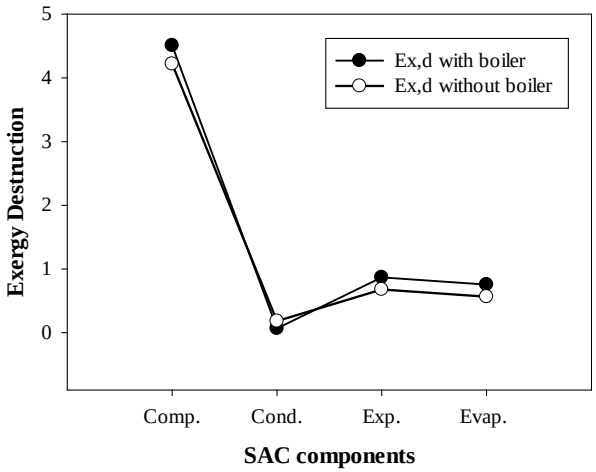

Figure 2. *Exergy destruction of basic components of split air conditioner.*

In figure 3 variations efficiency values versus basic components of the SAC are shown. As can be clearly seen from the figure all equipment's' efficiency of the SAC with boiler case are much higher than SAC without boiler case. Maximum efficiency value was computed as 0.97 and 0.93 for the condenser equipment in the case with boiler and without boiler respectively.

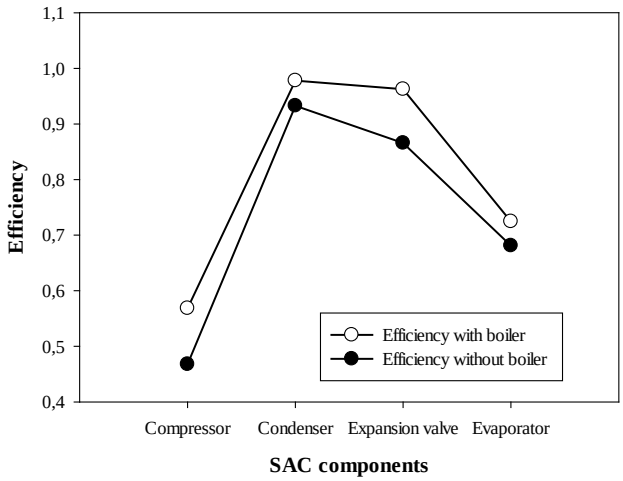

Figure 3. *Efficiency of basic components of split air conditioner*

In addition that according to calculated values from the Equation 16 the overall efficiency of the system was found 19.6% and 26.2% for the case without boiler and with boiler. From thermoeconomic point of view when it is compared with and without boiler the system was consumed 0.0395 EUR/h and 0.0465 EUR/h respectively.

4 CONCLUSION

Results of the experimental study of a split type air conditioner equipped with boiler show an improvement in system performance and reduction in energy consumption. A significant improvement in the air conditioner performance is observed for SAC with combined boiler compared to a conventional split type air conditioner system. Based on the results obtained, the following conclusions can be made:

- The cooling performance was computed as 19.6% and 26.2% for the air conditioner without and with boiler respectively.
- The energy consumption was decreased with the increase of efficiency
- When it is compared with and without boiler from the economical point of view the device was consumed 0.0395 EUR/h and 0.0465 EUR/h respectively.

ACKNOWLEDGMENT

The authors would like to thank the Karabük University Scientific Research Projects Unit, Karabük/TURKEY for providing the financial supports for this study under the KBÜ-BAP-16/1-YD-027 project.

REFERENCES

[1]. E. Gedik, E. Kılıçaslan, B.Acar, A.Ergün and E.Özbaş, "Experimental Investigation of a Household Refrigerator Performance Using Chimney-Type Condenser", Arab J Sci Eng (2016) 41:1691–1697.
[2]. D. Kumlutas¸ Z. H. Karadeniz and F. Kuru, "Investigation of flow and heat transfer for a split air conditioner indoor unit", *Applied Thermal Engineering*, vol. 51 pp. 262-272, 2013.
[3]. M. Tuztas, A.N. Egrican, Mathematical model of finned tube heat exchangers for thermal simulation software of air conditioner, Int. J. Heat Mass Transf. 29 (4) (2002) 547-556.
[4]. Y.C. Shih, H.C. Hou, H. Chiang, On smilitude of the cross flow fan in a split-type air-conditioner, Appl. Therm. Eng. 28 (2008) 1853-1864.
[5]. P. Martínez, J. Ruiz, C.G. Cutillas, P.J. Martínez, A.S. Kaiser and M. Lucas, "Experimental study on energy performance of a split air-conditioner by using variable thickness evaporative cooling pads coupled to the condenser", *Applied Thermal Engineering*, In press (doi: 10.1016/j.applthermaleng.2016.01.06.) 2016.
[6]. K. Sumeru, S. Sulaimon, H. Nasution and F. N. Ani, "Numerical and experimental study of an ejector as an expansion device in split-type air conditioner for energy savings", *Energy and Buildings*, vol. 79, pp. 98–105. 2014.
[7]. B.Xu, Y.Wang, J. Chen, F. Li, D. Li, X. Pan, "Investigation of domestic air conditioner with a novel low charge microchannel condenser suitable for hydrocarbon refrigerant" Measurement (2016), doi: http://dx.doi.org/10.1016/j.measurement.2016.04.034.
[8]. A.S., Padalkar V. M., Kundlik, D. Sukumar "Simulated and experimental performance of split packaged air conditioner using refrigerant HC-290 as a substitute for HCFC-22" Applied Thermal Engineering 2014; 62: 277-284.

ICENS
INTERNATIONAL CONFERENCE ON ENGINEERING AND NATURAL SCIENCES
24-28 May 2016 /Sarajevo

A Contour-Based Moving Object Segmentation Algorithm in H.264/AVC Bitstream

Yilmaz Eroglu[1], *Halil Ibrahim Eskikurt*[2]

Abstract

Moving object segmentation in compressed domain has very important role for multimedia applications, such as Video Surveillance, Video Optimization and Object-Based Video Coding. In this work, a new algorithm for the moving object segmentation is presented by using the motion vectors and DCT coefficients, obtained from the H.264 bitstream. For object segmentation, two different masks are implemented. The first object segmentation mask is created by applying Spatio-Temporal filters to the motion vectors and the second one is created by applying a Canny Edge Detector to DC image, obtained from DCT coefficients. At the end, object mask which is a combination of these two masks can be used for segmentation of moving objects.

Keywords: Canny Edge Detector, DCT Coefficient, H.264 Bitstream, Motion Vector, Moving Object Segmentation

1. INTRODUCTION

In the last decade, there has been a rapid increase in multimedia applications in several fields. In this process, a transition from analogue to digital information took place. Today, almost all processes, involving video recording, its storage and transmission are conducted in digital media. The need for higher bitrates and rapidly increasing need for storage have been promoting the compressed video standards. Known as the most popular video coding standard, H.264 is a standard developed with the cooperation of ITU and ISO standards. This video coding standard added several features to video coding algorithms providing better object video performance when compared to older video compression platforms such as MPEG-4, H.263, etc. [1], [2], [3]. However, digital technologies are now in every aspect of our lives, video object segmentation is still being considered as a problem for several fields. Examples of these fields are object-based video conversion, video database searching, video surveillance, etc. Although a number of methods are developed in the recent years in order to solve this problem, it is expected to take some time before obtaining satisfactory results. Common use of compressed formats in video storage has increased the importance of video object segmentation [4].

Developed for compressed formats, moving object segmentation algorithms usually use motion vectors and DCT (Discrete Cosine Transform) coefficients. DCT coefficients convert brightness and color values corresponding to brightness and color modulations in each block. As a result, high-frequency fine details which human eye is only able to distinguish to an extent are suppressed.

Motion vectors, on the other hand, involve direction vectors which indicate the change in the location of macro blocks obtained from video frames from one frame to another. However, motion vectors indicate the moving blocks in theory, this is not always the case in practice [5]. Frequently, there are a number of errors along with the motion we want to use as shown in Figure 1.

[1] *Corresponding author: Kastamonu University, Department of Computer Technology and Programming, Kastamonu Vocational School of Higher Education, 37100, Kuzeykent / Kastamonu, Turkey. yeroglu@kastamonu.edu.tr*

[2] *Sakarya University, Department of Electrical and Electronic Engineering, Faculty of Technology, 54100, Serdivan/Sakarya, Turkey. eskikurt@sakarya.edu.tr*

Figure 1. Noisy motion vectors

There are several studies in the literature which aimed at filtering the motion vector. Noisy motion vectors can be re-estimated with an interim valuation of the correctly estimated neighboring motion vectors. Median and mean filters may be used for this purpose [5].

Golam Sorwar et al. [6] suggested MAT (Mean Accumulated Filter) filter to remove noisy motion vectors. This method includes the following steps: first, an iterative mean filter is applied to the motion vectors, then, after several iterations with median and mean filters, new vectors are calculated in a way not overlapping with the maximum and minimum values of the neighboring vectors. Some of the results are shown in Figure 2.

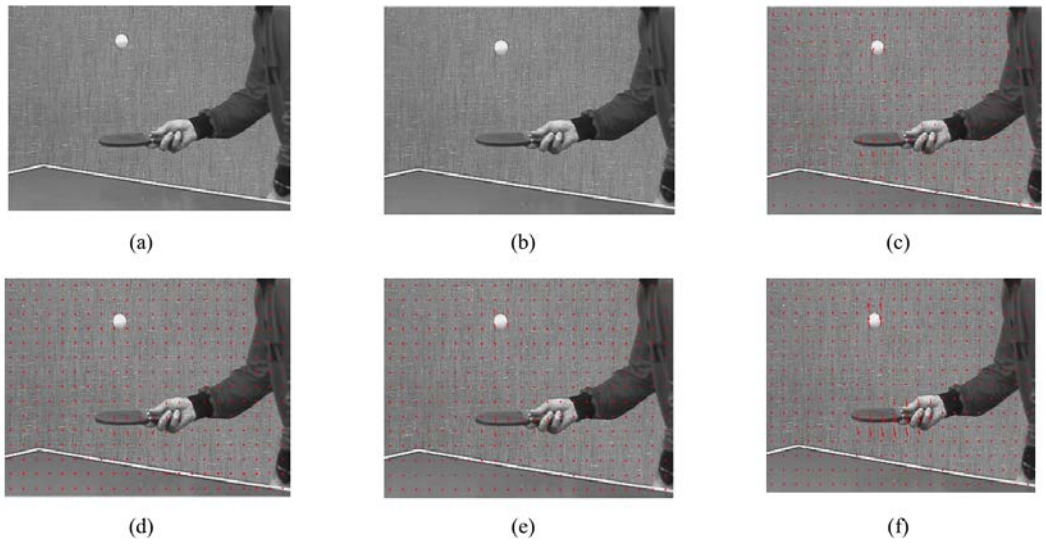

Figure 2. (a) 32th frame of the Tennis video; (b) 33th frame of the Tennis video; (c) Motion vectors

(d) Motion Vectors Using Median Filter of 3x3 Kernel; (e) Mean filter of 3x3 Kernel; (f) MAT filter

Using another method, Roy Wang et al. [7] developed a new technique for the motion vectors obtained from videos in Mpeg format. In order to remove the noises from motion vectors, frequency filters and spatial filters were compared in terms of calculation density, and it was found that spatial filters are faster in terms of calculation complexity. In this context, the study used the Cascade filter, a combination of Gauss and Median filters (spatial filters), on the motion vectors and positive results were obtained.

Another method reported by Moura et al. [8] motion vectors were filtered using a new technique for motion tracking. The Spatio-Temporal Filter (STF) used for filtering involves the following steps: MV Normalization, Temporal Consistency and Spatial Consistency. The illustration of the performance of this method is as follows (Figure 3).

Figure 3. (a) Motion Vectors; (b) Median Filter; (c) STF Filter

2. A CONTOUR-BASED MOVING OBJECT SEGMENTATION ALGORITHM IN H.264/AVC BITSTREAM

This study offers a new algorithm for moving object segmentation from an H.264 video in a bitstream format. According to this algorithm, motion vectors from the bitstream in H.264 video format and DCT coefficients are separated.

Object mask to be used in moving object segmentation is a combination of two masks. The first object mask is obtained using a Spatio-Temporal Filter on the motion vectors, while the second object mask is obtained using the edge change map applied to the DC images obtained from AC (Alternating Current) and DC (Direct Current) values which constitute the DCT coefficients. Here, low-frequency components are identified as DC, while high-frequency components are identified as AC. Finally, the Object Mask, a combination of two masks, is used to segment video objects. The general diagram of this algorithm is as follows (Figure 4). The course of the algorithm will be detailed in following chapters.

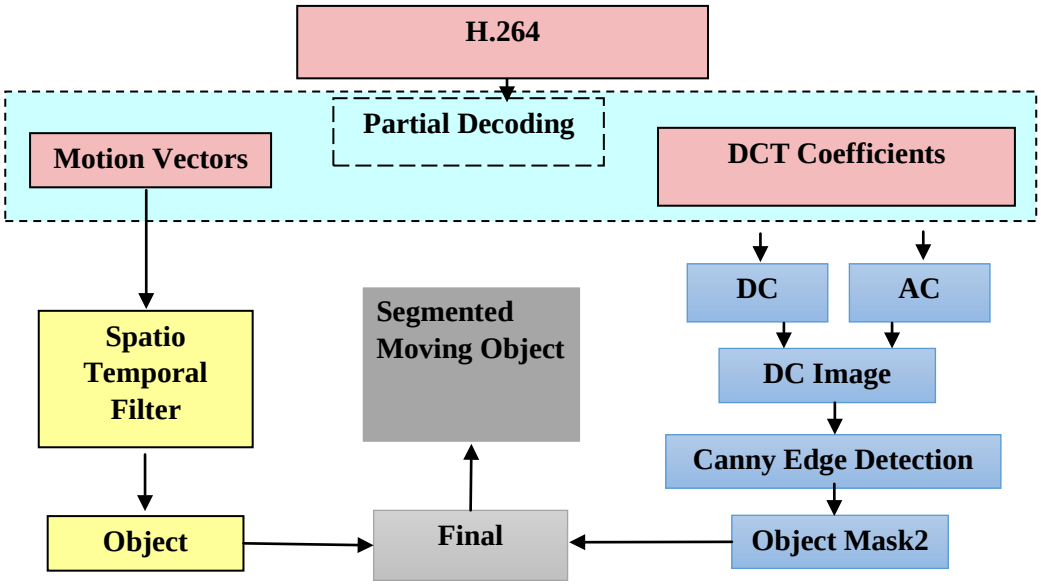

Figure 4. General diagram of the moving object segmentation

2.1. Spatio-Temporal Filter (STF)

Developed for object tracking by Moura et al. [8], this method is used in this study for moving object segmentation. Motion vectors are filtered in three essential steps in this method.

- **MV Normalization** (Normalization of the motion vectors):
  While P-frames take the previous frame as a reference, B-frames are also able to take the last frame as a reference too. In this step, motion vectors are normalized in order to be independent from the frame type (P or B).
- **Temporal Consistency** (The temporal consistency check between the previous and following MVs):
  In this step, blocks which are not in the frame yet generated according to the Noisy motion vectors are compared with the next motion vector temporally, filtering incorrect images.
- **Spatial Consistency** (Spatial consistency check of the motion vectors with neighboring vectors):
  In this step, blocks which are not moving with the superficially neighboring blocks –again as a result of incorrect motion vectors- are filtered.

Table 1 shows a comparison of Median Filter and STF Filter according to the Multiple Object Detection Accuracy (MODA) and Multiple Object Detection Precision (MODP) measurements [8].

***Table 1**. Multiple Object Detection Measurements (PETS2001 Dataset1/Testing/Camera1, 2500 frame, 7849 object)*

Filter Type	No Response	Incorrect Detection	MODP	MODA
None	4803	578	31%	31%
Median Filter	4899	380	28%	33%
STF	4089	329	42%	44%

As shown in Table 1, the performance of STF method in object detection precision (MODA) was 44% when compared to the 33% obtained with Median filter. MODP test which measures the consistency of the detected object and the actual object also proves the superiority of the STF over Median filter (28% vs. 42%).

The success of STF method in terms of filtering results proves its dominance over the other methods (Table 1, Figure 5). As a result, the first object mask is obtained with filtering the motion vectors of the objects with STF method.

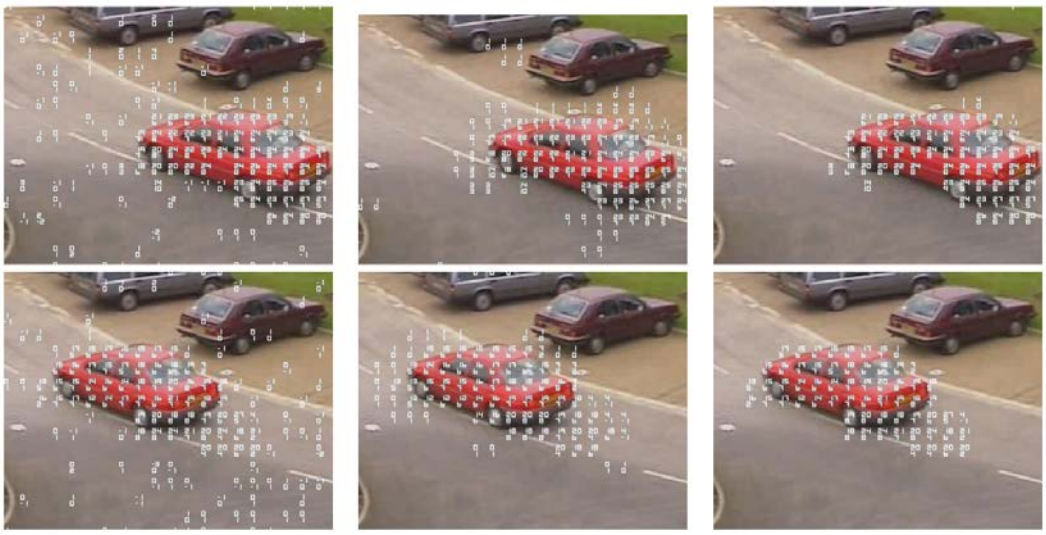

Figure 5. (a) Motion Vectors; (b) Median Filter; (c) STF Filter

2.2. Edge Mask Generation from DC Images

In this process, DC images obtained from the DCT coefficients will be used. Among several methods for edge mask obtained from DC images, Canny Edge Detection was selected as it was found to offer the best results. The general diagram of this process is as follows (Figure 6).

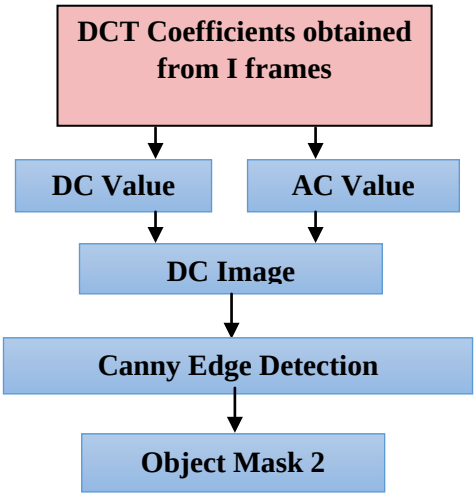

Figure 6. Diagram for the second object mask generation

2.3. Canny Edge Detection

The Canny Edge Detector [9] which is to be applied in this step involves 4 essential stages. These four stages are as follows:

- **Noise Removal with Gaussian Filtering:** Incorrect areas of the image are removed using the Gaussian method according to a specific sigma value.
- **Edge Detection by Gradient Calculation:** Magnitude and direction of the edge gradient are calculated with the application of gradient operator.
- **Non-Maxima Suppression:** Edges of the image are thinned using non-maxima suppression.
- **Hysteresis Thresholding:** Finally, the image is refined eliminating undesired details using Hysteresis Thresholding.

2.4. Final Moving Object Segmentation Mask

Consequently, the first Object Mast obtained with the STF filtering of the motion vectors and the second Object Mask obtained with the application of Canny Edge Detector on the DC images will provide the Final Segmentation Mask.

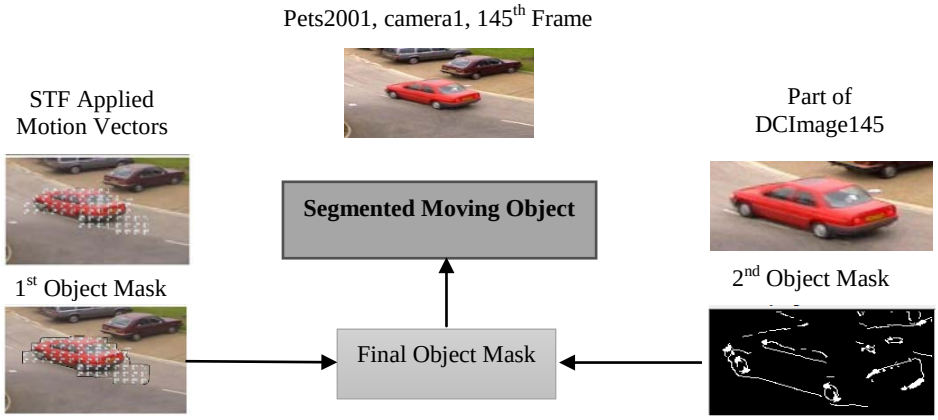

Figure 7. Diagram of the final object mask generation

2.5. Application Results for Canny Edge Detection

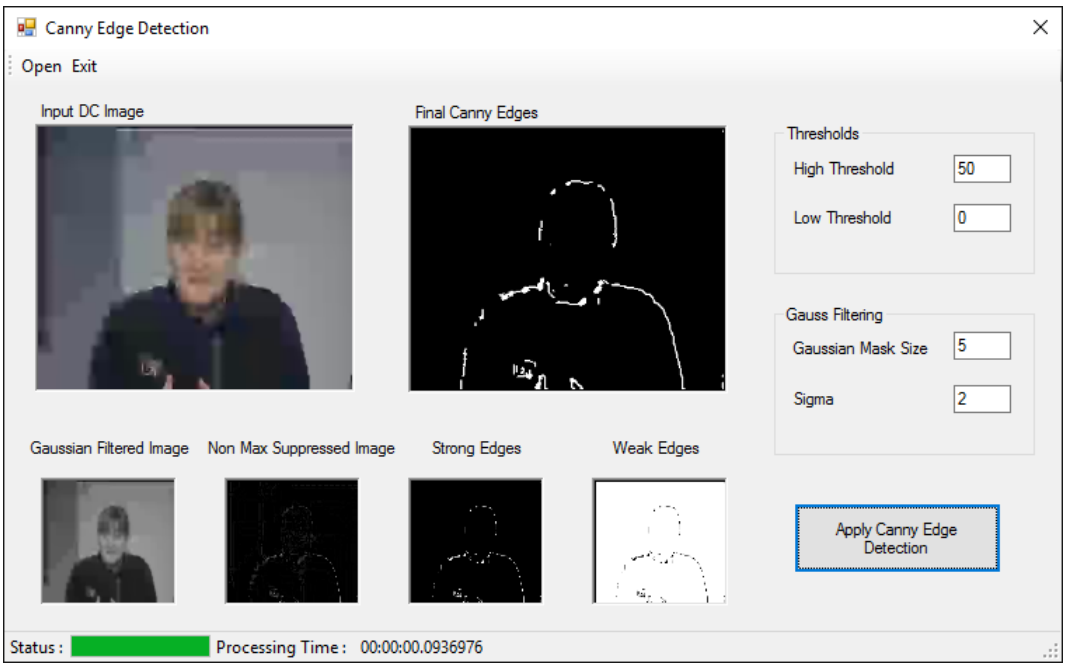

Figure 8. Australia.h264 Video, DCImage12

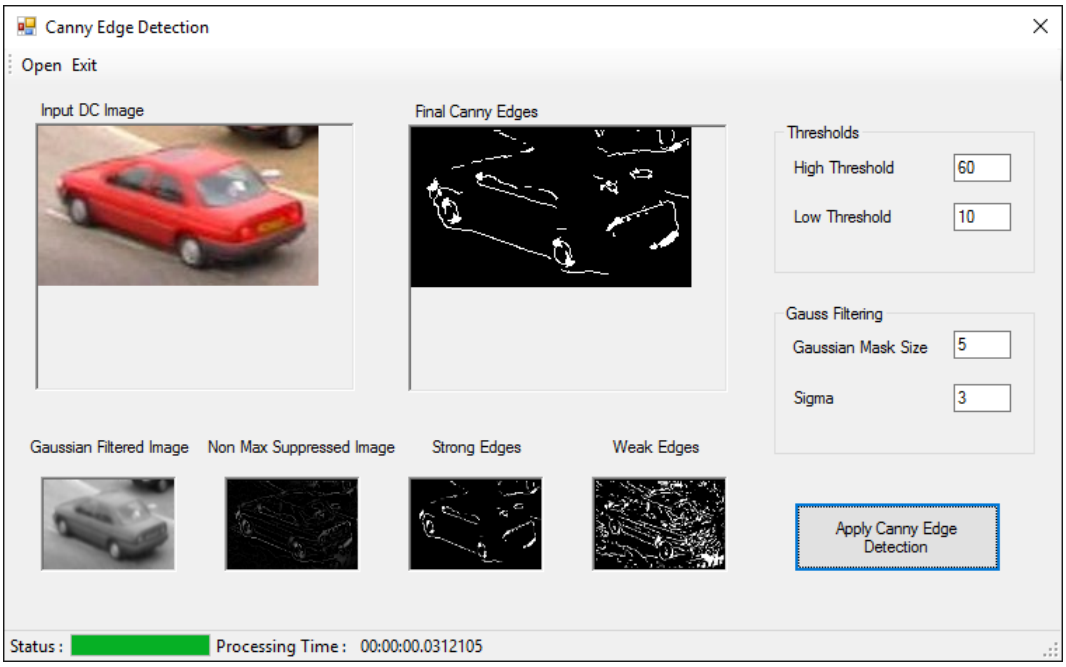

Figure 9. Pets2001, camera1, DCImage145

3. RESULTS

This study suggests a new video object segmentation algorithm for moving objects using motion vectors and DCT coefficients obtained from H.264 bitstream. The Spatio-Temporal Filter (STF) which is commonly used in video tracking offered a better performance in terms of quality when compared to the median filter which is commonly used in video processing. As shown in Table 1, the performance of STF method according to the MODP test was 44% when compared to the 33% obtained with Median filter using the same test. In general, the average performance of the STF method was 43% while it was 30.5% for

median filter. Adapted to moving object segmentation, STF is expected to increase the object segmentation performance. The Canny Edge Detection method employed in the second part of the process gave better results when compared to the other methods. It is expected to have better results from this algorithm when compared to the other methods after the actualization of the final object mask which is a combination of these two masks.

REFERENCES

[1]. Joint Video Team (JVT) of ISO/IEC MPEG & ITU-T VCEG, "Draft ITU-T Recommendation and Final Draft International Standard of Joint Video Specification (ITU-T Rec. H.264/ISO/IEC 14496-10 AVC)", JVT-G050, March, 2003.
[2]. King Ngan, Video Segmentation and Its Applications, Springer Media, 2011.
[3]. Al Bovik, Video Segmentation, Elsevier Academic Press, 2005.
[4]. Y.-M. Chen, I. V. Bajić, and P. Saeedi, "Moving region segmentation from compressed video using global motion estimation and Markov random fields," IEEE Trans. Multimedia, vol. 13, no. 3, pp. 421-431, Jun. 2011.
[5]. R.Rajkumar, D.SaiKrishna, and Jayanth.A.S, "Survey on Motion Vector Filtering and Object Segmentation Methods in Compressed Domain", International Journal of Advancements in Technology, 2011.
[6]. Golam Sorwar, Manzur Murshed, and Laurence Dooley, "A Novel Filter for Block-Based Object Motion Estimation", Digital Image Computing Techniques and Applications, Melbourne, Australia, 2002.
[7]. Roy Wang, Hong-Jiang Zhang, and Ya-Qin Zhang, "A confidence measure based moving object extraction system built for compressed domain", The 2000 IEEE International Symposium on Circuits and Systems (ISCAS 2000), Volume.5, pp. 21-24, Geneva, 2000.
[8]. Ronaldo C., Moura Monity, and Elder Moreira Hemerly, "A Spatiotemporal Motion-Vector Filter for Object Tracking on Compressed Video", 7th IEEE International Conference on Advanced Video and Signal Based Surveillance, 2010.
[9]. J. Canny, "A computational approach to edge detection," IEEE Trans. Pattern Analysis and Machine Intelligence, Vol. 8, no. 6, pp. 679-698, November 1986.

ICENS
INTERNATIONAL CONFERENCE ON ENGINEERING AND NATURAL SCIENCES
24-28 May 2016 /Sarajevo

Surface PGA Calculations by Using Dynamic Amplification Factor and Synthetic Accelerogram

Ozkan Cevdet Ozdag[1], Mustafa Akgun[2], Eren Pamuk[3]

Abstract

Quasi Transfer Spectrums (QTS) and Dynamic soil amplification factor defining which ratio earthquake acceleration will reach the soil surface by changing is one of the most important factors in seismic risk studies. When computing the value of DAF at a point without a strong motion station, peak horizontal acceleration values at the bedrock and soil transfer function are needed. PGA value at the bedrock can be obtained by using either real seismic records or the earthquake scenario. However, the soil transfer function can be computed observationally and theoretically. Observational soil transfer function is defined by microtremor horizontal/vertical spectral ratio. In case of theoretical computation, the density belonging to the soil layers between the bedrock and the soil surface is used together with the change of P-S wave rates with the depth and the damping factor. In this study, the dynamic amplification factor has been computed for 57 points by using observational QTS obtained by microtremor horizontal/ vertical spectral ratio as well as the earthquake scenario. Also, theoretical soil transfer function at 1 point was obtained through spatial autocorrelation method study and determined to be compatible with observational result.

Keywords: Synthetic Accelerogram, Dynamic Amplification Factor, PGA.

1. INTRODUCTION

Quasi Transfer Spectrums (QTS) and Dynamic soil amplification factor (DAF) defining which ratio earthquake acceleration will reach the soil surface by changing is one of the most important factors in seismic risk studies. When computing the value of DAF at a point without a strong motion station, peak horizontal acceleration values (PGA) at the bedrock and soil transfer function are needed. PGA value at the bedrock can be obtained by using either real seismic records or the earthquake scenario. However, the soil transfer function (soil transfer function) can be computed observationally and theoretically. Observational soil transfer function is defined by microtremor horizontal/vertical spectral ratio. In case of theoretical computation, the density belonging to the soil layers between the bedrock and the soil surface is used together with the change of P-S wave rates with the depth and the damping factor. In this study, the dynamic amplification factor (DAF) has been computed and mapped for 57 points by using observational soil transfer functions obtained by microtremor horizontal/ vertical spectral ratio as well as the earthquake scenario at a new city center located within the metropolitan area of Izmir. Also, theoretical soil transfer function at 1 point was obtained through spatial autocorrelation method (SPAC) study and determined to be compatible with observational result. It was observed that both peak period values are higher than 1 s and DAF values are higher than 2 throughout the area. Also, according to the soil profile obtained from the SPAC study, S wave rate changes up to a depth of 1300 m showing that acoustic impedance differences may occur in the frequencies and the magnitudes of the earthquake waves. The fact that peak period values obtained from microtremor studies are higher than 2 s supports this result. This means that acoustic impedance differences likely to occur in these depths should also be taken into consideration while computing the dynamic amplification factor.

2. THEORY

2.1 Dynamic Amplification Factor (DAF) Calculations

In the study carried out by Nakamura (1989) in the year 1989, Nakamura showed that horizontal/spectral ratio curves obtained observationally can be defined as a soil transfer function in the domain frequency. Nowadays,this argument is still used. The various applications of this acceptation were given in the study of Mucciarelli and Gallipoli 2001. Using these assumptions, observational soil transfer function is obtained. As is known, the soil transfer function gives information about how the earthquake waves passing from the bedrock to the soil is changed. Theoretical soil transfer functions are calculated by using viscoelasticity of soil layers in the frequency environment. During calculation of theoretical transfer spectrum process, P and S velocity values, thicknesses, densities, and damping factors to be included in the bedrock with in situ studies are used as

[1] *Corresponding author: Dokuz Eylül University, Aegean Implementation and Research Center, 35430, İnciraltı/İzmir Turkey.*
cevdet.ozdag@deu.edu.tr

input parameters (Akgün et al. 2013). The soil transfer function can be calculated separately with three different ways by common usage of S wave velocity, P wave velocity, and commonly used theoretically.

$$AMP_s(f) = \frac{ds_s(f)}{ds_b(f)} \quad (1)$$

$$AMP_p(f) = \frac{dp_s(f)}{dp_b(f)} \quad (2)$$

$$HVSR(f) = \frac{ds_s(f)}{dp_b(f)} = \frac{AMP_s(f)}{AMP_p(f)} \quad (3)$$

In Eqs. 1–3, dsa(f), dsy(f), dpa(f), and dpy(f) are defined as stable state magnitudes and changes with the frequency. Subscripts represent the spectrum calculations made according to S and P waves of the function d(f). "s" and "b" expressions again seen in the subscripts define the operations made for the soil surface and the bedrock, respectively. Similarly, they define the soil transfer functions obtained depending on the P and S waves in different frequencies of the layers forming the soil for AMP(f) calculations. Horizontal earthquake force to be formed on the soil surface is investigated in the seismic risk or microzoning studies to be carried out in the regions with high earthquake risk. Assumption is made about the fact that the spectrum AMPs(f) in Eq. 1 to be obtained depending on S wave velocity can be used for the investigation of this force (Nakamura 2000). As is known, the most important problem in designing earthquake-resistant structure is the prediction of the PGAs value on the soil surface. If a strong motion station and sufficient earthquake data are available at a point where the structure will be built, the PGAs value is found by carrying out direct reading and statistical processes. This value is also used for defining the points close to the station. This process includes the studies that are both difficult to apply in practice and of high cost. Therefore, the efforts are made for predicting the value PGAs mostly with theoretical calculations. When calculating the value PGAs, the prediction of the soil transfer function and the value PGAs in the bedrock must be made. Thus, the soil including the bedrock must be modeled according to P and S wave rates through earthquake scenarios and in situ studies. Both the PGA values belonging to the bedrock and the soil surface and the dynamic amplification factor can be calculated in this phase. Parseval's Theorem and Random oscillation theory as well as earthquake scenarios are utilize for this purpose. Detailed theoretical explanations related to these processes are given below. Earthquake scenarios are mostly defined with parameters M for magnitude, E for epicenter distance, H for hypocenter distance, and r for factor reflecting the earthquake wave propagation characteristic of the environment. As a result of this process, the PGAb and frequency spectrum curves belonging to the bedrock are obtained. Since PGA values can be defined depending on each other in time and frequency environment, the PGA value is defined inside the spectrum AMP(f). Parseval's theorem and Random oscillation theories are utilized for reaching the PGA value in time environment from the AMP(f). According to Parseval's theorem, Eq. 4 is obtained by assuming that the average of square root of the magnitudes in the frequency environment is identical to the average of square root of the magnitudes in time environment.

$$rms[A(f)] \propto rms[a(t)] \quad (4)$$

Equation 5 is obtained when this generalized approach is used for the wave S.

$$A_s(f) = A_b(f)AMP_s(f),$$

$$rms[A_s(f)] = rms[A_b(f)AMP_s(f)] \propto a_s(t) \quad (5)$$

As is known from random oscillation theory, maximum values of the time series are proportional to average values of square root and from this result, Eq. 6 is used for reaching the values PGAs and PGAb.

$$PGA_s \propto rms[a_s(t)] \propto kko[A_b(f)AMP_s(f)],$$

$$PGA_y \propto rms[a_b(t)] \propto rms[A_b(f)] \quad (6)$$

As a result of correlation of the parameters PGAs and PGAb with each other in frequency environment, the parameter DAF is calculated by Eq. 7 (Trifunac 1993; Lee and Trifunac 1995; Herak 2008).

$$DAF = \frac{PGAs}{PGAb} = \frac{rms[A_b(f)AMP_s(f)]}{rms[A_b(f)]} \quad (7)$$

2.2 Synthetic Accelerogram Generation and Adjustment

Synthetic accelerogram generation and adjustment process were applied by using Hallodorson and Papageorgiou 2005 algorithm. The artificial accelerogram is defined starting from a synthetic one, compatible with the target spectrum, and adapting its frequency content using the Fourier transformation method.

The correction of the random process is carried on at every iteration using the relationship given in eq. 8 (Mucciarelli et al., 2004);

$$F(f)_{i+1} = F(f)_i [SRT(f)/SR(f)_i] \quad (8)$$

SRT(f) is the value of the target spectrum and $SR(f)_I$ is the value of response spectrum corresponding to the accelerogram of the current iteration for frequency f. $F(f)_{I+1}$ and $F(f)_I$ are the values of the accelerogram in the frequency domain for the current and previous iteration respectively. A flow chart of this process is given figure 1.

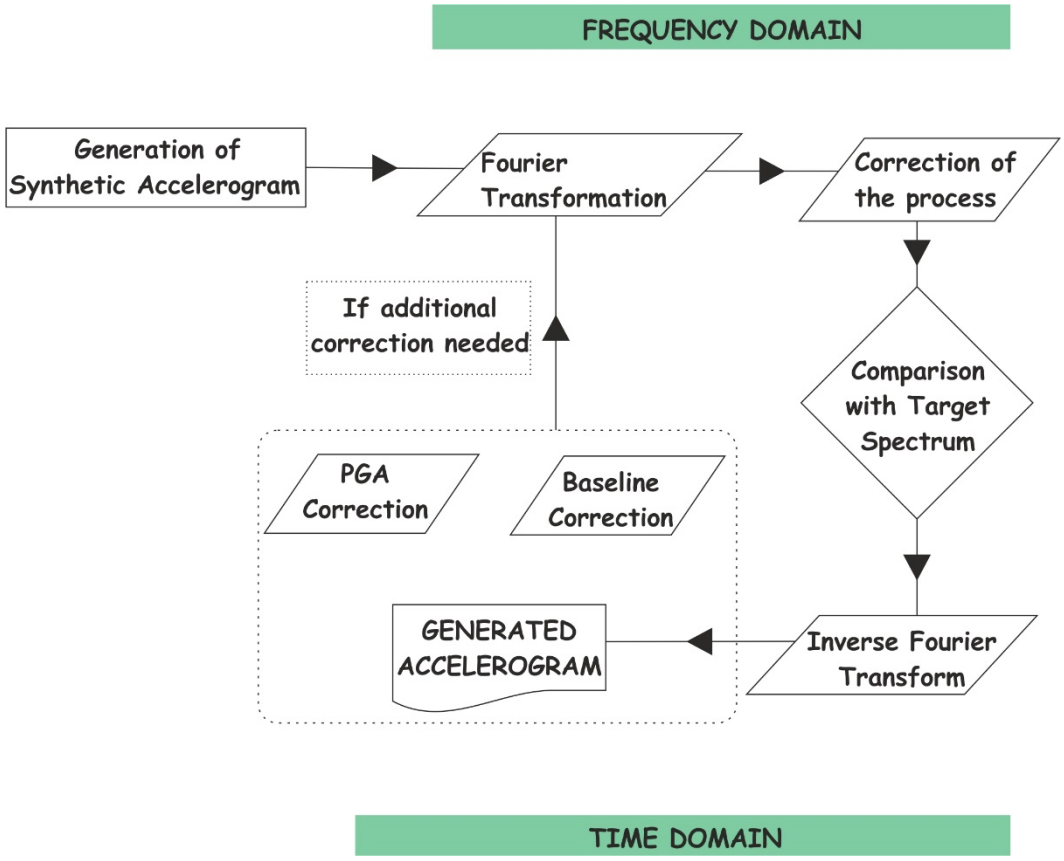

Figure 3. A flow chart of synthetic accelerogram generation and adjustment process.

3. APPLICATIONS, RESULTS AND CONCLUSION

The results obtained using geological researches, microtremor QTS, and DAF studies were combined and interpreted together with those from previous studies (Figure 2). Consequently, the following results are given below. Seven different layers were defined depending on P-S wave velocity changes obtained up to a depth of 1200– 1300 m in the investigation area (Figure 3, 4). Velocity values of Vs< 700 m/s observed between the depths of 0–200 m in average define the characteristic of engineering bedrock after this depth.

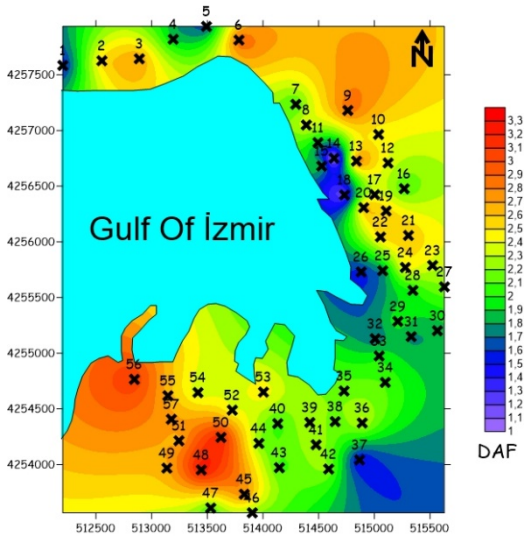

Figure 2. DAF map of Study Area.

On the other hand, when interfaces having the S wave rate differences of 100 m/s in average observed after this depth are taken into consideration, it is possible that amplitude and frequency contents of the earthquake waves coming from a depth of 1200–1300 m may be affected positively or negatively (Figure 3,4).

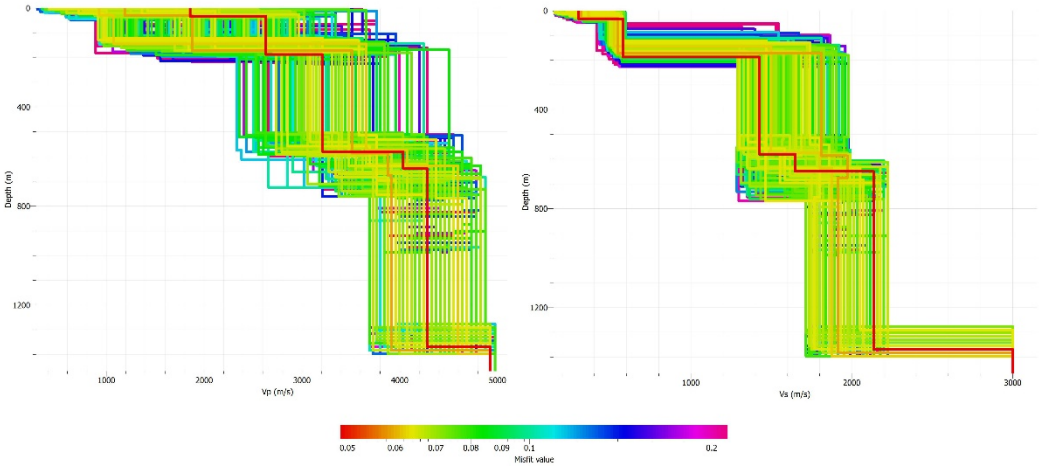

Figure 3. ESPAC Results.

This means that engineering and seismic bedrock models must also be taken into consideration in soil transfer function calculations for the investigation area. Peak period values obtained on the surface support the existence of a thick soil throughout the investigation area. Also, it must be expected that this thickness would be increased further at the points reaching the period value of 5 s.

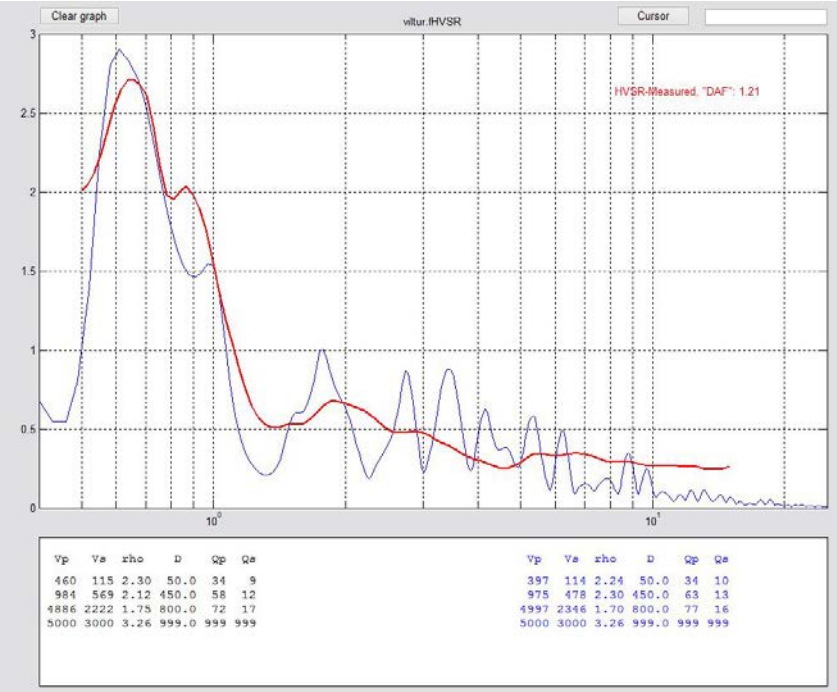

Figure 4. Theroretical and Observed QTS.

This means that the depth of bedrock must be taken into consideration according to these results when calculating the soil transfer functions. Displacement effect will be predominant in soil reaction spectra to be obtained in the areas with period values especially higher than 3 s. Variations in DAF values show that average magnitudes of earthquake waves progressing towards the soil surface from the bedrock at the points of basin characteristic would be increased at least two times. The investigation area presents a heterogeneous structure characteristic according to the variations in lateral direction of the DAF values. This means that the investigation area cannot be represented by an average magnification value. In the scope of these findings, investigation of bedrock and defining physical parameters of soil which new buildings will be constructed are very important factors to decrease mortality during earthquakes. Therefore, the areas having similar characteristics must be investigated by using in situ geophysical methods before starting construction of earthquake-resistant buildings.

REFERENCES

[1]. Herak, M., (2008), Model HVSR-A Matlab® tool to model horizontal-to-vertical spectral ratio of ambient noise, Computer and Geosciences, 34, 1514-1526.
[2]. Lee, V.W., Trifunac, M.D, (1995), Frequency dependent attenuation function, and Fourier amplitude spectra of strong earthquake ground motion in California. University of Southern California, Los Angeles, CA, USC Report no. CE 95-03, 190.
[3]. Nakamura, Y. (1989). A method for dynamic characteristics estimation of subsurface using microtremor on the ground surface, Quarterly Report of Railway Technology Research Institute, 30, 25-33.
[4]. Nakamura, Y. (2000). Clear Identification of Fundamental Idea of Nakamura's Technique and Its Applications, Proc. 12th World Conf. on Earthquake Engineering, 2656.
[5]. Trifunac, M.D., (1993), Broad band extension of Fourier amplitude spectra of strong motion acceleration. University of Southern California, Los Angeles, CA, USC Report no. CE 93-01, 109pp.

ICENS
INTERNATIONAL CONFERENCE ON ENGINEERING AND NATURAL SCIENCES
24-28 May 2016 /Sarajevo

Free Vibration Behaviors of Wind Turbine Towers for Various Geometrical Parameters

Ali I. Karakas[1], *Ayse T. Daloglu*[2]

Abstract

Frequency characteristics of wind turbine tower structures have a practical importance in rotor resonance prevention and seismic response analysis. For this purpose, the present study provides a parametric analysis focusing on the free vibration behaviors of wind turbine towers with different geometrical characteristic parameters and base support conditions. The geometrical parameters investigated are the ratio of top and bottom diameter, the ratio of top and bottom wall thickness, the ratio of slenderness and the ratio of diameter and thickness of foundation. Moreover, fixity and circular foundation resting on elastic subsoil conditions are examined as wall base support conditions. The finite element models of the towers are created in structural analysis software SAP2000 automatically with the help of OAPI (Open Application Programming Interface) feature of SAP2000. The OAPI functions employed in code developed in MATLAB to supply two-way data flow between SAP2000 and MATLAB during pre and post processing. The nacelle-rotor turbine system with blades is considered as rigid non-rotating mass at the top of the tower for structural analysis models. And, the soil foundation is considered as elastic half-space represented by linear springs. The fundamental frequencies of the wind turbine tower for various base conditions and geometrical properties are presented in graphical formats. As a result of the numerical analyses it can be stated that particular natural frequencies of the tower can be obtained reliably by altering certain geometrical parameters and considering soil-foundation-tower interaction.

Keywords: *Wind turbine tower, free vibration, open application programming interface*

1. INTRODUCTION

Wind turbine structures are used to transform kinetic energy of the moving air to electrical power without polluting the environment. The increasing need for clean energy results with larger wind structures. Designing of larger structures requires detailed investigations on the behavior of such structures. A number of researchers focused on the structural behaviors of steel and/or concrete wind turbine towers to accomplish safer designs. For instance, Lavassas et al. [1] analyzed a steel 1 MW wind turbine tower for gravity, seismic and wind loadings. Also, Bazeos et al. [2] conducted stability analyses of a prototype wind turbine steel tower and investigated the effect of the soil-structure interaction on the dynamic characteristics of the structure. Moreover, Zyl and Zijl [3] investigated the effect of crack formation and soil stiffness on the fundamental frequency of a concrete wind turbine tower using nonlinear finite element modeling as well as analytical models proposed for primary design stage. Hu et al. [4] examined the effect of internal stiffening rings and wall thickness on the wind responses of steel wind turbine towers with different heights. There are also several studies concerning structural optimization of wind tower structures for robust and cost efficient designs using deterministic or probabilistic optimization algorithms. In particular, Negm and Maalawi [5] described several optimization models for the design of a wind tower to be built from uniform segments using interior penalty function technique. Uys et al. [6] searched the optimum wall thickness and number of stiffeners ensuring minimum cost of the turbine tower considering the cost of assemblage and welding of the segments. Lagaros and Karlaftis [7] focused on the optimization of steel wind towers with different heights by imposing steel buckling and local buckling of ring-stiffeners as design constraints.

In most of the aforementioned studies the tower base conditions are assumed to be completely rigid or fixed. However, it is clear that a reliable structural design of a wind turbine tower system requires regarding of the flexibility of mat foundation and the compressibility of supporting soil. Also, a detailed investigation on the frequency behavior of wind tower structures depending on the geometrical parameters is not available in these studies. For this reason, in the current study a conical tubular concrete wind turbine tower with shallow flat disk base resting on elastic subgrade is investigated exhaustively for the free vibration behavior under changing geometrical parameters and base conditions. The parametric study is conducted with the help of a code developed in MATLAB which utilizes Open Application Programming Interface (OAPI) feature of SAP2000 [8].

2. TOWER FINITE ELEMENT MODEL

The finite element model of the wind turbine structure is developed using OAPI functions in the computer program SAP2000 that is integrated to the code including material and geometrical properties. The nacelle-rotor turbine system with three blades

[1] *Corresponding author: Karadeniz Technical University, Department of Civil Engineering, 61080, Trabzon, Turkey.* aliihsanka@yahoo.com

[2] *Karadeniz Technical University, Department of Civil Engineering, 61080, Trabzon, Turkey.*

is considered as rigid non-rotating mass at the top of the tower. The total mass of three blade turbine is taken as 100 tons for a wind turbine of 450-kW capacity. Figure 1 depicts structural configurations and finite element model of the structure.

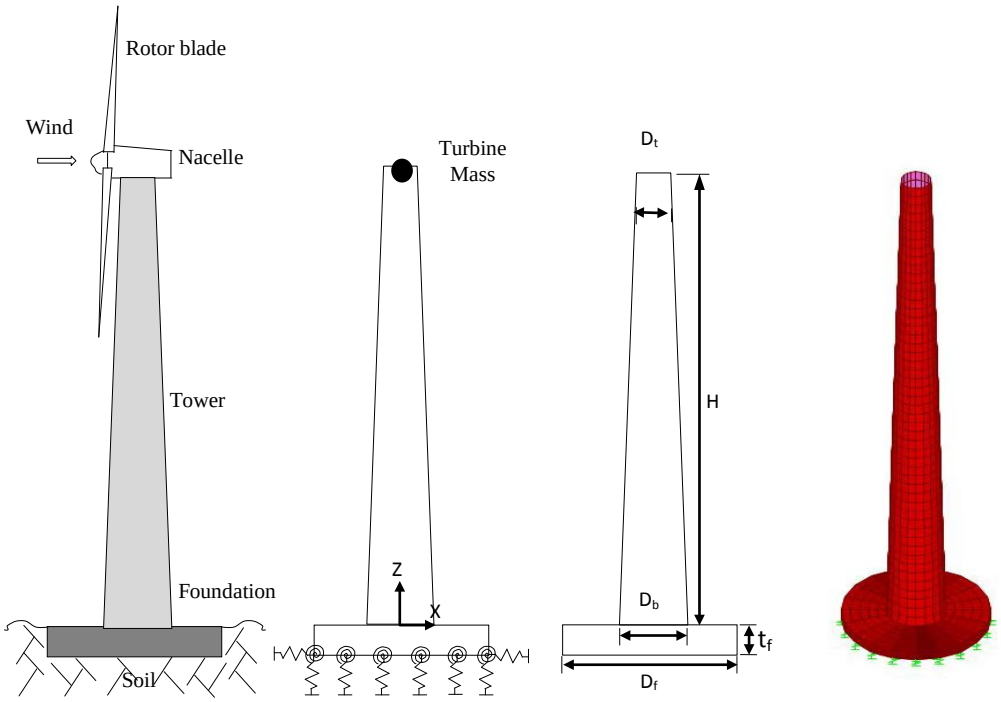

Figure 1. Structural configurations and finite element model of the turbine tower structure

The material properties of the concrete used in the study are given in Table 1.

Table 1. Material properties

Property	Concrete
Elasticity modulus (GPa)	30
Poisson's ratio	0.2
Unit weight (kg/m^3)	2500

For the finite element model the turbine tower wall is modeled using four-node thin-shell elements with six degrees of freedoms (dofs) at each node. Each shell element has linearly variable thickness through the height. Eight-node solid brick elements are used for concrete foundation discretization. And, soil foundation is represented by area spring elements with six dofs. Prior to optimization process a convergence study is conducted to decide the sufficient number of elements to be used in the finite element model.

3. ELASTIC SOIL FOUNDATION

In this study the soil-foundation interaction is taken into account by a commonly used method described by Gazetas [9] in which the soil stiffnesses are represented through linear uncoupled springs. In this way, the effect of soil stiffness on the behavior of wind turbine structure can be simulated in a simple and time efficient way. This method has been derived from the vibration of a rigid round disc on a linear elastic homogeneous half-space. The equations for directionally uncoupled linear spring constants are given in Table 2. Also, the embedment effect of the foundation constructed below the ground level can be taken into account by multiplying spring constants with the embedment coefficients provided by Indrajit and Shambhu [10]. Thus the modified spring constants for embedded foundations can be obtained. The modification coefficient formulations used in this study are also given in Table 2.

Table 2. Soil spring constants and embedment coefficients ([9],[10])

Direction	Spring Constant	Coefficient	Remarks
Vertical	$K_z = \frac{4Gr}{(1-v_s)}$	$\eta_z = 1 + 0.6(1-v_s)\frac{h}{r}$	This is in vertical Z direction
Horizontal	$K_x = K_y = \frac{32(1-v_s)Gr}{(7-8v_s)}$	$\eta_x = 1 + 0.55(2-v_s)\frac{h}{r}$	This induce sliding in horizontal X or Y direction
Rocking	$K_\varphi = \frac{8Gr^3}{3(1-v_s)}$	$\eta_\varphi = 1 + 1.2(1-v_s)\frac{h}{r} + 0.2(2-v_s)$	This produces rocking about X and Y axis
Twisting	$K_\varphi = \frac{16Gr^3}{3}$	None available	This produces twisting about vertical Z axis

The parameters in Table 2 are defined as *G*, dynamic shear modulus of the soil; v_s, Poisson's ratio of the soil; K, equivalent spring stiffness; η, embedment coefficient; r, radius of the circular foundation and h, depth of embedment of the foundation. The soil damping is ignored in the present study. The properties of various soil types investigated in the present study are given in Table 3.

Table 3. Properties of typical soil types,[3]

Soil type	Poisson's ratio	Dynamic shear modulus (MPa)
Clay	0.35	13
Sand	0.40	63
Gravel	0.40	111

4. FREE VIBRATION ANALYSIS

The governing equation for a structure subjected to a free vibration with no damping is

$$[M]\{\ddot{u}\} + [K]\{u\} = 0 \quad (1)$$

where [*K*] is the stiffness and [*M*] is the mass matrix of the structural system, u and $\ddot{u}$ are the displacement and acceleration of the structure, respectively. Substituting $u = W \sin wt$ into Equation 1, after intermediate process we can obtain the following equation:

$$([K] - \lambda[M])\{W\} = 0 \quad (2)$$

where {*W*} is a vector of nodal displacement amplitudes of vibration and λ is the frequency parameter defined as the square of natural circular frequency, ω. The solution of Equation 2 yields the frequency parameter and the corresponding mode shape vectors. In this study the natural frequencies (Hz) and particular mode shapes are presented for altering geometries and supporting conditions. It should be noted that to avoid dynamic amplifications, the first natural frequency of the tower structure should not be within the range of the excitation frequencies of the turbine.

5. NUMERICAL EXAMPLES

The geometric characteristic parameters considered in this study can be expressed as:

D_tD_b = the ratio of tower top diameter to bottom diameter

T_tT_b = the ratio of tower wall top thickness to bottom thickness

HD_b = the ratio of tower height to bottom diameter

D_bT_b = the ratio of tower bottom diameter to bottom thickness

D_fT_f = the ratio of foundation diameter to thickness

D_bD_f = the ratio of tower bottom diameter to foundation diameter

The lower and upper values of these parameters considered in the present study are given in Table 4.

Table 4. Lower and upper ratios for geometrical parameters

Parameter	Lower ratio	Upper ratio
D_tD_b	0.25	1.0
T_tT_b	0.25	1.0
HD_b	20	50
D_bT_b	10	40
D_fT_f	4	9
D_bD_f	0.4	0.9

Frequency analyses are performed for a wind tower with a height altering between 40 m and 100 m, an outer top diameter altering between 0.5 m and 3.4 m, an outer bottom diameter altering between 2.0 m and 13.6 m. Also, the thickness of the wall in these analyses is varied between 0.05 m and 0.8 m. The diameter of the tower foundation is varied between 4 m and 12 m and the foundation thickness is varied between 0.5 m and 2.0 m.

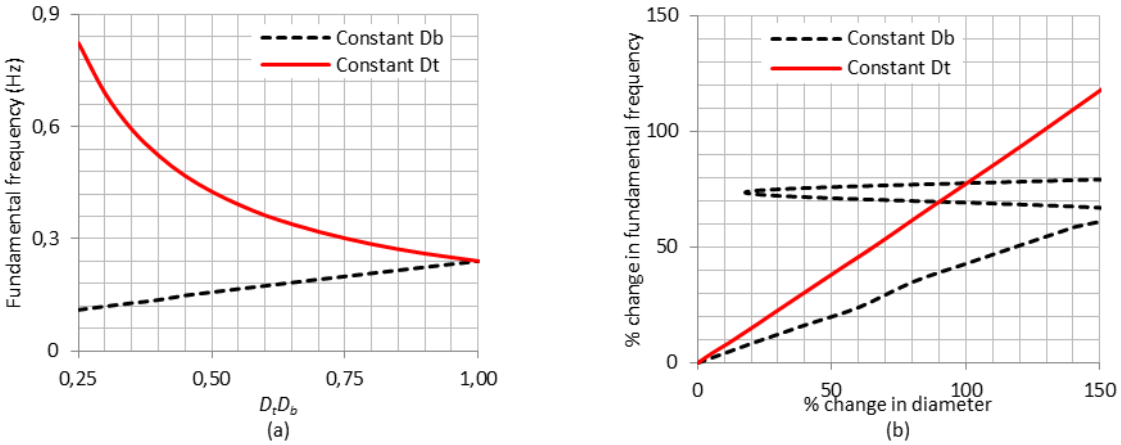

Figure 2. Frequency variations for various tower top and bottom diameters

Figure 2(a) shows the first natural (fundamental) frequencies for changing top and bottom tower diameter ratios. These ratios are obtained keeping one geometrical parameter as constant and the other one as variable. Figure 2(b) shows the percentage change in the fundamental frequency for the corresponding percentage change in top or bottom diameters of the tower. It can be seen that when the top diameter is doubled (100% change) the fundamental frequency of the tower system increases by about 40%. Also, when the bottom diameter is doubled the percentage change in frequency seems to be about 80%. Hence, it can be stated that the bottom diameter has nearly two times greater influence on the frequency of the tower than top diameter.

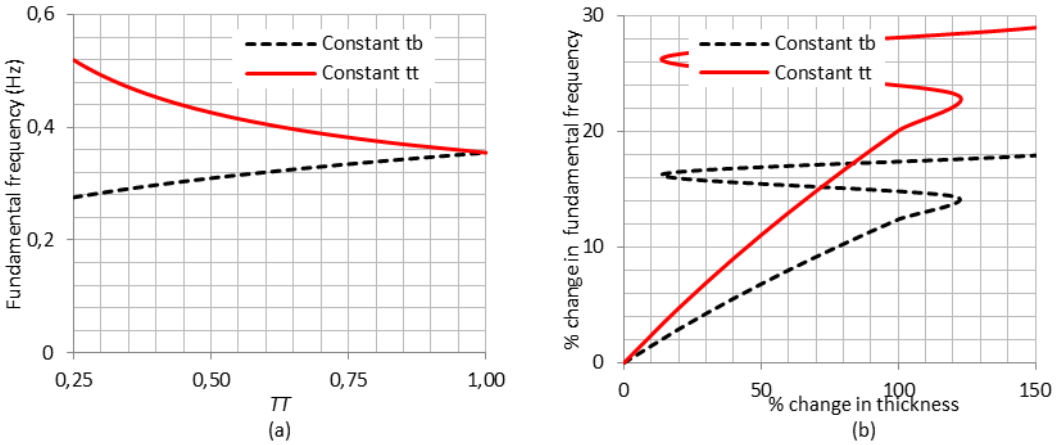

Figure 3. Frequency variations for various tower top and bottom thicknesses

Similarly, Figure 3(a) depicts the fundamental frequencies for changing top and bottom tower wall thickness ratios. Figure 2(b) shows the percentage change in the fundamental frequency for the corresponding percentage change in top or bottom

thicknesses of the tower wall. It is seen that when the top thickness is doubled (100% change) the fundamental frequency of the tower system increases by about 12%. And, when the bottom thickness is doubled the first natural frequency of the tower increases by 20%. Therefore, it can be noted that similar to the bottom diameter the bottom thickness has larger effect on the frequency of the tower than top thickness. Additionally, it can be concluded that the change in diameter has more critical effect on the frequency change than the change in wall thickness. In other words, the wall thickness influences the tower frequency as well, but the effect is not as dominant as for diameter change, because the stiffness increase due to a larger wall thickness is offset by the resulting higher mass of the tower.

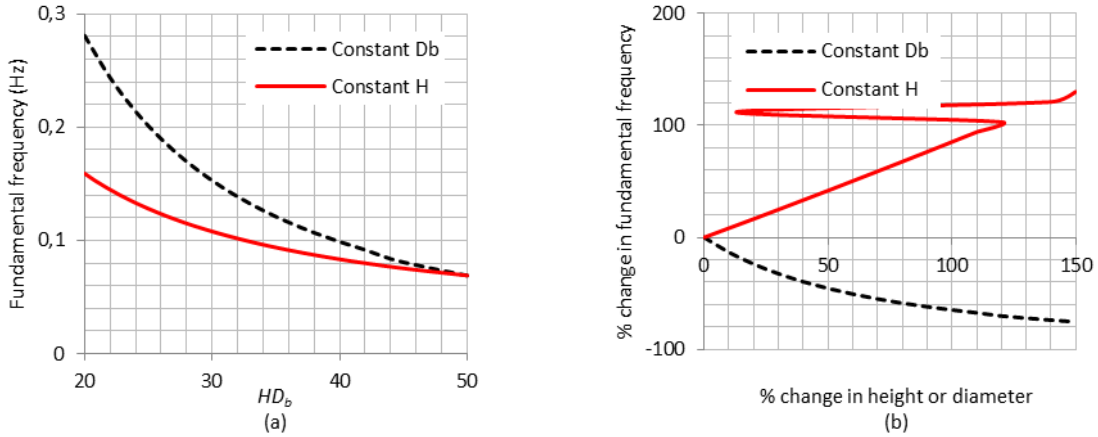

Figure 4. Frequency variations for various tower height and bottom diameters

The fundamental frequencies for altering tower height and bottom diameter ratios are depicted in Figure 4 (a). It is seen that the frequency decreases with increasing ratio of height to diameter. Figure 4(b) shows the percentage change in the fundamental frequency for the percentage changes in height or bottom diameter of the tower. It can be observed that when the tower height is increased by 100 % the fundamental frequency of the tower decreases nearly 65%. As expressed earlier when the bottom diameter is doubled the first natural frequency of the tower increases by 80%. Thus, it can be concluded that the main attribute influencing the frequency of the tower is its diameter.

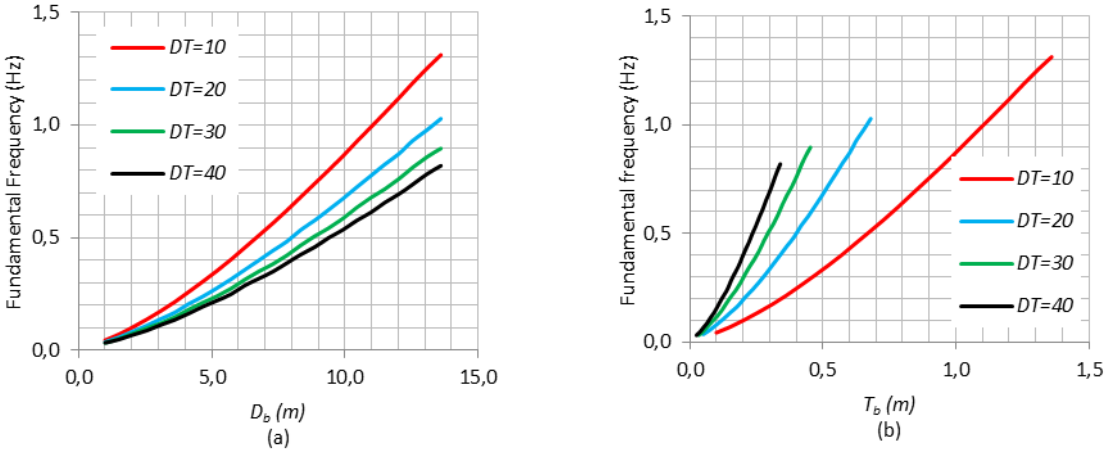

Figure 5. Fundamental frequencies for different tower bottom diameters and thicknesses

Figure 5 (a) and (b) display the fundamental frequencies of the tower structure with various diameter and thickness values at the bottom section of the wall for different ratios of bottom diameter to thickness. The influence of bottom diameter on the percentage change in fundamental frequency decreases when the bottom thickness of the wall becomes thicker. Similarly, the effect of thickness on the frequency change decreases as the tower wall diameter becomes larger.
Clayey (C), sandy (S) and gravel (G) soil types are taken into account as elastic soil beneath the tower foundation in order to investigate the influence of soil-structure interaction on the fundamental frequency of the wind turbine tower. The first natural frequencies obtained considering soil-structure interaction are compared with those obtained by assuming the tower foundation base as completely fixed (F).

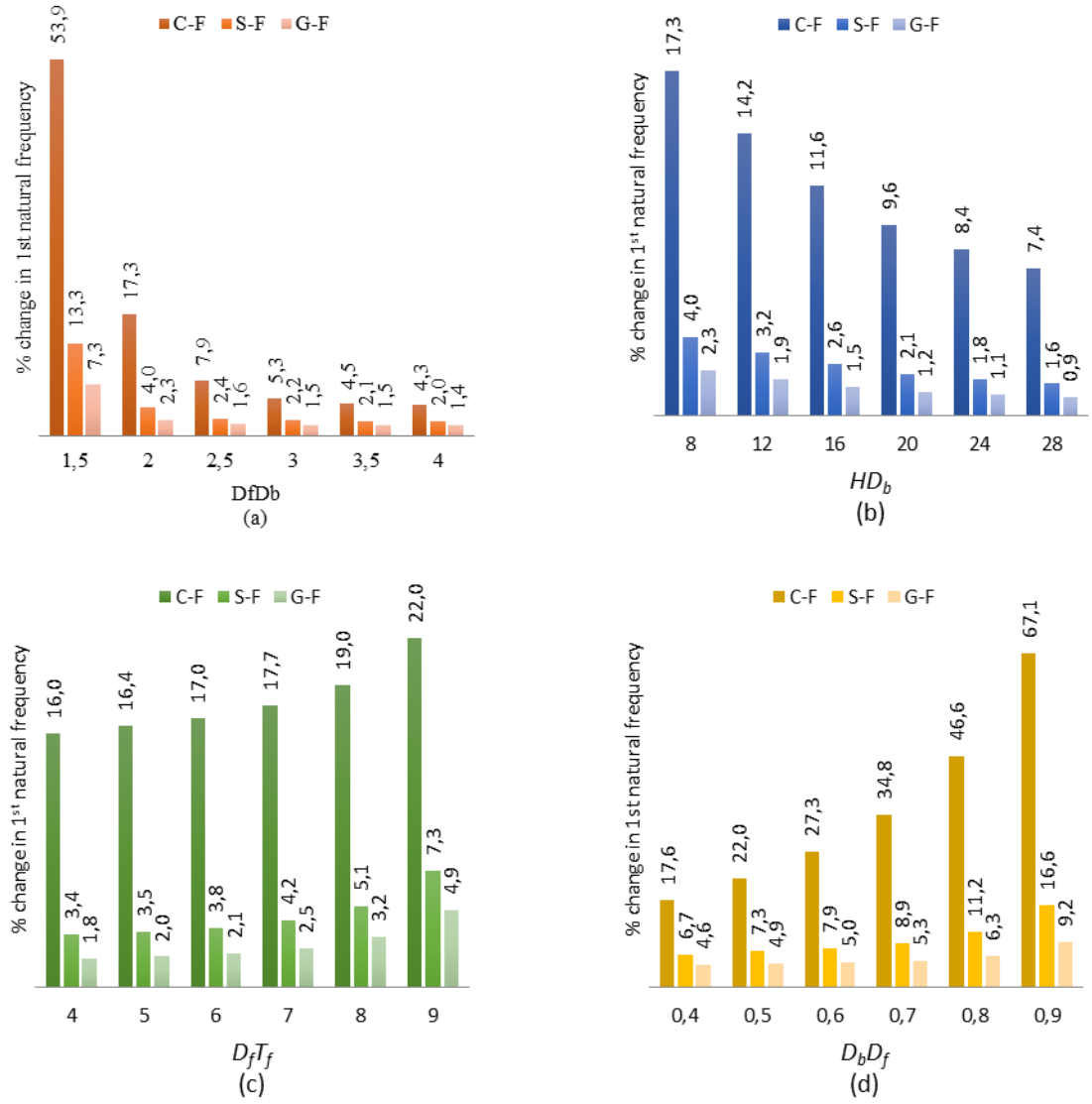

Figure 6. Frequency change for various soil types and geometrical parameters

The percentage differences between 1st natural frequencies of towers with clayey elastic soil and fixed base foundation (C-F), sandy elastic soil and fixed base (S-F), and gravel elastic soil and fixed base (G-F) conditions for different various geometrical parameters are depicted in Figure 6. All positive percentage changes indicate that the fundamental frequencies of the wind towers founded on elastic soils are smaller than those of towers with fixed base. Also, it can be seen that the largest difference occurs between clayey soil and fixed base conditions for each different geometrical parameters. The percentage changes for elastic and fixed conditions decrease with increasing D_fD_b and HD_b ratios while they increase with increasing D_fT_f and D_bD_f ratios. The influence of soil-structure interaction on the frequency decreases when the diameter of the tower foundation becomes larger and the tower height gets higher. Reduction in foundation thickness increases the effect of soil-structure interaction. On the contrary, the soil-structure interaction has smaller effect on the frequency when the bottom diameter of the tower becomes smaller. As a result it can be concluded that the soil-structure interaction has a major influence on the fundamental frequency of wind tower. Especially, soft soils with low dynamic shear modulus such as clay results with the largest reduction in the frequency.

The ten lowest representative mode shapes including extensional and torsional modes of the wind turbine tower with foundation fixed at the base are depicted in Figure 7. Since the tower is a slender structure the earlier modes reflects beam-like behaviors which are critical in earthquake analysis for horizontal ground motion. Moreover, beyond the 15th mode the mode shape produces undulating deformations around the cross section without translation. When the wall thickness of the tower becomes thinner the undulating modes occur earlier.

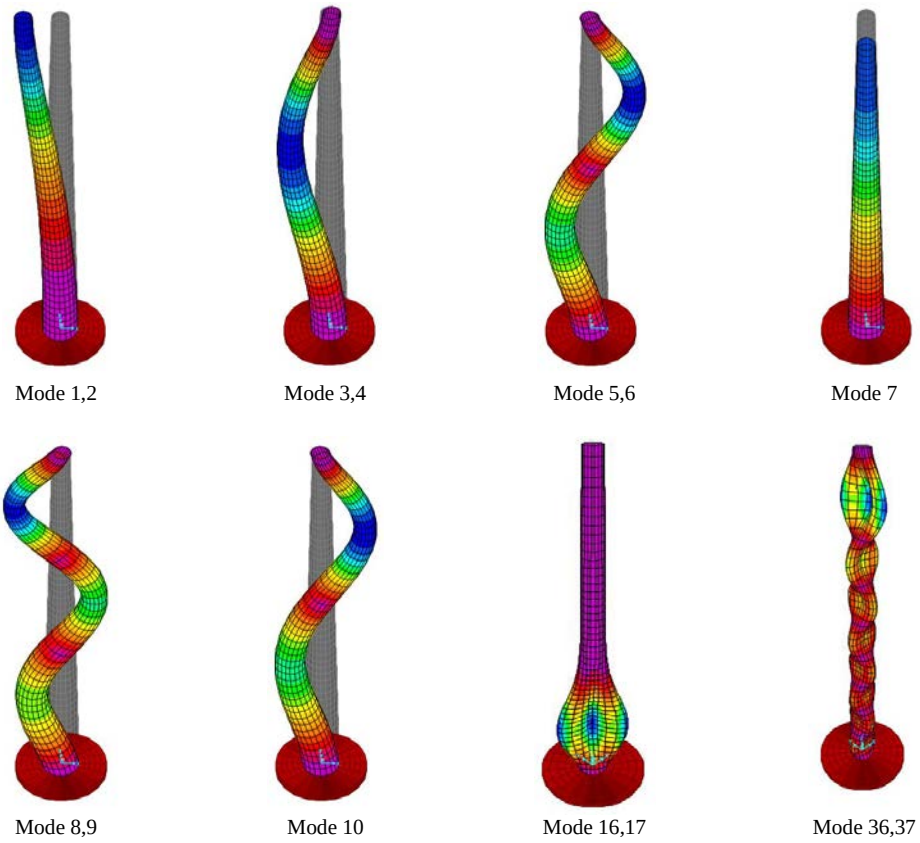

Figure 7. Representative mode shapes for fixed foundation base

6. CONCLUSIONS

A parametric study is conducted to investigate the fundamental frequency characteristics of a wind turbine tower structure with various geometrical parameters considering soil-structure interaction. The geometrical parameters altered in the analyses are top and bottom wall diameters and thicknesses, the height of tower, the diameter and thickness of foundation. Moreover, the soil-structure interaction is taken into account as elastic soil foundation represented by linear elastic springs with different stiffness properties depending on dynamic shear modulus of soil type. In structural analysis model the nacelle-rotor turbine system is considered as rigid non-rotating distributed mass at the top of the tower and the top section of the tower is prevented for undulating deformation around the circumference. The finite element models are obtained in structural analysis software SAP2000 practically with the help of OAPI (Open Application Programming Interface) feature of SAP2000. The OAPI feature contains particular functions employed in a code developed in MATLAB to supply two-way data flow between SAP2000 and MATLAB during pre and post processing. As a result of the numerical analyses it can be stated that the tower height and bottom diameter have major influences on the fundamental natural frequency of the tower. The tower wall thicknesses also influences the frequency, but the effect is not as dominant, since the stiffness increase due to a larger wall thickness is offset by the resulting higher mass of the tower. Additionally, it can be noted that the soil-structure interaction has a critical effect in reducing the fundamental frequency of the wind tower. Finally, it can be concluded that the fundamental frequency of the wind tower structure can be kept away from the excitation frequencies of the turbine to avoid dynamic amplifications by altering particular geometrical parameters and considering soil-structure interaction for reliability.

REFERENCES

[1]. I. Lavassas, G. Nikolaidis, P. Zervas, E. Efthimiou, I. N. Doudoumis, and C. C. Baniotopoulos, “Analysis and design of the prototype of a steel 1-MW wind turbine tower,” *Engineering Structures*, vol. 25, pp. 1097-1106, 2003.

[2]. N. Bazeos, G. D. Hatzigeorgiou, I. D. Hondros, H. Karamaneas, D. L. Karabalis, and D. E. Beskos, “Static, seismic and stability analyses of a prototype wind turbine steel tower,” *Engineering Structures*, vol. 24, pp. 1015-1025, 2002.

[3]. W. van Zyl and G. van Zijl, “Dynamic behavior of normally reinforced concrete wind turbine support structures,” *Journal of the South African Institution of Civil Engineering*, vol. 57, pp. 38-44, 2015.

[4]. Y. Hu, C. Baniotopoulos, and J. Yang, “Effect of internal stiffening rings and wall thickness on the structural response of steel wind turbine towers,” *Engineering Structures*, vol. 81, pp. 148-161, 2014.

[5]. H. M. Negm, and K. Y. Maalawi, “Structural design optimization of wind turbine towers,” *Computers and Structures*, vol. 74, pp. 649-666, 2000.

[6]. P. E. Uys, J. Farkas, K. Jarmai, and F. van Tonder, "Optimization of a steel tower for a wind turbine structure," *Engineering Structures*, vol. 29, pp. 1337-1342, 2007.
[7]. N. D. Lagaros, and M. G. Karlaftis, "Life-cycle cost structural design optimization of steel wind towers," *Computers and Structures*, 2015, http://dx.doi.org/10.1016/j.compstruc.2015.09.013
[8]. SAP2000, Analyses reference manual, in: Computers and Structures Berkeley, California, 2011.
[9]. G. Gazetas, "Analysis of machine foundation vibrations: state of the art," *Soil Dynamics and Earthquake Engineering*, vol. 2, pp. 2-43, 1983.
[10]. C. Indrajit, and P. D. Shambhu, "Dynamics of structure and foundation," USA; CRC Press, 2009.

ICENS
INTERNATIONAL CONFERENCE ON ENGINEERING AND NATURAL SCIENCES
24-28 May 2016 /Sarajevo

Optimum Design of Space Truss Bridges Including Soil-Structure Interaction

Ali I. Karakas[1], Musa Artar[2], Korhan Ozgan[3], Ayse T. Daloglu[4]

Abstract

In the present study the influence of soil-structure interaction on the optimum designs of steel space truss bridges are investigated. The optimization algorithm utilized in the design process is the metaheuristic harmony search (HS) method. The subsoil foundation is modeled using the three-parameter Vlasov elastic foundation model. This model takes the shear behavior of the soil into account unlike one-parameter Winkler model. Structural analyses required in the optimization algorithm are conducted in the structural analysis software SAP2000. The interaction between optimization algorithm coded in MATLAB and SAP2000 is provided with the help of OAPI (Open Application Programming Interface) feature of SAP2000. For this purpose, a code is developed in MATLAB utilizing OAPI functions to provide two-way data flow between SAP2000 and optimization algorithm in all optimization processes. The optimum designs are carried out by selecting suitable sections from a specified list including W-profiles taken from American Institute of Steel Construction (AISC). The stress limitations in accordance with the provisions of AISC-ASD (American Institute of Steel Construction-Allowable Stress Design), and the maximum lateral displacement are applied to steel space truss bridges as design constraints. The optimal design process inwhich the design objective is the minimization of the weight of the bridges is performed for the cases with and without subsoil effect. As a result of the optimization process it can be stated that the consideration of soil-structure interaction results with heavier space truss bridges.

Keywords: *Harmony search, Vlasov foundation, Open application programming interface, Space truss bridge*

1. INTRODUCTION

Harmony Search Algorithm, one of the basic metaheuristic techniques, mimics musical harmony procedures. This algorithm has been applied for the purpose of structural optimizations by many researchers in recent years.

Lee and Geem [1] substantially studied a basic study of a new structural optimization based on harmony search algorithm. The algorithm is commonly used for truss or frame structure optimization by several researchers ([2]-[6]). Morover, Carbas et al. [7] studied optimum design of cold-formed open thin-walled sections using harmony search algorithm. Carbas and Saka [8] focused on efficiency of improved harmony search algorithm for solving engineering optimization problems.

In the literature, there are many studies on optimum design of truss structures but fewer studies on truss bridges. Moreover, it is hard to see studies on three dimensional truss bridges including soil-structure interaction. Therefore, in the present study, optimum designs of two different truss bridges are carried out with and without soil-structure interaction. A program is coded in MATLAB [9] software incorporated with SAP2000-OAPI (Open Application Programming Interface) [10].

1.1 HARMONY SEARCH ALGORITHM

An Harmony Search Algorithm mimics musical harmony procedures and this method consists of three basic steps.

-Harmony memory matrix is initialized first as seen in Equation 1. It includes a specified number of solutions. Each row represents a steel design comprised of design variables selected a profile list. In this study, the specified profile list includes 128 W profiles taken from American Institute of Steel Construction (AISC).

$$H=\begin{bmatrix} x_1^1 & x_2^1 & .. & x_{n-1}^1 & x_n^1 \\ x_1^2 & x_2^2 & .. & x_{n-1}^2 & x_n^2 \\ .. & .. & .. & .. & .. \\ x_1^{HMS-1} & x_2^{HMS-1} & .. & x_{n-1}^{HMS-1} & x_n^{HMS-1} \\ x_1^{HMS} & x_2^{HMS} & .. & x_{n-1}^{HMS} & x_n^{HMS} \end{bmatrix} \begin{matrix} \rightarrow \\ \rightarrow \\ \rightarrow \\ \rightarrow \\ \rightarrow \end{matrix} \begin{matrix} \varphi(x^1) \\ \varphi(x^2) \\ .. \\ \varphi(x^{HMS-1}) \\ \varphi(x^{HMS}) \end{matrix} \quad (1)$$

- Each row of harmony memory matrix is evaluated and their corresponding objective function values are determined. The rows in the harmony memory matrix are sorted according to these values. First row indicates the best solution in the harmony matrix.

- New harmony memory matrix is improvised. A new solution is carried out by selecting each design variable from either harmony memory matrix or the entire section list depending on Harmony Memory Considering Rate (*HMCR)* which is between 0 and 1. The new value of the design variable selected from harmony memory matrix is checked whether this value should be pitch-adjusted or not depending on Pitch Adjustment Ratio (PAR). The detailed information about harmony search algorithm can be obtained from [1].

1.2 DESIGN PROBLEM

The minimum weight design of space truss bridge is defined as below,

$$\min W = \sum_{k=1}^{ng} A_k \sum_{i=1}^{nk} \rho_i L_i \qquad (2)$$

where *W* is the weight of the frame, A_k is cross-sectional area of group *k*, ρ_i and L_i are density and length of member *i*, *ng* is total number of groups, *nk* is the total number of members in group *k*.

The design constraints used in this study are presented as below,

- The stress constraints taken from AISC–ASD (1989) [11]
- The displacement constraints (length/1000)
- The constraints for mid-span deflection of floor beams (length/1000)

2. THREE-PARAMETER VLASOV ELASTIC FOUNDATION MODEL

Subsoil reaction of a structure resting on a two-parameter elastic foundation is given by

$$q_z = kw - 2t\Delta^2 w \qquad (3)$$

depending on the displacement function *w* of the subsoil surface. *k* and *2t* in the expression above are the subgrade reaction modulus and soil shear parameter respectively and defined as

$$k = \int_0^{H_s} \frac{E_s(1-\upsilon_s)}{(1+\upsilon_s)(1-2\upsilon_s)} \left(\frac{\partial\varphi(z)}{\partial z}\right)^2 dz \qquad (4)$$

$$2t = \int_0^{H_s} G_s \varphi(z)^2 \, dz \qquad (5)$$

where H_s is subsoil depth, υ_s and G_s are Poisson's ratio and the shear modulus of subsoil respectively. The subgrade reaction, *k*, and soil shear parameter, *2t*, are considered to be constant in the classical two-parameter foundation models like Pasternak Model, Hetenyi Model and Vlasov Model etc. The drawback of these models lies in the difficulty of establishing the soil parameters, *k* and *2t*. Vallabhan et al. [12] introduced another parameter, γ, to characterize the vertical deformation profile within the subsoil, and called the model as Modified Vlasov Model. The advantage of this model is the elimination of the necessity to determine the values of soil parameters, *k* and *2t*, arbitrarily because these values can be computed as a function of a new parameter, γ using an iterative procedure.

$\varphi(z)$ in Eqs. (4, 5) is the mode shape function describing the vertical displacement variation through the subsoil. The values of $\varphi(z)$ are stipulated such that $\varphi(0)=1$ and $\varphi(H_s)=0$. Mode shape function $\varphi(z)$ is given with respect to the subsoil surface vertical deformation parameter (γ) as below.

$$\varphi(z) = \frac{sinh\ \gamma\left(1-\frac{z}{H_s}\right)}{sinh\ \gamma} \tag{6}$$

where γ is calculated using the equation below.

$$\left(\frac{\gamma}{H_s}\right) = \frac{(1-2\upsilon_s)}{2(1-\upsilon_s)} \frac{\int_{-\infty}^{+\infty}\int_{-\infty}^{+\varphi} (\nabla w)^2\, dxdy}{\int_{-\infty}^{+\infty}\int_{-\infty}^{+\varphi} w^2 dxdy} \tag{7}$$

The important point here is that the modulus of subgrade reaction, *k*, and the soil shear parameter, *2t*, are both dependent on the mode shape function $\varphi(z)$ and the depth of the subsoil, H_s, as can be seen in Equations 4 and 5. Furthermore the value of the vertical deformation parameter within the subsoil, γ, varies with the subsoil surface displacement and the subsoil depth. Therefore, the solution of this complex soil-structure interaction problem can be performed using an iterative technique.

For this purpose, a computing tool is developed using MATLAB to model bridge in SAP2000 software considering soil-structure interaction. As is known, the modulus of subgrade reaction, *k*, which is the only soil parameter used in Winkler Model is represented by elastic area springs in SAP2000. However the interaction between springs is ignored due to the assumption that each spring acts independently. The interaction between springs is taken into account using subsoil shell elements connecting the top of the springs. Soil shear parameter, 2*t*, is appointed as shear modulus material property of subsoil shear element.

3. SOLUTION PROCEDURE

In the present study, a program is developed in MATLAB interacting with SAP2000-OAPI. All the steps used for MATLAB-SAP2000 OAPI interaction and the HS algorithm methods are listed as below,

1) Read input data and create harmony matrix (HM) randomly in MATLAB
2) Decode each row in HM
3) Calculate soil parameters *k* and 2*t* and transfer from MATLAB to SAP2000
4) Select corresponding sections from available list in SAP2000
5) Solve the system and calculate the displacements of the soil surface
6) Transfer the results from SAP2000 to MATLAB
7) Calculate the new value of soil parameters
8) Is the difference between new and previous value of third soil parameter within a prescribed tolerance, if no go to step 3.
9) Determine objective function values of each row in the harmony memory matrix.
10) Was the criterion of convergence provided? (if it is yes, write results)
11) Create the next harmony memory matrix with *HMCR* and *PAR* and go to 2th step

4. DESIGN EXAMPLES

Harmony Search Algorithm is used to obtain optimum designs of two different space truss bridges with and without consideration of soil-structure interaction. Design variables are taken from a specified section list including 128 W profiles in accordance with AISC. Modulus of elasticity is E=200 GPa, yield stress is f_y=250 MPa, material density is ρ=7.85 t/m^3. Harmony memory size in harmony matrix was selected as 20 for both the examples.

4.1 172-bar Space Truss Bridge

172-bar space truss bridge model is depicted in Figure 1. All members are categorized into eight groups as seen in Figure 2. The member group 8 shows floor beams. A single design loading is considered such that vertical loading including traffic and dead loads are on each floor beams as 100 kN/m. The maximum displacement of all nodes is 7.2cm (length/1000) and mid-span deflection of floor beams is restricted to 0.7 cm (length/1000).

The soil properties are considered such that modulus of elasticity is equal to 68950 kN/m^2 (medium dense soil), Poisson ratio is 0.25, and depth of the soil is *Hs*=15 m. Table 1 shows soil parameters and Table 2 shows the optimum results for both cases

and the design histories of both solutions are shown in Figure 3. Figure 4 shows optimum profiles and soil surface settlements of the truss bridge.

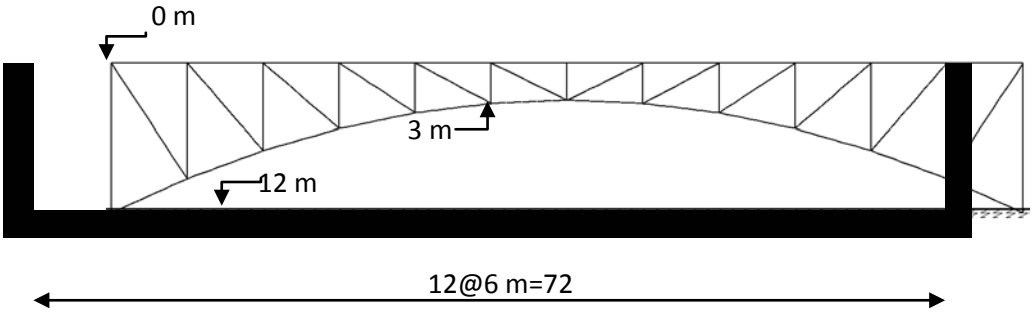

a) Side view

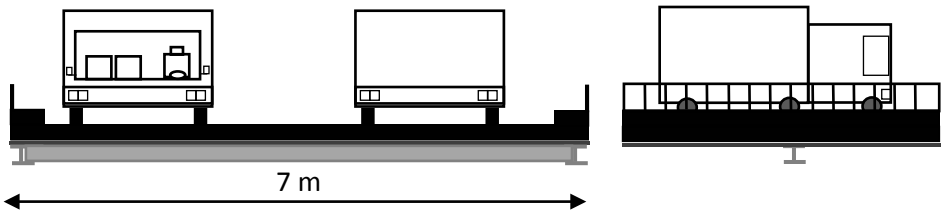

b) Traffic flow on floor beam

Figure 1. 172-bar space truss bridge

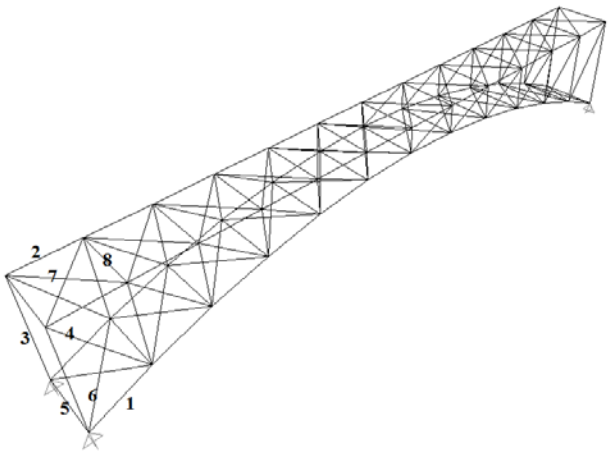

Figure 2. Member groups

Table 1. Soil parameters for 172-bar space truss bridge on elastic foundation

γ	k (kN/m^3)	2t (kN/m)
1.32323	5793.038	112221.219

Table 2. Optimum designs of 172-bar space truss bridge

Group No	Without soil-structure interaction	With soil-structure interaction
1	W44X224	W14X257
2	W10X15	W12X16
3	W10X26	W8X31
4	W10X15	W12X19
5	W10X15	W5X16
6	W8X15	W6X15
7	W8X15	W8X15
8	W40X167	W40X167
Weight, kN	968.32	1068.53
Max. disp.,cm	7.19641	6.81
Max. midspan deflection in floor beams, cm	0.316	0.316
Max. settlement of the soil surface, cm	-	-0.51

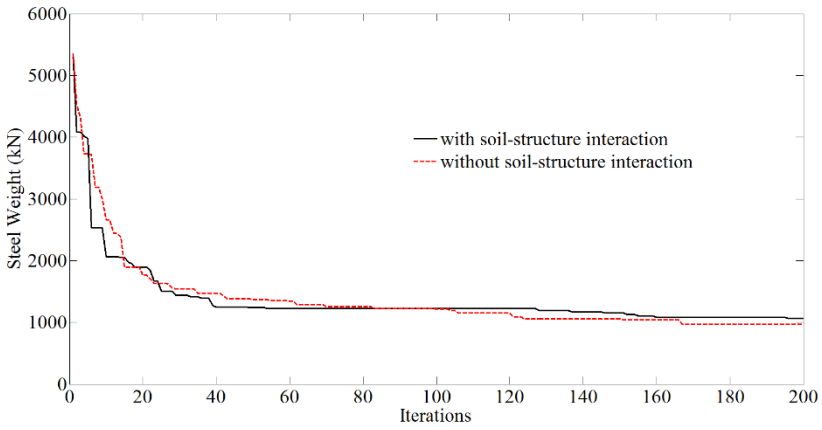

Figure 3. Design histories of 172-bar space truss bridge

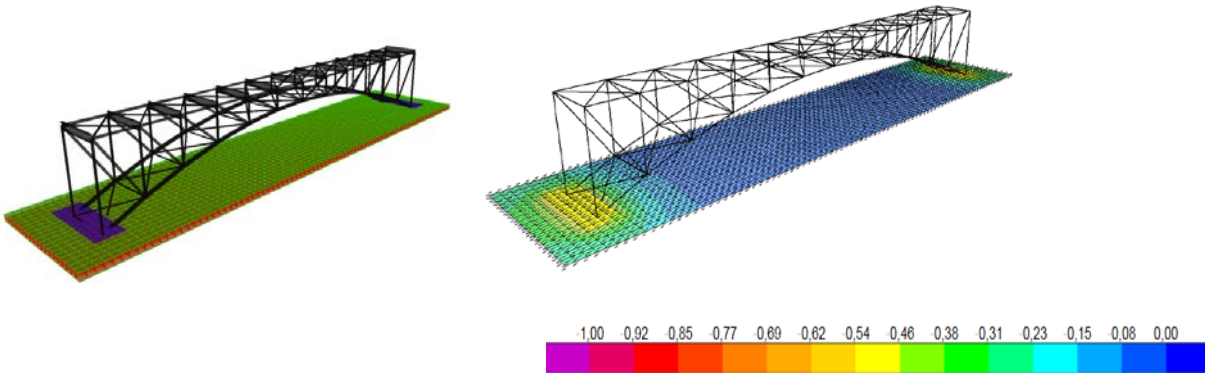

a) Optimum profiles b) soil surface settlement of the space truss (cm)

Figure 4. Optimum profiles and soil surface settlements of the truss

It is observed from Table 2 that the minimum weight of space truss bridge without soil-structure interaction is 968.32 kN which is nearly 10% lighter than the minimum value 1068.53 kN calculated for the case with soil-structure interaction. This table also shows that maximum displacement 7.196 cm is very close to the limit value of 7.2 cm. Therefore, these constraints play active roles in optimum designs of the space truss bridge.

4.2 396-bar Space Truss Bridge

Three dimensional view of 396-bar space truss bridge is seen in Figure 5. All members are collected into twelve groups presented in Figure 6. The member group 12 shows floor beams. The detailed information about loading and displacement constraint are mentioned in the previous example.

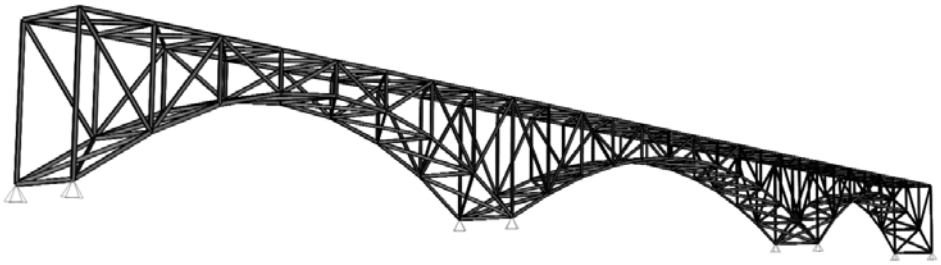

Figure 5. 3d view of 396-bar space truss bridge

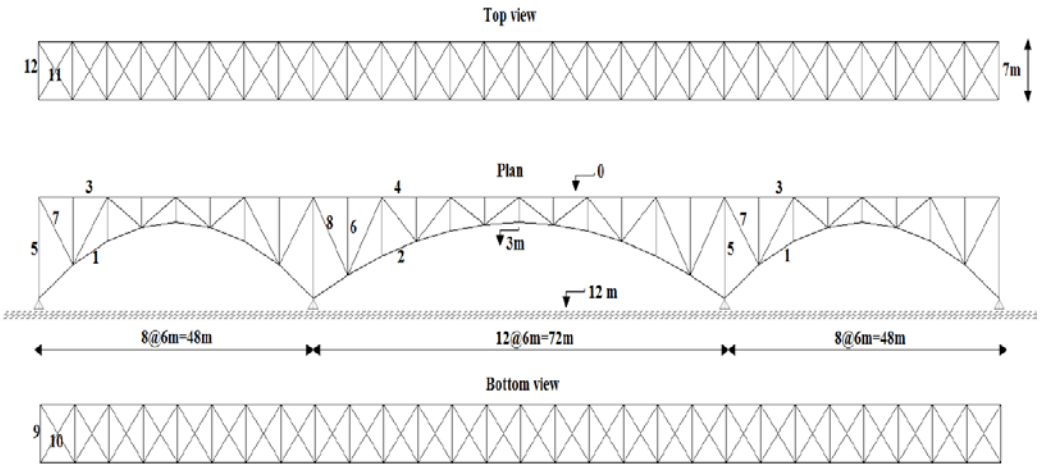

Figure 6. Member groups

The material properties of the soil are considered as the ones in previous example and soil parameters are obtained as presented in Table 3. Table 4 shows the optimum results for the bridge with and without soil effect. Design histories of both solutions are shown in Figure 7. Figure 8 shows soil surface settlements of the truss bridge.

Table 3. Soil parameters for 396-bar space truss bridge on elastic foundation

γ	k (kN/m^3)	2t (kN/m)
1.70940	6162.291	100237.260

As seen in Table 4, minimum weight of 396-bar space truss bridge is 2093.37 kN which is nearly 8.6% heavier than the minimum weight of the bridge without soil-structure interaction. This indicates that soil effects are critical for the optimum design of truss bridge structures. Figure 8 presents the soil surface settlements of the structure where maximum surface settlement value is -0.74 cm.

Table 4. Optimum designs of 172-bar space truss bridge

Group No	**Without soil-structure interaction**	**With soil-structure interaction**
1	W16X89	W24X94
2	W40X167	W40X244
3	W10X26	W18X35
4	W18X35	W16X31
5	W18X35	W16X36
6	W12X22	W14X26
7	W10X22	W10X22
8	W10X26	W12X22
9	W6X20	W12X19
10	W12X19	W10X15
11	W6X15	W10X15
12	W40X167	W40X167
Weight, kN	1927.32	2093.37
Max.disp.for spans 1 and 2, cm	3.15 and 6.73	2.94 and 5.94
Max.mid-span deflection cm	0.316	0.316
Max.settlement of soil surface, cm	-	-0.74

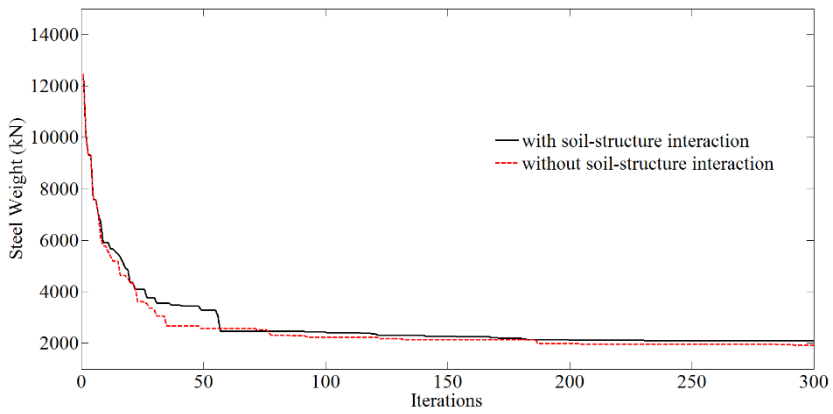

Figure 7. Design histories of 396-bar space truss bridge

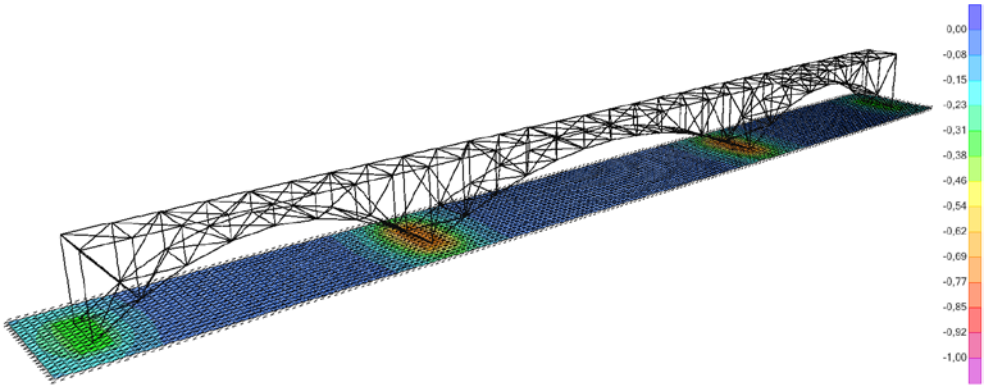

Figure 8. *Soil surface settlements of the truss bridge (cm)*

5. CONCLUSIONS

This paper presents an application of Harmony Search Algorithm for optimum designs of space truss bridge with and without soil-structure interaction. Stress constraints obeying AISC-ASD [11], the constraints of maximum displacement for all nodes and maximum mid-span deflection for floor beams are imposed on the problems. To conduct all analyses, a program is coded in MATLAB interacting with SAP2000-OAPI. The results obtained from the optimum solutions show that soil effects play active roles in designs. These effects increase the minimum weights as 10% and 8.6% for the first and the second examples investigated in the present study, respectively.

REFERENCES

[1]. K. S. Lee, and Z. W. Geem, "A new structural optimization method based on the harmony search algorithm," *Computer and Structures*, vol. 82, pp. 781–798, 2004.
[2]. S. O. Degertekin, M. S. Hayalioglu, and H. Gorgun, "Optimum design of geometrically non-linear steel frames with semi-rigid connections using a harmony search algorithm," *Steel and Composite Structures, International J*ournal, vol. 9, pp. 535-555, 2009.
[3]. S. O. Degertekin, and M. S. Hayalioglu, "Harmony search algorithm for minimum cost design of steel frames with semi-rigid connections and column bases," *Structural* and *Multidisciplinary Optimi*zation, vol. 42, pp. 755-768, 2010.
[4]. S. O. Degertekin, M. S. Hayalioglu, and H. Gorgun, "Optimum design of geometrically nonlinear steel frames with semi-rigid connections using improved harmony search method," *Mühendislik Dergisi, Dicle University, Department of Engineering*, vol. 2, pp. 45-56, 2011.
[5]. M. P. Saka, "Optimum design of steel sway frames to BS5950 using harmony search algorithm" *Journal of Constructural* and *Steel Research*, vol. 65, pp. 36-43, 2009.
[6]. V. Togan, A. T. Daloglu, and H. Karadeniz, "Optimization of trusses under uncertainties with harmony search," *Structural Engineering and Mechanics*, vol. 37, pp. 543-560, 2011
[7]. S. Carbas, I. Aydogdu, and M. P.Saka, "Optimum design of cold-formed open thin- walled sections using harmony search algorithm" 9th International Congress on Advances in Civil Engineering, 27-30 September 2010, Karadeniz Technical University, Trabzon, Turkey, 2010.
[8]. S. Carbas, and M. P. Saka, "Efficiency of improved harmony search algorithm for solving engineering optimization problems," *International. Journal of Optimization in Civil Eng*ineering, vol. 3, pp. 99-114, 2013.
[9]. MATLAB, The Language of Technical Computing, The Mathworks Inc.; Natick, MA, USA, 2009.
[10]. SAP2000, Integrated Finite Elements Analysis and Design of Structures. Computers and Structures, Inc, Berkeley, CA, 2008.
[11]. AISC – ASD, Manual of Steel Construction: Allowable Stress Design, American Institute of Steel Construction, Chicago, IL, USA, 1989.
[12]. C. V. G. Vallabhan, W. T. Straughan, and Y. C. Das, "Refined model for analysis of plates on elastic foundation", *Journal of Engineering Mechanics*, vol. 117, pp. 2830-2844, 1991.

ICENS
INTERNATIONAL CONFERENCE ON ENGINEERING AND NATURAL SCIENCES
24-28 May 2016 /Sarajevo

Design and Development of Wireless Building Lighting Management

Seyit Alperen Celtek[1], Hakki Soy[2]

Abstract

Lighting management systems play a significant role on energy consumption of buildings, especially commercial and public buildings like shopping malls, universities and hospitals. The aims of building lighting control system are increasing people's comfort and decreasing energy consumption. The development of the wireless technology provides opportunity for simplification in wiring requirements. This paper explores the design and development of a wireless sensor and actuator based lighting management systems that use a protocol providing minimum energy consumption for the lighting management process. A case study is simulated for a university building by using Simulink. The cost and power consumption results of proposed lighting controlling are compared with conventional systems.

Keywords: *Building Lighting Management, Smart Lighting, Wireless Sensor and Actuator Networks.*

1. INTRODUCTION

The potential of energy saving in building can describe with massive numbers because of building energy consumption is more than 40% of the total energy consumption [1]. Lighting accounts for a high percentage of electricity consumption in many countries. In Turkey, lighting accounts for nearly 15% of the electrical energy consumed [2]. The efficient lighting provides visual comfort and budgetary control. It must be done in compliance with the requirements of good lighting and without reducing the quality of the lighting. There are fundamentally two ways of reducing the consumption and costs of energy: using high efficient light bulbs and the lighting control systems. An efficient LED luminaires instead of conventional lighting bulbs could decreases energy consumption by up to % 80. Meanwhile, the lighting management systems are a key technology that will make it possible to decrease the energy consumption of lighting without impeding comfort goals.

The theoretical background and approach of it is based upon a simple energy consumption Formula. The general formula for calculating energy consumption of lighting equipments is shown below;

$$W = P \times T \quad Watt\ Hour\ (Wh) \qquad (1)$$

Where P is the power of the lambs (Watt, W) and t is the operating time (Hours, h). Within this scope,there are two ways for energy saving, reducing power and operation time of lighting. Power is directly proportionate to the luminosity of the lamb. Luminosity sensor and Light depended resistor (LDR) or photocell use for minimum luminosity value that desired comfort level. LDR is a very useful, especially in light/dark sensor circuits. Normally, the resistance of an LDR is very high, for instance, when a light level is 10 lux, the resistance value is 1 MΩ. They are illuminated with light and the light level reach up to 1000 lux, resistance drops dramatically to 400 Ω [3] . Luminosity sensor is an electronic component that is light to digital converters.

Luminosity sensors are useful for general purpose light sensing implementation due to transform the light intensity to a digital signal output [4]. The luminance data from luminosity sensor and LDR is significant for microprocessor -is a computer processor on a microchip. Microprocessor process and compares luminance data and desired brightness level. Then, it controls and commands drivers of the lighting components provide efficient lighting.

Automatic lighting management and smart controlling has been developing as a trend. Each and every day, building lighting management becomes stronger because of considering economic advantages (energy saving) and improvement in quality of life (comfort). Building lighting management is the integrated system that monitor, control and analyze compatible electrical devices in a building. Over the past decade, the researchers have been working on building lighting control systems. Using

[1] *Corresponding author: Karamanoglu Mehmetbey University, Department of Energy Systems Engineering, 70100, Karaman, Turkey.* salperenceltek@kmu.edu.tr

[2] *Necmettin Erbakan University, Department of Electric and Electronic Engineering, Konya,Turkey* hakkisoy@konya.edu.tr

efficient electric lighting with luminaire ballasts, sensors and controllers could reduce energy consumption between 17% to 32 [5]. Automatic lighting control systems decrease operation time of lighting equipments based on various several factors like occupancy, daylight, time of day and luminance information [6]. Especially, office building lighting systems consume more energy than houses. Higuera et al. have worked on hybrid smart lighting systems for buildings as shopping malls and office building. This intelligent system can detect natural lighting levels. The natural lighting level is a significant factor for the dim artificial lighting levels. Their results have shown that nearly 23% of overall energy saving is possible in the lighting [7].

A wireless sensor and actuator networks (WSANs) are a new generation of control systems that can react promptly and appropriately to events as they occur. The WSANs are the last version of the wireless sensor networks (WSNs). The WSN is a group of sensors that gather information about their environment conditions. WSN applications were the one of the trend topics of the last decade. The main difference between WSAN and WSN is the control function. The actuator nodes have ability to drive appliances and trigger the devices, while the sensor nodes just collect data from their surroundings. All nodes can process data and transfer them to a sink node through wireless path [8].

In our study, we present a lighting management system based on WSAN. The proposed system monitor and control lighting units to maintain more comfortable indoor conditions. The remainder of the paper is organized as follows: Section 2 briefly describes our system design and the communication framework of clustered WSAN architecture. The simulation results of the proposed lighting management are presented in Section 3. In the last section, the paper is being concluded with a brief summary about the research.

2. THE SYSTEM DESIGN AND COMMUNICATION FRAMEWORK

The system model can be considered as an automated WSAN architecture with single-tier, single hop cluster-tree topology as shown in Figure 1.The proposed lighting management system consists of three main parts; the sensor nodes (SNs), the actuator nodes (ANs) and the root node (RN) which is top of the central data management. In this study, we apply the proposed system to the university building. Each room is designed as a cluster which has two SNs and a AN. The SNs and ANs must place in appropriate locations of the room.

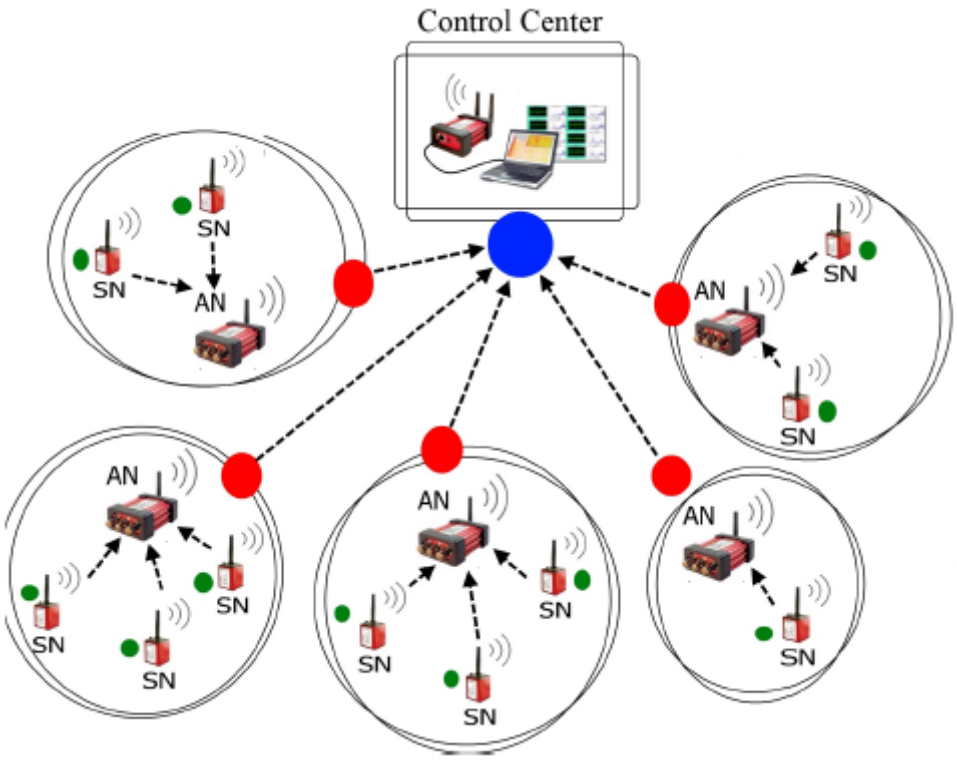

Figure 1. The proposed WSAN based building lighting management system model.

In the proposed model, each AN performs as a leader, which is also called the cluster head (CH). Each room has an occupancy sensor and a luminosity sensor. Cluster heads receive information about occupancy and luminosity of the space from SNs of the room. As mentioned above, the SNs just collect raw information about environment periodically and not process. But for the communication, these raw data must be processed and filtered. The other significant mission of the cluster head is data processing. The data processing and filtering is crucial for the data aggregation to actuate the required action as dim the artificial lighting. The cluster heads transfer the data to the root node which is control center. In smart systems, the

management system is accessible from virtually anywhere in the world via the Internet. Because of that the root node connected to the Internet through GSM module or an Ethernet adapter.

3. THE SIMULATION RESULTS

The simulation of the conventional lighting model is shown in Figure 2. The inputs of the simulation are average values which were collected different rooms. There are two lighting armature is in each office room. The hour of the work is 8 hours and the lighting equipment is on during the work hours. The input parameters of the simulation are given below (Table 1);

Table 1. The input parameters

Power of the Lighting Equipment (One Room):	140x2=280 watt
Time Period:	8 Hours
Number of the Office Room in the Building:	120
Electric Unit Price	0,213428 TL / 1 kW

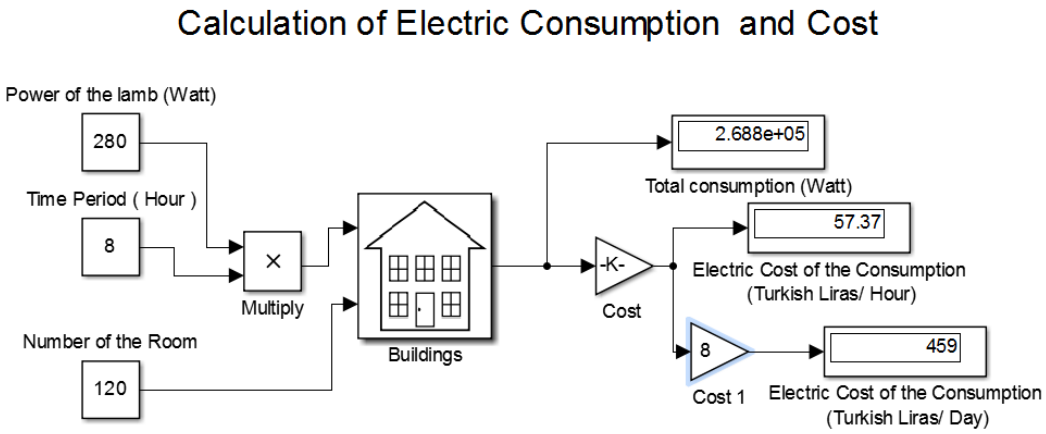

Figure 2. Conventional Lighting Systems with Outputs

The simulation model of proposed sensor node is shown in Figure 3. Each sensor node has a TSL2561 Digital luminosity/lux/light sensor and PIR motion sensor.the The desired luminance value can vary depending on person and office room. Actuator node compares the desired luminance value and luminosity value, and then calculate the needed of the artificial lighting (Figure 4).

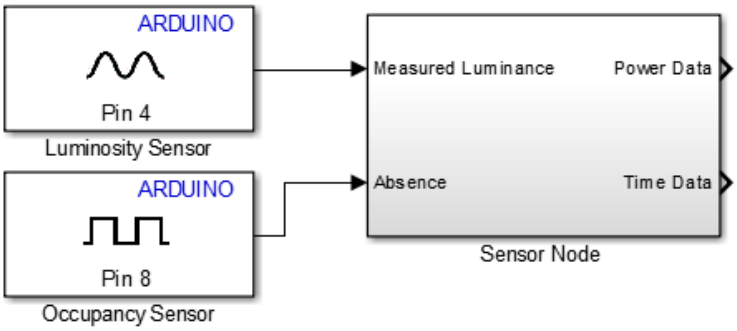

Figure 3. The simulation model of The Sensor Node.

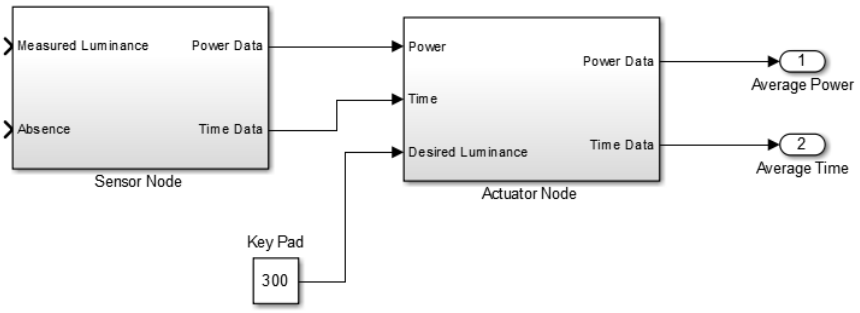

Figure 4. The simulation model of The Actuator Node.

The simulation results are total power consumption of lighting equipments, electric cost of the hourly and daily consumption. As can be seen from the figure 2 and figure 5, the proposed lighting management system can save approximately % 55 of energy and money.

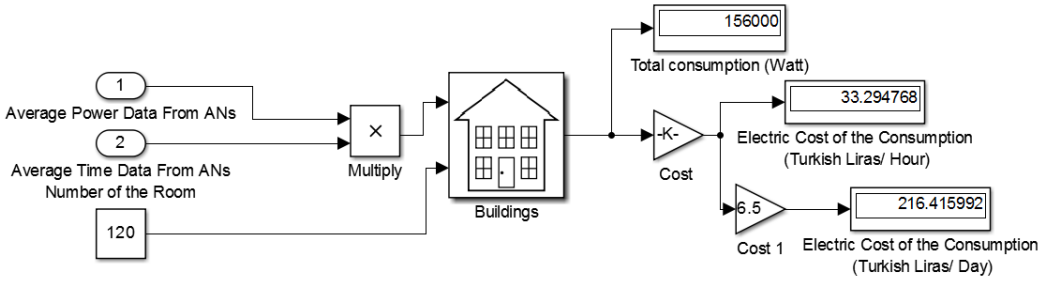

Figure 5. Proposed Lighting Systems with Outputs

4. CONCLUSION

In this study, we presented a building lighting management based on WSAN. We have simulated our system model with actual data for university building. This paper clearly showed that energy saving is possible without reducing the quality of the lighting by wireless management system. In addition to these, the need for human intervention is minimized because of WSAN does not require the deployment of wires. The results of this research suggest that the increase in lighting management usage has led to a sharp decrease in energy consumption.

REFERENCES

[1] American Society of Heating Refrigerating and Air-Conditioning Engineers, *2011 ASHRAE Handbook - HVAC Applications*. 2011.

[2] P. Waide and S. Tanishima, “Light ’ S Labour ’ S Lost,” 2006.

[3] R. Components, “Light dependent Resistors Datasheet,” *RS Compon.*, vol. 12, no. 651, 1997.

[4] A. Human, E. Response, U. Upper, L. Threshold, P. A. Gain, P. D. Mode, and R. Compliant, “Tsl2560, tsl2561 light-to-digital converter,” no. November, pp. 1–42, 2009.

[5] C. Aghemo, L. Blaso, and A. Pellegrino, “Building automation and control systems: A case study to evaluate the energy and environmental performances of a lighting control system in offices,” *Autom. Constr.*, vol. 43, pp. 10–22, 2014.

[6] M. A. U. Haq, M. Y. Hassan, H. Abdullah, H. A. Rahman, M. P. Abdullah, F. Hussin, and D. M. Said, “A review on lighting control technologies in commercial buildings, their performance and affecting factors,” *Renew. Sustain. Energy Rev.*, vol. 33, pp. 268–279, 2014.

[7] J. Higuera, W. Hertog, M. Perálvarez, and J. Carreras, “Hybrid smart lighting and climate control system for buildings,” *IET Conf. Futur. Intell. Cities*, pp. 1–5, 2014.

[8] S. A. C, “An Application of Building Automation System based on Wireless Sensor / Actuator Networks.”

ICENS
INTERNATIONAL CONFERENCE ON ENGINEERING AND NATURAL SCIENCES
24-28 May 2016 /Sarajevo

The Best Site Determination of Solar Farms: A case study

Hasan Eroglu[1]

Abstract

Today, renewable energy sources are one of the most important and indispensable part of our lives. Especially the number of solar energy applications are raising every day all over the world. With the increasing of the solar energy farms' applications around the world, the site selection problem of the solar energy farms is gaining importance every day. In some cases ignoring an important criteria will negatively affect environment, social life or cost of the project.

The objective of this research is determining the best place for solar farms by proposing some crucial criteria, weighting these criteria and making all the data processing of the criteria on a sample study area. The weighting of the criteria is made via Fuzzy Analytical Hierarchy Process. The Geographical Information Systems are used for processing the maps of determined criteria.

For the purpose 12 Main criteria and their sub criteria are determined from the opinion of experts, surveys and studies in literature. Finally the new proposed criteria are applied to the study and a suitability map for solar farms on the study area is obtained. This map shows the most suitable places, low suitable places and disallowed places for solar farms on the study area. The proposed criteria, their weights and the suitability map will help researchers to determine more environmental, social and economic sites for solar farms.

Keywords: Solar farm siting, Geographic Information Systems, Multi Criteria Decision Making, Fuzzy Analytical Hierarch Process, Suitability map

1. INTRODUCTION

In recent years, the installations of Renewable Energy Sources (RES) have been quite accelerated with the increase of tendency to clean energy. One of the most important preference reason of RES is having less damage to the environment than the other classical Energy sources (ES). The depletion of other ES by over time is also enhancing the importance of the RES [1].

Solar power is the one that has the most extensive application in the RES. RES emerge as the fastest growing ES in the world in terms of environmental benefits, government incentives, more flexible preference of installation area, modularity [1]. Site determination of a planning RES is an important problem. Determination of the criteria which affect the installation area of the RES emerges as the first operation. Application by detecting every important criteria and sub criteria will provide determination of a more accurate location in terms of environment, economy and sociology. In literature, there are many studies that present the criteria related to Solar farms (SF)'s site selection [1]–[8]. Giving the importance values of these presented criteria relative to each other is a difficult problem for human brain. In order to make this weighting the Multi Criteria decision making (MCDM) methods are developed. These methods are developed for evaluation of many alternatives according to many criteria [3]. One of the most commonly used in MCDM methods is Analytical Hierarchy process (AHP). In AHP, there is a structure that the objective is at the top and the alternatives are at the base. Alternatives are evaluated by making pair-wise comparisons according to the objective. The Fuzzy AHP (FAHP) is developed due to the decision maker's difficulties in giving precise judgments during pairwise comparisons process. Making the data based processes of the proposed and weighted criteria through printed maps have become impossible. Processing the data in digital environment and gathering the data consecutively by evaluating all the data as a whole of the Geographical information systems (GIS) have necessitated the use of GIS in site determination studies.

About SF's siting studies in literature, Janke J. [7] used a multi criteria GIS model for determination of suitable places for solar and wind farms' installation at Colorado. In the study seven main criteria belonging to SF are used.Charabi Y. and Gastli A. [4] is developed a Fuzzy Logic Ordered Weight Averaging (FLOWA) module integrated to the GIS for SF's installation of Oman by using nine criteria in sultanate.Aydin N.Y. [2] carried out a suitable place finding study for solar and wind farms in a specific region by using GIS and fuzzy logic methods. In the study, evaluating as "acceptable" or "unacceptable" without using intermediate values or sub criteria in criteria comparison process caused ignorance of some important values in the suitable place finding.Sanchez-Lozano J.M. at. al. [3] used GIS and AHP and Technique for Order Preference by Similarity to Ideal Solution (TOPSIS) from MCDM in SF's suitable place finding at South-east of the Spain. Ten criteria is used in the study and any sub criteria is not included in the study.Uyan M. [1] is used five main criteria and their sub criteria with the help of GIS and AHP for determination of possible SF's most suitable, suitable and low suitable places in Konya province. Kengpol at al. [5] contributed to the making of importance weighting made of users by developing a decision system interface with the help of FAHP and TOPSIS for SF's suitable place finding studies. Sanchez-Lozano J.M. at. al. [8] carried out a suitable place finding study for SF with the help of GIS and ELECTRE-TRI method by using ten criteria at South-east of the Spain.

[1] *Corresponding author: Gümüşhane University, Department of Electrical Electronics Engineering, 29100, Gümüşhane, Turkey.* hasan.eroglu@gumushane.edu.tr

It can be seen in literature that combined using of the GIS and MCDM is very common but the number of used criteria and sub-criteria is not enough. For example “Flora & Fauna” main criteria and the "The important plant species" and "tropical areas" sub criteria, Soil, Geology, Landslide and their sub criteria are not used in the studies in literature. It is necessary not to be ignored any criteria in order to select more economic, environmental and social areas in SF’s and other energy plants’ installation.

The rest of the paper is organized as follows: In Section 2, the criteria that will be used in SF’s suitable place finding studies are presented. In Section 3, the weighting of these criteria is made via FAHP. In Section 4, the suitability map for probable SF is derived by processing the geographical data belonging to the sample study area with the help of GIS. The conclusion is presented in the section 5.

2. DETERMINING THE CRITERIA

In the criteria determination process it has been benefitted from the electric transmission and natural gas pipeline path finding studies [9]–[15] and surveys [10] besides the criteria used for SF and other ES’s suitable place finding studies in literature [1]–[8].In this context 12 main criteria and 61 sub criteria shown in Table 1 are proposed for using in SF’s suitable place finding studies.

Table 1. The criteria and sub criteria proposed in the study.**Error! Not a valid link.**

3. WEIGHTING THE CRITERIA

FAHP -obtained by applying the fuzzy logic to the AHP- provides giving more accurate results of the weights obtained from decision makers’ decisions by easing slightly the difficulty of decision making [16]–[20].

The extent analyzes method proposed by Chang is used in many problem that the FAHP is used. Besides using synthetic degree values, this method come forward with simple level ranking and mixed total ranking. Being less of the calculations and following the steps used in classical AHP are the advantages of the FAHP. Using the Fuzzy triangular numbers is the disadvantage of the method [20].

In this study, the steps of Chang’s extend analyzes method [20] are used and the triangulated fuzzy numbers used in the study are presented in Table 2.

Table 2. Triangulated fuzzy numbers used in the study.

Statement	Triangulated fuzzy numbers (TFN)	TFN conjugate
Equally important	(1, 1, 1)	(1, 1, 1)
Moderately important with one over another	(1/2, 1, 3/2)	(2/3, 1, 2)
Strongly important	(1, 3/2, 2)	(1/2, 2/3, 1)
Very strongly important	(3/2, 2, 5/2)	(2/5, 1/2, 2/3)
Extremely important	(2, 5/2, 3)	(1/3, 2/5, 1/2)

All the weighting steps of the method are made via Microsoft excel. The weights calculated by the help of FAHP are presented in Table 3.

4. *TABLE 3. THE WEIGHTS CALCULATED BY THE HELP OF FAHP.*ERROR! NOT A VALID LINK.PROCESSING THE GEOGRAPHICAL DATA

The ArcMAP as a globally used software is used in the study for collecting, clipping, converting and gathering consecutively all the data in the SF’s suitable place finding application.

Gümüşhane province is selected as the sample study area. There is no SF in Gümüşhane which has an annual solar radiation value rising up to 1700 KWH/m^2. The data belonging to the criteria and sub criteria for the samle study area are obtained from related institutions, related departments in universities or people in the private sector. Some of the data is digitized from printed maps while others are obtained by processing in ArcMAP.

The Solar power potential map (SPPM) shown in Figure 1 is digitized from the solar radiation map of General Directorate of Renewable Energy.

The values of every map related to the criteria are calculated and assigned to the maps as multiplying the percentage of the criteria and sub criteria to each other.

After assigning the weight values to the databases of the maps, the main criteria maps consists of union of the sub criteria maps are converted to the Raster (Pixel-based) maps having 200 m x 200 m pixel size in order to make arithmetical processes on these maps. The restricted (Not allowed) regions for SF are classified as “NoData” meaning to the absence of data in ArcMAP.

In order to obtain the suitability map or Totally Weighted Surface Raster Map (TWSRM) the “Raster Calculator” (RC) function is used in ArcMAP. In RC function summation and other math operations can be applied to the raster maps. In addition, if any weighted region is summed with any “NoData” assigned region the result is “NoData” as resembling multiplying any number with zero. All the weighted and united maps used in this study are presented in Figure 2.

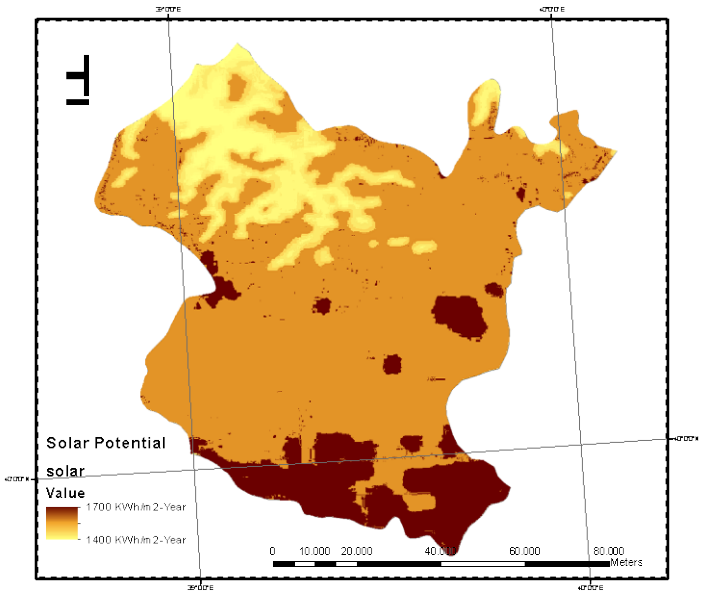

Figure 4. The Solar power potential map (SPPM) used in study.

The restricted and suitability map obtained with the help of RC function by gathering all the maps shown in Figure 2 is presented in Figure 3.

In Figure 3.a the restricted regions are shown in pink colors. As shown in the legend the higher values are shown red colors while the lower values are shown in blue colors. In this study it is proposed that the values between 0-2400 should be accepted as “low suitable places”, 2400-2900 should be accepted as “suitable places” and 2900-4000 should be accepted as “Most suitable places” for SF’s siting as shown in Figure 3.b.

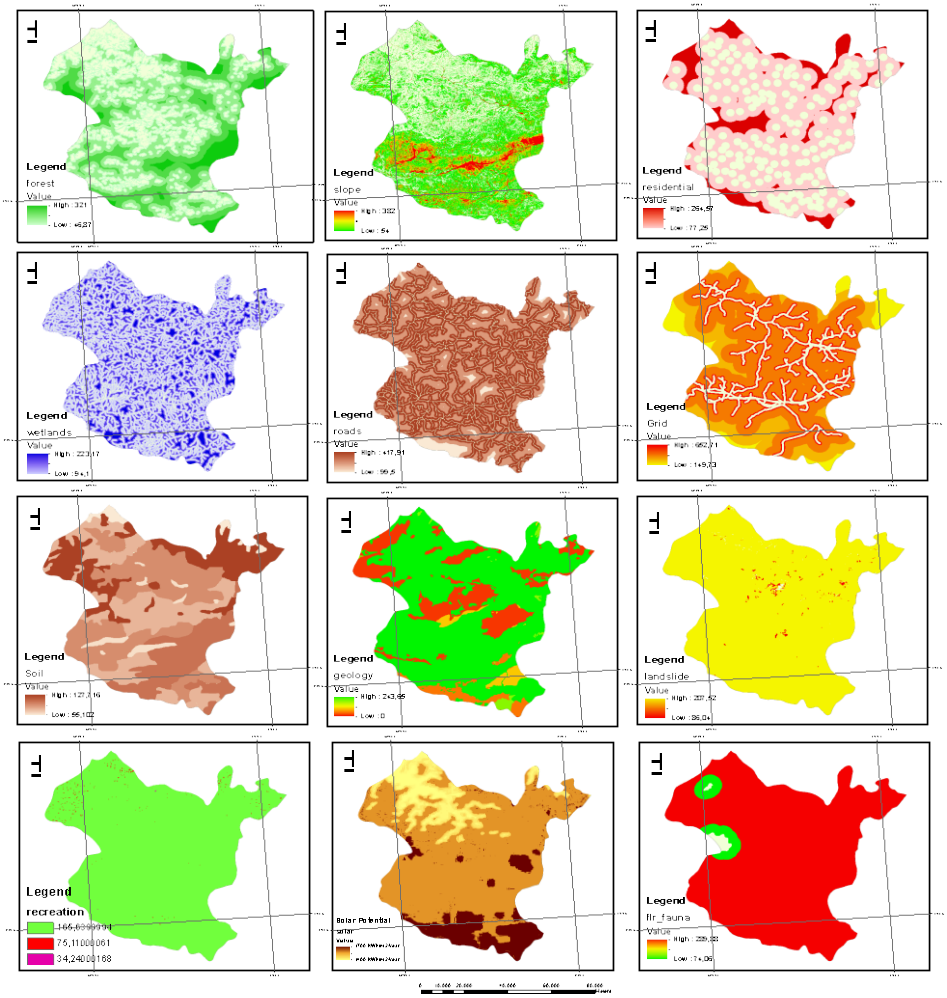

Figure 5. Weighted and united maps used in this study.

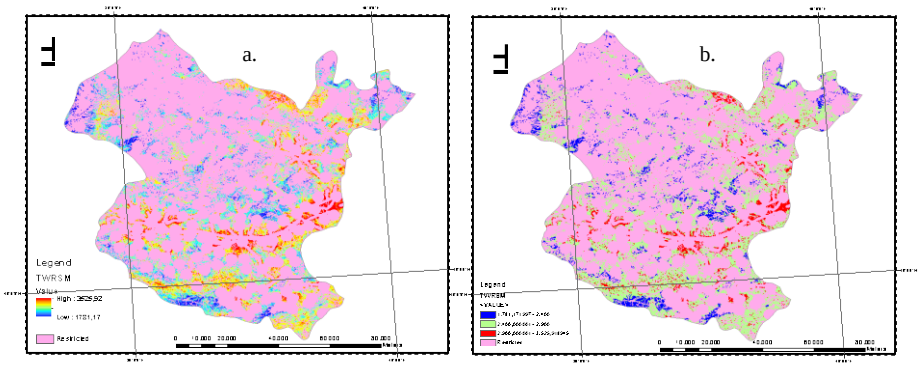

Figure 6. The suitability maps.

5. CONCLUSIONS

Increasing number of the RES has increased the importance of the suitable site determination studies that environmental, economic and sociological sites are preferred.

In this study, a quite wide range criteria and sub criteria are proposed for SF according to the studies, surveys in literature. The weighting of the criteria is made via FAHP a commonly used method. The restricted regions are determined and all the map processes are performed at GIS environment. The TWSRM is obtained by using the RC function. With the help of this study, the suitable site determination process for SF is performed more accurately by considering wider range of environmental, economic and sociological criteria.

REFERENCES

[1] M. Uyan, "GIS-based solar farms site selection using analytic hierarchy process (AHP) in Karapinar region, Konya/Turkey," *Renew. Sustain. Energy Rev.*, vol. 28, pp. 11–17, Dec. 2013.

[2] N. Y. Aydin, "GIS-Based Site Selection Approach for Wind and Solar Energy Systems: A Case Study from Western Turkey," D. Eng. thesis, Mıddle East Technıcal Unıversıty, Ankara, Turkey, July 2009.

[3] J. M. Sánchez-Lozano, J. Teruel-Solano, P. L. Soto-Elvira, and M. Socorro García-Cascales, "Geographical Information Systems (GIS) and Multi-Criteria Decision Making (MCDM) methods for the evaluation of solar farms locations: Case study in south-eastern Spain," *Renew. Sustain. Energy Rev.*, vol. 24, pp. 544–556, Aug. 2013.

[4] Y. Charabi and A. Gastli, "PV site suitability analysis using GIS-based spatial fuzzy multi-criteria evaluation," *Renew. Energy*, vol. 36, no. 9, pp. 2554–2561, Sep. 2011.

[5] A. Kengpol, P. Rontlaong, and M. Tuominen, "A Decision Support System for Selection of Solar Power Plant Locations by Applying Fuzzy AHP and TOPSIS: An Empirical Study," *J. Softw. Eng. Appl.*, vol. 6, no. September, pp. 470–481, 2013.

[6] N. Y. Aydin, E. Kentel, and H. Sebnem Duzgun, "GIS-based site selection methodology for hybrid renewable energy systems: A case study from western Turkey," *Energy Convers. Manag.*, vol. 70, pp. 90–106, Jun. 2013.

[7] J. R. Janke, "Multicriteria GIS modeling of wind and solar farms in Colorado," *Renew. Energy*, vol. 35, no. 10, pp. 2228–2234, Oct. 2010.

[8] J. M. Sánchez-Lozano, C. Henggeler Antunes, M. S. García-Cascales, and L. C. Dias, "GIS-based photovoltaic solar farms site selection using ELECTRE-TRI: Evaluating the case for Torre Pacheco, Murcia, Southeast of Spain," *Renew. Energy*, vol. 66, pp. 478–494, Jun. 2014.

[9] H. Eroğlu and M. Aydin, "Optimization of electrical power transmission lines ' routing using AHP , fuzzy AHP , and GIS," *Turkish J Electr Eng Comput Sci*, pp. 1–13, 2015.

[10] G. Houston and C. Johnson, "EPRI-GTC Overhead Electric Transmission Line Siting Methodology," *Georg. CA Georg. Transm. Corp.*, 2006.

[11] S. Demircan, M. Aydin, and S. S. Durduran, "Finding optimum route of electrical energy transmission line using multi-criteria with Q-learning," *Expert Syst. Appl.*, vol. 38, no. 4, pp. 3477–3482, Apr. 2011.

[12] C. Monteiro, "GIS spatial analysis applied to electric line routing optimization," *IEEE Trans. POWER Deliv.*, vol. 20, no. 2, pp. 934–942, 2005.

[13] C. Monteiro, V. Miranda, I. J. Ramírez-Rosado, P. J. Zorzano-Santamaría, E. García-Garrido, and L. A. Fernández-Jiménez, "Compromise seeking for power line path selection based on economic and environmental corridors," *IEEE Trans. Power Syst.*, vol. 20, no. 3, pp. 1422–1430, 2005.

[14] A. Schmidt, "Implementing a GIS methodology for siting high voltage electric transmission lines," *Pap. Resour. Anal.*, vol. 11, 2009.

[15] V. Yildirim and R. Nisanci, "Developing a Geospatial Model for Power Transmission Line Routing in Developing a Geospatial Model for Power Transmission Line Routing in Turkey," 2010, no. April 2010, pp. 11–16.

[16] E. Heo, J. Kim, and K.-J. Boo, "Analysis of the assessment factors for renewable energy dissemination program evaluation using fuzzy AHP," *Renew. Sustain. Energy Rev.*, vol. 14, no. 8, pp. 2214–2220, Oct. 2010.

[17] C. Kahraman and İ. Kaya, "A fuzzy multicriteria methodology for selection among energy alternatives," *Expert Syst. Appl.*, vol. 37, no. 9, pp. 6270–6281, Sep. 2010.

[18] A. Özdağoğlu and G. Özdağoğlu, "Comparison of Ahp and Fuzzy Ahp for the Multi- Criteria Decision Making Processes With Linguistic Evaluations," *İstanbul Ticaret Üniversitesi Fen Bilim. Derg.*, vol. 6, no. 1, pp. 65–85, 2007.

[19] C. Kahraman, U. Cebeci, and D. Ruan, "Multi-attribute comparison of catering service companies using fuzzy AHP: The case of Turkey," *Int. J. Prod. Econ.*, vol. 87, no. 2, pp. 171–184, Jan. 2004.

[20] H. Eroğlu, "Coğrafi Bilgi Sistemleri (CBS) ve Bulanık Analitik Hiyerarşi Metodu (FAHP) Kullanılarak Rüzgar Santralleri için En Uygun Yer Tayini," in *Proc* Eleco 2014,.pp. 27–29.

ICENS
INTERNATIONAL CONFERENCE ON ENGINEERING AND NATURAL SCIENCES
24-28 May 2016 /Sarajevo

Route Optimization of Electric Transmission Lines with ABC Algorithm

Hasan Eroglu[1], Musa Aydin[2]

Abstract

Finding the best route in electric transmission line (ETL) projects is a difficult process since there are many complex parts of the routing processes. These parts consist of determining the relevant criteria and sub-criteria; calculating the weights of these criteria (the importance values of the criteria to each other); collecting, digitizing, converting to raster format and all other map processes; assigning the weights to the maps; getting the Total Weighted Surface Raster Map (TWSRM) by combining all the maps with the Geographic Information Systems (GIS) and finding the optimum route on TWSRM.

Criteria determination and weighting of these criteria are crucial phases since one forgotten criteria or one wrongly calculated weight of an important criteria can change the course of the project by causing a great financial loss for the project. Besides, the last part of the routing process is the most difficult one since there are endless possible routes to be compared with each other. Many algorithms have been developed for finding optimum routing solutions for the problem. One of the most successful and used tool is "Cost Distance" (CD) toolbox embed in the GIS software. But it has some disadvantages like making many curves or turns with big angles in the proposed route. In ETL works, the curves on the route increases the cost of the project.

In this study, Artificial Bee Colony (ABC) algorithm was used for the route optimization problem for a possible ETL on a previously prepared sample TWSRM. The results of the proposed algorithm was compared with CD tool's results in order to present the performance of the algorithm. As a good alternative for researchers, the ABC algorithm gave better solutions for ETL optimization problems.

Keywords: Electrical Transmission Lines, Artificial Bee Colony algorithm, GIS, Route optimization.

1. INTRODUCTION

By the rising need of the people to energy, newly ETL will be considered to be installed. Finding the best route for ETL is a very difficult problem for engineers. As including many criteria like slope, landslide, road/railway/pipeline crossing, ice zone, distance to roads, national parks, archaeological areas, residential areas forests, river crossing etc. and their maps in one project is almost impossible for human brains in a perfect way without making any mistake.

So Multi Criteria Decision Making (MCDM) methods and GIS solutions should be included to the routing studies of ETL.

The path finding can be done on the Total Weighted Surface Raster Map (TWSRM) generated in GIS environment. So TWSRM should be obtained by weighting criteria related to ETL, collecting all the data about these criteria, processing these data, converting to raster format -basically a regular matrix of square cells where each cell represents an area and position- gathering consecutively all the data in ArcGIS in order to find the best route for ETL routing [1]–[4].

In the weighting processes Fuzzy Analytical Hierarchy Process (FAHP) method is used and the weighting is made by benefitting from electric transmission and natural gas pipeline path finding studies and surveys in literature [3]–[9]. All the data relevant to ETL routing are processed in ESRI's ArcGIS software and the TWSRM is gathered as shown in Figure 1.

[1] *Corresponding author: Gümüşhane University, Department of Electrical Electronics Engineering, 29100, Gümüşhane, Turkey.* hasan.eroglu@gumushane.edu.tr

[2] *Selçuk University, Department of Electrical Electronic Engineering, 42000, Konya, Turkey* aydin@selcuk.edu.tr

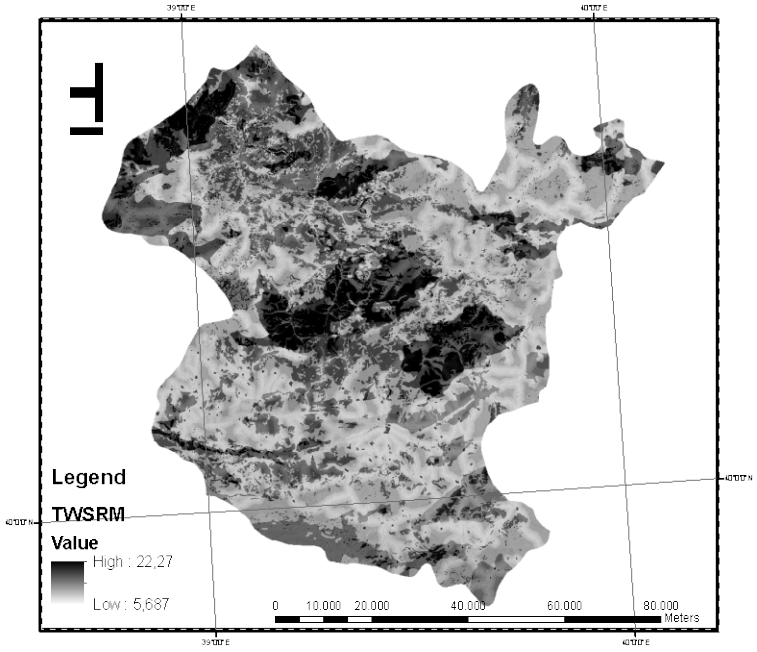

Figure1. TWSRM obtained by unifying the raster-based weighed maps.

In the map, the darkness of the pixels represents more passing difficulty. The size of the pixels is 25 meter that is a proper value for this kind of studies. Every cell has a value that represents the passing difficulty through them. If the value is higher it means the passing of the ETL will be difficult and vice versa.

The optimum path finding process can be made on this map by CD toolbox. In some cases the CD toolbox can find the best route with many big angle curves of routes. This situation is not desired in ETL routing studies. As an alternative to CD toolbox the ABC algorithm is applied on different start and end points of the TWSRM.

2. ABC ALGORITHM

ABC algorithm inspired by the behavior of the real bees for finding the honey sources and giving the information to other bees in the hive has drawn much attention [10]. There are many applications of ABC algorithm about the optimization studies in literature.

There are three types of bees in the hive: the employed bees, the onlooker bees and the scouts. The employed bees find the food sources and memorize the surroundings' food information in order to give the information to the onlooker bees in the hive. The onlooker bees select one of the food sources from the information taken from the employed bees and gather the nectar. The finding the new nectars, foods and sources duty is made by scouts. When a scout or onlooker bee finds a food sources it becomes an employed bee.

As illustrated in Figure 2, every food information that represents a randomly generated route consists of addresses and the nectar values of the source. These information represent "nrows" and "ncols" values of the text file matrix of the TWSRM. The addresses of the information are memorized with their rows and columns number in a series named "Map Series" (MS). Also the nectar values of these information are memorized with another series named "Value Series" (VS).

The food source and its address is represented as a randomly generated route in the algorithm.

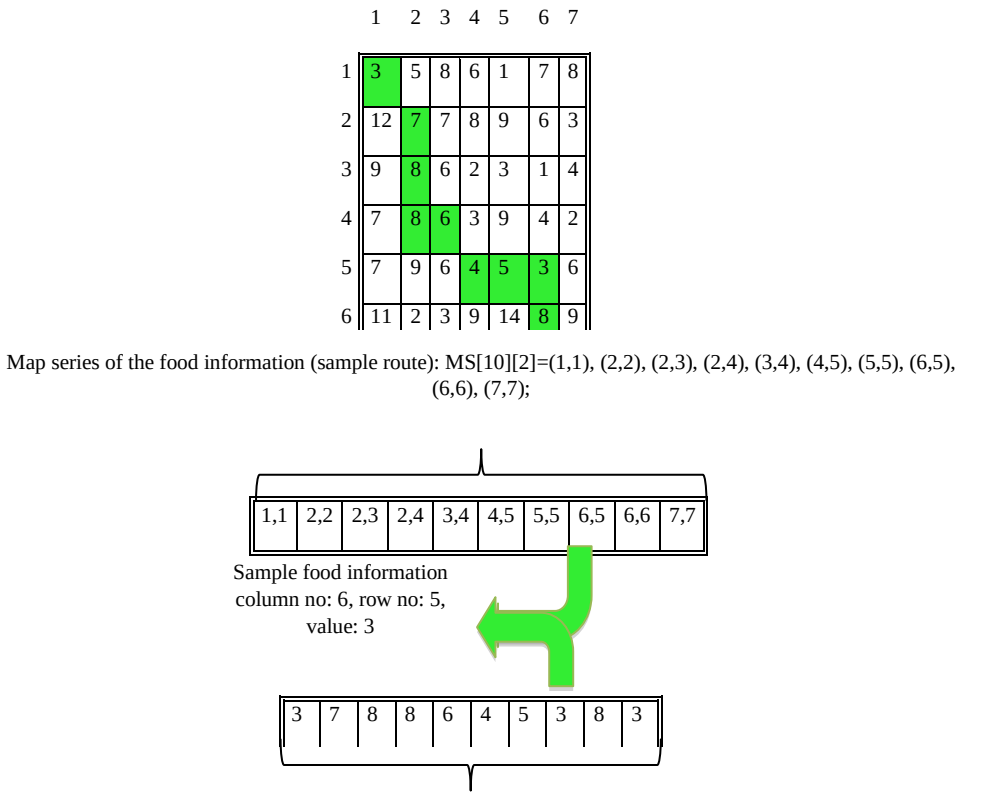

Figure. 2. Sample food information (route) generated by the algorithm.

General representation of the ABC used in this study is shown in Figure 3. The employed bees perform the neighbor operation by finding a new food source or generating a new solution from the present. This operation is made as generating a new route part from the present. The new part is changed with the old if the new route value is better.

The fitness function of every solution is calculated by summation of all pixel values in the sample route. The abandoned routes are determined by controlling the fitness values of the solutions. If the fitness value of a solution in the last rows doesn't increase after many iteration named "Limit" it is accepted as abandoned and scouts generate new solutions.

After these processes, the algorithm runs until the number of the iteration is reached and then selects the best solution.

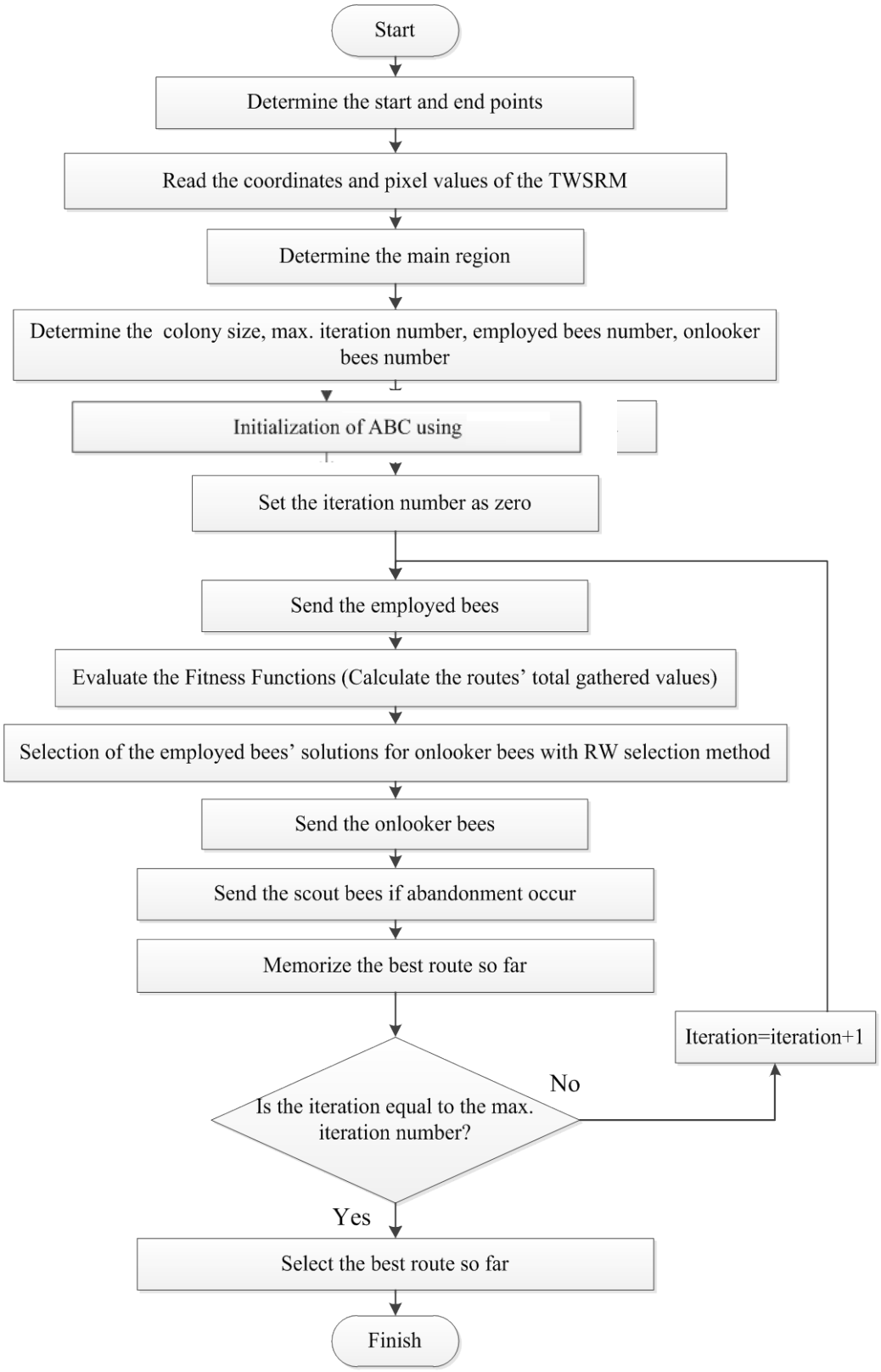

Figure 3. General representation of the ABC used in the study.

3. EXPERIMENTAL RESULTS

The results of the proposed algorithm are compared with CD tools' results. With the help of many experiences by the algorithm, the colony size is selected as 50 and the max. number of iteration is used as between 500-1000 iteration. The number of the artificial bees is accepted as the half of the colony [11].

Two different start and end points are selected for two experiments and the results of the algorithm and CD tool are shown in Figure 4.

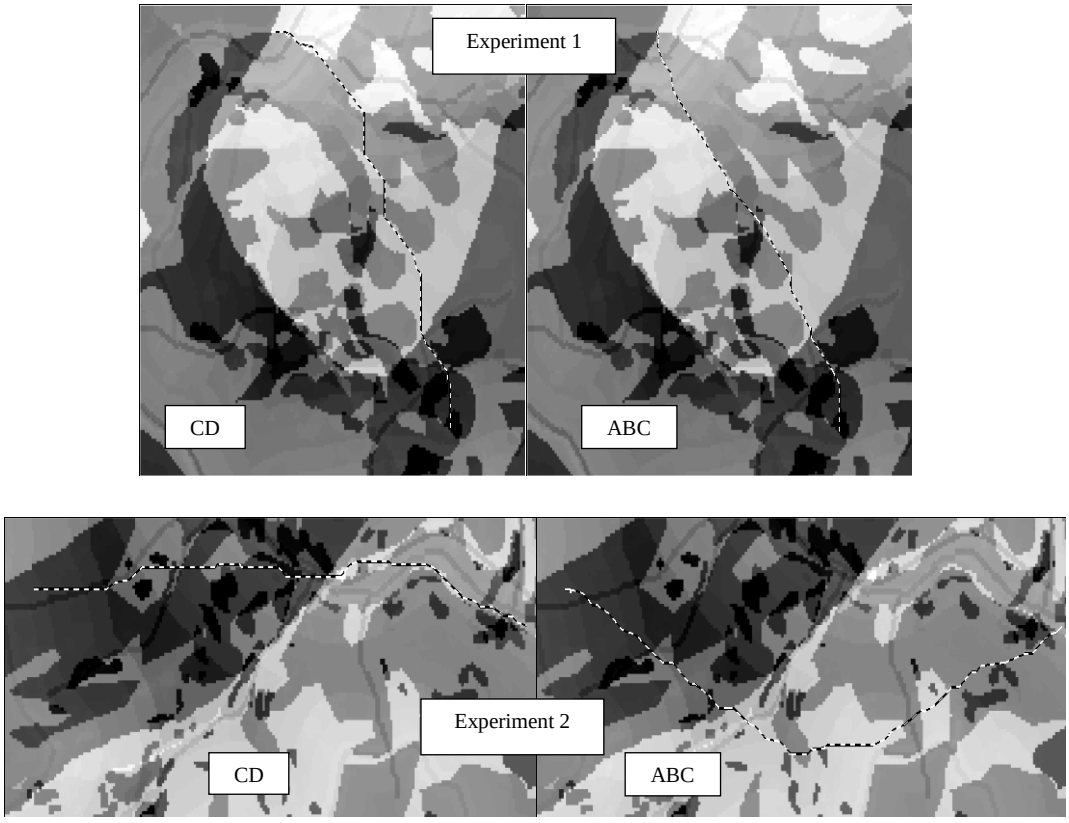

Figure 4. The Routes generated from the proposed Algorithm and CD tool.

Both in the first and second experiment the fitness values of ABC algorithm are better than the CD tool's. Also in experiment 1, the ABC algorithm's route is straighter than the CD tool's. The fitness values of algorithms for two experiments are shown in Table 1. The time performance of the ABC algorithm is not as better as CD tool.

Table 1. The fitness values of algorithms.

	Fitness Values	
	ABC	**CD**
Experiment 1	1500	1517
Experiment 2	2299	2397

4. CONCLUSIONS

In this study, ABC algorithm is adopted the route optimization problem of ETL on raster-based maps. The results of the proposed algorithm are compared with the most common tool of the GIS software. As the CD tool has the disadvantage of making many curves with big angles through the result route, the ABC algorithm is used as an alternative to the CD tool. The prosed algorithm gives better alternatives in terms of straightness and fitness values. But the proposed algorithm finds the alternative routes slower than the CD tool.

REFERENCES

[1] I. J. Ramirez-Rosado, V. Miranda, P. J. Zorzano-Santamaria, E. Garcia-Garrido, L. A. M. C., and Fernandez-Jimenez, "GIS spatial analysis applied to electric line routing optimization," *Ieee Trans. Power Deliv.*, vol. 20, no. 2, pp. 934–942, 2005.

[2] C. Monteiro, V. Miranda, I. J. Ramírez-Rosado, P. J. Zorzano-Santamaría, E. García-Garrido, and L. A. Fernández-Jiménez, "Compromise seeking for power line path selection based on economic and environmental corridors," *IEEE Trans. Power Syst.*, vol. 20, no. 3, pp. 1422–1430, 2005.

[3] V. Yildirim and R. Nisanci, "Developing a Geospatial Model for Power Transmission Line Routing in Developing a Geospatial Model for Power Transmission Line Routing in Turkey," 2010, no. April 2010, pp. 11–16.

[4] V. Yildirim, "DOĞALGAZ İLETİM HATLARININ BELİRLENMESİ İÇİN COĞRAFİ BİLGİ SİSTEMLERİ İLE RASTER TABANLI DİNAMİK BİR MODELİN GELİŞTİRİLMESİ," 1937.

[5] F. Husain, N. A. Sulaiman, K. A. Hashim, and A. M. Samad, "Multi-criteria selection for TNB transmission line route using AHP and GIS," *2012 Int. Conf. Syst. Eng. Technol.*, pp. 1–6, Sep. 2012.

[6] S. Demircan, M. Aydin, and S. S. Durduran, "Finding optimum route of electrical energy transmission line using multi-criteria with Q-learning," *Expert Syst. Appl.*, vol. 38, no. 4, pp. 3477–3482, Apr. 2011.

[7] W. Shu-Xi, "The Improved Dijkstra's Shortest Path Algorithm and Its Application," *Procedia Eng.*, vol. 29, pp. 1186–1190, 2012.

[8] A. Schmidt, "Implementing a GIS methodology for siting high voltage electric transmission lines," *Pap. Resour. Anal.*, vol. 11, 2009.

[9] G. Houston and C. Johnson, "EPRI-GTC Overhead Electric Transmission Line Siting Methodology," *Georg. CA Georg. Transm. Corp.*, 2006.

[10] P. TSai, J. Pan, B. Liao, and S. Chu, "Enhanced artificial bee colony optimization," *Int. J. Innov. Comput. Inf. Control*, vol. 5, no. 12, pp. 5081–5092, 2009.

[11] D. Karaboga, "An idea based on Honey Bee Swarm for Numerical Optimization," *Tech. Rep. TR06, Erciyes Univ.*, no. TR06, p. 10, 2005.

ICENS
INTERNATIONAL CONFERENCE ON ENGINEERING AND NATURAL SCIENCES
24-28 May 2016 /Sarajevo

An Iterated Local Search Based Algorithm for Curriculum Based Course Timetabling Problems

Mehmet Hacibeyoglu[1], Kemal Alaykiran[2]

Abstract

Determining a timetable for courses, exams and for other events at all educational institutes is a time consuming and hard problem to be solved under a number of constraints in order to maximize a number of goals. Most common constraints of these problems are class capacities, course and lecture clashes at the timetable, available time zones for events etc. As a special class of all timetabling problems, curriculum based course timetabling is also a NP-hard problem. The problem structure and its parameters are generalized at International Timetabling Competitions (ITC) which were held in 2002, 2007 and 2011. In this study, the problem set used at ITC 2007 are solved using an iterated local search based algorithm. The results achieved are encouraging but compared to the best solutions to the problems provided, it is obvious that iterated local search method may be used with other methods in a hybrid way.

Keywords: Curriculum based course timetabling problem, iterated local search, international timetabling competition

1. INTRODUCTION

Timetabling of courses, exams and other events at an educational institution is a hard and complex problem. As a sub branch of scheduling problems, timetabling problems are NP-hard combinatorial optimization problems [1]. Briefly defined, timetabling problems are assigning a number of events to a number of resources satisfying a number of constraints in order to maximize / minimize one or multiple objectives. Based on this definition there are many forms of timetabling problems investigated in the literature. In this paper, curriculum based course timetabling (CB-CTT) problem is considered. In order to evaluate the solution performances of different methods, three timetabling competitions, International Timetabling Competition (ITC), are organized in 2002, 2007 and 2013. At ITC 2007, one of the branches of the competition is CB-CTT problems where a data format for the problem instances is structured, a number of specific constraints (both soft and hard) are defined and also 21 hard problem instances are proposed. This kind of a standardization in problem definition and its modelling has given a precious tool for the researchers, in addition, the instances proposed has been attacked using different exact and heuristic approaches.

Di Gaspero et. al [2], proposed a technical report on CB-CTT problems for ITC 2007 where one may find all information about the rules of competition and deep comprehension of the problem. Since this paper concentrates on solving CB-CTT problems using a heuristic approach, research using exact methods are not taken into consideration for a literature review, for more information about this literature one may refer to [3]. At [4], an adaptive tabu search method is proposed for CB-CTT problems. Lü et. al [5] solved CB-CTT instances of ITC 2007 using three different metaheuristic algorithms, tabu search, iterated local search and adaptive tabu search respectively. At [6], a simulated annealing based approach is given. At [7], the problems is solved using a hybrid of genetic algorithms and tabu search. At [8], suggest a hybrid solution method of simulated annealing with tabu search. At [9], a local search method based on threshold accepting is given. At [10], the problem is solved using simulate annealing algorithm.

In this paper, CB-CTT problem instances of ITC 2007 are solved using an iterative local search (ILS) algorithm. At the next chapter, the CB-CTT problem is defined using the definition of ITC 2007 where an example problem is given. At chapter 3, the ILS algorithm used is defined. At chapter 4, the experimental results are given and analyzed. The paper is finished with conclusions.

2. PROBLEM DEFINITION

In order to understand and solve the CB-CTT problem instances proposed at ITC 2007, one should understand the notation used. The terms and constraints are given below [3].

Time periods: Each time period denotes to a pair of (day, time_slot) where a week is divided into days and each day is divided into a fixed number of time_slots.

Courses, Lectures, Curriculum, Teachers, Number of students: Each course consists of a number of lectures given by the a teacher where all lectures of a course is given by the same teacher, and a course is attended by a number of students where

[1] *Corresponding author: Necmettin Erbakan University, Department of Computer Engineering, 42090, Meram/Konya, Turkey.* hacibeyoglu@konya.edu.tr

[2] *Necmettin Erbakan University, Department of Industrial Engineering, 42090, Meram/Konya, Turkey.* kalaykiran@konya.edu.tr

each course should be a member of at least one curricula where a curricula refers to a set of courses that must be taken a number of students.

Rooms: Rooms are the resources where the lectures take place where every room has a capacity.

Using these basic terminology of CB-CTT problems, the hard and soft constraints taken into consideration at ITC 2007 are as below [3]. The hard constraints denote to the feasibility conditions of a timetable where the soft constraints are the performance criteria for a feasible solution.

Lectures: All lectures of all courses must be assigned to available time periods;

Room occupancy: A room can host at most one lecture per time periods;

Conflicts: At a specific time period at most one lecture of a curriculum can be scheduled also a teacher can be scheduled exactly one lecture at a time period.

Availabilities: A lecture of a course cannot be assigned to an unavailable time period.

Since the objective of CB-CTT is to minimize the weighted sum of the soft constraints, the soft constraints denote to the cost of violation. There are 5 different weighting methods with different soft constraints in the literature which are called as UD1, UD2, UD3, UD4, UD5. Since this study considers the ITC 2007 formulation, the UD2 weighting is taken into consideration and the weights are given below. These soft constraints are:

Minimum number of working days: A minimum working day is determined for each course at the problem instances, where for each day below this minimum working day is resulted in a penalty. The penalty for UD2 is 5 per day per course below minimum working day of that individual course.

Curriculum compactness: It is intended to minimize the idle time for students of a curricula. In order to achieve this, a penalty of 2 units is given per empty time periods for a lecture which is not adjacent to any other lecture of that curricula in the same day.

Room capacity: It is intended to achieve a solution where the number of students of a course does not exceed the capacity of the room the course is assigned. For every student exceeding the capacity, a penalty of 1 unit is calculated.

Room stability: It is preferred that all lectures of a course are taught in the same room. A penalty of 1 unit is given to each additional room assignment of a course.

For a better understanding of the instances of ITC 2007 and the solution evaluation (weighting) procedure an example problem with 5 courses and 3 curriculum is given below. Since the number of courses are so few, days are taken as 3 and time_slots are taken as 4. The data of the problem is given just the same as it is given at ITC 2007 cases.

The datasets provided at ITC 2007 for CB-CTT problems start with a brief definition of the problem where the name of the problem, number of courses, rooms, days, periods, curricula and constraints. These values for Example-1 are given in Table 1 below:

Table 4. The properties of the Example-1

Name	Example-1
Courses	5
Rooms	2
Days	3
Periods_per_day	4
Curricula	3
Constraints	10

The dataset continues with course parameters. The sequence of the data is, name of the course, teacher of the course, number of lectures, minimum working days, number of students. These values for this Example-1 are given in Table 2 below:

Table 2. The properties of the courses in Example-1

Courses				
Name of the course	**Teacher of the course**	**Number of Lectures**	**Minimum working days**	**Number of students**
c1	t001	5	2	30
c2	t002	5	2	50
c3	t003	4	3	40
c4	t004	3	1	80
c5	t005	1	1	40

As it may be seen at the above example, total number of lectures in the system is 18 where total available time slots are 24 (number_of_rooms * number_of_days* number_of_periods). The next data part consists of the data for the rooms and data for the curricula respectively. These are given in Table 3 and Table 4 respectively.

Table 3. The properties of the rooms in Example-1

Rooms	
Name of room	**Capacity of room**
A	40
B	80

Table 4. The properties of the curriculum in Example-1

Curricula		
Name of curricula	**Number of Courses**	**Courses**
q1	3	c1 c2 c4
q2	2	c2 c3
q3	4	c2 c3 c4 c5

The data sets ends with unavailability constraints which denote to the unavailable time periods for courses where the sequence is as course name, day, period where days and periods start with 0. The unavailability constraints for Example-1 are given in Table 5 below.

Table 5. The properties of the unavailability constraints in Example-1

Unavailability_Constraints		
Name of course	**Day**	**Period**
c1	0	0
c1	0	1
c2	2	0
c2	2	1
c3	3	1
c3	3	2

3. ITERATIVE LOCAL SEARCH (ILS) ALGORITHM

Consider a local optimum solution for a problem derived using a local search algorithm, ILS improves this solution by perturbing other local optimum solutions. The algorithm presented in this study start with a Random Initial Solution where all lectures are assigned to feasible time slots considering all of the hard constraints. Then, a local search method based on 1 point swap method to improve the solution. Once the local search ends, the best solution is perturbed for the last unaccepted solution and the algorithm stops at 208 s. of CPU time which is determined as a rule at ITC 2007. The pseudo code of the algorithm is given below in Fig.1 [11]:

```
procedure ILS
    s0 ← GenerateInitialSolution
    s* ← LocalSearch(s0)
    while Stopping criteria is not met do
        s' ← Perturb(s*)
        s*' ← LocalSearch(s')
        s* ← AcceptanceCriterion(s*, s*')
    end
end
```

Figure 7Pseudo code of ILS

4. EXPERIMENTAL RESULTS

In this study, 21 datasets of ITC 2007 are solved using ILS on a computer with an I7-3840QM CPU at 2.80 GHz with 16 GB of ram working on Windows 10 operating system. The algorithm is coded using C# on Microsoft Visual Studio 2013 builder. Due to the competition rules, this configuration of a computer should use at most 208 s. The results of the problems are given at Table 1. As it may be seen from the results, all hard constraints are satisfied for all problems and the weighed penalties for RoomCapacity, MinWorkingDays, Cost of IsolatedLectures, and Cost of RoomStability are given for all instances. The bold values at Best Known column indicates that the optimal solution for that problem is known.

Table 6. The results found using ILS and the best known

Dataset	Cost of RoomCapacity	Cost of MinWorkingDays	Cost of IsolatedLectures	Cost of RoomStability	Total Cost	Best Known
Comp01	4	-	-	1	5	**5**
Comp02	-	35	118	6	159	24
Comp03	-	30	130	2	162	64
Comp04	-	10	56	6	72	**35**
Comp05	110	145	402	6	663	284
Comp06	-	35	70	14	119	**27**
Comp07	2	-	48	31	81	**6**
Comp08	-	-	74	8	82	**37**
Comp09	-	35	118	6	159	**96**
Comp10	-	15	62	11	88	**4**
Comp11	-	-	-	-	0	**0**
Comp12	11	205	336	4	556	294
Comp13	-	15	92	7	114	**59**
Comp14	-	15	92	4	111	**51**
Comp15	-	40	110	3	153	62
Comp16	-	30	60	13	103	**18**
Comp17	-	30	110	4	144	**56**
Comp18	-	55	84	2	141	**61**
Comp19	-	20	122	5	147	**57**
Comp20	2	35	82	15	134	**4**
Comp21	-	65	114	11	190	**74**

If the results shown at Table 1 are analyzed one may figure out that the results found using ILS are encouraging but not good enough when compared to the best known results. As it is mentioned the primary goal of this study is to find feasible results to these problems to satisfy hard constraints. The next step in this ongoing research will be hybridizing ILS with other metaheuristics to provide better results to the problems.

5. CONCLUSIONS

Timetabling of courses, exams and other events at an educational institution is a hard and complex problem. From the complexity point of view this problem is an NP-Hard problem. Three international challenges are organized to compare and compete solution methods for these problems. In this study, the curriculum-based course timetabling problem dataset of ITC 2007 are considered with the original constraints defined at this organization. These problems are solved using ILS. The main objective of this study is to find feasible and reasonable solutions to these problems. Furthermore, the results found in this study will be improved using other metaheuristic methods, mathematical methods and with hybrid applications.

REFERENCES

[1]. E. Burke, J. Marecek, A. Parkes and H. Rudova, "*Decomposition, reformulation, and diving in university course timetabling*", Computer Operations Research, 37(3), 582–597, 2010.

[2]. L. Di Gaspero, B. McCollum and A Schaerf, The second international timetabling competition (itc-2007): curriculum-based course timetabling (track 3). Technical report, School of Electronics, Electrical 123348, 2007.

[3]. A. Bettinelli, V. Cacchiani, R. Roberti and P. Toth, "*An overview of curriculum-based course timetabling*", TOP, 23, 313-349, 2015.

[4]. Z. Lü and JK. Hao, "*Adaptive tabu search for course timetabling*", European Journal of Operational Research, 200(1), 235–244, 2010.

[5]. Z. Lü and JK. Hao and F. Glover, "*Neighborhood analysis: a case study on curriculum-based course timetabling*", Journal of Heuristics 17(2), 97–118, 2011.

[6]. MJ Geiger, "*Applying the threshold accepting metaheuristic to curriculum based course timetabling*", Annals of Operations Research, 194(1), 189–202, 2012.

[7]. S. Abdullah, H. Turabieh, *"On the use of multi neighbourhood structures within a tabu-based memetic approach to university timetabling problems*", Information Science, 191,146–168, 2012.

[8]. R. Bellio, L. Di Gaspero and A. Schaerf, *"Design and statistical analysis of a hybrid local search algorithm for course timetabling"*, J Sched, 15(1):49–61, 2012.

[9]. M. Geiger, *"Applying the threshold accepting metaheuristic to curriculum based course timetabling"*, Annals of Operations Research, 194:189-202, 2012.

[10]. R. Bellio, S. Ceschia, L. Di Gaspero, A. Schaerf and T. Urli, *Feature-based tuning of simulated annealing applied to the curriculum-based timetabling problem*, Computers and Operations Research, 65: 83-92J, 2016.

[11]. PVZ. Penna, A. Subramanian and LS. Ochi, *"An Iterated Local Search heuristic for the Heterogeneous Fleet Vehicle Routing Problem"*, Journal of Heuristics, 19:2:201-232, 2013.

ICENS
INTERNATIONAL CONFERENCE ON ENGINEERING AND NATURAL SCIENCES
24-28 May 2016 /Sarajevo

A Simulated Annealing Approach for the Uncapacitated P-median Problem

Kemal Alaykiran[1], Mehmet Hacibeyoglu[2]

Abstract

The p-median problem is one of the basic problems in location theory of operations research where it is shown to be a NP-hard problem. The problem has been intensively studied in the literature using both exact and heuristic approaches. P-median problem may be defined as finding the location of p facilities on a graph where the positions of a number of demand points and the cost of satisfying these demand points from other points which are potential facility locations are given. The objective of the problem is to minimize the sum of the transportation costs. In this study, a well-known data set which consists of 40 uncapacitated p-median problem instances with increasing values of total number of nodes and p and which is provided by OR-LIB. In order to solve these instances a simulated annealing algorithm is proposed. The results show that for all the problems in the data set simulated annealing shows a significant success considering both the quality of the results and CPU times used for solution.

Keywords: Metaheuristic, p-median, simulated annealing, OR-Lib

1. INTRODUCTION

Location problems are a wide portion of problems in operations research literature and in practice. These problems arise where a number of decisions are to be made on a network such as: Which facility/facilities are to be opened in order to satisfy demand of a number of entities in the network, which customers' demand will be satisfied by which facility etc. P-Median problem is one of the basic problems of location theory which has been studied widely in the literature. The problem is classified as a discrete, minisum, deterministic, linear optimization problem with single objective [1]. Also the problem is a NP-Hard problem [2]. P-median problem may be defined as finding the location of p facilities on a graph where the positions of a number of demand points and the cost of satisfying these demand points from other points which are potential facility locations are given. The objective of the problem is to minimize the sum of the transportation costs. If the capacity of these facilities to be opened are considered than the problem becomes "capacitated" else it is "uncapacitated". In this study the uncapacitated p-median problem is considered.

P-median problem is widely studied in the literature. One of the former reviews about the studies on this problem is [3] where the studies from 1869 to 1983 are analyzed. The studies on the problem may be divided into two broad classes: Studies using exact solution methods and studies using heuristic or metaheuristic methods. Since this research considers a metaheuristic based approach, the studies proposing metaheuristic methods are taken into consideration for a brief literature review. At [4,5], genetic algorithms are used for the solution of the problem. Hansen, et. al, proposed a variable neighborhood search algorithm for p-median problems with different node sizes [6]. At [7], both ant colony optimization and simulated annealing metaheuristics are used to propose a solution to the p-median problems. At [8], tabu search metaheuristic is used to solve a set of p-median problems. At [9], a simulated annealing approach is proposed for the solution of the problem. For a more detailed review of articles for p-median problems one may refer to [1].

In this paper, one of the basic problems of location theory, p-median, is solved using simulated annealing approach. A well-known data set of OR-LIB [10] consisting of 40 problem instances with different values for number of nodes and p. In the next chapter, the problem is defined and an example problem is given. In chapter 3, the simulated annealing metaheuristic is presented and the algorithm used in this study is given in detail. In chapter 4, the experimental results are given and the solutions are analyzed. The paper is finished with conclusions.

2. PROBLEM DEFINITION

P-median problem may be defined as finding the location of p facilities on a graph where the positions of a number of demand points and the cost of satisfying these demand points from other points which are potential facility locations are given. The objective of the problem is to minimize the sum of the transportation costs. The transportation cost mostly regards as the physical distances between medians and customers. For a better understanding of the problem, an example with ten customers and 2-medians are given.

[1] *Corresponding author: Necmettin Erbakan University, Department of Industrial Engineering, 42090, Meram/Konya, Turkey.* kalaykiran@konya.edu.tr

[2] *Necmettin Erbakan University, Department of Computer Engineering, 42090, Meram/Konya, Turkey.* hacibeyoglu@konya.edu.tr

Consider an example graph where there are 10 nodes denoting the customers. As seen on Figure 1., some nodes have direct flow and some do not. For those of the nodes which don't have direct flow, the cost of transportation is calculated based on Dijkstra's algorithm which is used to solve shortest path problems. The cost of transportation from nodes to nodes are given at Table 1, where the costs calculated using Dijksta's algorithm are shown in bold.

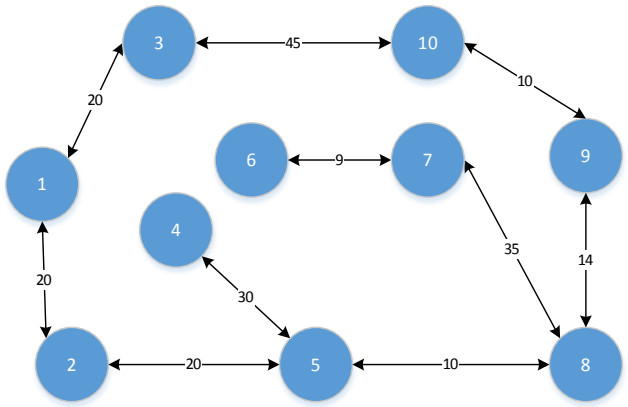

Figure 8. An example problem

Table 5. Sample table

Nodes	**1**	**2**	**3**	**4**	**5**	**6**	**7**	**8**	**9**	**10**
1	0	25	20	**67**	**37**	**91**	**82**	**47**	**61**	**65**
2		0	**45**	**42**	12	**66**	**57**	**22**	**36**	**46**
3			0	**87**	**57**	**111**	**102**	**67**	**57**	45
4				0	30	**84**	**75**	**40**	**54**	**64**
5					0	**54**	**45**	10	**24**	**34**
6						0	9	**44**	**58**	**68**
7							0	35	**49**	**59**
8								0	14	**24**
9									0	10
10										0

In order to solve the example problem below one has to determine on which nodes the medians are to be opened. Consider a feasible solution given at Figure 2, where the medians are determined to be opened at nodes 7 and 3. After this determination, the next step is to calculate the objective function which is the total of costs from medians to customers. Since no capacity constraints are considered here, the median which has the least cost to a customer will serve it. This calculation is showed at Table 2.

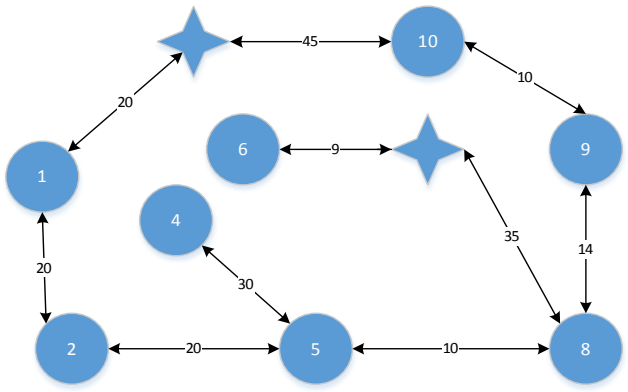

Figure 2. A feasible solution for p=2

Table 2. Sample calculation for a feasible solution

Node	Median-1(Node:3)	Median-2(Node:7)	Cost
1	45	59	45
2	45	57	45
3	0	102	0
4	87	75	75
5	57	45	45
6	111	9	9
7	102	0	0
8	67	35	35
9	57	49	49
10	45	59	45
		Total Cost:	348

As it may be calculated, for a p-median problem with n nodes and p medians, total number of feasible solutions is C(n,p). As it is mentioned at previous chapter the problem is NP-Hard which means that the complexity increases exponentially for increasing values of n and/or p. The mathematical model of this problem is given below [11]:

Parameters:

I: set of customers (i ∈ I = {1, . . ., n)

J: set of potential sites (j ∈ J = {1, . . . , m})

(I, J) : set of customers (i ∈ I = {1, . . . , n}) and set of potential sites (j ∈ J = {1, . . ., M})

c_{ij}: total cost of transportation potential site j to customer i;

p: number of facilities(median) to locate;

Decision Variables:

Y_{ij} = 1, if customer i is served by a facility at site j;

X_j = 1, if a facility is opened at potential site j;

$$Minimize \sum_{i \in I} \sum_{j \in J} c_{ij} Y_{ij} \quad (1)$$

Subject to

$$\sum_{j \in J} Y_{ij} = 1 \quad \forall i \in I \quad (2)$$

$$\sum_{j \in J} X_j = p \quad (3)$$

$$Y_{ij} \leq X_j \quad \forall i,j \quad (4)$$

$$X_j \in \{0,1\}$$

$$Y_{ij} \in \{0,1\}$$

Equation (1) is the objective function and minimizing the total cost of transportation. With constraint (2), it is assured that a customer is served exactly by one median. Constraint (3) guarantees that p medians are opened.

3. SIMULATING ANNEALING (SA)

SA is a metaheuristic approach which is based on the foundations of Metropolis et. al. [12] which are shown to be used for solution of large size optimization problems in order to find acceptable results in reasonable run times by Kirkpatrick et. al. [13]. SA is a local search algorithm where the solution starts with an initial solution and on each iteration, until the termination criteria is met, M different neighbors are evaluated. If at any iteration a better solution than the current best solution is found it is accepted. The main distinguishing feature of SA from other metaheuristics is that a bad solution may be accepted at any iteration with a probability. The SA approach used in this study is given at Figure 3, where the acceptance criteria is calculated as an exponential function as given at (4).

$Accept = e^{-\frac{\Delta}{T}}$ where Δ refers to the difference between the bad solution and the best solution, T refers to the system temperature at that iteration, and t refers to cooling plan.

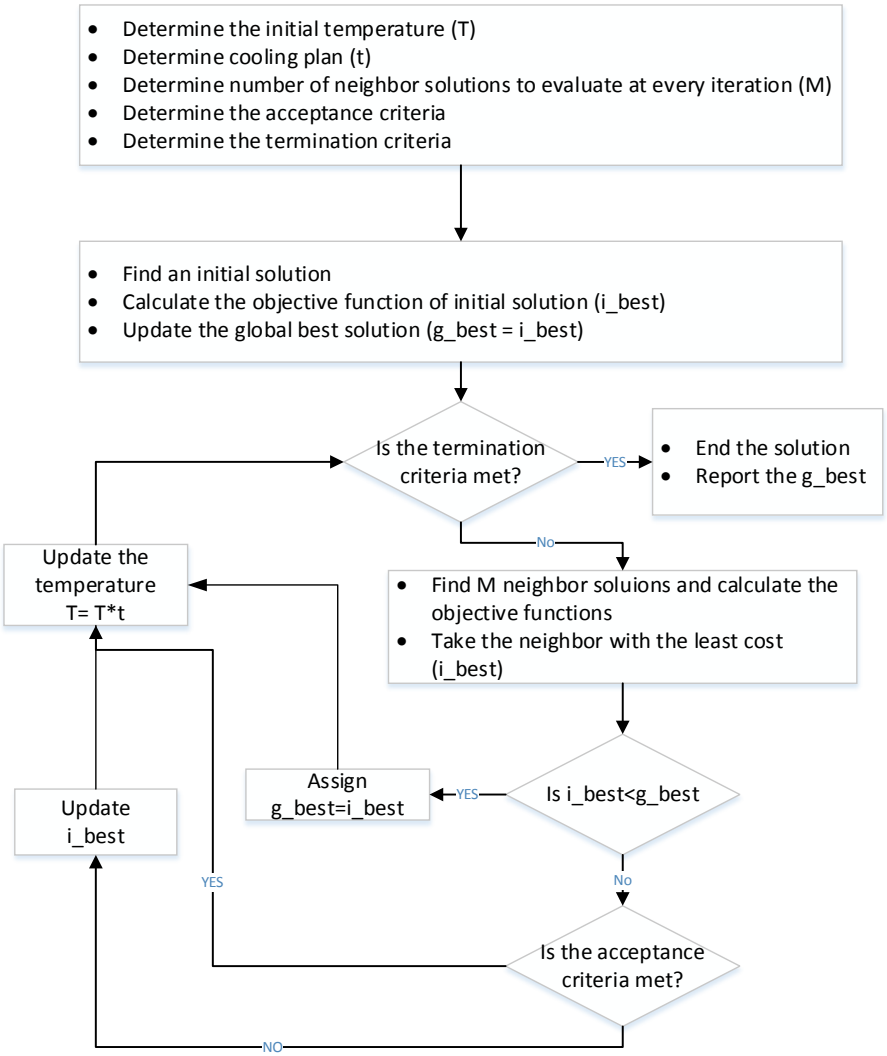

Figure 3. SA approach used

4. COMPUTATIONAL RESULTS

In order to analyze the performance of simulated annealing algorithm, a well-known data set of OR-LIB consisting of 40 problem instances is used. These problem instances have different number of vertices, edges and P. SA algorithm is run 20 times for each problem instance on a computer with an I7-3840QM CPU at 2.80 GHz with 16 GB of ram working on Windows 10 operating system. The algorithm is coded using C# on Microsoft Visual Studio 2013 builder. At the beginning of the experiments, system temperature (T) and the cooling plan (c) parameters are initialized to 5000000 and 0.995. These parameter values are determined due to empirical experiments on different problems. The algorithm stopped when T is smaller than 1. In the experiments the best solution, the average of 20 solutions and the average of CPU-Time are measured. The features of the datasets and experimental results are shown in Table 3.

Table 3. The features of the datasets and experimental results

Pmed	OR - Library				SA		
	Nodes	Edges	P	Best	Best Solution	Average Solution	Average of CPU-Time (sec)
1	100	200	5	5819	**5819**	5819	0.2
2	100	200	10	4093	**4093**	4093	0.2
3	100	200	10	4250	**4250**	4250	0.2
4	100	200	20	3034	**3034**	3034	0.2
5	100	200	33	1355	**1355**	1355.85	0.2
6	200	800	5	7824	**7824**	7824	0.8
7	200	800	10	5631	**5631**	5631	0.8
8	200	800	20	4445	**4445**	4445.4	0.8
9	200	800	40	2734	**2734**	2736,3	0.8
10	200	800	67	1255	1256	1256.9	0.8
11	300	1800	5	7696	**7696**	7696	0.2
12	300	1800	10	6634	**6634**	6634	1.7
13	300	1800	30	4374	**4374**	4374.9	1.7
14	300	1800	60	2968	**2968**	2972.75	1.7
15	300	1800	100	1729	1731	1735.15	1.7
16	400	3200	5	8162	**8162**	8162	3.5
17	400	3200	10	6999	**6999**	6999	3.3
18	400	3200	40	4809	**4809**	4812.05	3
19	400	3200	80	2845	2847	2854.55	3
20	400	3200	133	1789	1791	1793.65	3
21	500	5000	5	9138	**9138**	9138	5.6
22	500	5000	10	8579	**8579**	8579	5.3
23	500	5000	50	4619	4620	4627.85	4.7
24	500	5000	100	2961	2963	2968.55	4.7
25	500	5000	167	1828	1833	1836,2	4.7
26	600	7200	5	9917	**9917**	9917	8.4
27	600	7200	10	8307	**8307**	8307	7.8
28	600	7200	60	4498	4499	4505.3	6.6
29	600	7200	120	3033	3034	3038.45	6.6
30	600	7200	200	1989	1990	1996.4	6.9
31	700	9800	5	10086	**10086**	10086	12.2
32	700	9800	10	9297	**9297**	9297	11.3
33	700	9800	70	4700	4702	4706.9	9.3
34	700	9800	140	3013	3016	3021.6	9.1
35	800	12800	5	10400	**10400**	10400	17.9
36	800	12800	10	9934	**9934**	9934	16.7
37	800	12800	80	5057	5060	5066.55	13.1
38	900	16200	5	11060	**11060**	11060	22.7
39	900	16200	10	9423	**9423**	9423	21
40	900	16200	90	5128	5132	5138.95	17

When the results shown at Table 3 are analyzed, it may be seen that the SA algorithm proposed in this study yields the optimal solution for 27 out of 40 instances where for the rest of the instances the average error is about 0.01 %. From another point of view, if the CPU times are investigated, it may be figured out that the greatest CPU time used for solution is 22.7 seconds where the average of CPU times is approximately 6 seconds.

5. CONCLUSIONS

In this study, one of the basic problems of location theory, uncapacitated p-median problem is solved using simulated annealing approach. The data set proposed at OR-LIB consisting of 40 problem instances for different values of number of nodes and p is considered for solution. Every problem instance is solved using the algorithm proposed for 20 times. The best solution, the average of solutions, average CPU times are recorded. As the results are analyzed, it is seen that the simulated annealing algorithm proposed in this study yields very good results to the problems considered both from the solution quality point of view and from the CPU times point of view.

REFERENCES

[1]. N. Mladenovic, J. Brimberg, P. Hansen and J.A.M. Perez, "*The p-median problem: A survey of metaheuristic approaches*", European Journal of Operational Research, 179, 927-939, 2007.
[2]. O. Kariv and S.L. Hakimi, "*An algorithmic approach to network location problems; part 2. The p-medians*", SIAM Journal on Applied Mathematics 37, 539–560, 1969.
[3]. B.C. Tansel, R.L. Francis and T.J. Lowe, "*Location on networks: A survey. Part I: The p-Center and p-Median Problems*", Management Science, 29, 4, 482-497, 1983.
[4]. C.M. Hosage and M.F. Goodchild, "*Discrete space location allocation solutions from genetic algorithms*", Annals of Operations Research 6, 35–46, 1986.
[5]. O. Alp, E. Erkut and D. Drezner, "*An efficient genetic algorithm for the p-median problem*", Annals of Operations Research 122, 21–42, 2003.
[6]. P. Hansen, N. Mladenovic and D. Perez-Brito, "*Variable neighborhood decomposition search*", Journal of Heuristics 7(4), 335–350, 2001.
[7]. T. Levanova and M.A. Loresh, "*Algorithms of ant system and simulated annealing for the p-median problem*", Automation and Remote Control, 65, 431–438, 2004.
[8]. S. Salhi, "*Defining tabu list size and aspiration criterion within tabu search methods*", Computers and Operations Research 29, 67–86, 2002.
[9]. A.T. Murray and R.L. Church, "*Applying simulated annealing to planning-location models*", Journal of Heuristics 2, 31–53, 1996.
[10]. J. Beasley, "*OR-Library: Distributing Test Problems by Electronic Mail*", Journal of the Operational Research Society, 41(3), 1069-1072, 1990.
[11]. C.A. Irawan and S. Salhi, "*Solving large p-median problems by a multistage hybrid approach using demand points aggregation and variable neighbourhood search*", J. Glob. Optim, 63, 537-554, 2015.
[12]. N. Metropolis, A. Rosenbluth, M. Rosenbluth, A. Teller and E. Teller, "*Equation of state calculations by fast computing machines*", Journal of Chemical Physics, 21, 1087-1092, 1953.
[13]. S. Kirkpatrick, C.D. Gelatt and M.P. Veechi, "*Optimization by simulated annealing*", Science, 220, 671-679, 1983.

ICENS
INTERNATIONAL CONFERENCE ON ENGINEERING AND NATURAL SCIENCES
24-28 May 2016 /Sarajevo

CFD Analysis of a Divided Combustion Chamber of Single Cylinder Spark Ignition CNG Engine

Feyyaz Arslan[1], Yasin Ust[2]

Abstract

There are several software applications for CFD modelling of cold flow and combustion in internal combustion engines. The reliability of these applications are verified with previous studies. In preliminary studies prior to the experiment it is convenient to use CFD analysis methods. In this study, analysis of a project that is planned to do experiments of single cylinder divided chamber spark ignition CNG engine are evaluated with a commercial CFD code. CFD analysis were performed by using the G-equation for turbulent, partial premixed combustion in divided combustion chamber. The obtained results are presented comparatively for two different fuels of methane and iso-octane. These results include cylinder pressure, temperature and mass fraction at different equivalence ratios. It is observed from the results of this study that methane use in divided chamber instead of iso-octane provides higher performance in terms of indicated power output, thermal efficiency and specific fuel consumption.

Keywords: Engine performance; divided chamber; CFD combustion model; methane; iso-octane; equivalence ratio

1. INTRODUCTION

The methane, as the main component of natural gas, allows a combustion almost completely free of particulate and its high octane number leads to high resistance to knock, that allows higher compression ratios and a high level of efficiency. Divided chamber provides micro-turbulence in the chamber and it also provides heating of the mixture by walls of the chamber. These characteristics lead to providing practically complete combustion with swirl and squish motions and shifting of the lean burn limit [1].

Crane and King conducted a study to assess the effects of various pre-chamber design, operating and control parameters on exhaust emissions of a natural gas engine. Their results revealed that NO_X and hydrocarbon emissions may be shortened via pre-chamber design [2]. Mueller presented landfill gas application to a spark ignited pre-chambered engine. The study includes also natural gas application and its results presented comparatively. Employing pre-chamber to the spark ignition (SI) engine and sophisticated electronic control provide very low emissions and adjusting required fuel quality [3]. Christensen et al. compared using natural gas in homogeneous charge compression ignition (HCCI) and SI modes. The indicated efficiency of HCCI mode is better than SI operation. However, hydrocarbon and CO emissions are less generated in SI mode. SI mode provides more lean burn when it compared with HCCI mode [4]. Roethlisberger and Favrat studied the natural gas cogeneration engine with pre-chamber. They conducted four different studies in this context. First study is about engine geometrical parameters and results of this study shows pre-chamber intensifies and accelerates the combustion process and it reduces the emissions significantly [5]. The second study presents operating parameters and turbocharger characteristics. Optimization of ignition timing decreases HC and CO emissions and the optimization of turbocharger results in an increase of fuel conversion efficiency [6]. The third study is CFD analysis of pre-chamber geometrical configuration and it shows geometry of pre-chamber effects the charge, flow and combustion in engine [7]. The forth study presents the experiments of geometrical configuration of pre-chamber. Results of the study shows impacts of geometry on fuel conversion efficiency, gas flow and combustion [8]. Manivannan et al. presented an overview study about lean burn natural gas SI engines. The study provides the effects of combustion chamber geometry, fuel composition, pre-chamber and etc. according to the study, pre-chamber with the successfully implemented lean burn strategy provides lower exhaust emissions and higher thermal efficiencies [9]. Zuo et al. developed a swirl chambered combustion system for a SI engine that uses coal-bed gas and they carried out the experiments of engine. Their results show that the higher concentration methane in coal-bed gas and higher loads provides higher performance and lower emissions [10]. Shah et al. performed the experiments on a single cylinder SI engine equipped with divided chamber that is capable of fuel injection and pressure measurement. They concluded that divided chamber operated with rich charge provides a better source of ignition for lean charge in main chamber when they compared with their previous study [11]. Thelen and Toulson analyzed effects of the location of ignition source in pre-chamber by using CFD. Comparison of CFD simulations show that more distant source from orifice generates better ignition and more close source from orifice generates hotter jets with slower velocities [12]. Perini et al. studied on CFD of gas fueled SI engines with pre-chamber. They used G-Equation for turbulent flame propagation in solver at different mesh types. They suggest that the presented method by them can be successfully implemented for the gas fueled SI engines with pre-chambers [13]. Biswas and Qiao developed an experiment to assess the ignition characteristics ultra-lean premixed H_2/air mixtures by a

[1] *Yildiz Technical University, Department of Naval Architecture and Marine Engineering, 34349, Besiktas/İstanbul, Turkey.* fyarslan@yildiz.edu.tr

[2] *Corresponding author: Yildiz Technical University, Department of Naval Architecture and Marine Engineering, 34349, Besiktas/İstanbul, Turkey.* yust@yildiz.edu.tr

supersonic hot-jet. They designed a new chamber for this aim that called as dual-chamber [14]. Shah et al. conducted an experimental study on scalability aspects of pre-chamber ignition on a single cylinder marine natural gas engine. Their results demonstrate that the performance of pre-chamber strongly affected by size of the engine [15].

2. COMBUSTION ANALYSIS

Combustion analyses of a single cylinder spark ignition CNG engine equipped with divided chamber are evaluated with a commercial CFD code. In CFD analysis, G-equation for turbulent and partial premixed combustion is used.

2.1 CFD Combustion Model

Partially premixed turbulent combustion model used for CFD analysis. G-equation was used for numerical simulation of partially premixed turbulent flames. In SI DI engines partially premixed flame propagation, where a spray of fuel is injected directly into the cylinder instead of into the inlet manifold as in conventional homogeneous charge SI engines. The advantage of this technology is improved efficiency at partial load. But the increased HC emissions and soot are handicaps of stratified combustion mode [16].

2.2 Method

CFD analyses were carried out for 6 different equivalence ratios (φ_1=0.967, φ_2=0.95, φ_3=0.90, φ_4=0.85, φ_5=0.80, φ_6=0.75) at the compression ratio $\varepsilon = 10$ for two different kind of fuel which are named as methane and iso-octane. Totally 12 analyses were carried out [17]. Combustion chamber that used in the analyses is shown in Fig. 1. Divided chamber connected the main chamber with an orifice. And the main chamber has a hemispherical shape.

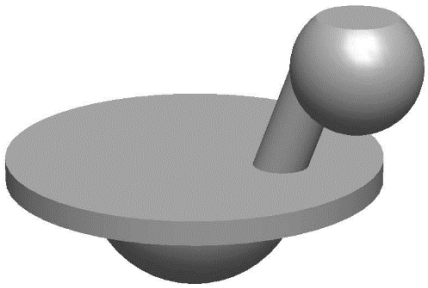

Figure 1. Combustion chamber model that used in the analyses

In the analyses, single cylinder spark ignition divided chambered CNG engine is based on. Specifications of the engine are shown in Table 1. Inlet valve opening (IVO) timing, inlet valve closing (IVC) timing, exhaust valve opening (EVO) timing and exhaust valve closing (EVC) timing are shown in the table.

Table 1. Specifications of engine

	Specifications
Type	4 Strokes, Water cooling
Number of cylinders	1
Air charging	Natural aspiration
Rated Power/Speed	4.5 kW / 1800 rpm
Bore/Stroke	87.5 mm / 110 mm
IVO	4.5° BTDC
IVC	35.5° ABDC
EVO	35.5° BBDC
EVC	4.5° ATDC

Spark timing 26 CA° BTDC is selected according to previous studies in the analysis [18]. And according to engine performance data, equivalence ratio φ_1=0.967 is selected as approximately stoichiometric equivalence ratio.

3 RESULTS AND DISCUSSION

In CFD analyses, for methane combustion, the parameters selected as six different equivalence ratios (φ_1=0.967, φ_2=0.95, φ_3=0.90, φ_4=0.85, φ_5=0.80, φ_6=0.75) at the compression ratio $\varepsilon = 10$. Variation of absolute pressure in cylinder with the CA for various equivalence ratios are shown in Fig. 2. Decrease in the equivalence ratio leads to decrease in maximum pressure. At the equivalence ratio φ_1=0.967, maximum pressure is 36.9 bar. While maximum pressure of φ_1 is shown at 9 CA° ATDC, 27.8 bar maximum pressure of the equivalence ratio φ_6=0.75 is shown at 14 CA° ATDC.

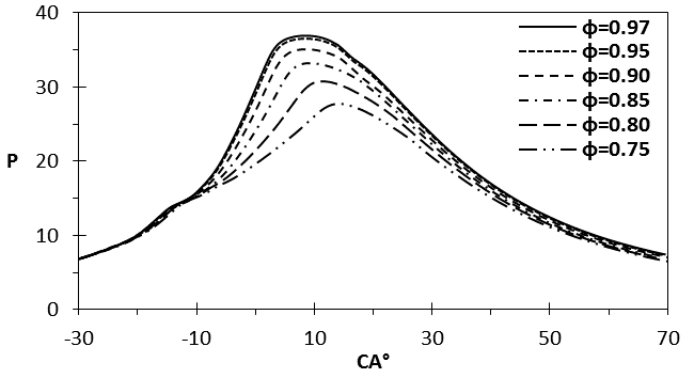

Figure 2. In-cylinder pressure at various equivalence ratios for methane

Variation of temperature in cylinder with the crank angle (CA) for various equivalence ratios are shown in Fig. 3. Temperature decreases with the decrease of equivalence ratio. Maximum temperature is 2435 K at the equivalence ratio φ_1=0.967. While maximum temperature of φ_1 is shown at 22 CA° ATDC, 2134 K maximum temperature of the equivalence ratio φ_6=0.75 is shown at 27 CA° ATDC.

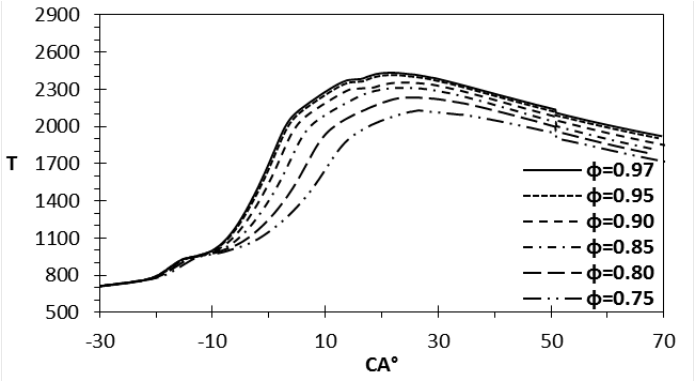

Figure 3. In-cylinder temperature at various equivalence ratios for methane

Variation of mass fraction of methane with the CA for various equivalence ratios are shown in Fig. 4. As can be seen from the Fig. 4 burning velocity decreases with the decrease of equivalence ratio.

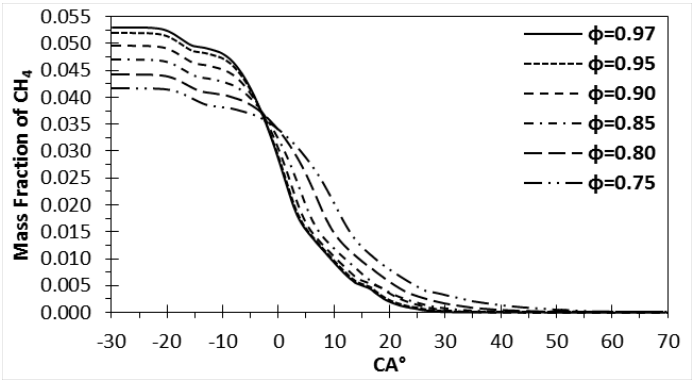

Figure 4. Mass fraction of methane at various equivalence ratios

For iso-octane combustion, the parameters selected as six different equivalence ratios (φ_1=0.967, φ_2=0.95, φ_3=0.90, φ_4=0.85, φ_5=0.80, φ_6=0.75) at the compression ratio $\varepsilon = 10$. Plots of pressure versus CA for various equivalence ratios are shown in Fig. 5. Decrease in the equivalence ratio of premixed charge leads to decrease in maximum pressure. Maximum pressure is 24.9 bar at the equivalence ratio φ_1=0.967. While maximum pressure of φ_1 is shown at 20 CA° ATDC, 18 bar maximum pressure of the equivalence ratio φ_6=0.75 is shown at 11 CA° ATDC.

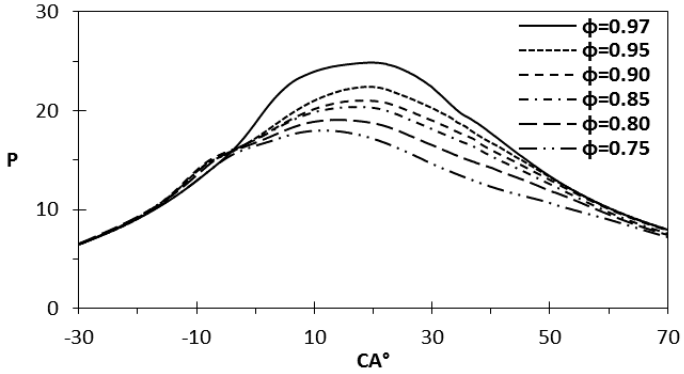

Figure 5. In-cylinder pressure at various equivalence ratios for iso-octane

Plots of temperature versus CA for various equivalence ratios are shown in Fig. 6. Temperature decreases with the decrease of equivalence ratio. Maximum temperature is 2350 K at the equivalence ratio φ_1=0.967. While maximum temperature of φ_1 is shown at 41 CA° ATDC, 1890 K maximum temperature of the equivalence ratio φ_6=0.75 is shown at 51 CA° ATDC.

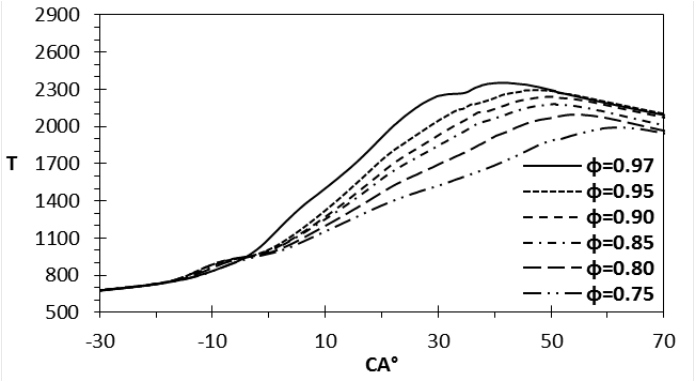

Figure 6. In-cylinder temperature at various equivalence ratios for iso-octane

Variation of mass fraction of iso-octane with respect to CA for various equivalence ratios are shown in Fig. 7. As can be seen from the Fig. 7 burning velocity decreases with the decrease of equivalence ratio.

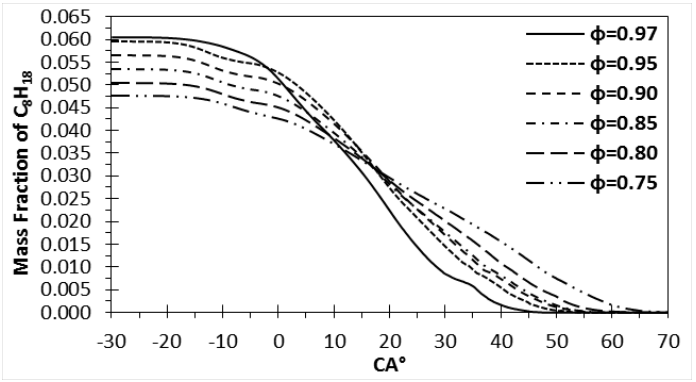

Figure 7. Mass fraction of iso-octane at various equivalence ratios

Comparison of the pressures of methane and iso-octane at the equivalence ratio $\varphi = 0.95$ is shown in Fig. 8. As can be seen from the figure methane is more favorable fuel for the divided chambered engine. There is 14 bar difference between maximum pressures of two conditions.

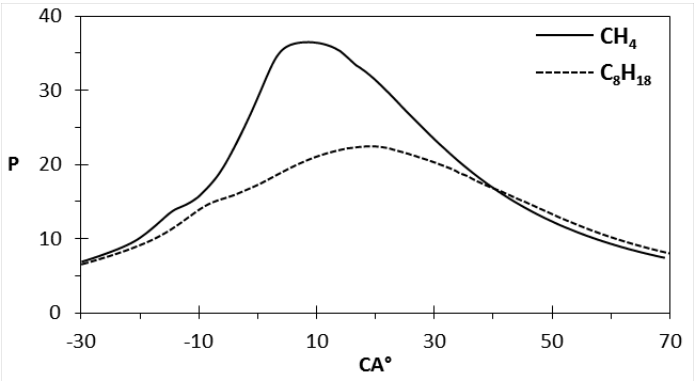

Figure 8. Comparison of the maximum pressures of CH_4 and C_8H_{18} at the equivalence ratio $\varphi = 0.95$

Comparison of the temperatures of methane and iso-octane at the equivalence ratio $\varphi = 0.95$ is shown in Fig. 9. As can be seen from the figure methane has higher maximum temperature value and it is more favorable fuel for the divided chambered engine. There is approximately 120 K difference between maximum temperatures of two conditions. And the figure also shows the burning velocity of methane is more favorable.

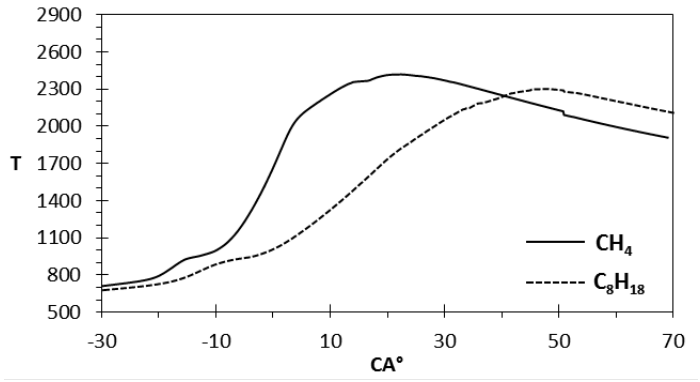

Figure 9. Comparison of the maximum temperatures of CH_4 and C_8H_{18} at the equivalence ratio $\varphi = 0.95$

Comparison of the mass fractions of methane and iso-octane at the equivalence ratio $\varphi = 0.95$ is shown in Fig. 10. As can be seen from the figure methane has burning velocity and it is more favorable fuel for the divided chambered engine. There is approximately 20 CA° difference between complete combustion of two conditions.

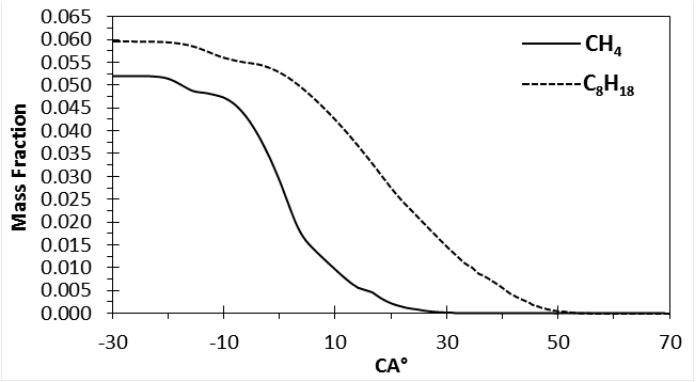

Figure 10. Comparison of the mass fractions of CH_4 and C_8H_{18} at the equivalence ratio $\varphi = 0.95$

Table 2 shows the performance outputs of divided chambered model for methane and iso-octane at the equivalence ratio $\varphi = 0.95$. It can be concluded from these results that the methane has higher indicated power output, thermal efficiency and it has lower indicated specific fuel consumption. It is observed that there is a great difference between specific fuel consumptions at approximate power ratings.

Table 2. Performance outputs of analyses for methane and iso octane at the equivalence ratio $\varphi = 0.95$

	Power	Thermal Efficiency	Specific Fuel Consumption
Methane	5.94 kW	% 36	197 g/kWh
Iso-octane	5.92 kW	% 33	244 g/kWh

4 CONCLUSION

In the present study, the analysis of the performance of a single cylinder divided chambered SI CNG engine is presented as a preliminary study of a project that planned to do experiments. In this perspective, analyses were carried out for various equivalence ratios and two different fuels. The results of the CFD analyses were given in comparison in Table 2. Present study shows that the methane is favorable fuel for divided chambered engine in terms of burning velocity, maximum pressure and temperature, indicated power, thermal efficiency and specific fuel consumption. The results can provide guidance for the performance evaluation, optimization and improvement of real divided chambered SI CNG engines.

ACKNOWLEDGMENT

This study is a part of MSc thesis of first author and it was conducted as a preliminary study for the 214M329 numbered project of TUBITAK's 3501 program. I would like to thank TUBITAK, TUBA-GEBIP, Yildiz Technical University Graduate School of Natural and Applied Sciences, Prof. Dr. Yasin UST, Assoc. Prof. Dr. Guven GONCA and Asst. Prof. Dr. Mehmet CAKIR.

REFERENCES

[1] *Natural gas and renewable methane for powertrains: future strategies for a climate-neutral mobility*. New York, NY: Springer Berlin Heidelberg, 2016.
[2] M. E. Crane and S. R. King, "Emission Reductions Through Precombustion Chamber Design in a Natural Gas, Lean Burn Engine," *Journal of Engineering for Gas Turbines and Power*, vol. 114, no. 3, p. 466, 1992.
[3] G. P. Mueller, "Landfill Gas Application Development of the Caterpillar G3600 Spark-Ignited Gas Engine," *Journal of Engineering for Gas Turbines and Power*, vol. 117, no. 4, p. 820, 1995.
[4] M. Christensen, B. Johansson, and P. Einewall, "Homogeneous Charge Compression Ignition (HCCI) Using Isooctane, Ethanol and Natural Gas - A Comparison with Spark Ignition Operation," 1997.
[5] R. P. Roethlisberger and D. Favrat, "Comparison between direct and indirect (prechamber) spark ignition in the case of a cogeneration natural gas engine, part I: engine geometrical parameters," *Applied Thermal Engineering*, vol. 22, no. 11, pp. 1217–1229, Aug. 2002.
[6] R. P. Roethlisberger and D. Favrat, "Comparison between direct and indirect (prechamber) spark ignition in the case of a cogeneration natural gas engine," *Applied Thermal Engineering*, vol. 22, no. 11, pp. 1231–1243, Aug. 2002.
[7] R. P. Roethlisberger and D. Favrat, "Investigation of the prechamber geometrical configuration of a natural gas spark ignition engine for cogeneration: part I. Numerical simulation," *International Journal of Thermal Sciences*, vol. 42, no. 3, pp. 223–237, Mar. 2003.
[8] R. P. Roethlisberger and D. Favrat, "Investigation of the prechamber geometrical configuration of a natural gas spark ignition engine for cogeneration: part II. Experimentation," *International Journal of Thermal Sciences*, vol. 42, no. 3, pp. 239–253, Mar. 2003.
[9] A. Manivannan, P. T. Porai, S. Chandrasekaran, and R. Ramprabhu, "Lean Burn Natural Gas Spark Ignition Engine - An Overview," 2003.
[10] C. Zuo, Y. Qian, J. Tan, and H. Xu, "An experimental study of combustion and emissions in a spark-ignition engine fueled with coal-bed gas," *Energy*, vol. 33, no. 3, pp. 455–461, Mar. 2008.
[11] A. Shah, P. Tunestal, and B. Johansson, "Effect of Relative Mixture Strength on Performance of Divided Chamber 'Avalanche Activated Combustion' Ignition Technique in a Heavy Duty Natural Gas Engine," 2014.
[12] B. C. Thelen and E. Toulson, "A Computational Study of the Effects of Spark Location on the Performance of a Turbulent Jet Ignition System," 2016.
[13] F. Perini, Y. Ra, K. Hiraoka, K. Nomura, A. Yuuki, Y. Oda, C. Rutland, and R. Reitz, "An Efficient Level-Set Flame Propagation Model for Hybrid Unstructured Grids Using the G-Equation," *SAE International Journal of Engines*, vol. 9, no. 3, Apr. 2016.
[14] S. Biswas and L. Qiao, "Prechamber Hot Jet Ignition of Ultra-Lean H_2 /Air Mixtures: Effect of Supersonic Jets and Combustion Instability," *SAE International Journal of Engines*, vol. 9, no. 3, Apr. 2016.
[15] A. Shah, P. Tunestal, and B. Johansson, "Scalability Aspects of Pre-Chamber Ignition in Heavy Duty Natural Gas Engines," 2016.
[16] N. Peters, *Turbulent combustion*. Cambridge, [England] ; New York: Cambridge University Press, 2000.
[17] F. Arslan, "Investigation on the effects of Divided Combustion Chamber Use in an Otto Engine the Performance with Using Two-Zone Combustion Model and CFD," MSc. thesis, Yildiz Technical University, Istanbul, TURKEY, 2016.
[18] S. Soylu, "Autoignition modeling of natural gas for engine modeling programs: an experimental and modeling study," PhD Thesis, Iowa State University, 2001.

Biographical notes: Feyyaz ARSLAN graduated from Naval Architecture and Marine Engineering Department at YILDIZ Technical University with MSc degree in 2016. Feyyaz ARSLAN is working as the Research Assistant of the Naval Architecture and Maritime Faculty, YILDIZ Technical University, Istanbul. His main research areas are internal combustion engines, CFD analysis, thermodynamics and ship machinery.

Biographical notes: Yasin UST graduated from Naval Architecture and Marine Engineering Department at YILDIZ Technical University with PhD degree in 2005. Yasin UST is working as the Vise Dean of the Naval Architecture and Maritime Faculty, YILDIZ Technical University, Istanbul. His main research areas are thermodynamic simulation of energy conversion systems, ship machinery and cogeneration systems.

ICENS
INTERNATIONAL CONFERENCE ON ENGINEERING AND NATURAL SCIENCES
24-28 May 2016 /Sarajevo

IAQ Modeling and Estimating for a Meeting Room

Nesibe Yalcin[1], Deniz Balta[2], Ahmet Ozmen[3],

Abstract

Carbon dioxide (CO_2) gas amount is widely used for Indoor Air Quality (IAQ) determination in densely occupied environments such as schools, homes, and offices. The most important CO_2 source in these environments is human metabolic generation. In this study, IAQ modeling tool has been developed to estimate the distribution of CO_2 concentration inside an unventilated meeting room and to observe the status of indoor air in terms of CO_2. Information of their weight, height and activity level in addition to the number of occupants are considered in the model. Indoor CO_2 concentrations are presented graphically by the modeling tool as a function of time and total number of the occupants. The data obtained from the model are compared with real measurements to validate the model, and promising results are obtained.

Keywords: carbon dioxide, indoor air quality, modeling, prediction.

1. INTRODUCTION

Recent research has shown that people spend an average 2 hours of their day outside; therefore they are interacting further with indoor air. Indoor air can affect human health, comfort and performance [1]. Indoor Air Quality (IAQ) refers to the acceptability levels of the buildings' air.

A demand control ventilation system is a supplementary part in the ventilation system design of a building and IAQ modeling and simulation studies help examining the buildings before they built to determine ventilation rate and to optimize energy use. CO_2 gas breathed out by humans in the buildings plays an important role in the regulation of ventilation for acceptable IAQ. Occupant behavior and actual occupants are counted in the IAQ simulation studies in order to improve the accuracy of the IAQ modeling. Reference [2] has proposed CO_2 gas as the best predictor of occupant behavior. A method to predict occupant-generated CO_2 concentration in naturally ventilated elementary classrooms is presented in [3]. The prediction CO_2 generation rate per child is similar to the literature in terms of the activity level and age of students.

In this study, a meeting room in Bilecik Şeyh Edebali University is mathematically modeled and simulated to predict IAQ in terms of CO_2. The predicted CO_2 concentration is presented in graphical form. CO_2 concentrations in the meeting room are measured to verify model prediction results and then it is found an encouraging relationship between them.

2. IAQ MODELING METHOD

The first thing coming to mind is oxygen when breathing is mentioned ever so carbon dioxide (CO_2) is as important as oxygen (O_2) for healthy breathing. CO_2 is a colorless and odorless gaseous contaminant at room temperatures. CO_2 concentration can be used to indicate IAQ.

CO_2 production rate per person V_{CO2} is calculated using rate of O_2 uptake V_{O2} and respiratory quotient RQ given as in Eq. (1). RQ is the ratio between CO_2 production and O_2 uptake (V_{CO2}/V_{O2}) and 0.83 for an average size person busy with light activities. V_{CO2} increases in the same proportion with $V_{O2.}$

$$V_{CO_2} = RQ \times V_{O_2} \tag{1}$$

The characteristics such as age, gender, health status, body sizes and physical activity level affect the inhaled and exhaled O_2 and CO_2 amounts. V_{O2} based activity level M and DuBois surface area A_D can be estimated by Eq. (2) [4].

[1] *Corresponding author: Bilecik Şeyh Edebali University, Department of Computer Engineering, 11230, Merkez/Bilecik, Turkey.* nesibe.yalcin@bilecik.edu.tr

[2] *Sakarya University, Institute of Natural Sciences, 54187, Serdivan/Sakarya, Turkey.*

[3] *Sakarya University, Department of Computer Engineering, 54187, Serdivan/Sakarya, Turkey.* ddural@sakarya.edu.tr, ozmen@sakarya.edu.tr

$$V_{O_2} = \frac{0.00276\,A_D M}{(0.23\,RQ + 0.77)} \quad (2)$$

A_D can be determined using Eq. (3) where H is body height and W is body weight.

$$A_D = 0.20247 H^{0.725} W^{0.425} \quad (3)$$

Metabolic equivalent (met) levels for various physical activities are given in Table 1.

Table 6. Met levels for various activities [5]

Activity	met level
Seated, quiet	1.0
Reading, seated	1.0
Writing	1.0
Typing	1.1
Standing, relaxed	1.2
Stead, filing	1.2

The production amount of CO_2 in a room increases linearly with the number of people *N* in the room [6].

$$G = V_{CO_2} \times N \quad (4)$$

Pollutant concentration is calculated by mass entering and leaving the environment in IAQ models based on mass balance equation. Pollutant mass balance equation can be given as follows.

$$V\frac{dC}{dt} = S - LC \quad (5)$$

V is the effective volume of the environment, C is indoor pollutant concentration and t is time. S and L are source and sink parameters, respectively. In this study, S and L parameters are computed by (6) and (7) equations.

$$S = \frac{1}{V}\left(C_O Q_{inf} + G\right) \quad (6)$$

$$L = \frac{Q_{exf}}{V} \quad (7)$$

C_O is outdoor pollutant concentration, Q_{inf} is infiltration rate and Q_{exf} is exfiltration rate. Balanced airflows are used in this study, so Q_{inf}=Q_{exf}. The analytical solution of Eq. (5) used to predict the pollutant concentration of the environment is as the following [7].

$$C = C_O e^{-Lt} + \frac{S}{L}\left(1 - e^{-Lt}\right) \quad (8)$$

The body volume of an average person is 0.06 m^3 and used in calculation of the effective volume.

3. EXPERIMENTAL DESIGN

A meeting room is modeled for IAQ simulation study. The modeled room as shown in Figure 1 is located in the third floor in Engineering Faculty Bilecik Şeyh Edebali University. The dimensions of the room 5.34 m in length, 3.27 m in height, 3.51 m in width. It has one door (2.1 m × 0.95 m) and one window (the size of its openable part is 1.1 m × 0.95 m). The leakage area under the door is 0.03 m^2.

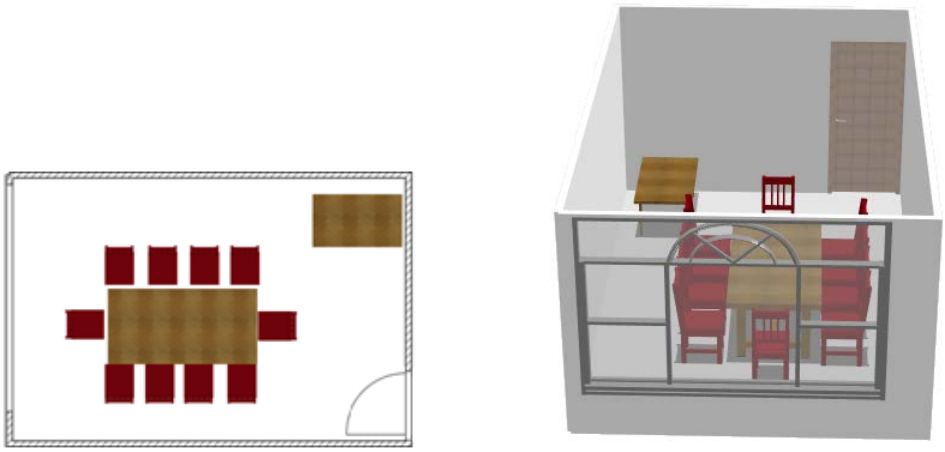

Figure 9. (a) Schematic representation of the meeting room (b) 3D view of the meeting room

As CO_2 source, 5 people take part in the room during modeling and their characteristics are given in Table 2.

Table 2. The characteristics of people

Occupant Id	Height (m)	Weight (kg)	A_D
1	1.65	62	1.6819
2	1.60	50	1.5011
3	1.68	56	1.6319
4	1.64	51	1.5411
5	1.71	85	1.9737

The calculation of CO_2 generation amount is based on the number of people and their physical activity level. The total number of people and the mean of their physical activity levels in the meeting room are presented as a function of time in Figure 2.

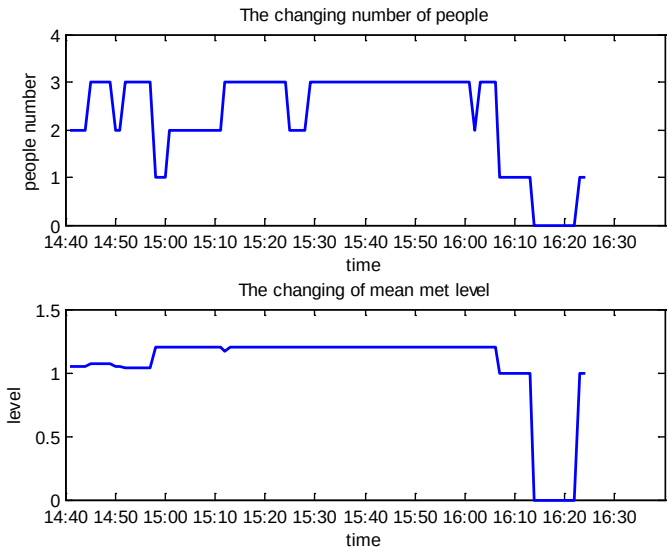

Figure 2. The number of people and the mean of their activity levels

The CO_2 concentration, air temperature and relative humidity were measured by a CO2 & TEMP. & RH meter as shown in Figure 3. Measuring range is 0 ~ 9999 ppm; accuracy ±30 ppm + %5 of the reading (0 ~5000 ppm).

Figure 3. CO2/Temp./RH meter

4. RESULTS AND DISCUSSION

Real measurements were performed under standard conditions. The air temperature and relative humidity results obtained by the data logger are illustrated in Figure 4. The measured air temperature and relative humidity in the meeting room were 22.5 – 23.5 ^{o}C and 38.9 – 40.7%, respectively.

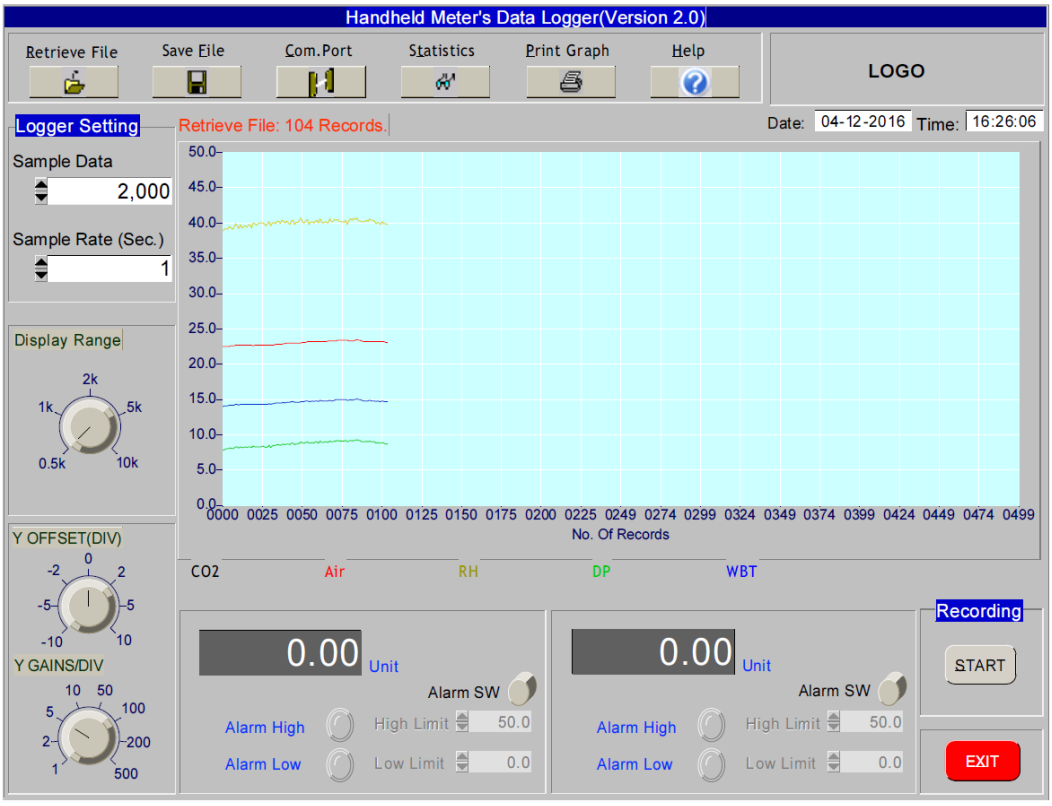

Figure 4. Air temperature and relative humidity data logger

CO_2 measurements are performed between 14:40 and 16:25 on Tuesday. The CO_2 measurement results by using the readings of CO2 & TEMP. &RH meter are shown in Figure 5.

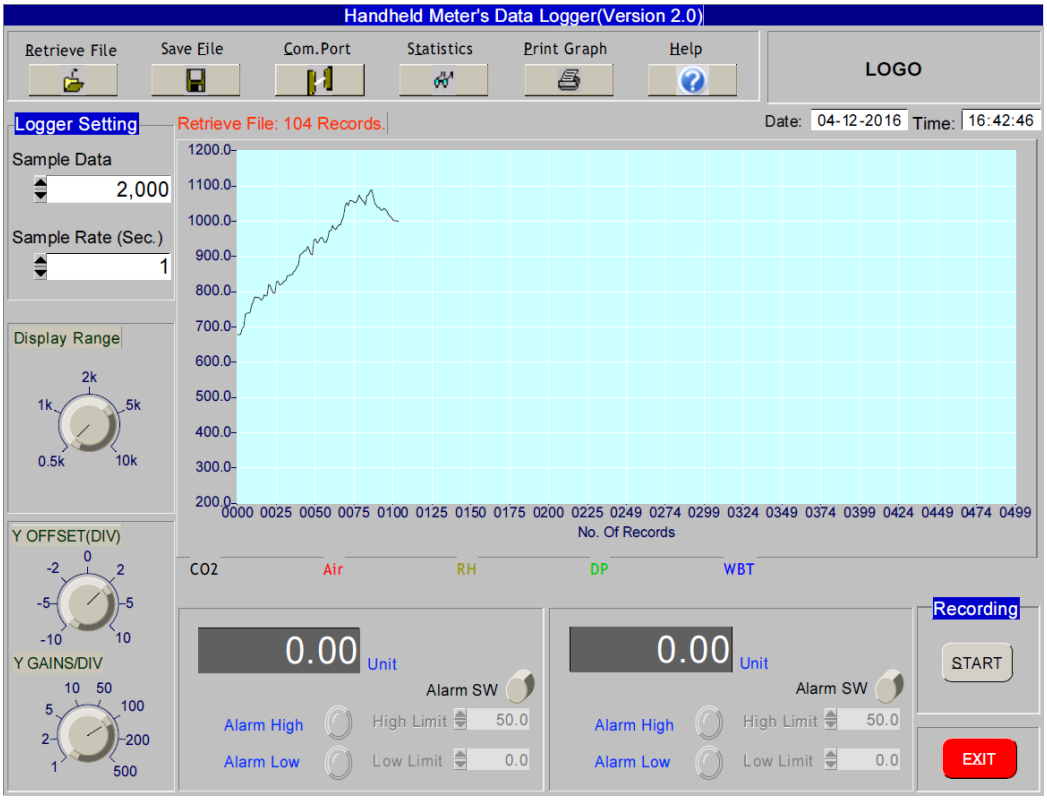

Figure 5. CO_2 readings

Initial and outdoor CO_2 concentrations are 677 ppm and 400 ppm, respectively. Time (sampling) duration is about 2 hours and time interval 1 min. The maximum, minimum, mean and standard deviation values and the histogram graphic of indoor CO_2 concentrations obtained from measurements are represented in Figure 6.

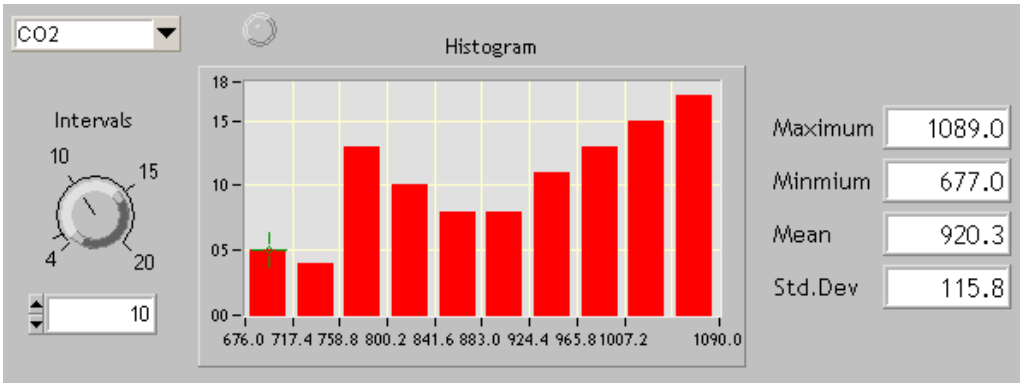

Figure 10. The histogram graphic of CO_2

CO_2 prediction results are given in Figure 7. The threshold value is determined as 1000 ppm for indoor CO_2 concentration by Environmental Protection Agency. CO_2 concentration in the room exceeds the threshold between 15:40 and 16:20 and so ventilation is required during this time.

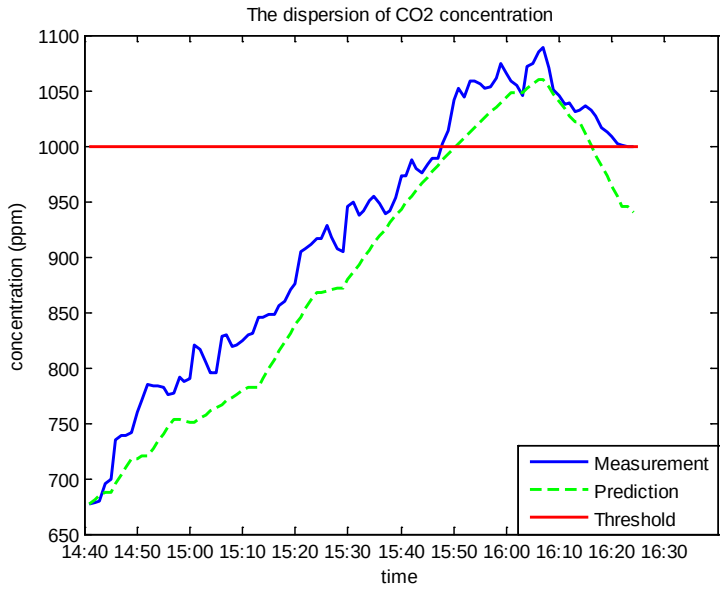

Figure 7. The results of CO_2 prediction

The prediction and measurement graphics are similar. The CO_2 concentration increases and reduces depending on the number of people in the room. Although the maximum number of people in the room is 3, indoor air has been bad in about 2 hours.

5. CONCLUSION

In this study, an IAQ model is developed and simulated to estimate the CO_2 concentration in a meeting room. This study indicates how CO_2 generated by people affect IAQ. A user can observe graphically the changing of CO_2 amounts and IAQ variations for a defined period of time.

IAQ should be investigated in other places where the large numbers of people occupy, such as offices, homes and factories, to increase their health, well-being, productivity and safety, and to decrement energy usage.

REFERENCES

[1]. A. Soysal, and Y. Demiral, "Indoor Air Pollution," *TAF Prev Med Bull*, vol. 6 (3), pp. 221-226, 2007.
[2]. Y. Jian, Y. Guo, J. Liu, B. Zhen, and L. Qingrui. "Case Study of Window Opening Behavior Using Field Measurement Results," *Building Simulation*, vol. 4, pp. 107-116, 2011.
[3]. K. H. Bartlett, M. Martinez, and J. Bert, *Modeling of Occupant-Generated CO2 Dynamics in Naturally Ventilated Classrooms*, Journal of occupational and Environmental Hygiene, 2004, vol. 1, pp. 139–148.
[4]. A. K. Persily, "Evaluating Building IAQ and Ventilation with Indoor Carbon Dioxide," *ASHRAE Transactions*, vol. 103 (2), pp. 4072 (1–12), 1997.
[5]. *Thermal Environmental Conditions for Human Occupancy.* ANSI/ASHRAE Addendum g to ANSI/ASHRAE Standard 55-2010, 2013.
[6]. N. Nassif, "CO2-based Demand-Controlled Ventilation Control Strategies for Multi-Zone HVAC Systems," *in Proc. Eleventh International Conference Enhanced Building Operations*, 2011, New York City, pp. 18–20.
[7]. M. Jamriska, *Modeling of Indoor Particle Concentration: Indoor Environment – Airborne Particles and Settled Dust*, L. Morawska and T. Salthammer, Ed. Wiley-VCH, 2003..

The Effect Of Reaction Parameters On The Yield And Fuel Properties Of Biodiesel From Algae Oil

Fevzi Yasar[1*] Sehmus Altun [21]

Abstract

In this study, the effect of catalyst concentration, reaction temperature and time on the conversion of algae oil into biodiesel via alkali-catalyzed transesterification using methanol at fixed molar ratio of 6:1was studied. It was observed that less catalyst than necessary resulted in a lower yield, while a maximum yield was obtained when moderate amount was used as further increase in catalyst caused a decrease in the yield. The similar results were obtained for viscosity and density values. In the case of moderate amount of KOH, kinematic viscosity and density was measured as 4,812 mm^2/s and 876 kg/m^3, respectively for produced ester.

Keywords: *Chlorella, algae oil, biodiesel, fuel properties.,*

1. INTRODUCTION

Petroleum, particularly the raw material of transportation, construction vehicles, automotive, electric generation, metallurgy, construction and chemical industry in the world, has the lion's share in energy consumption. Developing alternative fuels apart from petroleum for these sectors carries weight with a possible petroleum crisis. On the other hand, considerable amount of harmful gases spread around since the consumption petroleum products have increased lead to global climate changes which may cause dangerous events to the environment, human health and the globe [1]. Due to the fact that the number of vehicles in use globally increases, many rearrangements including redesigning the engines have been carried out in order to reduce the effects of emissions of vehicles on environment and ecosystem [2]. One of the comprehensive works conducted is to investigate and develop alternative fuels without any change in diesel engines. It is necessary that the alternative fuel resources should be obtainable from local sources, renewable, applicable and easily accessible for a sustainable economic development and a cleaner environment. Countries focus on various renewable energy sources (biomass, solar, wind, hydroelectric, geothermal, wave etc.) regarded with their economic, environmental, natural and social features. In this respect, biodiesel, obtained from renewable resources such as vegetable and animal fats, has been investigated as alternative to petroleum diesel.

In the studies carried out [3-5], with the use of biodiesel fuel obtained from such renewable resources as vegetable and animal fallows, it was pointed out that oil dependence could be reduced; and that they were taken into consideration as promising alternative fuels for decreasing air pollution stemming from exhaust emissions. That vegetable and animal fats with high edible quality will be used in biodiesel production means additional cost for the countries importing great deal of their cooking oil need. Particularly, without using the resources and without making use agriculture areas, looking for environmentally friendly energy resources has been accelerated before the increase in food cost. Within this context, studies about biodiesel production from different types of algae have been carried out recently [6]. The fact that some types of algae contain more fat than those of arable crops, and that their growing up processes are easier, and that they are not affected from the changing climatic conditions and that they are producible in high amounts in a short time have made biodiesel production attractive [7]. Another important property of algae is that they can flourish very fast in

[1]*Department of Refinery and Petro-Chemistry, University of Batman, 72100, Batman, Turkey. E-mail: yasarf75@gmail.com Telephone: +(90) 488-2173500 Fax: +(90) 488-2173601*
[2]*Department of Automotive Engineering, University of Batman, 72100, Batman, Turkey*

very small areas [8]. Moreover, because of the reasons that there is no need for fertile agricultural fields to grow them, and that they can flourish in small ponds, and that they can adapt desert conditions, and that they can grow in plastic bags and tanks and nearby energy plants which emit carbon dioxide, studies related to biodiesel production from different kinds of algae have been conducted lately.

In this study, the effect of transesterification conditions on the yield, viscosity and density of biodiesel from algae oil, which is obtained from unicellular and heterotroph Chlorella type algae, have been examined.

2. MATERIAL and METHOD

In this study, the algae oil used for biodiesel production was supplied by a commercial firm (Soley Biotechnology, Istanbul, Turkey). The algae oil, here, has been obtained from unicellular and heterotroph type Chlorella. Some of the properties of algae oil were analysed before it was converted into biodiesel. In the analyses carried out, it was determined that the water content, viscosity and density values of algae oil were particularly high. In order to lower the water content of algae oil, it was subjected pre-heating for 2 hours by being mixed with magnetic mixer at a temperature over 100^{o}C (between 110-120^{o}C) after it was filtered. After the pre-heating, the analyses of the same parameters were performed after the oil was rested in convenient conditions.

Initially, 300 gr of algae oil was heated up to 60^{o}C to produce biodiesel out of algae oil. According to this raw material, the calculations of reactants needed to be used for reaction are as follows:

According to the calculations done above, 2.25 g KOH was solved in 65.485 g methyl alcohol in another container under room conditions. The reaction was started by adding the obtained mixture into the pre-heated oil under convenient conditions. In Figure 1, in transesterification reaction transfer of the methyl alcohol-KOH mixture into the reaction container and completion of reaction can be seen

*Figure **1** Transfer of the methyl alcohol-KOH mixture into the reaction container and completion of reaction*

At the end of the reaction, the reaction was terminated switching off the heater and mixer and the obtained ester-glycerine mixture was left to rest for 12 hours after it was transferred into the separating funnel. At the end of the duration, the glycerine accumulated at the bottom of separating funnel due to the density difference was transferred into another container and weighed. Afterwards, the ester whose glycerine was taken was washed four times with distilled water at 22, 40, 50 and 60^{o}C, so the unwanted alcohol and solid particles, if there were any, were able to be removed.

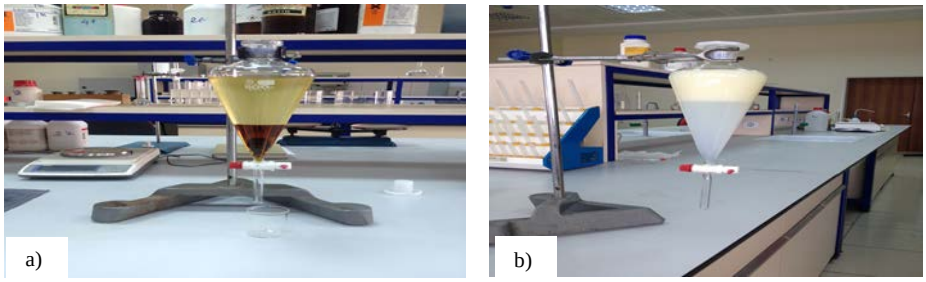

*Figure **2** Taking glycerine from separating funnel (a), washing ester (b)*

For ester remaining after the forth washing, water and alcohol were vaporized by heating methyl ester at 110°C for nearly 60 min since there may have left partly a little water and alcohol. Then, the remaining ester amount was weight on a sensitive balance and noted down. In Figure 3, the process of removing water and alcohol can be seen.

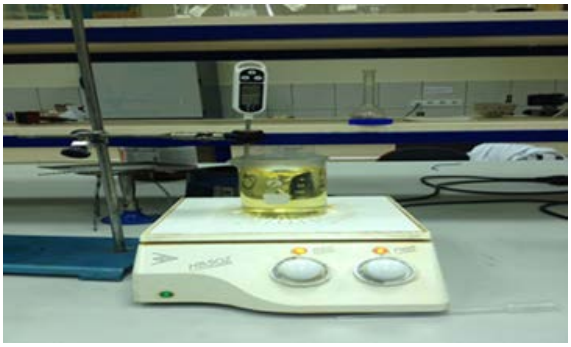

*Figure **3** Removing the remaining water and alcohol in ester*

3. TEST RESULTS

0.5%, 0.75% and 1.00% KOH of oil by weight at 6:1 molar ratio under 60°C and 60 min conditions was experimented in order to examine the effect of catalyst amount on the yield, viscosity and density. The viscosity and density parameters of product obtained as a result of these works were determined, and their alteration is shown in Figure 4 (a), (b) and (c).

As seen in Figure 4 (a), with the use of 0.5% KOH catalyst, while the lowest yield of 88.33% was obtained, the maximum product yield of 91.93% was reached with the use of 0.75% KOH catalyst. When the amount of catalyst was increased to 1.00%, it was observed that the yield of product achievement decreased.

When Figure 4 (b) is examined, with the use of 0.5% KOH catalyst, kinematics viscosity value could not catch the 5.00 mm^2/s of limit value as required in EN 14214. However, with the use of 0.75% and 1.00% KOH catalyst, the viscosity values of 4.812 mm^2/s and 4.902 mm^2/s were obtained, respectively; and it was seen that these values are within the context of standards.

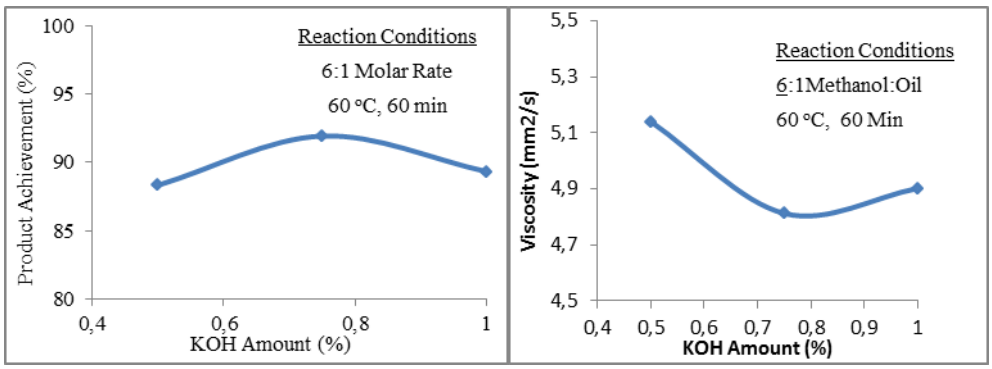

*Figure **4(a)** Change of product achievement with KOH amount **Figure 4(b)** Change of viscosity with KOH amount*

In Figure 4 (c), it is seen that the density changes depending upon the amount of catalyst. Under constant transesterification conditions, while the density of obtained ester was determined as 898 kg/m^3 with the use of 0.5% KOH catalyst, it is seen that the density dropped when 0.75% KOH was used, but there was partial increase in density when 1.00% KOH was used. As a result of the study, maximum product achievement and minimum viscosity and density values were obtained when 0.75% catalyst was used.

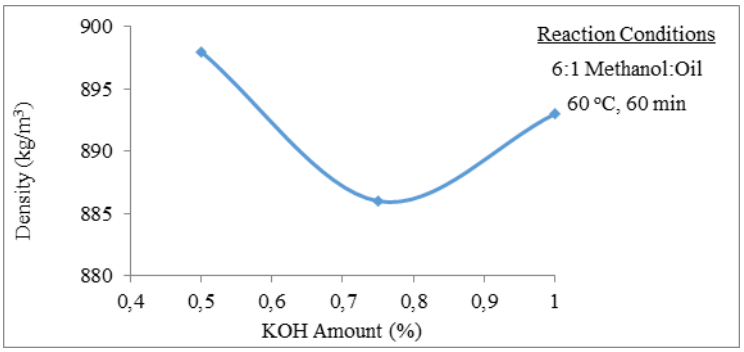

*Figure **4.(c).** Change of density with amount of KOH*

The most important aspect that should be taken into consideration for the amounts of these catalysts can be interpreted as the drop of product achievement, causing saponification during reaction and also aggravating glycerol phase separation when more catalyst than necessary is used.

After determining the suitable catalyst amount for reaction, in order to optimize the reaction temperature under 0.75% KOH and 60 min and 6:1 molar ratio it was changed as 60, 63, 65, 68 and 70°C. When the reaction temperature was increased to 68^{o}C gradually, the yield increased depending upon the temperature and at 68^{o}C; and the maximum yield was obtained as 98.70%. Nevertheless, when the temperature was increased 70^{o}C, it was determined that the product achievement decreased. Furthermore, it was seen that the viscosities of products obtained at all temperature values caught the limit value of 5.00 mm^2/s required by EN 14214. While the highest viscosity value (4.812 mm^2/s) was seen at 60^{o}C, the most convenient viscosity (4.491 mm^2/s) was obtained at reaction temperature. When the temperature was increased to 70^{o}C, however, amount increase in viscosity was observed.

The density decreases relatively until temperature increase reaches to 68^{o}C. When the temperature is increased to 70^{o}C, a partial increase is observed in density as in viscosity. In optimization works, after determining proper catalyst amount and reaction temperature for reaction, 5 reactions were realized within 60, 70, 80, 90 and 100 min reaction times to determine the effects of reaction time. The highest yield was obtained with 80 minutes reaction. When reaction time is increased to 90 and 100 min, it was determined that the product achievements decreased as 98.33% and 98.23%, respectively. While ester viscosity obtained at the end of 60 minute reaction time gave the highest value as 4.585 mm^2/s, it was established that when reaction time was increased gradually, the ester viscosity obtained at the end of 80 minute time was at the lowest value with 4.491 mm^2/s. It was observed that the viscosity increased again when reaction times were increased to 90 and 100 minutes. It was found that the density values of ester obtained at the end of all reaction times are between the values of 860-900 kg/m^3, which are required by EN 14214. The lowest density values are obtained as 881 kg/m^3 at the end of 80 minute reaction. On the contrary, the highest density value is found as 884 kg/m^3 in 60 min.

ACKNOWLEDMENT

This study was supported by by the Unit of Scientific Research Projects of Batman University, Batman, Turkey with Research Project No. BTUBAP-2015-Doktora-2.

REFERENCES

[1]. Kumbur, H., Özer, Z., Özsoy, H.D., Avcı, E.D., 2005, The Comparison of Potential of Traditional and Renewable Energy Resources and their Environmental Affects in Turkey, III Symposium and Exhibition of Renewable Energy Sources, Mersin.
[2]. Buğra Otken, B., Gümüşay, M.Ü, Preparation of Interfaces of GIS for Analysing Emissions the Vehicles on the Move onHighways, www.hkmo.org.tr/resimler/ekler/.)
[3]. Kumar, M.S., Kerihuel, A., Bellettre, J. and Tazerout, M., 2006, Ethanol animal fat emulsions as a diesel engine fuel – Part 2: Engine Test Analysis, Fuel, 85, 2646–2652.
[4]. Altun, Ş., Öner, C., 2009, Biodiesel production from inedible animal tallow and an experimental investigation of its use as alternative fuel in a direct injection diesel engine, Applied Energy, 86, 2114–2120.
[5]. Işıklı, İ., E. Açıkkalp, E., Yamık, H., Kurban, M., 2011, Biyodizelin dizel santrallerde kullanım analizi, 6th International Advanced Technologies Symposium (IATS'11), , Elazığ, Turkey.
[6].]. Chen, Z., Wang, X., Pei, Y., Zhang, C., Xiao, M., He, J., 2015, Experimental investigation of the performance and emissions of diesel engines by a novel emulsified diesel fuel, Energy Conversion and Management, 95, 334–341.

[7]. Xu, H., Miao, X., Wu, Q., 2006, High quality biodiesel production from a microalga Chlorella protothecoides by heterotrophic growth in fermenters, Journal of Biotechnology, 126, 499–507.
[8]. Mata, T.M., Martins, A.A., Caetano, N.S., 2010, Microalgae for biodiesel production and other applications: A review, Renewable and Sustainable Energy Reviews, Vol.14, 217–232.
[9]. . www.allaboutalgae.com/open-pond

ICENS
INTERNATIONAL CONFERENCE ON ENGINEERING AND NATURAL SCIENCES
24-28 May 2016 /Sarajevo

Grounded and Floating Real Inductor Simulations and Experimentations using Second Generation Current Conveyors

Mehmet Demirtas[1], Salih Gunes[2], Saadetdin Herdem[2]

Abstract

Current Conveyors (CC) are active circuit elements which perform analog signal processing. CCs were developed as an alternative to the classical Operational Amplifiers (OPAMP). Unlike OPAMPs, CCs are current-based and they operate according to the principle of 'current conveying' from one terminal to another. As a modified version of the First Generation Current Conveyor (CCI), Second Generation Current Conveyors (CCII) is versatile and useful in designing analog circuits such as filters, amplifiers, inductor simulators etc. In this paper, one grounded and one floating inductor simulator designs are given. These simulator designs are based on CCII's and passive elements like resistors and capacitors. Both inductor simulator designs are lossy and simulate real inductors that have internal resistance. The simulators simulate an inductance in series with an internal resistance. Since inductors are non-ideal, noisy, bulky circuit elements, it is reasonable to simulate their behavior under certain frequency range using CCII's as active elements. In this study, inductor simulators are created first by BJTs & passive elements in SPICE environment and created inductor simulators are tested in a Low Pass Filter (LPF) for a frequency range up to 10MHz. Moreover, both simulators are realized for experimentation using commercially available Analog Device's AD844's which can perform as a CCII & using resistors and capacitors. Realized inductor simulators are tested in the same LPF. The gain of the filter is measured for 15 different frequency values which are located between 10 Hz-10MHz. Finally, both SPICE simulation and experimental results are compared for the same LPF which is constructed using ideal inductor. It is concluded that a lossy, real inductor can be simulated up to certain frequencies by using CCIIs both in simulation environment and experiment.

Keywords: second generation current conveyors; inductance simulation; current conveying; analog design

1. INTRODUCTION

1.1 Second Generation Current Conveyors

Second Generation Current Conveyors (CCII) are first proposed as a revised version of First Generation Current Conveyors(CCI) [1]. Compared to CCIs, CCIIs are more useful and versatile in analog signal processing implementations such as voltage/current sources, amplifiers, filters, differentiators, integrators and inductance simulations [2]. The main principle of current conveyors is conveying current from one terminal to another terminal.

In Figure 1, block diagram of a CCII is shown. Under ideal conditions, the principle of operation of CCII is as follows:

- If a V_y voltage is applied to the Y terminal, the same amount of voltage will appear at terminal X. Therefore, $V_x = V_y$ will be observed.

[1] *Corresponding author: Selçuk University, Department of Electrical and Electronics Engineering, 42000, Selçuklu/Konya, Turkey.* mdemirtas@selcuk.edu.tr

[2] *Selçuk University, Department of Electrical and Electronics Engineering, 42000, Selçuklu/Konya, Turkey.* sgunes@selcuk.edu.tr,sherdem@selcuk.edu.tr

Figure 1. CCII Block Diagram

- There is no current flowing into to the Y terminal which makes $i_y = 0$ which is the only difference between CCI and CCII. In CCI, if there is a current flowing into the X terminal, the same amount of current will flow into the Y terminal.
- If there is a current flowing into the X terminal, the same current will also flow into the Z terminal which is $i_x = i_z$.

Under ideal conditions, Y terminal should not draw current from the circuit which means there is infinite impedance at that terminal. Also, since voltage at X terminal follows the voltage at Y terminal, the impedance at X terminal should be very low, ideally zero.

$$\begin{bmatrix} i_y \\ V_x \\ i_z \end{bmatrix} = \begin{bmatrix} 0 & 0 & 0 \\ 1 & 0 & 0 \\ 0 & \pm 1 & 0 \end{bmatrix} \begin{bmatrix} V_y \\ i_x \\ V_z \end{bmatrix} \quad (1)$$

The matrix which explains the relation between input and output characteristics of CCII in ideal conditions is as shown in (1). In hybrid matrix, ±1 notation indicates the direction of the current at Z port. If it is +1, then CCII is called as positive type second generation current conveyor (CCII+). If it is -1, that type of CCII is called as negative type second generation current conveyor(CCII-).

1.2 Inductance Simulation

Inductors are non-ideal passive circuit elements. The reasons for their non-ideality are the length of wire to wrap up inductors, the internal resistance of that wire and parasitic capacitance which occurs between parallel wirings [3]. Moreover, inductors are bulky, expensive and noisy circuit elements which contain too much unwanted characteristics [4]. Because of these reasons, physical inductors are not generally preferred in integrated circuits. Instead of physical inductors, 'inductance simulator' circuits are used. Inductance simulator circuits operate like inductors under certain frequency range.

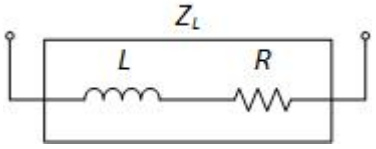

Figure 2. Real Inductor Model

In Figure 2, a real inductor model is shown. In this model, R in series with L is the resistance of the wire used to form inductor. The impedance observed between terminals of a real inductor is given as follow:

$$Z_L = R + sL \quad (2)$$

Using CCIIs and certain combination of passive elements like resistors and capacitors, it is possible to simulate both floating and grounded inductors.

2. MATERIALS AND METHODS

One grounded and one floating lossy, real inductor models are given. The proposed models use CCII's and passive circuit elements such as resistors and capacitors as seen in Figure 3 and Figure 9. Those models are tested in test circuits which behave as low pass filter. Also, Analog Device's AD844[5] integrated circuit is used as CCII+ so that the test circuit is built and measured experimentally. For experimental testing, the gain is measured for 15 different frequency points to compare simulation and experimental results.

2.1 Grounded Inductance Model

In Figure 3, a grounded inductance simulation circuit which consists of one CCII+ and three passive elements is given [6]. This circuit simulates a real inductor which consists of a resistance and an inductor in series with each other. When the impedance is observed from Z_{in} point of view, considering the terminal equations of the CCII+ and passive element characteristics, the Z_{in} is calculated as follows:

$$Z_{in} = Z_1 + Z_2 + \frac{Z_1 Z_2}{Z_3} \tag{3}$$

If Z_1 and Z_2 passive elements are selected as resistors R_1 and R_2 respectively and Z_3 is selected as capacitor C, the following input impedance equation that fulfills the requirement of a real inductor can be obtained:

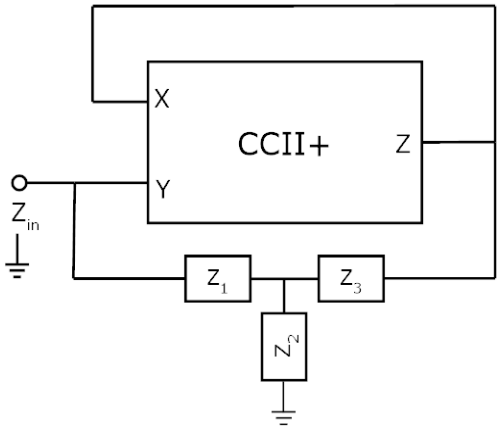

Figure 3. Grounded Inductance Simulator

$$Z_{in} = R_1 + R_2 + sCR_1R_2 = R_{eq} + sL_{eq} \tag{4}$$

Therefore, a lossy (due to the resistance term in the equation) grounded inductance is simulated using one CCII+ with 2 resistors and 1 capacitor.

To model CCII+, Figure 4[7] is used along with NR200N and PR200N SPICE model parameters [8].

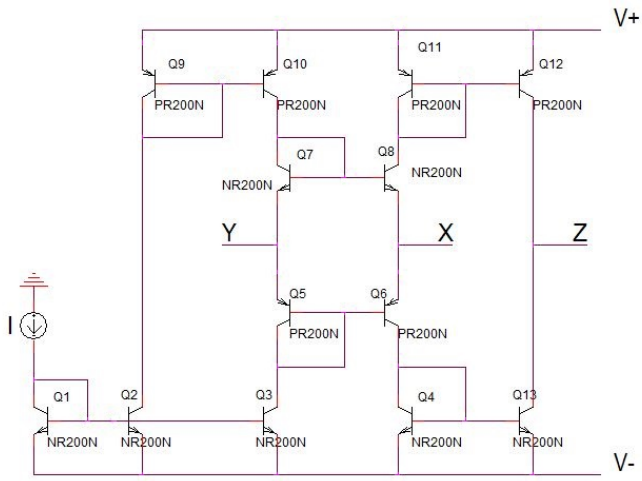

Figure 4. Schematic Implementation of CCII+

2.2 Grounded Inductance Model Experimental Setup

In order to test the suggested inductance model experimentally, an integrated circuit AD844 fabricated by Analog Devices which behave as CCII+ is used as shown in Figure 5. Since it is commercially available, AD844 is useful in putting simulation level studies into practice. Therefore, experimental results can be obtained.

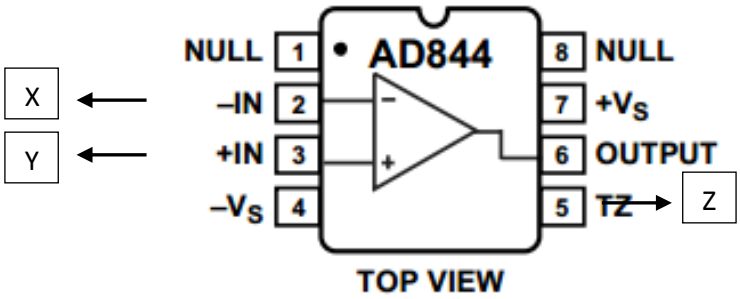

Figure 5. AD844 Block Diagram

For this grounded inductor simulator, if passive element are chosen such that R_1 = 10 Ω, R_2 = 10 Ω and C = 10 μF then R_{eq} = 20 Ω and L_{eq} = 1 mH is obtained. For the experimental setup, the circuit in Figure 6 is constructed using these resistor and capacitor values.

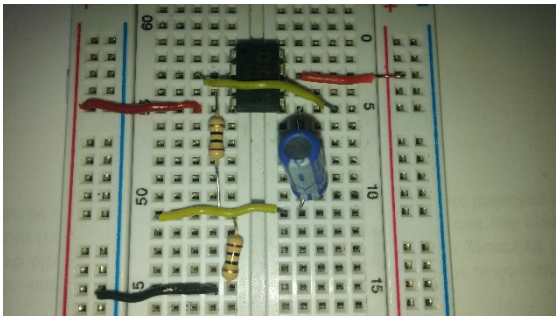

Figure 6. Grounded Inductance Simulator Experimental Setup

2.3 Grounded Inductance Model Test Circuit

We can test this grounded inductance simulator designing a low pass filter as shown in Figure 7.

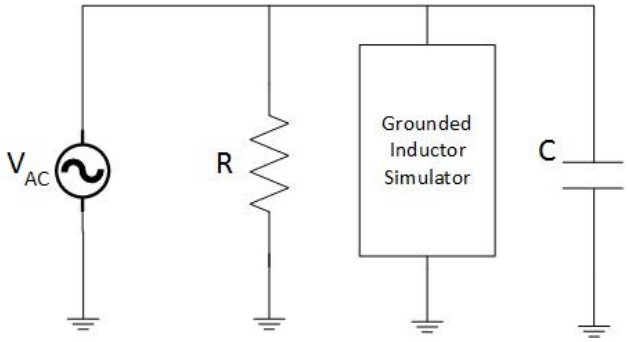

Figure 7. Grounded Inductance Simulator Test Circuit

The frequency response of the test circuit is observed from the current in the grounded inductor simulator point relative to the input current. Three different graphs are obtained as shown in Figure 8. The first graph is the ideal response as if using an ideal inductor in series with a resistor. The second one is simulation results which are obtained in SPICE environment. Second graph is obtained using Figure 4. schematic representation. The third graph is the experimental results. For 15 different frequencies in between 10 Hz-10MHz, experimental results are measured.

From Figure 8, it can be concluded that the cut-off frequency is found at 200 kHz for ideal situation while it is 7 MHz for the SPICE simulation. Experimentally it is found out to be 300 kHz. It is fair to say that SPICE simulated circuit operates very close to the ideal situation until 100 kHz. The experimental circuit can model the lossy inductor up to 40 kHz.

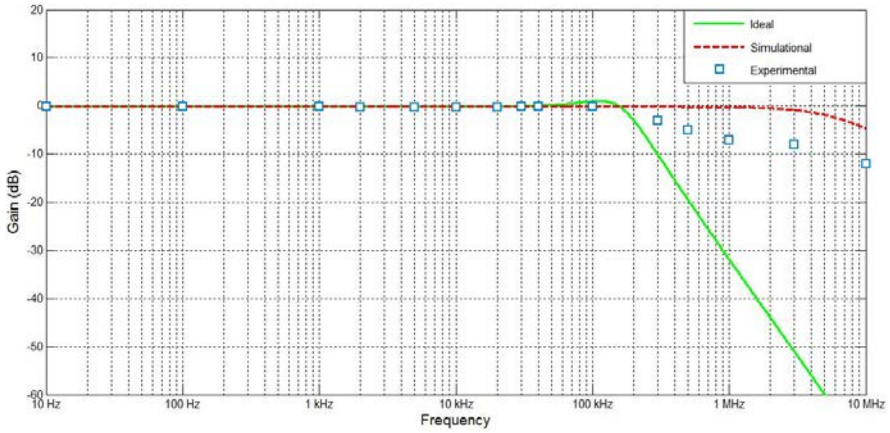

Figure 8. Simulation, Experimentation & Ideal Frequency Responses for Grounded Inductance Simulator

2.4 Floating Inductance Model

In Figure 9, a real/lossy floating inductance simulator that is built with 2 positive-type CCII's and 3 passive elements is given [9]. If Z_1 and Z_2 are chosen as resistor R and Z_3 is chosen as capacitor C; the impedance value between the terminals of the floating inductance simulator can be obtained as follows:

$$Z_L = R + sCR^2 \tag{5}$$

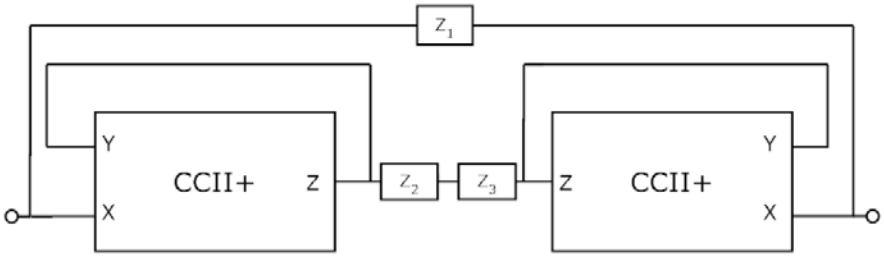

Figure 9. Floating Inductance Simulator

Therefore, the obtained impedance Z_L can model a lossy floating inductor. In order to test the designed floating inductance simulation a PSPICE simulation is run. To model the CCII+'s, NR200N and PR200N SPICE model parameters are used.

2.5 Floating Inductance Model Experimental Setup

For this model, if passive element are chosen such that R = 1k Ω and C = 1 nF; then

$$Z_L = 1000 + s0.001\,\Omega \tag{6}$$

impedance value is found. This model simply simulates a 1 mH lossy inductor with 1000 Ω internal resistance. For the experimental setup, the circuit in Figure 10 is constructed using 2 AD844s, 2 1k Ω resistors and one 1 nF capacitor.

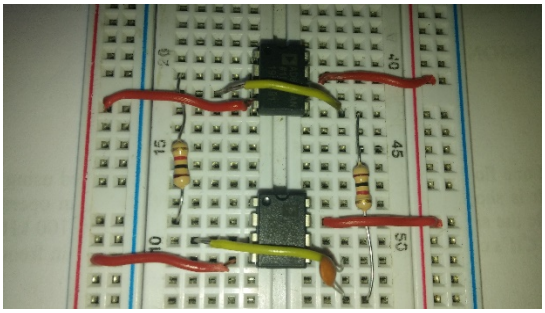

Figure 10. Floating Inductance Simulator Experimental Setup

2.6 Floating Inductance Model Test Circuit

In order to test the floating inductance simulation a test circuit is set as shown in Figure 11.

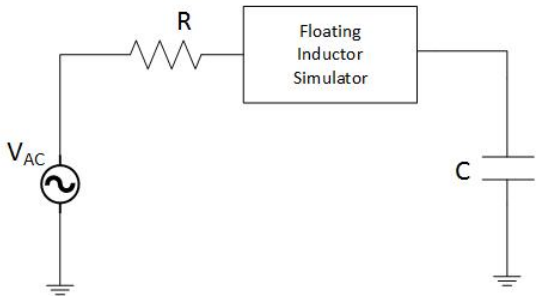

Figure 11. Floating Inductance Simulator Test Circuit

The frequency response of the voltage of capacitor in the test circuit is observed relative to the input voltage. The graphs of ideal, SPICE simulation and experimentation results are shown in Figure 12.

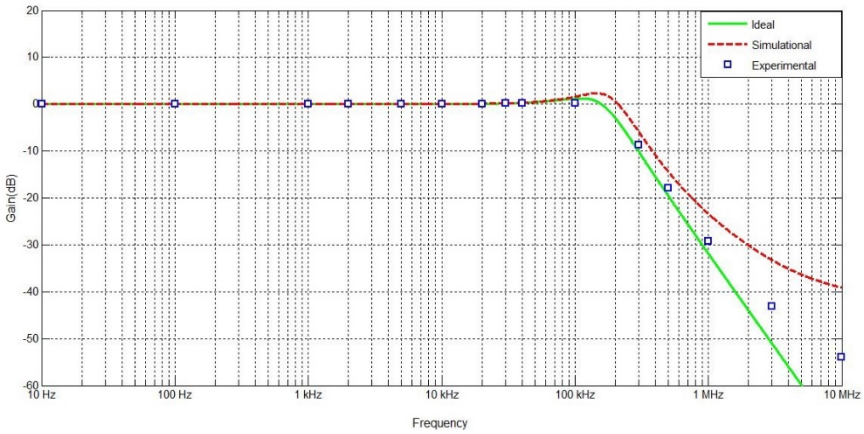

Figure 12. Floating Inductance Simulation, Ideal and Experimental Frequency Responses

In Figure 12, it can be seen that the cut-off frequency is found at 202 kHz for ideal situation while it is 256 kHz for the SPICE simulation. In experiments, the cut-off is found out to be 150 kHz. It can be said that this floating inductor simulator can operate close to the ideal situation up to 90 kHz for the SPICE simulation. Also, experimental results show that the circuit in Figure 10 can operate as if a lossy inductor up to 50 kHz.

3. RESULTS AND DISCUSSION

As a passive electronic circuit element, inductors have many applications. However, using physical inductors in circuit design is somehow problematic due to their size and cost. In order to overcome this issue, instead of physical inductors, inductor simulations could be utilized.

In this paper, two kinds of inductor simulators are given and tested both in simulation and experimentation. Grounded inductor simulator is designed with one CCII+, 2 resistors and 1 capacitor. This design can simulate a lossy inductor such that 1 mH inductance in series with 20 Ω resistance. CCII+ is first modeled by BJTs and simulation results are taken. Also, the same circuit is realized with AD844 and experimental data is obtained. Using the test circuit, the performance of those simulation and experimentation are compared to the ideal response. The simulator can perform up to 100 kHz similar to the ideal response. The experimental results also show that up to 40 kHz realized AD844 circuit can be used instead of a lossy inductor.

Floating inductor simulator is designed 2 CCII+'s, 2 resistors and 1 capacitor. This simulator can simulate an inductor 1 mH with a 1 kΩ internal resistance. The performance of the floating inductor simulator is tested in a test circuit. Simulation and experimentation data is taken and compared to ideal situation. The simulator can perform up to 90 kHz for simulation case and 50 kHz for experimentation very close to the ideal response.

4. CONCLUSION

In this paper, one grounded and one floating inductance simulator is designed and tested using CCII+'s and some passive circuit elements. It is shown that the simulator for grounded inductor can operate like a real inductor up to the

180 kHz, while the simulator for floating inductor can operate up to 100 kHz. With these results, it can be concluded that CCII's can be employed to simulate inductors up to certain frequencies.

REFERENCES

[1]. Smith, K.C. ve Sedra, A., 1968, The current conveyor: A new circuit building block. IEEE Proc., 56: 1356-1369.
[2]. Smith, K. C. ve Sedra, A., 1970, A second generation current conveyor and its applications. IEEE Trans. Circuit Theory, CT-17: 132-134.
[3]. Soliman, A. M., 1973, Inductorless realization of an all-pass transfer function using the current conveyor. IEEE Trans. On Circuit Theory, CT-20: 80-81.
[4]. Pal, K., Singh, R., 1982. Inductorless current conveyor allpass filter using grounded capacitors. Electronics Letters, 18(1): 47.
[5]. Analog Devices AD844, 1989, "60 MHz 2000 V/µs Monolithic Op Amp", Rev. 2009
[6]. Nandi, R., 1978, Active inductance using current conveyors and their application in a simple bandpass filter realization. Electronics Letters, 14: 373-375.
[7]. Fabre, A., Saaid, O., Wiest, F. ve Boucheron, C., 1995. Current controlled bandpass filter based on translinear conveyors. Electronics Letters, 31(20): 1727-1728.
[8]. Frey D.R., 1993, "Log-domain filtering: An approach to current-mode filtering", IEEE Proceedings-G: Circuits, Devices and Systems, Vol. 140, pp. 406-416.
[9]. Senani, R., 1985. Novel high-order active filter design using current conveyors. Electronics Letters, 21(22): 1055-1056.

BIOGRAPHY

Mehmet DEMİRTAŞ was born in Konya, Turkey in 1990. He graduated from Electrical and Electronics Engineering from Bilkent University in 2011. He continues his Phd studies in Electrical and Electronics Engineering at Selcuk University. His interests are current conveyors, MEMS design and fabrication.

ICENS
INTERNATIONAL CONFERENCE ON ENGINEERING AND NATURAL SCIENCES
24-28 May 2016 /Sarajevo

Effects on Microstructure and Mechanical Properties of the Additional 1% Si and Different Cooling Rate to AZ91 Magnesium Alloys

Halil Ahmet Goren[1], Mehmet Unal[2], Erkan Koc[3], Yunus Turen[3]

Abstract

In this study, the effects of silicon addition and different cooling rates on the microstructure and mechanical properties of AZ91 magnesium alloys which are used in various industries have been investigated. For this aim, the AZ91 alloys have been poured to ceramic mould cooled with copper. Additionally, silicon element has been added in the 1 wt. % to AZ91 to obtain AZ91+1 wt.% Si alloy and changes of different cooling rates have been observed. Results showed that hardness of alloys has been increased with cooling rates increase and silicon addition to this alloy. Also, with silicon addition in the 1 wt. % to AZ91 that have been occurred Mg_2Si phases. Depending on change in the cooling rate, phase of $Mg_{17}Al_{12}$ has been changed and thinner grains have been obtained.

Keywords: Mg Alloys, AZ91, Cooling Rate, Microstructure

1 INTRODUCTION

Of the metallic materials used as engineering material, Magnesium (Mg) is the lightest one. Because of its low density, it is preferred in microelectronic, telecommunication, aviation and automobile industries [1,2]. Moreover, it is predicted that, it will be used in orthopedic implant applications as screw and plate as potential implant material because of low toxic feature of Mg [3,4].

Mg is 78% lighter than Iron (Fe) and Steel and 36% lighter than Aluminium (Al) in terms of heaviness [5]. Due to the superior features of Magnesium such as specifically durability and processability, it is a very efficient material and it has a good castability under controlled athmosphere [1].

In developed production industries, combining different materials not only makes the features of the materials better, but also provides major flexibility in production stage in terms of different material usage [6,7].

Mg-Al based alloys has low creep resistance because of thermal instability of $Mg_{17}Al_{12}$ phase [8,9]. $Mg_{17}Al_{12}$ intermetallic is formed under low temperatures ($\leq$ 120 °C) in Mg alloys and it develops the endurance of the alloy. In Mg based alloys, Al develops solid precipitate endurance of Mg, castability of the melt and decreases the microporosity of the cast alloys. However, the alloys which contain excess Al are tend to microporosity.

Al additive increases the hardness, endurance and concretion time of the alloy, but decreases its ductility [10,11].

In the literature, commonly, the effect of $Mg_{17}Al_{12}$ (β-intermetallic) intermetallic phase present on the mechanical properties of the alloy in AZ91 magnesium alloy was studied[12,13]. Studies were conducted by changing the % proportions of Al amounts in AZ91 alloy which had a common usage potential.

However, the changes in Al amounts change both $Mg_{17}Al_{12}$ (β-intermetallic) phase amount produced in the alloy and solid melting limit in the matrix. In that case, not only basing mechanical property comments upon the effect of β-intermetallic phase, but also matrix combination should be taken into consideration [14,15].

AZ91 Mg alloy (Mg-9 % Al-1 % Zn) is used more commonly because of its better castability and mechanical properties [2]. Furthermore, in order to develop mechanical, microstructural, casting and corrosion features of AZ91 with microalloying, elements such as Ca, Sr, Si, Zr, Ti are added in small amounts [16-19].

For instance, Si is used in order to develop mechanical properties of Mg alloys in high temperatures [20-21]. It is reported that Si decreases castability and fluidity of Mg alloys [22-24]. Si atoms generate solid Mg_2Si intermetallic in room temperature [25].

Because the solubility of Si in Mg is pretty low, Mg matrix composite material is strengthened with Mg_2Si which is formed by adding Si into the alloy. Mg_2Si composed with Si additive is a very beneficial intermetallic composite with its high melting point, low density and high elastic modulus [26].

[1] *Sinop University, Vocational School, Department of Mechatronics, Orduköyü /Sinop, Turkey. agoren@sinop.edu.tr*

[2] *Corresponding author: Faculty of Technical Education, Karabük, Türkiye, munal@karabuk.edu.tr*

[3] *Department of Metallurgy Materials Engineering, Karabük, Türkiye,, ekoc@karabuk.edu.tr , yturen@karabuk.edu.tr*

In a study conducted by Ünal et. al., they stated an increase in hot tearing and a decrease in fluidity depending on the increase in Si additive into AZ91. The increase in Si proportion increased tensile and yield strength proportionally. When microstructure results are examined, it was observed that grains got thinner depending on Si amount and $Mg_{17}Al_{12}$ intermetallic phase was modified, besides, Mg_2Si phase was generated [27].

In the literature, studies for thinning microstructure with the help of rapid solidification process except micro alloying in order to increase mechanical properties of AZ series of magnesium alloys are few [14,15]. It is known that rapid solidification technology makes grain size thinner.

Mg alloys generated with rapid solidification process have many advantages, it liquidates grains and sediments considerably, besides widens solid solubility and generates out of balance phases [28,29].

In a study conducted by Candan et. al. [30], they reported that with the increase in cooling rate of AZ91 magnesium alloy its grain structure gets thinner, $Mg_{17}A1_{12}$ phase amount decreases and network shape, also mechanical properties of the alloy gets better [30]. In the study on AZ91 and other alloys, it was detected that with the increase in cooling rate grain size gets smaller [31].

In this study, it was aimed to investigate how microstructure and hardness features were affected when Mg alloys containing AZ91 and AZ91+1 wt.%Si were produced in different cooling rates.

2. EXPERIMENTAL STUDIES

Mg alloys were melted in a steel crucible which had the capacity of melting 2 kilograms of Mg alloy and which was placed in a furnace. In order to cut the contact of environment with atmosphere, protective gas was given to the furnace during the melting.

Furnace and metal temperature was 750 $^{\circ}$C, by considering the casting conditions. When the furnace was at the desired temperature, it was kept about 10 minutes and the alloy was provided to reach casting temperature.

After the alloy was at casting temperature, the bottom of the melting crucible was opened in a controlled way with the help of on-off valve of the melting furnace and liquid metal was provided to flow into the mould. During the casting process, SF_6 protective gas was given to the liquid metal and moulds [32].

In the preparation of AZ91 magnesium alloy, 99.9 wt.% pure Mg, Al and Zn besides Al-Si master alloy was used. With a second melting, test specimens were casted from the prepared master alloys.

In the experimental studies, surface inactive 1 wt.% silicon was added into AZ91 alloy as an alloy element. Analyses of the alloys used in the experiments are shown in Table 1.

Table 1.. The chemical compounds of the alloys used at the experiments

Alloys	% Compounds					
	Mg	Al	Zn	Mn	Si	Diğer
AZ91	89.42	9.35	0.83	0.20	-	0.20
AZ91+1 wt.% Si	88.53	9.25	0.77	0.20	1.05	0.20

Circular cross section ceramic mould with copper refrigerator, of 20x200 millimeters sizes was used in the experimental studies. The measurements were transferred into the PC by connecting thermocouples whose solidification rates depended on the mould to ADAM 45-20 data collection module. Moreover, a program that could measure and record 10 temperatures in a second was utilized in the module.

The ceramic mould used in the experimental studies is demonstrated in Figure 1. It is stated that the nearest point to the copper refrigerator is 1st area and the nearest point to the atmosphere is 5th area. Solidification rates, hardness and microstructure evaluations of equally spaced 5 different areas were made.

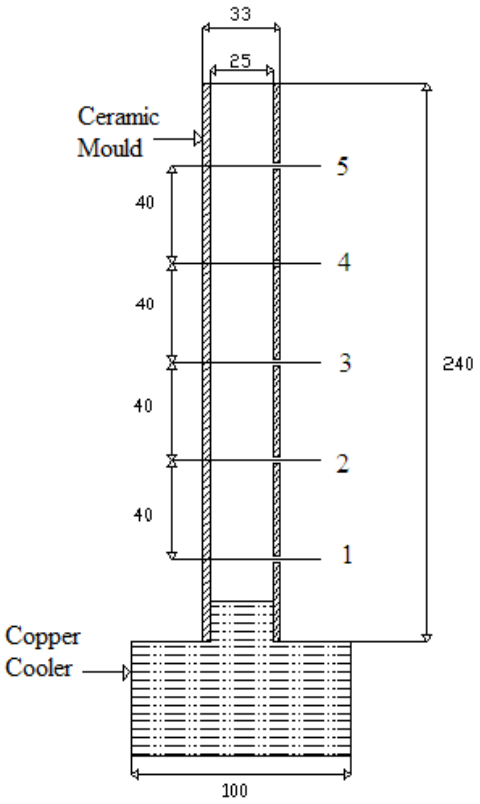

Figure 1. Cross sectional view of ceramic mould that cooled with copper that used at the casting process

Time based temperature data obtained at synchronous time periods were used respectively and cooling graphics of both alloys were drawn.

The hardness values were determined by Vickers hardness testing with a load of 50N. Hardness measurements were taken from 5 different points of the surface of the samples. For hardness and microstructure experiments, the surface of the samples were subsequently ground with 220, 400 and 600 grit emery papers followed by polishing with 1µm alumina solution paste

3. RESULTS AND DISCUSSION

3.1. Microstructure

AREAS	AZ91	AZ91+ 1 wt.% Si
1st	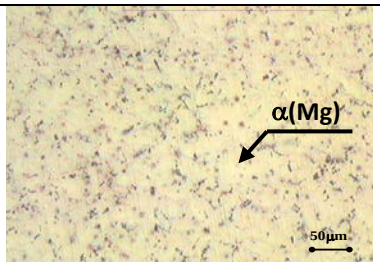	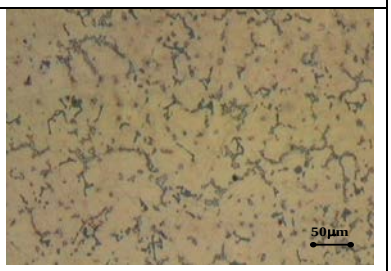

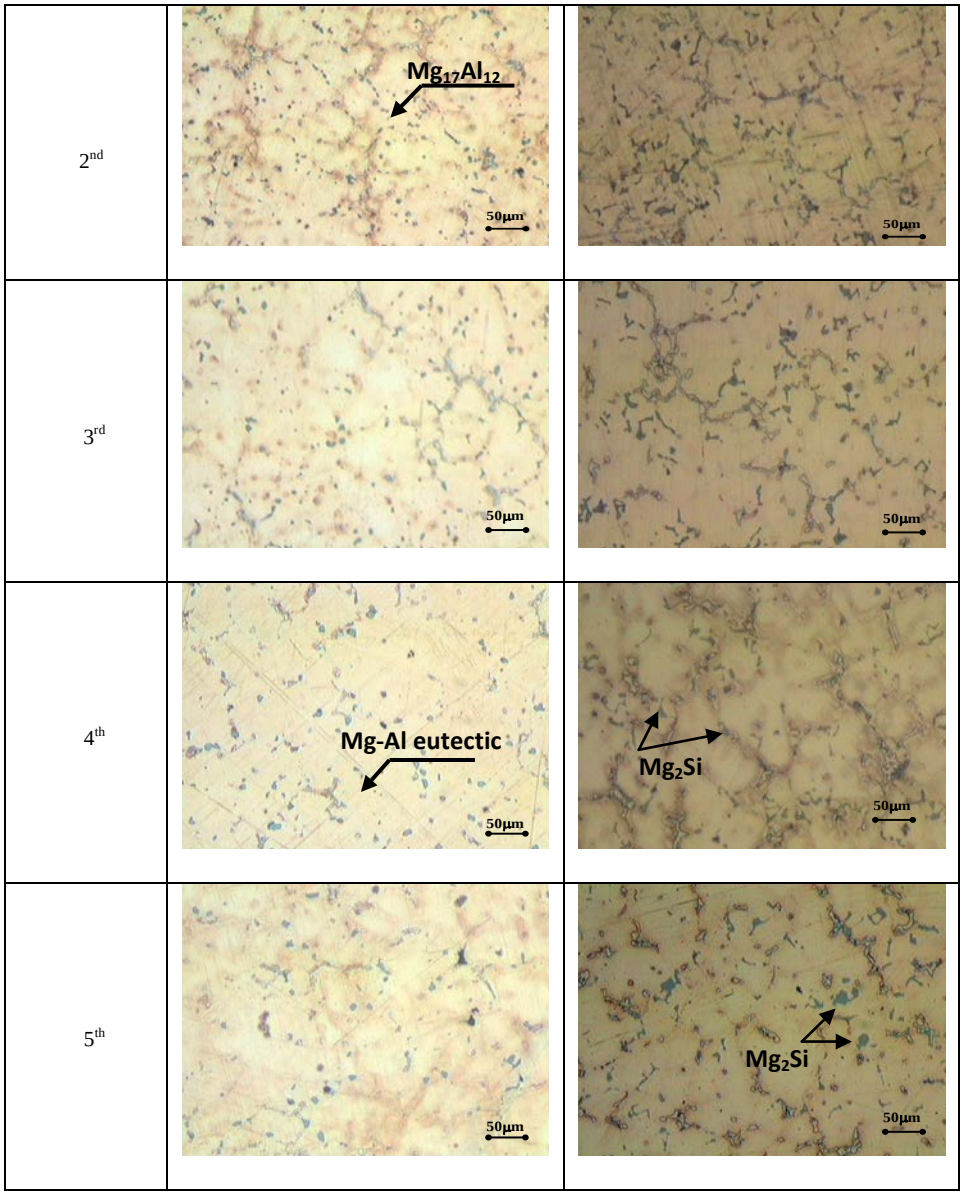

Figure 2.The microstructural views of AZ91 and AZ91+ 1 wt.% Si alloys. 1st Area, 2nd Area, 3rd Area, 4th Area, 5th Area

Microstructure studies were made on the castings in ceramic mould. In the experimental studies, AZ91, AZ91+ 1 wt.% Si alloys were casted into ceramic moulds respectively and microstructure examinations were obtained from samples which were taken from 5 different areas and which solidified at different cooling rates.

The obtained microstructure images depending on the cooling rates and the alloy are shown in Figure 2. In the microstructure of AZ91 alloy that was poured into ceramic mould is α+Mg main matrix phase. It is seen that the structure consists of eutectic that extends through grain boundaries and intermetallic phases, in the main matrix. These phases are assumed to be Mg-Al eutectic and $Mg_{17}A1_{12}$ intermetalic [33].

The examined microstructure images showed that grain structure of the alloy was getting thinner with the increasing in cooling rate and grain boundaries of $Mg_{17}Al_{12}$ intermetallic phase increased. When compared to the previous studies, AZ91 starts at about 600°C with α (Mg) solid solution nucleation which is primary Mg in the equilibrium solidification. these nuclei grow and solidification ends at 470°C [10,22].

A discrete eutectic formation generated from $Mg_{17}Al_{12}$ and α (Mg) phase is seen in microstructure. Thus, it is understood that the microstructure of out of balance AZ91 consists of α (Mg) and $Mg_{17}Al_{12}$ which is an intermetallic phase [34,35].

It was observed that phases in grain boundaries of AZ91 alloy underwent a change with Si addition. $Mg_{17}Al_{12}$ phase in the grain boundaries was shivered, additionally Mg_2Si phase occurred. This case was reported by Aizawa (25) and Candan (36), too [25,36].

3.2 Cooling Diagrams

Cooling curve was obtained for each solidification rate with the aim of comparing with classical casting method by cooling Mg alloys in different cooling rates. The casting process of the examined alloys was made into ceramic mould at room temperature. Time-dependant temperature change graphics obtained from the casting of alloys that were prepared with AZ91 and AZ91+ 1 wt.% Si additives into ceramic mould are given in Figure 3 (a), (b) respectively.

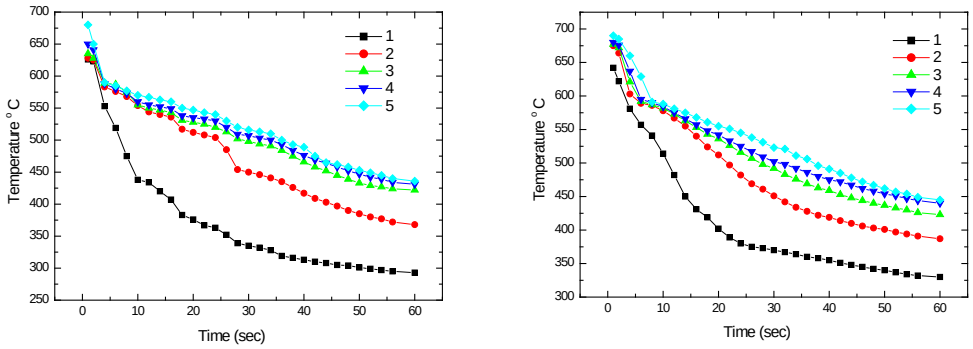

Fig3. (a) The heat change graphics of AZ91 Alloy (b) The heat change graphics of AZ91+1 wt.% Si Alloy

Both in AZ91, and in AZ91+1 wt. % Si alloys, the nearest point to the copper refrigerator, in other words 1st area was observed to cool in the fastest way in the examined cooling graphics. Although the difference between 1st and 2nd areas was seen clearly, the difference between 3rd, 4th and 5th areas was not much.

The difference between 4th and 5th areas was small. That case is assumed to result from the fact that these areas were close to the atmosphere.

3.3. Mechanical Test Results

Tensile specimen could not be obtained in ceramic mould. Only hardness values were obtained. In this study, hardness of the alloys was measured with Vickers hardness measurement method from 5 different areas. Changes occurred in the hardness of AZ91 and AZ91+ 1 wt.% Si Mg alloys depending on the cooling rates are demonstrated in Figure 5. In parallel with the decrease in cooling rate for both alloys in the first 3 areas, decrease in hardness was observed, while a little increase in the 4th and 5th areas was observed because they were close to the atmosphere. Hardness values are as follows respectively; in AZ91 alloy, 57.43 HV for the 1st area, 56.76 HV for the 2nd area and 52.73 HV for the 3rd area, while in AZ91+ 1 wt.% Si alloy, 64.50 HV for the 1st area, 64.26 HV for the 2nd area and 63.80 HV for the 3rd area.

With microstructure examination, as expressed in Figure 2, grain size gets smaller with the increase in cooling rate. It is stated in literature that decrease in grain size increases grain number and accordingly grain boundary proportion and grain boundaries have an effect of inhibiting dislocation activity. It is expected to increase the hardness and endurance of the material as long as grain size decreases [30].

In the hardness graphic in Figure 4, 1st areas are the ones that cool most rapidly, 5th areas are the ones that cool most slowly. Hardness results obtained from the ceramic mould with copper refrigerator experiments increased in direct proportion to silicon amount and cooling rate.

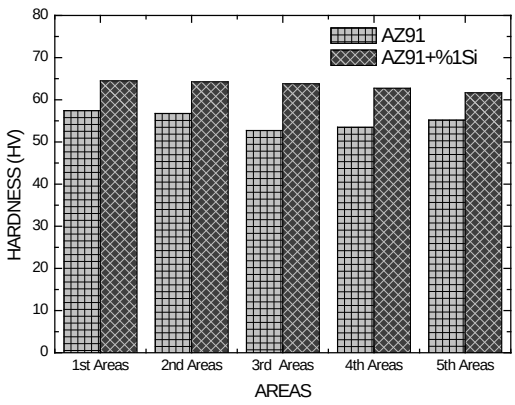

Fig 4. Hardness change graphics as depending on the different cooling rates of AZ91 and AZ91+1 wt.% Si alloys

RESULTS

When microstructures were investigated, it was observed that microstructure of AZ91 consisted of α+Mg main matrix and $Mg_{17}Al_{12}$ intermetallic phase was generated on grain boundaries. With the Si addition into AZ91, Mg_2Si intermetallic phase was generated in the structure at room temperature.

When cooling curves were investigated, it was detected that transformation points were the same but arrived times were different.

According to the hardness values, it was observed that the hardness of the alloy increased with 1 wt.% amount of Si addition into AZ91. Moreover in the test results, it was observed that with the increase in cooling rate, hardness increased, too.

REFERENCES

[1]. B.L. Mordike, T. Ebert, ''Magnesium: properties application-potential,'' Mater. Sci. Eng., vol. 302, pp. 37-45, 2001.
[2]. M.V. Manuel, A. Singh, M. Alderman, N.R. Neelameggham, Magnesium Technology, TMS, Wiley Publishing 2015, 2015
[3]. Y. Chen, Z. Xu, C. Smith, J. Sankar, Recent advances on the development of magnesium alloys for biodegradable implants, Acta Biomater, vol. 10, pp.4561-4573, 2014.
[4]. F. Witte, V. Kaese, H. Haferkamp, E. Switzer, A. Meyer-Lindenberg, C.J. Wirth, H. Windhagen, ''In vivo corrosion of four magnesium alloys and the associated bone response,'' Biomaterials, vol. 26, pp. 3557-3563, 2005.
[5]. L. Gaines, R. Cuenca, F. Stodolsky, S. Wu, ''Potential Automotive Uses of Wrought Magnesium Alloys,'' Automotive Technology Development, Detroit, Michigan, pp. 1-7, 1996.
[6]. L. Liu, D. Ren, F. Liu, ''A review of dissimilar welding techniques for magnesium alloys to aluminum alloys,'' Materials, vol. 7, pp. 3735–3757, 2014.
[7]. Z. Sun, J. C. Ion, ''Laser welding of dissimilar metal combinations,'' J. Mater. Sci., vol. 30, pp. 4205–4214, 1995.
[8]. W. Blum, P. Zhang, B. Watzinger, B. V. Grossmann, H. G. Haldenwanger, ''Comparative study of creep of the die-cast Mg-alloys AZ91, AS21, AS41, AM60 and AE42'' Materials Science and Engineering A, vol. 319/321, pp. 735−740, 2001.
[9]. I. H. Jung, D. H. Kang, W. J. Park, N. J. Kim, S. H. Ahn. ''Thermodynamic modeling of the Mg-Si-Sn system,'' Computer Coupling of Phase Diagrams and Thermochemistry, vol. 31, pp. 192−200, 2007.
[10]. L.P. Barber, ''Characterization of the Solidification Behavior and Resultant Microstructures of Magnesium-Aluminum Alloys,'' A Thesis of Master, Worcester Polytechnic Institute, Worcester, 10-46, 2004.
[11]. D. Schwam, J.F. Wallace, Y. Zhu, S. Viswanathan, S. Iskander, "Enhancements in Magnesium Die Casting Impact Properties," Final Report, Case Western Reserve University, Ohio, 5-22, 2000.
[12]. M. Anık, P. Avcı, A. Tanrıverdi, I Çelikyürek, B. Baksan, R. Gürler, ''Effect of the eutectic phase mixture on the anodic behavior of alloy AZ91,'' Materials and Design, vol. 27, pp. 347-355, 2006.
[13]. G. Song, A. Atrens, X. Wu, B.Zhang, ''Corrosion behavior of AZ21, AZ501, and AZ91 in sodiumchloride,'' Corros Sci, vol. 40, pp. 1769–1791, 1998.
[14]. A. Tanverdi, ''Effect of Si and Y Element with Solidification Rate on Corrosion Behavior of AZ91 Magnesium Alloy,'' M.Sc. Thesis, Institute of Science, Osmangazi University, 2005.
[15]. Govind, K. Suseelan Nair, M. C. Mittal, K. Lal, R. K. Mahanti, and C. S. Sivaramakrishnan, ''Development of rapidly solidifed magnesium-aluminum-zinc alloy, Mater. Sci. Eng. A, 304-306, pp.520-523. 2001.
[16]. K. Hirai, H. Somekawa, Y. Takigawa, K. Higashi, ''Effects of Ca and Sr addition on mechanical properties of a cast AZ91 magnesium alloy at room and elevated temperature,'' Mater. Sci. Eng. vol. 403, pp. 276-280, 2005.
[17]. Ş. Candan, M. Unal, E.Koc, Y. Turen, E. Candan, ''Effects of titanium addition on mechanical and corrosion behaviours of AZ91 magnesium alloy,'' Journal of Alloys and Compounds, vol. 509, pp. 1958–1963, 2011.
[18]. E. Koç, M. Ünal, E. Candan, Y. Türen, H. A. Gören, ''Effect of Zirconium on Microstructure and Mechanical Properties of AZ91 Magnesium Alloy,'' The International Conference on Material Science and Technology IMSTEC 2016, Nevşehir, Turkey.
[19]. H. A. Gören, M. Ünal, E. Koç, Y. Türen, ''Effect Of Si Additions And Different Cooling Rates On Microstructure and Mechanichal Properties of AZ91 Magnesıum Alloys,'' 1st International Conference on Engineering Technology and Applied Sciences, ICETAS 2016, Afyon, Turkey.
[20]. G. H. Li, H. S. Gill, R. A. Varin, ''Magnesium silicide intermetallic alloys,'' Metall. Trans. vol. 24A, pp. 2383-2391, 1993.
[21]. M. Mabuchi, K. Kubota, K. Higashi, Scripta Metall. Mater. vol. 33 pp. 331– 335, 1995.
[22]. Z. Zhang, ''Development of Magnesium-Based Alloys for Elevated Temperature Applications,'' Doctor of These, Faculte Des Sciences Et De Genie Universite, Quebec, Canada, 2-75, 2000.
[23]. H. K. Kazdal, ''Magnesium Alloys: Application and Future of the Automotive Industry,'' Tubitak, Marmara Research Center, Kocaeli, 3-39, 1999.
[24]. M. Vogel, ''Mikrostruktur und Kriechverhalten von Magnesium-Druckgusslegierungen im System Mg-Zn- Al-Ca,'' Doktors, Max-Planck-Institut für Metallforschung, Stutgart, 6-20, 2002.
[25]. T. Aizawa, R.Song, ''Mechanically induced reaction for solid-state synthesis of Mg_2Si and Mg_2Sn,'' Intermetallics, vol.14, pp. 382-391, 2006.
[26]. Z.H. Chen, W.J. Xia, J.H. Chen, ''Heat-Resisting Magnesium Alloy,'' Chemistry Industry Press, pp. 296, 2007.
[27]. M. Ünal, E. Koç, Y. Türen, F. Gül, E. Candan, ''Effect Of Silicon on Casting and Mechanical Properties of AZ91 Magnesium Alloy,'' The 5th International Advanced Technologies Symposium (IATS'09), 2009, Karabük, Türkiye, 13-15.
[28]. T. Shibata, M. Kawanishi, J. Nagahora, Mater. Sci. Eng. vol. A 179/180 632– 636, 1994.
[29]. D. Shechtman, ''Project of High Specific Strength Magnesium Alloy,'' Israel Ministry of Army Forces and Israel Ministry of Industry and Trade, Produced by RSP[R], Israel, 1999.
[30]. Ş. Candan, M. Çelik, E. Candan, ''Effect of Cooling Rates on Mechanical and Corrosion Behaviour of AZ91 Magnesium Alloys,'' Journal of Bilecik Şeyh Edebali University Science, vol. 1, pp. 2, 2014.
[31]. Ş. Candan, M. Celik, E. Candan, ''Effectiveness of Ti-micro alloying in relation to cooling rate on corrosion of AZ91 Mg alloy,'' Journal of Alloys and Compounds, vol. 672, pp. 197-203, 2016.

[32]. Ünal, M., ‘‘Examination of casting properties of magnesium alloys’’ Ph.D. Thesis, Gazi University, Institute of Science, Ankara, 2008.
[33]. H. A. Gören, ‘‘Effect of Cooling Rate on Microstructure and Mechanical Properties of Magnezyum Alloys’’ M. Sc. Thesis, Karabük University, Karabük, Turkey, 2010.
[34]. M. C. Lin, C.Y. Tsai, J.Y. Uan, ‘‘Converting hcp Mg-Al-Zn alloy into bcc Mg-Li-Al-Zn alloy by Electrolytic deposition and diffusion of reduced lithium atoms in a molten salt electrolyte LiCl-KCl,’’ Scripta Materialia, vol. 56 pp. 597-600, 2007.
[35]. W. Qudong, L. Yizhen, Z. Xiaqin, D. Wenjiang, Z. Yanping, L. Qinghua, L. Jie, ‘‘Study on the fluidity of AZ91+xRE magnesium alloy,’’ Materials Science and Engineering, vol. 271, pp. 109-115, 1999.
[36]. E. Candan, ‘‘Wettability and Pressurized Infiltration of Ceramic Powder Compacts by Metallic Melts,’’ Ph.D. Thesis, Department of Engineering Materials University of Sheffield, Sheffield, U.K., 38-39, 1998.

ICENS
INTERNATIONAL CONFERENCE ON ENGINEERING AND NATURAL SCIENCES
24-28 May 2016 /Sarajevo

Efficient Multi-Scale Scene Representation for Augmented Reality Applications

Erkut Arican[1], Tarkan Aydin[2]

Abstract

In this work, we are presenting an Augmented Reality (AR) system. Using multiple images which are generated by rotation and zooming from end user camera, are using for create a semi-complete panoramic representation. Our previous studies can explain multi-scale panoramic representation with using tree structure. First, we need to find zoom level information for each images. We use mean-shift algorithm for detecting a scale information. Finding zoom levels is not enough for build our multi-scale panoramic tree. Second problem is reducing number of images. Tree structure relevant to zoom levels and needs to minimum number of images. Main contribution of this study is to use integer programming methods to select the minimum number of images from the image set, which best represent the scene.

Keywords: multi-scale augmented reality, integer programming, automatic image selection, mean-shift algorithm, multi-scale panoramic tree

1. INTRODUCTION

With development of mobile technology, augmented reality and virtual reality systems became popular again. Many applications use pinned information for images and videos in correct position. Thus, we can learn about real-world objects, and even interact with them easily. GPS information is important for augmented reality and provide 3D position and orientation information. Scale is also important but zoom vibration is a big problem for augmented reality objects.

In our system, we know the limitations and present a method for augmented reality system. We create a multi-scale panoramic representation with using tree structure. You can find more detailed explanation in our previous studies. Previous studies find images scale and image selection process manually. Important points of our study is as follows:

- We find zoom levels for each image automatically then we create tree structure using these information. Mean-shift method is a key point of finding zoom levels.
- Finding zoom levels for each image is not enough our multi-scale panoramic tree. Other big limitation is number of images. Our tree needs to minimum number of images fit our tree to cover maximum area. Main contribution is using an integer programming methods to select images from image set which represents the best scene.

There exist lots of studies is about augmented reality and panoramic representation for computer vision but we cannot find a lot of studies about multi-scale panoramic representation in literature. We expect that our study will contribute to the literature. SIFT **Invalid source specified.** technique is a milestone in local feature based image analysis. SIFT attributes are used successfully to produce panoramic images **Invalid source specified.**. Matching images using such high dimensional vectors is an open research topic, such as FLANN **Invalid source specified.** method which is fast and return approximately correct result. Geometric relation between the images in static environments is a well-studied problem and assumed to be solved **Invalid source specified.**. "Bag of Word" **Invalid source specified.** approach led to significant progress in retrieval of large image databases. For integer programming, we use **Invalid source specified.** for calculation. As well as AR is quite and old topic, lately regained interest from academic and business world. For example, Project Glass **Invalid source specified.** is an AR goggles from Google to be used in daily life. Qualcomm **Invalid source specified.** 's and Turk Telekom **Invalid source specified.** 's AR libraries are good examples for single image anchor based approaches. Also there is a standardization research of AR meta-data **Invalid source specified.** .

[1] *Corresponding author: Bahcesehir University, Faculty of Engineering and Natural Sciences, Department of Computer Engineering, 34353, Besiktas/İstanbul, Turkey.* erkut.arican@eng.bahcesehir.edu.tr

[2] *Bahcesehir University, Faculty of Engineering and Natural Sciences, Department of Computer Engineering, 34353, Besiktas/İstanbul, Turkey.* tarkan.aydin@eng.bahcesehir.edu.tr

2. MATERIALS AND METHODS

2.1 Basic Techniques

Matching images through their local features and fitting a homography motion model is the critical sub-routine in our technique. We depend on OpenCV **Invalid source specified.** library for such critical routines. Now a brief overview of these techniques will be presented.

2.1.1 Matching Image Attributes

In this stage Lowe**Invalid source specified.** 's classical approach is deployed. SIFT is robust against scale and in-image rotation. After feature extraction, we use FLANN **Invalid source specified.** for fast but approximate matching of the features

2.1.2 Mean-shift

Mean-shift is a classical vision algorithm which seeks to find the peak of a nonparametric distribution. **Invalid source specified.** . Since we are building a tree in recursive way, in this step we are only interested in the first modality in the distribution, which corresponds to the children of the node.

2.1.3 Calculation of Homography

The relationship between the pictures produced by the camera rotation is typically modeled as 2D homography transformation. This transformation can be written in a homogeneous coordinate system.

$$\begin{bmatrix} a & b & c \\ d & e & f \\ g & h & i \end{bmatrix} * \begin{bmatrix} x_1 \\ y_1 \\ 1 \end{bmatrix} = \begin{bmatrix} x_2 \\ y_2 \\ w_2 \end{bmatrix} \quad (1)$$

This 3x3 homography matrix calculate the transformation of the first image points to the second image. Conjugate point of each pair gives a relation as above. Homogeneous equations are insensitive to scale so it turns into two equations. With the same reasoning homography matrix have 8 unknowns so 4 conjugate points are enough to solve it.

Figure 1 Two different images with the different scale, after the RANSAC elimination

To remove the wrong pairs and to get most of the right pairs for the solving equations, we use the

RANSAC technique for eliminating bad pairs. After RANSAC, Levenberg-Marquardt non-linear technique using for optimization **Invalid source specified.** . Figure 1 shows the pairs between 2 different zoom level images.

2.1.4 Integer Programming

Another critical stage in the proposed approach is to reduce the number of images on a zoom-level while not losing from the visual scope for the level. Our solution is a sub-set selection problem with discretization of the panoramic landscape. In order to solve it, we applied integer programming optimization **Invalid source specified.**. We select Lindo **Invalid source specified.** integer programming tool for this calculation. Lindo can solve linear, nonlinear, and integer models and using standard spreadsheet equations.

2.2 Method

2.2.1 System Summary

Tree structure in the heart of the system is constructed from images taken with rotating and zooming levels. Levels of the tree are ordered by zoom degree (see Figure 2). Every parent node, covers its child nodes. Finding the user image's best match image in this tree structure is main aim in the online stage.

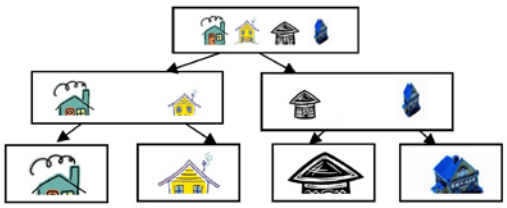

Figure 2 Tree Structure

This representation has numerous important points. Firstly, the tree structure discovering best match to the client information results in logarithmic complexity. It additionally makes it conceivable to do multi-scale AR labeling and mapping. Moreover, the strategies for traditional display procedures, for example, tube shaped mapping, worldwide arrangement and other complex methods are not used as a part of this framework.

In our system we have got a two stages. In the offline stage, we expect the data pictures can originate from a moving and zooming camera as a video stream, since it is the easiest way for the user. One critical assumption of the proposed tree is the assumption that images on that level do not overlap significantly. In the online stage, the best match to an input match is searched for, similar to any search tree algorithm.

2.2.2 Finding Zoom Levels with Mean-Shift

After we discover descriptors for all pictures, we have to discover zoom levels for each. We accept to know zoom level of one picture in the root level. Whatever remains of the tree will be worked by utilizing this picture as the seed. To begin with we characterize two 2D focuses on a sanctioned position (for instance a line fragment with 100 pixels in length). Every picture is coordinated against this root picture and through the figured homographies and and the deformation of the canonical line segment, we compute a rough estimate of the overall scaling affect. We store these calculations in a sorted array and use mean shift algorithm to find the "first" peak of the scale distribution.

2.2.3 Reducing Number of Images with Integer Programming

Image subset selection step tries to find minimal number of images which is extensively covering a certain portion of the panoramic scene. Since the proposed tree structure is essentially a search tree, it is important that sibling nodes coverage areas do not overlap in the context of parent node. We attempt to minimize the intersection areas. Since at last, the final aim is not to locate the best image but rather compute a reasonable transformation from input image to the panorama. Likewise, utilizing minimum number of pictures are better for run-time execution and memory necessities.

Fig. 3 describes the problem. Dashed rectangle represents a parent node and small rectangles represents child nodes. As mentioned before, a subset of these images must selected in a way that the overlap between the selected images must be minimal while trying to keep the most coverage area. It must be noted that, in case the images are coming from videos, the overlap and redundancy will even be more problematic.

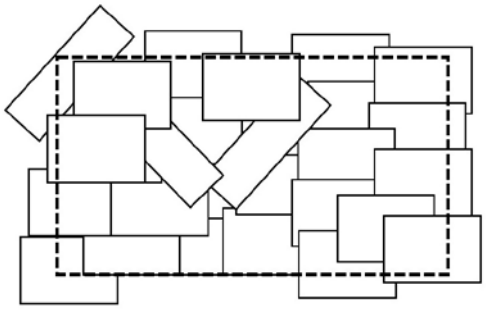

Figure 3 Image Selection Problem

Fig. 4 shows example of this process. Child images (more closer) cell are shown "A". In parent images matched and attached cells are shown "X". In this iteration, child image matches cover empty parent image cell are shown "A" and if it is not empty it is shown "AX". We expect in each iteration, images cover less cells coverage.

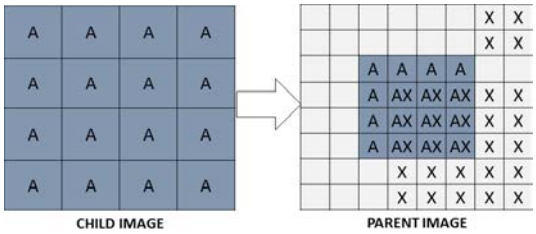

Figure 4. Child Image Match with Parent Image

Initially, each candidate image is transformed into grid space using the precomputed homographies and the number of grid-cells they cover is computed. The problem is cast as minimum subset selection problem where "minimal number of images which cover all possible grid nodes" is searched for. These information using in integer programming tool program Lindo [8] is used for the calculations. Output shows minimum number of images and these images are cover the most area in the parent image.

3. RESULTS AND DISCUSSION

Considering the complexity of the proposed system, experiments are conducted on various sub-routines exclusively in addition to integration tests.

3.1 Finding Levels and Reducing Number of Images

Four image datasets are created by standard camera and find the these images cover area. All image resolutions are 720x576. In Fig. 7a - 7b, show the cover cell in parent image for each iteration. In Besiktas Image dataset have got 279 images and parent image's grid 12x12, child image's grid 6x6. After the 6 iterations, we reached the optimal solution. In Kozyatagi Image dataset has got 94 images and parent image's grid 6x6, child image's grid 2x2. After the 10 iterations, we reached the optimal solution.

In Besiktas image set sampling rate approximately 2 therefore as is seen in Table 1 grid size should be two fold. As it seen child image edge is split 6 or more intense segmentations than the covering area is not change but rate of increase in solution set naturally continues. So these sampling rate can be used for ideal solution.

In Kozyatagi image set sampling rate approximately 3 therefore as is seen in Table 2 grid size should be two threefold. First row coverage rate is 97,3148% and select the best solution.

Table 7 Number of Image and Cover Area with Grid Size in Besiktas Dataset

Child Image One Edge Grid Size	Parent Image One Edge Grid Size	Number of Image Selected	Cover Area
2	4	4	63,6446
4	8	5	73,4318
6	12	6	78,3003
8	16	9	77,8837

Table 8 Number of Image and Cover Area with Grid Size in Kozyatagi Dataset

Child Image One Edge Grid Size	Parent Image One Edge Grid Size	Number of Image Selected	Cover Area
2	6	10	97,3148
4	12	18	98,7074
6	18	20	99,7642
8	24	26	99,9579

3.2 Creating Tree Structure

System is tested in 2 datasets and these images are taken by standard end user cameras. Image resolution does not affect the results. In Fig. 5, you can see some examples of our Galata dataset in 3 different scales. Fig. 6 shows us three images. One is different scale, and has AR markings. User input, in Fig. 7, searched in the tree and matches with top of the second image in Fig. 6. All points of AR data, some of them not in the best match image, are shown in correct position and with correct scale information. A similar set of experiments were conducted on the other Uskudar dataset.

Figure 5. Galata test set: various scale images

Figure 6. Galata test set: AR points mapped on the original pictures

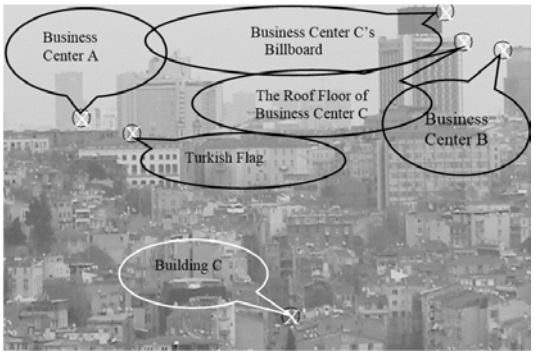

Figure 7. Galata test set: AR information moved from the diffent scales of image on the user input

In these two experiments, black speech bubbles come from same level AR object and white speech bubble comes from a top-level AR object. One of the critical points in these systems is positioning the AR object in the correct location on user input with minimum error. In this situation our system targets two key scenarios. Fig. 15 describes those. First one is the case where relevant AR objects are on the best matching image.

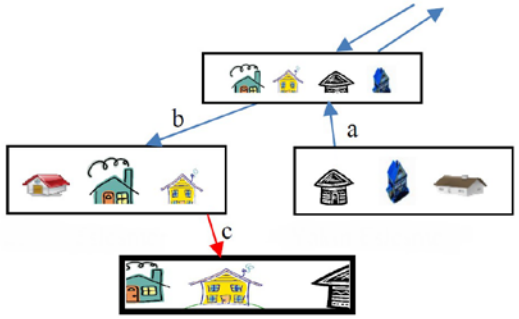

Figure 8. Augmented Reality Object's Transfer Path

The other situation is relatively few AR points come from images other than the best matching one but still in the neighborhood. In this case 3 homographies must be applied to AR objects (Fig. 15 at a, b and c are shown by arrows) and larger error is expected in comparison to the other scenario.

In Table 3, we can see the di_erent threshold values for RANSAC and transfer error is calculated by the pixel errors. As shown the errors are quite low. Our observations from the other test concludes that best RANSAC threshold level is around 2 pixels.

Table 9 Uskudar Dataset Errors

Ransac Threshold Level	Average Pixel Error	Median Pixel Error
6	2,16576	2,97564
5	2,41566	3,39651
4	1,67173	2,45491
3	0,86795	0,26557
2	0,82947	0,53763
1	1,03112	0,82621

4. CONCLUSIONS

In this study, we developed a visual augmented reality system based on hierarchical semi-complete panoramic representation which helps people to interact with environment easily. We provide an innovative approach to store attributes of the images in a tree structure so matching process is accelerated. Automatic detection of the image zoom-level is provided which is critical during assignment of images to tree levels. System gives the satisfactory results in highly zoomed-in scenarios. Multi-scale augmented reality with automatic image scaling is presented.

REFERENCES

There are no sources in the current document.

ICENS
INTERNATIONAL CONFERENCE ON ENGINEERING AND NATURAL SCIENCES
24-28 May 2016 /Sarajevo

Spectrum Occupancy Measurements for Terrestrial TV Bands in Turkey

Ibrahim Seflek[1], Ercan Yaldiz[2], Huseyin Duysak[3]

Abstract

Wireless communication applications which demand broadband have increased intensively. This situation has revealed that the electromagnetic spectrum has been a very valuable and finite resource. Cognitive Radio (CR) is seen as a solution to provide growing requirement and eliminate spectrum scarcity. Especially, determination of CR standards such as Wireless Regional Area Network (WRAN), IEEE 802.19 has boosted interest in the VHF and UHF TV bands. This paper presents spectrum occupancy measurements results for VHF (174-230 MHz) and UHF (470-790 MHz) frequency bands in an outdoor environment both suburban and urban locations in Konya, Turkey. Average occupancy results for urban areas for VHF and UHF bands are 18.07 %, and 11.17%. On the other hand, these results for suburban area are 9.80% and 10.84% respectively. The obtained results show that TV bands is foremost candidate for implementation of CR.

Keywords: spectrum occupancy measurement, spectrum monitoring, cognitive radio, UHF-VHF TV Bands

1. INTRODUCTION

Mankind had not used wireless communication devices in the past. There was no spectrum management and confusion. But nowadays, wireless communication applications have proliferated in every area where we live and the lack of spectrum has become a challenge. Fixed spectrum allocation method has led to the emergence of this condition. That is why, the world has tended dynamic spectrum access and cognitive radio was born in 1999 by Mitola. CR allows to use idle or underutilize frequency band for unlicensed (secondary) user without disturbance to licensed user (primary) [1]. CR is seen a key solution for spectrum scarcity because of its feature.

Federal Communications Commission (FCC) and other regulatory agencies have realized dynamic spectrum access and CR which are technologies that will relieve the spectrum. Therefore, FCC released a report on this subject to use low-power unlicensed devices for VHF and UHF TV bands [2]. Besides, WRAN standard was presented for TV bands by IEEE in 2011. This standard organizes unused TV band re-used for secondary users in rural area. Another standard is IEEE 802.19. The aim of the standard is to make possible co-existence for IEEE 802 networks and devices to productively use TV bands [3].

TV bands are more promising solution because of transition from analog to digital broadcast. Bandwidth for analogue TV is 8 MHz but for digital broadcast this value 6 or 8 times reduces with different technological properties [4].Besides, TV bands frequency range has shown good feature in terms of propagation in electromagnetic spectrum. Many countries have completed this transition. Especially, USA and large portion of Europe has used digital TV broadcast. For spectrum, this transition from analogue to digital is quite helpful. A large part of spectrum (TV) has become empty and appropriate for dynamic spectrum applications such as cognitive radio. In this context, a lot of spectrum occupancy measurements were carried out in different scenarios for the world TV bands. Some studies were performed to determine the occupancy of the indoor and outdoor environments after passing from analog to digital broadcast status [5]-[10]. Despite the onset of digital TV test broadcasts, Turkey has not yet switched to digital broadcasts. The goal set for the transition to digital broadcasting in 2015 has not been met. This paper presents spectrum occupancy measurement results for TV bands which broadcast analogue.

2. MEASUREMENT SETUP

Measurements were made in two separate regions. The first region was the Selçuk University campus, which is about 25 km from the city center. The measurement system was set up on faculty of engineering building (latitude: 38º 01’38” north, longitude: 32º 30’ 38” east, altitude: 1140 meters). The second area was a detached house in Konya and system was established on the detached house’s roof (latitude: 37º 51’09” north, longitude: 32º 30’ 28 east altitude: 1020 meters). Measurements were carried out for a week and 24 hours in both regions. The study was conducted between

[1] *Corresponding author:İbrahim Şeflek, Selçuk University, Department of Electrical & Electronics Engineering, 42250, Selcuklu/Konya, Turkey.* iseflek@selcuk.edu.tr

[2] *Ercan Yaldiz, Selçuk University, Department of Electrical & Electronics Engineering 42250, Selcuklu/Konya, Turkey.* eyaldiz@selcuk.edu.tr

[3] *Hüseyin Duysak, Karamanoğlu MehmetBey University, Department of Electrical & Electronics Engineering, 70200, Karaman, Turkey.* huseyinduysak@kmu.edu.tr

December 7th and December 21st 2015. Locations are selected carefully as possible for precise measurements and line of sight transmitters. The same instruments and setup for measurements made in both areas were used. AOR DA 3200 antenna was used during the studies. Antenna has vertically polarized with omni-directional receiving pattern in the horizontal plane. Especially for the university measurements, pre-amplifier was used because measurements are made far from transmitters. Rigol DSA 1030 spectrum analyzer which have 9 kHz-3000 MHz frequency range was used in measurement campaign. The connection between the antenna and spectrum analyzer was provided with a low loss coaxial cable. Laptop connection with spectrum analyzer was performed with USB connection cable. Data acquisition, data analysis and measurement system control was carried out via laptop with MATLAB program. Spectrum analyzer configuration was conducted by MATLAB too. Table 1 shows this configuration parameters. Measurement system which established in two measuring points is shown in Figure 1.

Table 10. Spectrum Analyzer Configuration

Parameter	Value
Frequency Span	60 MHz
Resolution Bandwidth (RBW)	10 kHz
Video Bandwidth (VBW)	10 kHz
Reference level	-10 dBm
Scale	10 dB/div
Detection Type	RMS detector
Sweep Time	Automatically Selected

a)

b)

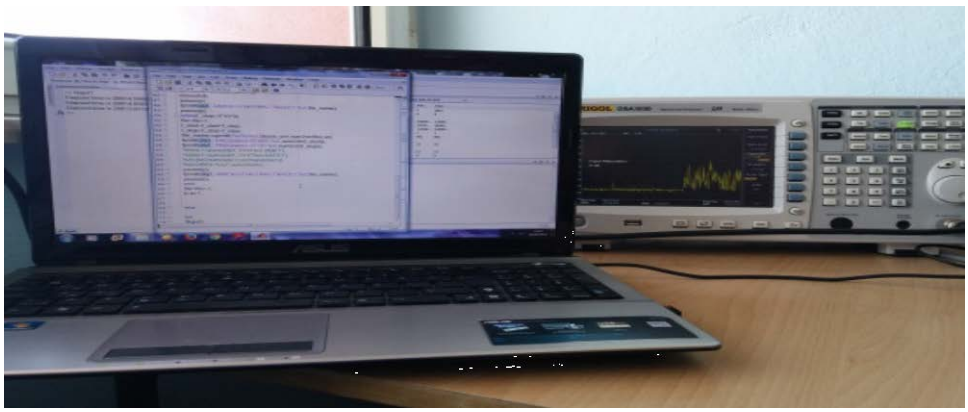

c)

Figure 1. Spectrum Occupancy Measurement System a) University Campus b) Suburban Area c) Measurement Equipment

3. METHODOLOGY

Spectrum sensing is the basis of spectrum occupancy measurements. Matched filtering, Waveform based sensing, cyclostationary detection and energy detection are some of the detection methods used in the literature. Energy detection method is simple and have low computational complexities. The reason for this, while other methods need to signal parameters of transmitters, energy detection does not need. In energy detection method, primary user's presence is determined by comparing energy value of the signal in the environment and the predetermined threshold value [11]. If value of the signal received from the ambient is higher than the threshold, spectrum is considered to be occupied. Otherwise, the spectrum is idle.

The process for setting the threshold value is extremely important. While high threshold that leads to the perception of noise, such as low-power licensed users, low threshold value provides noise values to be perceived as a licensed user. Thus, in both cases the spectrum is evaluated incorrectly and those cases allow the occurrence of false occupancy rate.

Determination of the measurement system's noise figure forms the basis for identifying the threshold value. The identification process is performed instead of the antenna connected match load (50 Ω). After the system noise margin determined for each frequency band, using any of the methods of determining the threshold values, are determined for each frequency band. Maxnoise criterion, m-dB method and probability of false alarm (PFA) criterion are used for determination of threshold. In Maxnoise method, the maximum noise values obtained for each frequency point is determined as the threshold value. This method can lead to underestimation.

$$T(f) = Nmax(f) \quad (1)$$

where $Nmax(f)$ represents maximum noise value for each frequency point. In m-dB method, threshold is determined by adding m decibel the average noise level

$$T(f) = Nmean(f) + m \quad (2)$$

where m represents constant value of the amount added to the average noise level. In PFA method, the empirical distribution of the noise samples are computed and the set the threshold so that no more than 1% of the measured noise samples are above that threshold.

$$T(f) = F_{X(f)}^{-1}(1-P_{fa}) \quad (3)$$

where $F^{-1}_{X(f)}(.)$ represents the inverse of $F_{X(f)}(.)$, the cumulative distribution function of the noise values $X(f)$ [12]. As it mentioned in the reference [12], PFA 1 % method give better results than others. This method has been used in this measurement study.

During the measurement studies, TV bands are separated 60 MHz frequency band. Each 60 MHz frequency band has 301 frequency points. The separation between two consecutive frequency points is 200 kHz and a similar algorithm in the reference [13], thousands of data are obtained. After that data post-processing is conducted and results have been obtained.

4. MEASUREMENT ANALYSIS AND RESULTS

As a result a total of 15 daily measurement campaign for TV bands, the data obtained from urban and suburban area are compared with predetermined threshold for VHF and UHF TV bands. Presentation of spectrum occupancy is shown with the average duty cycle ratio. The duty cycle can be described as the ratio of the time the signal is above threshold value. Average duty cycle is calculated as follow.

$$ADC = Nf/Ti.N \quad (4)$$

where Nf refers to the amount of the power value exceeds the threshold value for each frequency point. While N indicates the total frequency points for measurement campaign, Ti is time instances during measurement for each frequency points. For each measurement point of the TV bands, analysis is performed and is presented with figures. Figures consist of 3 parts:

a) average power spectral density

b) whether the instantaneous spectrum is full or empty

c) how often the threshold has been exceeded at each frequency (average duty cycle)

Figure 2 indicates VHF TV bands measurements for university campus. This frequency band showed 18.07% occupancy for 7 day period.

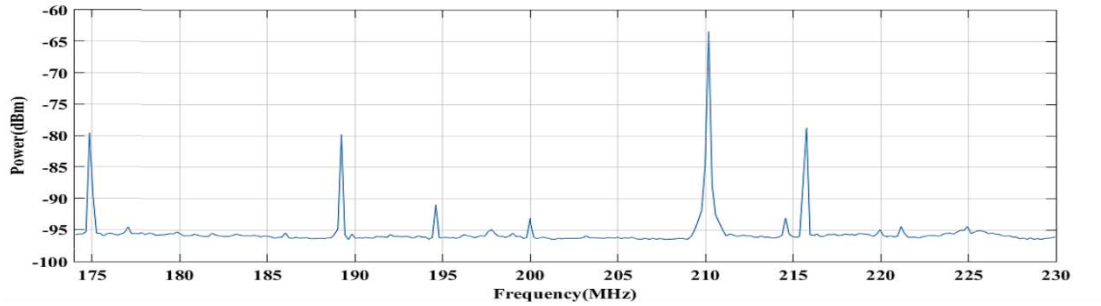

a)

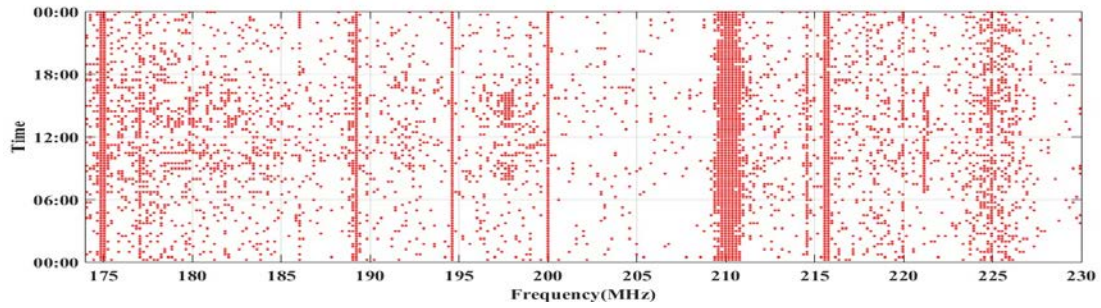

b)

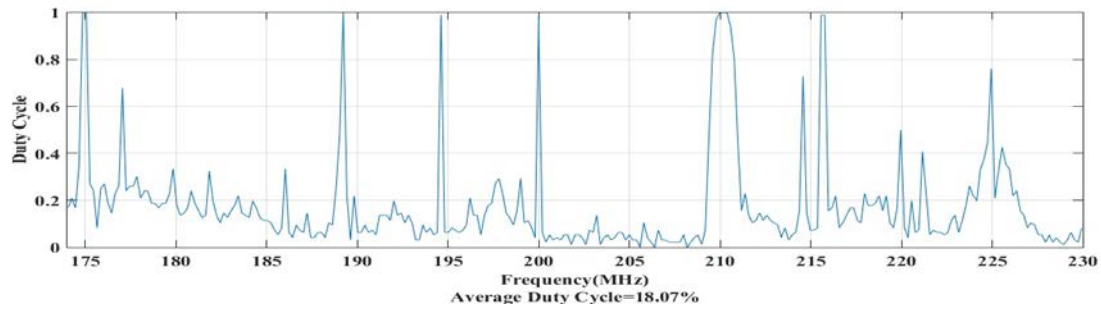

c)

Figure 2. VHF TV Band Measurement Results for Urban Area (University Campus)

Figure 3 illustrates VHF TV bands measurements for suburban area. This frequency band's occupancy rate is 9.80% for 7 day period.

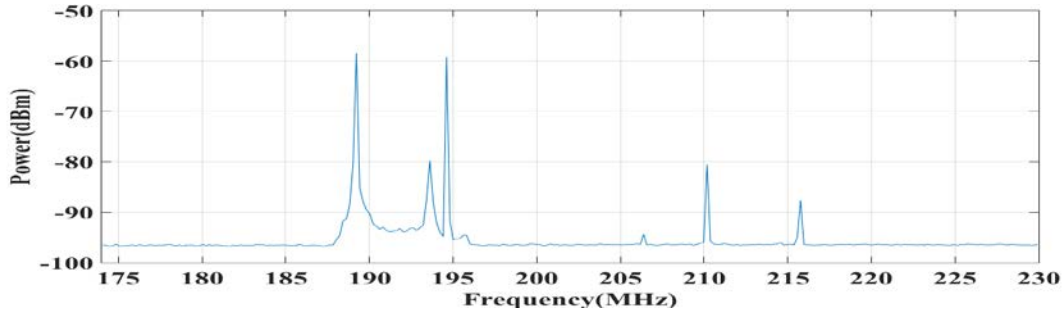

a)

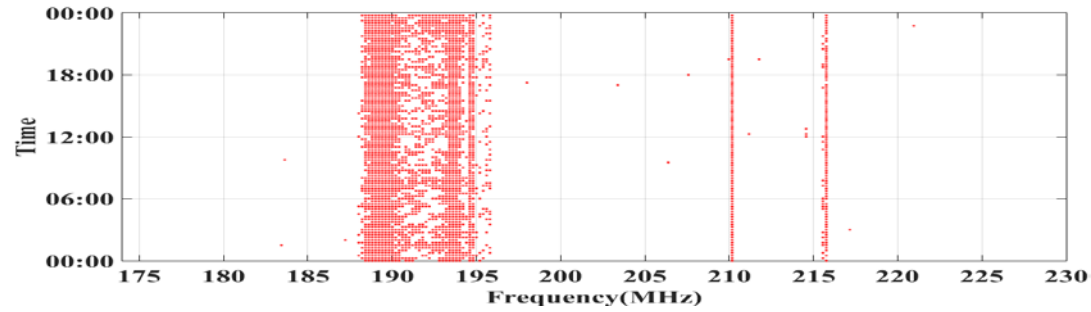

b)

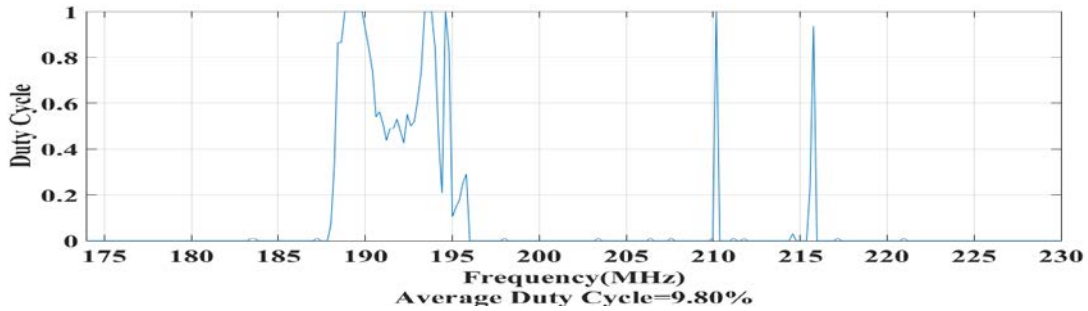

c)

Figure 3. VHF TV Band Measurement Results for Suburban Area

Distance of urban and suburban measurement points to TV transmitters approximately are 25.8 and 13.5 km respectively. Figure 4 demonstrates UHF TV band measurement results for urban area. Occupancy for Figure 4 is 11.17%.

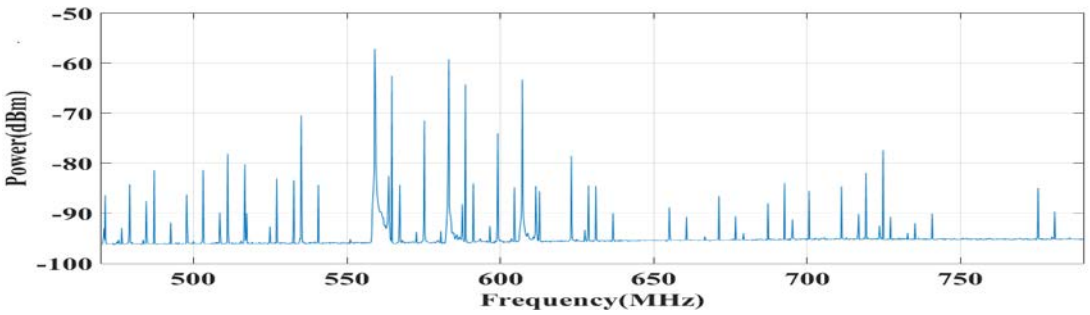

a)

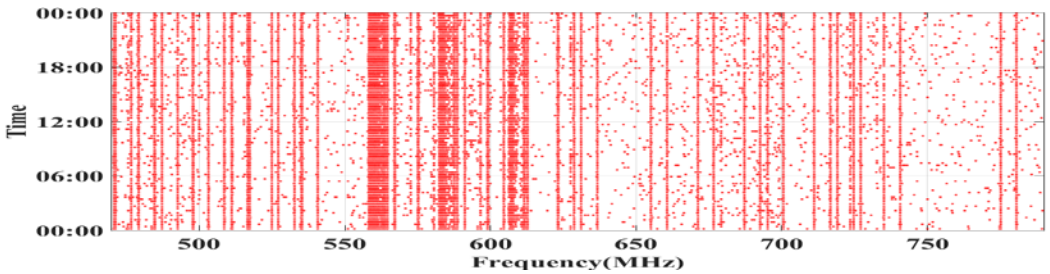

b)

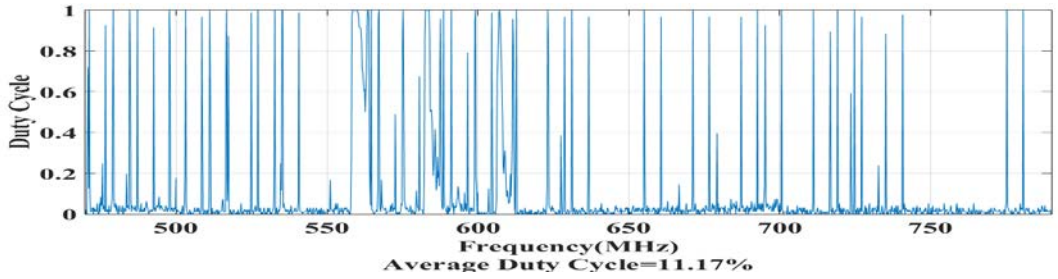

c)

Figure 4. UHF TV Band Measurement Results for Urban Area (University Campus)

UHF TV bands results for suburban area is showed in Figure 5. 7-day measurement result obtained occupancy rate is 10.84%.

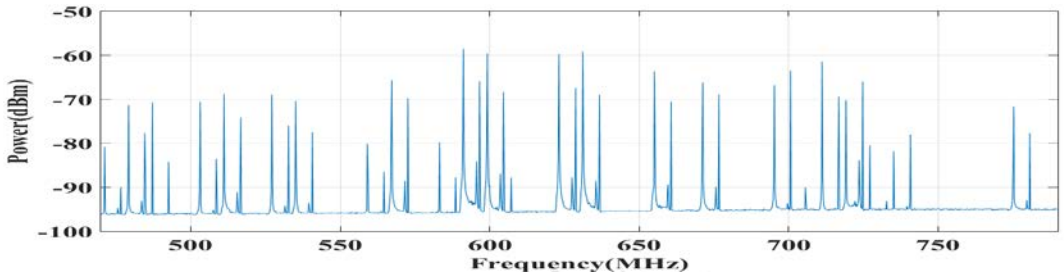

a)

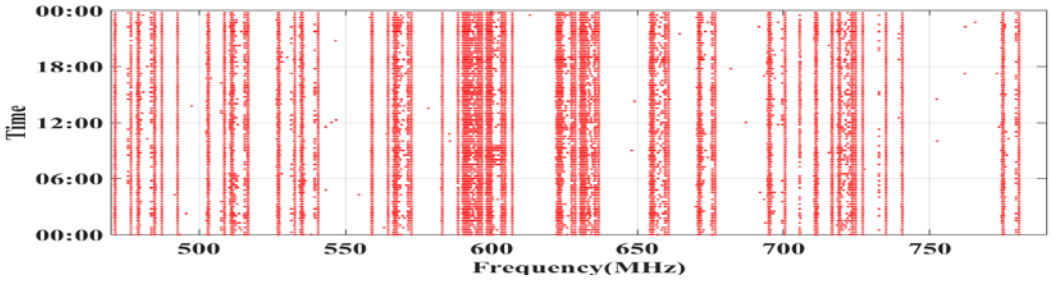

b)

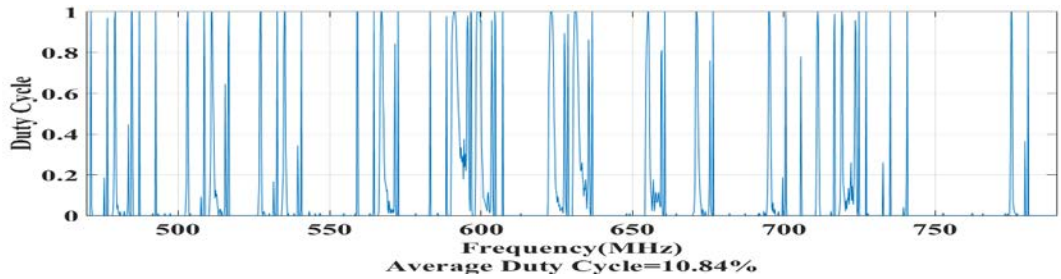

c)

Figure 5. UHF TV Band Measurement Results for Suburban Area

5. CONCLUSIONS

In this paper, the overall process of how to perform the spectrum occupancy measurement is explained. Additionally, measurements are performed in the TV bands for two different areas and results obtained from the analysis are presented in different forms. For urban area measurement results, VHF and UHF bands are 18.07% and 11.17% respectively. Due to the transmitting distance, pre-amplifiers are also used in urban (university campus) measurements.

Suburban measurement results in context of occupancy are less than urban results. For VHF band occupancy rate is 9.80%. This rate is 10.84% for UHF band. At VHF band, suburban occupancy results are almost half of urban occupancy results. On the other hand, UHF band results are quite similar. These results indicate that TV bands are quite suitable for the implementation of cognitive radio.

REFERENCES

[1]. J. Mitola III and G.Q. Maguire Jr. "Cognitive radio: making software radios more personal," *Personal Communications, IEEE* vol.6, no:4, pp.13-18, Aug 1999.
[2]. M. J. Marcus, "Unlicensed cognitive sharing of TV spectrum: The controversy at the Federal Communications Commission," *Communications Magazine, IEEE* vol.43 no:5, pp.24-25, May 2005.
[3]. K. Patil, K. E. Skouby, and R. Prasad., "Spectrum measurement and analysis of TV band support of Cognitive Radio operation in India," *Wireless Communications, Vehicular Technology, Information Theory and Aerospace & Electronic Systems* (VITAE), Atlantic City, 2013, pp. 1-5.
[4]. A. Henten, R.Tadayoni, I. Windekilde, "Spectrum war the battle for the digital dividend spectrum", *Proceeding of the 18th Biennial ITS conference*, Tokyo, 2010.
[5]. C. Konig, P. Guirao and R. Lubben, "Distributed indoor spectrum occupancy measurements in the UHF TV band." *Communications* (ICC), Sydney, 2014, pp. 1373-1378.
[6]. J. Van De Beek, J. Riihijärvi, A. Achtzehn, P. Mähönen, "TV white space in Europe," *Mobile Computing*, IEEE vol.11, no:2, pp.178-188, Feb 2012.
[7]. S Contreras, et al., "An investigation into the spectrum occupancy in Japan in the context of TV White Space systems," *Cognitive Radio Oriented Wireless Networks and Communications (CROWNCOM)*, Osaka, 2011, pp. 341-345.
[8]. T. X. Brown, et al., "A Survey of TV White Space Measurements," *e-Infrastructure and e-Services for Developing Countries*, Springer International Publishing pp.164- 172, Nov 2014.
[9]. A. Pintor, et al., "Spectrum survey of VHF and UHF bands in the Philippines,'' *in TENCON 2012-2012 IEEE Region 10 Conference*, Cebu, 2012, pp. 1-6.
[10]. G. M. Kagarura, D.K. Okello and R.N.Akol, "Evaluation of spectrum occupancy: a case for cognitive radio in Uganda." *Mobile Ad-hoc and Sensor Networks (MSN)*, Dalian, 2013, pp. 167-174.
[11]. T. Yücek, and H Arslan, "A survey of spectrum sensing algorithms for cognitive radio applications," *Communications Surveys & Tutorials, IEEE* vol.11, no:1, pp.116-130, Mar 2009.
[12]. M. López -Benítez, and Fernando Ca
cognitive radio," European Transactions on Telecommunications, vol.21, no:8, pp.680-693, Dec 2010.
[13]. M. López -Benítez, and Fernando Ca
radio," *Testbeds and Research Infrastructure. Development of Networks and Communities*, Springer Berlin Heidelberg, 2011.

BIOGRAPHY

İbrahim ŞEFLEK was born in Konya, Turkey in 1988. He graduated from Electrical and Electronics Engineering in Erciyes University in 2012. He continues M.Sc. in Electrical and Electronics Engineering from Selcuk University. He has been a research assistant since 2013. He is interested in spectrum management, cognitive radio, 5G communication.

ICENS
INTERNATIONAL CONFERENCE ON ENGINEERING AND NATURAL SCIENCES
24-28 May 2016 /Sarajevo

Dipeptidyl Peptidase IV Inhibitory Activity of *Alchemilla vulgaris* L.

Ali Zeytunluoglu[1], Figen Zihnioglu[2]

Abstract

Type 2 diabetes mellitus (T2DM) is a common metabolic/endocrine disorder throughout the world and cause serious medical problems to human health. Dipeptidyl peptidase IV(DPPIV) enzyme is closely associated with the T2DM disease that responsible for the degradation of glucose dependent insulinotropic polypeptide (GIP) and glucagon-like peptide-1 (GLP-1) that play a pivotal role in glycemic regulation. One of the new approaches to the management of type 2 diabetes mellitus (T2DM) is inhibiton of DPP-IV enzyme. There is a growing interest to develop natural DPP-IV inhibitors that will be potent without undesirable side effects. In this study; DPPIV inhibitory activity of the aqueous and methanolic extracts obtained from Alchemilla vulgaris were tested. The aqueous extracts showed the more inhibitory activity on the enzyme than methanolic extracts. IC_{50} value was calculated for the aqueous extract as 16.9 µg/ml. Herewith Diprotin-A was used as reference standard. The results indicated that aqueous extracts of A. vulgaris had the significantly inhibitory effect on DPPIV. The results suggest that aqueous extracts would be a beneficial ingredient for nutraceuticals and pharmaceuticals acting against DPPIV inhibition.

Keywords: *Alchemilla vulgaris*, Dipeptidyl Peptidase IV, Enzyme inhibition, Type 2 diabetes

1. INTRODUCTION

Incretin hormones[insulinotropic polypeptide (GIP) and glucagon-like peptide-1 (GLP-1)] secreted by intestinal L cells have many physiological functions, such as promoting glucose dependent insulin secretion, suppressing pancreatic glucagon release and inhibiting gastric emptying(Fig 1). Dipeptidyl peptidase IV (DPP-IV; EC 3.4.14.5) rapidly inactivates by proteolytic cleavage both of them as endogenous substrates [1]. Therefore, the use of DPPIV inhibitors for elongation of the half-life of incretins is a new therapeutic approach for managing type 2 diabetes[2].

Several DPP-IV inhibitors, e.g., sitagliptin, vildagliptin, saxagliptin and alogliptin, are antidiabetic agents approved by the United States and Europe governments. However, several adverse effects of these chemicals have been recently reported, including nasopharyngitis, headache, nausea, hypersensitivity and skin reactions. Therefore, to develop DPP-IV inhibitors from natural sources without any side effects is important for the novel therapy of diabetes [3].

The species *Alchemilla vulgaris* (lady's mantle) belongs to the Rosaceae family is known with astringent, anti-hemorroidal and anti-diarrheal properties (Fig 2). The plant infusion is used externally in the cases of stomatitis and wound healing [4].

[1] *Corresponding author: Pamukkale University, Electron Microscopy Research Center 20100 Denizli-Turkey. azeytun@pau.edu.tr*

[2] *Ege University, Faculty of Science, Department of Biochemistry, , 35100, İzmir-Turkey. figen.zihnioğlu@ege.edu.tr*

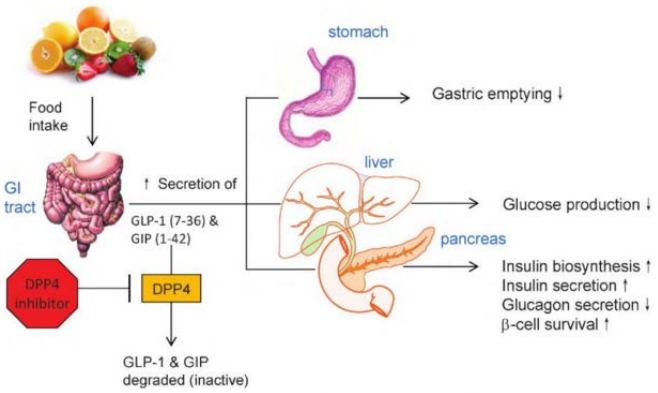

Fig 1: Incretion action and incretin inactivation by DPPIV [5].

*Fig **2 :** Alchemilla vulgaris (lady's mantle)*

The aim of this study was to screen *in vitro* inhibitory activity of DPP-IV from aqueous and methanolic extracts of *A. vulgaris.*

2. MATERIALS AND METHODS

Chemicals

Glycyl-prolyl-paranitroanilide (Gly-Pro-pNA) (Bachem), Diprotin A (Bachem), Methanol (Sigma-Aldrich), Nonidet P40 (Fluka), Tris (Sigma), Sucrose (Riedel) were purchased from commercial suppliers. All other reagents were used in highest analytical grade.

Preparation of Plant Extracts

Alchemilla vulgaris was *obtained from local* herbal market (Yelken Baharat-izmir, Turkey). The plant sample was dried in a vacuum *oven* at *60*°C for 24 hours and then was ground by a Grinder and sieved through 35 mesh. In order to prevent the samples from absorbing moisture, the ground samples were stored in the dark and plastic bags. Plant extracts were prepared as aqueous(with infusion and decoction method) and methanolic extracts.

In infusion method; 10 g of the powder plant material was solved in 100 ml of boiled distilled water. The mixture was stirred in room temperature for 20 min. and then filtered by the double-layered cheesecloth. Obtained filtrate was centrifuged at 10.000 rpm for 10 min and then the separated supernatant volume was completed to 100 ml and stored in a dark glass bottle (in +4 °C) until use.

In decoction method; 10 g of the powder plant material was solved in 100 ml of distilled water. The mixture was refluxed with stirring. After boiling water; the stirring was continued for 20 minutes. The mixture was allowed to cool at the end of 20 minutes. The later; steps used in the infusion method were followed.

In methanolic extraction method; 10 g of the powder plant material was solved in 100 ml of methanol (100 %). The mixture was stirred on the hot-plate in room temperature for a week and then filtered by the double-layered cheesecloth. Obtained filtrate was centrifuged at 10.000 rpm for 10 min. The methanol in supernatant was evaporated with a vacuum *oven* at 65°C.

Tissue Preparation

Preparation of the crude enzyme from lung tissue and all purification procedures were performed at 4°C. Sheep lungs were brought to the laboratory on ice from slaughterhouses (Bircan fattening, Izmir) immediately after slaughter. To remove blood, The lungs were perfused with 10 mM Tris pH (7.4). Lungs were weighed, minced, and homogenized in 20 mM Tris-HCI (pH 7,4) contain 0.25 M sucrose and 1.0 % (v/v) Nonidet P40 with blender. The homogenate was centrifuged at 600 rpm for 15 min. The supernatant was centrifuged for 30 min at 10000 rpm. and the supernatant filtered through glass wool. The filtrate was used for measurement of DPPIV inhibitor activity. Protein contents were estimated by Bradford method using bovine serum albumin as a standard [6].

Measurement of DPPIV inhibitor activity

DPPIV inhibitor activity was performed by using glycyl-prolyl-paranitroanilide (Gly-Pro-pNA) as chromogenic substrate. The enzyme activity was measured as with inhibitor (Diprotin A) and without inhibitor. In a 96-well plate 10 µl enzyme were mixed with 10 µl plant extracts and then preincubated for 15 min at 37 C. Then the reaction was started with adding 100 µl substrate (1 mM Gly-Pro-pNA) and buffer (100 mM Tris buffer pH 7.4) in a final volume of 200 µl. DPPIV activity was determined kinetically during 15 min at 37 °C by measuring the velocities of pNA release (405 nm) from the chromogenic substrate and quantified by reference to a standard curve prepared with *p*-nitroaniline. One unit enzyme activity was defined as the amount of enzyme that catalyzes the release of 1µmol pNA from the substrate/min under assay conditions. All measurements were performed as three replicates. Enzyme inhibitory activity was calculated as mean ± SD(n=3).

3. RESULTS AND DISCUSSION

Dipeptidyl peptidase IV inhibitory activity of the aqueous and methanolic extracts of *Alchemilla vulgaris* leaves were tested in *in vitro* conditions. DPPIV enzyme inhibiton were observed effect *in changing ratio* of aqueous and methanolic extracts of *Alchemilla vulgaris* **(Table 1).** The IC_{50} value was calculated from aqueous extract which highest enzyme inhibition observed. IC_{50} values were determined by nonlinear regression curve fit using Graph pad Prism 5.0 with appropriately diluted of lyophilized *Alchemilla vulgaris* aqueous extracts. Diprotein-A (Ile-Pro-Ile) was used as reference inhibitör. The inhibitory potential of *Alchemilla vulgaris* aqueous extracts showed IC_{50} 16.9 µg/ml while the standard (positive control) Diprotin A displayed the IC_{50} value of 10.1 µg/ml (Table 2) (Fig 3).

*Table **1:** Dipeptidyl peptidase IV inhibitory activity in Alchemilla vulgaris extracts prepared with different methods*

Sample name	Method	DPPIV specific activity (U/mg)	% Inhibition
Sheep lung extract (without inhibitor)	-	0.244± 0.022	0
Sheep lung extract (With inhibitor : *Alchemilla vulgaris* L.)	Infusion	0.026 ± 0.014	89
	Decoction	0.080 ± 0.020	67
	Methanolic extraction	0.047 ± 0.020	81

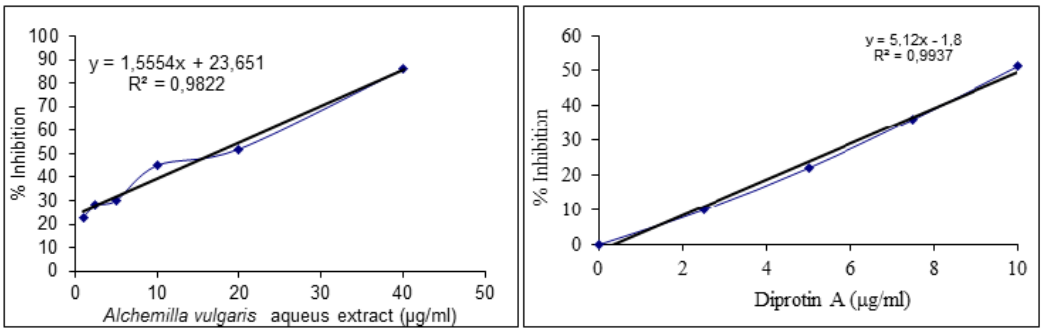

*Figure **3:** Dipeptidyl peptidase IV inhibitory activity of Alchemilla vulgaris (infusion extract) & Diprotin A*

Table 2 : Dipeptidyl peptidase IV inhibitory activity of Alchemilla vulgaris(infusion extract) & Diprotin A

Sample No	Tested Material	Concentration (µg/ml)	% Inhibition	IC_{50} ♥ (µg/ml)	Lineer regression (% Inhibition) ♣
1	*Alchemilla vulgaris*	1	23	16.9	y = 1.5554x + 23.651
		2.5	28		
		5	30		
		10	45		
		20	52		
		40	86		
2	Diprotin A (positive control)	2.5	10	10.1	y = 5.12x – 1.8
		5	22		
		7.5	36		
		10	51		

♣ x; $IC_{50;}$ y DPPIV activity values in 50 % inhibition

♥ The IC_{50} value was defined as the concentration of lyophilized plant extract required to inhibit 50% of DPPIV activity.

4. CONCLUSIONS

Researches of active compounds that have antidiabetic activity should be developed in order to obtain better therapeutic outcomes. Active compounds of plants have potency as antidiabetic that can be used in diabetes mellitus treatment [7].

Dipeptidyl peptidase IV inhibitors are the newest and most promising anti-diabetic drugs for the treatment of diabetes [1].

In recent years, many papers have reported inhibition of DPPIV enzymatic activity by plant extracts; *Camelia sinensis* [7], *Syzygium cumini* [8-9], *Berberis aristata* [10], *Mangifera indica* [11], *Vitis vinifera, Artemisia dracunculus, Prunus laurocerasus., Rubus caesius and Olea europaea* [12]. *Hippophaë rhamnoides* [13], *Helichrysum arenarium* [14], *Urena lobata*[15], *Aronia* sp. [16], *Castanospermum australe* [17], Vitis thunbergii var. Taiwaniana [18], *Allophylus cominia* [19], *Pterocarpus marsupium* [20], *Hedera nepalensis* [21], *Ocimum sanctum* and *Momordica charantia* [22], *Cistus incanus L. ssp. incanus* [23], Annona squamosal [24]. Results of the researches work on DPPIV inhibiton clearly demonstrated that plant extracts had DPPIV inhibitory activity in different levels (Table 3).

*Table **3**: Dipeptidy peptidase IV % inhibition and IC_{50} values in different plant species*

Plant name	% Inhibiton	IC_{50} (µg/ml)	Extraction type
Syzygium cumini	87	65.8	EtOH extract
Berberis aristata	73	14.46	MetOH extract
Mangifera indica	68.2	182.7	MetOH extract
Hippophaë rhamnoides	80.5	2500	Aqueous extract
Helichrysum arenarium	-*	41.2	MetOH extract
Urena lobata	74.4	1654.6	MetOH extract
	62.2	6489.8	Aqueous extract
Castanospermum australe	-*	13.9	EtOH extract
Vitis thunbergii var. taiwaniana	26	-*	Ethanol extract
Camelia sinensis	30	62.5	EtOH extract
Allophylus cominia	52	344.3	Aqueous extract
Ocimum sanctum	66.8	-*	MetOH extract
Momordica charantia	53.2		

*The data is not given in the article.

This study demonstrates that *Alchemilla vulgaris* extract (obtained with infusion method) could be a good lead for further development as a new antidiabetic agent.

ACKNOWLEDGEMENTS

This work was supported by Scientific Research Projects Coordination Unit of Ege University. Project number 08FEN011.

REFERENCES

[1]. Zeng, Z., Luo, J., Zuo, F., Zhang, Y., Ma, H.., Chen, S., Screening for potential novel probiotic Lactobacillus strains based on high dipeptidyl peptidase IV and α-glucosidase inhibitory activity, Journal of Functional Foods 2016: 486-495.

[2]. Huang, S.L., Hung, C.C., Jao, C.L., Tung, Y.S., Hsu, K.C., Porcine skin gelatin hydrolysate as a dipeptidyl peptidase IV inhibitor improves glycemic control in streptozotocin-induced diabetic rats, Journal of Functional Foods 2014: 235-242.

[3]. Scheen, A., Gliptins (dipeptidyl peptidase-4 inhibitors) and risk of acute pancreatitis. Expert Opinion on Drug Safety, 2013; 12:545–557.

[4]. Neagu, E., Paun ,G., Albu,C., Radu, G.L., Assessment of acetylcholinesterase and tyrosinase inhibitory and antioxidant activity of *Alchemilla vulgaris* and *Filipendula ulmaria* extracts, Journal of the Taiwan Institute of Chemical Engineers, 2015; 52:1–6.

[5]. Jones, R.M., Thurston, D.E., Rotella, D., Guccione, S., Martinez, A., New Therapeutic Strategies for Type 2 Diabetes: Small Molecule Approaches, Royal Society of Chemistry, 2012; 515 page.

[6]. Bradford, M., A rapid and sensitive method for the quantification of microgram quantities of protein utilizing the principle of protein-dye binding, *Analytical Biochemistry*, 1976; 72:248–54

[7]. Elya, B., Handayani, R., Sauriasari,R., Ahwati, A., Hasyyati, U.S., Permana, I.T., Permatasari, Y.I., Antidiabetic Activity and Phytochemical Screening of Extracts from Indonesian Plants by Inhibition of Alpha Amylase, Alpha Glucosidase and Dipeptidyl Peptidase IV, Pakistan Journal of Biological Sciences,2015; 18 (6): 279-284.

[8]. Bellé, L.P., Bitencourt, P.E., Abdalla, F.H., Bona, K.S.,Peres, A., Maders, L.D., Moretto, M.B., Aqueous seed extract of *Syzygium cumini* inhibits the dipeptidyl peptidase IV and adenosine deaminase activities, but it does not change the CD26 expression in lymphocytes in vitro, J Physiol Biochem., 2013;69(1):119-24.

[9]. Taldone, T., Isolation and characterization of a dipeptidyl peptidase-IV (DPP-IV) inhibitor from the ayurvedic herb *Syzygium cumini* (Linn.) Skeels. St. John' university(New York), School of Pharmacy, 2008; 201 pages.

[10]. Chakrabarti, R., Bhavtaran, S., Narendra, P., Varghese, N., Vanchhawng, L., Shihabudeen, M.S.H., Thirumurgan, K., Dipeptidyl Peptidase- IV Inhibitory Activity of *Berberis aristata*, Journal of Natural Products, 2011; 4: 158-163.

[11]. Yogisha, S., Raveesha, K.A., Dipeptidyl Peptidase IV inhibitory activity of *Mangifera indica*, , Journal of Natural Products, 2010; 3:76-79.

[12]. Zeytunluoglu, A., Zihnioglu, F., Evaluation of some plants for potential dipeptidyl peptidase IV inhibitory effects in vitro, Turkish Journal of Biochemistry, 2015; 40(3): 217–223.

[13]. Mardanyan, S., Sharoyan, S., Antonyan,A., Zakaryan, N., Dipeptidyl peptidase IV and adenosine deaminase inhibition by Armenian plants and antidiabetic drugs, Int J Diabetes & Metab, 2011;19:69-74.

[14]. Morikawa, T., Ninomiya, K., Akaki, J., Kakihara, N., Kuramoto, H., Matsumoto, Y., Hayakawa, T., Muraoka, O., Wang, L., Wu, L.J., Nakamura, S., Yoshikawa, M., Matsuda, H., Dipeptidyl peptidase-IV inhibitory activity of dimeric dihydrochalcone glycosides from flowers of *Helichrysum arenarium*, J Nat Med,2015; 69:494–506.

[15]. Purnomo, Y., Soeatmadji, D.W., Sumitro, S.B., Widodo, M.A., Anti-diabetic potential of *Urena lobata* leaf extract through inhibition of dipeptidyl peptidase IV activity, Asian Pac J Trop Biomed 2015; 5(8): 645–649.

[16]. Kozuka, M., Yamane, T., Nakano, Y., Nakagaki, T., Ohkubo, I., Ariga, H., Identification and characterization of a dipeptidyl peptidase IV inhibitor from aronia juice, Biochemical and Biophysical Research Communications, 2015; 465:433-436.

[17]. Bharti, S.K., Krishnan, S., Kumar, A., Rajak, K.K., Murari, K., Bharti, B.K., Gupta, A.K., Antihyperglycemic activity with DPP-IV inhibition of alkaloids from seed extract of Castanospermum australe: Investigation by experimental validation and molecular docking, Phytomedicine. 2012; 20(1):24-31.

[18]. Lin, Y.S., Chen,C.R., Wu,W.H., Wen,C.L., Chang,C.I., Hou, W.C., Anti-α-glucosidase and Anti-dipeptidyl Peptidase-IV Activities of Extracts and Purified Compounds from *Vitis thunbergii var. taiwaniana*, J. Agric. Food Chem., 2015; 63(28):6393–6401.

[19]. Calero, J.S., Young, L.C., Faz, E.M., Harvey, A.L., Inhibitory effect of *Allophylus cominia* (L.) Sw leaves aqueous extract on tyrosine phosphatase 1B and dipeptidyl peptidase IV proteins, Revista Cubana de Farmacia., 2014;48(4):672-683.

[20]. Kosaraju, J., Dubala, A., Chinni, S., Khatwal, R.B., Satish Kumar, M.N., Basavan, D., A molecular connection of *Pterocarpus marsupium*, *Eugenia jambolana* and *Gymnema sylvestre* with dipeptidyl peptidase-4 in the treatment of diabetes, Pharm. Biol., 2014; 52: 268-271.

[21]. Saleem, S., Jafri, L., Haq, I.U., Chee Chang, L., Calderwood, D., Green, B.D., Mirza, B., Plants *Fagonia cretica* L. and *Hedera nepalensis* K. Koch contain natural compounds with potent dipeptidyl peptidase-4 (DPP-4) inhibitory activity, J. Ethnopharmacol., 2014; 1156:26-36.

[22]. Singh, A.K., Jatwa, R., Joshi, A.J., Cytoprotective and dipeptidyl peptidase IV (DPPIV/CD26) inhibitory roles of *Ocimum sanctum* and *Momordica charantia* extract, Asian J Pharm Clin Res, 2014; 7(1):115-120.

[23]. Lendeckel, U., Arndt, M., Wolke, C., Reinhold, D., Kahne, T., Ansorge S. Inhibition of human leukocyte function, alanyl aminopeptidase (APN, CD13) and dipeptidylpeptidase IV (DP IV, CD26) enzymatic activities by aqueous extracts of Cistus incanus L. ssp. incanus. J Ethnopharmacol., 2002;79:221-7.

[24]. Davis, J.A., Sharma, S., Mittra, S., Sujatha, S., Kanaujia, A., Shukla, G., et al., Antihyperglycemic effect of *Annona squamosa* hexane extract in type 2 diabetes animal model: PTP1B inhibition, a possible mechanism of action ?, Indian J Pharmacol. 2012;44:326-32.

BIOGRAPHY

Ali Zeytunluoglu was born in Denizli, Turkey, in 1975., He received the Bachelor degree in Biology from the University of Ankara, Turkey, in 1998, and the Master degree in biology from the University of Pamukkale, Denizli, Turkey, in 2004, and Ph.D degree in biochemistry from the University of Aegean, Izmir, Turkey, in 2012. In 1999, he joined the Department of Biology, University of Pamukkale, as a Research assistant. He become an Assistant Professor in 2013. He has been worked in department of biomedical equipment technology as Assistant Professor since year 2013. His current research interests include enzyme purification and characterization, enzyme inhibition, diabetes, hypertension, and cancer.

ICENS
INTERNATIONAL CONFERENCE ON ENGINEERING AND NATURAL SCIENCES
24-28 May 2016 /Sarajevo

Standart Penetration Test Correlation for Kocaeli,Turkey

Utkan Mutman[1], Murat Karadeniz[2]

Abstract

In any geotechnical design procedure, the fundemantal point to be initially clearified is the characterization of existing soil profile at a site. Standard Penetration Test is considered one of the most common in-situ tests to evaluate the the soil parameters. The parameters to be determined in the ground examination sometimes cannot be obtained due to various reasons. In this case, from the correlations of Standard Penetration Tests, soil parameters are obtained. Up to the present day, many researchers have done Standard Penetration Test correlations. However; because they work in different areas, each correlation gives different results. In this study, the correlation was made between the values obtained from the Standard Penetration Test made in soil examinations which were done in Kocaeli (Turkey) and laboratory tests. In the first stage of this study, the fieldwork done in the ground examinations in Kocaeli /Turkey has been analyzed. The parameters obtained as a result of soil mechanics tests on disturbed and undisturbed samples taken from drills huddled together. These parameters are liquid limit, plastic limit, compression index, cohesion and internal friction angle. The SPT-N value obtained as a result of Standard Penetration Test done on each borehole and these soil parameters were matched. In the second stage of this study, by performing regression analysis between determined parameters, correlations were obtained between Standard Penetration Test and undrained shear strength (S_u) of fine-grained soil. In this way, special Standard Penetration Test correlations for Kocaeli /Turkey were obtained. Soil parameters which could be obtained in this way are determined more accurately by Standard Penetration Test results.

Keywords: Cohesion, In-situ Test , Soil Shear Strength Parameters, , Unconfined Compression Test.

1. INTRODUCTION

The standard penetration test (SPT) is routinely used in the geotechnical engineering practice for in situ investigation of soil deposits. Due to the longtime and worldwide use of this test, comprehensive data have been accumulated in the past resulting in a number of SPT-based empirical correlations for clayed soils. In these correlations, the SPT blow count is used as a parameter for in situ characterization of field deposits. On the other hand, extensive information on the behavior of clayed soils has been obtained from laboratory tests on reconstituted and undisturbed samples. In these laboratory studies, cohesion is commonly identified as a principal factor influencing the deformation and strength characteristics of clays. Thus, in order to establish a correspondence between the field and laboratory parameters for soil characterization, the first step would be to provide a link between the penetration resistance and cohesion of clayed soils [1].

In order to find this correlation between cohesion of clayey soil and penetration resistance, studies have attempted to establish since the first implementation of the standard penetration test and numerous empirical correlations have been proposed in this direction in contemporary literature. On the other hand the proposed correlations have usually been derived for the grounds located in a certain geographical area. In the case of using these correlations in different regions, results of the regional differences are affected. In the process of determining any parameter, it is important to reveal which range parameters can be changed using all available correlations and to do parameter selection considering all values with an engineering standpoint [2].

In Turkey, SPT is the field test most used in ground investigations. In most of the ground investigations, laboratory tests are done in the required soil layer. Therefore, the parameters required in the calculation of construction projects are used to be obtained by correlation. In this study, a new correlation between SPT penetration resistance and cohesion has been identified for Kocaeli/Turkey. In this way, by making a specific correlation for Kocaeli /Turkey, it will be ensured to obtain more accurate soil shear strength in construction activities.

[1] *Corresponding author: Civil Engineering Department, Kocaeli University, 41000, Kocaeli, Turkey . utkanmutman@gmail.com*

[2] *Co-author:Civil Engineering Department,Kocaeli University , Kocaeli, Turkey,41000,karadenizmurat61@gmail.com*

1.1 Standart Penetration Test (SPT)

Fletcher and Hanry A. Mohr standardized the penetration test for the first time with the hammer at 140 lb. being nailed on by dropping it from 30 in. using a sampling spoon [3]. "Standard Penetration Test" (SPT), which was first come out in about 1927 and developed by "Raymond Concrete Pile Company" and introduced to the public by Terzaghi and Peck has been used in nearly 90 years [4]. SPT is widely used in North and South America, Australia, South Africa, India, Portugal, Israel, Turkey, Great Britain and Japan [5].Until now, various improvements have been achieved on this test [6].

In order to interpret the results of the SPT correctly, equipment used in the experiment and how the test has been done need to be known. The tools used for SPT varies more from country to country than the static penetrometer equipment. Many variables affect the validity and availability of SPT results [7].As a result of these variables, the measured penetration resistance (SPT-N_{field}, N_f) may be excessively high or excessively low. In order to reduce the effects of these variables on geotechnical design and the determination of engineering properties of soils, SPT resistance corrections should be made. Within the frame of these corrections, geological load correction (C_N), energy correction (C_E), rod length adjustment (C_R), boring diameter correction (C_B), sampler sheath correction (C_S) require to be used depending on instrumental details and the test experiment method [7]. Farrar stated that making C_N correction in fine-grained soils, shallow cases would be normal but it was still controversial, especially for experiments performed in deep-set[8]. Although still controversial, CN correction for clay soils is applied in practice [9]. Therefore, this study has not taken into account the CN [10].

The correction shown in N60 is given by the following expressions [7].

$$N_{60} = \frac{C_E . C_B . C_S . C_R . N_a}{60} \quad (1)$$

Here N_{60} = Corrected SPT resistance according to the 60% of the theoretical free-fall energy mallet,

$N_f = N_a$ =SPT resistance in the field.

2. METHODOLOGY

To estimate the correlations needed N (SPT) and Laboratory S_u, plasticity index (PI),sampling depths, boreholes diameter, drilling methods and other geotechnical properties of study area soil.In this study, ground investigation reports made in province of Kocaeli/Turkey were collected. SPT results in the report and cohesion values (S_u) obtained from experiments performed in the laboratory on undisturbed soil samples taken during the ground investigation have been recorded. In order to correlate these data, first of all the necessary correction have been made in SPT resistance. For energy correction (C_E) value of 45% was used; that is suitable for the conditions of Turkey. Because in Kocaeli/Turkey, boring are made in 100 mm diameter, drilling diameter correction (C_B) was accepted as 1. Also because the SPT sampler is used for unshielded, sampler sheath correction (C_S) was taken as 1. For the rod length correction (C_R), values given in the table below were used in relevant depts.

Table 1. Rod length correction (C_R)

Depth (m)	C_R
> 10	1.00
6-10	0.95
4-6	0.85
0-4	0.75

In measured 113 SPT resistance (N_f), correction was performed using the first number formula. The collected physical and mechanicsl properties of Kocaeli fine-grained soils is presented in Table (2).

Table 2. Geotechnical properties of studied fine-grained soil of Kocaeli

Properties	Min	Max	Ave.	S.D
Plasticity limit (PL)	12,9	39,5	20,89	20,89
Liquid limit (LL)	23	69,3	40,67	8,17
Plasticity Index (PI)	7	38	19,95	5,09
Natural water content (w_n)	5,5	38,8	21,75	5,59
Number of SPT (N_{field})	4	39	18,71	8,13

N_{60}	2,25	27,08	11,13	5,23
Undrained shear strength (S_u)	13	131,5	72,48	23,8

To estimate undrained shear strength of fine- grained soils for the mentioned sites was investigated in two phases. In the first phase, only N (SPT) considered as independent parameter. İn the second phase the parameter of of natural water content (w_n) and plasticity index (PI) considered as independent effective parameters, in addition to N (SPT) content.

In the first phase, between N_f ,N_{60} and Su linear regression analysis were performed. In this analysis first correlation coefficient was found and then the regression equation was obtained. The correlation coefficient (r) is 0.92 ,0.90 between N_f, N_{60} and Su respectively , r values close to 1.00 has been found. Because when the N_f value is zero, the Su value should also be zero, the regression equation was calculated as the Eq. (2,3)

$S_u=5.604.N_{60}$ r=0,90 SD= 32,8 (2)

$S_u=3,43.N_f$ r=0,92 SD= 30,47 (3)

SD= Standart Deviation

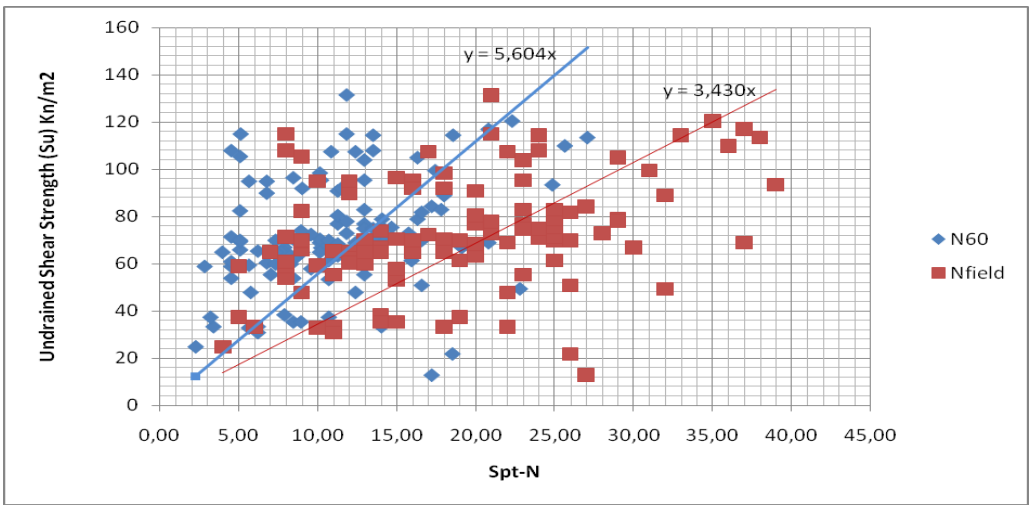

Figure 1. For this study , relationsips between SPT-N value and undrained shear strength of fine-grained soils

İn the second phase the parameter of natural water content (w_n) and plasticity index (PI) considered as independent effective parameters, in addition to N (SPT) content. The correlations Eq.(4,5) were develop using multi linear regression between indepented parameters (SPT-N_f,N_{60},w_n ,PI) and Su .

$S_u= 1,54.N_{60}+0,52. w_n+2,93. PI$ r=0,94 SD=26,7 (4)

$S_u= 3,47.N_f+0,06.w_n-0,18.PI$ r=0,98 SD=6,12 (5)

With regression analysis of data revealed that relationships in the second phase have beter correlation than first phase. (first phase: r = 0.92 and r = 0.90 for correlations based on N_{field} and N_{60} respectively, second phase: r = 0.94 and r = 0.98 for correlations based on N_{field} and N_{60} respectively that r is correlation coefficient).

Correlations suggested in earlier research done on this topic and Su values obtained in the correlation suggested in this study results are given in Figure 2.

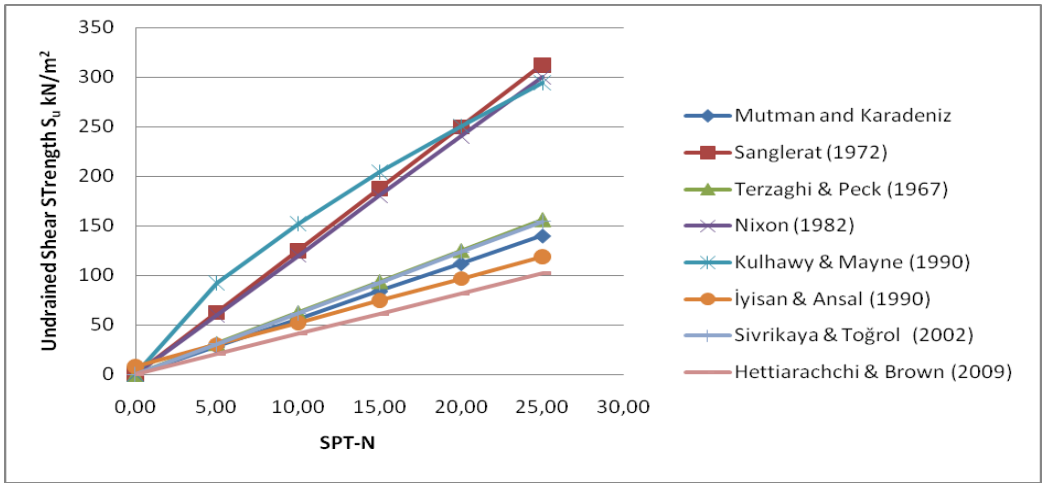

Figure 2. The comparison of the correlation, used in the study and Mutman and Karadeniz Eq.(2)

Compared to previous correlations, correlations presented by Sirvikaya (2009), Terzaghi & Peck (1967) and İyisan & Ansal (1990) had conformity with present proposed correlations but correlation presented by Saglerat(1972) , Nixon (1982), Kulhawy & Mayne (1990) had relatively large differences[2,4,11,12]. These differences could have been caused by soil physical as well as mechanical properties of each region.

3. CONCLUSION

In the present study , between SPT-N and undrained shear strength for fine -grained soils correlations were obtained. Compared first phase and second phase result showed that considering other parameters such as water content (w_n)and plasticity index (PI) in addition to SPT-N, increase the correlation coefficient of estimation. In order to obtain more realistic cohesion value with the N_{60} value, the use of natural water content and plasticity index is required for Kocaeli /Turkey. Soil properties and the tools used in the test , they differ from region to region.Therefore, for different regions, when predicting soil parameter we must chose specific correlations that used in area or near.

REFERENCES

[1]. Cubrinovski, M. and Ishihara, K., Empirical correlation between SPT N-value and relative density for sandy soils, *Soils and Foundations*, 39(5): 61-71, 1999.
[2]. Erol,A. O. and Çekinmez, Z., Geoteknik Mühendisliğinde Saha Deneyleri, *Yüksel Proje Yayınları No: 14 - 01*,2014.
[3]. Sanglerat, G, The Penetrometer and Soil Exploration, *Elsevier Publishing Co.*, Amsterdam, 1972.
[4]. Terzaghi, K. and Peck, R.B., Soil Mechanics in Engineering Practice, *John Wiley*, New York, 1967.
[5]. Durgunoğlu, H.T. and Toğrol, E., Penetration testing in Turkey: State-of-the-art report, Proceedings of the European Symposium on Penetration Testing, Stockholm, Sweden, p. 137, June 1974.
[6]. Sivrikaya, O., Toğrol, E., Türkiye'de SPT-N Değeri ile İnce Daneli Zeminlerin Drenajsız Kayma Mukavemeti arasındaki İlişkiler, *İMO Teknik Dergi,* 4229 -4246, 2007.
[7]. McGregor, J.A. and Duncan, J.M., Performance and use of the standard penetration test in geotechnical engineering practice, *A Report of a study performed by Virginia Tech Center for Geotechnical Practice and Research*, Virginia Polytechnic Institute and State University, October 1998.
[8]. Farrar, J.A. and Chitwood, D., CME Automotic Hammer Operations, *U.S. Department of the Interior Bureau of Reclamation Earth Sciences and Research Laboratory, Dam Safety Office*, DSO-99-03, November 1999
[9]. Decourt, L, The Standard Penetration Test: State-of-the-Art-Report, *Norwegian Geotechnical Institute Publication*, 179, Oslo, Norway, 1990
[10]. Sivrikaya, O., Toğrol, E., Relations between SPT-N and q_u, *5th International Congress on Advances in Civil Engineering*, p. 943-952, Istanbul, Turkey, 2002.
[11]. Nixon, I.K., Standard penetration test: State-of-the-art report, *Proceedings of the 2nd Europen Symposium on Penetration Testing*, Amsterdam, Netherlands, 3-21, May 1982.
[12]. Kulhawy, F.H. and Mayne, P.W., Manual on estimating soil properties for foundation design, *Electric Power Institute*, Palo Alto, CA,

BIOGRAPHY

Name Surname: Murat Karadeniz Place and Date of Birth: 25.07.1986/ Trabzon

E-Mail: karadenizmurat61@gmail.com

EDUCATION: B.Sc.: 2010, Karadeniz Technical University, Civil Engineering Department

M.Sc: 2015, Kocaeli University, Institute of Natural Science of Civil Engineering Department

PROFESSIONAL EXPERIENCE: 2010~2012 : Civil Engineer of Eksı Group of Companies

2012 Research Assistant at Kocaeli University

ICENS
INTERNATIONAL CONFERENCE ON ENGINEERING AND NATURAL SCIENCES
24-28 May 2016 /Sarajevo

Determination of Heavy Metals in Polypropylene Materials Used in Food Packaging by WDXRF Spectrometer

Gokce Borand[1], Faruk Demir[2]

Abstract

Plastics used in food packaging include many additives that could result in changing some properties such as physical, chemical and mechanical. It affects the quality of the product, human health and the environment. Considering this situation, there are some legislations and regulations developed in the U.S. and the European Union about food contact materials like food packaging. Also in Turkey, certain additives must be determined according to the Turkish Food Codex and notification of Plastic Stuff and Materials that is contact to food. These materials are analyzed using spectroscopic methods such as AAS, ICP-AES, ICP-MS. Unlike these spectroscopic methods, X-ray fluorescence spectrometry is also widely used in different industries; since it is a quick, non-destructive, sensitive and an easy method. Among XRF methods, Wavelength Dispersive X-ray fluorescence spectrometry is being preferred for industrial applications due to its analytical assessment and sensitivity. These spectrometers provide analysis in ppm levels for determination of concentration. In this study; polypropylene bulk materials from some different food sectors which are mostly used in food packaging were examined via semi-quantitative analysis used in WDXRF. Detected some heavy metals in these materials were compared with certain additives which are determined the Turkish Food Codex and notification of Plastic Stuff and Materials that is contact to food. In this way, using of WDXRF spectrometry methods will be developed to determine metal additives in plastic food packaging industry.

Keywords: Food Contact Polymer Materials, Food Packaging, Migration, Plastic Additives, Polypropylene (PP), WDXRF.

1. INTRODUCTION

Food packaging is an industrial material product which stores the product it contains, keeps and protects from external influences until the consumer from the first stage of the process. Metal, plastic, paper, glass and wooden are main groups of materials used for food packaging. Plastics are the most common materials used in the food packaging. These plastics are following: Polyethylene (PE), polypropylene (PP), polystyrene (PS), polyvinyl chloride (PVC), polycarbonate (PC), ethylene vinyl acetate (EVA), polyvinylidene chloride (PVdC), styrene butadiene (SB), acrylonitrile butadiene styrene (ABS), ethylene vinyl alcohol (EVOH), polymethyl pentene (TPX), polyvinyl acetate (PVA), polyamide (PA) and polyvinyl alcohol (PVOH).

Migration is the transfer of substances originally present in the plastic material into a packaged product. The compounds that transfer are called migrants. Examples of migrants include residual monomers, solvents, residual catalysts, and polymer additives [1]. According to that metal additive are also used to change physical, chemical and mechanic properties of plastic materials contacting with food. The concentration of these metals within plastic matrix must be determined according to the Turkish Food Codex and notification of Plastic Stuff and Materials contacting with food and beverages. Analysis of these metals is conducted using spectroscopic methods which are slower and more costly in comparison with X-ray fluorescence (XRF) spectrometry. XRF spectrometry is widely used in analysis of metals, since it is a quick, non-destructive, sensitive and an easy method. Among XRF methods, Wavelength Dispersive X-ray fluorescence (WDXRF) spectrometer is being preferred for industrial applications due to its analytical assessment and sensitivity. These spectrometers provide analysis in ppm levels for determination of concentration. In recent years, producers of these spectrometers have been trying to determine accurate concentration values by developing software that provide semi-quantitative analysis using fundamental parameter methods. These analyses can only give accurate results when quantitative analysis is applied by using reference materials (standard

[1] *Bursa Technical University, Institute of Science, Material Science and Engineering, gborand@gmail.com*

[2] *Correspondig author: Bursa Technical University, Natural Sciences, Architecture and Engineering Faculty, Metallurgy and Materials Engineering, 16190 Bursa, Turkey farukdemir1977@hotmail.com.tr*

methods). For these spectrometers, reference materials belonging to various field of industry are produced by international research centers.

In this study; polypropylene bulk materials from some different food sectors which are mostly used in food packaging were examined via semi-quantitative analysis used in WDXRF. Detected some heavy metals in these materials were compared with certain additives which are determined the Turkish Food Codex and notification of Plastic Stuff and Materials that is contact to food. In this way, using of WDXRF spectrometry methods will be developed to determine metal additives in plastic food packaging industry. Adaptation of X-ray fluorescence spectroscopy in food industry and ensuring economic contribution in this filed are aimed. In the next study, reference material will be preparation by using standard addition method with WDXRF spectrometer for quantization of certain metals in plastic materials contacting food such as packaging.

2. EXPERIMENTAL PROCEDURE

2.1. Sample Preparation

Polypropylene food packaging materials were obtained from different sectors. The samples were cut for sample holder that belongs to WDXRF.

2.2. Measurements

Each sample was placed in sample holder. Semi-quantitative (SQX) analysis carried out by using WDXRF. SQX is a qualitative analysis that carries out quantification to some extent. Rigaku has improved their semi-quantitative software package further with the introduction of SQX [2]. It usually gives analyte concentration as derived from intensities measured with speed and convenience, rather than precision, as primary objectives and from standards applicable to a variety of related sample types [3].

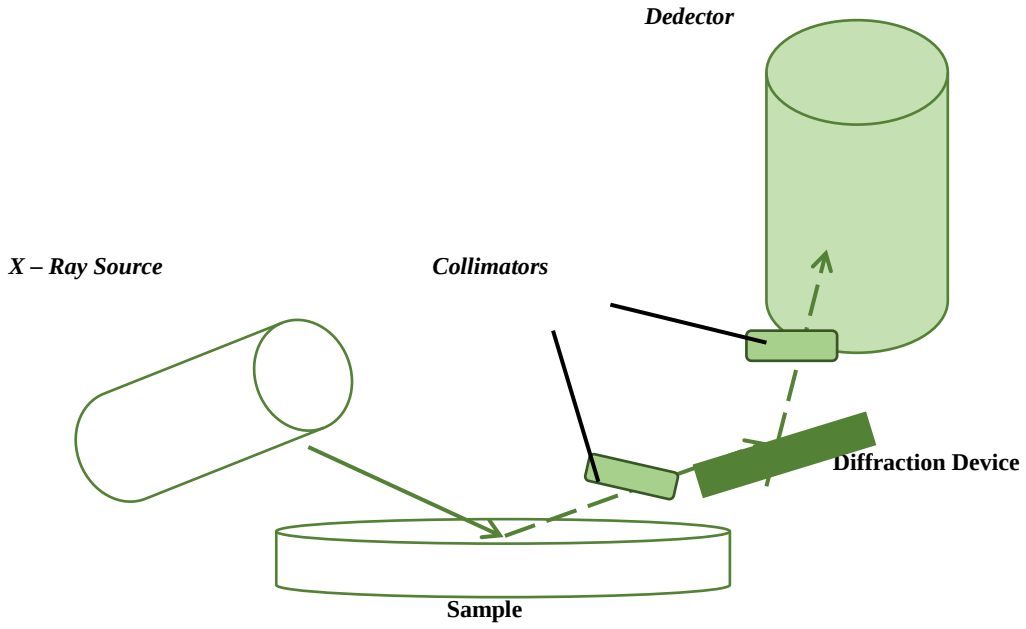

Figure 1: Basic Principle of WDXRF

Wavelength Dispersive X-ray Fluorescence (WDXRF) is one of two general types of X-ray Fluorescence spectrometer. *Figure 1* shows basic principle of WDXRF. Heavy metals in food packaging were determined in 30 mm diameter with using Pd target. Total measuring time for each sample is 26 minute. The X-ray tube was operated at 50 kV and 40mA. PP was selected balance element to determine heavy metals in food packaging accurately. Vanadium, chromium, iron, nickel, copper, arsenic, zinc, zircon, cadmium, antimony, barium, hafnium, mercury, lead from heavy metals were particularly selected due to the Turkish Food Codex and notification of Plastic Stuff and Materials that is contact to food in the software for WDXRF.

3. RESULTS and DISCUSSIONS

SQX results of polypropylene food packaging materials belong to sector 1 were shown in *Table 1*. These results were obtained from multiple analyses of packaging materials. So, average and standard deviation were calculated for these materials. Na, Al, Si, P, S, Cl, K, Ca are allowed to use as metal or metallic additives for plastic stuff. They are not problem for this study. The concentration of Fe in food plastic packaging must be 48 mg/kg for the Turkish Food Codex and notification of Plastic Stuff and Materials that is contact to food. This concentration for this sector can be ignored due to results.

Table 1. SQX Results of Polypropylene Food Packaging Materials belong to sector 1

Element	Sample 1 Average (%)	Sample 1 Std. Dev.	Sample 2 Average (%)	Sample 2 Std. Dev.	Sample 3 Average (%)	Sample 3 Std. Dev.	Sample 4 Average (%)	Sample 4 Std. Dev.
Na	0.0355	0	0.0357	0.0020	0.0102	0.0006	-	-
Al	0.0064	0.0013	0.0068	0.0006	0.0068	0.0006	0.0088	0.0004
Si	0.0034	0.0009	0.0024	0.0004	0.0019	0.0003	0.0020	-
P	0.0033	0.0001	0.0038	0.0001	0.0035	0.0005	0.0035	0.0001
S	0.0134	0.0030	0.0063	0.0029	0.0055	0.0036	0.0052	0.0032
Cl	0.0062	0.0001	0.0052	0	0.0029	0.0003	0.0030	0.0004
K	0.0150	0.0020	0.0175	0.0010	0.0152	0.0010	0.0162	0.0001
Ca	0.0045	0.0009	0.0046	0.0013	0.0050	0.0001	0.0050	0.0011
Fe	0.0027	0	0.0022	0	0.0029	-	0.0026	0.0006
PP (Balance)	99.9070	0.0056	99.915	0.0021	99.9470	0.0042	99.950	0

Table 2 shows SQX results of polypropylene food packaging materials belong to sector 2. In the same way; Na, Mg, Al, Si, P, S, Cl, K, Ca, Ti are allowed to use as metal or metallic additives for plastic stuff. They are not problem for this study. However, unlike the first sector, Ti element has been observed. It is considered to this element is used as a additive from colorants. The concentration of Fe for this sector can be ignored due to results.

Table 2. SQX Results of Polypropylene Food Packaging Materials belong to sector 2

Element	Sample 1 Average (%)	Sample 1 Std. Dev.	Sample 2 Average (%)	Sample 2 Std. Dev.	Sample 3 Average (%)	Sample 3 Std. Dev.	Sample 4 Average (%)	Sample 4 Std. Dev.
Na	0.0210	0.0031	0.0230	0.0082	0.0256	0.0004	0.0692	0.0861
Mg	0.1591	0.0071	0.1586	0.0012	0.1364	0.0056	0.1422	0.1006
Al	0.0196	0.0021	0.0188	0.0011	0.0179	0.0014	0.0154	0.0018
Si	0.1924	0.0024	0.1880	0.0061	0.1855	0.0063	0.1889	0.0009
P	0.0059	0.0009	0.0059	0.0005	0.0056	0.0001	0.0051	0.0001
S	0.0048	0.0021	0.0064	0.0026	0.0049	0.0026	0.0052	0.0023
Cl	0.0036	0.0001	0.0049	0.0001	0.0043	0	0.0027	0.0004
K	0.0153	0	0.0157	0.0003	0.0173	0.0010	0.0161	0.0023
Ca	0.3532	0.0006	0.3741	0.0047	0.3293	0.0049	0.3080	0.0002
Ti	0.3624	0.0067	0.3861	0.0163	0.3098	0.0004	0.2907	0.0064
Fe	0.0048	0.0006	0.0048	0.0004	0.0051	0.0009	0.0043	0.0006
PP (Balance)	98.8570	0.0127	98.8020	0.0537	98.9580	0.0035	99.0210	0.0240

Table 3 and *Table 4* show SQX results of polypropylene food packaging materials belong to sector 3 and sector 4, respectively. In the same way, allowable metals were present in these food plastic packaging.

Table 3. SQX Results of Polypropylene Food Packaging Materials belong to sector 3

Element	Sample 1 Average (%)	Sample 1 Std. Dev.	Sample 2 Average (%)	Sample 2 Std. Dev.	Sample 3 Average (%)	Sample 3 Std. Dev.	Sample 4 Average (%)	Sample 4 Std. Dev.
Na	0.0120	0.0085	0.0076	0.0054	0.0190	0.0024	0.0132	0.0093
Mg	0.0118	0.0004	0.0116	0.0004	0.0133	0.0031	0.0145	0.0015
Al	0.0144	0.0021	0.0140	0.0006	0.0142	0.0004	0.0136	0.0008
Si	0.0153	0.0002	0.0156	0	0.0175	0.0004	0.0162	0.0013
P	0.0048	0.0001	0.0041	0.0003	0.0047	0	0.0037	0.0004
S	0.0036	0.0018	0.0026	0.0009	0.0027	0.0014	0.0030	0.0016
Cl	0.0046	0.0006	0.0037	0	0.0040	0.0003	0.0037	0.0001
K	0.0137	0.0015	0.0157	0.0008	0.0155	0.0011	0.0155	0.0011
Ca	0.6111	0.0010	0.6012	0.0034	0.5814	0.0035	0.5792	0.0066
Ti	0.7105	0.0030	0.7024	0.0058	0.6871	0.0012	0.6644	0.0124
PP (Balance)	98.6050	0.0035	98.6240	0.0070	98.6410	0.0014	98.6800	0.0148

Table 4. SQX Results of Polypropylene Food Packaging Materials belong to sector 4

Element	Sample 1 Average (%)	Sample 1 Std. Dev.	Sample 2 Average (%)	Sample 2 Std. Dev.	Sample 3 Average (%)	Sample 3 Std. Dev.	Sample 4 Average (%)	Sample 4 Std. Dev.
Na	0.0191	0.0045	0.0132	0.0021	0.0212	0.0055	0.0229	0.0014
Al	0.0042	0.0016	0.0046	0.0008	0.0053	0.0013	0.0056	0.0011
Si	0.0034	0.0024	0.0030	0.0003	0.0028	0.0020	0.0032	0.0007
P	0.0039	0.0009	0.0038	0.0006	0.0041	0.0003	0.0035	0.0001
S	0.0037	0.0026	0.0026	0.0009	0.0027	0.0012	0.0029	0.0010
Cl	0.0032	0.0006	0.0028	0.0001	0.0032	0.0001	0.0043	0.0001
K	0.0175	0.0002	0.0149	0.0021	0.0142	0.0001	0.0160	0.0007
Ca	0.0032	0.0003	0.0036	0	0.0029	0.0020	0.0034	0.0010
PP (Balance)	99.9430	0.0007	99.0230	0.0029	99.9450	0.0049	99.9350	0.0021

SQX results of polypropylene food packaging materials belong to sector 5 was shown in *Table 5.* This sector was shown different results compared with other four sectors, Zn element was obtained from the results. The concentration of Zn in food plastic packaging must be 25 mg/kg for the Turkish Food Codex and notification of Plastic Stuff and Materials that is contact to food. It was observed that limit has been exceeded for this sector due to the results. This result is an important point for the sensitivity of these spectrometers. *Figure 2* shows a graph with well-defined sharp lines for zinc element peaks at $2\theta \approx 42°$ in this sector.

Table 5. SQX Results of Polypropylene Food Packaging Materials belong to sector 5

Element	Sample 1 Average (%)	Sample 1 Std. Dev.	Sample 2 Average (%)	Sample 2 Std. Dev.	Sample 3 Average (%)	Sample 3 Std. Dev.	Sample 4 Average (%)	Sample 4 Std. Dev.
Na	0.0334	0.0033	0.0199	0.0141	0.0190	0.0134	0.0239	0.0129
Mg	0.0404	0.0026	0.0359	0.0007	0.0476	0.0033	0.0443	0.0002
Al	0.0219	0.0002	0.0196	0.0014	0.0149	0.0006	0.0126	0.0012
Si	0.0427	0.0035	0.0415	0.0009	0.0158	0.0010	0.0163	0.0003
P	0.0101	0.0010	0.0104	0.0008	0.0085	0.0006	0.0089	0.0013
S	0.0055	0.0024	0.0044	0.0013	0.0040	0.0011	0.0038	0.0010
Cl	0.0064	0.0010	0.0057	0.0001	0.0060	0.0003	0.0058	0.0002
K	0.0142	0.0013	0.0137	0.0017	0.0144	0.0008	0.0119	0.0001
Ca	7.1555	0.9878	7.1599	0.1301	6.9185	0.6534	7.0694	0.2885
Ti	0.7692	0.0310	0.7295	0.0344	0.5132	0.0204	0.5616	0.0051
Zn	0.0278	0.0005	0.0295	0.0001	0.0350	0.0010	0.0383	0.0021
PP (Balance)	91.8620	0.0021	91.9400	0.0014	92.4100	0.0339	92.1930	0.0509

Calcium element is present for all samples. This element may be come from reinforcement and filler materials as additive for polypropylene food packaging. However the concentration of the calcium element increased for sector 5. The presence of zinc may be affecting this concentration. Calcium may be used to avoid the use of excessive zinc.

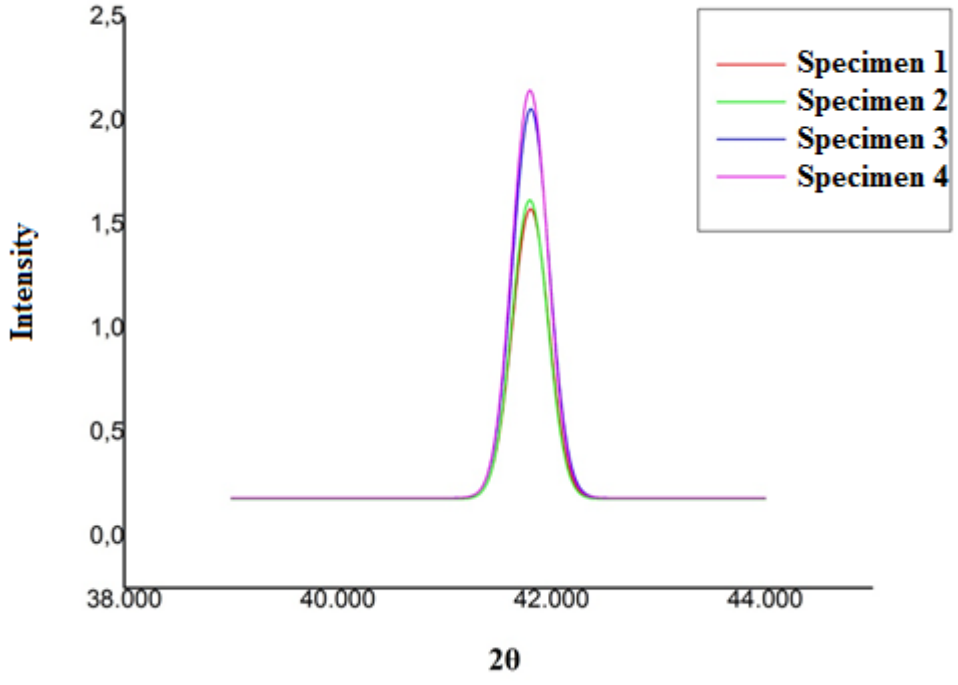

Figure 2. Graph of Zinc Element Peaks in Polypropylene Food Packaging belongs to sector 5

4. CONCLUSIONS

In recent years, producers of these spectrometers have been trying to determine accurate concentration values by developing software that provide semi-quantitative analysis using fundamental parameter methods. These analyses can only give accurate results when quantitative analysis is applied by using reference materials. For these spectrometers, reference materials belonging to various field of industry are produced by international research centers. There is no prepared reference material in the World in the field of food industry and in any fields in Turkey. In this study, polypropylene is the most commonly used plastic food contact materials was examined via WDXRF (SQX Software) so heavy metals from additives were determined. So that, quantitative analysis methods developed in WDXRF will be a preparatory study to produce of polymer standard materials for food packaging.

ACKNOWLEDGMENT

The authors would like to acknowledge Bursa Technical University through the grant 2015-02-001 for financial supports.

REFERENCES

[1]. Susan E.M. Selke, John D. Culter and Ruben J. Hernandez, *Plastics Packaging, Properties, Processing, Applications, & Regulations*, 3rd ed., Carl Hanser Verlag, Munich 2015.
[2]. R. Dumlupinar, F. Demir, T. Sisman, G. Budak, A. Karabulut, Ö.K. Erman and E. Baydas, *Trace element changes during hibernation of Drosophila melanogaster by WDXRF analyses at chilling temperature*, J. Quant. Spectrosc. Radiat. Transfer, 102, 492 (2006).
[3]. Eugene P. Bertin, *Principles and Practice of X-Ray Spectrometric Analysis*, 2nd ed.,New York-London, 1975.

ICENS
INTERNATIONAL CONFERENCE ON ENGINEERING AND NATURAL SCIENCES
24-28 May 2016 /Sarajevo

Reduction of Waves Magnitudes by Offshore Submerged Breakwater in Akyazi Sport Complex Area, Turkey

Fatih Saka[1], Osman Kara[2], Emrah Kaplan[3], Onur Bulut[1]

ABSTRACT

A shore is a place where sea and land across each other and the land is affected by the sea waves. Shores are important for many aspects including, economical, political, and cultural sides. Spoiled, unregulated, messy or unsteady shores are neither valuable nor protecting against damages from waves. Shore protection constructions are built up to protect beaches and lands behind them from the destructive effects of waves.

In this study, the shore protection subject of Akyazı Sport Complex, Trabzon, Turkey was studied. The experiments were performed on a model system to establish a breakwater type to get a more reductive effect on wave magnitudes. For this purpose, four offshore submerged breakwater models in different sizes were experimentally tested. The breakwaters were filled with sand in varying diameters (10 cm,7,6 and 5 cm) and located 6.5 cm away from the breakwater. After the implementation, the damages and wave climbings on breakwater, and wave breaking points were determined. The experimental results obtained before and after the submerged breakwater constructions with varying diameters were compered.

Results showed the breakwater with 10 cm diameter caused 0.6 m of reduction on wave climbing. Moreover, the wave was broken at a 7.5 cm farther location from the breakwater, comparing to the no breakwater setup. Overall results proved that, the submerged breakwaters, can reduce the wave magnitudes and cause a more effective protection. Therefore, the required size and amount of the rocks used for inshore construction can be reduced which also makes the construction more cost effective.

Keywords: *Shore protection, reduction of wave magnitudes, mitigation.*

1. INTRODUCTION

It is called shore that the place where sea and land across each other and the land is affected by sea waves. The beach and nearshore zone of a coast is the region where the forces of the sea react against the land. The physical system within this region is composed primarily of the motion of the sea, which supplies energy, and the shore, which absorbs this energy [1]. Wave energy is a concern for any structure placed in the coastal zone. Uncontrolled wave forces can damage piers and roads, cause operational problems in harbors, and erode coastal lands and recreational beaches [2]. There are many considerations when designing a project for reducing the offshore wave heights. The primary concern must be to provide a functional design that reduces the wave climate to acceptable levels [3]. Coastal engineers have commonly relied on breakwaters, seawalls, groins, and recreation applications to mitigate wave-induced problems.

Conventional offshore rubblemound breakwaters are commonly used to provide sheltered areas and they do an excellent job of reducing wave heights [3]. Offshore submerged breakwater applications can also provide another potential tool for protecting the coastal zone. These breakwaters are not piercing surface thus maintaining natural appearance and also allow aquatic life to bypass the structure relatively unimpeded.

It was investigated in this research that the reduction of wave magnitudes, and so the onshore structures built for the Akyazı Sport Complex area, Trabzon, Turkey, can protect more effectively. For this purpose, four offshore submerged breakwater models were experimentally tested. Breakwaters in the experiments are cylindirical and have different diameters (10 cm,7,6 and 5 cm). They were filled with sand and located 6.5 cm away from the breakwater. After the implementation, the damages and wave climbings on breakwater, and wave breaking points were determined. The experimental results obtained before and after the submerged breakwater constructions with varying diameters were compered.

1 Corresponding author: Gümüşhane University, Department of Civil Engineering, 29000, Merkez/Gümüşhane, Turkey. sakafatih@hotmail.com

[2] Gümüşhane University, Department of Civil Engineering, 29000, Merkez/Gümüşhane, Turkey. drosmankara@yandex.com.tr

3 Gümüşhane University, Department of Electrical Electronic Engineering, 29000, Merkez/Gümüşhane, Turkey. ekaplan@gumushane.edu.tr

2. MATERIAL AND METHOD

Akyazı Spor Complex located in Trabzon, a city of northeast Turkey on the Black Sea, is currently under construction and major social, cultural and economic dignity for the people of the region (Figure 1). Akyazı Stadium is expected to open to public in August 2016 and will have a capacity of 41,513 spectators. It will be the new home of Trabzonspor of the Süper Lig. It will replace the club's current home, Hüseyin Avni Aker Stadium [4].

Figure 1. Gross construction area of the Akyazi Spor Complex and the Akyazı Stadium viewing [4;5]

Akyazı Sport Complex was planned on filling area and designed as rubblemond breakwater with 1/5 slope. 6-10 tons of rocks were used at this part. Waves in the East Black Sea Region were found between 4.00-6.55 m for 10 year recurrence intervals, between 4.65-7.75 m for 25 year recurrence intervals, and between 5.15-8.60 m for 50 year recurrence intervals after researches. Wave magnitudes were found as in Table 1 below for a site which is around the project area.

Table 1. Significant wave heights and periods for various recurrence intervals at the site around the project area

Recurrence Interval (Year)	Synoptic Map		Weather Station	
	H1/3 (m)	T1/3 (sn)	H1/3 (m)	T1/3 (sn)
10	5.80	9.57	2.90	6.83
20	6.80	10.36	3.68	7.69
30	7.69	11.02	3.90	7.92

Experiments of model having two dimensions were conducted to provide for keeping balance of breakwater. This model experiments were fitted with the theory of Froude Model. Model scale was chosen 1/45 for experiments for the shoreline of the Akyazı Sport Complex. While chosing that, properties of experimental channel and machine generating wave were corresponded. Four models with different submerged breakwater's diameters have been prepared like looking cross section in Figure 2. Then experiments have done and results have taken.

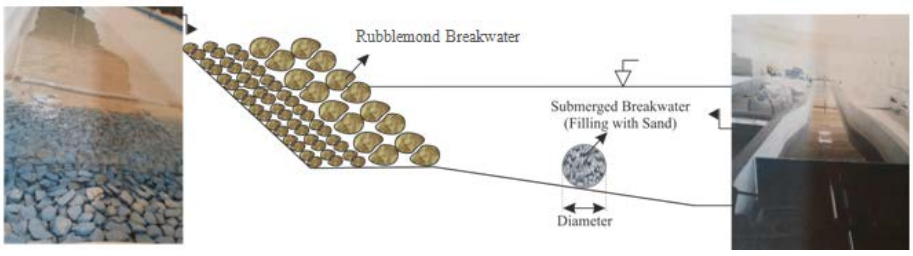

Figure 2. Cross section of models and channel viewings from two sides

3. RESULTS

Four different offshore submerged breakwater models were performed in different sizes and taken results of them. The textiles of the breakwater models were filled with sand in varying diameters (10,7,6 and 5 cm) and located 6.5 cm away from the breakwater. 10-yr recurrence interval waves implemented to the models and the damages, wave

climbings on breakwater, and wave breaking points on each model were determined. After implemented, damages on the experimental breakwater, wave climbing and breaking point were obtained for every model (Table 2, Table 3).

Table 2. Damages on breakwater, wave climbing and breaking point data after implemented models in experiment scale

	Diameters (cm)	Damages on breakwater	Wave climbing (from SWL) (cm)	Breaking point (from breakwater) (cm)
Model 1	10	None	3.2	32
Model 2	7	None	3.4	35
Model 3	6.5	None	3.45	36
Model 4	5	None	3.5	37

Table 3. Wave climbing and breaking point data after implemented models in real scale

	Diameters (m)	Wave climbing (from SWL) (m)	Breaking point (from breakwater) (m)
Model 1	4.5	1.44	14.4
Model 2	3.15	1.53	15.75
Model 3	2.93	1.55	16.2
Model 4	2.25	1.58	16.65

4. CONCLUSIONS

In Model 1, offshore submerged breakwater provides that wave climbing was reduced 0.6 m for breakwater point with using 4.5 m diameter, also wave was broken 3.38 m farther than before in real scale.

It has achieved using sand filled offshore breakwater can reduce wave magnitudes and strengthen resistance. So it has chosen less size of rocks and amount than without offshore breakwater.

Submerged breakwater conceptual designs of different sizes were also found to be successful at reducing the overall wave heights.

Submerged breakwaters should be researched deeper to provide more information to know their capabilities and deficiencies.

ACKNOWLEDGMENT

We also thank academicians of the Hydraulic Laboratory of the KTU-Department of Civil Engineering for assistance.

REFERENCES

[1]. US Army Coastal Engineering Research Center, *Shore Protection Manual Vol. II*, 1984.
[2]. Foley, “Submerged Breakwater Modeling and Coral Reef Ecological Analyses for Harbor Protection,” PhD thesis, Department of Civil Engineering, University of Hawaii at Manoa, 2015.
[3]. Knox, “Examination of the Performance of a Longitudinal Submerged Breakwater System,” M. Eng. thesis, Department of Civil Engineering, Queen's University, Canada, 2001.
[4]. (2016) Akyazi Stadium website. [Online]. Available: http://akyazistadi.com
[5]. Google Inc. 2015. Google Earth (Version 6.0.0.1735) [Software].

ICENS
INTERNATIONAL CONFERENCE ON ENGINEERING AND NATURAL SCIENCES
24-28 May 2016 /Sarajevo

Synthesis, Characterization and Thermal Decomposition Kinetics of ABC Triblock Copolymer Synthesized by ROP and ATRP

Gulben Torgut[1], Kadir Demirelli[2]

Abstract

In this study to examine thermal degradation mechanism and kinetic parameters of the poly(1,2-epoxy-3-phenoxy propane-b-ε-caprolactone-b-benzyl methacrylate), poly(PEPP-b-Pε-CL-b-PBMA) triblock copolymer synthesized by ring opening polymerization (ROP) and atom transfer radical polymerization (ATRP). ABC type block copolymer was characterized by FT-IR, ^{1}H-NMR. Thermogravimetric analysis (TGA) was used at different heating rates. Polymer was heated from room temperature to 500^{o}C with heating rate of 5, 10, 20, 30, 40 ^{o}C/min^{-1} under a nitrogen atmosphere. TGA curves showed that the thermal decomposition occurred in one stage. The activation energies (E_a) of thermal decomposition were determined using the method of Kissinger's, Flynn–Wall–Ozawa and Tang which does not require knowledge of the reaction mechanism at different conversions. Average E_a values for ABC polymer were calculated 196.36 Kj/mol, 193.65 Kj/mol and 194.90 Kj/mol, respectively.
Keywords: *ATRP, ABC triblock copolymer, ε-caprolactone, ring opening polymerization*

1. INTRODUCTION

ABC type block copolymers can be synthesized by combining the ''living''/controlled polymerization techniques such as ATRP and ROP [1]. Aliphatic polyesters, such as poly(ε-caprolactone) (PCL), polylactide (PLA) and polyglycolide (PGA), are a group of which synthesized by ATRP and ROP. Among these aliphatic polyesters, PCL has been widely used as poor hydrophilic block in amphiphilic ABC triblock copolymers, owing to its striking properties, such as, crystallizability, biodegradable, biocompatibility permeability and good mechanical properties [2]- [4]. But low melting temperature (Tm) and slow degradation rate severely limit its application [5]. Various catalysts such as oxides, carboxylates, and alkoxides have been used for the synthesis of polyesters by ROP [6]. For hydroxyl-end group-containing compounds used as initiators in the synthesis, tin(II) 2-ethylhexanoate ($SnOct_2$) is the most extensively used catalyst [7], [8]. $SnOct_2$ is commercially available, and can produce polymers in high yield with controlled molecular weight and narrow distribution.

Thermogravimetric analysis (TGA) has been used to investigate the thermal stability characteristic of many substances, including polymers. Numerous investigations can be used to determine thermal behavior, kinetic and thermodynamic parameters of many polymeric materials using different thermogravimetric methods at different heating rates in nitrogen. The kinetic parameters of degradation processes, such as the rate constants, activation energies, reaction orders, and Arrhenius pre-exponential factors, can be assessed from thermograms [8]- [11].

In this article, to synthesize of well defined triblock copolymer, ROP and ATRP have been used. The activation energies related to the decomposition kinetics of a ABC block copolymers characterizationed FT-IR and ^{1}H-NMR were calculated using the Kissinger, Flynn–Wall–Ozawa and Tang methods under an N_2 dynamic atmosphere and at different heating rates of 5, 10, 20, 30 and 40◦C/min.

[1] *Corresponding author: Tunceli University, [1]Department of Chemistry and Chemical processes,Tunceli Vocation School, 62100, Tunceli, Turkey.* gtorgut@tunceli.edu.tr

[2] *Kadir Demirelli, Department of Chemistry, Faculty of Science, Elazığ, Turkey,* kdemirelli@firat.edu.tr

2. EXPERIMENTAL

2.1 Synthesis of ABC polymer

In first step poly(1,2-epoxy-3-phenoxy propane) (PEPP) homopolymer was synthesized using stannous 2-ethylhexanoate as an initiator and benzyl alcole as a catalyst in ROP. The reaction mixture was heated at 120 ^{o}C for a 48 h. The product was precipiated into cold hexane and dried for 24 h at 40 ^{o}C in vacuum. Scheme 1 is the reaction of ring opening polymerization of 1,2-epoxy-3-phenoxy propane. This homopolymer was used as an initiator for ROP of ε-CL (Scheme 2).

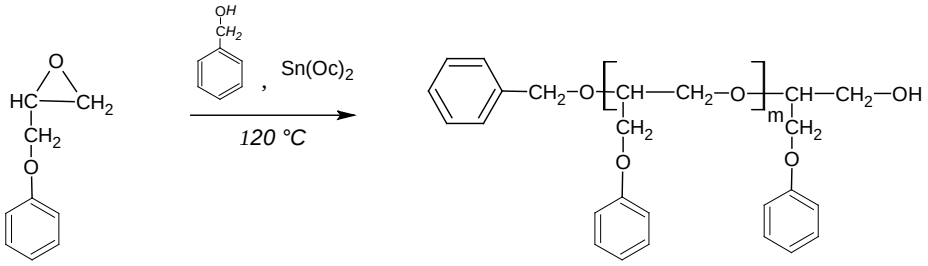

Figure 1: ROP of 1,2-epoxy-3-phenoxy propane

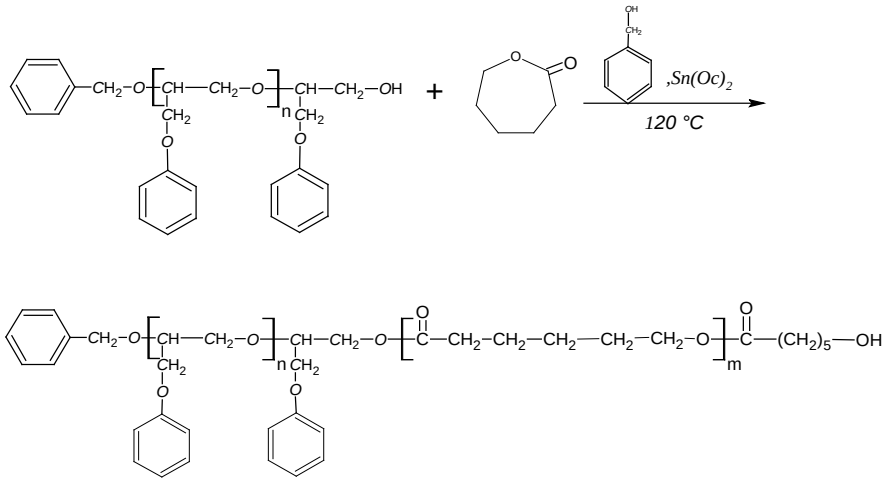

Figure 2. Synthesis of (PEPP-b-Pε-CL) diblock copolymer

To synthesis macroinitiator (PEPP-b-Pε-CL)-Cl for ATRP, (PEPP-b-Pε-CL) diblock copolymer was dissolved in dry THF, triethylamine (NEt_3) (relative of -OH groups) added and stirred 20 min. Then choloroacetyl cloride was dropped under ice bath. After the reaction solution stirred for 5 hours at room temperature the solution was filtated to remove salt and precipiated in cold hexane for dry in vacuum**.** Finally ABC triblock copolymer was synthesized by atom transfer radical polymerization (ATRP). First CuBr and ligand (bpy) were added into a glass tube to compose ATRP complex. The macroinitiator (PEPP-b-Pε-CL)-Cl was dissolved in THF to initiate the polymerization. Then monomer (benzyl methacrylate) was added and sealed after degassed by argon for 10 min and tube was immersed in a preheated oil bath. The polymerization run out at 110 ^{0}C for 24h. The reaction was demonstrated in schme 3.

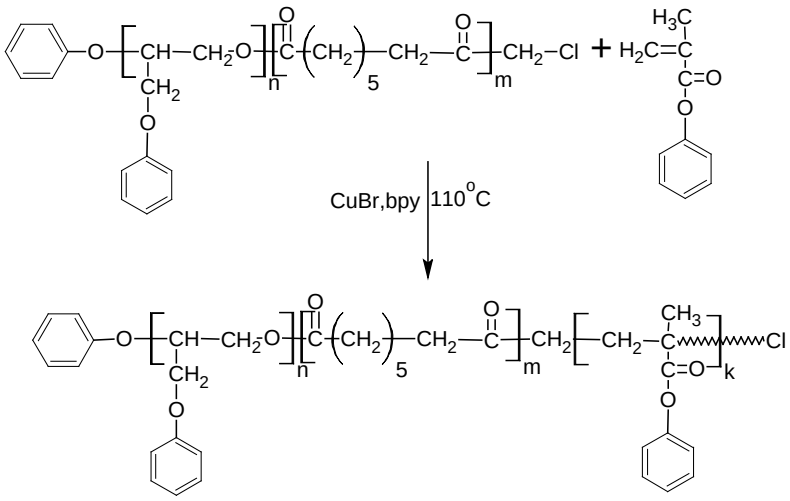

Figure 3. ATRP of BMA with macroinitiator

2.2 Measurements:

Infrared spectra were obtained on Perkin Elmer Spectrum One. Avence III Bruker 400 MHz spectrometer was used for the ^{1}H-NMR with $CDCl_3$ as the solvent and tetramethylsilane (TMS) as internal referance. Termogravimetric analysis (TGA) was realized on an Shimadzu TA-50 insrument in a nitrogen atmosphere. The thermal stability and the decomposition activation energy measurements were run out from room temperature to 500^{o}C with heating rate of 5, 10, 20, 30, and 40^{o}C/ min^{-1}.

2.3 Thermal degradation kinetics

The kinetics methods of thermal degradation are investigated the single heating rate method and the multi-heating rate method. Kissinger, Flynn-Wall-Ozawa (FWO) and Tang method were applied to analyze the kinetic parameters of the copolymers in this work.

2.3 1. Kissinger method

Kissinger method is a technique to the study of thermal degradation behaviors without a precise knowledge of the reaction mechanism [12]. Activation energy values can be calculated high accuracy by Kissinger's using the following equation:

$$ln\frac{\beta}{T_{max}^2} = -\frac{E_a}{RT_{max}} + ln\frac{AR}{E_a} \quad (1)$$

where β is the heating rate, T_{max} is the absolute temperature under the maximum weight loss rate, E_a is the activation energy, A is the pre-exponential factor and R is the universal gas constant. From a plot of $\ln(\beta /T^2_{max})$ versus $1000/T_{max}$ and fitting to a straight line, the activation energy E_a can be calculated from the slope.

2.3.2. Flynn-Wall-Ozawa (FWO) method

This method is a analysis to make a model-free evaluation of the activation energy from a series of non-isothermal measurements carried out at different heating rates [13].

It is used to determine the activation energy for given values of conversion. The equation is as follows:

$$log\beta = log\frac{AE_a}{-Rln(1-\alpha)} - 2.315 - 0.4567\frac{E_a}{RT} \quad (2)$$

2.3.3. Tang method

Tang method are an integral isoconversional method similar to the FWO. The plots of $\ln(\beta/T^{1.894661})$ versus 1/T give a group of straight lines. The activation energy (E_a) can be obtained from the slope $-1.001450\ E_a/R$ of the regression line.

$$\ln\left(\frac{\beta}{T^{1.894661}}\right) = \ln\left(\frac{AE}{Rg(\alpha)}\right) + 3.635041 - 1.894661\ lnE - \frac{1.001450E}{RT} \quad (3)$$

3. RESULTS and DISCUSSION

3.1. Characterization of Polymers

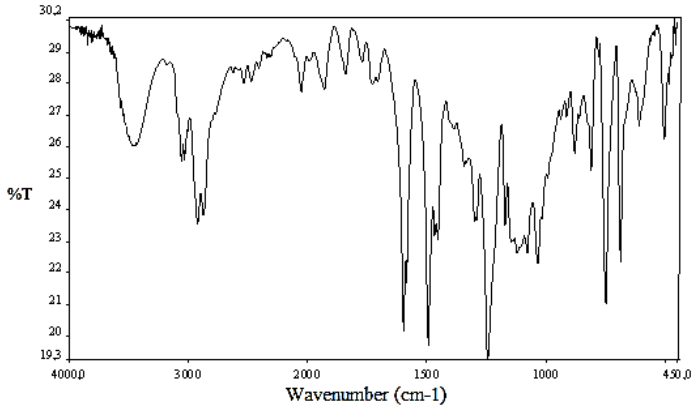

Figure 1. IR spectrum of PEPP

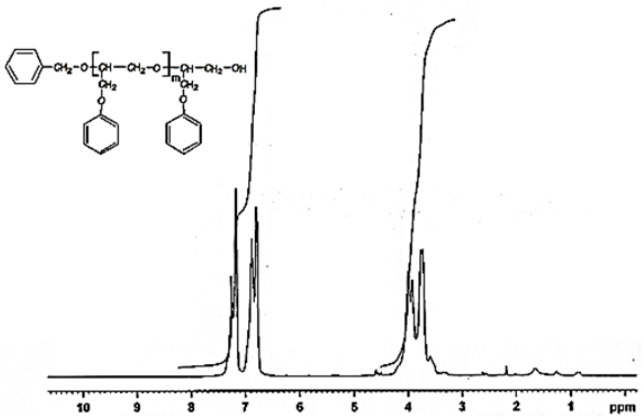

Figure 2. ^{1}H-NMR spectrum of PEPP

The FT-IR spectra (Figure 1.) of PEPP showed that C-H stretching vibration in the methyl and methylene groups at 2876–2927 and aromatic C-H stretching vibration at 3062–3039 cm^{-1}. OH stretching vibration seen at 3465 cm^{-1} proved the ring opening polymerization of the epoxide end group. The ^{1}H-NMR spectra of PEPP illustrated in Figure 2. and showed that 6.79 - 7.34 ppm aromatic ring protons, 4.15 and 3.87 ppm aliphatic CH_2 protons of homopolymer.

PEPP-b-Pε-CL diblock copolymer was synthesized by ring opening polymerization by using PEPP as an initiator. The strong band at 1732 cm^{-1} is the stretching vibration of the carbonyl ester group of ε-CL and 3452 cm^{-1} confirming of –OH group. IR Spectrum of triblock (ABC) copolymer was showed in Figure 3. and the ^{1}H-NMR spectra of ABC copolymer was showed in Figure 4. The peaks at 4.95 ppm reveal the $–COOCH_2$ protons, 2.25 and 1.70 ppm reveal the methylene protons of BMA.

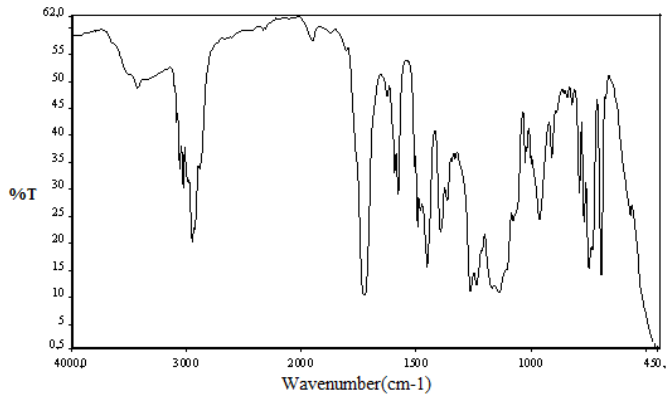

Figure 3. IR spectrum of PEPP-b-Pε-CL-b-PBMA triblock copolymer

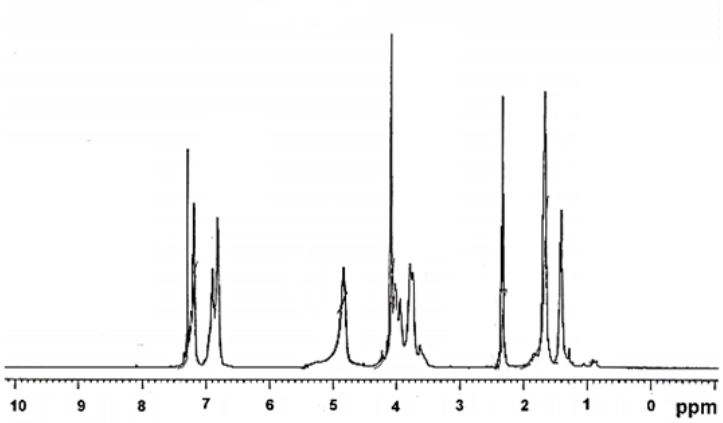

Figure 4. ^{1}H-NMR spectrum of PEPP-b-Pε-CL-b-PBMA

3.2. Kinetics of thermal degradation

The TGA curves of the synthesized ABC block copolymer heated in N_2 at different heating rates 5, 10, 20, 30 and 40°C/min showed in Figure 5. All TG curves of (PEPP-b-Pε-CL-b-PBMA) showed that the thermal decomposition took place in one stage. The initial decomposition temperature (T_i), decomposition temperature at 50% weight loss, the weight loss (%) at 350°C and residual mass at 500°C after complete degradation can be determined from these curves and are shown in Table 1. From the corresponding DTG profiles, it is clear that the decomposition temperature depends on the heating rate. Kissinger plot of (PEPP-b-Pε-CL-b-PBMA) copolymer are shown in Figure 6 and the activation energy was calculated as 196.37 from fitting to a straight line using eq. (1).

Furthermore, the activation energy can be determined using the Flynn–Wall–Ozawa analytic method. It was used to investigate the relationship between Ea and the fractional weight loss. The plots were shown in Figure 7.eq. (2) and E_a were calculated from a linear fitting of log β versus 1000/T at different conversions. This equation was derived using the Doyle approximation, only conversions values in the range 3–18% can be used. For this study, the conversion values 3, 5, 7, 9, 11, 15 and 18% have used. Figure 7. shows that the fitting straight lines are nearly parallel, thus indicating the applicability of this method to (PEPP-b-Pε-CL-b-PBMA) triblock copolymer in the studied conversion range. Also it was observed that the correlation is quite well, and confirms that the fitting of linear and plots are reliable. Table 2 shows that the variation of effective activation energy with fractional conversion for ABC polymer. Avarage E_a value calculated by Flynn–Wall–Ozawa method was found 193.65 kJ/mol. Also it was shown in Table 2 the activation energy corresponding to 7% conversion (193.78 kJ/mol) is very close to the avarage value.

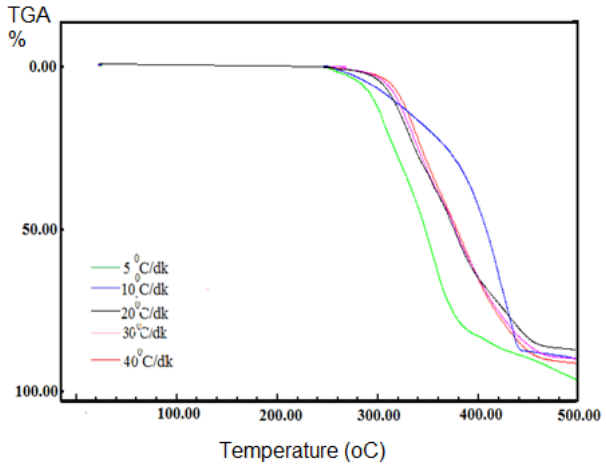

Figure 5. TG curves of PEPP-b-Pε-CL-b-PBMA at different heating rates

Table 1. TGA Data for ABC Copolymer at Different Heating Rates

Reaction rate (^{O}C/min)	$^{a}T_i$ (^{o}C)	$^{b}T_f$(^{o}C)	T%50 (^{o}C)	%Weight loss at 350 ^{o}C	%Residue at 500^{o}C
5	281	500	348	58	5
10	263	420	410	20	10
20	290	460	379	32	12
30	305	460	380	35	8
40	310	460	381	28	10

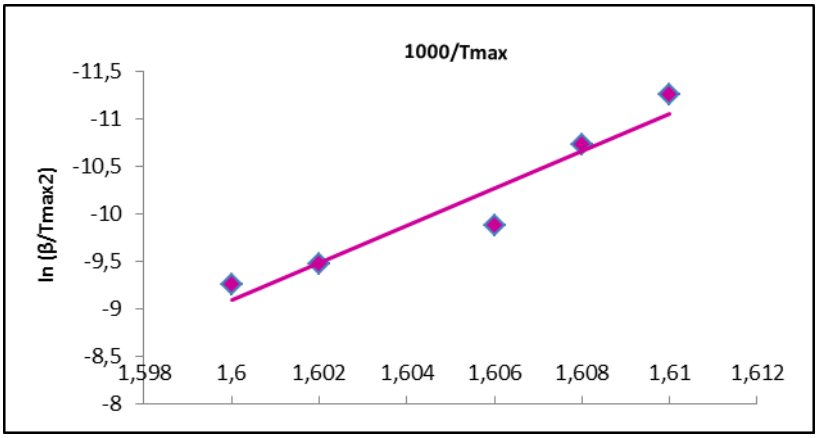

Figure 6. Linear plot of ln β/T_{max}^2 against $1000/T_{max}$ for PEPP-b-Pε-CL-b-PBMA copolymer

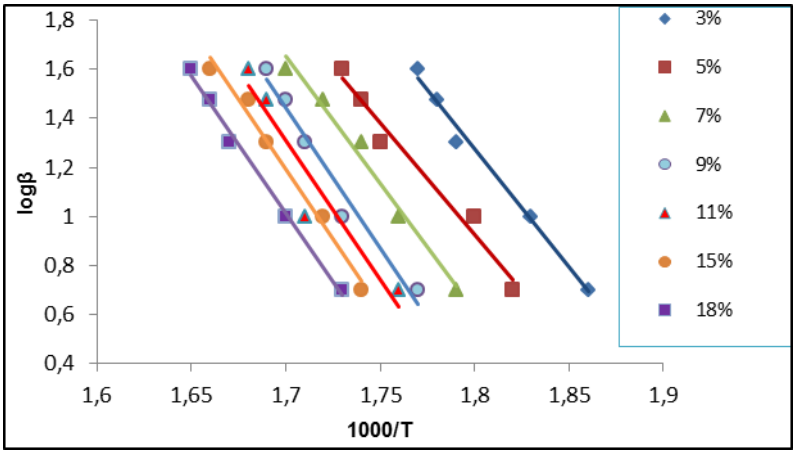

Figure 7. Linear plots of log β against 1/T for PEPP-b-Pε-CL-b-PBMA copolymer

Table 2. Activation Energies Obtained Using the Different methods

α (%)	Flynn-Wall-Ozawa method		Tang method		Kissenger method	
	E_a (kJ/mol)	R	E_a (kJ/mol)	R	E_a (kJ/mol)	R

3	175.67	0.9877	197.09	0.7907		
5	166.25	0.9712	189.12	0.7965		
7	193.78	0.9835	192.06	0.9227		
9	208.04	0.9685	193.90	0.7599	196.37	0.9215
11	204.56	0.905	195.20	0.7491		
15	207.71	0.9849	197.05	0.9037		
18	203.59	0.9926	199.9	0.8025		
ORT	**193.65**		**194.90**			

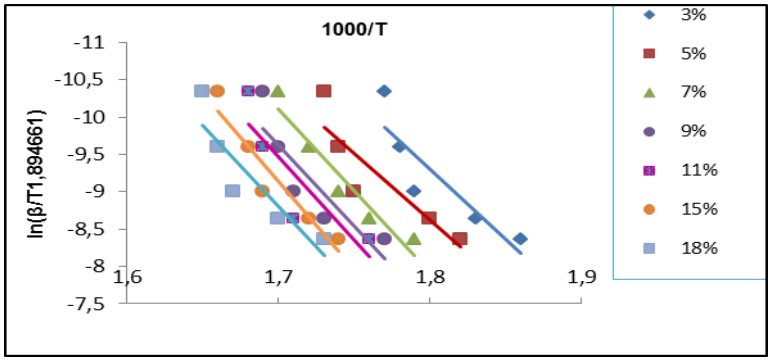

Figure 8. Linear plot of ln β/T_{max}^2 against $1/T_{max}$ for PEPP-b-Pε-CL-b-PBMA copolymer

Tang method was also used for determining of activation energy. eq. (3) was used to obtain E_a, which could be calculated from the plot of ln $\beta/T^{1.894661}$) versus 1000/T fit to a straight line shown in Figure 8. The mean value of the E_a of the thermal degradation of PEPP-b-Pε-CL-b-PBMA triblock copolymer was 194.90 kJ/mol. The calculated results are summarized in Table 2. Compared with other methods, these three methods present the advantage that they do not require previous knowledge of the reaction mechanism for determining of activation energy [14].

4.CONCLUSIONS

ABC (PEPP-b-Pε-CL-b-PBMA) triblock copolymer was prepared by combination of ROP and ATRP successfully. IR and ^{1}H-NMR techniques were used to characterization of synthesized polymers. The kinetics of the thermal degradation of ABC triblock copolymer were investigated by thermogravimetric analysis at different heating rate values. The E_a values of the thermal degradation of copolymer in N_2 calculated by the Kissinger's, Flynn–Wall–Ozawa, and Tang methods were 196.36 Kj/mol, 193.65 Kj/mol and 194.90 Kj/mol, respectively, for the decomposition stage.

ACKNOWLEDGEMENT

The authors wish to thank FUBAP FF-11-34 for financial support of this project.

REFERENCES

[1]. G. Deng, L. Zhang, C. Liu, L. He, Y. Chen, ''Synthesis of miktoarm star (block) polymers based on a heterofunctional initiator via combination of ROP, ATRP and functional group transformation'', *European Polymer Journal*, vol. 41, pp. 1177–1186, 2005.

[2]. W. Dai, J. Zhu, A. Shangguan, M. Lang, ''Synthesis, characterization and degradability of the comb-type poly(4-hydroxyl-ε-caprolactone-co-ε-caprolactone)-g-poly(L-lactide)'', *European Polymer Journal*, vol. 45, pp. 1659–1667, 2009.

[3]. J. Li, Y. Deng, S. Jie, B. Li, ''Zinc complexes supported by (benzimidazolyl)pyridine alcohol ligands as highly efficient initiators for ring-opening polymerization of ε-caprolactone'', *Journal of Organometallic Chemistry*, vol. 797, pp. 76–82, Nov. 2015.

[4]. Engelberg, J. Kohn, ''Physico-mechanical properties of degradable polymers used in medical applications: a comparative study'', *Biomaterials*, vol. 12, pp. 292-304, 1991.

[5]. Bilgin, C. Yağcı, ''Octa-armed star-shaped poly(e-caprolactone)s with a

[6]. phthalocyanine core by ring-opening polymerization: Synthesis and characterization'', *European Polymer Journal*, vol. 61, pp. 240–252, 2014.

[7]. Y.J. Cui, X.M. Ma, X. Z. Tang, Y. P. Luo, ‘‘Synthesis, characterization, and thermal stability of star-shaped poly(ε-caprolactone) with phosphazene core’’, *European Polymer Journal*, vol. 40, pp. 299–305, 2004.

[8]. J. Xu, W. Shi, ‘‘Synthesis and crystallization kinetics of silsesquioxane-based hybrid star poly(ε-caprolactone)’’, *Polymer*, vol. 47, pp. 5161–5173, June. 2006.

[9]. Z. Terzopouloua, V. Tsanaktsisa, M. Nerantzakia, D. S. Achiliasa, T. Vaimakisb, G. Z. Papageorgioub, D. N. Bikiaris,‘‘Thermal degradation of biobased polyesters: Kinetics anddecomposition mechanism of polyesters from 2,5-furandicarboxylicacid and long-chain aliphatic diols’’, *Journal of Analytical and Applied Pyrolysis*, vol. 117, pp. 162–175, Dec. 2016.

[10]. F..Doğan, İ. Kaya, A. Bilici, ‘‘Azomethine-based phenol polymer: Synthesis, characterization and thermal study’’, *Synthetic Metals*, vol. 161, pp. 79–86, Dec. 2011.

[11]. G. Kök, K. Ay, E. Ay, Fatih Doğan, İ. Kaya, ‘‘Synthesis, characterization and non-isothermal decomposition kinetic of a new galactochloralose based polymer’’, *Carbohydrate Polymers*, vol. 101, pp. 324– 331, Sep. 2013.

[12]. H. Mostaan, F. Karimzadeh, M.H. Abbasi, ‘‘Non-isothermal kinetic studies on the formation of Al_2O_3/Nb composite’’, *Thermochimica Acta*, vol. 511, pp. 32–36, July 2010

[13]. Q. Li, Y. Wang, M. Fan, J. Zhang, J. Cheng, ‘‘Thermal degradation kinetics of poly(acrylate/a-methyl styrene) copolymers’’, *Polymer Degradation and Stability*, vol. 128, pp. 158-164, Oct. 2016.

[14]. J. Opfermann, E. Kaisersberger, ‘‘An Advantageous Variant of the Ozawa–Flynn–Wall Analysis’’, *Thermochimica Acta*, vol. 203, pp. 167-175, July. 1992.

[15]. Kurt, ‘‘Thermal Decomposition Kinetics of Poly(nButMA-b-St) Diblock Copolymer Synthesized by ATRP’’, *Journal of Applied Polymer Science*, DOI 10.1002/app.30576, June. 2009.

ICENS
INTERNATIONAL CONFERENCE ON ENGINEERING AND NATURAL SCIENCES
24-28 May 2016 /Sarajevo

Biosorption of Cadmium(II) Ions from Aqueous Solutions by Oriental Hornbeam

Betul Tuba Gemici[1],*, Ercan Berberler[1], Handan Ucun Ozel[1], Halil Barıs Ozel[2]

Abstract

Cadmium is dangerous heavy metal for the environment and human health due to its toxicity. The common use of cadmium in various industrial activities such as electroplating, metallurgy, phosphate fertilizers, pigments, nuclear and Ni–Cd batteries causes the cadmium release into the environment. Several treatment methods including precipitation, ion exchange by ionic resins, electrodialysis and ultrafiltration have been proposed for removal of cadmium from wastewaters. However, each of these processes has restrictions and disadvantages. Biosorption is a promising alternative method to treat heavy metals, mainly because of its low cost and high metal binding capacity. In this study the biosorption of cadmium ions from aqueous solution by Oriental hornbeam (Carpinus orientalis) was studied in batch systems. The removal of cadmium(II) from aqueous solution was investigated under conditions such as initial concentration (10, 20, 30 and 45mg/L) and contact time (3h). Batch studies indicated that the biosorption efficiency decreased with increasing initial concentration of cadmium(II). It was observed that the removal efficiency at 10, 20, 30 and 45 mg/L of initial cadmium ions were found 95.90, 89.65, 73.83 and 56.67%, respectively. Biosorption equilibrium was reached within 5 min. Further increase in contact time did not show an increase in biosorption. In conclusion, abundant and cheap biosorbent of Oriental hornbeam, is a potent candidate for efficient biosorbent capable of removing cadmium(II) from aqueous solutions.

Keywords: *Oriental Hornbeam, Cadmium(II), Heavy metals, Biosorption*

1. INTRODUCTION

Technological developments and industrialization contribute to lives of peoples more comfortable, on the other hand it leads to serious environmental problems. Environmental pollution is one of the most important problems of our century. Especially increased levels of heavy metals in the environment caused by various industrial activities are a major threat to natural resources, human health and ecological systems.

One of the toxic heavy metal cadmium has an extremely dangerous effect on biological systems even at low concentrations. Cadmium is generated by various industrial activities including electroplating, metallurgy, phosphate fertilizers, pigments, nuclear, Ni–Cd batteries and other uses [1],[2]. Toxicity of cadmium, in general, causes severe damages to human health that accumulated in the kidney and liver, particularly in the renal cortex cause erythrocyte destruction, nausea, salivation, diarrhoea and muscular cramps, renal degradation, chronic pulmonary problems and skeletal deformity [3],[4]. Cadmium compounds are listed an carcinogenic substance by Environmental Protection Agency, USA [5]-[7]. Also The World Health Organization (WHO) has reported an allowable limit of cadmium in drinking water is 3 ppb [8]. Therefore as a heavy metal, cadmium must be removed from drinking and wastewater systems.

Although there are several methods for treatment and recovery of heavy metals, the most economical and efficient one is biosorption process. Biosorption process, due to the use of inexpensive and easy obtainable biosorbent, getting fast results and being repeatable, is preferred over others. Besides this method is preferable for not cause water and air pollution. Biosorption process is adsorption of dissolved contaminants by a suitable interface. This method can be performed a wide variety of mechanisms such as physical, chemical and ionic adsorption. Progress of mechanism depends on heavy metals and biosorbent used. Biosorption kinetic of heavy metals affected by several factors. In the process of biosorption, the dissolved compounds first have to encounter the boundary layer and then diffuse from the boundary layer film into the porous structure of biomass [9]. However mixing speed, pH, temperature, property of biosorbent, substance and solvent are affecting factors of biosorption. It is known that many aquatic organisms (bacteria, yeast, algae, etc.), and plant-based biosorbents have the ability of adsorb of dissolved heavy metals and radioactive elements [10],[11]. There are several studies using inexpensive and easily obtainable agricultural wastes and forest elements (leaf, pine, needle etc.) for heavy metal treatment. Some biosorbents are widely use potential for heavy metal removal such as pine cone biomass as forest biowaste [11],[12], chestnut shell [13] papaya peel biowaste [14], crab shell and orange peel [15], tea pulp and coffe grounds [16] etc.

[1] *Department of Environmental Engineering, Faculty of Engineering, University of Bartin, 74100-Bartin, Turkey*

[2] *Department of Silviculture, Faculty of Forestry, University of Bartin, 74100-Bartin, Turkey*

[*] *Corresponding author; E-mail:btakcay@bartin.edu.tr*

In this study, the removal of cadmium ions was investigated from aqueous solution using an Oriental hornbeam (*Carpinus orientalis*) as a cheap and readily available biosorbent. The effect of two important parameters including initial cadmium concentration and contact time were studied in batch system on the performance of biosorption process.

2. EXPERIMENTAL

2.1 Chemicals

All purchased chemicals were analytical grade provided by Sigma Aldrich. $CdCl_2$ was used as aqueous solutions and desired concentration of cadmium was prepared by making various dilutions with distilled water. Oriental Hornbeam used in investigation was washed with distilled water and dried at 80 ^oC for 24 hours. The dried biomass was ground in a mortar to a very fine powder.

2.2 Experimantal Apparatus and Cadmium Analysis

Orbital shaker (N-Biotek, NB-101MC Model) was used to homogenize aqueous solutions stirred for 3 h at 20 °C and at a fixed agitation speed of 150 rpm. Biosorption experiments were carried out in 250 ml Erlenmeyer flasks using 100 mL metal bearing solution with a 5 mg/L dried biosorbent (Oriental Hornbeam). Samples were taken at regular time intervals and centrifuged to remove biomass by centrifuge (Nüve NR200). Then Cd(II) in the remaining solution were determined using an atomic absorption spectrophotometer (Shimadzu AA7000).

2.3 Equations

Equations are used to examine the performance of the system parameters used for biosorption. Removal Efficiency (RE) defined as follows was used as a determination of biosorption process performance:

$$RE(\%) = (1 - \frac{C}{C_o}) \times 100 \quad (1)$$

where C_o is the initial concentration of cadmium and C is the final concentration of cadmium.

3. RESULT and DISCUSSION

3.1 Effect of Initial Metal Concentration

The concentration of both metal ions is a significant factor to be considered for effective biosorption [17]. In this study, the effects of initial metal concentration (10, 20, 30, 45 mg/L) were investigated for removal cadmium ions from aqueous solutions. The concentration of biosorbents, temperature and mixing speed of solutions were kept constant at 5 gr/L, 20 ^oC and 150 rpm respectively. The result is shown in Figure 1a and b. The experimental data showed that the cadmium removal efficiency was increased as the initial metal concentration decreased and optimum initial concentration was found 10 mg/L. On the other hand, unadsorbed Cd^{2+} increased as the initial metal concentration increased. Biosorbents have active binding sites which are bounded by pollutant molecules. In this experiment biosorption was occurred successfully at lower cadmium concentrations because all of the active site in the biosorbent surface wasn't occupied by adsorbed cadmium molecules. On the other hand, at higher concentrations, metal ions competed for the active binding sites of biosorbents and because of the lack of sufficient free sites metal ions didn't interact with biosorbents. Therefore, biosorption processes is affected significantly by the initial metal concentration. Similar results have been reported by others [11],[12],[17],[18].

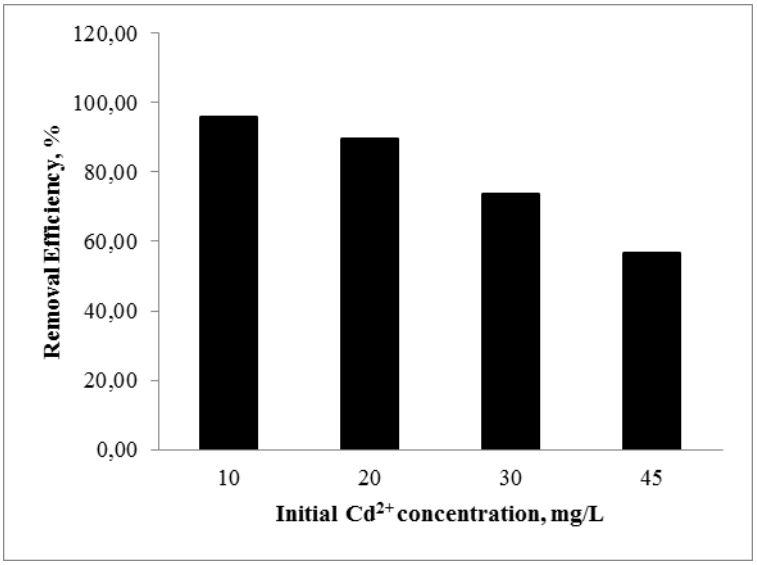

Figure 1.a. Effect of initial metal concentration as removal efficiency

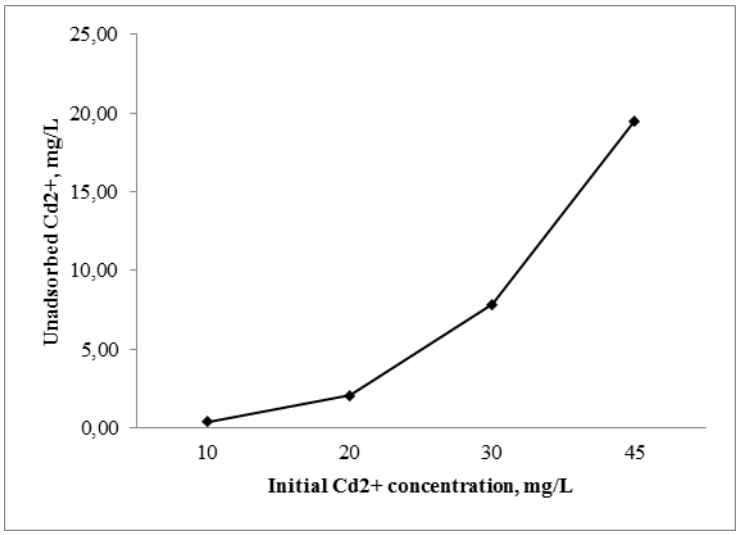

Figure 1.b. Effect of initial metal concentration as unsorbed Cd^{2+} concentrations

3.2 Effect of Contact Time

In the process of Cd(II) biosorption, the metal ions first have to encounter the boundary layer and then diffuse from the boundary layer film into the porous structure of plant biomass [9]. These phenomena shows that the importance of contact time. The rate of metal ion biosorption was highest in the beginning due to high affinity of free metal ion binding sites on bio sorbent but after few minutes the rate of biosorption slowed and reached to equilibrium [17]. In this study the effect of contact time at 10 mg/L initial cadmium solution was investigated for 3 hours keeping the temperature and mixing of the solution constant at 20 ^{o}C and 150 rpm respectively. The result is shown in Fig. 2. It was found that biosorption equilibrium occurred within 5 min. After this equilibrium time, the amount of biosorbed cadmium ions did not significantly change with time.

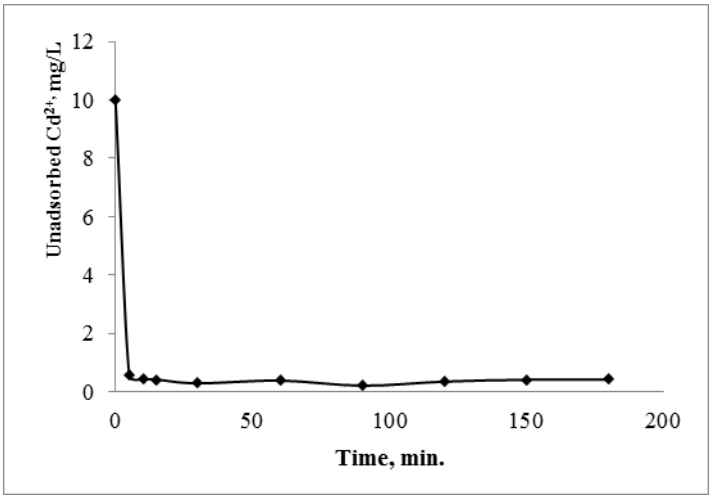

Figure 2. Effect of contact time

CONCLUSION

In this study the important parameters of biosorption method including initial metal concentration and contact time are investigated for removal of cadmium ions from aqueous solutions. The biosorption processes was evaluated at 10-45 mg/L initial concentrations and the batch system experiments showed that biosorption processes are strongly dependent on initial metal concentrations. Removal efficiency decreased as the initial metal concentrations increased and the optimum cadmium concentrations was found 10 mg/L due to the lack of sufficient active binding site at higher metal concentrations. Biosorption equilibrium was reached within 5 min. and after this equilibrium time, the amount of biosorbed cadmium ions did not significantly change with time. The study indicated that the Oriental hornbeam, is a potent candidate for efficient biosorbent capable of removing cadmium(II) from aqueous solutions.

REFERENCES

[1]. N. S. Rathore, A. Leopold, A. K. Pabby, A Fortuny, M. T. Coll, A. M. Sastre, "Extraction and permeation studies of Cd(II) in acidic and neutral chloride media using Cyanex 923 on supported liquid membrane," *Hydrometallurgy*, vol. 96, pp. 81-87, 2009.

[2]. D.L Tsalev, Ed., *Cadmium*; *Atomic Absorption Spectrometry in Occupational and Environmental Health Practice*. Florida, 1993, vol.1.

[3]. M. Hutton, *Human health concerns of lead, mercury, cadmium and arsenic;* Lead, Mercury, Cadmium and arsenic in the Environment, 1987.

[4]. G. Lee, "Effects of operating parameters on the removal performance of electrodialysis for treating wastewater containing cadmium," *Desalination and Water Treatment*, vol. 35, pp. 150-157, Nov. 2011.

[5]. C.P. Huang, M. Asce, F.B. Ostovic, "Removal of Cadmium (II) by activated carbon adsorption" *Journal of The Environmental Engineering Division*, pp. 863-878.

[6]. Gaballah, G. Kilbertus, "Recovery of heavy metal ions through decontamination of synthetic solutions and industrial effluents using modified barks," *Journal of Geochemical Exploration*, vol. 62, pp. 241-286, 1998.

[7]. S. L. Brown, R. L., Chaney, , J. S. Angle, A. J. M. Baker, "Zinc and cadmium uptake by hyperaccumulator Thlaspi caerulescens grown in nutrient solution" *Soil Sci. Soc. Am. J*. vol. 59, pp. 125-133.

[8]. *World Health Organization WHO*, Guidelines for Drinking-Water Quality, vol. 4. 327- 383, 2011.

[9]. K. M. Al-Qahtani, "Water purification using different waste fruit cortexes for the removal of heavy metals," *Journal of Taibah University for Science, Article in press, 2016.*

[10]. L. D.Benefield, , J. R, J. F.Judkins, , and B. L.Weand, "Process Chemistry For Water And Wastewater Treatment", Englewood Cliffs, New Jersey, p 433-435, 1982.

[11]. H. Ucun, Y. K. Bayhan, Y. Kaya, A. Çakıcı, O.F. Algur, "Biosorption of lead (II) from aqueous solution by cone biomass of *Pinus sylvestris" Desalination*, vol. 154, pp. 233-238, 2003.

[12]. H Ucun., Y. K. Bayhan, Y. Kaya, A, Çakıcı, O. F. Algur, "Biosorption of chromium(VI) from aqueous solution by cone biomass of *Pinus sylvestris*," *Bioresource Technology*, vol.85, pp.155–158, 2002.

[13]. N. Kim, P. Munsik, D. Park, D., "*A new efficient* forest biowaste *as biosorbent for removal of cationic heavy metals*, *Bioresource Technology*, vol. 175, pp. 629-632, 2015.

[14]. S. Abbaszadeh, S.R.W. Alwi, C. Webb, N. Ghasemi, "Treatment of lead-contaminated water using activated carbon adsorbent from locally available papaya peel biowaste," *Journal of Cleaner Production*, Artical in press, pp. 1-13.

[15]. C J.S.Varshini, D. Das, N. Das, Optimization of parameters for praseodymium(III) biosorption onto biowaste materials using response surface methodology: Equilibrium, kinetic and regeneration studies. *Ecological Engineering*. vol. 81, pp. 321-327, 2015.

[16]. H. D. Utomo, ve K. A. Hunter, Particle Concentration Effect: Adsorption of Divalent Metal Ions on Coffee Grounds. Bioresource Technology, vol. 101, pp. 1482-1486, 2010.
[17]. Ö. Aksakal, H. Ucun, Y. Kaya1, "Removal of nickel from aqueous solution by nordmann fir (abies nordmanniana (stev.) spach subsp. nordmanniana) cones," *Environmental Engineering and Management Journal*, vol. 7 (4), pp. 359-363, 2008.
[18]. M. Oves, M.S. Khna, A. Zaidi, "Biosorption of heavy metals by *Bacillus thuringiensis* strain OSM29 originating from industrial effluent contaminated north Indian soil," *Saudi Journal of Biological Sciences*, vol. 20, pp. 121-129, 2013.

ICENS
INTERNATIONAL CONFERENCE ON ENGINEERING AND NATURAL SCIENCES
24-28 May 2016 /Sarajevo

Estimation of the Flow Velocity Effected by Submerged Vanes with Regression Models

Fikret Kocabas[1], Ercan Gemici[1,], Mehmet Ardiclioglu[2]*

Abstract

Water structures are also made in order to reduce erosion and flood damage, as well as the more effective use of limited water resources. The most important design parameters for these structures which costs high is river flows that flow velocity indirectly. The flow velocity must be known in the problems of rivers slope protection, bed protection and sediment transport. Submerged vanes placed at the bottom of the stream are easy to build, economical and effective regulating structure compared to other water structure. Submerged vanes changing the sediment and velocity distribution reduce the slope and bed erosion at vanes downstream. River section properties, vane section properties and vane arrangements are the main factors affecting velocity distribution.

In this study, some experiments are made for finding effect on the flow velocity downstream of the vanes at some conditions such as different channel width/channel depth (B/d), submergence/vane height ratio (S/H), the Froude number (Fr), vane arrangement, vane length/vane height (L/H) and the approach angle (α) in rectangular open channel.

End of this study it was seen that the effect of vanes to the flow velocity increased when the water level is low and vane width is more effective than the height of the vanes, vane effect increased as approach angle increased. Generated linear and nonlinear regression models have been quite good and given similar results. The coefficient of determination obtained from linear and nonlinear regression models (R^2) were obtained 0.81 and 0.84 and the root mean squared error (RMSE) 1.02 and 0.97, respectively.

Keywords: *Submerged vane, multiple linear regression, nonlinear multiple regression, flow velocity.*

1. INTRODUCTION

3/4 of the human body is water and water is a necessary requirement for the continuation of life. As water problems in the world increases, studies in order to avoid more damage than benefit from rivers is increasing. Bed slope in streams and cross-sectional narrowing or changing speed expansion is a direct data used in the studies. Velocity is less on the coast and bottom than on the right side of the bed. When the slope increased, flow velocity increases accordingly and with velocity, running water erodes and moves river bed materials along. Solid matters carried by water and wind forces called sediments. Transported sediments, would scour if below river capacity on the other hand they precipitation if above river capacity. Depends on the case river bottom and slope formed. Structures in order to prevent the deterioration of the river bed, prevent floods, protect the water structure, provide the desired stream depth, provide breeding streams referred to as river training structures. River protection structures, narrowing structures, carved protection structures, flood structures examples of river regulation structures.

Scour on the river bed varies with the flow. Meandering rivers, because having inner coast secondary currents, inner coast speed reduce wile outer coast speed increase , with this peeling occurs in the outer slope and bed bottom near here. Stresses that cause movements in the bottom and slopes are different from each other [1]. For a trapezoidal channel that difference explain by Chow at figure 1.

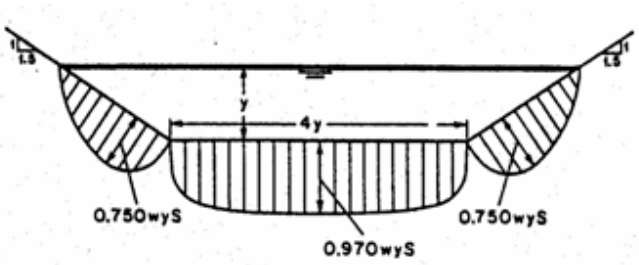

[1] *Bartın University, Department of Civil Engineering, 74100, Bartın/ Turkey.fkocabas@bartin.edu.tr*

[2] *Erciyes University, Department of Civil Engineering, 38039, Kayseri/ Turkey. mardic@erciyes.edu.tr*

[*] *Corresponding author: egemici@bartin.edu.tr*

Figure 1. Shear stress distribution in the bottom and slopes [1]

Shear stress is seen to be more at bottom and part of slope that close to bottom at figure 1. Considering the size and velocity of stream substrate on whether to move the bed material is most commonly used chart diagram created by Shields. If Shields diagram calculated shear stress and Reynolds number intersect on curve, that means base material is moving.

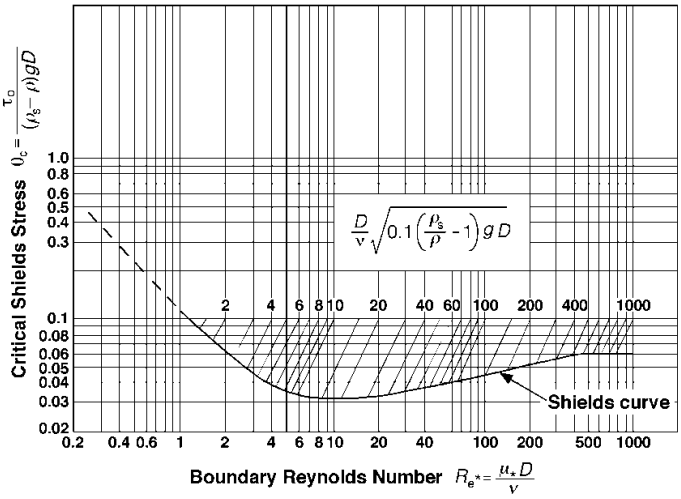

Figure 2. Shields diagram [1]

Protection structures are created to prevent scouring the bottom or slope. This structures directing flow to reducing scouring the slop and the bottom to prevent soil erosion. Bed sediment deposition causes water retention of the river. Below capacity and sufficient performance can not be taken from the rivers. It is intended to reduce the flow velocity and change the flow direction of slope and bottom with river regulation structures. Flow and sediment movement is one of the problems encountered in hydraulic engineering. Protection and guidance aimed regulating structures are perpendicular to the coast, quite expensive and made in accordance with upstream and downstream. In may 1982 "Analysis of Sacramento river bend flows, and development of new methods for bank protection" report was prepared by Odgaard and Kennedy [2]. Submerged vane tested and introduced as an alternative method for the protection of the river bottom and slope. Placed at an angle to the bottom of the stream according to the current direction, the structures below the top level of the water surface built from concrete, rocks or steel plate is described as submerged vanes. As sediment accumulates behind the buildings from shore structures such as spurs and prevents the flow of water. Submerged vanes which has less effect on water passage brings a more advantageous situation. In general submerged vanes that placed near the outer slope alter the channels flow and sediment distribution by creating reverse vortex (secondary circulation) to avoid distortion of the channel bed. There is no clear design criteria of a submerged vane which is new, economic and easy-to-built than other regulatory structures. Today the information obtained by laboratory tests are the basis of vane design. Vortex created by submerged vanes cause changes in the flow velocity, sediment and current depth magnitude and direction of shear stres at the river bottom. Vanes circulation is in accordance with vanes heigth, width, shape and angle of laying. Mostly are used at the mouth of the water intake channel or routing.

The first study about submerged vane is made for slope protection on the Sacramento River by Kennedy and Odgaard [2] in 1982. Boniforti et al. [3] has examined the sediment move around the vane with 4 different featured submerged vane placed by 10° and 20° angle of flow direction. Ouyang [4] investigated the sediment routing performance using a single rectangular and trapezoidal vane with different width and height. Ouyang et al. [5], investigated the interaction of each side of the meandering channel sequence. The expected slope protection and building operating costs can be achieved by determining the optimum vane system is indicated. Tan et al. [6] studied the effects of submerged vanes on sediment orientation. Voisin and Townsend [7], investigated the effect of the angle of approach to the channel, ratio of the flow height to the vane height and width ratio of the channel length of the vane. Duan et al. [8], investigated which measured flow velocity with ADV in upstream and downstream flow and sediment distribution around the vane by used different diameters sediment. Ouyang and Lai [9], used a genetic algorithm method for optimizing the submerged vanes. Moghadam and Keshavarzi [10], used submerged vanes in order to examine sediment and velocity distribution in lateral channel. Ghorbani and Kells [11], investigated effect of submerged vane height, angle of approach and the constant flow (10-30 cm) to scour around cylindrical feet by constant Froude number (0.15). Marius and Sinha [12] investigated the relationship between the submerged vane angle and sediment input to lateral channel input and it can not be definitely stated relationship.

Velocity formed in slope one of the most important parameters used in the design of slope protection structures. Instead of velocity measurements which is quite troublesome, its possible with created models to estimate the approximate velocity change cause by vanes. Today, saving both time as well as economic regression model is one of the effective methods used quite often.

In this study estimated the relative velocities experimentally obtained with with linear and nonlinear regression models by using various vanes, channel and flow properties as arguments. Experimental studies are made rectangular channel, 3 different vane type, different vane placements and different sort of approach angles. Throughout the establishment of the model 162 data is used. Submerged vanes behavior depending on changing flow characteristics and flow velocity effect of different vane properties was estimated with the help of models.

2. EXPERIMENTS

Experiments made in Bartin University Central Research Laboratory Hydromecanic Lab. Estabilised on open channel that 1.80 m over floor with properties of 10 m total height, 0.5 m bottom width and channel side walls created from 0.5 m height glass. In order to placement of the vanes, 4 m long and 15 cm deep sediment pool created from 5th meter of channel by filling with the washed coarse sand. The channel is made with reference to previous studies about the submerged vanes.

2.1 Experiment Equipments

Rectangle vanes with different aspect ratios were used in the working. Rectangle vanes created with 15/10 cm, 10/10 cm and 15/10 cm aspect ratios. Vanes placed at sediment pool by making working lenght 5 cm longer. Special plate (40 x 60 cm2) created to ensure the placement angle of the vanes and prevent the movement of the vanes from flow effect, Vane angles able to adjust to be 20, 25 and 30 degree by opening six holes to plate and placing vanes from inside out to slots in order. Vanes and placement of vanes used in the experiments shown in Figure 3.

Figure 3. Vanes and placement of vanes

Consisting of propeller and digital display Micro Muline used for speed measurement at specified points in the channel. Muline have propellers with different diameters and angles for use on different flow velocity. Muline depends on probs diameter can measure at 3 mm from bottom [13].

Seen on the Figure 4. Pump provided water recirculation in channel. Water depth is increased to the desired level with aid of an adjustable valve placed at the end of channel. Flow adjustable via the valve located at the pump outlet that provided water recirculation in channel and ultrasonic flow meter seen at Figure 5. placed at the inlet of the pump is measured flow entering the system. Device able to measure speed between 0,03-12,2 m/s [14].

Figure 4. Experimental setup

Seen on the Figure 4. Pump provided water recirculation in channel. Water depth is increased to the desired level with aid of an adjustable valve placed at the end of channel. Flow adjustable via the valve located at the pump outlet that provided water recirculation in channel and ultrasonic flow meter seen at Figure 5. placed at the inlet of the pump is measured flow entering the system. Device able to measure speed between 0,03-12,2 m/s.

Figure 5. Ultrasonic flow meter

2.2 Experimental Procedure

In this experiment, effect of vanes was investigated by measured flow velocity in the middle of channel and close to the slopes. In order to determine this placement, flow velocity were measured without vanes and different angles, sections and by placing the vane arrangement. Measurements were carried out the midpoint of the channel cross-section side walls 10 cm away from the water surface at a depth in the downstream 0.6d. Vanes are placed with adjustments in the arrangement of vanes type, vane arrangement, vane angle used in the experiment set up in the channel. With the operation of pump, water passes through the gravel filter and reaches channels with pacified form. To set the desired experiment, flow is adjusted by valve and flow is read passing from the pipe and reachin channel with ultrasonic flow meter.

Submergence on vanes is set on the help of the adjustable gate. Flow is expected 15-20 minutes to reach equilibrium. Muline brought the point to be measured and the water level is read by lasermeter. Water level and flow velocity is recorded. By the end of the measurements channel bottom corrected prepared for further experiments. Experiments are repeated in this way creating different conditions.

Change in the flow velocity was investigated placing the blades at different angles for different flow, water level, vane arrangement in this experiment. In the experiments, the vane section length / height ratio was chosen as (L/H) 10/10, 10/15 and 15/10; discharge (Q) 16.0, 22.0 and 28.0 l / s; water level (d), 13.0, 23.0 and 33.0 cm vane arrangement of (r) double and triple; vane approach angle (α), 20°, 25° and 30°. The relative velocity expresses change of the flow velocity was found using $|(V_{non\text{-}vane}-V_{vane})/ V_{non\text{-}vane}|*100$ equations with the by addition the absolute value at the right wall, in the middle and the left wall.

3 METHODS

3.1 Multiple Linear Regression

The aim of multiple linear regression to determine the dependent variable values with the independent variables and to find which independent variables effect dependent variables [15].

In the multiple regression analysis, the dependent variable y, the independent variables x_1, x_2, ..., when indicated by their relationship is expressed by equation 1 x_p.

$$y=b_0+b_1x_1+b_2x_2+\ldots+b_jx_j+\ldots+b_px_p+\varepsilon \quad (1)$$

Here; b_0, b_1, b_2, ..., b_j, ... b_p called the regression coefficients of the unknown. Any b_j regression coefficient, when other variables are held constant (eliminating the effect when other variables are removed) in response to a change occurring in the x_j unit variable variable y represents the amount of change expected. In other words; b_1, b_2, ..., b_j, ... b_p; independent variables y to determine their relative contributions are related to weight. Therefore, b_j (j = 1, 2, ..., p) parameters are usually referred to as partial regression coefficients. b_0 is called the cut-off point or fixed and variable values in all x_j shows the value taken by the dependent variable is zero. ε is the error term [16].

3.2 Multiple Nonlinear Regression

Purpose of nonlinear regression which is same with basic idea of linear regression is establish the non-linear relationship between dependent and independent variables. Different model equation can be used in nonlinear regresion, the most used ones logistics, exponential and polinominal equations. In this model equations, there are several unknown parameters must be found using related variable and dependent parameters. In this study, nonlinear regression analyzed by thinking exponential relation between dependent Q variable and independent variables thats given at equation 2.

$$y=ax_1^{\beta_1}x_2^{\beta_2}x_3^{\beta_3}\ldots x_n^{\beta_n} \quad (2)$$

θ_i model parameter represents 'a' multiplicative error term and variable 'n' .This model parameters optimized with Least Squares technique [17].

4 DISCUSSION

162 experimental data were used in the study. Among them 108 data used to train model, 54 data used to test model. Independent variables that used in models are shown in Table 1.

Table 11. Model Parameters

Dependent Variable	Effective Parameters (Independent Variable)
Relative velocity ($V_{relative}$)	Vane angle (α), Arrangement (r), Section (L/H), Water level (d) and Discharge (Q)

Estimation results of models compared according to Square Root Mean Square Error(RMSE) and Coefficient of Determination(R2) criteria. RMSE and R2 calculated with help of equation 3 and 4.

$$RMSE = \sqrt{\frac{1}{N}\sum_{i=1}^{N}\left(V_{relative,measured} - V_{relative,model}\right)^2} \quad (3)$$

$$R^2 = 1 - \frac{\sum_{i=1}^{N}\left(V_{relative,measured} - V_{relative,model}\right)^2}{\sum_{i=1}^{N}\left(V_{relative,measured} - V_{relative,average}\right)^2} \quad (4)$$

After training of model ended, performans of model tested with the previously unused test data. Data used in the training stage together with linear and nonlinear regression relation used to get equation 5 and 6. (5) for linear, (6) for non-linear models equation.

$$V_{relative} = -9.528 + 0.348(\alpha) + 1.827(r) + 0.215\left(\frac{10L}{H}\right) - 0.035(d) + 0.0214(Q) \quad (5)$$

$$V_{relative} = -2.853(\alpha)^{0.916}(r)^{0.493}\left(\frac{10L}{H}\right)^{0.180}(d)^{-0.089}(Q)^{0.520} \quad (6)$$

R^2 and RMSE values are shown in Table 2 by using these equations on test data. Predicted values obtained from models are shown in Table 3.

Table 2. R^2 and RMSE Statistics of Models

Model	R^2	RMSE
Linear	0.84	0.97
Nonlinear	0.81	1.02

Although, R^2 values high and RMSE values low for both model to estimate Vrelative ; values very close to the measured results of the model were obtained.

Linear model results and measured values obtained using equation 5 shown with figure 6 and 7.

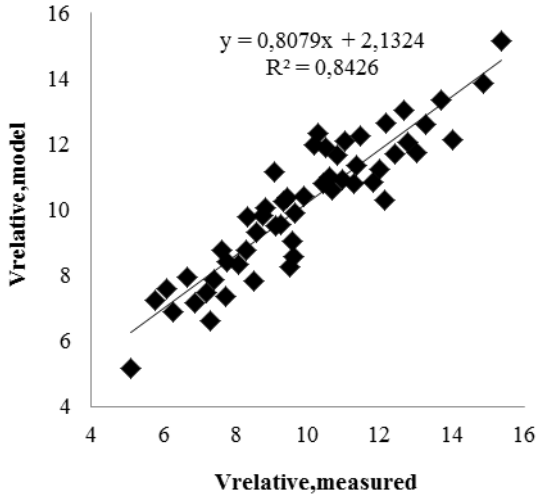

Figure 6. Scatter plot of measured and linear model test data

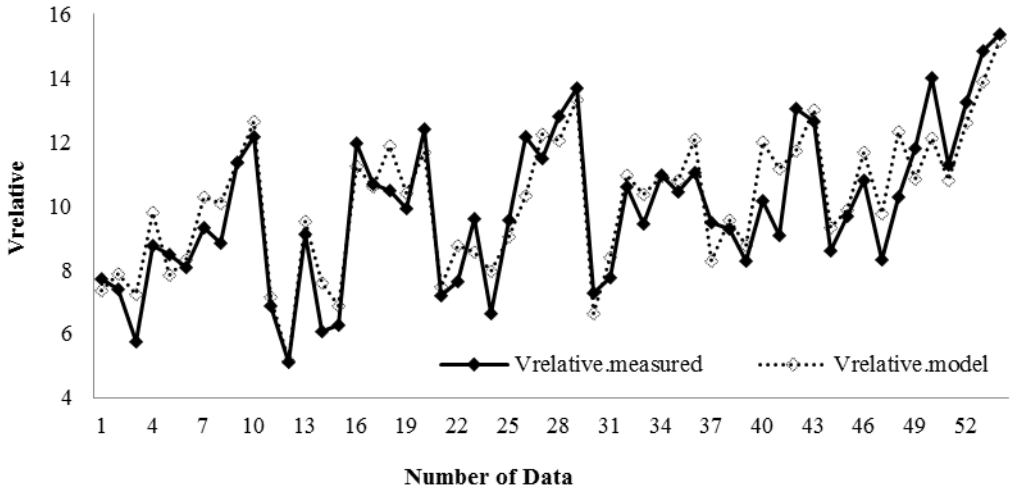

Figure 7. Predicted values of measured and linear model

Linear model results and measured values obtained using equation 6 shown with figure 8 and 9.

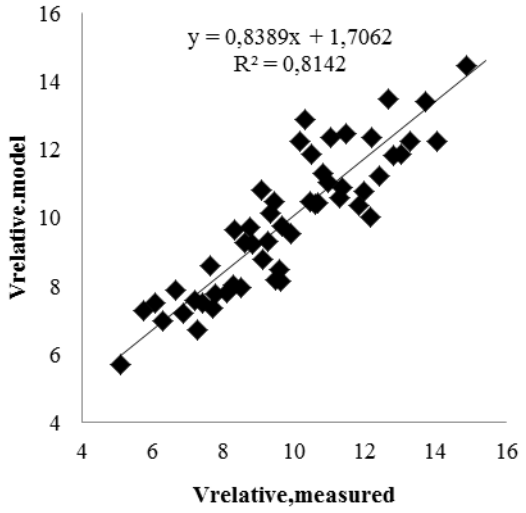

Figure 8. Scatter plot of measured and nonlinear model test data

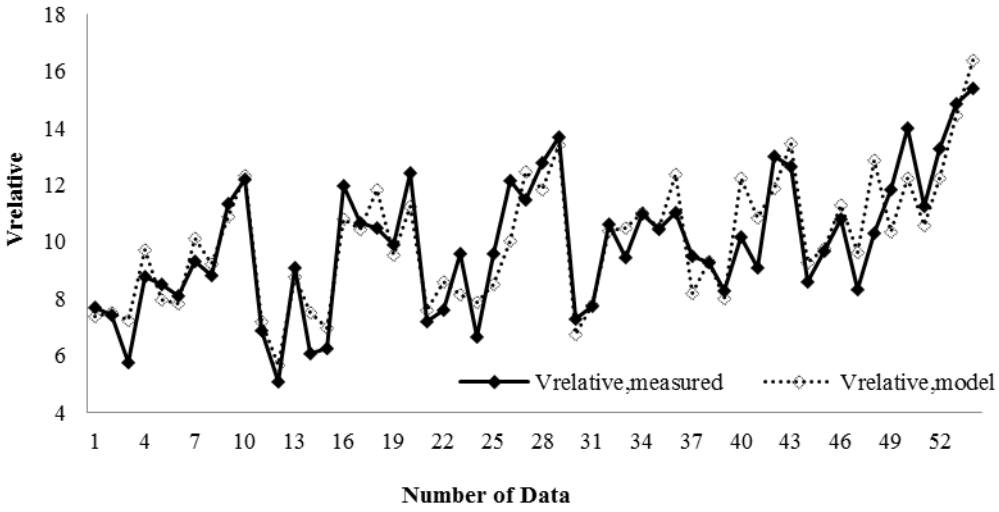

Figure 9. Predicted values of measured and nonlinear model

CONCLUSIONS

In the experiments conducted in an open channel with different discharge, different water levels and vane arrangement conditions, by changing the angle of approach and vane sections, between the accordance of the measured values for the downstream water surface at a depth of from 0.6d flow velocity of side effects and linear and nonlinear regression models were investigated.

The change flow velocity is reduced with the increasing the water level while increased discharge and the number of vanes increases the change flow velocity. Flow velocity are affected by vane width more than the vane length.

Performance of both models were seen close together and pretty good. Model independent variables angle (α), vane arrangement (r), section (L/H), depth (d) and discharge (Q) has been shown to be highly effective direct on the flow velocity.

ACKNOWLEDGMENT

The Authors acknowledged the Financial assistance by the Bartin University through the Scientific Research Project commission (BAP) for funding project number 2013.1.94.

REFERENCES

[1]. V. T. Chow, *Open Channel Hydraulics*, Mc Graw-Hill Book Co., New York, USA, 1959.
[2]. J. Odgaard, Kennedy, J. F., "Analysis of Sacramento River Bend Flows, and Development of a New Method for Bank Protection," University of Iowa, Iowa City, IHHR Report 328, 86s, 1982.
[3]. M. A. Boniforti , R. Guercio, R. Magini, "Effects of Submerged Sheet Pile Vanes on Mobile River Beds," *Journal of Zhejiang University-Science*, 16 (3): 182-193, 2015.
[4]. H. T. Ouyang, "Investigation on the Dimensions and Shape of a Submerged Vane for Sediment Management in Alluvial Channels," *Journal of Hydraulic Engineering*, ASCE 135 (3): 209-217, 2009.
[5]. H. T. Ouyang, J. S. Lai, H. Yu, "Interaction Between Submerged Vanes for Sediment Management," *Journal of Hydraulic Research*, 46 (5): 620-627, 2008.
[6]. S. K. Tan, G. L. Yu, S. Y. Lim, "Flow Structure and Sediment Motion Around Submerged Vanes in Open Channel," *Journal of Waterway Port Coastal and Ocean Engineering*, ASCE, 131 (3): 132-136, 2005.
A. Voisin, R. D. Townsend, "Model Testing of Submerged Vanes in Strongly Curved Narrow Channel Bends," *Canadian Journal of Civil Engineering*, 29 (1): 37-49, 2002.
[7]. J. G. Duan, A. Acharya, M. Yeager, "Sediment Sorting Experimental Spur Dike," *World Environmental and Water Resource Congress*, May 12-16, 2008, Honolulu, Hawaii, USA.
[8]. H.T. Ouyang, J. S. Lai, "Design Optimization of a Submerged Vane with Streamlined Profile for Sediment Management in Rivers," *Journal of Marine Science and Technology-Taiwan* 21 (3): 325-332, 2013.
[9]. M. K. Moghadam, A. R. Keshavarzi, "An Optimised Water Intake with the Presence of Submerged Vanes in Irrigation Canals," *Irrigation and Drainage* 59 (4): 432-441, 2010.
[10]. Ghorbani, J. A. Kells, "Effect of Submerged Vanes on the Scour Occuring at a Cylindrical Pier," *Journal of Hydraulic Research*, 46 (5): 610-619, 2008.
[11]. F. Marelius, S. K. Sinha, "Experimental Investigation of Flow Past Submerged Vanes – Closure," *Journal of Hydraulic Engineering*, ASCE 125 (8): 898-899, 1999..

[12]. E. Gemici, "Flow Management with Submerged Vanes in Open Channels", Ph. D. thesis, Erciyes University, Graduate Scholl of Natural and Applied Sciences, Kayseri/Turkey, 2015.
[13]. F. Kocabaş, E. Gemici, M. Ardıçlıoğlu. "Dikdörtgen Kesitli Açık Kanallarda Batık Kanatların Şev Stabilitesi Üzerinde Etkisi," *Mühendislik ve Teknoloji Bilimleri Dergisi*, 4 (1): Baskıda, 2016.
[14]. F. Kocabaş, N. Yıldırım, E. Gemici, "Sirkülasyonun Su Alma Borusuna Ait Kritik Batıklığa Etkisi," *Mühendislik ve Teknoloji Bilimleri Dergisi*, 1 (1): 1-21, 2013.
[15]. R. Alpar, *Uygulamalı Çok Değişkenli İstatistiksel Yöntemlere Giriş 1*, Nobel Yayın, Ankara/Turkey, 2003.
[16]. N. Seçkin, A. Güven, R. Yurtal, "Taşkın Debilerinin Yapay Sinir Ağları ile Modellenmesi: Batı Karadeniz Havzası Örneği", *Ç.Ü. Müh. Mim. Fak. Dergisi*, Cilt 25 (1-2), 45-57, 2010.

ICENS
INTERNATIONAL CONFERENCE ON ENGINEERING AND NATURAL SCIENCES
24-28 May 2016 /Sarajevo

Chelate-Induced Phytoextraction Potential of *Brassica rapa* for Soil Contaminated with Nickel

***Aydeniz Demir*[1*], *Nurcan Koleli*[1]**

Abstract

The aim of present study is to induce for phytoextraction of Ni by Brassica rapa from contaminated soil by application of EDTA. Brassica rapa seeds were planted in pots with Ni concentrations ranging from 0 to 2000 mg/kg in the absence or presence of 10 mg/kg EDTA. After 60 days of growth, Ni concentration of plants were observed. Brassica rapa showed the remarkable resistance to Ni toxicity with no visual toxic symptoms as chlorosis and necrosis. The addition of 10 mg/kg EDTA significantly increased both the plant growth and the Ni concentration, compared with the control. Especially the addition of 10 mg/kg EDTA and 500 mg/kg Ni produced fertilizer effect and maximum dry matter achieved to 1.96 mg/plant from 0.82 mg/plant. While Brassica rapa accumulated 3763 mg/kg Ni in the absence of EDTA, the addition of 10 mg/kg EDTA increased Ni accumulation to 3942 mg/kg Ni at Ni application dose of 2000 mg/kg. Experimental results indicated that Brassica rapa is Ni hyperaccumulator plant (>1000 mg/kg in shoots) both in the absence or presence of EDTA. The bioaccumulation coefficient (BAC) for Ni by Brassica rapa was greater than 1, providing further evidence for the transport of Ni from Ni contaminated soils.

Keywords: *Brassica rapa, EDTA, Hyperaccumulator, Nickel, Phytoextraction*

1. INTRODUCTION

There is a great worldwide interest surrounding issues of soil contamination including heavy metals [1]. Soil contamination with Ni has become a worldwide problem [2]. Nickel (Ni) is an important heavy metal in soil and is an essential element required for nitrogen (N) metabolism. Nickel plays a role in the structure and activity of the urease and hidrogenaz enzyme in plants [3]. In recent years, Ni pollution has gained importance due to negative potential impact on agriculture and human health. Nickel contamination mainly results from volcanic eruptions, land fill, forest fire, bubble bursting and gas exchange in ocean, weathering of soils and geological materials, effluent disposal from mining and smelting, fossil fuel burning, vehicle emissions, disposal of household, municipal and industrial wastes, fertilizer application and organic manures [4-6].

Phytoextraction is a non-destructive, cost-effective and safe alternative to conventional clean up techniques of contaminated soils with heavy metals such as Ni [7]. Phytoextraction is either a continuous (natural) process (using metal hyperaccumulating plants, or fast growing plants), or an induced process (using chemicals to increase the bioavailability of metals in the soil) [8].

The success of phytoextraction, either natural or chemically assisted, is largely determined by plant biomass, metal concentration in the plant tissue, and the phytoavailable fraction of metals in the rooting medium [9]. Researchers initially applied hyperaccumulator plants to clean metal polluted soils. However, many such plants have limited utility for phytoremediation, because of their slow growth, difficult propagation, seasonal growth, and low biomass [2]. Then, chelates such as EDTA, hydroxy ethylethylenediaminetriacetic acid (HEDTA), and ethylenebis-2(o-hydroxyphenyl) glycine (EDDHA) are used to enhance the phytoextraction of a number of metal contaminants including cadmium (Cd), chromium (Cr), cooper (Cu), lead (Pb), zinc (Zn) and Ni.

[1] *Corresponding author: Mersin University, Faculty of Engineering, Department of Environmental Engineering, 33342 Mersin-Turkey.* demiraydeniz@gmail.com, aydenizdemir@mersin.edu.tr

[2]*Mersin University, Faculty of Engineering, Department of Environmental Engineering, 33342 Mersin-Turkey.* kolelinurcan@gmail.com, nkoleli@mersin.edu.tr

This chelate-assisted accumulation of toxic quantities of metal in a non-accumulator species is termed "chelate-induced hyperaccumulation" [10]. Chelate-induced phytoextraction is an innovative technique for cleaning metal contaminated soil [11]. Ethylenediaminetetraacetic acid is the most effective chelating agent for chelate-induced hyperaccumulation because it has a strong chelating ability for different metals and increases the bioavailability and uptake of metals in the plant from soil [11-12]. Several researchers have screened on chelate-induced hyperaccumulation of some fast-growing, high-biomass-accumulating plants, including agronomic crops, for their ability to tolerate and accumulate metals in their shoots [13]. Huang et al. [10] reported a 1000-fold increase of Pb in in agronomic crops such as corn (*Zea mays* L.) and pea (*Pisum sativum* L.) after HEDTA application in comparison to soil solution of a control (no HEDTA addition). Under these conditions Pb concentrations in the shoots of corn and pea increases from less than 500 mg/kg to more than 10.000 mg/kg within one week after HEDTA application.

Brassica species are well known as metal accumulators and are being used for phytoremediation of contaminated soils. However, the metal tolerance mechanism in the plant still remains unclear [14]. Purakayastha *et al.* [15] reported that in a pot culture experiment, five different species of Brassica (*Brassica juncea, Brassica campestris, Brassica carinata, Brassica napus, and Brassica nigra*) were grown for screening possible accumulators of heavy metals, viz. Zn, Cu, Ni, and Pb. Among all species, *Brassica carinata* showed the highest concentration (mg/kg) as well as uptake (µg/pot) of Ni and Pb at maturity. Grčman *et al*. [16] studied the effect on the uptake of Pb, Zn and Cd by *Brassica rapa* and found that the concentrations of Pb, Zn and Cd in shoots were detected, up to 104.6, 3.2 and 2.3-times as much as that in the control.

In a study performed by Putnik-Delic *et al.* [17] had been determined the biggest concentration of Ni (300 ppm), both in leaf and in stem, was in *B. rapa*, with 64.25 times increase in concentration compared with the control group, and 66.5 times in stem in comparision with the respective control group.

In this study, Ni was choosen as target metal because it is widespread on serpentine rocks and the area in which the study was performed. It is known that serpentine soils are high in several heavy metals (e.g. nickel, cobalt and chromium) and these high heavy metal concentrations are thought, in part, to lead to varying levels of plant adaptation and soil affinities (i.e. endemic vs. non-endemic plant species) [18]. Koleli *et al.* [19] defined common soil formations distinguished in this area as follows: brown forest soils, reddish Mediterranean soils and brown calcareous soils reported that the maximum concentrations of metals in 11 soil samples collected from Mersin-Findikpinari (as dry mass) were 909 mg/kg Cr, 3615 mg/kg Ni, 246 mg/kg Cu, 467 mg/kg Zn, 8.2 mg/kg Cd and 111 mg/kg Pb. As it can be seen from the results, Ni concentration is always higher than the other metals. Because of that reason in this study investigated only nickel.

The objectives of this study were to evaluate the effect of EDTA application on Ni phytoextraction by *Brassica rapa* growing in artificially Ni contaminated soil, and to evaluate EDTA application effects on toxicity symptom, dry matter production, Ni concentration, Ni content and BAC of the plant. *Brassica rapa* is preferred because of its high yield (1.5 tons- 4.0 tons per ha) and high oil content of 42-46% [20], resist to soil and climate conditions and efffective root depth is ~1-1. 20 cm.

2. MATERIAL AND METHODS

2.1 Soil Sample and Analysis

Surface soil sample (0-30 cm) was collected from the experimental farm on General Directorate of Agricultural Research, Tarsus-Mersin, Turkey. After collecting soil from the surface (0–30 cm), it was brought to a laboratory, air dried, ground to pass through a 2-mm sieve, and stored in plastic bags for analyses and pot experiments. The some initial physical and chemical properties of the soil used in pot experiment were measured with routine analytical methods. Soil organic matter was determined using the Walkley and Black method [21]. Soil particle size distribution was estimated by the hydrometer method after pre-treating soil with H_2O_2 and dispersing overnight in sodium hexametaphosphate by the hydrometer method [22]. The carbonate content was determined by a calcimeter method, and the soil pH was measured at 1:1 soil:water ratio [23]. The concentrations of *diethylenetriamine pentaacetic acid (*DTPA)-extractable Ni were estimated using the method described by [24]. Total Ni concentrations in soil sample were digested according to [25] Anonymous (1995) with aqua regia method using inductively coupled plasma mass spectrophotometer (ICP-MS, Agillent 7500ce). Certified reference material (CRM 7003) was also analyzed in order to control the data quality. All results were given in terms of mg Ni per kg soil. All tests were performed in triplicates.

2.2. Artificial Soil Contamination

Two kg air-dried soils were weighed and loaded into a plastic bags and were contaminated by nickel nitrate [$Ni(NO_3)_2 \cdot 6H_2O$] salt solution containing 0, 500, 1000, 1500 and 2000 mg Ni kg^{-1} onto it and spread uniformly on plastic sheet. Then, soil was thoroughly mixed to achieve uniformity with respect to metal spiking.

After contamination and mixing, soil was left on plastic sheet and allowed to equilibrate at room temperature for almost three months with frequent and thorough mixing and by adding distilled water to maintain water content in soil at 60% of water-holding capacity and to periodic alternating wetting and air-drying cycles.

2.3. Greenhouse Pot Experiments

Total 4 seeds were planted in plastic pots, each containing 2 kg soil supplemented with increasing supply of Ni (0, 500, 1000, 1500 and 2000 mg/kg soil) in the absence or presence of 10 mg EDTA per kg soil. Ethylendiaminetetraacetic acid was added in the form of Na_2EDTA ($C_{10}H_{14}N_2Na_2O_8.2H_2O$).

A basal treatment of 200 mg/kg N as $Ca(NO_3)_2$ and 100 mg/kg P as KH_2PO_4 was applied to all pots. After germination, the seedlings were thinned to 2 plants per pot. During this 60 days, soils in the pots were kept humid (~80% water holding capacity). After 60 days of growth in the greenhouse, only the shoots of the plants were harvested, and dried at 70 ^oC for the determination of dry matter production.

2.4. Plant Sampling and Analysis

The oven-dried shoot samples were first ground and digested using 2 mL 30% H_2O_2 and 5 mL 65% HNO_3 in sealed vessels of a microwave (MarsXpress) apparatus. The digested samples were then analyzed with ICP-MS for Ni. Certified reference materials (*SRM 1573A, SRM 1547*) were also used in order to check the accuracy of the extraction technique used in the study. All analyses were carried out in triplicates, and the results were presented in terms of mg Ni per kg biomass (DW) or µg Ni per plant biomass. In this study, Ni was choosen as target metal because phytoextraction efficiency is related to both plant metal concentration and dry matter yield. Thus, the ideal plant species to remediate a contaminated site should be a high yielding crop that can both tolerate and accumulate the target contaminants [26].

2.5. Statistical Analysis

All data collected were subjected to statistical analysis of variance (ANOVA), and t*wo-tailed t-tests* with *p*-values less than 0.05 were used for *statistical* comparison between averages.

3. RESULTS AND DISCUSSION

3.1. Some Initial Physical and Chemical Properties of the Soil Used in Pot Experiment

Some physical and chemical properties of the soil used in pot experiment are summarized in Table 1. The greenhouse pot experiments were performed using unpolluted agricultural soils with a clayey loam texture, a pH of 8.1, 26.2% $CaCO_3$ and 1.3% organic matter contents. The analysis of soils for total and DTPA-extractable Ni contents indicates Ni concentrations of 57.0 and 2.2 mg/kg soil, respectively.

In serpentine soils, Ni is not strongly held by clay and Fe-oxyhydroxide surfaces relative to other transition elements; consequently, Ni was more mobile than other metals in the serpentinitic landscape surrounding the study area. The soils derived from serpentine, displayed strong chemical fertility limitations due to a very low Ca/Mg ratio and limited available phosphorus [27]. Therefore, the application rate for 200 mg/kg N as $Ca(NO_3)_2$ and 100 mg/kg P as KH_2PO_4 amended in the study soil.

The total metal contents are much lower than the typical concentration ranges observed for unpolluted soils as set by the “Turkish Soil Contamination and Control Legislation”, and were under the critical value (100 mg/kg) according to KabataPendias [28].

Table 1. *Some initial physical and chemical properties of the soil used in pot experiment*

Parameters	**Tarsus Soil**
pH (1:2)	8.1
Organic Matter (%)	1.3
$CaCO_3$ (%)	26.2
Particle Size Distribution	
Sand (%)	41
Silt (%)	36
Clay (%)	23
Texture Class	Clay Loam (CL)
Total Ni (mg/kg)	57
DTPA Extractable Ni (mg/kg)	2.2

3.2. Effect of EDTA on Ni Toxicity and Plant Growth

Following Ni application, visual symptoms were also monitored throughout the experiments. The toxicity effects were observed based on plant growth, chlorosis, and necrosis symptoms of the plant. Although *Brassica rapa* did not exhibit any significant symptoms as observed in a typical Ni toxicity including chlorosis and necrosis, increasing Ni application led to a visual reduction in the growth of plants, especially in absence of EDTA.

Toxic effects of high concentrations of Ni in plants have been frequently reported as reductions in plant growth and adverse effects on fruit yield and quality ([2], [29]). Plants are known to tolerate metals to some extent, but high concentrations of available metals affect and induce disorders in the plant metabolism [30]. Plants can absorb and distribute metals internally in many different ways and may localize selected metals mostly in leaves and roots [31]. As a mechanism of metal tolerance or accumulation in plants, the response to metal stress is observed in both the leaves and roots. This response and accumulation of metals is more dependent on the type of metal rather than metal concentration [31].

Fig. 1 shows the effects of Ni and EDTA application on dry matter production (shoot) after 60 days of growth. Application of 2000 mg/kg Ni decreased dry matter production of *Brassica rapa*. But the addition of 10 mg/kg EDTA significantly increased the plant growth compared with the control. The addition of EDTA promoted an increase in DW by *Brassica rapa*, up to 74% in the shoots.

Especially the addition of 10 mg/kg EDTA and 500 mg/kg Ni produced fertilizer effect and maximum dry matter achieved to 1.96 mg/plant from 0.82 mg/plant. EDTA is a synthetic chelator. In this study, it has been studied in fairly low concentration against the possibility of damaging the soil structure. Increases in the doses of EDTA and DTPA applied increased the mobilization of heavy metals; however, environmental risk associated with synthetic chelators is consequently increased regardless of the EDTA and DTPA application rate under such saturation [27]. According to Chaturvedi *et al.* [32] considering the overall plant growth as it is highly essential for efficient phytoextraction we conclude that the low molecular weight organic acids (LMWOAs), such as citric acid, are a better and environmentally compatible alternative to synthetic chelators such as EDTA [32].

When our results are evaluated, we can conclude that EDTA is also used as a kind of plant micronutrient fertilizers**.** Because pot experiments data showing the effect of 10 mg/kg EDTA on soluble nickel levels at each of the soil concentrations would be benefical.

A two-sided t-test with *p*-values less than 0.05 confirmed that the EDTA application had a positive effect on plant growth. The findings obtained were in agreement with the results obtained by Alam *et al.* [33]-[35]. This reduction in yield parameters might be attributed to poor plant development and reduced photosynthesis as a consequence of reduction in photosynthetic pigments in the leaves of the Ni-treated plants which resulted in suppressed supply of nutrients and photosynthates to the reproductive parts that ultimately affected yield [36].

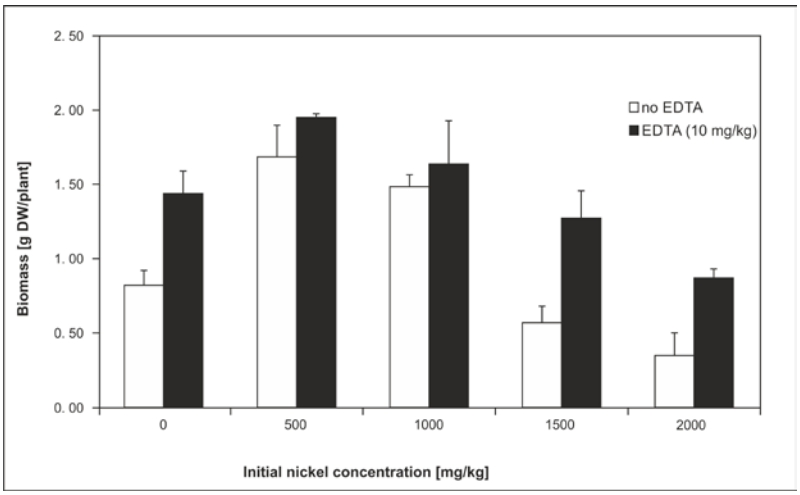

Fig. 1. *Effect of Ni and EDTA on dry matter production (shoot) of Brassica rapa.*

3.3. Effect of EDTA on Ni Concentration in Plant Shoots

The added EDTA remained most effective in increasing Ni accumulation in plants shoots and thus enhanced the phytoextraction [37]. The synthetic chelators EDTA was the most efficient amendments for increasing concentrations of Ni in soil solutions. In the present study, the concentrations of Ni in the soil solutions treated with EDTA were markedly higher than in the control soil.

As seen Figure 2 plots the Ni concentration in shoots in the control treatment and following the application of 0 and 10 mg/kg EDTA. Concentrations of Ni in the shoots of the control *Brassica rapa* varied between 23 and 61 mg/kg. This concentration according to Kabata and Pendias [28] was the pyhototoxic range of Ni (30 and 100 mg/kg). Experimental results indicate that the accumulation of Ni was significantly greater than those of control plants and the strong dependence of Ni concentration on initial Ni dose and EDTA concentration. *Brassica rapa* accumulated more Ni in the presence of EDTA. While *Brassica rapa* accumulated 3763 mg/kg Ni in the absence of EDTA, the addition of 10 mg/kg EDTA increased Ni accumulation to 3942 mg/kg at Ni application dose of 1500 mg/kg. (Fig.2) Experimental results indicated that applying 10 mg/kg EDTA could significantly increase the concentrations of Ni in the soil solution and remarkably enhance Ni accumulation in the shoots of *Brassica rapa*.

The addition of 10 mg/kg EDTA increased Ni uptake in the shoots from 61 mg/kg in the control to 3942 mg/kg. Shoots of *Brassica rapa* exceeded the Ni hyperaccumulation threshold value (>1000 mg/kg) according to the criteria described by [38]. Experimental results indicated that *Brassica rapa* is Ni hyperaccumulator plant (>1000 mg/kg in shoots) (Fig. 2). Nickel concentrations are >1000 mg/kg in shoots both the absence and presence of EDTA which these result confirm Ni hyperaccumulator of *Brassica rapa*. This result was higher than value reported Wenzel *et al.* [39] for *Brassica rapa*. Authors found that chelate effects were significant in the order EDDS > EDTA, control for *Brassica rapa and* EDDS enhanced only Ni content up to 10 mg/kg in *Brassica rapa* [40].

Chelating agents such as EDTA had positive effects on the enhancement of the bioavailability of heavy metals in soils, thereby increasing the amount of metals accumulated in the plants [41-43].

The amounts of metal removed from the soil via phytoremediation are affected by different factors. One important factor controlling the amount of Ni removed through phytoremediation is distribution of chemical forms of this metal in the soil. As the proportion of Ni in insoluble forms increased, the amount of Ni removed via phytoremediation

decrease [44]. The increase in Ni accumulation by plants can be explained through the formation of highly soluble and less toxic Ni-EDTA complexes. This finding is in agreement with the results obtained by Barona *et al*. Panwar *et al.* [45-46]. Nascimento *et al.* [47] reported that EDTA increased Ni concentration in plant shoots to maximum and is confirmed by high concentration of AB-DTPA-extractable Ni in the soil in EDTA treatment; this could be due to greater stability constants of Ni-EDTA.

Some investigations have used the *Brassica* species for phytoremediation of sites contaminated with heavy metals [11,14, 48]. But they have not examined the use of EDTA, to increase plant phytoextraction capacity. Kumar et al. [48] tested many fast growing Brassicas for their ability to tolerate and accumulate metals, including Indian mustard (*Brassica juncea*), black mustard (*Brassica nigra* Koch), turnip (*Brassica campestris* L.), rape (*Brassica napus* L.), and kale (*Brassica oleracea* L). Although all *Brassicas* accumulated metal, *Brassica juncea* showed a strong ability to accumulate and translocate Cu, Cr (VI), Cd, Ni, Pb, and Zn to the shoots. Kos *et al.* [49] studied that the Pb, Zn and Cd phytoextraction potential of 14 different plants including *Brassica rapa* was assessed in a chelate (as EDTA and ethylenediamine-disuccinic acid (EDDS) induced phytoextraction experiment. But they no study has been performed on this plant species to show whether the EDTA could efficiently improve its phytoextraction in Ni contaminated soil [6] (Muhammad *et al.* 2009).

Statistical analysis (two-sided t-test) ($p < 0.05$) indicates that the differences obtained for Ni concentration in the absence and presence of EDTA are statistically significant.

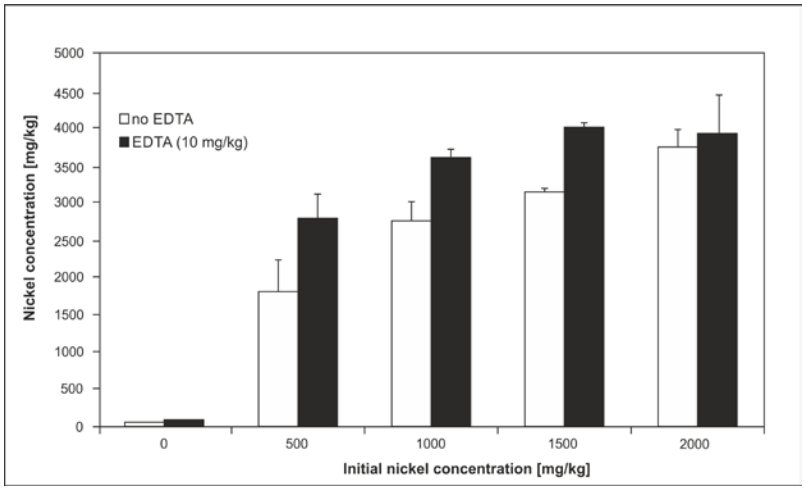

Fig. 2. *Effect of Ni and EDTA on shoot Ni concentration (mg/kg) of Brassica rapa.*

3.4. Effect of EDTA on Ni Content in Plant Shoots

Plant Ni content (µg/plant) was calculated as dry weight (mg/plant) multiplied by Ni concentration (mg/kg). The maximum Ni content by *Brassica rapa* was 4111 µg per plant in the absence of EDTA, the addition of 10 mg/kg EDTA increased Ni uptake to 5878 µg per plant at an initial Ni application of 1000 mg/kg. Wenzel *et al.* [39] (2003) reported that overall extracted mass per plant varied between 7and 50 µg in the control, between 29 and 135 µg in the EDTA treated pots, which were not consistent with the our study. The enhanced Ni accumulation in the presence of EDTA indicates the formation of less toxic Ni-EDTA complexes, which led to an increase in plant growth. Nickel content by plants reached a maximum at an initial Ni application of 1000 mg/kg, and then decreased sharply with increasing initial Ni level due to the fact that excess Ni reduced the biomass of plant (Fig. 1), thereby decreasing the amount of Ni accumulation. EDTA at selected concentration (10 mg/kg) increased uptake of the heavy metals from the soils it also resulted in low plant biomass. Greater biomass production is a desired parameter for plants being used for phytoextraction so that these plants can extract more amounts of heavy metals from the soil. A decrease in biomass production might be due to increased metal uptake because of the destruction of the physiological barrier by these acids in roots, which controls the uptake of solutes [37] (Sabir *et al.* 2014).

In a study carried out Wu *et al.* [26] has shown EDTA increased shoot Cu and Pb concentrations in Indian mustard (*Brassica juncea*) plants growing in the soil. There were no visible symptoms of heavy metal toxicity in Indian mustard during germination and growth. However, 2–4 days after EDTA addition into the soil there were numerous brown dots on the leaves, and the whole leaf became yellow and died slowly, indicating phytotoxicity of EDTA metals [26].

These findings are consistent with the results of present study. In our study, after Ni content in plants reached 1000 mg/kg, it was observed that biomass of plant was decreasing sharply with increasing initial Ni concentration.

The correlation analyses were performed between Ni content and the plant growth and correlation was much stronger ($r > 0.95$, $p < 0.01$). This strong correlation can be explained through much higher affinity of *Brassica rapa* to accumulate Ni species as shown in Fig. 3. The enhanced Ni accumulation in the presence of EDTA indicates the formation of less toxic Ni-EDTA complexes, which led to an increase in plant growth (Fig. 1), thereby increasing both Ni tolerance and capacity for Ni transport to the shoot [50].

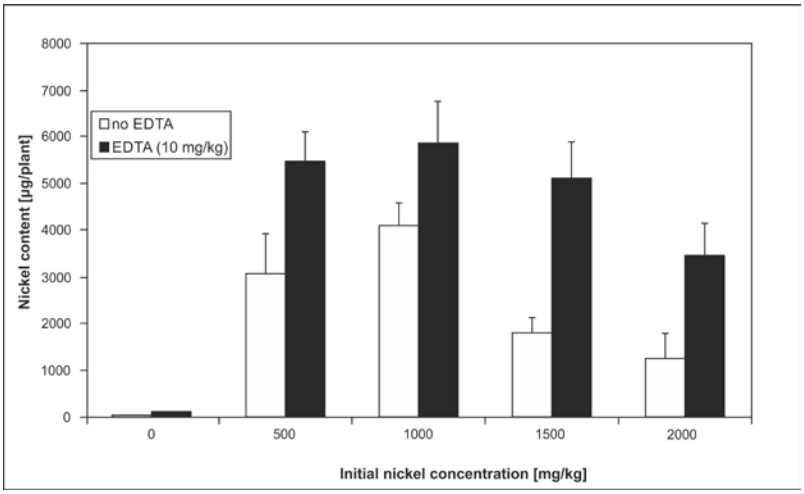

Fig. 3. *Effect of Ni and EDTA on Ni uptake by Brassica rapa plotted in terms of initial nickel dose versus shoot Ni content (µg/plant).*

According to Laurie *et al*. [51] and Molas and Baran [35], there are mainly two different patways for the uptake of metal ions from contaminated soils. The first path involves the transport of free metal ion (M^{2+}) to cell root across plasmalemma following the dissociation of metal-ligand complex in the diffuse layer. The second pathway, on the other hand, involves the absorption of metal-ligand complex by root cell membrane where the metal-ligand complex is either transported to root cells across plasmalemma, or dissociated in the cell membrane; free metal is then transported to cell, and the ligand goes back to solution [52] (Wang *et al.* 2007). Here, the increase in Ni uptake in the presence of EDTA may be explained through a mechanism similar to the second pathway mentioned above. Molas and Baran [35] suggests that Ni is absorbed by plants in the form of a free ion rather than a Ni-ligand complex.

3.5 Biological accumulation coefficient (BAC)

In addition to total Ni concentration and content, the BAC needs to be considered while evaluating hyperaccumulators. The BAC commonly used commonly to evaluate metal accumulating capacity of plants relative to the degree of soil contamination [53]. According to the criteria described by Brooks [38] to define hyperaccumulators, bioaccumulation coefficient (ratio of metal concentration in plant to soil) is greater than 1. Biological accumulation coefficient (BAC) was defined as the concentration of heavy metals in plant shoots divided by the heavy metal concentration in soil [BAC = [Metal] $_{shoot}$ / [Metal] $_{soil}$] [54] and indicate the ability of plants to tolerate and accumulate heavy metals.

The bioaccumulation coefficients of Ni in *Brassica rapa* growing in a artifically contaminated soil are shown in Table 2. *Brassica rapa* was between 1.9 and 5.6 for Ni, providing further evidence for the transport of Ni from Ni contaminated soils to plant shoots. Adding 10 mg/kg EDTA significantly increased the bioaccumulation coefficient of Ni in *Brassica rapa* shoots (Table 2). This information confirm also Ni hyperaccumulation of *Brassica rapa.*

,

Table 2. *Bioaccumulation coefficients of Ni in Brassica rapa growing in a artifically contaminated soil*

Application (mg/kg)		**Bioaccumulation Coefficient**
Ni	**EDTA**	
500	0	3.6
1000	0	2.8
1500	0	2.1
2000	0	1.9
500	10	5.6
1000	10	3.6
1500	10	2.7
2000	10	2.0

4. CONCLUSION

Greenhouse experiment was carried out to evaluate the potential for phytoextraction of Ni,

with or without with the use of EDTA. Nickel hyperaccumulation was defined by [38] Brooks *et al.* (1989) as the accumulation of at least 1000 mg/kg Ni in the dry biomass of plants grown on a natural substrate. As indicated in the results, the pot experiment conducted with contaminated soils indicated that *Brassica rapa* had the capability to accumulate high levels of Ni. Ethylenediaminetetraacetic acid is a good chelating agent for enhancing phytoextraction of Ni by *Brassica rapa*, especially when 10 mg/kg EDTA is applied, because it exceeded the threshold value (1000 mg/kg) as a Ni hyperaccumulator [11, 55-56] (Baker and Brooks 1989; Alkorta *et al.* 2004; Gupta *et al.* 2011). Moreover, the BAC value were 1.9 and 5.7, respectively, which were higher than 1 with or without with the use of EDTA. Therefore, *Brassica rapa* might be useful for the remediation of soil contaminated with Ni. Since *Brassica rapa* is fast and easy growing a agronomic crop plant. In recent years, *Brassica rapa* is seen as a key and strategic crop for raw material supply in the biodiesel (green diesel) industry throughout the world and Turkey [20,57] (Baydar 2005; Mahasi and Kamundia, 2007). Therefore, the distribution of the accumulated Ni within the plant and whether the transport to *Brassica rapa* seeds of Ni should be also study in the future.

ACKNOWLEDGMENTS

This research was supported by a grant from General Directorate of Agricultural Research (GDAR), Project No: TAGEM/TA/05320C01.

REFERENCES

[1]. S. P. McGrath, E. Lombi, C. W. Gray, N. Calille, S. J. Dunham and F. J. Zhao, Field evaluation of Cd and Zn phytoextraction potential by the hyperaccumulators *Thlaspi caerulescens*and *Arabidopsis halleri*. Environ Poll 141:15-125, 2006.

[2]. C. Chen, D. Huang and J. Liu, Functions and toxicity of nickel in plants: recent advances and future prospects. Clean 37:304–313, 2009.

[3]. I.E. Akinci and U. Caliskan Effect of Lead on Seed Germination and Tolerance Levels in Some Summer Vegetables. Ecology 19(74): 164-172, 2010.

[4]. M. S. Abdullahi, A. Uzairu , G. F. S. Harrison, M. L. Balaraabe and O. J. Okunola, Comparative study of tomatoes and onions from irrigated farmlands on the bank of river Challawa, kano, Nigeria. Int J Environ Res 2(1): 65- 70, 2007.

[5]. M. S. Abdullahi, A. Uzairu and O. J. Okunola, Quantitative determination of heavy metal concentration in onion leaves. Int J Environ Res 3(2): 271-274, 2009.
[6]. D. Muhammad, F. Chen, J. Zhao, G. Zhang and F. Wu, Comparison of EDTA- and citric acid-enhanced phytoextraction of heavy metals in artificially metal contaminated soil by *Typha angustifolia.* Int J Phytoremediat 11(6): 558-574, 2009.
[7]. G. Garg and S. .K. Kataria, Phytoremediation potential of *Raphanus sativus* (L.), *Brassica juncea* (L.) and *Triticum aestivum* (L.) for copper contaminated soil. E-Proceedings of International Society of System Sciences, Univertity of Queensland, Brisbane (Australia), July 12-17, 2010.
[8]. S. Greipsson, Phytoremediation. Nature Education Knowledge, 2(1): 7, 2011.
[9]. D. Aydin and O. F. Coskun, Effects of EDTA on Cr^{+3} Uptake, Accumulation, and Biomass in *Nasturtium officinale* (Watercress). Ecology 22 (87): 16-23, 2013.
[10]. J. W. Huang, J. J. Chen, W. R. Berti and S. D. Cunningham, Phytoremediation of lead contaminated soils: role of synthetic chelates in lead phytoextraction. Environ Sci Technol 31:800–805, 1997.
[11]. A. Gupta, S. Shaw-Wei and C. Zueng-Sang, Heavy-metal bioavailability and chelate mobilization efficiency in an assisted phytoextraction process by *Sesbania sesban* (L.) Merr, Commun Soil Sci Plant Anal 42 (2): 231-245, 2011.
[12]. D. E. Salt, R. D. Smith and L. Raskin, Phytoremediation. Annu Rev *Plant* Biol 49(1): 643-668, 1998.
[13]. M. N. V. Prasad and H. Freitas, Metal hyperaccumulation in plants-Biodiversity prospecting for phytoremediation technology. Electron J Biotechn 6:275-321, 2003.
[14]. M. Jahangir, I. B. Abdel-Farid, Y. H. Choi and R. Verpoorte, Metal ion-inducing metabolite accumulation in *Brassica rapa.* J Plant Physiol. 165(14): 1429-37, 2008.
[15]. T. J. Purakayastha, T. Viswanath, S. Bhadraray, P. K. Chhonkar, P. P. Adhikari and K. Suribabu, Phytoextraction of zinc, copper, nickel and lead from a contaminated soil by different species of Brassica. Int J Phytoremediat 10 (1):61-72, 2008.
[16]. H. Grčman, S. Velikonja-Bolta, D. Vodnik, B. Kos and D. Lestan, EDTA enhanced heavy metal phytoextraction: metal accumulation leaching and toxicity. Plant Soil 235:105–114, 2001.
[17] M. Putnic-Delic, I. Maksimovic, I. Gani-Novakovic, T. Zeremski and A. M. Jeromela, The Effect of Ni on Concentration of The Most Abundant Essential Cations In Several Brassica Species. Jour Nat Sci 126: 15-23, 2014.
[18]. G. A. Meindl, D. J. Bain and T. L. Ashman, Nickel accumulation in leaves, floral organs and rewards varies by serpentine soil affinity. AoB PLANTS 6, plu036;, 2014.
[19]. N. Koleli, A. Demir, M. Eke and O. Cakmak, Accumulation of Heavy Metals in Some Plants Grown on Serpentine Soils of Mersin-Turkey. Oral presentation, 2nd International Symposion on Sustainable Development (ISSD'2010), 8-9 June, Sarajevo, 2010, pp. 499-507, ISBN:978-9958-9965-7-3.Sarajevo, 2010.
[20]. M. J. Mahasi and J. W. Kamundia, Cluster analysis in rapeseed (*Brassica napus* L.). Afr J Agric Res 2 (9):409-411, 2007.
[21]. D. W. Nelson and L. E. Sommers, Total carbon, organic carbon, and organic matter. In: Page AL, Miller RH, Keeney DR, eds. Methods of Soil Analysis. Part 2. Chemical and Microbiological Properties. 2nd ed. Madison (WI): Agronomy Monograph, p. 539–577, 1982.
[22]. G. J. Bouyoucous, Hydrometer method improved for making particle size analysis of soil. Agron J 54 (5):466- 465, 1952.
[23]. E. O. McLean, Soil pH and lime requirement. In: Page AL, Miller RH, Keeney DR, eds. Methods of soil analysis. 2nd ed. Madison, (WI): Agronomy Monograph p. 595-624, 1982.
[24]. W. L. Lindsay, and W. A. Norvell, Development of DTPA soil test for zinc, iron, manganese and copper. Soil Sci Soc Am J 42:421–448, 1978.
[25]. Anonymous, Soil quality, extraction of trace elements soluble in aqua regia, DIN ISO 11466, Berlin, Germany, 1995.
[26]. L. H. Wu, Y. M. Luo, X. R. Xing and P. Christie, EDTA-enhanced phytoremediation of heavy metal contaminated soil with Indian mustard and associated potential leaching risk. Agric. Ecosyst. Environ. 102: 307–318, 2004.
[27]. Z. Y. Hseu, Concentration and distribution of chromium and nickel fractions along a serpentinitic toposequence. Soil Sci 171: 341–353, 2006.
[28]. A. Kabata-Pendias, Trace elements in soils and plants. 3nd edition, Boca Raton, USA, 2001.
[29]. H. Daghan and N. Koleli, Comparative Evaluation of Transgenic and Non Transgenic Tobacco for the Phytoextraction of Nickel-Contaminated Soils. Ecology 21(84): 90-97, 2012.
[30]. T. R. Guo, G. P. Zhang, Y. H. Zhang, Physiological changes in barley plants under combined toxicity of aluminum, copper and cadmium. Colloids Surf. B. 57, 182–8, 2007.
[31]. A. R. Memon, D. Aktoprakligul, A. Zdemur and A. Vertii, Heavy metal accumulation and detoxification mechanisms in plants. Turk. J. Bot. 25:111–21, 2001.
[32]. N. Chaturvedi, N. K. Dhal and H. K. Patra, EDTA and citric acid-mediated phytoextraction of heavy metals from iron ore tailings using Andrographis paniculata: a comparative study. Int. J. Min. Reclam. Env. 29(1): 33-46, 2015.
[33]. M. G. M. Alam, S. Tokunaga and F. Stagnitti, Removal of arsenic from contaminated soils using different salt extractants. J Environ Sci Health Part A 42 (4): 447-451, 2007.
[34]. P. M. Kopittke, C. J. Asher and N. W. Menzies, Toxic effects of Ni^{2+} on growth of cowpea (*Vigna unguiculata*). Plant and Soil 292:283-289, 2007.
[35]. J. Molas and S. Baran, Relationship between the chemical form of nickel applied to the soil and its uptake and toxicity to barley plants. Geoderma 122:247-255, 2004.
[36]. M. S. Ahmad, M. Hussain, R. Saddiq and A. K. Alvi, Mung Bean: A nickel indicator, accumulator or excluder? Bull Environ Contam Toxicol 78(5): 319-24, 2007.
[37]. M. Sabir, M. M. Hanafi, M. Zia-Ur-Rehman, H. R. A. Saifullah, K. R. Hakeem and T. Aziz, Comparisonof Low-Molecular-Weight Organic Acids and Ethylenediaminetetraacetic Acid to Enhance Phytoextraction of Heavy Metals by Maize. Commun Soil Sci Plant Anal 45(1): 42-52., 2014.

[38]. R. R. Brooks, Plants that Hyperaccumulate Heavy Metals: Their Role in Phytoremediation, Microbiology, Archaeology Mineral Exploration and Phytomining. CAB International, Wallingford, UK, 380 p, 1998.

[39]. W. W. Wenzel, R. Unterbrunner, P. Sommer and P. Sacco, Chelate assisted phytoextraction using canola (*Brassica rapa* L.) in outdoors pot and lysimeter experiments. Plant Soil 249:83-96, 2003.

[40]. E. Meers, A. Ruttens, M. Hopgood, E. Lesage and F. M. G. Tack , Potential of *Brassica rapa*, *Cannabis sativa*, *Helianthus annuus* and *Zea mays* for phytoextraction of heavy metals from calcareous dredged sediment derived soils. Chemosphere 61:561-572, 2005.

[41]. H. Y. Lai and Z. S. Chen, The EDTA effect on phytoextraction of single and combined metals-contaminated soils using rainbow pink (*Dianthus chinensis*). Chemosphere 60:1062-1071, 2005.

[42]. C. Luo, Z. Shen and X. Li, Enhanced phytoextraction of Cu, Pb, Zn and Cd with EDTA and EDDS. Chemosphere 59:1–11, 2005.

[43]. L. Jean, F. Bordas, C. Gautier-Moussard, P. Vernay, A. Hitmi and J. C. Bollinger, Effect of citric acid and EDTA on chromium and nickel uptake and translocation by *Datura innoxia*. Environ. Pollut. 153: 555-563, 2008.

[44]. B. H. Robinson, R. R. Brooks, P.E. H. Gregg and J. H. Kirkman, The nickel hytoextraction potential of some ultramafic soils as determined by sequential extraction. Geoderma. 87: 293–304, 1999.

[45]. A. Barona, I. Aranguiz and A. Elias, Metal associations in soils before and after EDTA extractive decontamination: implications for the effectiveness of further clean-up procedures. Environ Pollut 113:79-85, 2001.

[46]. B. S. Panwar, K. S. Ahmed and S. B. Mittal, Phytoremediation of nickel-contaminated soils by *Brassica* species. Environ Dev Sustain, 4:1-6.

[47]. C. W. A. Nascimento and B. Xing, Phytoextraction: A review on enhanced metal availabilityand plant accumulation. *Scientia Agriculture* 63, 299–311, 2006.

[48]. N. P. B. A. Kumar, V. Dushenkov, H. Motto and I. Raskin, Phytoextraction: The use of plants to remove heavy metals from soils. Environ Sci Technol 29:1232-1238, 1995.

[49]. B. Kos, H. Grčman and D. Lestan, Phytoextraction of lead, zinc and cadmium from soil by selected plants. Plant Soil and Environ 49(12):548–553, 2003.

[50]. J. Agrawal , I. Sherameti and A. Varma Detoxification of heavy metals: State of art. In: Sherameti I, Varma A, eds. Detoxification of heavy metals. Germany: Springer-Verlag. p.1-34. 2011.

[51]. S. H. Laurie, N. P. Tancock, S. P. McGrath and J. R. Sanders,Influence of complexation on the uptake by plants of iron, manganese, cooper and zinc: II. Effect of DTPA in a multi-metal and computer stimulation study. J Exp Bot 42(4):515–519, 1991.

[52]. H. Wang, X. Shan, T. Liu, Y. Xie, B. Wen, S. Zhang, F. Han and M. Van Genuchten, Organic acids enhance the uptake of lead by wheat roots. Planta 225:1483–1494, 2007.

[53]. M. Rafati, N. Khorasani, F. Moattar, A. Shirvany, F. Moraghebi and S. Hosseinzadeh, Phytoremediation potential of *Populus alba* and *Morus alba* for cadmium, chromium and nickel absorption from polluted soil. Int J Environ Health Res 5(4): 961-970, 2011.

[54]. Y. Q. Zu, Y. Li, J. J. Chen, H. Y. Chen, L. Qin and C. Schvartz, Hyperaccumulation of Pb, Zn and Cd in herbaceous grown on lead-zinc mining area in Yunnan, China. Environ Int 31: 755-762, 2005.

[55]. A. J. M. Baker and R. R. Brooks, Terrestrial higher plants which hyperaccumulate metallic elements-a review of their distribution, ecology and phytochemistry. Biorecovery 1:81-126, 1989.

[56]. I. Alkorta, H. Hernandez-Allica, J. M. Becerril, I. Amezaga, I. Albizu and C. Garbisu, Recent findings on the phytoremediation of soils contaminated with environmentally toxic heavy metals and metalloids such as zinc, cadmium, lead, and arsenic. Rev Environ Contam Toxicol 3:71–90, 2004.

[57]. H. Baydar, Yield and quality properties of canola (*Brassica rapa* L.) cultivars under Isparta condition. Dissertation, University of Suleyman Demirel, 2005.

ICENS
INTERNATIONAL CONFERENCE ON ENGINEERING AND NATURAL SCIENCES
24-28 May 2016 /Sarajevo

A Posision Model Evaluation of Earthquake Hazard Parameters for the East Anatolian Fault

Tugba Turker[1], Yusuf Bayrak[2]

Abstract

The purpose of this study; The East Anatolian Fault (EAF) estimated earthquake hazard parameters using the Poisson model in the between years 1900-2015. Firstly, for this purpose, the EAF divided into 5 seismic source regions with tectonic structure and focal mechanism solutions and epicentral distribution of occurrence earthquakes. The 5 different seismic source regions determined the relationships between the cumulative number-magnitude which estimated a and b parameters using the equation of LogN=a-bM in the Gutenberg-Richter. Later, annual occurring the number of earthquakes and return periods of occurring earthquakes estimated for the next 5, 10, 20, 50 and 100 years with Poisson model. A homogenous earthquake catalog for M_s magnitude equal or larger 3.5 prepared in the period between 1900 and 2015. The probabilities of the earthquake occurring estimated for the next 10, 20, 30, 40, 50, 60, 70, 80, 90 and 100 years in the 5 different seismic source regions. The chi-square test applied to Poisson model determined as $\alpha=0.05$ in this study. The highest earthquake occurs probabilities estimated into 5 different seismic source regions in the next years. According to, the computed earthquake hazard parameters, the most dangerous region was the Bingöl-Karlıova (Region 1) and this region estimated that %89 with an earthquake occur probability for a magnitude 6 which the return period 44.9 year, %70 with an earthquake occur probability for a magnitude 6.5 which the return period 83.9 year, %47 with an earthquake occur probability for a magnitude 7 which the return period 157 year.

Keywords: *The East Anatolian Fault, Earthquake hazard, Poisson model*

1. INTRODUCTION

In southern Turkey ongoing differential impingement of Arabia into the weak Anatolian collisional collage resulting from subduction of the Neotethyan Ocean has produced one of the most complex crustal interactions along the Alpine–Himalayan Orogen (Tatar et al. 2004). The East Anatolian Fault consisted from left-lateral strike slip fault which extended the south westward from the triple combination of the intersection with the North Anatolian Fault Zone and Maraş around created a triple junction combined with Türkoğlu and extended up to Türkoğlu. The EAF is one of the most important faults in and around Turkey.

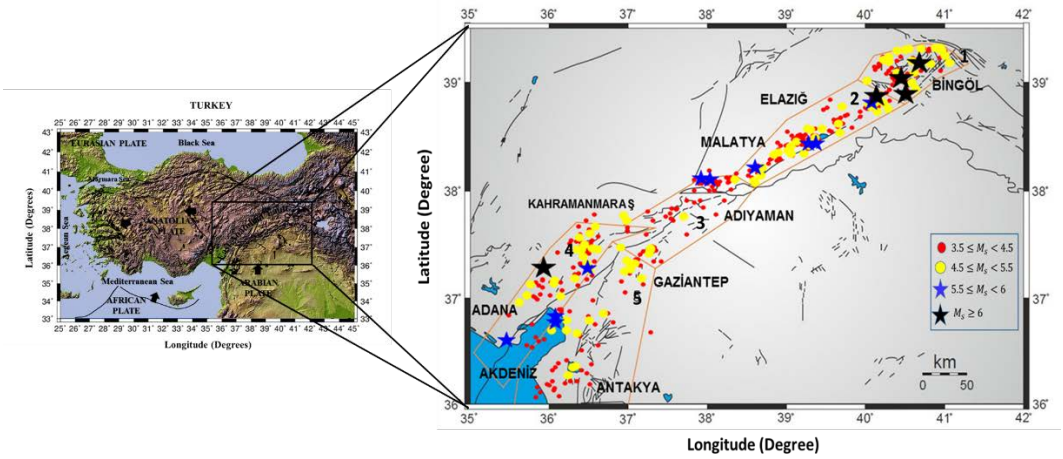

[1] *Corresponding author: Karadeniz Technical University, Department of Geophysical Engineering, Trabzon/Turkey.* tturker@ktu.edu.tr

[2] *Ağri Ibrahim Ceçen University, Ağri/Turkey* ybayrak@agri.edu.tr

Figüre 1. The EAF for Ms≥ 3.5 earthquakes between 1900-2015 years are divided into 5 different seismic source regions with epicenter distribution of formed earthquakes in the instrumental period, focal mechanism solutions, and existing tectonic structures (Right figure). The EAF is demonstrated on Turkey map (Left figure).

2. DATA AND METHOD

In this study; is used the instrumental earthquake catalog by Bayrak et al. (2009). A homogenous earthquake catalog for M_s magnitude which is equal or larger than 3.5 is used for the time period between 1900 and 2015. The catalogs contain the origin time, different magnitudes scales (M_b-body wave magnitude, M_S-surface wave magnitude, M_L-local magnitude, M_D-duration magnitude, and M_W-moment magnitude), epicenter and depth information of earthquakes. The database of catalog used in the study has been created from International Seismological Center (ISC) and Boğazici University Kandilli observation and earthquake research institute (KOERI). The earthquake data were obtained until from 1900 to 1974 from KOERI and ISC until from 1974 to 2015 from KOERI.

We divided into 5 different seismic source regions with tectonic structure and focal mechanism solutions and epicentral distribution of occurrence earthquakes in the EAF. The Region 1 (Bingöl-Karlıova) was the Karlıova Triple Junction, the Region 2 (between Pütürge-Palu) was the Elazığ-Malatya, the Region 3 (Tut and Sürgü Faults) was the Adıyaman-Kahramanmaraş, the Region 4 (Karataş-Osmaniye Faults) was the Adana and the Region 5 (between Kırıkhan-Islahiye) was the Gaziantep-Antakya that taken into the regions. The 5 different seismic source regions shown in Figure 1 are defined to study earthquake hazard parameters of EAF.

The 5 different seismic source regions determined the relationships between the cumulative number-magnitude which estimated a and b parameters using the equation of LogN=a-bM in the Gutenberg-Richter and are shown in Figure 2. The earthquake parameters are estimated for the 5 different seismic source regions of the EAF and shown in Table 1.

3. POISSON MODEL

The Poisson method used one of the most commonly models to estimate the earthquake occurrences. According to the Poisson model wasn't affected since passing time by the formation of a previous earthquake, distribution of waiting time by the formation of the a next earthquake (Özdemir et. al. 2000). The Poisson model is especially important for large earthquakes.

The earthquake hazard parameters for investigated area with the Poisson model were calculated using different equations.

$a' = a - \log(b*\ln 10)$ (1)

$a_1 = a - \log T$ (2)

$a_1' = a' - \log T$ (3)

T in this equation shows period for the next years and calculated for 100 years. The normal frequency value is used for determining of the earthquake risk which is shown by the following equation.

$$N(M) = 10^{a_1' - b*M}$$ (4)

N(M) value indicates annual average the number occurring of earthquakes and has been calculated according to the seismic parameters.

$$R(M) = 1 - e^{-N(M)*T}$$ (5)

T value in this model is more different than other models and used to calculate of the earthquake occurring risk.

The return periods according to the Poisson method is calculated for the next years using the following equation.

$$Q(M) = \frac{1}{N(M)}$$ (6)

The earthquake hazard parameters are computed occurrence probabilities of the different magnitude earthquakes and return periods, earthquake risks (%) for the 5 different seismic source regions of the EAF and shown in Figures 3, 4 and 5.

4. RESULTS

The b values which is one of the most important earthquake hazard parameters are estimated with Poisson method for the 5 different seismogenic source regions of the EAF. The map of estimated b values is plotted. The highest b value is observed in the Tut ve Sürgü Faults region. The lowest b value is observed in the Bingöl-Karlıova.

The a/b values are estimated with Poisson method for 5 different seismogenic source regions of the EAF. The map of estimated a/b values is plotted. The highest b value is observed in region 5 covering the Bingöl-Karlıova. The lowest b value is observed in the Tut ve Sürgü Faults region.

The annual occurring the number of earthquakes and return periods of occurring earthquakes are estimated for the next 5, 10, 20, 50 and 100 years with Poisson model. The probabilities of the earthquake occurring are estimated for the next 10, 20, 30, 40, 50, 60, 70, 80, 90 and 100 years in the 5 different seismic source regions. The chi-square test applied to Poisson model determined as α=0.05 in this study.

The highest earthquake occurs probabilities estimated into 5 different seismic source regions in the next years. According to, the computed earthquake hazard parameters, the most dangerous region was the Bingöl-Karlıova (Region 1) and this region estimated that %89 with an earthquake occur probability for a magnitude 6 which the return period 44.9 year, %70 with an earthquake occur probability for a magnitude 6.5 which the return period 83.9 year, %47 with an earthquake occur probability for a magnitude 7 which the return period 157 year.

In the past, Bayrak and Türker (2015) is estimated an earthquake occurrence probability (in the next 100 years) in region Bingöl-Karlıova using the Bayesian method for the EAF. In this study, we are estimated the same of results. Both the Bayesian method and the Poisson method are estimated an earthquake occurrence probability with most probably in the region Bingöl-Karlıova for the next 100 years in the EAF.

Table 1. The earthquake hazard parameters are estimated for 5 different seismic source regions on the EAF.

Region	**Region Name**	**a**	**b**	**σ_b**	**a/b**	**a'**	**a_1**	**a_1'**
1	Bingöl-Karlıova	3.71	0.544	0.07	6.82	3.61	1.71	1.61
2	Between Pütürge-Palu	4.47	0.693	0.07	6.45	4.26	2.47	2.26
3	Tut ve Sürgü Faults	4.56	0.824	0.1	5.53	4.81	2.56	2.81
4	Karatas-Osmaniye Faults	3.99	0.596	0.05	6.69	3.85	1.99	1.85
5	Between Kırıkhan-Islahiye	4.60	0.741	0.08	6.21	4.36	2.60	2.36

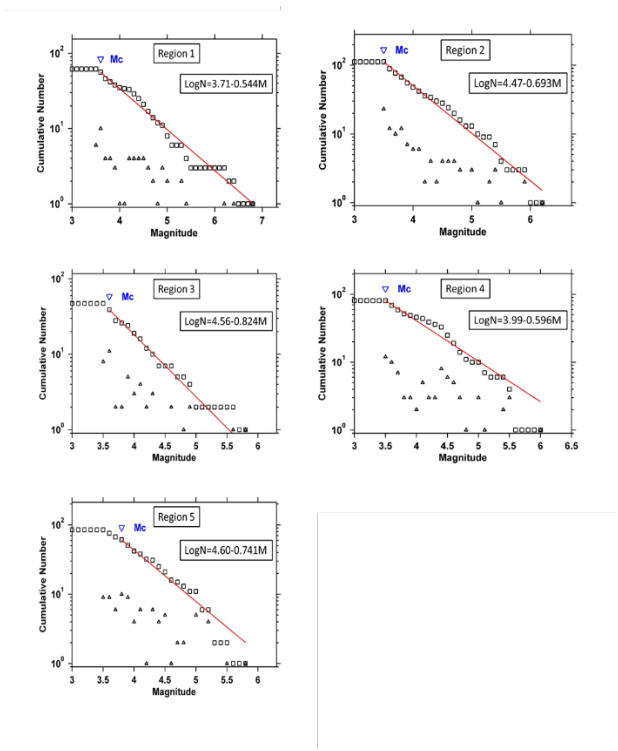

Figüre 2. The Magnitude-Frequency (Gutenberg-Richter) relationships are shown for occurring earthquakes on the EAF. The overall catalog plotted is both the cumulative (squares) and noncumulative form (triangles) in frequency magnitude distribution.

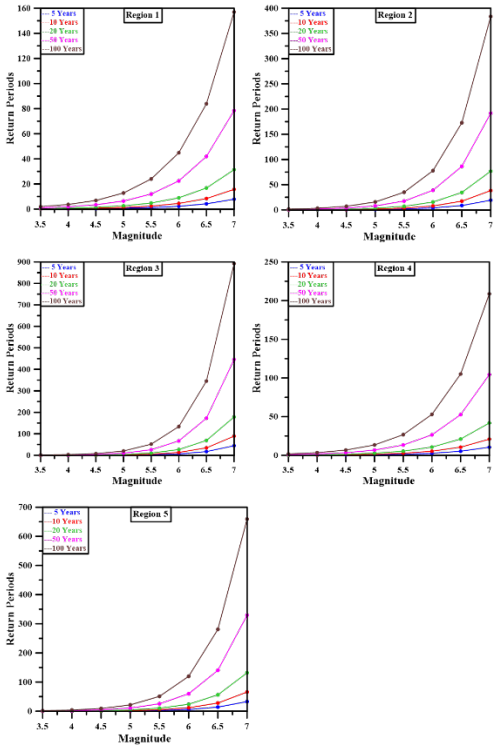

Figüre 3. The 5 different seismic source regions of the EAF are estimated the return periods for next 5, 10, 20, 50 and 100 years.

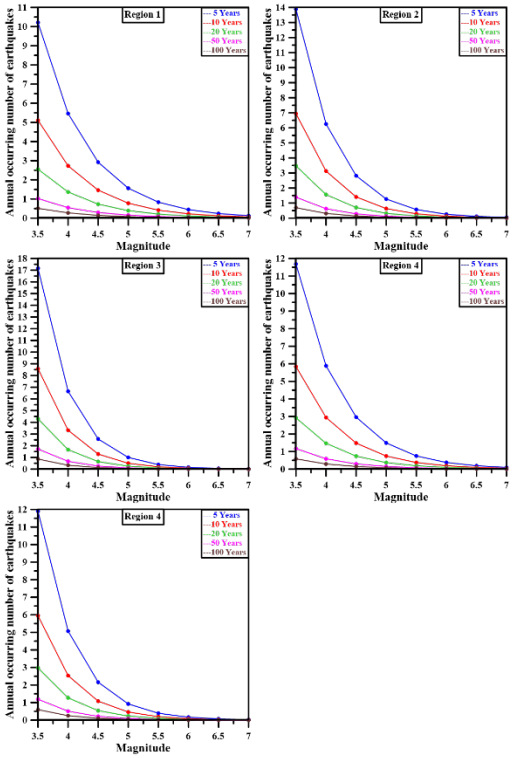

Figüre 4. The 5 different seismic source regions of the EAF are estimated the annual occurring number of earthquakes for next 5, 10, 20, 50 and 100 years.

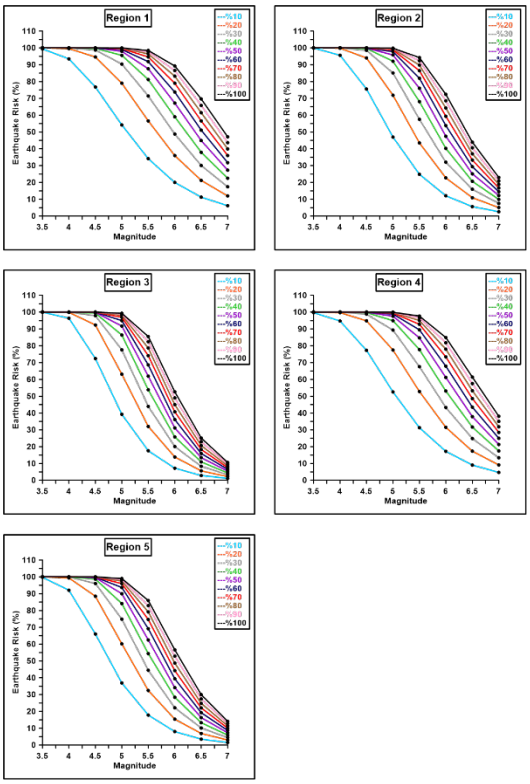

Figure 5. The 5 different seismic source regions of the EAF are estimated the earthquake risk (%) for next 10, 20, 30, 40, 50, 60, 70, 80, 90 and 100 years.

ACKNOWLEDGMENT

We acknowledge GMT program, are used for plotting of epicenter distribution of the earthqukaes. The computer program, the earthquake hazard parameters were calculated with MATLAB.

REFERENCES

[1]. F. Özdemir, A. Necioğlu, and G. Bağcı, Jeofizik, JFMO Yayını **14**, 1-2, 2000.
[2]. T. Türker and Y. Bayrak, "Assessment with Bayesian method of earthquake hazard parameters for East Anatolian Fault", (Genç Yerbilimciler Kongresi). 366-367, 2015.
[3]. O. Tatar, J. D. A. Piper, H. Gürsoy, A. Heimann, F. Koçbulut, "Neotectonic deformation in the transition zone between the Dead Sea Transform and the East Anatolian Fault Zone, Southern Turkey: a palaeomagnetic study of the Karasu Rift Volcanism, Tectonophysics, 385, 17-43, 2004.
[4]. Y. Bayrak, S. Öztürk, H. Çinar, D. Kalafat, T. M. Tsapanos, G. CH. Koravas, and G. A. Leventakis, "Engineering Geology", **105**, 200-210, 2009.

ICENS
INTERNATIONAL CONFERENCE ON ENGINEERING AND NATURAL SCIENCES
24-28 May 2016 /Sarajevo

A Conceptual Design of a Rotary Cup Atomizer and a Fluidized Bed for Dry Granulation of Molten Slag in Iron-Steel Industry

***Semih Akin*[1], *Yusuf A.Kara*[2]**

Abstract

Iron-steel industry, the milestone of the international economy, has showed tremendous improvements in energy efficiency in the last decades especially developing new methods for heat recovery. Particularly, molten slag, as kind of by-product during iron steel making process, has attracted the attention since it is exhausted critically high temperature (1450-1550 °C) and seen a potential resource of e
recovery methods like water quenching effects heat recovery efficiency negatively, and also it consumes a huge amount of water and harms to environment. Due to these reasons, different heat recovery technologies based on dry granulation have been proposed in many researches. These technologies divide into two groups as physical methods and chemical methods. In this study, rotary cup atomizer (RCA) technology as a physical method is evaluated, its mechanism is revealed and a RCA design for dry granulation is performed. In addition, a conceptual design of a fluidized bed is proposed in order to provide a sensible heat recovery from molten slag by using RCA granulation method.

Keywords: *Dry Granulation, Energy Efficiency, Iron-Steel Industry, Molten Slag, Rotary Cup Atomizer, Waste Heat Recovery*

1. INTRODUCTION

Iron and steel industry is the milestone of global economy. In the last decades, iron and steel industry has showed a remarkable development. According to World Steel Association, total crude steel production has reached to approximately 1.6 million tons by 2015 [1]. However, the iron-steel industry is the most energy consuming industry, which consumes nearly 4-5% of total world energy consumption [2]. Due to the fact that iron and steel industry consumes tremendous amount of energy, it is the leading industry which many waste heat recovery studies are intensively done. As shown in Figure 1, high temperature waste heat in iron and steel industry is mainly stored in the products, molten slag and waste gas. As it can be seen from the Figure 1, considerable amount of waste heat energy is stored in molten slag. Molten slag is a kind of by-product which occurs during the steel production process and it is exhausted in critically high temperature. Thanks to this characteristic feature, molten slag carries a great deal of heat energy which is nearly 10% of waste energy in steel industry and %35 of total high-temperature waste heat [2]. Although molten slag carries a substantial amount of high quality thermal energy, this energy is usually not recovered. Because, molten slag is also used as feedstock for cement production and this can be only provided when the internal structure of slag has more than 90% glassy-phase and this problem can be achieved by rapid cooling [3].

Nowadays, conventional water quenching method is used to reach this glassy phase ratio. On the other hand, water granulation method has several drawbacks. Firstly, it consumes huge amount of water. This method consumes 1.0-1.2 ton water for granulating 1 ton slag. Secondly, in this method most of sensible heat is wasted. Thirdly, it brings along an important pollution. Because, during the granulation process, sulfur dioxide and other sulfur compounds emit. Finally, water granulation method requires additional energy for drying up the slag particles [2].

[1] *Corresponding author: Bursa Technical University, Department of Mechanical Engineering, 16330, Yıldırım/Bursa, Turkey.* *semih.akin@btu.edu.tr*

[2] *Bursa Technical University, Department of Mechanical Engineering. Bursa, Turkey* *yusufali.kara@btu.edu.tr*

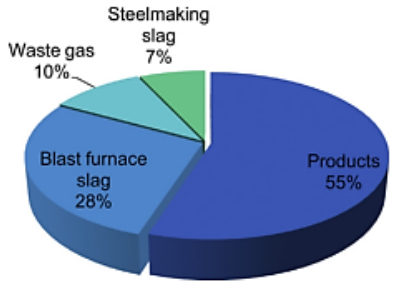

Figure 11.Distribution of high-temperature waste heat in steel industry [2]

In order to prevent the stated reasons, several physical dry granulation methods were proposed such as mechanical crushing method, air blast method, centrifugal granulation method etc. These methods are categorized according to crushing mechanism.

In this study, RCA technology as a centrifugal granulation method is analyzed and a RCA design for dry granulation is performed. In addition to that, a conceptual design of a fluidized bed is proposed to recover sensible heat energy from molten slag by using RCA technology.

2. ROTARY CUP ATOMIZER (RCA) PROCESS

The prototype of RCA was first designed in Britain by Pickering et al in early 1980s [4]. As shown in Figure 2, RCA process consists of combined actions of a rotating cup, air blast and cooling the slag droplets to obtain a glassy product. In the first step of this process, the slag particles are cooled as they are travelling through air. Then, the cooled and granulated particles which have nearly 2 mm diameter are dropped into the fluidized bed. In the last step, waste heat energy of the slag particles is recovered by fluidized bed and it is transported to the air. Thus, the hot air is obtained by recovering the waste heat energy of molten slag [3].

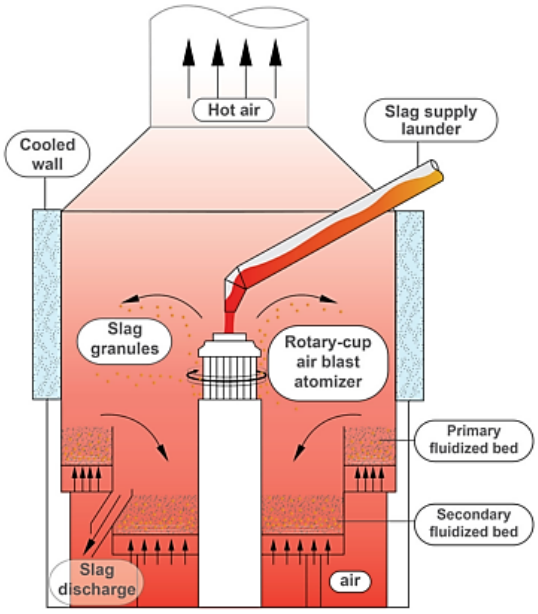

Figure 2. Rotary cup atomizing process schematics [5]

In RCA process, there are some important parameters which affect the heat recovery operation. These parameters are the effect of temperature, the effect of the granulation device speed and the effect of granulation device diameter.

2.1 The effect of temperature

The viscosity of molten slag is a key factor on continuous flow. Slag normally begins to melt between $1250^{\circ}C - 1450^{\circ}C$. When the temperature of molten slag exceeds $1320^{\circ}C$, its viscosity increases sharply. It can be inferenced from this statement; the temperature of slag must be kept above $1320^{\circ}C$ before it falls on the RCA [6].

2.2 The effect of granulation device speed

The speed of granulation device is a vital factor in centrifugal granulation. Because, the speed of granulation device directly affects the centrifugal force which an important factor for granulating the molten slag successfully. In a study performed by Zou et al, if the granulation device speed is increased, it was seen that solid slag particles which has less than 3 mm diameter can be gained [6]. In another study by Yu et al, it has been found that when the RCA speed exceeds 1000 rpm, the decrease in particle diameter becomes less important and also the temperature of slag does not have a significant effect on the slag granule diameter [7]. Also, when the velocity exceeds 1000 rpm, the effect of cup size can be neglected [2].

2.3 The effect of granulation device diameter

The RCA diameter is an important parameter in the molten slag granulation. The large cup diameter has a negative effect on revolution and this situation affects the granulation process negatively. On the other hand, if the cup diameter is too small, molten slag will be thrown out in a short time. This causes undesired situations on granulation process [6].

3 ROTARY CUP ATOMIZER DESIGN

In this section, a RCA is designed based on average annual 175000 ton/year crude iron production. For designed system, molten slag is charged into the RCA with $1450^{o}C$ and in the production process of 1 ton crude iron, 0.3 ton slag occurs. If these values are evaluated, the total capacity of annual slag production can be calculated like following.

$$\text{Annual slag production capacity} = 175000 \times 0.3 = 52500 \text{ ton/year}$$

The mass flow rate of molten slag can be calculated as 1.67 kg/s by using Equation 1.

$$\dot{m} = \frac{52500}{365 * 24} \cong 6 \text{ ton/hour } \cong 1.67 kg / s \qquad (1)$$

The physical properties of molten slag are given in Table 1. Volumetric flow rate of molten slag can be also calculated as $5.57 \times 10^{-4} m^3/s$ by using the Equation 2 given below.

Table 1. The physical properties of molten slag

Quantity	Value
Density	3000 kg/m^3
Dynamic viscosity	0.7 Pa.s

$$\dot{Q} = \frac{\dot{m}}{\rho} = \frac{1.67}{3000} \cong 5.57 \times 10^{-4} m^3 / s \qquad (2)$$

By using the calculated values above, in the first step of this section, RCA material selection is realized. Secondly, the granulator design is proposed. In the last step, finite elements model of the designed RCA is constructed and the reliability of the designed RCA is checked by using finite elements method (FEM).

3.1 Material selection

1.4462 duplex stainless steel is selected for RCA since it is resistant against high temperature and corrosion. Also, the internal surface of the RCA is coated with dolomite refractory in order to increase the thermal resistance of RCA material. The properties of 1.4462 duplex stainless steel are given at the Table 2.

Table 2. 1 .4462 duplex stainless steel properties

Quantity	Value
Yield strength	205 MPa
Density	800 kg/m^3
Young's modulus	193 GPa

3.2 Sizing of granulator

In RCA process, the solidification of molten slag under the influence of centrifugal forces and air flow occurs in 0.5-6 second. If the maximum solidification period (6-second) is taken into account, the slag volume for this time period can be calculated by using the Equation 3. The granulator must have a bearing capacity which is bigger than the maximum molten slag value. Thus, the granulator is designed as shown in Figure 3 by considering the related parameters and using the vanes for obtaining more homogeneous slag particles[8].

$$V_{slag} = Q.t = 5.57 \times 10^{-4} \times (6) = 3.342 \times 10^{-3}\, m^3 \quad (3)$$

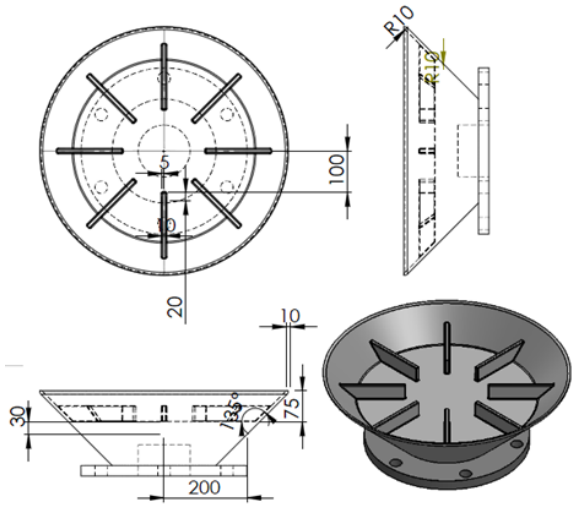

Figure 3. Technical drawing of designed granulator

For designed granulator, the diameter of the solid slag particles which occurs after granulation process should be calculated. In this context, it is benefited from the Equation 4 which derived by Purwanto et al. In Equation 4, D_p is the diameter of the slag particles, r radius of the granulator and v is the tangential velocity. For RCA design, the angular velocity of the granulator is selected as 1200 r/min since in this velocity rather small and homogenous slag particles occur.

$$D_p = 16.86 / rv \quad (4)$$

By using Equation 4, dimeter of slag particles is calculated as 3.35 mm and according to literature, this value represents a good approximation for energy efficient.

3.3 Finite elements model of designed granulator

FEM of the designed granulator is constructed in order to predict the working condition of granulator and determine the safety level. While the granulator is dividing into finite elements, local meshed was used in the sharp edges and the radiuses. FEM model of the granulator is constructed by using ANSYS 15.0 software. The FEM and the boundary conditions of the granulator are illustrated in Figure 4 below.

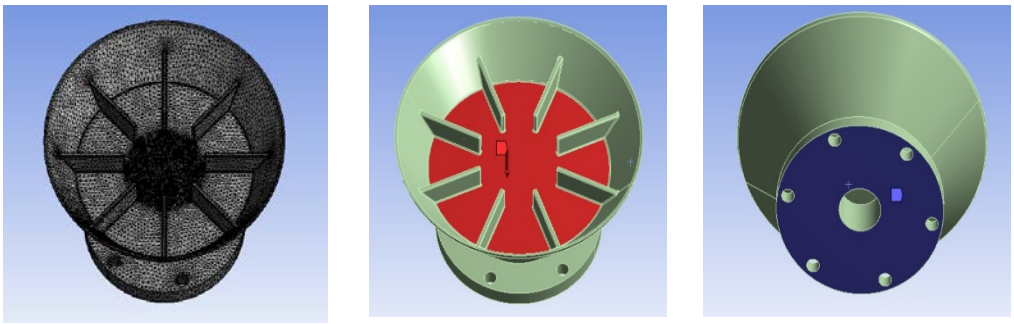

Figure 4. FEM model of designed granulator

According to finite elements results, maximum Von-Mises Stress and Von-Mises Strain values are obtained $0.01\,MPa, 5.664 \times 10^{-5}\,mm$ respectively. It can be easily said that, the granulator is pretty reliable in terms of structural strength.

3.4 Designing of shaft

Shafts are rotating machine elements, usually circular in cross section which is used to transmit power from one part to another [9]. For RCA system, the shaft is designed by using 304 stainless steel. The shaft is exposed to buckling load due to granulator and slag mass. In addition to that, the shaft is exposed to torsional load due to motor torque. The force value which applied to the shaft is 234 N, also the torsional moment value is 11940 Nmm. Designed shaft, its boundary conditions, total force applied on shaft and FEM model of the shaft are showed in Figure 5.

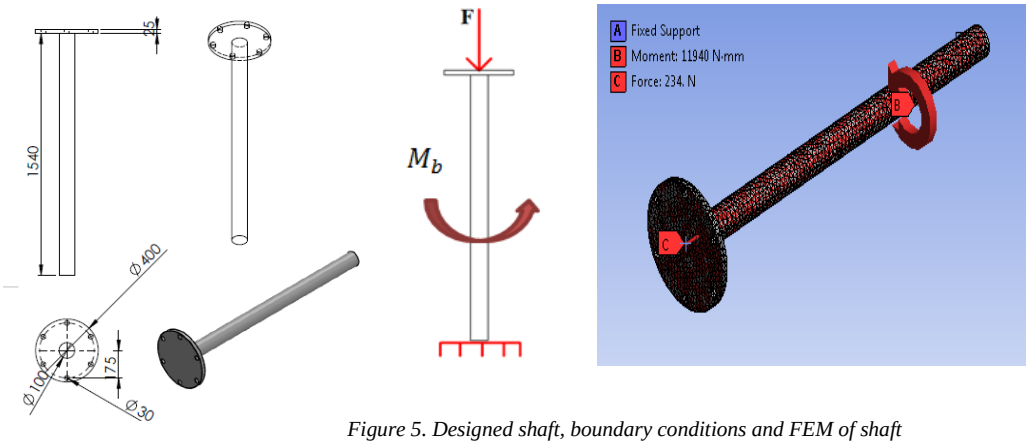

Figure 5. Designed shaft, boundary conditions and FEM of shaft

According to linear buckling analysis of shaft, maximum Von-Mises Stress is obtained as 0.25 MPa. If this value is evaluated, it can be said that the shaft is quite reliable. Finally, the RCA is designed as shown in Figure 6. Designed RCA consists of six components: granulator, insulation materials, shaft, coupling, electric motor and motor holder block.

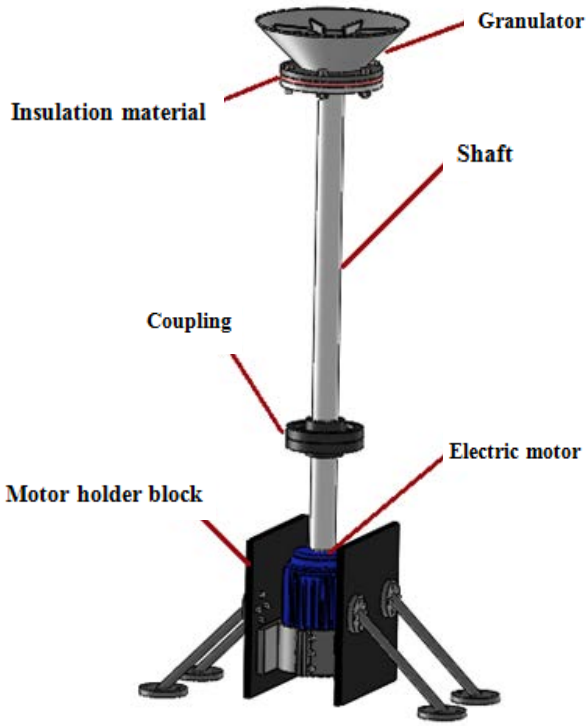

Figure 6. Designed Rotary cup atomizer

4 FLUIDIZED BED DESIGN

A fluidized bed is a state of a two-phase mixture of particulate solid material and fluid, which is widely used in many modern technologies to increase the efficiency of the various physical and chemical processes [10]. In RCA process, fluidized bed is used in increasing the efficiency of energy recovery. As can be seen from Figure 7, granulated slag particles fall into the fluidized bed where the heat is recovered.

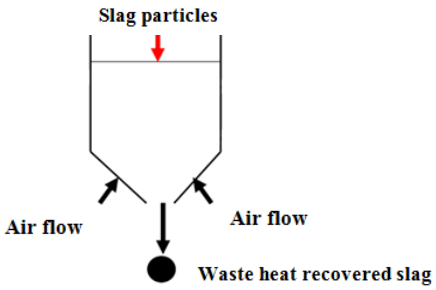

Figure 7. Schematic of fluidized bed

The air flow is supplied from the under of the fluidized bed and so the waste heat of slag particles is carried to the air. Then, this hot air is used in generating electricity or heating. In this context, heat recovery system which consists of RCA and fluidized bed is designed as illustrated in Figure 8.

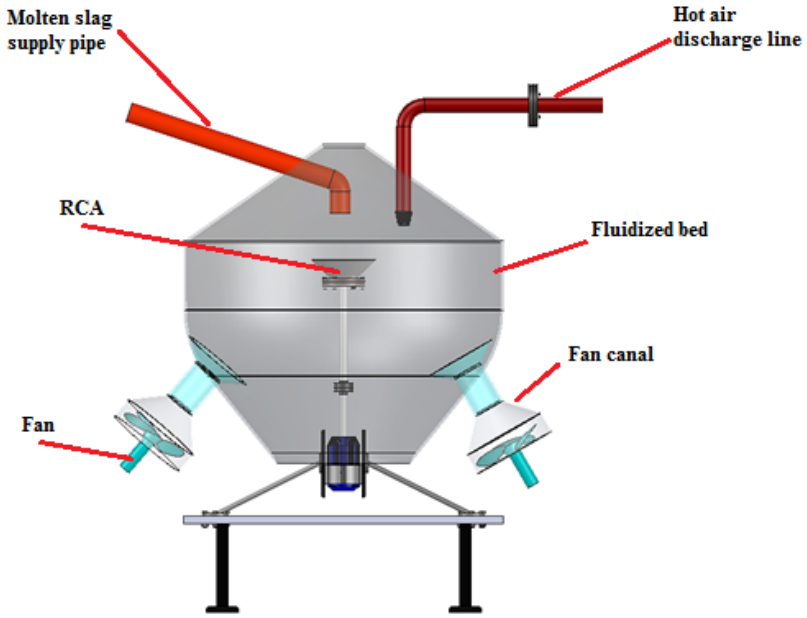

Figure 8. Designed heat recovery system

4.1 Heat transfer calculation for fluidized bed

The energy conservation in a slag droplet is given by Equation 5, where c_p is the molten slag specific heat, ε the emissivity, A_d cross sectional area of slag droplet, σ the Stephan-Boltzman constant and V_d is the volume of the droplet [11].

$$-hA_d\left(T_1 - T_0\right) - A_d\varepsilon\sigma\left(T^4 - T_0^4\right) = V_d\rho_d c_p\frac{dT}{dt} \qquad (5)$$

In the fluidized bed there will be no big temperature difference between the inside of fluidized bed and its walls, and so radiative heat transfer does not play a significant role in heat transfer. Thus, the Equation 5 is converted to Equation 6 given below.

$$-hA_d\left(T-T_0\right)=V_d\rho_d c_p\frac{dT}{dt} \quad (6)$$

If this ordinary differential equation is solved, Equation 7 is obtained. In this equation, T_2 is the latest temperature of the slag particle during the heat transfer process, T_0 temperature of air and T_1 is the initial temperature of the molten slag (1450°C).

$$-\Delta t=\frac{V_d\rho_d c_p}{hA_d}\ln\left|\frac{T_2-T_0}{T_1-T_0}\right| \quad (7)$$

In order to obtain the latest temperature of the slag particles, convective heat transfer coefficient should be calculated. The convective heat transfer coefficient between a droplet and the air can be calculated by using the Equation 8 where Re is the Reynolds number and Pr the Prandtl number for gas, K_g thermal conductivity of gas and d is the diameter of the slag droplet [11]. The related parameters of the slag droplet and the air are given in Table 3, below.

$$h=\frac{K_g}{d}\left(2+0.6\sqrt{\mathrm{Re}}\sqrt[3]{\mathrm{Pr}}\right) \quad (8)$$

$$\mathrm{Re}=\frac{\rho v d}{\mu} \quad (9)$$

Table 3. Constant, physical, and thermal properties of slag droplet and air [11]

Quantity	Value
Density of slag droplet (ρ_s)	3000 kgm^{-3}
Dynamic viscosity of slag droplet (μ_s)	0.7 Pa.s
Density of air	1.184 kgm^{-3}
Dynamic viscosity of air (μ_a)	1.849$\times 10^{-5}$ kg/ms
Specific heat of slag droplet (C_s)	1200 J/kgK
Initial temperature of slag droplet (T_1)	1450 °C
Temperature of air (T_0)	25 °C
Specific heat of air (C_a)	1007 J/kgK
Thermal conductivity of air (K_a)	2.6$\times 10^{-2}$ W/mK
Prandtl number of air at 25 °C	0.7296

As it can be seen from Equation 8, velocity of slag droplets should be determined for calculating the Reynolds number to obtain convective heat transfer coefficient. In accordance with this purpose, it was benefited from force balance equation and Newton's second law. During the granulation process, tangential and radial velocity components occur and this velocity are calculated by using Equation 10 and 11 and the parameters of these equations are presented in Table 4 [11]. From these equations, tangential velocity and radial velocity are calculated 25.134 m/s and 0.542 m/s respectively. Finally, resultant velocity of the slag droplet is obtained as 25.14 m/s by using Equation 12.

$$V_t=\frac{\omega D}{2} \quad (10)$$

$$V_m=\sqrt[3]{\frac{\rho_d\omega^2Q^2}{6\pi^2D\mu_d}} \quad (11)$$

$$V_x=\sqrt{V_x^2+V_m^2} \quad (12)$$

Table 4. Velocity parameters of the related equations [11]

Quantity	Unit
Tangential velocity (V_t)	m/s
Radial velocity (V_m)	m/s
Angular velocity of granulator (ω)	r/min
Diameter of granulator (D)	m
Volumetric flow rate of slag	m^3/s

The vertical length between the RCA and the air fans is 2 meters and it is assumed that falling down of slag particles until the fan level takes 7 seconds. The acceleration of the slag particles can be calculated as 0.082 m/s^2 by Equation 13. The forces applied on a slag particle are illustrated in Figure 10.

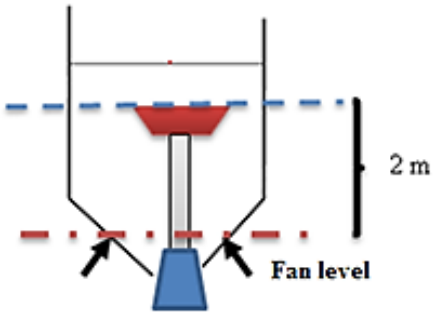

Figure 9. The length between the granulator and the fan

$$X = V_o t \pm \frac{1}{2} a t^2 \qquad (13)$$

After calculation of acceleration, the net force applied on slag particle can be calculated by using Equation 14. If the net force value is put into Equation 15, the drag force is calculated as $5.744 \times 10^{-4}\ N$. In Equation 15, W represents the weight of the slag particles, C_d is the drag coefficient for slag particles and for cylindrical shapes this value can be considered as 0.5 [12]. By using Equation 16, the resultant air velocity exerted by fan is obtained as 16.145 m/s for each fan.

$$F_{net} = F_y = ma \Rightarrow \quad F_{net} = \rho_d V_d a = 4.842 \times 10^{-6}\ N \qquad (14)$$

$$\sum F_y = W - F_D = m \times a \qquad (15)$$

$$F_D = C_D A_s \rho \frac{v^2}{2} = 5.744 \times 10^{-4}\ N \qquad (16)$$

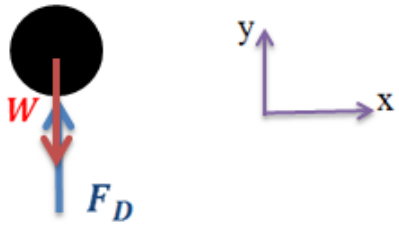

Figure 10. The forces applied on a slag particle

Fans are located at an angle of 45° with respect to fluidized bed, and velocity of fan air for each fan is calculated by Equation 17 as 11.416 m/s. Furthermore, if the diameter of fan canal is selected as 35 mm, the mass flow rate of air for each fan can be calculated by using Equation 18.

$$V_1 = V_2 = \frac{V_B}{\sqrt{2}} \Rightarrow V_1 = V_2 = 11.455 m/s \quad (17)$$

$$\dot{m} = \rho A V = 1.184 \times \pi \left(\frac{0.35^2}{4} \right) \times 11.416 \cong 1.3 \text{ kg/s} \quad (18)$$

After calculation of the air velocity, Reynold number can be easily obtained by Equation 9. Then, if the Reynolds number is used in Equation 8, the convective heat transfer coefficient is calculated as 257.28 W/m^2°C. Thereafter, the convective heat transfer coefficient is substituted in Equation 7, discharge temperature of slag is calculated as 606°C. Heat transfer during 7 seconds which occurs between the slag particles and the air is obtain by Equation 19.

$$Q = \dot{m} c_p \left(T_\infty - T_i \right) \text{ (kW)} \quad (19)$$

If the calculated values are substituted in Equation 19, heat transfer is obtained as 1691 kW for the 6 ton/hour molten slag production capacity. This heat transfer value is also equal to the energy change of the air. Thus, the outlet temperature of air can be calculated as 670°C by using Equation 20.

$$Q = 1691 \text{ kW} = \dot{m}_h c_p \left(T_{2h} - T_0 \right) \Rightarrow T_{2h} = \frac{1691}{2.6 \times 1.007} + T_0 \cong 670^\circ C \quad (20)$$

5 RESULTS and DISCUSSIONS

Energy efficiency is a vital component of iron-steel industry and molten slag is a key factor for energy recovery in iron-steel industry. Molten slag poured into the fluidized bed at 1450°C, and it leaves from the RCA with 2 mm diameter solid form. In fluidized bed, waste heat of the solid slag particles is recovered by air flow for obtaining hot air. Then this hot air is used in generating electricity or heating. Finally, the residual slag particles are discharged from the fluidized bed under the influence of net force. However, in this study the heat transfer which occurs from the top of the fluidized bed until the granulator level is not considered since the slag is liquid phase. In addition, the waste heat of residual molten slag particles can be recovered by using one more fluidized bed due to the fact that the slag particles leave from the fluidized bed at 606°C. If these parameters are considered, more reliable results can be provided.

CONCLUSIONS

In this study, RCA technology is evaluated and a conceptual design of RCA is performed. In addition, a conceptual design of a fluidized bed is proposed to provide a sensible heat recovery from molten slag by using RCA granulation method. The results show that, energy efficiency in iron and steel industry can be enhanced by recovering the waste heat energy of molten slag. Moreover, this improvement can be achieved by integrated system approach which consists of RCA and fluidized bed technology.

REFERENCES

[1] (2015) The WSA website. [Online]. Available: https://www.worldsteel.org/statistics/crude-steel-production.html
[2] H. Zhang, H. Wang, X. Zhu, Y.-J. Qiu, K. Li, R. Chen, and Q. Liao, "A review of waste heat recovery technologies towards molten slag in steel industry," *Applied Energy*, vol. 112, pp. 956-966, 2013.
[3] M. Barati, S. Esfahani, and T. A. Utigard, "Energy recovery from high temperature slags," *Energy*, vol. 36, no. 9, pp. 5440-5449, 2011.
[4] S. J. Pickering, N. Hay, T. F. Roylance, and G. H. Thomas, "New Process for Dry Granulation and Heat-Recovery from Molten Blast-Furnace Slag," *Ironmaking & Steelmaking*, vol. 12, no. 1, pp. 14-21, 1985.
[5] B. Lee, and I. Sohn, "Review of Innovative Energy Savings Technology for the Electric Arc Furnace," *Jom*, vol. 66, no. 9, pp. 1581-1594, 2014.
[6] Y. M. Zhou, C. Li, L. L. Xu, S. Y. Luo, and C. J. Yi, "The Experimental Study of Molten Blast Slag Dry Granulation," *Advanced Materials Research*, vol. 356-360, pp. 1882-1885, 2011.
[7] Yu Q-b, Liu J-x, Dou C-x, Hu X-z. Dry granulation experiment of blast furnace slag by rotary cup atomizer. Journal of Northeastern University (Natural Science). 2009;30:1163e5
[8] J. B. Zhu, S. Z. Wang, and M. Luo, "Progress in molten blast furnace slag treatment using dry centrifugal granulation technology," En*vironmental Technology and Resource Utilization Ii*, vol. 675-677, pp. 1406-1410, 2014.

[9] Khurmi R S, (2014), 'A text book of machine design', Eurasia publishing house(P) ltd., New-Delhi,2005
[10] (2015) The Thermopedia website. [Online]. Available: http://www.thermopedia.com/content/46/
[11] Q. Yuelin, L. Xuewei, B. Chenguang, C. Pan, Q. Guibao, and Z. Jie, "Mechanism of Dry Molten Slag Granulation Using a Rotating Multi-Nozzle Cup Atomizer," ste*el research international, vo*l. 85, no. 1, pp. 44-52, 2014.
[12] Çengel Y.A, Cimbala J.M, "Fluid Mechanics: Fundamentals and Applicatonsi" 3rd Edition, 2014

BIOGRAPHY

Semih Akın was born in İstanbul, Turkey. He received his bachelor's degree from Mechanical Engineering Department and Industrial Engineering Department (Double Major) of Uludağ University, Bursa, Turkey, in 2013. Mr. Akın's major fields of study are renewable energy sources and energy efficiency. He is currently is a research and teaching assistant at Bursa Technical University.

Yusuf Ali Kara is a Professor in the Department of Mechanical Engineering at Bursa Technical University, Turkey. He received his Ph.D. degree from Ataturk University, Erzurum, Turkey. His main research interests are heat pumps, heat exchangers, and renewable energy sources. He has published twelve articles in international journals.

ICENS
INTERNATIONAL CONFERENCE ON ENGINEERING AND NATURAL SCIENCES
24-28 May 2016 /Sarajevo

A Case Study of Installation of a Wind Power Plant in Sinop Province, Turkey

Semih Akin[1], Yusuf A.Kara[2]

Abstract

World energy demand is increasing very rapidly, and environmental issues such as the greenhouse effect and pollution are growing in importance. This situation incites the developing countries to benefit more efficiently from alternative energy sources. In parallel to this policy, Turkey as a developing country, is promoting the incentives and investments to the wind power conversion systems. Thanks to these investments, number of wind power plants (WPP) has been increasing in the country each passing day. In this study, Sinop Province in which has a remarkable wind power potential, is analyzed in terms of establishment of a WPP. Four years of hourly average wind speed data of the selected region is applied to the Windsim software: annual energy production, capacity factor and also power and energy curves of selected wind turbines are obtained as output. The study shows that with 5 Vestas V90 commercial wind turbines, establishment of a WPP which has approximately 29 GWh/y annual energy production and %33 capacity factor is feasible.

Keywords: *Renewable Energy Sources, Sinop Province, Wind Energy, Windsim, Wind Power Plant*

1. INTRODUCTION

Renewable energy technologies including solar, wind, biomass, geothermal, etc., has become more important since they are clean, sustainable and efficient energy sources. In addition, renewable energy sources are seen as a hope for decreasing the global fossil fuel usage. Wind energy as a renewable energy source has shown a remarkable growth all around the world [1]. Turkey as a developing country, has been investing in wind energy by increasing the number of incentives and investments. As it can be seen from Figure 1, Turkey's installed wind power capacity has been increasing consistently. According to the wind statistic report published by Turkish Wind Energy Association, installed wind capacity of Turkey has reached 4,718 MW by the January of 2016 [2]. It is predicted that Turkey's technical and economical wind energy potential are 83,000 MW and 10,000 MW respectively [3]. However, Turkey is a foreign dependent country in terms of energy sector and it imports nearly 70% of current energy source to meet the current energy demand [4]. Also, this issue causes some economical problem such as current deficit, soaring inflation etc. Moreover, it leads to decrease the competitive power of Turkey. When considered from this aspect, investment in renewable energy sources is inevitable for Turkey's future.

In this study, Sinop Province where located in the most northern edge of Turkey is studied for WPP investment. The wind atlases which developed by the Turkish Electric Affairs Etude Administration are used for evaluating the wind potential of Sinop Province. Wind data of the selected region is obtained from the mast which owned by Turkish State Meteorological Service. In addition, four years of hourly average wind speed data of the selected region is applied to the Windsim software and annual energy production, capacity factor and also power curves of selected wind turbines are obtained as output.

[1] *Corresponding author: Bursa Technical University, Department of Mechanical Engineering, 16330, Yıldırım/Bursa, Turkey.* semih.akin@btu.edu.tr

[2] *Bursa Technical University, Department of Mechanical Engineering. Bursa, Turkey* yusufali.kara@btu.edu.tr

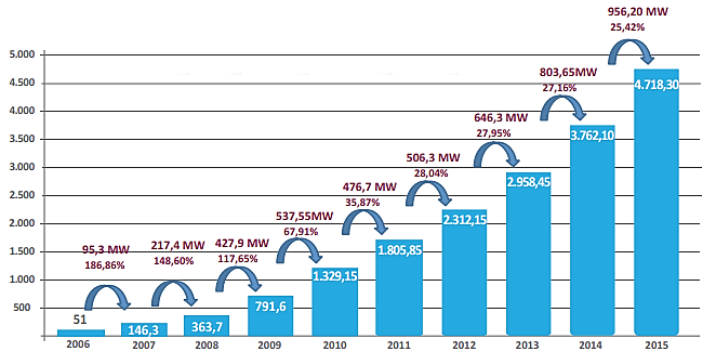

Figure 12. Cumulative installations for wind power plants in Turkey by years (MW) [5]

2. MATERIALS and METHODS

In this section, firstly wind power potential of Turkey is evaluated by using wind atlases which developed by the Turkish Electric Affairs Etude Administration. Secondly, wind power potential of Sinop Province is analyzed. Finally, terrain selection for WPP is performed by considering wind power potential, accessibility and distance to energy transmission lines (ETL).

2.1 Assessment of Turkey's Wind Power Potential

Turkey is located in the northern hemisphere between the 36°-42° northern parallels and the 26°-45° eastern meridians. Thanks to this unique geographical position, Turkey has a significant wind energy potential when compared with most of European countries [3]. Turkey has realized this remarkable potential in recent years and according to Turkey's 2023 vision, Turkey wants to supply 30% of total energy demand from renewable energy sources [6]. In this context, wind energy comes into prominence for Turkey's future. The wind investments in Turkey are concentrated in the western and southern regions [7]. In order to determine the wind power potential of Turkey, wind atlases were developed by Turkish Electric Affairs Etude Administration as shown in Figure 1 and Figure 2, below.

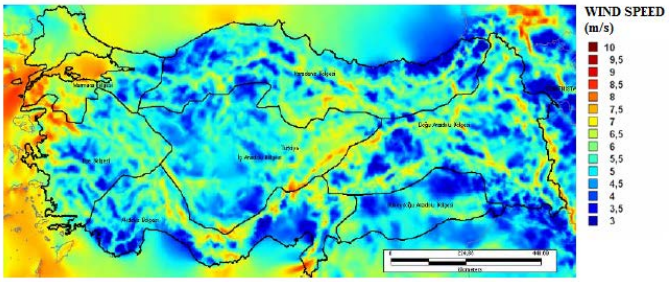

Figure 2. Yearly average wind speed distribution map of Turkey (50m) [8]

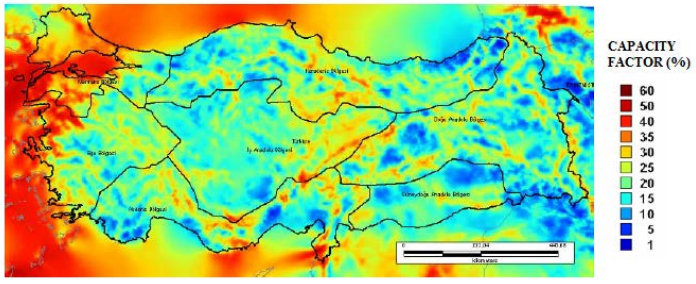

Figure 3. Average wind capacity factor in Turkey (50m) [8]

According to Figure 2, the average wind speed at 50 meters elevation is approximately 7.0m/s throughout of country. Also, average wind capacity factor is nearly 35% for most northern part of Turkey including Sinop Province. It can be deduced from the wind atlases, Turkey is a rich country in terms of wind power potential.

2.2 Assessment of Wind Power Potential in Sinop Province, Turkey

Sinop is a province of Turkey and it is located the most northern edge of the Turkish side of Black sea. The surface area of the city is 5,862 m^2, equivalent to 0.8% of Turkey's surface area. The borders of the city are 475 km and it consists of 300 km of land and 175 km seaside borders [9].

Figure 4. Location of Sinop Province in Turkey [10]

In order to evaluate the wind power potential of Sinop Province, the wind atlas which prepared for Sinop is analyzed. Yearly average wind speed and capacity factor distribution at 50 meters elevation for Sinop Province are given in Figure 4 and Figure 5. If the wind atlases of Sinop Province are evaluated, it can be said that northern part of the city is more convenient for WPP investment. In northern part of Sinop, hourly average wind speed changes between 6.5 and 7.0 m/s. Besides, average wind capacity of northern part of the province is approximately %35. For economical WPP investments, %35 or more capacity factor is required for the selected site [11]. When considered from this point of view, northern part of Sinop Province is feasible for a WPP establishment.

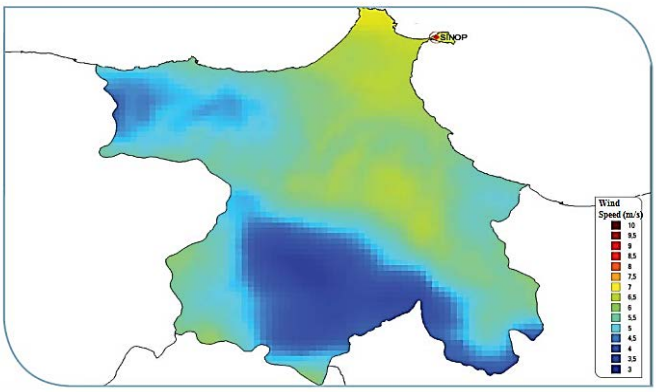

Figure 5. Average wind speed distribution map of Sinop Province (50m) [12]

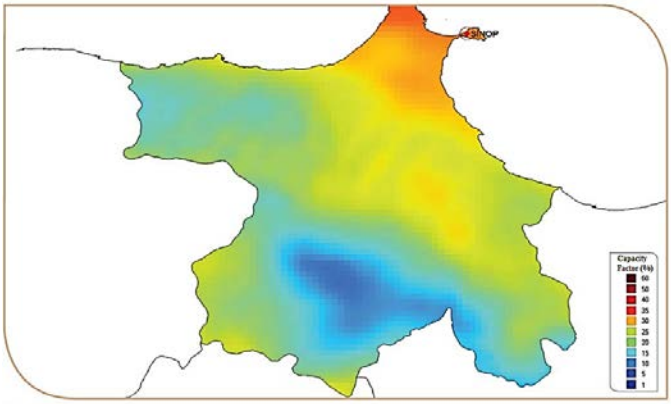

Figure 6. Average wind capacity factor in Sinop Province (50m) [12]

2.3 Site Selection for Wind Power Plant

Modern wind turbines are installed near the coasts, on the hills, and the opening valleys through the sea to obtain maximum efficiency [13]. Sinop is a coastal city of the Black Sea and thanks to this characteristic feature, the coastal terrains of the

province is pretty convenient for WPP investment. Unusable lands for WPP investments are shown in Figure 7. According to Figure 7, most area of Sinop Province is inconvenient for WPP investment since northern part of the province consists of forestland. When ETL parameter is evaluated for WPP investments, it can be seen from Figure 8 that there is a transformer station near the city and it can reduce the initial investment cost.

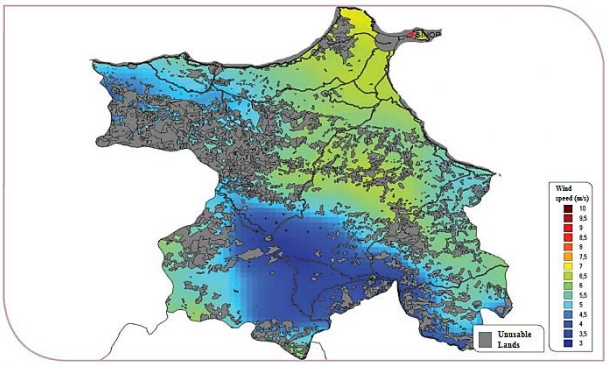

Figure 7. Unusable fields for the WPP in Sinop Province [12]

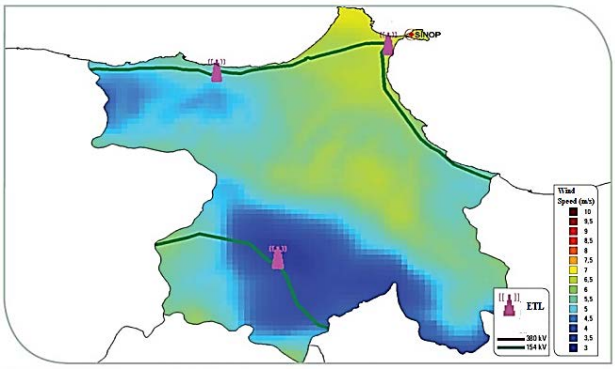

Figure 8. ETL and transformer stations in Sinop Province [12]

When these parameters are considered, the wind farm site selection is carried out in Sinop Cape as shown in Figure 9.

Figure 9. Selected Wind farm site in Sinop Province [12]

In selected site there is no settlement and it is a big advantage of wind power security of supply. In addition, commercial wind turbines have a noise problem for the environment during the operation. This noise problem is caused by mechanical and aerodynamic effects [14]. In this context, it can be said that the selected site is suitable in terms of noise and environmental issues.

3 DESIGN OF WIND FARM LAYOUT

In this section, wind farm layout design is carried out for Sinop Cape by using Windsim software. In order to gain 25 GWh/y energy or more, 5 Vestas V90 wind turbines are installed in the region by considering wake affect and air density change. Beside, Weibull distribution is obtained for the region, its parameters are calculated for all sectors and calculated values are compared with the wind atlas.

3.1 Assessment of Wind Power Potential for Bursa Province by Computational Fluid Dynamics (CFD) Analysis

CFD approach is a numerical method for solving problems which include fluid flow. In Windsim software, the region is divided by cells and these cells are used for CFD analysis to estimate the wind potential of the terrain. In the first analysis, the region was divided into 172,800 cells as shown in Figure 10. Then, the model was solved under the fixed pressure boundary condition and the results were obtained as shown in Figure 11, below.

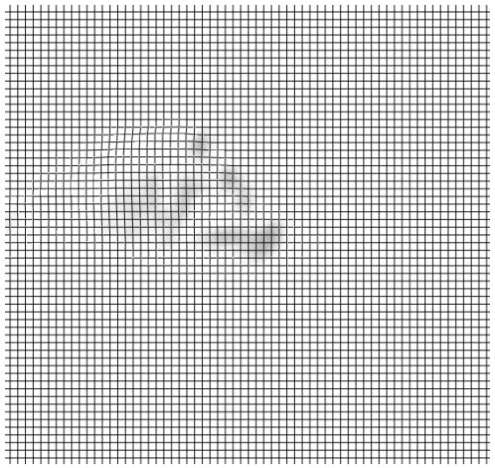

Figure 10. Cell structure of the region

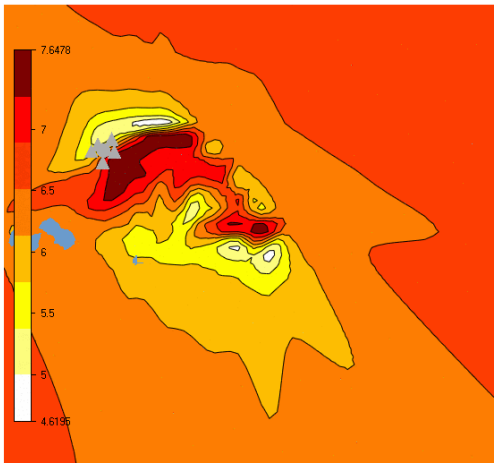

Figure 11. Wind resource map at the hub height of 80 meter (m/s)

According to CFD results given in Figure 11, average wind speed in the wind farm region is nearly 6.5-7 m/s. When the CFD result is compared with the wind atlas of Sinop Province, it can be seen that the results are quite similar.

3.2 Assessment of Wind Power Potential by Weibull Distribution

Weibull distribution is one of the most popular statistical methods used in engineering and also it is widely used for modeling the wind speed data [15]. The Weibull probability density function is given by Equation 1 where k and c are the Weibull parameters and v is wind speed [16]. Weibull distribution of the wind farm site is obtained as shown in Figure 12.

$$f(v) = \frac{k}{c}\left(\frac{v}{c}\right)^{k-1} \exp\left[-\left(\frac{v}{c}\right)^{k}\right] \qquad (1)$$

According to Weibull distribution, average wind speed is obtained 6.49 m/s for 80 meters elevation. Also, Weibull parameters, shape factor and scale factor are calculated 1.37 and 6.97 respectively. When these calculated values are compared with the CFD analysis and wind atlas, it can be said that the results match pretty well.

3.2 Turbine Layout

In the wind farm design process, commercial Vestas V90 wind turbines which have 80 meters hub height were selected. Selected turbine characteristics with power and thrust coefficient are given in Figure 13. In addition, turbine layout design was carried out by considering wake affect which reduce the wind speed behind the rotor and swirl the air flow [17].

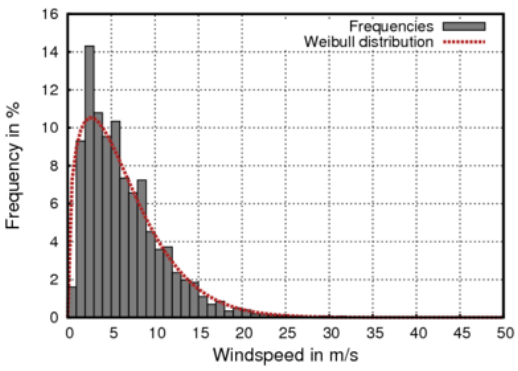

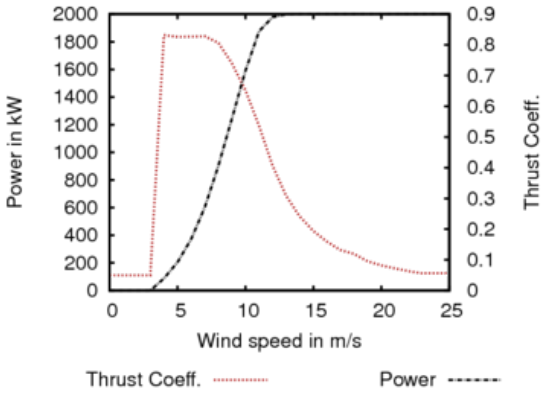

Figure 12. Weibull distribution for all sector]

Figure 13. Turbine characteristics with power and thrust coefficient

As shown in Figure 14, wake effect occurs when the wind turbines embower themselves and it has a negative effect on wind farm efficiency. In this study, Jensen wake model was selected since it is widely used, quite simple and effective wake model [18].

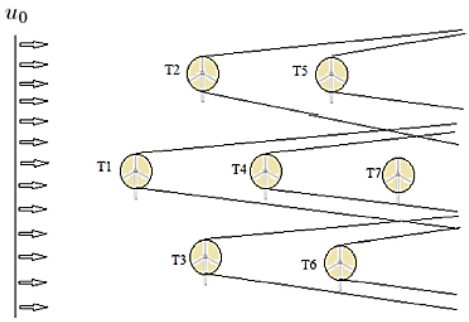

Figure 14. Multiple wake effect *in wind farm [17]*

In order to prevent wake affect, adequate separation distance at the dominant wind direction must be ensured among the wind turbines. As shown in Figure 15, all turbines were installed horizontally and the distance between two adjacent wind turbines was set as 400 m. Thus, wake loss was calculated as %0.2 of total energy generation and this value is pretty satisfactory in terms of wake effect.

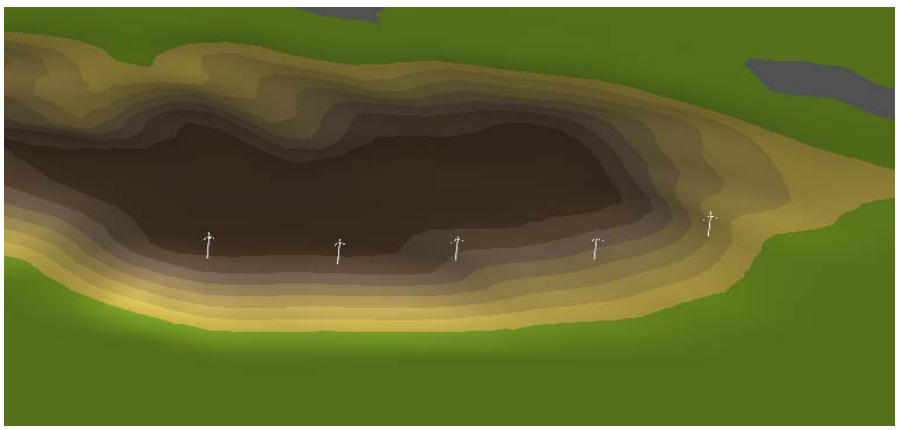

Figure 15. Wind farm layout

4 ENERGY ANALYSIS

In this section, wind farm energy analysis was performed considering wake affect and air density change. In this study, U.S Standart Atmosphere Model was used to calculate the air density change with elevation. U.S Standart Atmosphere Model is given in Equation 2 where ρ and z are density and elevation respectively [19].

$$\rho = 1.225 - (1.194 \times 10 - 4) \times z \quad (2)$$

After this step, the model was applied to Windsim software and then it was solved by using 172,800 cells. According to first analysis, AEP and capacity factor were calculated 28.7 GWh/y and 32.8% respectively. Also, wake loss was obtained as 0.4%. Hereupon, in order to ensure mesh independent result, a new analysis was run by 239,800 cells. In second analysis, AEP, capacity factor and wake loss were calculated as given in Table 1. When the analysis results are evaluated, AEP value is same for all analysis. Also, when first and second analyses are compared, it can be seen that relative error for capacity factor is %0.6. Finally, it can be deduced that, establishment of a WPP which has 28.7 GWh/y AEP, 33% capacity factor and %0.2 wake loss is feasible in Sinop Cape.

Table 1.Analyses Results

Cell Number	AEP(GWh/y)	Capacity Factor (%)	Wake Loss (%)
172,800	28.7	32.8	0.4
239,800	28.7	33.0	0.2

5 RESULTS and DISCUSSIONS

Turkey's economy has been growing significantly and this development brings along the energy challenges for Turkey's future. According to Turkey's 2023 vision, the main target is to increase the share of renewable energy sources to at least 30%. Also, this target is containing 10,000 MW installed wind power capacity [20]. In the current situation, Turkey's installed wind power plant capacity is 4,718 MW [2]. When viewed from this aspect, investment in renewable energy sources should be increased to accomplish this objective. In this context, Sinop Province becomes important since its remarkable wind power potential. Currently, there is a licensed WPP named Fener WPP in Sinop. The Fener Wind Energy Plant project will have a 5 MW installed power with 2 Enercon turbines, each 1,000 kW. It is expected that, 17.2 million kWh of electricity will be produced in a year and for 5,000 houses will be provided with this electricity [21]. However, this investment is not enough for exploiting the wind power potential of Sinop Province. Number of WPP should be increased in order to benefit from the wind potential of the province.
In this case study, AEP, capacity factor and wake loss of the designed WPP were calculated by Windsim software. The wind data was obtained from Turkish State Meteorological Service mast in Sinop. However, height of this measurement mast is only 10 meters and it is required to extrapolate the data to the hub height of wind turbine. In this context, Wind Power Law is used for this aim but this approach causes some errors on the results. If a special measurement mast whose elevation is same with the hub height of the turbines is installed in the wind farm site, more reliable data can be acquired. Although the data was extrapolated for 80 meters elevation, convergence was provided for the wind potential of the region. Thus, CFD result, Weibull distribution results and the wind atlas values were obtained fairly similar. Moreover, AEP and capacity factor was calculated as 28.7 GWh/y and 33.0% respectively. When these results are evaluated, it can be easily said that WPP converged to be an economical WPP with the rate of 33% capacity factor. On the other hand, cost analysis such as cost of turbine acquisition, installation and running cost along with grid connection was not taken into account in this study. If these parameters are considered, more reliable results can be obtained.

6 CONCLUSIONS

In this work, a case study of installation of a WPP was revealed for Sinop Province, Turkey. The study shows that, hourly average wind speed is 6.5-7.0 m/s at 80 meters elevation in Sinop and this wind speed is a satisfactory value for a WPP investment. In addition, the regions where located near the coast side of Sinop Cape are pretty convenient in terms of roughness formation and distance to ETL. The study also indicates that establishment of a WPP which has 28.7 GWh/y energy production capacity is feasible by using five number of Vestas V90 commercial wind turbines. Also, the capacity factor of designed wind farm was calculated as %33 and this value is convenient for an economical investment. The main objective of this study is providing inputs to the investors and the policy makers for exploiting the wind potential of the region.

ACKNOWLEDGMENT

The authors would like to thank Turkish State Meteorological Service for their support given to this work.

BIOGRAPHY

Semih Akın was born in İstanbul, Turkey. He received his bachelor's degree from Mechanical Engineering Department and Industrial Engineering Department (Double Major) of Uludağ University, Bursa, Turkey, in 2013. Mr. Akın's major fields of study are renewable energy sources and energy efficiency. He is currently is a research and teaching assistant at Bursa Technical University.

Yusuf Ali Kara is a Professor in the Department of Mechanical Engineering at Bursa Technical University, Turkey. He received his Ph.D. degree from Ataturk University, Erzurum, Turkey. His main research interests are heat pumps, heat exchangers, and renewable energy sources. He has published twelve articles in international journals.

REFERENCES

[1] A. K. Azad, M. G. Rasul, R. Islam, and I. R. Shishir, "Analysis of Wind Energy Prospect for Power Generation by Three Weibull Distribution Methods," *Energy Procedia*, vol. 75, pp. 722-727, 2015.
[2] (2016) The WSA website [Online] Available: http://www.tureb.com.tr/files/bilgi_bankasi/turkiye_res_durumu/new_report_by_turkish_wind_energy_association.pdf
[3] M. Bilgili, and E. Simsek, "Wind Energy Potential and Turbine Installations in Turkey," *Energy Sources, Part B: Economics, Planning, and Policy*, vol. 7, no. 2, pp. 140-151, 2012.
[4] Y. A. Kaplan, "Overview of wind energy in the world and assessment of current wind energy policies in Turkey," *Renewable and Sustainable Energy Reviews*, vol. 43, pp. 562-568, 2015.
[5] (2016) The WSA website [Online] Available: http://www.tureb.com.tr/files/bilgi_bankasi/turkiye_res_durumu/2016_turkiye_ruzgar_enerji_istatistik_raporu_ocak_2016.pdf
[6] B. Atilgan, and A. Azapagic, "Renewable electricity in Turkey: Life cycle environmental impacts," *Renewable Energy*, vol. 89, pp. 649-657, 2016.
[7] M. Çapik, A. O. Yılmaz, and İ. Çavuşoğlu, "Present situation and potential role of renewable energy in Turkey," *Renewable Energy*, vol. 46, pp. 1-13, 2012.
[8] (2016) Turkey's Wind Energy Potential. [Online]. Available: http://www.mgm.gov.tr/FILES/haberler/2010/rets-seminer/2_Mustafa_CALISKAN_RITM.pdf
[9] (2016) The Wikipedia website [Online] Available:https://en.wikipedia.org/wiki/Sinop_Province
[10] (2016) Sinop-Art website [Online] Available: http://www.sinop-art.eu/city-of-sinop/location/
[11] Y. Oner, S. Ozcira, N. Bekiroglu, and I. Senol, "A comparative analysis of wind power density prediction methods for Çanakkale, Intepe region, Turkey," *Renewable and Sustainable Energy Reviews*, vol. 23, pp. 491-502, 2013.
[12] (2016) Ministry of Energy and Natural Resources website [Online] Available: http://www.eie.gov.tr/YEKrepa/SINOP-REPA.pdf
[13] C. İlkiliç, "Wind energy and assessment of wind energy potential in Turkey," *Renewable and Sustainable Energy Reviews*, vol. 16, no. 2, pp. 1165-1173, 2012.
[14] O. Jianu, M. A. Rosen, and G. Naterer, "Noise Pollution Prevention in Wind Turbines: Status and Recent Advances," *Sustainability*, vol. 4, no. 6, pp. 1104-1117, Jun, 2012.
[15] F. G. Akgul, B. Senoglu, and T. Arslan, "An alternative distribution to Weibull for modeling the wind speed data: Inverse Weibull distribution," *Energy Conversion and Management*, vol. 114, pp. 234-240, Apr 15, 2016.
[16] D. Solyali, M. Altunc, S. Tolun, and Z. Aslan, "Wind resource assessment of Northern Cyprus," *Renewable & Sustainable Energy Reviews*, vol. 55, pp. 180-187, Mar, 2016.
[17] R. Shakoor, M. Y. Hassan, A. Raheem, and Y. K. Wu, "Wake effect modeling: A review of wind farm layout optimization using Jensen's model," *Renewable & Sustainable Energy Reviews*, vol. 58, pp. 1048-1059, May, 2016.
[18] Jensen, N.O, " A note on wind generator interaction" Tec rep. RISØ-M-2411, Denmark; 1983
[19] (2016) Wikipedia website [Online] Available: https://en.wikipedia.org/wiki/U.S._Standard_Atmosphere
[20] (2015) Ministry of Energy and Natural Resources website [Online] Available: http://www.enerji.gov.tr/tr-TR/Sayfalar/Ruzgar
[21] (2015) Ortadoğu Energi website [Online] Available: http://ortadoguenerji.com.tr/en/projelerimiz-ve-santrallerimiz/proje-ve-lisans-haritasi/fener-ruzgar-santral-projesi-2/

ICENS
INTERNATIONAL CONFERENCE ON ENGINEERING AND NATURAL SCIENCES
24-28 May 2016 /Sarajevo

Does Fitness Scaling Boost the Performance of Single Objective Genetic Algorithm?

Engin Ufuk Ergul[1], Ilyas Eminoglu[2], Cenk Gezegin[3]

Abstract

Fitness scaling is an important method to boost the performance of single objective genetic algorithm (SOGA). In this paper, an external parameter is systematically used to improve the performance of SOGA. A power-law fitness scaling method is used for this purpose. This method is named as gamma (γ) correction based fitness scaling (GCFS). GCFS is embedded SOGA algorithm and the efficiency of GCFS is tested by 6 different static gamma values (including 0.1, 0.2, 1, 2, 5 and 10) on two benchmarks (Ackley and Rastrigin test functions). According to the results, it is seen that SOGA converges the optimal solution of the benchmarks speedily and accurately. GCFS can be embedded on SOGA easily and without extra computational burden.

Keywords: *GCFS, Genetic algorithm, fitness scaling.*

[1] *Corresponding author: Amasya University, Department of Electrical and Electronics Engineering, 05100, Merkez/Amasya, Turkey.* *engin.ergul@amasya.edu.tr*

[2] *Ondokuz Mayis University, Department of Electrical and Electronics Engineering, 55139, Kurupelit/Samsun.* *ilyaseminoglu@hotmail.com*

[3] *Amasya University, Technical Sciences Vocational School, 05100, Merkez/Amasya, Turkey.* *cenkgezegin@gmail.com*

1. INTRODUCTION

Genetic Algorithms (GAs) are very efficient search techniques. While searching the optimal result/results of a problem, GAs use some operators such as crossover, mutation and selection. Also, GAs assign fitness values to individuals/solutions in early steps of their algorithms. Some very detailed information about GAs can be found in [1] and [2].

Hopgood and Mierzejewski [3] say that "generally speaking, fitness scaling can be applied at the early stages of evolution to reduce overall the selection pressure and thereby encourage exploration of the whole search space and increase the diversity. Conversely, at the late stages of evolution, fitness scaling is intended to strengthen the selection pressure in order to converge on the exact optimum". Fitness scaling methods were generally applied to SOGAs. There are some fitness scaling methods proposed in literature: linear scaling [4],[5], rank scaling [4], exponential scaling [6],[7], sigma scaling [4],[5], transform ranking [3], Boltzman scaling [8] and power-law scaling [4],[5],[9]. Hao, Chen, Wei, Gong, & Hu [10] proposed two conditions for efficient fitness scaling and also studied two new fitness scaling methods named as fitness scaling based on logarithmic and trigonometric functions. In the work of Bakinde, Zhu, Gao, & Nandi [11], the effects of proportional and rank fitness scaling methods on the performance of a genetic algorithm (GA) based equalization approach was presented. Hill, Newell, & O'Riordan [12] compared the effectiveness of an inversion operator in a basic GA and in a GA using linear scaling.

In this study, a kind of power-law scaling ([4],[5],[9]) named as gamma correction based fitness scaling (GCFS) is applied to SOGA. In GCFS, fitness values generated by SOGA are powered by a gamma value (γ), and selection pressure of a population can be then regulated. Therefore, selection probabilities of the best individuals can be increased and, fit and unfit individuals may be separated very well in fitness-wise before going to the selection mechanism.

GCFS is embedded SOGA algorithm and the efficiency of GCFS is tested by 6 different static gamma values (including 0.1, 0.2, 1, 2, 5 and 10) on two benchmarks (Ackley and Rastrigin test functions). According to the results, it is seen that SOGA with GCFS converges the optimal solution of the benchmarks speedily and accurately.

This paper is organized as follows: Materials and methods are given in Section 2. Results and discussion is presented in Section 3. Finally, overall conclusions and future directions are given in Section 4.

2. MATERIALS AND METHODS

In this paper, a kind of power-law fitness scaling method is employed to SOGA and named as gamma correction based fitness scaling (GCFS) because of historical and structural similarity to gamma correction operator used in digital image processing. It should be noted that in this paper, externally and adjustable fitness scaling in SOGA is questioned and explored.

Generally and philosophically speaking, a digital image can be darkened or brightened to improve the overall image quality by applying gamma correction (Figure 1(a)) [13]. In this way, the image is visually appealing to viewers, and it has become more understandable and meaningful. Now, SOGA generates a set of fitness values and these fitness values can easily be altered by GCFS to obtain a new set of fitness values to be fed into the selection mechanism (Figure 2). Instructively, GCFS is a simple nonlinear method and it is used just after fitness assignment block to alter the fitness values (and therefore the selection pressure of the population) depending on the selected value of gamma (γ). If γ is greater than one, the selection pressure is increased. If γ is lower than one, the selection pressure is decreased (Figure 1(b)). Therefore, selection probabilities of the best individuals can be increased and fit and unfit individuals may be separated very well before going to the selection mechanism.

Hao et al. [10] proposed two conditions for fitness scaling. The first is that individuals with high fitness values should also have high fitness values after fitness scaling. The second is that fitness scaling will change the diversity of the population or accelerate the convergence. Proposed GCFS provides these two conditions.

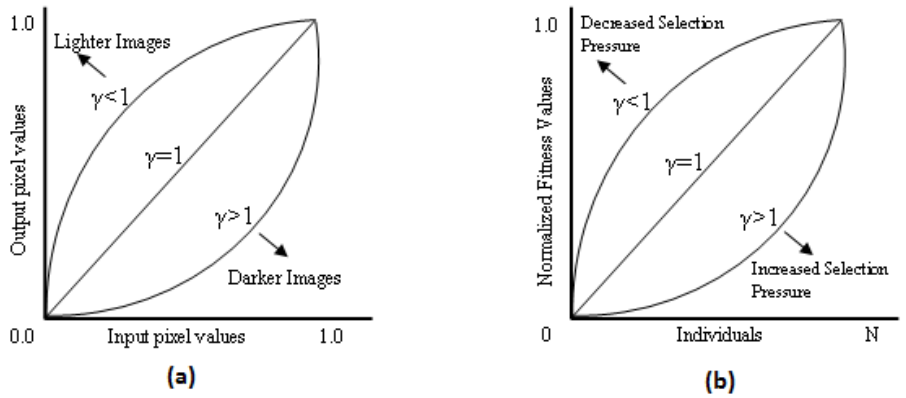

Figure 1. (a) Gamma correction in digital image processing, (b) Gamma correction in evolutionary algorithms

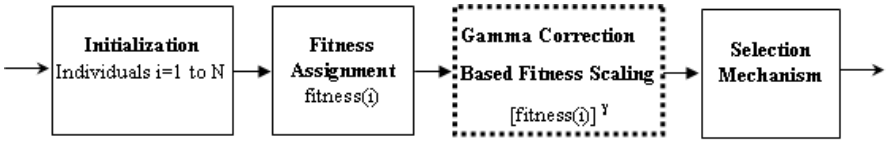

Figure 2. Usage of GCFS before the selection mechanism

The power law scaling transforms the fitness value of an individual *i* as follows:

$$f_i(new) = (f_i)^{\gamma} \tag{1}$$

Hence, the gap between fit and unfit individuals can be adjusted with the value of γ. In the study of Leclerc & Potvin [14], a methodology for dynamically modifying the power value γ was introduced and used for SOGAs. A general outline of GCFS algorithm is given as:

Step 1: Fitness values assigned by MOEAs are normalized as, (for *i=0,1,…,population_size*):

$$Normalized\_Fitness(i) = Fitness(i) / Max\_fitness \tag{2}$$

Step 2: New fitness values of individuals are calculated by using gamma correction operator (γ) as:

$$New\_Fitness(i) = Normalized\_fitness(i)^{\gamma} \tag{3}$$

Step 3: New fitness values are fed into the selection mechanism.

3. RESULTS AND DISCUSSION

Rastrigin and Ackley test functions are used for determining the effect of GCFS on SOGA. These test functions are minimization problems. Minimum value of Rastrigin function is 5 and minimum value of Ackley function is 0. Mathematical definitions of Rastrigin and Ackley functions are given in Eq.4 and Eq.5 respectively. Graphical representations of Rastrigin and Ackley functions are depicted in Figure 3 and Figure 4 respectively.

$$f(x_1, x_2) = (x_1^2 - 10\cos(2\pi x_1) + 10) + (x_2^2 - 10\cos(2\pi x_2) + 10) + 5 \tag{4}$$

$$f(x_1, x_2) = -20 \cdot \exp\left(-0.2 \cdot \sqrt{\frac{1}{2} \cdot \sum_{i=1}^{2} x_i^2}\right) - \exp\left(\frac{1}{2} \cdot \sum_{i=1}^{2} \cos(2\pi \cdot x_i)\right) + 20 + e \tag{5}$$

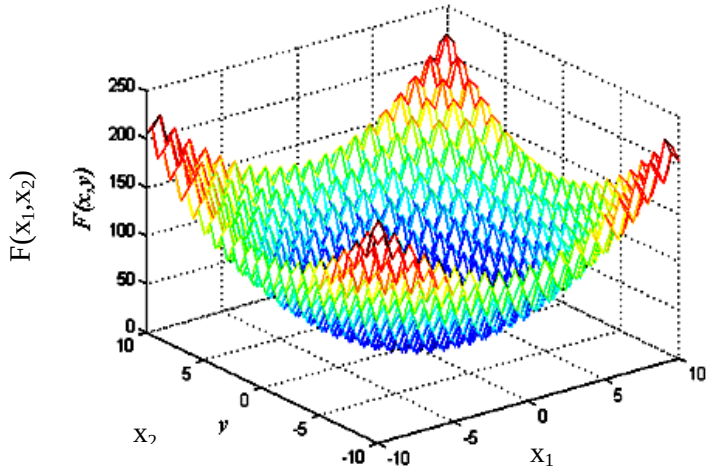

Figure 3. Rastrigin test function

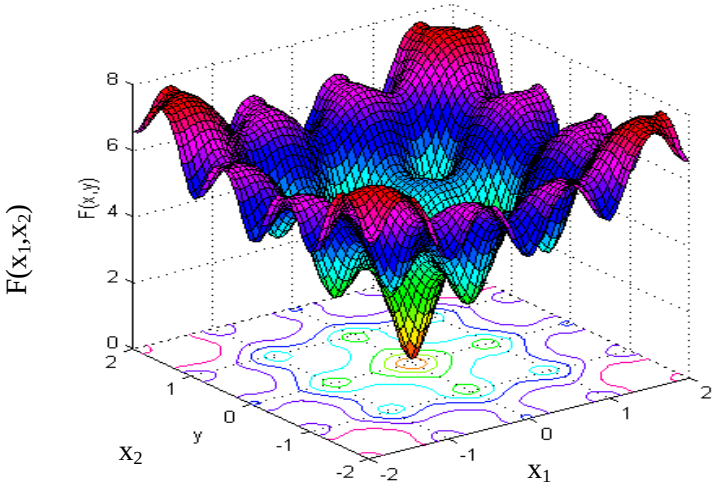

Figure 4. Ackley test function (for x1,x2 =[-2,2])

SOGA with GCFS is run for six different gamma values (0.1, 0.2, 1, 2, 5 ve 10). SOGA parameters are given in Table I.

Table I. Parameters of SOGA

Population Size	20
Number of Bits	30
Maximal Number of Generations	300
Crossover Rate	1
Mutation Rate	0.1
Upper and Lower Limits of Parameters for Rastrigin Function	[-10,10]
Upper and Lower Limits of Parameters for Ackley Function	[-500,500]

Obtained results from running SOGA with GCFS with given parameters on Rastrigin and Ackley test functions are shown in Figure 5 and Figure 6 respectively.

It is seen from Figure 5 and Figure 6, when the gamma values are increased, GA reaches the optimum value in fewer steps. In both test functions, GA converges the optimum value for γ=10.

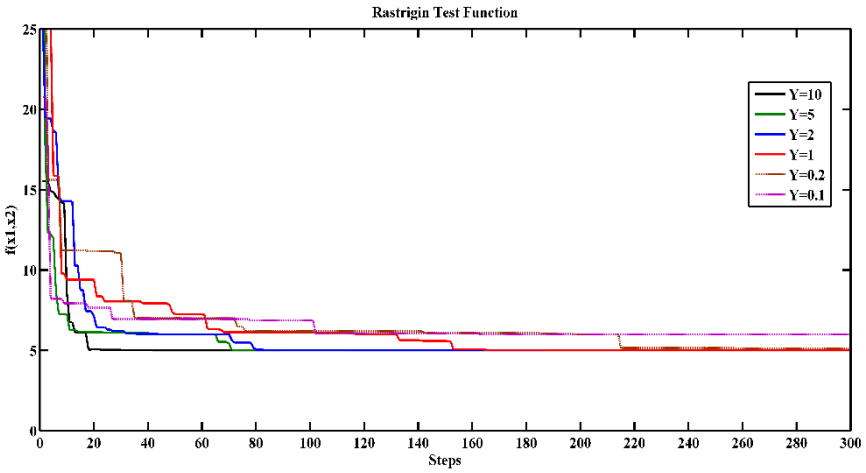

Figure 5. Effect of GCFS on Rastrigin test function

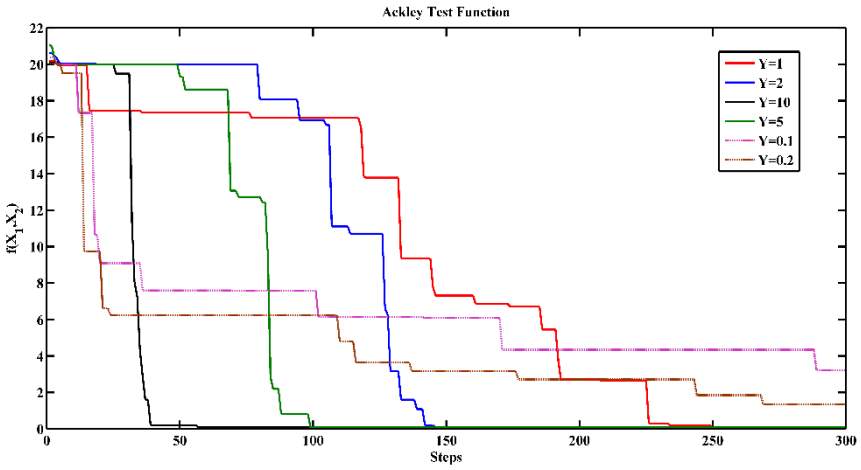

Figure 6. Effect of GCFS on Ackley test function

CONCLUSIONS

Simulated cases show that gamma correction based fitness scaling (GCFS) can be used to generate variable selection pressures to improve the convergence ability of SOGA. GCFS is a simple nonlinear fitness scaling operator and it is used just after fitness assignment block to alter the fitness values. Intuitively, the selection pressure of the population can also be altered by the chosen value of gamma (γ). According to the results, it is seen that SOGA converges the optimal solution of the benchmarks speedily and accurately. GCFS can be embedded on SOGA easily and without extra computational burden. In future work, an adaptive version of GCFS will be investigated.

ACKNOWLEDGMENT

This work is supported by the Scientific Research Project Fund of Amasya University under the project number FMB-BAP 15-0138.

REFERENCES

[1]. Coello, C.A.C., Lamont, G.B., and Veldhuizen, D.A. *Evolutionary Algorithms For Solving Multi-Objective Problems*, Second Edition, Springer, New York, U.S.A, 2007.

[2]. Deb, K. *Multiobjective Optimization Using Evolutionary Algorithms*, Wiley, Chichester, U.K., 2001.

[3]. Hopgood ,A., and Mierzejewsk, A. Transform Ranking: A New Method for Fitness Scaling in Genetic Algorithms, *Proc. AI-2008: Research and Development in Intelligent Systems XXV*, pp. 349-354, 2008.

[4]. Goldberg, D. E. *Genetic Algorithms in Search, Optimization & Machine Learning*, Addison-Wesley Pub., Reading, MA, 1989.

[5]. Michalewicz, Z. *Genetic Algorithms + Data Structures = Evolution Programs*, Springer-Verlag, New York, 1994.

[6]. Hopfield, J.J. Neural Networks and Physical Systems with Emergent Collective Computational Abilities, *Proceedings of the National Academy of Sciences*, Vol. 79, pp. 2554-2558, 1982.

[7]. Gen, M., Liu, B., and Ida, K. Evolution Program for Deterministic and Stochastic Optimizations, *European Journal of Operational Research*, 94, pp. 618-625, 1996.

[8]. Hopgood, A.A. *Intelligent Systems for Engineers and Scientists Second Edition*, CRC Press, 2001.

[9]. Gillies, A.M. Machine Learning Procedures for Generating Image Domain Feature Detectors, Doctoral Dissertation, University of Michigan, Ann Arbor, MI, 1985.

[10]. Hao, G.S., Chen, Y.Y., Wei, K.X., Gong, G., and Hu, X.T. Parameter Selection of Fitness Scaling in Genetic Algorithm and Its Application, *Control and Decision Conference (CDCC 2010)*, pp.2475-2480, 2010.

[11]. Bakinde, N.S., Zhu, X., Gao, J., and Nandi, A.K. Effects of Fitness Scaling and Adaptive Parameters on Genetic Algorithm based Equalization for DS-UWB Systems, *International Conference on Computers and Devices for Communication*, pp.1-4, 2009.

[12]. Hill, S., Newell, J., and O'Riordan, C. Analysing the Effects of Combining Fitness Scaling and Inversion in Genetic Algorithms, *Proceedings of the 16th IEEE International Conference on Tools with Artificial Intelligence (ICTAI 2014)*, pp.380-387, 2004.

[13]. Gonzales, R.C., and Woods, R.E. *Digital Image Processing. 3rd Edition*, Pearson Prentice Hall, New Jersey, USA, 2008.

[14]. Leclerc, F., and Potvin, J.Y. A Fitness Scaling Method Based on a Span Measure, *IEEE International Conference on Evolutionary Algorithms*, Vol.2, pp.561-565, 1995.

ICENS
INTERNATIONAL CONFERENCE ON ENGINEERING AND NATURAL SCIENCES
24-28 May 2016 /Sarajevo

The Best Vehicle Engine System Selection Using VIKOR and TOPSIS Methods

Engin Ufuk Ergul[1], Aytac Yildiz[2], Levent Ugur[3]

Abstract

Today, in parallel with the rapid depletion of fossil fuels, alternative engines used in vehicles begin to increase rapidly. Although more options are available for vehicle engines using fossil fuels, the importance of other engine systems also begin to rise. Because, expected features from vehicles is increased compared to the past. Besides the price; power, torque, acceleration, and emission values have become very important. Therefore, the engine systems which meet these features become more advantageous. In this study, VIKOR (VIseKriterijumska Optimizacija I Kompromisno Resenje) and TOPSIS (Technique for Order Preference by Similarity to an Ideal Solution) methods are used for determining the best vehicle engine system among six main engine systems (gasoline, diesel, LPG, hybrid, electric and hydrogen). For this purpose, six main criteria and their weights about six vehicles which use these engine systems are determined by ten experts. Then, by using the catalog data of vehicles, criteria and criteria weights are analyzed by using VIKOR and TOPSIS methods separately. The results of these methods are compared and it is determined that the vehicle which use the electric engine systems are the best one.

Keywords: *MCDM, Selection, TOPSIS, Vehicle Engine Systems, VIKOR.*

1. INTRODUCTION

Today, a large portion of the world's energy needs is met by using conventional energy sources such as coal, natural gas and petroleum. Because world energy demand rises day by day, conventional fuel needs increase gradually.

On the other hand, reserves of conventional fuels are limited and they run out due to the increasing energy needs. Besides, emission of greenhouse gases is increased with the usage of conventional fuels and, global warming problem is emerged [1]. Considering the rate of current reserves to production, it is estimated that about 40 years petroleum reserve remains. Because of these reasons, there is a need for alternative fuels that can be used instead of fossil-based fuels [2]. Due to the rapid development of the automotive industry which uses fossil fuels, the deterioration of petroleum reserves in the world and supply-demand balances Etc.; internal combustion engine technology is constantly being developed [3]. Usage of fossil-fuels in internal combustion engine causes to reduce of naturel sources. Accordingly, the ecological balance is deteriorated. Therefore, development activities about eco-friendly, cheap, safe fuels become very important. As a result, various engine systems have been used [4]. One of these is the engines which use LPG (Liquid Petroleum Gas). LPG is launched to the markets cheaper. And also, it is preferred to gasoline, because it is cleaner than gasoline [5-6]. LPG has superior anti-detonation features than gasoline. According to diesel and gasoline, LPG has better calorific power and as a result, LPG engines give better performance (%8) compared to diesel and gasoline eight percent [7].

Another alternative is hydrogen fuel engines. Hydrogen becomes an important alternative, because it can be produced by electrolysis, it has better physical and chemical properties it provides more power and it is eco-friendly. Usage of hydrogen as a fuel helps to elimination of fossil fuels and to reduce pollutant emissions [2]. Exhaust emission values of hydrogen is less than gasoline [8-9].

Vehicles which have hybrid engines fundamentally take power from at least two different energy sources. According to the system structure, they move with the help of only electric engine or only internal combustion engine or both of them [10]. Hybrid vehicles have an important place, because it provides the ability to use alternative forms of energy together [11].

Vehicles which use electric engine systems use one or more electric engines and some batteries to store the energy. These electric engines produces instantaneous torque and it provides powerful and balanced acceleration. These electric vehicles provide fuel safe and reduce environmental pollution and CO_2 emission. Despite the potential

[1] *Corresponding author: Amasya University, Department of Electrical and Electronics Engineering, 05100, Merkez/Amasya, Turkey.* engin.ergul@amasya.edu.tr

[2] *Amasya University, Department of Automotive Engineering, 05100, Merkez/Amasya, Turkey.* aytac.yildiz@amasya.edu.tr

[3] *Amasya University, Department of Automotive Engineering, 05100, Merkez/Amasya, Turkey.* levent.ugur@amasya.edu.tr"

benefits, electric engines have some limitations. Due to the Lithium-Ion batteries, they are more expensive than vehicles which use internal combustion engine and hybrid electric engine. Their range is low and charge time is long [12].

Vehicle engine systems have some advantages and disadvantages to each other. Determining the best engine system is a complex problem. So, the use of multi-criteria decision-making (MCDM) methods in solving this problem can be quite useful.

In this study, VIKOR and TOPSIS methods are used for determining the best vehicle engine system among six main engine systems (gasoline, diesel, LPG, hybrid, electric and hydrogen). For this purpose, six main criteria and their weights about six vehicles which use these engine systems are determined by ten experts. Then, by using the catalog data of vehicles, criteria and criteria weights are analyzed by using VIKOR and TOPSIS methods separately. The results of these methods are compared and it is determined that the vehicle which use the electric engine systems are the best one.

This paper is organized as follows: Materials and methods are given in Section 2. Results and discussion is presented in Section 3. Finally, overall conclusions are given in Section 4.

2. MATERIALS AND METHODS

In this study, two MCDM methods (VIKOR and TOPSIS) are used to select the best vehicle engine system. These methods are described briefly below. VIKOR method was proposed by Serafim Opricovic in 1998 [13]. It was developed for the multi-criteria optimization of complex systems. This method is known as a method focused on selecting among the alternatives and ranking them when there are conflicted criteria [14]. VIKOR method aims maximum group benefit and to get minimum individual regret of competitors [13]. In VIKOR method, feasible solutions which are the closest to ideal solution are produced by evaluating many criteria together. Afterwards, the best alternative is selected and alternatives are ordered according to the performances. VIKOR provides a compromise order. It provides to reach a compromise common solution under the determined weights. It is obtained a compromise order of alternatives by comparing the closeness values to ideal solution. The compromise alternative is determined by under some conditions [14].

Ar et al. [15] use VIKOR and TOPSIS methods to determine which sectors need to take place primarily in organized industrial areas. Opricovic and Tzeng [16] use VIKOR, TOPSIS, PROMETHEE and ELECTRE methods were applied to evaluate alternative hydropower systems on the Drina River in the former Yugoslavia. Chang and Hsu [17] use VIKOR for determining land usage constraint strategies in reservoir basin. Cristobal [18] applied VIKOR method for selecting renewable energy projects in Spain. Babashamsi et al. [19], Kim et al. [20], Qin et al. [21] and, Mohantya and Mahapatra [22] used VIKOR in their studies. Detailed information about VIKOR method and its algorithm can be found in [23].

TOPSIS was proposed by Hwang and Yoon [24] in 1981. In TOPSIS, a positive ideal solution is a combination of the best values of evaluation criteria and a negative ideal solution is a combination of the worst values of evaluation criteria. In the solution of the problem, alternatives must be the closest distance to the positive ideal solution and the furthest distance to the negative ideal solution [25,26]. In 2016; Tavana et al. [27] and Wang et al. [28] use DEA and TOPSIS, Abedi and Norouzi [29] use TOPSIS, Kermani et al. [30] use TOPSIS and genetic algorithm and Mir et al. [31] use TOPSIS and VIKOR for selecting the best alternative. Detailed information about TOPSIS method can be found in [24,32].

When comparing VIKOR and TOPSIS, it is concluded that VIKOR offers more choice than TOPSIS to decision makers, it reflects the opinions of the group better than TOPSIS and also its solutions are nearer to ideal solution than the solutions of TOPSIS. TOPSIS performs operations between the two reference points by using vector normalization and it cares relative importance of distances to these reference points. VIKOR uses linear normalization to reach the nearest solution to the ideal solution [13].

In this study, the purpose of using VIKOR and TOPSIS together is that comparing the results of these methods, because MCDM methods can give different results.

3. RESULTS AND DISCUSSION

In this paper, two of MCDM methods are implemented to a decision problem which investigates the vehicle engine system. For this purpose six vehicles and six engine systems are determined by the experts and their catalogue values are collected. For this purpose, six main criteria and their weights about six vehicles which use these engine systems are determined by ten experts respectively.

3.1. Application of VIKOR

Data sets (or parameters) about six vehicles are given in Table I. Criteria weights and criteria specifications are also given in Table I.

Table 1. Data set of the best vehicle engine system selection problem

		CRITERIA					
		Maximum Power (HP) (K1)	**Maximum Tork (Nm) (K2)**	**Acceleration (for 0-100 km/h) (sn) (K3)**	**Maximum Velocity (km/h) (K4)**	**Fuel cost in 100 km (TL) (K5)**	**CO2 Emission (gr/km) (K6)**
Criteria Weights		0,18	0,12	0,08	0,08	0,3	0,24
		MAX	**MAX**	**MIN**	**MAX**	**MIN**	**MIN**
ALTERNATIVE ENGINE SYSTEMS	**LPG (A1)**	125,00	152,00	12,20	200,00	16,73	157,00
	Gasoline (A2)	132,00	160,00	11,10	190,00	26,60	142,00
	Diesel (A3)	90,00	205,00	14,70	180,00	14,97	109,00
	Hydrogen (A4)	87,00	230,00	12,00	128,00	7,66	0,00
	Hybrid (A5)	100,00	111,00	12,00	165,00	15,70	82,00
	Electric (A6)	102,00	250,00	7,20	150,00	5,42	0,00
	The best criteria values f_j^*	132,00	250,00	7,20	200,00	5,42	0,00
	The worst criteria values f_j^-	87,00	111,00	14,70	128,00	26,60	157,00

Normalization matrix of the problem is given in Table II. Weighted normalization matrix of the problem is given in Table III.

Table 2. Normalization matrix of the best vehicle engine system selection problem

		CRITERIA					
		Maximum Power (HP) (K1)	**Maximum Tork (Nm) (K2)**	**Acceleration (for 0-100 km/h) (sn) (K3)**	**Maximum Velocity (km/h) (K4)**	**Fuel cost in 100 km (TL) (K5)**	**CO2 Emission (gr/km) (K6)**
ALTERNATIVE ENGINE SYSTEMS	**LPG (A1)**	0,156	0,705	0,667	0,000	0,534	1,000
	Gasoline (A2)	0,000	0,647	0,520	0,139	1,000	0,904
	Diesel (A3)	0,933	0,324	1,000	0,278	0,451	0,694
	Hydrogen (A4)	1,000	0,144	0,640	1,000	0,106	0,000
	Hybrid (A5)	0,711	1,000	0,640	0,486	0,485	0,522
	Electric (A6)	0,667	0,000	0,000	0,694	0,000	0,000

Table 3. Weighted normalization matrix of the best vehicle engine system selection problem

		CRITERIA					
		Maximum Power (HP) (K1)	**Maximum Tork (Nm) (K2)**	**Acceleration (for 0-100 km/h) (sn) (K3)**	**Maximum Velocity (km/h) (K4)**	**Fuel cost in 100 km (TL) (K5)**	**CO2 Emission (gr/km) (K6)**
ALTERNATIVE ENGINE SYSTEMS	**LPG (A1)**	0,0280	0,0846	0,0533	0,0000	0,1602	0,2400
	Gasoline (A2)	0,0000	0,0777	0,0416	0,0111	0,3000	0,2171
	Diesel (A3)	0,1680	0,0388	0,0800	0,0222	0,1353	0,1666
	Hydrogen (A4)	0,1800	0,0173	0,0512	0,0800	0,0317	0,0000
	Hybrid (A5)	0,1280	0,1200	0,0512	0,0389	0,1456	0,1254
	Electric (A6)	0,1200	0,0000	0,0000	0,0556	0,0000	0,0000

Calculated S, R and Q values of the problem are given in Table IV.

Table 4. S_i, R_i and Q_i values

	S_i	**R_i**	**Q_i (v=0)**	**Q_i (v=0.25)**	**Q_i (v=0.5)**	**Q_i (v=0.75)**	**Q_i (v=1)**
LPG (A1)	0,5661	0,2400	0,6667	0,7069	0,7472	0,7874	0,8276
Gasoline (A2)	0,6475	0,3000	1,0000	1,0000	1,0000	1,0000	1,0000
Diesel (A3)	0,6110	0,1680	0,2667	0,4307	0,5946	0,7586	0,9226
Hydrogen (A4)	0,3602	0,1800	0,3333	0,3478	0,3623	0,3768	0,3912
Hybrid (A5)	0,6090	0,1456	0,1423	0,3363	0,5304	0,7245	0,9186
Electric (A6)	0,1756	0,1200	0,0000	0,0000	0,0000	0,0000	0,0000

S*	0,1756
S-	0,6475
R*	0,1200
R-	0,3000

Table 5. Ranking orders of alternatives and control of conditions

	Q_i (v=0)	Q_i (v=0.25)	Q_i (v=0.5)	Q_i (v=0.75)	Q_i (v=1)
LPG (A1)	5	5	5	5	3
Gasoline (A2)	6	6	6	6	6
Diesel (A3)	3	4	4	4	5
Hydrogen (A4)	4	3	2	2	2
Hybrid (A5)	2	2	3	3	4
Electric (A6)	**1**	**1**	**1**	**1**	**1**
Q(A2)	0,1503	0,2017	0,2530	0,3044	0,3557
Q(A1)	0,0000	0,0000	0,0000	0,0000	0,0000
Q(A2)-Q(A1)	0,1503	0,2017	0,2530	0,3044	0,3557
D(Q)=1/(6-1)	0,2000	0,2000	0,2000	0,2000	0,2000
Condition 1	FALSE	TRUE	TRUE	TRUE	TRUE
Condition 2	TRUE	TRUE	TRUE	TRUE	TRUE

Alternatives are ordered by using S_i, R_i and Q_i values and three ranking list are obtained (See Table V). After that, it is controlled that the alternative which has minimum Q_i value satisfies two conditions. These conditions are acceptable advantage and acceptable stability in decision making [23].

These two conditions are satisfied for Q(v=0.25, v=0.5, v=0.75 and v=1). So, vehicle which has electric engine system is the best alternative for these values. For Q(v=0), the first condition is not satisfied, in this situation all alternatives are located in a set of compromise solutions, but when alternatives are ordered by using Q(v=0) values, again electric engine system is the best one.

3.2. Application of TOPSIS

Decision matrix and criteria weights are given in Table I. For TOPSIS implementation, normalization and weighted normalization matrices are given in Table VI and Table VII respectively.

Table 6. Normalization matrix

		CRITERIA					
		Maximum Power (HP) (K1)	**Maximum Tork (Nm) (K2)**	**Acceleration (for 0-100 km/h) (sn) (K3)**	**Maximum Velocity (km/h) (K4)**	**Fuel cost in 100 km (TL) (K5)**	**CO2 Emission (gr/km) (K6)**
ALTERNATIVE ENGINE SYSTEMS	**LPG (A1)**	0.475447	0.325213	0.423984	0.478626	0.425479	0.623438
	Gasoline (A2)	0.502072	0.342329	0.385756	0.454695	0.676493	0.563874
	Diesel (A3)	0.342322	0.438609	0.510866	0.430764	0.380718	0.432833
	Hydrogen (A4)	0.330911	0.492098	0.417034	0.306321	0.19481	0
	Hybrid (A5)	0.380357	0.237491	0.417034	0.394867	0.399284	0.325617
	Electric (A6)	0.387965	0.534889	0.25022	0.35897	0.137842	0

Table 7. Weighted Normalization matrix

		CRITERIA					
		Maximum Power (HP) (K1)	**Maximum Tork (Nm) (K2)**	**Acceleration (for 0-100 km/h) (sn) (K3)**	**Maximum Velocity (km/h) (K4)**	**Fuel cost in 100 km (TL) (K5)**	**CO2 Emission (gr/km) (K6)**
ALTERNATIVE ENGINE SYSTEMS	**LPG (A1)**	0,085580	0,039025	0,033918	0,038290	0,127643	0,149625
	Gasoline (A2)	0,090372	0,041079	0,030860	0,036375	0,202947	0,135329
	Diesel (A3)	0,061617	0,052633	0,040869	0,034461	0,114215	0,103879
	Hydrogen (A4)	0,059563	0,059051	0,033362	0,024505	0,058442	0
	Hybrid (A5)	0,068464	0,028498	0,033362	0,031589	0,119785	0,078148
	Electric (A6)	0,069833	0,064186	0,020017	0,028717	0,041352	0

Table 8. The relative closeness values and ranking orders of alternatives

ALTERNATIVES	THE RELATIVE CLOSENESS VALUE (C_i^*)	RANKS
LPG (A1)	0,318419	5
Gasoline (A2)	0,156541	6
Diesel (A3)	0,438189	4
Hydrogen (A4)	0,838753	2
Hybrid (A5)	0,480832	3
Electric (A6)	0,908260	1

The relative closeness values and ranking order is given in Table VIII. According to the relative closeness values (C_i^*) of the alternatives, the best alternative which has the biggest closeness value is Electric Engine System. As can be seen from the results, electric engine system in vehicles is more preferable than the other systems.

In both VIKOR and TOPSIS methods, electric engine system is the best one and gasoline engine system is the worst one.

CONCLUSIONS

In this paper, VIKOR and TOPSIS methods are used to determine the best vehicle engine system. Criteria and their weights are determined by ten experts. After the implementation of the methods to this multi-criteria decision making problem, it is seen that electric engine system is selected the best one in both methods. Also, the results of these two methods are compatible. Electric engine systems are very efficient and eco-friendly. In future, electric engine systems will be more used than the others.

REFERENCES

[1]. Hadjipaschalis, I., Poullikkas, A., and Efthimiou, V. Overview of current and future energy storage technologies for electric power applications. *Renewable and Sustainable Energy Reviews*, 13(6), 1513-1522, 2009.
[2]. Ider, S. K. Hidrojen Enerji Sistemi. *TMMOB Metalurji Muhendisler Odası Metalurji Dergisi*, 134, 1-8, 2003.
[3]. Koca A., and Gun, F. Degisken supap zamanlamasinin motor performansina etkilerinin deneysel incelenmesi. *Politeknik Dergisi*, 9(4), 271-277, 2006.
[4]. Ultanır, M. O. 21. Yuzyila girerken Turkiye'nin enerji stratejisinin degerlendirilmesi. TÜSİAD Yayınları, Yayın No: TÜSİAD, 98-12, 1998.
[5]. Icingur, Y., and Haksever, R. Using of LPG for internal combustion engines-experimental analysis of its effects on performance and emission. *Journal of Polytechnic*, 1(3-4), 69-76, 1998.
[6]. Scharff, R. Complete Fuel Systems and Emission Control, Delmar Publishers, Inc., Albany, NY, 1989.
[7]. Salman, M.S., and Batmaz, I. Sivilastirilmis petrol gazi kullanan tasitlarda performans ve emisyonlar. *G.Ü. Tek. Eğit. Fak. Politeknik Dergisi*, 1(1-2), Ankara, 1998.
[8]. Gorgulu A. Hidrojenin yakit olarak icten yanmali motorlarda kullanimi ve diger yakitlarla mukayesesi. Yüksek Lisans Tezi, Osmangazi Universitesi Fen Bilimleri Enstitüsü, Eskişehir, 1994.
[9]. Ciniviz, M., Hasimoğlu, C., and Ucar, G. Gunumuzde icten yanmali motorlarda hidrojen yakitinin kullanilmasi. *Selcuk Univ. On-Line Dergisi*, 1-2, 2002.
[10]. Erbeyler, S. A. Hibrid elektrikli hafif ticari aracta dizel motoru azot oksit (NOx) emisyonlarının optimizasyonu, Yuksek Lisans Tezi, ITU Fen Bilimleri Enstitusu, Istanbul, 2007.
[11]. Chan, C. C.. The state of the art of electric and hybrid vehicles. *Proceedings of the IEEE*, 90(2), 247-275, 2002.
[12]. Sandalow, D. B. (Ed.). Plug-in electric vehicles: what role for Washington?. Brookings Institution Press, 2009.

[13]. Peker, I, Korucuk, S., Ulutas, Ş., Okatan, B. S., and Yasar, F. Afet lojistigi kapsaminda en uygun dagitim merkez yerinin AHS-VIKOR butunlesik yontemi ile belirlenmesi: Erzincan ili ornegi. *Yonetim ve Ekonomi Arastirmaları Dergisi*, *14*(1), 82-103, 2016.
[14]. Ozden, U. H. AB'ye uye ulkelerin ve Turkiye'nin ekonomik performanslarina gore VIKOR yontemi ile siralanmasi. *Istanbul Ticaret Universitesi Sosyal Bilimler Derqisi*, 11(21), 455-468, 2012.
[15]. Ar., I.M., Ozdemir, F., and Baki, B. Oncelikli sektörlerin belirlenmesinde AHS-TOPSIS ve AHS-VIKOR yaklasimlarının kullanimi: Rize organize sanayi bolgesi ornegi. *Journal of Yasar University*, *35*(9), 6159-6174, 2014.
[16]. Opricovic, S., and Tzeng, G. H. Extended VIKOR method in comparison with outranking methods. *European Journal of Operational Research*, 178(2), 514-529, 2007.
[17]. Chang, C. L., and Hsu, C. H. Multi-criteria analysis via the VIKOR method for prioritizing land-use restraint strategies in the Tseng-Wen reservoir watershed. *Journal of Environmental Management*, *90*(11), 3226-3230, 2009.
[18]. San Cristóbal, J. R. Multi-criteria decision-making in the selection of a renewable energy project in Spain: the Vikor method. *Renewable Energy*, 36(2), 498-502, 2011.
[19]. Babashamsi, P., Golzadfar, A., Yusoff, N. I. M., Ceylan, H., and Nor, N. G. M. Integrated fuzzy analytic hierarchy process and VIKOR method in the prioritization of pavement maintenance activities. *International Journal of Pavement Research and Technology*, in press, 2016.
[20]. Kim, Y., Park, D., Um, M. J., and Lee, H. Prioritizing alternatives in strategic environmental assessment (SEA) using VIKOR method with random sampling for data gaps. *Expert Systems with Applications*, 42(22), 8550-8556, 2015.
[21]. Qin, J., Liu, X., and Pedrycz, W. An extended VIKOR method based on prospect theory for multiple attribute decision making under interval type-2 fuzzy environment. *Knowledge-Based Systems*, *86*, 116-130, 2015.
[22]. Mohanty, P. P., and Mahapatra, S. S. A compromise solution by VIKOR method for ergonomically designed product with optimal set of design characteristics. *Procedia Materials Science*, *6*, 633-640, 2014.
[23]. Opricovic, S., and Tzeng, G. H. Compromise solution by MCDM methods: A comparative analysis of VIKOR and TOPSIS. *European Journal of Operational Research*, 156(2), 445-455, 2004.
[24]. Hwang, C.L. ve Yoon, K. Multiple Attribute Decision Making Methods and Applications, Springer-Verlag, New York, NY, 1981.
[25]. Ayvaz, B., Bolturk, E., and Kactioglu, S. Supplier selection with TOPSIS method in fuzzy environment: an application in banking sector. *Sigma*, *33*(3), 351-362, 2015.
[26]. Demireli, E. TOPSIS cok kriterli karar verme sistemi: Turkiye'deki kamu bankalari uzerine bir uygulama. *Girisimcilik ve Kalkinma Dergisi*, *5*(1), 101-112, 2010.
[27]. Tavana, M., Li, Z., Mobin, M., Komaki, M., and Teymourian, E. Multi-objective control chart design optimization using NSGA-III and MOPSO enhanced with DEA and TOPSIS. *Expert Systems with Applications*, *50*, 17-39, 2016.
[28]. Wang, P., Zhu, Z., and Wang, Y. A novel hybrid MCDM model combining the SAW, TOPSIS and GRA methods based on experimental design. *Information Sciences*, *345*, 27-45, 2016.
[29]. Abedi, M., and Norouzi, G. H. A general framework of TOPSIS method for integration of airborne geophysics, satellite imagery, geochemical and geological data. *International Journal of Applied Earth Observation and Geoinformation*, *46*, 31-44, 2016.
[30]. Kermani, M. A., Badiee, A., Aliahmadi, A., Ghazanfari, M., and Kalantari, H. Introducing a procedure for developing a novel centrality measure (Sociability Centrality) for social networks using TOPSIS method and genetic algorithm. *Computers in Human Behavior*, *56*, 295-305, 2016.
[31]. Mir, M. A., Ghazvinei, P. T., Sulaiman, N. M. N., Basri, N. E. A., Saheri, S., Mahmood, N. Z., ... and Aghamohammadi, N. Application of TOPSIS and VIKOR improved versions in a multi criteria decision analysis to develop an optimized municipal solid waste management model. *Journal of Environmental Management*, *166*, 109-115, 2016.
[32]. Behzadian, M., Otaghsara, S. K., Yazdani, M., and Ignatius, J. A state-of the-art survey of TOPSIS applications. *Expert Systems with Applications*, 39(17), 13051-13069, 2012.

ICENS
INTERNATIONAL CONFERENCE ON ENGINEERING AND NATURAL SCIENCES
24-28 May 2016 /Sarajevo

Enzyme Resistant Starch As a Functional Fiber

Ozen Ozboy Ozbas [1], Merve Sert Aribas

Abstract

Starch is the major source of carbohydrates in the human diet. Starch is present in many different fruits, vegetables, roots, and grains. Being a major constituent, starch contributes to the texture, body and organoleptic qualities of the prepared food. Food materials are generally consumed after being processed which includes heating, cooling, drying, roasting, deep-fat frying, etc. It is now well recognised that during such processing treatments the dietary starch partially undergoes physical modification leading to the formation of resistant starch (RS), that escapes from digestion in the small intestine but later is fermented by the gut microflora. The amylose/amylopectin ratio also influence food RS content. RS has been classified into five different types (RS1-5). RS is made up of different fractions: retrograded, physically inaccessible, chemically modified fragments, starch complexes with other related food components, etc. RS contents in food range between 0 and approximately 4%. This type of starch has been the subject of intensive investigations recently and may prove to be a source of dietary fiber. For health preventing or therapeutical effects, a higher amount of RS in food is recommended. RS has been recognised as a functional fiber performing an important role in digestive physiology. Similar to oligosaccharides, it escapes digestion and provides fermentable carbohydrates for colonic bacteria. RS has also been shown to provide benefits such as the production of desirable metabolites including short-chain fatty acids in the colon. In addition to its therapeutic effects, RS provides better appearance, texture, and mouthfeel than conventional fibers. At present, RS have drawn broad interest worldwide for both their potential health benefits and functional properties. As a functional fiber, its quality characteristics make possible the formulation of a number of food products (breads, snack crackers, muffins, etc) with better consumer acceptability and greater palatability than those made with traditional fibers.

Keywords: *Resistant starch, Dietary fiber*

1. INTRODUCTION

Starch is the major source of energy in most human diets. Starchy foods are derived from plant sources such as potatoes and cereal products. Chemically, starches are polysaccaharides, i.e. they are composed of a number of monosaccarides or sugar (glucose) molecules linked together with α1-4 and/or α1-6 linkages. Two main structural types of starch exist: amylose which is a linear α1-4 molecule and typically constitutes 15-20% of starch, and amylopectin which is a larger branched molecule with α1-4 and α1-6 linkages and is a major component of starch. Starch and starch derivatives are a nutritive, abundant, and economical food source. Food starches contribute to the characteristic viscosity, texture, mouthfeel, and consistency of many food products. It is not known that not all starch is digested in the small intestine. Non-gelatinized and retrograded starches are exampes of non-digested starch [1] . These and other types of non-digested starches have been defined as enzyme resistant starch (ERS). The physiological effects of RS are similar to those observed with dietary fiber (DF). Starch is not only the major source of energy for most humans, it appears it is the major source of energy for the microbiota in the large intestine. As a functional fiber, many of RS's quality characteristics make possible the formulation of a number of breads, snack crackers, muffins, cookies with better consumer acceptability and greater palatability than those made with conventional fibers.

2. ENZYME RESISTANT STARCH

Starch and non-starch polysaccharides (dietary fiber) are the major carbohydrate constituents. Dietary starch has been classified into three main categories, readily digestible starch (RDS), slowly digestible starch (SDS) and resistant starch ([2], 3]). The term "resistant starch" was first coined by [4] to describe a small fraction of starch that was resistant to hydrolysis by exhaustive α-amylase and pullulanase treatment *in vitro*. RS is the starch not hydrolyzed after 120 min of incubation [5]. However, because starch reaching the large intestine may be more or less fermented by the gut microflora, RS is now defined as that fraction of dietary starch, which escapes digestion in the small intestine. It is measured chemically as the difference between total starch obtained from homogenized and chemically treated sample and the sum of RDS and SDS, generated from non-homogenized food samples by enzyme digestion [6]. RS has been classified into five general subtypes named RS1-RS5, which are described below ([7], [8]):

[1]*Corresponding author: Aksaray University, Department of Food Engineering, 68000, Aksaray Turkey. ozenozboy@yahoo.com*

Type 1 includes physically inaccessible starch that is locked within cell walls and food matrixes, thus preventing amylolysis. Milling and chewing can make these starches more accessible and less resistant. RS1 is heat stable in most normal cooking operations, which enables its use as an ingredient in a wide variety of conventional foods.

Type 2 is composed of native starch granules from certain plants containing uncooked starch or starch that was gelatinized poorly and hydrolyzed slowly by α-amylases (e.g., high-AM corn starches). RS2 describes native starch granules that are protected from digestion by the conformation or structure of the starch granule. This compact structure limits the accessibility of digestive enzymes (has low bioaccesibility), various amylases, and accounts for the resistant nature of RS2 such as, ungelatinized starch. In the diet, raw starch is consumed in foods like banana. A particular type of RS2 is unique as it retains its structure and resistance even during the processing and preparation of many foods; this RS2 is called high-AM maize starch [9].

Type 3 refers to retrograded or crystalline non-granular starch formed after cooking, like the starch found in cooked and cooled potatoes, bread crusts, cornflakes, and retrograded high AM maize starch. RS3 refers to non-granular starch-derived materials that resist digestion. RS3 is of particular interest, because of its thermal stability. This allows it to be stable in most normal cooking operations, and enables its use as an ingredient in a wide variety of conventional foods. During food processing, in most cases in which heat and moisture are involved. RS1 and RS2 can be destroyed, RS3 can be formed. The RS3 content of the foods is generally low; levels up to 3% have been reported in baked foods, pasta and processed cereals and tubers ([10], [11], [12]).

Type 4 includes chemically modified or re-polymerized starches (e.g., chain linkage altered dextrins, ethers, or esters) used by food manufacturers to alter the functional characteristics of the starch, and include starches which have been etherized, esterified, or cross-bonded with chemicals in such a manner as to decrease their digestibility.

Type 5 RS is an AM-lipid compexed starch, which is formed from high AM starches that require higher temperatures for gelatinization and are more susceptible to retrograde. In general, the structure and amount of starch-lipid in foods depend on their botanical sources. Also, [13] defined as RS5 a polysaccharide that consists of water-insoluble linear poly-alpha-1,4-glucan that is not susceptible to degradation by alpha-amylases. They also found that the poly-alpha-1,4-D-glucans promote the formation of short-chain fatty acids (SCFA), particularly butyrate, in the colona and are thus suitable for use as nutritional supplements for the prevention of colorectal diseases ([6], [8]). Although RS has been classified into 5 major components, it is difficult to experimentally differentiate between them.

RS is naturally found in cereal grains and in heated starch or starch-containing foods. The manufacture of RS usually involves partial acid hydrolysis and hydrothermal treatments, heating, retrogradation, extrusion cooking, chemical modification, and repolymerisation [14]. The content of RS formed depends on the severity of processing conditions such as temperature, pH, moisture content and number of heating and cooling cycles adopted. Chemically, RS is derived from the highly retrograded amylose fraction (linear) of starch, and it is likely that the amount of RS generated is proportional to the linear α-glucan content of starch [15].

RS occurs basically in all starchy foods but not in a fixed quantity. In addition to the structure of the starch as laid down during biosynthesis, methods used to prepare process and store foods, either domestically or industrially also determine the proportion of the starch that escapes digestion ([16], [8]). Table 1 provides a summary of the RS content of some basic and processed foods. According to the Table 1, cereal grains and legumes are an important natural source of RS.

RS may be categorized as a type of dietary fiber, as defined by the American Association of Cereal Chemists and the Food Nutrition Board of the Institute of Medicine of the National Academies. RS is measured in part by the methodology recommended by the Association of Official Analytical Chemists for measuring dietary fiber ([3], [11], [1]). In addition to the natural food sources of RS, some commercially manufactured forms of RS are also available such as HYLON VII, Hi-maize 1043, Novelose 240, ActiStar and CrystaLean etc. There are a number of advantages to using commercially manufactued sources of RS in food products [17]. Unlike natural sources of RS (*e.g.* legumes, potatoes, bananas), commercially manufactured RS are not affected by processing and storage conditions [1].

Comparison of the RS content of different foods and the food intake records showed that Americans on average consumed an estimated 3-8 g of RS per day. In Europe, the intake of RS has been estimated to be between 3 and 6 g per day while the intake in developing countries has been estimated to be between 30 and 40 g per day [18].

Isolated RS has a small particle size, white appearance, bland flavor and low water-holding capacity. RS typically replaces flour in foods such as bread and other bakes goods, pasta, cereal and batters, because it can produce foods with similar color and texture of the original food. It has also been used for its textural properties in imitation cheese

[19]. It has desirable physicochemical properties such as swelling, viscosity increase, gel formation, and water-binding capacity, making it useful in a variety of foods. RS not only fortifies fiber but also imparts special characteristics not otherwise attainable in high-fiber foods. Some of these properties have been succesfully used in a range of baked and extruded products as described subsequently.

Table 1. Approximate total dietary fiber, starch and resistant starch of some food sources (g/100 g as eaten)[1,2]

Source	Total Starch	Total Dietary Fiber	Resistant Starch
Legumes			
Red kidney beans	42.6	36.8	24.6
Lentils	53.3	33.1	25.4
Cereal grains			
Barley	55.2	17.0	18.2
Corn	77.9	19.6	25.2
White rice	95.1	1.5	14.1
Wheat	50.8	17.0	13.6
Oats	43.4	37.7	7.2
Flours			
Corn	84.3	2.8	11.0
Wheat	68.8	12.1	1.7
Rice	86.9	5.1	1.6
Potato	81.0	2.1	1.7
Grain-based food products			
Spaghetti	73.0	5.6	3.3
Cereal products			
Crisp bread	67.4	n/a	1.4
White bread	46.7	n/a	1.9
Extruded oat cereal	57.2	n/a	0.2
Puffed wheat cereal	67.0	n/a	1.2
Cooked spaghetti	n/a	n/a	
Cooked rice	n/a	n/a	2.9
Potato products			3.7
Boiled potatoes	n/a	n/a	2.0
Chips	29.5	n/a	4.8
Mashed potatoes	n/a	n/a	2.4

[1]*Adapted from [16], [8]).*

2 n/a: not available

2.1 Health Benefits of Resistant Starch

A number of physiological effects have been ascribed to RS [1], which have been proved to be beneficial for health (Table 2). There is ample justification through nutritional studies that RS behaves physiologically like fiber, and should be retained in the TDF assay. RS assays as insoluble fiber, but has the physiological benefits of soluble fiber.

By definition, RS escapes digestion in the human small intestine. RS therefore passes into the colon where like other dietary fibers, it may be fermented. Fermentation of carbohydrates in the colon leads to the production of SCFAs. SCFAs are the metabolic products of anaerobic bacterial fermentation and consist of butyrate, propionate, and acetate. The SCFAs produced by bacterial fermentation in the human gut are the preferred fuel for the cells lining the colon and have been shown to lower luminal pH, increase the excreation of bile acids, and help prevent the development of abnormal colonic cells. There is indication that RS like guar, a soluble fiber, influences tumorigenesis, and reduces serum cholosterol and triglycerides. RS can increase the production of SCFA and therefore may help improve colonic health. RS has been suggested for use in probiotic compositions to promote the growth of such beneficial microorganisms as *Bifidobacterium*. Since RS almost entirely passes the small intestine, it can behave as a substrate for growth of the probiotic microorganisms [6]. Among the different physiological roles of RS, its prebiotic effect is of great interest [8]. The slow digestion of RS has implications for its use in controlled glucose release applications, particularly for diabetics [11]. The metabolism of RS occurs 5 to 7 h after consumption, in contrast to normally cooked starch, which is digested almost immediately. This reduces postprandial glycemia and insulinemia and has the potential for increasing the period of satiety. RS is found also to reduce the incidence of gallstones. RS has been shown to have significant effects of serum triglyceride and cholesterol concentrations. RS also could have a positive

effect on intestinal calcium and iron absorption ([17], [6]). The effects of RS consumption on satiety and weight management are not as clear.

Table 2. Physiological effects of resistant starch

Potential physiological effects	Conditions where there may be a protective effect
Improve glycaemic and insulinaemic responces	Diabetes, impaired glucose and insulin responces, the metabolic syndrome
Improved bowel health	Colorectal cancer, ulcerative colitis, inflammatory bowel disease, diverticulitis, constipation
Improved blood lipid profile	Cardiovascular disease, lipid metabolism, the metabolic syndrome
Prebiotic and culture protagonist	Colonic health
Increased satiety and reduced energy intake	Obesity
Increased micronutrient absorption	Enhanced mineral absorption, osteoporosis
Adjunct to oral rehydration therapies	Treatment of cholera, chronic diarrhoea
Synergistics interactions with other dietary components, e.g. dietary fibers, proteins, lipids	Improved metabolic control and enhanced bowel health
Thermogenesis	Obesity, diabetes

2.1 Food Applications for Resistant Starch

Starch-based food products have diverse nutritional properties, which are influenced by the origin of the starch, its composition, processing method used, and process conditions applied. Increasing health awareness and growing demand for functional foods by consumers are driving the food industry internationally to look at ways to produce innovative food products with health benefits [20]. Considerable scientific research has confirmed the beneficial role of the DF in the reduction of several chronic diseases. So consumer awareness about the healthy role of DF intake has raised, gaining popularity especially fiber-enriched cereal based products [8]. RS is the term that has been applied to starch which resists degradation by amylolytic enzymes *in vitro* and *in vivo*. This type of starch has been the subject of intensive investigations and may prove to be a source of DF.

The physical properites of RS, particularly its low water-holding capacity, allow it to be a functional ingredient that provides good handling in processing and crispness, expansion, and improved texture in the final product. Bread is commonly fortified with DF. However, dark color, reduced loaf volume, poor mouthfeel, and masking of flavor are all negative attributes that are often associated with high-fiber breads. A study was conducted at the American Inst. of Baking (AIB) to evaluate the effects of RS on bread characteristics and to compare their performance to traditional fibers. As a result, bread containing 40%TDF RS had greater loaf volume and better cell structure compared with traditional fibers tested ([21], [3]). Breads with varying levels of ERS were also obtained by replacing 24% of wheat flour with 4% vital wheat gluten and 20% of one of the following: corn starch, high-amylose corn starch, or extruded retrograded high amylose corn starch [22]. It is now also recognised that as much as 30% of the total 'apparent' dietary fiber of white bread is RS [23].

RS was incorporated in a various of baked goods, many of which include batter systems, such as in cakes, cake-like muffins, or brownies. In general, application tests showed that RS acts as texture modifier, imparting a favorable tenderness to the crumb. A low-fat, loaf cake was formulated with RS and various fibers to obtain approximately 3% TDF or 2.5 g of fiber. The baked cakes made with RS were similar to that containing oat fiber and the control in the amount of moisture loss after baking, height, specific volume, and density ([6], [3]).

In another research study, utilization of resistant starch preparation (RSP) and apricot kernel flour (AKF) as fat replacers in cookies were examined and effects of fruit powders on the quality of low-fat cookies were investigated. A slight increase in the spread ratios of RSP/AKF supplemented cookies were observed up to 20% level. The hardness of RSP and RSP/AKF supplemented cookies increased above 10% level. Sensory scores of RSP and RSP/AKF supplemented cookies were not different from the control. Total dietary fiber (TDF) contents of RSP and RSP/AKF supplemented cookies increased with increasing level. Apricot powder (APR-P) supplemented cookies had higher spread ratios compared to the apple powder (APL-P) supplemented ones above 10% level. TDF contents of the cookies increased with increasing fruit powder supplementation level. APR-P appeared to be a more suitable replacer than APL-P up to 30% level [24].

Among other functional properties, RS can be used as an ingredient that improves crispness in foods where high heat is applied to aproduct's surface during processing. French toast and waffles, especially frozen reheated types, represent foods in which surface crispness is desired. Tests were conducted to compare the functionality of RS and various fibers in a buttermilk waffle formulation. Based on the evaluation of the toasted waffles for initial crispness,

crispness after 3 min, moistness, and overall texture by a trained sensory panel RS waffle indicated greater crispness than control or traditional fiber [6].

Traditional food fibers have a detrimental effect on the texture of many items, such as baked goods and extruded products. Fibers tend to strengthen the physical structure of a food and limit its ability to expand [11]. Along with textural enhancement, RS can improve expansion in extruded cereals and snacks. Various cereals were formulated to contain 40% TDF RS (Novelose 240 starch) alone and in combination with oat fiber. The cereal with RS and no oat fiber had greater volumetric expansion than control. Refrence [17], also summurized the comparison of TDF content, expansion and textural characteristics of an oat puffed cereal with or without Novelose^{TM}. Dried pasta products containing up to 15% RS can be made with little or no effect on dough reology during extrusion [6].

RS may also be used in thickened, opaque health beverages in which insoluble fiber is desired. Insoluble fibers generally require suspension and add opacity to beverages. Compared with insoluble fibers, RS imparts a less gritty mouthfeel and masks flavors less [6]. Recently, RS has become available as an ingredient that can be used to produce high quality foods.

3 CONCLUSIONS

ERS refers to the portion of starch and starch products that resist digestion as they pass through the gastrointestinal tract. RS is an extremely broad and diverse range of materials and a number of different types exist. RS is a dietary fiber and can be used to replace digestible starch in foods. RS may be fermented in the colon and resulting SCFA production has been linked to a number of health benefits such as reduced pH, which has been associated with the suppression or growth of potentially pathogenic organisms and reduction of the absorption of toxic compounds. RS is generally found as a component of a RS-containing ingredient or food. The goal of including an ingredient high in RS should be to combine physical functionality, processing stability, and nutritional functionality. The physical functionality of RS-containing ingredient is required for appropriate physical characteristics of the food, such as texture, water holding capacity, etc. The processing stability of RS is important in order to preserve the nutritional functionality of the RS-containing ingredient. The nutritional functionality of the RS-containing ingredient can involve both resistance to digestion in the small intestine and resistance to fermentation in the colon. To fully take advantage of the prospects for use of RS in foods, to understand the physical bases for enzyme resistance in the small intestine and in the colon. With such knowledge it might be possible to develope a wide range of RS-containing materials for use in manufactured foods [7]. In conclusion, the positive results seen in applications testing suggest that a RS can serve many purposes in the development of healthy foods.

REFERENCES

[1]. Nugent, A.P., 2005, Health Properties of Resistant Starch, British Nutrition Foundation Nutrition Bulletin, 30, 27-54.
[2]. Cairns, P., Morris, V.J., Botham, R.L., Ring, S.G., 1996, Physicochemical Studies on Resistant Starch *In Vitro* and *In Vivo*, Journal of Cereal Science, 23, 265-275.
[3]. Yu, P., Waring, S., 1998, Resistant Starch in Food Applications, Cereal Foods World, 43 (9), 690-695.
[4]. Englyst, H.N., Wiggins, H.S., Cummings, J.H., 1982, Determination of the Non-Starch Polysaccharides in Plant Foods by Gas-Liquid Chromatography of Constituent Sugars as Alditol Acetates, Analyst, 107, 307-318.
[5]. Englyst, H.N., Kingman,S.M., Cummings, J.H., 1992, Classification and Measurement of Nutritionally Important Starch Fractions, Eurapean Journal of Clinical Nutrition, 46, S33-S50.
[6]. Sajilata, M.G., Singhal, R.S., Kulkarni, P.R., 2006, Resistant Starch-A Review, Comprehensive Reviews in Food Science and Food Safety, 5, 1-17.
[7]. Thompson, D.B., 2000, Strategies for the Manufacture of Resistant Starch, Trends in Food Science and Technology, 11, 245-253.
[8]. Fuentes-Zaragoza, E., Sanchez-Zapata, E., Sendre, E., Sayas, E., Navarro, C., Fernandez-Lopez, J., Perez-Alvarez, J.A.P., 2011, Resistant Starch as Prebiotics: A review, Starch-Starke, 63, 406-415.
[9]. Jiang, G., Liu, Q., 2002, Characterization of Residues from Partially Hydrolyzed Potato and High Amylose Corn Starches by Pancreatic α-Amylase, Starch, 54, 527-533.
[10]. Vasanthan, T., Bhatty, R.S., 1998, Enhancement of Resistant Starch (RS3) in Amylomaize, Barley, Field Pea and Lentil Starches, Starch, 50 (7), 286-291.
[11]. Haralampu, S.G., 2000, Resistant Starch-A Review of the Physical Properties and Biological Impact of RS_3, Carbohydrate Polymers, 41, 285-292.
[12]. Lehmann, U., Rössler, C., Schmiedl, D., Jacobasch, G., 2003, Production and Physicochemical Characterization of Resistant Starch Type III Derived from Pea Starch, Nahrung, 1,60-63.
[13]. Frohberg, C., and Quanz, M., 2008, Use of Linear Poly-Alpha-1-4 Glucans as Resistant Starch, United States Patent Application 20080249297, Available on line at: http://www.wipo.int/pctdb/en/wo.jsp?WO-2005040223.
[14]. Charalampopoulos, D., Wang, R., Pandiella, S.S., Webb, C., 2002, Applications of Cereals ans Cereal Components in Functional Foods: A Review, International Journal of Food Microbiology, 79, 131-141.
[15]. Tharanathan, M., Tharanathan, R.N., 2001, Resistant Starch in Wheat-Based Products: Isolation and Characterisation, Journal of Cereal Science, 34, 73-84..
[16]. Lunn, J., Buttriss, J.L., 2007, Carbohydrates and Dietary Fiber, Nutrition Bulletin, 32, 21-64.

[17]. Gordon, D.T., Topp, K., Shi, Y.-C., Zallie, J., Jeffcoat, R., 1998, Resistant Starch: Physical and Physiological Properties. In: New Technologies for Healthy Foods & Nutraceuticals. M. Yalpani, Ed. ATL Press, Inc. Science Publishers, Shrewsbury, MA
[18]. Evans, A., 2015, Resistant Starch and Health, Encyclopedia of Food Grains, http://dx.doi.org/10.1016/B9/8-0-12-394437-5.0009/-3
[19]. Homayouni, A., Amini, A., Keshtiban, A. K., Mortazavian, A. M., Esazadeh, K., Pourmoradian, S., 2014, Resistant Starch in Food Industry. A Changing Outlook for Consumer and Producer. Starch-Starke, 66 (1-2), 102-114.
[20]. Htoon, A.K., Uthayakumaran; S., Piyasiri, U., Appelqvist, I., 2010, The Effect of Acid Dextrinisation of Enzyme-Resistant Starch Content in Extruded Maize Starch, Food Chemistry, 120, 140-149.
[21]. Baghurts, B.A., Baghurst, K.I., Record, S.J., 1996, Dietary Fiber, Non-Starch Polysaccharides and Resistant Starch-A Review, Food Aust., 48 (3), S3-S35.
[22]. Eerlingen, R.C, Vanhaesendonck, I.P., Depaepe, G., Delcour, J.A., 1994, Enzyme-Resistant Starch. 3. The Quality of Straight-Dough Bread Containing Varying Levels of Enzyme-Resistant Starch, Cereal Chemistry,71 (2), 165-170.
[23]. Berry, C.S., 1986, Resistant Starch: Formulation and Measurements of Starch that Survives Exhaustive Digestion with Amylolytic Enzymes during the Determination of Dietary Fiber, Journal of Cereal Science, 4, 301-314.
[24]. Ozboy-Ozbas, O., Seker, I.T., Gokbulut, I., 2010, Effects of Resistant Starch, Apricot Kernel Flour, and Fiber-rich Fruit Powders on Low-fat Cookie Quality, Food Sci. Biotechnol. 19 (4), 979-986.

ICENS
INTERNATIONAL CONFERENCE ON ENGINEERING AND NATURAL SCIENCES
24-28 May 2016 /Sarajevo

Formation, Occurrence, and Control of Disinfection By-Products in Drinking Water

***Sibel Aslan*[1]**

Abstract

Drinking water disinfection is one of the most important advancements for public health of the last century and has been used to eradicate and inactivate the pathogens from drinking water. Chemical disinfectants are effective for killing harmful microorganisms in drinking water, but they are also powerful oxidants, oxidizing the organic matter, anthropogenic contaminants, and bromide/iodide naturally present in most source waters. However, disinfection processes can lead to formation of potentially toxic disinfection by-products (DBPs). Disinfection by-products result from the reactions between disinfectants and naturally occurring organic matter, bromide, and iodide. Chlorine, ozone, chlorine dioxide, and chloramines are the most commonly used disinfectants and these produce its own DBPs in drinking water. There are various strategies for controlling formation of DBPs such as usage of alternative disinfectants, precursor removal, and source control.

Keywords: Disinfection, disinfectant, disinfection by-products

1. INTRODUCTION

Drinking water disinfection is one of the most important public health advances of the last century and disinfection process has been routinely carried out since the dawn of the 20th century [1, 2]. Drinking water disinfection is applied to eradicate and inactivate the pathogenic microorganisms from water, and to prevent microbial recontamination throughout the treated water distribution system [2, 3]. Disinfection methods fall into three major categories: (1) physical, (2) radiation, (3) chemical. Physical methods of disinfection include heat and ultraviolet radiation. Gamma rays are emitted from a radioactive source and are effectively to disinfect water [4].

Chemical disinfectants are also used for following reasons in addition to removing pathogens in drinking water treatment: (i) to act as an oxidant in water treatment, (ii) to remove taste and colour, (iii) to oxidize iron and manganese, (iv) to improve coagulation and filtration efficiency, (v) to prevent algal growth in sedimentation basins and filters, (vi) to prevent biological re-growth in the water distribution system [5, 2, 6]. Chemical disinfectants include (1) oxidizing agents, such as halogens (chlorine, bromide, and iodine), ozone, hydrogen peroxides, potassium permanganate; (2) alcohols; (3) phenol and phenolic compounds; (4) heavy metals; (5) quaternary ammonium compounds; (6) soaps and synthetic detergents; and (7) alkalies and acids. Among all these chemicals, oxidizing agents are commonly used for disinfection of water [4].

Five disinfection agents commonly used in drinking water treatment are chlorine, chloramines, ozone, chlorine dioxide, and UV light [3, 7]. Among disinfectants, chlorine and its compounds are the most commonly used disinfectants for the treatment of water and its popularity is due to higher oxidizing potential, provides a minimum level of chlorine residual throughout the distribution system and protects against microbial recontamination [8]. Chlorine dioxide is an excellent choice among disinfectants. Chloramines that result from reactions between chlorine and ammonia are useful disinfectants in some situations [9]. Ozone is an excellent disinfectant and can even be used to inactivate microorganisms such as protozoa which are very resistant to conventional disinfectants [10]. However, chemical disinfection has also raised a public health issue: the potential for cancer and reproductive/developmental effects associated with chemical DBPs [1].

2. DISINFECTION BY-PRODUCFORMATION OF DISINFECTION BY-PRODUCTS (DBPS)

Disinfection by-products (DBPs) are an unintended consequence of using chemical disinfectants to kill harmful pathogens in water [11, 7]. Disinfection by-products result from the reactions between disinfectants and naturally occurring organic matter, bromide, and iodide, as well as from anthropogenic pollutants [11]. The formation of DBPs in drinking water depends on several other factors such as temperature, pH, dose, contact time, concentrations of bromide or iodide, and concentrations of natural organic matter [8, 1].

DBP formation involves either halogen substitution and/or oxidation reactions [6].

{Precursor Material} + {Disinfectant} = {Disinfectant by-product or DBP}

[1] *Corresponding author: Firat University, Department of Environmental Engineering, 23119, Elazig, Turkey.* sibela@firat.edu.tr

In 1974, DBPs were first identified in the form of trihalomethanes (THMs) and nowadays over 600 DBPs have been identified. However, a small number of DBPs has been assessed either in quantitative occurrence or health-effects studies [1]. Table 1 lists major classes of DBPs formed due to various disinfectants [12]. The major by-products of water disinfection include trihalomethanes (THMs), haloacetic acids (HAAs), haloacetonitriles (HANs), haloketones (HKs), halonitromethanes, cyanogen halides, nitrosamines, aldehydes, carboxylic acids, and oxyhalides [3, 13-16]. Usually, THM and HAA concentrations are substantially higher than other organic DBP classes. Haloacetaldehydes represent the third highest concentration by class, followed by haloketones, halonitriles, haloamides, and halonitromethanes. Within each DBP class, the formation potential followed the general trends: Cl>Cl–Br>Br-DBPs, and trihalo>dihalo>monohalo-DBPs [16].

Several DBPs, such as THMs, HAAs, bromide, and chlorite, are regulated in the U.S. and in other countries, but other "emerging" DBPs, such as iodo-acids, halonitromethanes, haloamides, halofuranones, and nitrosamines, are not widely regulated. DBPs have been reported for the four major disinfectants: chlorine, chloramines, ozone, and chlorine dioxide (and their combinations), as well as for newer disinfectants, such as UV treatment with post-chlorination. Each disinfectant can produce its own suite of by-products. Several classes of emerging DBPs are increased in formation with the use of alternative disinfectants (e.g., chloramines), including nitrogen-containing DBPs ("N-DBPs"), which are generally more genotoxic and cytotoxic than those without nitrogen [11].

The formation of chlorinated DBPs in drinking water like trihalomethanes has emphasized the need for exploring alternate disinfectants and new treatment technologies. The trihalomethanes viz. chloroform, dichlorobromomethane, dibromochloromethane and bromoforms are the major byproducts of chlorination. In addition to trihalomethanes, haloacetic acids and haloacetonitriles are the products of both chlorination and chloramination. Chloramination also leads to the production of cyanogen chloride and *N*-organochloramine. Chlorine dioxide is a strong water disinfectant over a wide pH range and is most efficient in killing bacteria and especially successful in deactivating viruses. Chlorite and chlorate ions are DBPs formed by chlorine dioxide treatment and are often the limiting factor in the dose of chlorine dioxide that is applied for disinfection [1, 8]. The sources of chlorite are from the process used to generate the chlorine dioxide and from the reduction of chlorine dioxide. The chlorate ion can be derived from the oxidation of chlorine dioxide, from the impurities in the sodium chlorite feedstock, and from the photolytic decomposition of chlorine dioxide [12]. Ozone disinfection results in formation of numerous organic by-products such as aldehydes, aldoketoacids, and carboxylic acids [3]. Bromate is generated as a DBP primarily when high bromide source waters are treated with ozone, but it can also be formed by chlorine dioxide when the disinfection is carried out in the presence of sunlight. Bromate can also be introduced into chlorinated drinking water from an impurity in hypochlorite solutions [1, 17].

Many of the DBPs have been classified as probable or possible carcinogens; thus, the presence of DBPs in drinking water is considered as a human health risk factor; therefore, occurrence of DBPs in drinking water has been regulated in most countries [18]. The WHO reported that the highest concentration of chlorine by-products was THMs which consist of four compounds: chloroform ($CHCl_3$), bromodichloromethane ($CHCl_2Br$), dibromochloromethane ($CHClBr_2$), and bromoform ($CHBr_3$). USEPA reported that these four THMs are human carcinogens, of which $CHCl_3$, $CHCl_2Br$ and $CHBr_3$ are carcinogen type B2 (probable human carcinogens) and $CHClBr_2$ is carcinogen type C (possible carcinogens) [19]. Table 2 summarizes the toxicological effects of DBPs [2, 6].

Table 1. Important groups of DBPs produced using chlorine, chloramine, ozone, and chlorine dioxide during drinking water treatment

Class of DBPs	By-product	Chemical agent	Molecular formula
Trihalomethanes	Chloroform	Chlorine	$CHCl_3$
	Bromodichloromethane	Chlorine	$CHBrCl_2$
	Dibromochloromethane	Chlorine	$CHBr_2Cl$
	Bromoform	Chlorine, ozone	$CHBr_3$
	Dichloroiodomethane	Chlorine	$CHICl_2$
	Chlorodiiodomethane	Chlorine	CHI_2Cl
	Bromochloroiodomethane	Chlorine	CHBrICl
	Dibromoiodomethane	Chlorine	$CHBr_2I$
	Bromodiiodomethane	Chlorine	$CHBrI_2$
	Triiodomethane	Chlorine	CHI_3
Haloacetic acids	Monochloroacetic acid	Chlorine	$CH_2ClCOOH$
	Dichloroacetic acid	Chlorine	$CHCl_2COOH$
	Trichloroacetic acid	Chlorine	CCl_3COOH
	Bromochloroacetic acid	Chlorine	CHBrClCOOH
	Bromodichloroacetic acid	Chlorine	$CBrCl_2COOH$
	Dibromochloroacetic acid	Chlorine	$CBr_2ClCOOH$
	Monobromoacetic acid	Chlorine	$CH_2BrCOOH$
	Dibromoacetic acid	Chlorine	$CHBr_2COOH$
	Tribromoacetic acid	Chlorine	CBr_3COOH
Haloacetonitriles	Trichloroacetonitrile	Chlorine	$CCl_3C{\equiv}N$
	Dichloroacetonitrile	Chlorine	$CHCl_2C{\equiv}N$
	Bromochloroacetonitrile	Chlorine	$CHBrClC{\equiv}N$
	Dibromoacetonitrile	Chlorine	$CHBr_2C{\equiv}N$
Haloketones	1,1-Dichloroacetone	Chlorine	$CHCl_2COCH_3$
	1,1,1-Trichloroacetone	Chlorine	CCl_3COCH_3
Aldehydes	Formaldehyde	Ozone, chlorine	HCHO
	Acetaldehyde	Ozone, chlorine	CH_3CHO
	Glyoxal	Ozone, chlorine	OHCCHO
	Methyl glyoxal	Ozone, chlorine	CH_3COCHO
Aldoketoacids	Glyoxylic acid	Ozone	OHCCOOH
	Pyruvic acid	Ozone	$CH_3COCOOH$
	Ketomalonic acid	Ozone	HOOCCOCOOH
Carboxylic acid	Formate	Ozone	$HCOO^-$
	Acetate	Ozone	CH_3COO^-
	Oxalate	Ozone	$OOCCOO^{2-}$
Oxyhalides	Chlorite	Chlorine dioxide	ClO_2^-
	Chlorate	Chlorine dioxide	ClO_3^-
	Bromate	Ozone	BrO_3^-
Nitrosamines	N-nitrosodimethylamine	Chloramines	$(CH_3)_2NNO$
Cyanogen halides	Cyanogen chloride	Chloramines	ClCN
	Cyanogen bromide	Chloramines	BrCH
Miscellaneous	Chloral hydrate	Chlorine	$CCl_3CH(OH)_2$
Trihalonitromethanes	Trichloronitromethane (Chloropicrin)	Chlorine	CCl_3NO_2
	Bromodichloronitromethane	Chlorine	$CBrCl_2NO_2$
	Dibromochloronitromethane	Chlorine	CBr_2ClNO_2
	Tribronitromethane	Chlorine	CBr_3NO_2

Table 2. Toxicological effects of DBPs

Class of DBPs	Compound	Class	Effects
THM	Chloroform	B2	Cancer, liver, kidney and reproductive effects
	Dibromochloromethane	C	Nervous system, liver, kidney and reproductive effects
	Bromodichloromethane	B2	Cancer, liver, kidney and reproductive effects
	Bromoform	B2	Cancer, nervous system, liver and kidney effects
HAN	Trichloroacetonitrile	C	Cancer, mutegenic and clastogenic effects
Halogenated aldehydes and ketones	Formaldehyde	B1	Mutagenic
Halophenol	2-Chlorophenol	D	Cancer, tumour promoter
HAA	Dichloroacetic acid	B2	Cancer, reproductive and developmental effects
	Trichloroacetic acid	C	Liver, kidney, spleen and developmental effects
Inorganic compounds	Bromate	B2	Cancer
	Chlorite	D	Developmental and reproductive effects

A: Human carcinogen; B1: Probable human carcinogen (with some epidemiological evidence); B2: Probable human carcinogen (sufficient laboratory evidence); C: Possible human carcinogen; D: Non classifiable

2.2. Precursors of Disinfection By-Products

Natural organic matter (NOM) is a heterogeneous mixture of several organic materials including macromolecular humic substances, smaller molecular weight hydrophilic acids, proteins, lipids, carboxylic acids, amino acids, carbohydrates, and hydrocarbons [20]. It can be divided in hydrophobic and hydrophilic compounds, being humic substances part of hydrophobic compounds [21]. The hydrophilic fractions of NOM are composed mostly of aliphatic carbon and nitrogen compounds (such as carbohydrates, sugars, and amino acids), while hydrophobic NOM primarily consists of humic and fulvic acids and is rich in aromatic carbon, phenolic structures and conjugated double bonds. The hydrophobic compounds of NOM are the most important precursors for DBP formation and hydrophilic compounds may play a significant role in the formation of new compounds [22]. The most problematic of the humic substances are aromatic organics and they are more reactive than other organics having a double bond ring structure that results in free electrons that are readily available to react with other molecules. Non-aromatic (aliphatic) organics, such as fulvic acids, tend to be less reactive [6]. The presence of NOM causes a broad range of problems in drinking water treatment operations, because NOM is the organic precursor in the formation of suspected carcinogenic chlorination by-products such as THMs and HAAs as a result of reactions between NOM and oxidants/disinfectants such as chlorine [23, 20]. Various treatment processes not only reduce the amount of NOM, but also induce changes in NOM characteristics, and accordingly result in changes of DBP reactivity. All of these factors affect chlorination DBP formation. Other than NOM, the formation of chlorination DBPs including THMs and HAAs is dependent on many factors such as Br^-, pH, temperature, reaction time, and chlorine dose [23].

The presence of bromide (Br^-) and iodide (I^-) in source waters can result in the formation of brominated and/or iodinated DBPs, which are often more carcinogenic and mutagenic than their chlorinated analogues [24, 25]. Both natural processes, including seawater intrusion and dissolution of geologic sources, and anthropogenic activities, such as seawater desalination, generation of mining tailings, chemical production, production of sewage and industrial effluents, may contribute to bromide concentrations in drinking water sources. Similarly, seawater intrusion, seawater desalination and dissolution of geologic sources contribute to iodide concentrations in drinking water sources, although biological activity of microorganisms and marine algae can contribute to iodide removal from water sources through specific metabolic processes [25].

Bromide and iodide present in water may react differently with different disinfectants. HOBr, formed from bromide, may then react with NOM and generate bromine containing DBPs [25]. Iodide can react with ozone, chlorine, chloramines or

chlorine dioxide to first form hypoiodous acid (HOI). Ozone or chlorine can then further react with HOI to form iodate, which acts as a sink for the iodide. Alternatively, HOI can react with NOM to form iodinated DBPs [26].

In the presence of excess free chlorine, HOI is largely oxidized to iodate (IO_3^-), but in the presence of chloramines it is relatively stable, as shown by the relevant rate constants. Therefore, in the presence of chloramines, HOI will react with certain organic precursors producing iodine substitution and the generation of iodinated analogues of many of the chlorine- and bromine-containing DBPs [25].

NOM inhibits BrO_3^- formation on an ozone dose basis, largely in response to its positive influence of ozone decay in case of ozonation process. BrO_3^- formation, a major ozonation by-product, also depends on Br^-, pH, temperature, contact time, and ozone dose. Since water qualities and operating conditions vary with time and space, associated DBP formation also shows spatial and temporal variations [23].

3. CONTROL OF DBPs FORMATION

3.1. Control of Chlorination By-Products

3.1.1. Precursor Removal

There are various strategies for controlling formation of DBPs such as usage of alternative disinfectants, precursor removal, and source control [3, 13, 27]. Other control strategy is the DBP removal after formation, however, the most of studies on minimizing the formation of DBPs have focused on improving the removal of DBP precursors before disinfection.

Reduction in NOM before disinfection can minimize the formation of DBPs, it is thus very important to increase the removal of precursors of DBPs in drinking water treatment plants [22]. The major technologies for removal of organic DBP precursors are enhanced coagulation, granular activated carbon (GAC) adsorption, biologic treatment, membrane processes, anion exchange, and advanced oxidation processes (AOPs) [13, 16]. The removal of NOM by enhanced coagulation occurs largely through adsorption to metal hydroxide floc particles, and depends on the type and dosage of coagulant, pH of coagulation, and the type and concentration of NOM [28, 29]. Enhanced coagulation and GAC process are two best available technologies for DBP control under the Stage 1 D-DBP Rule. However, enhanced coagulation of water containing bromide may result in a higher level of brominated DBPs [16].

Kitis et al. [20] investigated the adsorptive NOM removal from waters of pumice coated with iron. They found that iron oxide surfaces preferentially removed high UV absorbing fractions of NOM, with UV absorbance reductions up to 90%. Therefore, they concluded that iron oxide coated pumice may also be effective in controlling the formation of disinfection by-products in drinking water treatment.

Removal of DBPs and their precursors is very low when using coagulation by organic polymers, physical processes like settling, deep bed filtration or pressure driven porous membrane processes. Therefore, the introduction of adsorption process is found to be the most suitable and significant for its removal. Granular activated carbon (GAC) and powdered activated carbon (PAC) have been used to remove these organic compounds from the water. It is suggested that the formation of the compounds with NOM and chlorine are referred as THM precursors and the complete reaction is known as trihalomethane formation potential and can be determined directly or by measuring total organic carbons [8].

In the study of Fan et al. [30], an integrated process including coagulation, ozonation, ceramic ultrafiltration, and biologic activated carbon (BAC) filtration was developed for the removal of organic matter and DBPs precursors from micro polluted surface water. The integrated process removed 73% of dissolved organic carbon (DOC), 87% of UV254, 77% of trihalomethane (THMs) precursors, 76% of haloacetic acid (HAAs) precursors, 83% of trichloracetic aldehyde (CH) precursor, 77% of dichloroacetonitrile (DCAN) precursor, 51% of trichloroacetonitrile (TCAN) precursor, 96% of 1,1,1-trichloroacetone (TCP) precursor and 63% of trichloronitromethane (TCNM) precursor.

Bromide is another precursor to many chlorination DBPs. Preventing or reducing salt-water intrusion may reduce bromide concentrations and thus the levels of chlorinated DBPs formed after chlorination [3].

Despite reported higher removal efficiencies, the removal strategies of DBP precursors such as enhanced coagulation, adsorption, ion exchange or advanced oxidation are expensive and have variable removal efficiencies. Moreover, oxidative processes can generate a series of unknown intermediates [27].

3.1.2. Usage of Alternative Disinfectants

Chlorine is the one used most commonly throughout the world in drinking water treatment; but is not only disinfectant available to disinfect water [3, 12]. Chloramination is the most commonly alternative to chlorine resulted a significant decrease in the by-product formation than with the use of chlorine, however its use requires longer contact time because it is less effective than chlorine [8]. Chloramination can also result in a higher level of nitrogenous DBPs, including CNCl and NDMA, and iodinated DBPs. Formation of these emerging DBPs may offset the benefits in reduction of THMs and HAAs [16]. Moreover, it tends to produce volatile products responsible for tastes and odors. The use of chlorine dioxide is of a

particular interest because it does not form THMs and produce low levels of organic byproducts as compared to chlorine disinfection [8]. Ozone has been widely used to reduce or eliminate the formation of THMs and HAAs; but it has been reported that by USEPA that there is an increase in mutagenicity in ozonated water [1, 31].

3.1.3. Source Control

Source control strategies involve management of the water source to lower the concentrations of NOM and bromide. As algal growth leads to the production of DBP precursors, one approach to controlling DBP formation is to control nutrient inputs to waters that are used as drinking-water sources, in order to limit the algal growth potential of these waters. Another source-control strategy, this one aimed at controlling bromide levels, is the control of saltwater or brine intrusion into the water source [13].

3.1.4. Removal of DBPs

Another effective DBP control and regulatory compliance strategy is the DBP removal after formation [27]. DBPs formed can be removed by treatment processes in the treatment plants, or treatment processes in the clear wells or distribution systems [16]. Since chlorination by-products are organic chemicals, they can be removed from water several trace-chemical removal technologies such as adsorption on granular activated carbon, aeration, and air stripping [3]. However, frequent GAC replacement (e.g., every other month or every quarter) makes the process unpractical in treatment plants [16]. Removal of the formed DBPs by air stripping is inefficient for non-volatile DBPs [27].

3.2. Control of Chloramination By-Products

The control of DBPs produced when chloramines are used the disinfectant is more challenging [12]. Nitrosodimethylamine (NDMA) is produced when chloramines are used for disinfection. NDMA is classified as a probable human carcinogen by the USEPA and IARC based on the carcinogenesis observed in animal studies [24]. The NDMA formation can be reduced with strategies such as reducing the dose of chloramines, increasing the pH, and minimizing contact time in the distribution system. The NDMA can be removed by reverse osmosis and photolysis [3].

3.3. Control of Chlorine Dioxide By-Products

The principal inorganic by-products of chlorine dioxide reactions within water treatment are chlorite (ClO_2^-) and chlorate (ClO_3^-) and they are potentially toxic [9, 12, 24]. The formation of chlorite can be controlled by careful management of the feedstock or by increasing the chlorine dose beyond the stoichiometric amount [12]. Treatment methods for the removal of the chlorite ion involve reduction with ferrous ion, adsorption on activated carbon, and oxidation with ozone [3, 12]. The control of the chlorate ion depends primarily on the effective management of the facilities used for the production of chlorine dioxide [12].

3.4. Control of Ozonation By-Products

Ozone form DBPs including aldehydes, various acids, and aldo- and keto- acids when significant amounts of bromide are not present [12, 31]. In the presence of bromide, the produced DBPs are inorganic bromate ion, bromoform, brominated acetic acid, bromopicrin, brominated acetonitriles, cyanogen bromide, and bromate [12]. Bromate is a concern because it has been shown to be a carcinogen in laboratory animals [1]. Bromate formation can be controlled by ozonation at acidic pH values or ammonia addition [3, 13]. Moreover, bromate can be removed from through the following water treatment technologies: (i) ion exchange, (ii) membrane separation, (iii) biological reduction, and (iv) chemical reduction. Organic ozonation by-products appear to be readily biodegradable, therefore they can be controlled by biologically active filtration [12, 13].

CONCLUSIONS

DBP formation is an unintended consequence of water disinfection. Chlorine is by far the most commonly used chemical disinfectant. Although the DBPs occurring most frequently and with highest concentration are THMs and HAAs that result from chlorination, other disinfectants commonly used such as ozone, chloramines, and chlorine dioxide can also produce its own suite of by-products. Formation of DBPs is of great concern due to the potential health risks. DBP control can be achieved by removing of DBP precursors, using of alternative disinfectants, and removing of DBPs after formation.

REFERENCES

[1]. S. D. Richardson, M. J. Plewa, E. D. Wagner, R. Schoeny, and D. M. DeMarini, “Occurrence, genotoxicity, and carcinogenicity of regulated and emerging disinfection by-products in drinking water: A review and roadmap for research,” *Mutation Research*, vol. 636, pp. 178-242, 2007.
[2]. R. Sadiq and M. J. Rodriguez, “Disinfection by-products (DBPs) in drinking water and predictive models for their occurrence: a review,” *Sci. Total Environ.*, vol. 321, pp. 21-46, 2004.
[3]. J. C. Crittenden, R. R. Trussell, D. W. Hand, K. J. Howe, and G. Tchobanoglous, *Water Treatment: Principles and Design/MWH*, 2nd ed., John Wiley & Sons, Inc., Hoboken, New Jersey, 2005.
[4]. S. R. Qasim, *Wastewater Treatment Plants: Planning, Design, and Operation*, 2nd ed., CRC Press, New York, 2000.

[5]. US EPA, Microbial and disinfection by-product rules-simultaneous compliance guidance manual, United States Environmental Protection Agency, EPA 815-R-99-015, 1999.
[6]. Government of Newfoundland & Labrador Department of Environment and Conservation Water Resources Management Division, *Best Management Practices for the Control of Disinfection by-Products in Drinking Water Systems in Newfoundland and Labrador*, April 2009.
[7]. C. Zwiener and S. D. Richardson, "Analysis of disinfection by products in drinking water by LC-MS related MS techniques," *Trend. Anal. Chem.*, vol. 24(7), pp. 613-621, 2005.
[8]. K. Gopal, S. S. Tripathy, J. L. Bersillon, and S. P. Dubey, "Chlorination byproducts, their toxicodynamics and removal from drinking water," *J. Hazard. Mater.*, vol. 140, pp. 1-6, 2007.
[9]. American Water Works Association and American Society of Civil Engineers, *Water Treatment Plant Design*, 3rd ed., USA, 1997.
[10]. U. von Gunten, "Ozonation of drinking water: Part II. Disinfection and by-product formation in presence of bromide, iodide or chlorine," *Water Res.*, vol. 37, pp.1469-1487, 2003.
[11]. S. D. Richardson and C. Postigo, *Drinking Water Disinfection By-Products, Emerging Organic Contaminants and Human Health*, Volume 20 of the series The Handbook of Environmental Chemistry, pp. 93-137, 2012.
[12]. T. Asano, F. L. Burton, H. L. Leverenz, R. Tsuchihashi, and G. Tchobanoglous, *Water Reuse: Issues, Technologies, and Applications*, Metcalf & Eddy Inc., USA, 2007.
[13]. P. C. Singer, "Control of disinfection by-products in drinking water," *J. Environ. Eng.*, vol. 120 (4), pp. 727-744, 1994.
[14]. S. K. Golfinopoulos, A. D. Nikolaou, and T. D. Lekkas, "The Occurrence of Disinfection By-Products in the Drinking Water of Athens, Greece," *ESPR – Environ. Sci. & Pollut. Res.*, vol.10 (6), pp. 368-372, 2003.
[15]. H. H. Chang, H. H. Tung, C. C. Chao, and G. S. Wang, "Occurrence of haloacetic acids (HAAs) and trihalomethanes (THMs) in drinking water of Taiwan," *Environ. Monit. Assess.*, vol. 162, pp. 237-250, 2010.
[16]. X. Wang, Y. Mao, S. Tang, H. Yang, and Y. F. Xie, "Disinfection byproducts in drinking water and regulatory compliance: A critical review," *Front. Environ. Sci. Eng.*, vol. 9(1), pp. 3-15, 2015.
[17]. W. J. Huang, C. Y. Chang, and F. H. Shih, "Disinfection by-product formation and mutagenic assay caused by preozonation of groundwater containing bromide," *Environ. Monit. Assess.*, vol. 158, pp. 181-196, 2009.
[18]. L. Rezaei, V. Alipour, S. Shokooheyan, and A. Ghanbarnejad, "Trihalomethanes formation potential in water supply system of Bandar Abbas (Southern Iran): from source to distribution network," *J. Health Sci. Surveillance Sys.*, vol. 2(1), January 2014.
[19]. B. S. Mishra, S. K. Gupta, and A. Sinha, "Human health risk analysis from disinfection by-products (DBPs) in drinking and bathing water of some Indian cities," *J. Environ. Health Sci. and Eng.*, vol. 12(73), pp. 1-10, 2014.
[20]. M. Kitis, S. S. Kaplan, E. Karakaya, N.O. Yigit, and G. Civelekoglu, "Adsorption of natural organic matter from waters by iron coated pumice," *Chemosphere*, vol. 66, pp. 130-138, 2007.
[21]. M. R. Teixeira, S. M. Rosa, and V. Sousa, "Natural organic matter and disinfection by-products formation potential in water treatment," *Water Resour. Manag.*, vol. 25, pp. 3005-3015, 2011.
[22]. Y. Zhao, F. Xiao, D. Wang, M. Yan, and Z. Bi, "Disinfection byproduct precursor removal by enhanced coagulation and their distribution in chemical fractions," *J. Environ. Sci.*, vol. 25(11), pp. 2207-2213, 2013.
[23]. J. Sohn, D. Gatel, and G. Amy, "Monitoring and modeling of disinfection by-products (DBPs)," *Environ. Monit. Assess.*, vol. 70, pp. 211-222, 2001.
[24]. E. Agus, N. Voutchkov, and D. L. Sedlak, "Disinfection by-products and their potential impact on the quality of water produced by desalination systems: A literature review," *Desalination*, vol. 237(1-3), pp. 214–237, February 2009.
[25]. K. Watson, M.J. Farré, and N. Knight, "Strategies for the removal of halides from drinking water sources, and their applicability in disinfection by-product minimisation: A critical review," *J. Environ. Manage.*, vol. 110, pp. 276-298, 2012.
[26]. S. W. Krasner, "The formation and control of emerging disinfection by-products of health concern," *Phil. Trans. R. Soc. A*, vol. 367, pp. 4077-4095, 2009.
[27]. J. Radjenović, M. J. Farré, Y. Mu, W. Gernjak, and J. Keller, "Reductive electrochemical remediation of emerging and regulated disinfection byproducts," *Water Res.*, vol. 46, pp. 1705-1714, 2012.
[28]. A. Mesdaghinia, M. T. Rafiee, F. Vaezi, A. Mahvi, A. Torabian, and A. Ghasri, "Control of disinfection by products formation potential by enhanced coagulation," *Int. J. Environ. Sci. Tech.* vol. 2(4), pp. 335-342, 2006.
[29]. E. K. Kim and H. W. Walker, "Effect of cationic polymer additives on the adsorption of humic acid onto iron oxide particles," *Colloid Surface A*, vol. 194, pp. 123-131, 2001.
[30]. X. Fan, Y. Tao, D. Wei, X. Zhang, Y. Lei, and H. Noguchi, "Removal of organic matter and disinfection by-products precursors in a hybrid process combining ozonation with ceramic membrane ultrafiltration," *Front. Environ. Sci. Eng.*, vol. 9(1), pp.112-120, 2015.
[31]. J. Y. Hu, Z. S. Wang, W. J. Ng, and S. L. Ong, "Disinfection by-products in water produced by ozonation and chlorination," *Environ. Monit. Assess.*, vol.59, pp. 81-93, 1999.

ICENS
INTERNATIONAL CONFERENCE ON ENGINEERING AND NATURAL SCIENCES
24-28 May 2016 /Sarajevo

Effects of High Copper Concentrations on Performance of Anaerobic Process

Sibel Aslan[1], Nusret Sekerdag[2]

Abstract

Heavy metals are an important class of pollutants and they may originate from domestic, commercial, and industrial sources. Copper is one of the most important and potentially toxic metallic pollutants. In this study, the effect of high copper concentrations on performance of anaerobic process was investigated using four laboratory scale upflow anaerobic sludge blanket (UASB) reactors. While three reactors were fed with synthetic wastewater containing high concentrations of copper, one reactor was intended for control. The tested copper concentrations were 500, 750, and 1000 mg l^{-1}. COD removal efficiency and biogas production was significantly decreased with time for all copper concentrations. Although copper removal efficiencies between 70 and 90% during experimental period were obtained, the effluent copper concentrations were very high.

Keywords: *Heavy metal, copper, anaerobic process, UASB.*

1. INTRODUCTION

The term "heavy metals" refers to metals and metalloids having densities greater than 5 g cm^{-3} and is usually associated with pollution and toxicity although some of these elements (essential metals) are required by microorganisms at low concentrations [1]. Heavy metals are nonbiodegradable and can accumulate to potentially toxic concentrations [2-5]. The most common heavy metals contaminants are: cadmium (Cd), chromium (Cr), copper (Cu), iron (Fe), lead (Pb), nickel (Ni) and zinc (Zn) [1].

Heavy metals can affect the biochemical reactions that take place during anaerobic digestion processes of organic matter through: (a) essential microelements necessary for growth of microorganisms, (b) inhibitors of the toxicity produced by the sulfide, (c) inhibitors and toxic agents of microbial populations, (d) agents binding substances, and (e) promotors of bacterial aggregation [1, 6]. Heavy metals can be stimulatory, inhibitory, or even toxic in biochemical reactions depending on their concentrations [1]. The toxic effect of heavy metals is attributed to disruption of enzyme function and structure by binding of the metals with thiol and other groups on protein molecules or by replacing naturally occurring metals in enzyme prosthetic groups [7, 8]. Whether heavy metals would be stimulatory or inhibitory to anaerobic microorganisms is determined by factors such as the total metal concentration in a soluble, ionic form in the solution, type of metal species, and process-related factors such as pH and redox potential, presence of bacteria that resistant to metal or will detoxify the metal [1, 4, 8-12,]. Heavy metals are inhibitory to anaerobic microorganisms including acetogens, acidogens, methanogens and sulphate-reducing bacteria (SRB) [5, 13]. Among anaerobic microorganisms, acidogens are believed to be more resistant to heavy metal toxicity than methanogens [5].

In an anaerobic environment, heavy metals may be involved in many physico-chemical processes including (1) precipitation as sulphide (except Cr), carbonate and hydroxides, (2) sorption to the solid fraction, either biomass or inert particulate matter, and (3) formation of complexes in solution with intermediates and product compounds produced during digestion, e.g. soluble microbial products (SMPs) [1, 8, 12].

Copper is a common heavy metal found in wastewaters from industrial processing of paper, pigments, metals, fertilizers, and effluents from mines [14, 15]. Copper is a trace element that is required by microorganisms as vital cofactors for metalloproteins and certain enzymes [16-18]. Also, it was shown that copper is one of the heavy metals stimulated methane production in anaerobic reactors [19]. However, at high concentrations, it may be toxic and inhibitory to anaerobic microorganisms.

Anaerobic digestion is increasingly being used to treat wastes from many sources because of its manifold advantages over aerobic treatment, e.g. low sludge production and low energy requirements. However, anaerobic digestion is sensitive to toxicants, and a wide range of compounds can inhibit the process and cause upset or failure [5]. High-rate anaerobic treatment configurations such as the anaerobic contact process (ACP), anaerobic filter (AF), upflow anaerobic sludge blanket (UASB)

[1] *Corresponding author: Firat University, Department of Environmental Engineering, 23119, Elazig, Turkey.* sibela@firat.edu.tr

[2] *Firat University, Department of Environmental Engineering, 23119, Elazig, Turkey.* nusretsekerdag@firat.edu.tr

reactor, fluidized bed (FB) reactor, expanded granular sludge bed (EGSB) reactor, internal circulation (IC) reactor, anaerobic baffled reactor (ABR), receive great interests due to their high loading capacity and low sludge production [20, 21]. Among them, UASB reactors are certainly the most commonly used anaerobic reactors worldwide [22]. The main feature of a UASB reactor which makes it the popular high-rate anaerobic digester worldwide is the availability of granular or flocculent sludge, allowing it to achieve high chemical oxygen demand (COD) removal efficiencies without the need of a support material [20]. Furthermore, the compactness of the UASB reactors, their low operational cost, and low sludge production make the UASB technology very attractive [19].

The aim of this study was to investigate the inhibitory effect of copper on performance of anaerobic process using UASB reactors fed by synthetic wastewater. Inhibition was evaluated by monitoring the removal of the organic matter and biogas production. Moreover, copper removal of UASB reactors was investigated.

2. MATERIALS AND METHODS

2.1 Source of biomass

Methanogenic granular sludge was obtained from anaerobic digester of brewery wastewater treatment located at Adana. The total suspended solids (TSS) and volatile suspended solids (VSS) concentration of sludge 37855 mg l^{-1} and 20965 mg l^{-1}, respectively.

2.2 Feed Composition

The reactors were fed a synthetic wastewater consisting of glucose, peptone, meat extract, macronutrients, and a trace metal solution dissolved in demineralized water. Each liter of synthetic wastewater contained 1.4 g of glucose, 0.4 g of peptone, 0.25 g of meat extract, 0.2 g of NH_4Cl, 0.045 g of KH_2PO_4, 0.3 g of $CaCl_2$, 0.025 g of $MgSO_4$, 0.020 g of $FeSO_4.7H_2O$, 0.045 g of $Na_2S.7H_2O$ and trace element solution. Each liter of trace elements solution contained 0.05 mg of H_3BO_3, 0.05 mg of $ZnCl_2$, 0.03 mg of $CuCl_2$, 0.50 mg of $MnSO_4$. H_2O, 0.05 mg of $(NH_4)_6Mo_7O_{24}.4H_2O$, 0.05 mg of $AlCl_3$, 0.05 mg of $CoCl_2.6\ H_2O$, 0.05 mg of $NiCl_2$. $NaHCO_3$ of 2 g l^{-1} was added to provide the buffering capacity in the anaerobic system.

2.3 UASB Reactor Operation

The experiments were performed using four lab-scale fiberglass UASB reactors with an inner diameter of 10 cm. The working volume of the reactors were 5 L (bottom zone 3.70 L and upper zone 1.3 L). The feeding tanks and the effluent collection tanks were made plexiglass and the volume of each tank was 9 L. The reactors were operated in a temperature-controlled room at 37 ^oC. Synthetic wastewater was fed into the UASB reactors using peristaltic pump (type 323 S/D, Watson-Marlow, Falmouth, UK).

2.4 Experimental design

Three reactors were fed with synthetic wastewater containing different concentrations of copper, while one reactor fed with metal-free synthetic wastewater was used as a control reactor (R4). The tested copper concentrations were 500 g l^{-1} (R1), 750 g l^{-1} (R2), and 1000 g l^{-1} (R3), which were added as aqueous $CuCl_2$. Hydraulic retention time was kept constant at 1 d. The influent COD concentration was about 2000 mg l^{-1} through experimental period.

2.5 Analytical Procedure

Chemical oxygen demand (COD), total suspended solids (TSS), volatile suspended solids (VSS) analysis were done according to Standard Methods (1989). pH measurements were done by using ORION 420A pH meter. Copper concentration was measured by an ATI UNICAM Model 929 flame atomic absorption spectrophotometer equipped with ATI UNICAM hollow cathode. The gas production was measured by liquid displacement method.

3 RESULTS

The adverse effects of copper on anaerobic process was evaluated in terms of COD removal and biogas production. Moreover, copper removal of UASB reactors was investigated. pH is an important parameter affecting metal toxicity as it influences both form and mobility of Cu. The influent pH values of R1, R2, and R3 were 6.6, 6.0, and 5.6, respectively, while their effluent pH values were decreased to 6.5, 5.6 and 4.6. Although influent alkalinity was 2000 mg l^{-1} $CaCO_3$, the effluent alkalinity of R1, R2, and R3 was decreased to 720, 420, and 200 mg l^{-1} $CaCO_3$, respectively. As copper forms complexes with hydroxide and carbonate, alkalinity in effluent decreased.

3.1 Effect of Copper Concentration on COD Removal and Biogas Production

COD removal efficiencies were calculated by using in following equation:

$$E = \left(1 - \frac{S}{S_o}\right) * 100 \qquad (1)$$

where E is COD removal efficiency (%), S_0 and S are influent and effluent COD concentration (mg l^{-1}), respectively. The variation of COD removal efficiencies with different copper concentrations in the wastewater are shown in Figure 1. COD removal efficiency of R4 was remained in between 89% to 95%. The COD removal efficiency of reactors fed with wastewater containing copper decreased with increasing initial copper concentration. The similar results to ours were obtained in the study carried out by Sarioglu et al. [23]. They investigated the inhibition effect of copper (1-1000 mg l^{-1}) on anaerobic sludge with serum bottle assays and observed that when the copper concentration was increased from 250 to 1000 mg l^{-1}, COD removal efficiency decreased.

Biogas production is one of the major parameters used in measuring the effects of metals [11]. The daily biogas production of control reactor was between 2.55 and 3.26 l. At first day of experiment, biogas production of all reactors was nearly 3.0 l day^{-1}, while it was decreased to 0.40, 0.38, and 0.36 l day^{-1} for R1, R2, and R3, respectively. Leighton and Forster [24] found that copper compared to other tested heavy metals (nickel, lead, zinc) had the greatest long-term impact. Lin [25] also demonstrated that Cu and Zn were more toxic to acidogens than to methanogens. Bae et al. [26] studied the effect of Cu^{2+} on methanogenesis, acetate degradations at various Cu^{2+} concentrations. They reported that in the presence of Cu^{2+}, the methane production was more significantly inhibited than acetate consumption.

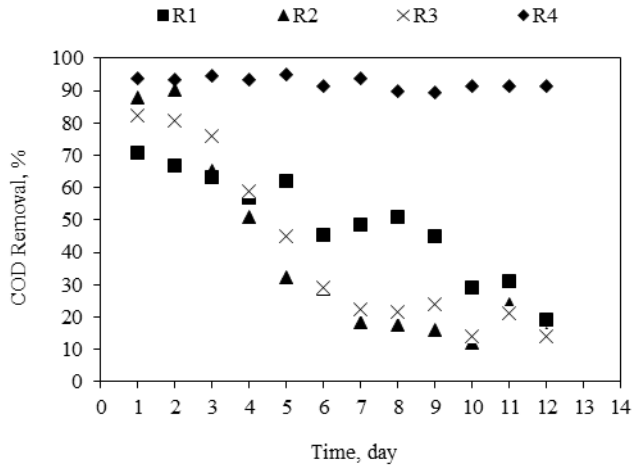

Figure 1. COD removal efficiencies at different initial copper concentrations

3.2 Copper Removal Efficiency of UASB Process

The copper removal of UASB process during experimental period is given in Figure 2. The copper removal efficiencies for three reactors were over 90% first 5 days. At the last day of the experiments, the copper removal efficiencies were 85%, 80%, 71% for R1, R2, and R3, respectively. Metal removal from solution is mainly achieved by precipitation of metals with carbonate, sulphide, hydroxide and phosphate ions, with the first two anions being most important in an anaerobic digester [27-29]. As precipitated metals show a low bio-availability [30], the biomass in the reactor depends heavily on this mechanism to reduce the toxicity of extremely poisonous heavy metal ions [29]. The other heavy metal removal mechanisms are adsorption on the surface of microbial cells and by microbial absorption, i.e. uptake of metals into microorganisms [29, 31, 32]. The higher copper removal obtained at this study was probably due to production of CuS that have very low solubility and precipitate even at pH values as low as pH 1 [33, 34]. Because many metals precipitate as hydroxide at neutral pH and solubility of metal precipitates increases with lower pH values [34]. Moreover, it was reported that adsorption of metals on the surface of solid matter in the sludge seems to make a small contribution to the removal of Cd, Cr, Cu, Ni, Pb and Zn [29]. Gould and Genetelli [35] found that the affinity of sludge for heavy metals was as (in decreasing order): Cu > Cd > Zn > Ni [8].

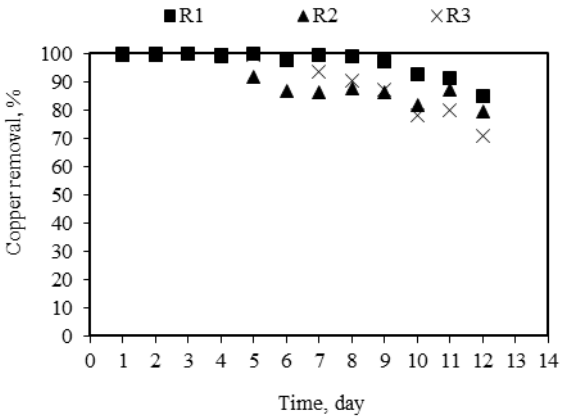

Figure 2. Copper removal efficiency of UASB process

CONCLUSIONS

The toxicity of copper to anaerobic process was evaluated using UASB reactors. The adverse effects of copper on performance of anaerobic process was investigated in terms of COD removal and biogas production. COD removal efficiency was significantly decreased at tested copper concentrations. Copper removal of UASB process was over 71%.

REFERENCES

[1]. A. Mudhoo and S. Kumar, "Effects of heavy metals as stress factors on anaerobic digestion processes and biogas production from biomass," *Int. J. Environ. Sci. Technol.*, vol. 10, pp. 1383–1398, 2013.
[2]. R. M. Sterritt and J. N. Lester, "Interaction of heavy metals with bacteria," *Sci. Total Environ.*, vol. 14 (1), pp. 5–17. 1980
[3]. C. Liu, R. Bai, and Q. S. Ly, "Selective removal of copper and lead ions by diethylenetriamine-functionalized adsorbent: behaviors and mechanisms," *Water Res.*, vol. 42, pp.1511–1522, 2008.
[4]. R. H. Krishna and W. B. Gilbert, "Toxification and detoxification of heavy metals in anaerobic reactors used in the production of bio hydrogen: future fuel," *Int. J. Environ. Eng. Res.*, vol. 3(1), pp. 1–6, 2014.
[5]. J. L. Chen, R. Ortiz, T. W. J. Steele, and D. C. Stuckey, "Toxicants inhibiting anaerobic digestion: A review," *Biotechnol. Adv.*, vol. 32, pp. 1523–1534, 2014.
[6]. J. C. Codina, M. A. Muñoz, F. M. Cazorla, A. Pérez-García, M. A. Moriñigo, and A. Vicente, "The inhibition of methanogenic activity from anaerobic domestic sludges as a simple toxicity bioassay," *Wat. Res.*, vol. 32, no. 4, pp. 1338–1342, 1998.
[7]. B. L. Vallee and D. D. Ulner, "Biochemical effects of mercury, cadmium, and lead," *Annu. Rev. Biochem.*, vol. 41, 91–128, 1972.
[8]. Y. Chen, J. J. Cheng, and K. S. Creamer, "Inhibition of anaerobic digestion process: a review," *Bioresource Technol.*, vol. 99(10), pp. 4044–4064, July 2008.
[9]. F. E. Mosey, J. D. Swanwick, and D. A. Hughes, "Factors affecting the availability of heavy metals to inhibit anaerobic digestion," *Water Pollut. Control*, vol. 70, pp. 668–679, 1971.
[10]. C. W. Kuo and B. R. S. Genthner, "Effect of added heavy metal ions on biotransformation and biodegradation of 2-chlorophenol and 3-chlorobenzoate in anaerobic bacterial consortia," *Appl. Environ. Microb.*, vol. 62(7), pp. 2317–2323, July 1996.
[11]. C. Y. Lin and C. C. Chen, "Effect of heavy metals on the methanogenic UASB granule," *Water Res.*, vol.33, pp.409–416, 1999.
[12]. G. Zayed and J. Winter, "Inhibition of methane production from whey by heavy metals-protective effect of sulfide," *Appl. Microbiol. Biotechnol.*, vol. 53, pp. 726–731, 2000.
[13]. S. Karri, R. Sierra-Alvarez, and J. A. Field, "Toxicity of copper to acetoclastic and hydregonotrophic acitivities of methanogens and sulfate reducers in anaerobic sludge," *Chemosphere*, vol. 62, pp. 121–127, 2006.
[14]. L. Y. Lee, S. L. Ong, H. Y. Ng, J. Y. Hu, and Y. N. Koh, "Simultaneous ammonium-nitrogen and copper removal, and copper recovery using nitrifying biofilm from Ultra-Compact Biofilm Reactor," *Bioresource Technol.*, vol. 99, pp. 6614–6620, 2008.
[15]. J. Bouzid, Z. Elouear, M. Ksibi, M. Feki, and A. Montiel, "A study on removal characteristics of copper from aqueous solution by sewage sludge and pomace ashes," *J. Hazard. Mater.*, vol. 152, pp. 838–845, 2008.
[16]. R. J. Sani, B. M. Peyton, and L. T. Brown, "Copper-induced inhibition of growth of *Desulfovibrio desulfuricans* G20: assessment of its toxicity and correlation with those zinc and lead," *Appl. Environ. Microb.*, vol. 67, pp. 4765–4772, 2001.
[17]. M. Y. Pamukoglu and F. Kargi, "Mathematical modeling of copper(II) inhibition on COD removal in activated sludge unit," *J. Hazard. Mater.*, vol.146, pp.372–377, 2007.
[18]. C. S. Carvalho and M. N. Fernandes, "Effect of copper on liver key enzymes of anaerobic glucose metabolism from freahwater tropical fish *Prochilodus lineatus*," *Comp. Biochem. Physiol. Part A*, vol. 151, pp. 437–442, 2008.
[19]. T. Abbasi and S. A. Abbasi, "Formation and impact of granules in fostering clean energy production and wastewater treatment in upflow anaerobic sludge blanket (UASB) reactors," *Renew. Sust. Energ Rev.*, vol. 16, pp. 1696–1708, 2012.
[20]. S. Chong, T. K. Sen, A. Kayaalp, and H. M. Ang, "The performance enhancements of upflow anaerobic sludge blanket (UASB) reactors for domestic sludge treatment-A State-of-the-art review," *Water Res.*, vol. 46, pp. 3434–3470, 2012.
[21]. J. B. van Lier, F. P. van der Zee, C. T. M. J. Frijters, and M. E. Ersahin, "Celebrating 40 years anaerobic sludge bed reactors for industrial wastewater treatment," *Rev. Environ. Sci. Biotechnol.*, vol. 14, pp. 681–702, 2015.
[22]. R. G. Veronez, A. A. Orra, R. Ribeiro, M. Zaiat, S. M. Ratusznei, and J. A. D. Rodrigues, "A simplified analysis of granule behavior in ASBR and UASB reactors treating low-strength synthetic wastewater," *Braz. J. Chem. Eng.*, vol. 22(03), pp. 361–369, July - September 2005.
[23]. M. Sarioglu, S. Akkoyun, and T. Bisgin, "Inhibition effects of heavy metals (copper, nickel, zinc, lead) on anaerobic sludge," *Desalin. Water Treat.*, vol. 23, pp. 55–60, 2010.

[24]. I. R. Leighton and C. F. Forster, "The effect of heavy metals on an thermophilic methanogenic upflow anaerobic sludge blanket reactor," *Bioresource Technol.*, vol. 63, pp. 131–137, 1998.
[25]. C. Y. Lin, "Effect of heavy metals on acidogenesis in anaerobic digestion," *Wat. Res.*, vol. 27, pp. 147–152, 1993.
[26]. J. W. Bae, S. K. Rhee, A. Jang, I. S. Kim, and S. T. Lee, "Copper ion toxicity causes discrepancy between acetate degradation and methane production in granular sludge," *J. Microbiol. Biotechnol.*, vol. 12(5), pp. 849–853, 2002.
[27]. R. M. Smith and A. E. Martell, Critical Stability Constants, Inorganic Complexes, vol. 4, Plenum Press, New York, 1976.
[28]. I. J. Callander and J. P. Barford, "Precipitation, chelation, and the availability of metals as nutrients in anaerobic digestion, II. Applications," *Biotech. Bioeng.*, vol. 25, pp. 1959–1972, 1983.
[29]. M. O. Ginter and A. M. Grobicki, "Manganese removal mechanisms in a stirred UASB reactor," *Wat. Res.*, vol. 31(6), pp. 1261–1268, 1997.
[30]. J. A. Oleszkiewicz and V. K. Sharma, "Stimulation and inhibition of anaerobic processes by heavy metals: A review," *Biol. Waste*., vol. 31, pp. 45–67, 1990.
[31]. E. D. van Hullebusch, A. Peerbolte, M. C. Zandvoort, and P. N. L. Lens, "Sorption of cobalt and nickel on anaerobic granular sludges: isotherms and sequential extraction," *Chemosphere*, vol. 58, iss. 4, pp. 493–505, 2005.
[32]. E. D. van Hullebusch, J. Gieteling, M. Zhang, M. C. Zandvoort, W. V. Daele, J. Defrancq, and P. N. L. Lens, "Cobalt sorption onto anaerobic granular sludge: isotherm and spatial localization analysis," *J. Biotechnol*,. vol. 121, pp. 227–240, 2006.
[33]. R. F. Mueller and A. Steiner, "Inhibition of anaerobic digestion caused by heavy metals," *Water Sci. Technol.*, vol. 26, pp. 835–846, 1992.
[34]. M. K. Tiwari, S. Guha, C. S. Harendranath, and S. Tripathi, "Influence of extrinsic factors on granulation in UASB reactor," *Appl. Microbiol. Biot.*, vol. 71, pp. 145–154, 2006.
[35]. M.S. Gould and E. J. Genetelli, "Effects of complexation on heavy metal binding by anaerobically digested sludges," *Water Res.*, vol. 18, pp. 123–126, 1984.

ICENS
INTERNATIONAL CONFERENCE ON ENGINEERING AND NATURAL SCIENCES
24-28 May 2016 /Sarajevo

Effects of Voltages to the Equivalent Circuit Parameters of Transformers

Cenk Gezegin[1], Hasan Dirik[2], Engin Ufuk Ergul[3], Muammer Ozdemir[4]

Abstract

The equivalent circuit parameters which are a function of physical structure of the transformers provide important information about the status of the transformers. These parameters can give the possibility of monitoring the status of a transformer. These paramet[2]ers which can change according to many factors can also change depending on the voltages applied to the transformers. With true understanding of these changes, the evaluations through the transformer parameters will be better. For instance, knowing the changes in the value of iron core resistance according to voltage deviations can provide the comments on the changes of the iron core losses better. For the monitoring of loss change through the parameters, firstly the direction and rate of the changes in these parameters with the voltages should be well known. In this study, the effects of the voltages that are applied to transformer on the equivalent circuit parameters are investigated by using a series of experiments done on a transformer rated 5kVA, 380V/220V. These results are also evaluated by considering theoretical knowledge.

Keywords: *Effects of voltage, Equivalent Circuit Parameters, Transformer.*

1. INTRODUCTION

Transformers are one of the most important and vital elements of power transmission and distribution systems. The studies on the operation of the transformers are generally about some physical features such as oil temperature, chemical features of oil, water and dissolved gas content in oil, resistance of winding insulation, leakage currents and vibration [1-3]. There are some studies that suggest the determination of the status of transformers over equivalent circuit parameters [4-6]. The effects of applied voltage value on the parameters are ignored in these studies. This sometimes causes some lacks of the analysis. Conventionally, transformer parameters are found by using the data of open-circuit and short-circuit experiments. In short-circuit experiment; applied voltage is much lower than the nominal value, so the reliability of the obtained results should also be examined. The values of the equivalent circuit parameters of transformers change in some cases due to many factors. These values can also change according to the value of applied voltage, and they give important information about the status of the transformers. These parameters can be calculated by using directly measured electrical quantities [7-8]. This offers significant opportunities for monitoring the status of the transformer. The proper understanding of the relationship between the voltage and the equivalent circuit parameters will provide that the studies on this subject are more reliable. In this paper, the relationship between the equivalent **T** circuit parameters and level of voltage applied to transformer are investigated by utilizing a series of experiments. Experimental studies consist of open-circuit and on-load experiments in constant temperature of winding and core and have been done in different voltage levels. A single phase dry-type transformer which has 5kVA, 380V/220V nominal values is used in experiments. An energy analyzer is used for the measurement of voltage and current. Equivalent circuit parameters are calculated in MATLAB/Simulink environment by using the measured voltage and current data. As the main purpose of the study is to investigate the relationship between voltage and equivalent circuit parameters, it has been paid attention to be same the value of transformer winding temperature during each experiment.

This paper is organized as follows: Materials and methods are given in Section 2. Results and discussion is presented in Section 3. Finally, overall conclusions and future directions are given in Section 4.

2. MATERIALS AND METHODS

In this study, it is investigated the effect of applied voltage to transformer to R_p, X_p, R_s', X_s', R_{fe} and L_m parameters of the equivalent T circuit of Steinmetz [9] that given in Figure 1. These parameters are respectively winding resistance and leakage

[1]*Corresponding author: Technical Sciences Vocational School, Department of Electric and Energy, Amasya University, Amasya, Turkey, cenkgezegin@gmail.com*

[2]*Vocational School, Department of Electric and Energy, Sinop University, Sinop, Turkey, hasan_dirik@hotmail.com*

[3]*Department of Electrical and Electronics Engineering, Faculty of Technology, Amasya University, Amasya, Turkey, engin.ergul@amasya.edu.tr*

[4] *Department of Electrical and Electronics Engineering, Faculty of Engineering, Ondokuz Mayis University, Samsun, Turkey, mozdemir@omu.edu.tr*

reactance of primary side, winding resistance and leakage reactance of secondary side referred to the primary side, resistance corresponding iron loss and magnetizing reactance.

This circuit is often used for representing transformer behaviors in low frequencies. In this circuit, it is assumed that magnetizing characteristic of the transformer is linear. Here, $u_p(t)$, $i_p(t)$, $u_s(t)$ and $i_s(t)$ values respectively represent the voltages and currents of primary and secondary sides. $u_s^{'}(t)$, $i_s^{'}(t)$, $i_o(t)$, N_p, N_s values are also represent the voltage and current values of secondary side referred to primary side, no-load current, number of turns of primary and secondary windings.

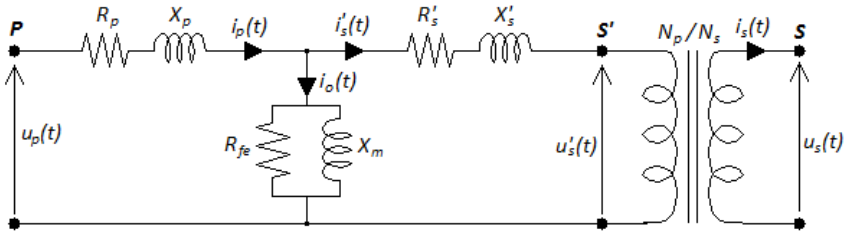

Figure1. Equivalent T circuit of the transformer

Valid equations for referring the secondary side values to the primary side are (here, r_t shows turns ratio):

$$r_t = \frac{N_p}{N_s} \tag{1}$$

$$u_s^{'}(t) = r_t \cdot u_s(t) \tag{2}$$

$$i_s^{'}(t) = \frac{i_s(t)}{r_t} \tag{3}$$

$$R_s = \frac{R_s^{'}}{r_t^2} \tag{4}$$

$$X_s = \frac{X_s^{'}}{r_t^2} \tag{5}$$

Here, data obtained from open-circuit and on-load experiments are used for calculation of the parameters. Current and voltage values obtained from primary and secondary sides of transformer are obtained by using the energy analyzer. These values are raw data which contain harmonics because of nonlinear magnetizing current characteristic of transformers. Amplitude and angle values of fundamental frequency components of these data are obtained by using Discrete Fourier Transform (DFT) in MATLAB/Simulink.

Cartesian forms of these components are calculated as (A is amplitude and α is angle):

$$A_x = A \cdot \cos(\alpha) \tag{6}$$

$$A_y = A \cdot \sin(\alpha) \tag{7}$$

$$A = A_x + j \cdot A_y \tag{8}$$

According to this, Cartesian forms of voltages and current obtained from open-circuit and on-load work are given in eqs. (9)-(14).

$$U_o^p = U_{ox}^p + j \cdot U_{oy}^p \tag{9}$$

$$I_o^p = I_{ox}^p + j \cdot I_{oy}^p \tag{10}$$

$$U_s^p = U_{sx}^p + j \cdot U_{sy}^p \tag{11}$$

$$I_s^p = I_{sx}^p + j \cdot I_{sy}^p \tag{12}$$

$$U_s^{s'} = U_{sx}^{s'} + j \cdot U_{sy}^{s'} \tag{13}$$

$$I_s^{s'} = I_{sx}^{s'} + j \cdot I_{sy}^{s'} \tag{14}$$

R_{fe} and X_m parameters are computed by using open-circuit voltages and currents as in the following equations.

$$R_{fe} = \frac{1}{\mathrm{Re}\left(\frac{I_o^p}{U_o^p}\right)} \tag{15}$$

$$X_m = \frac{1}{\mathrm{Im}\left(-\frac{I_o^p}{U_o^p}\right)} \tag{16}$$

R_p, R_s, X_s and X_p are computed by using the data obtained from on-load experiments. Practically, I_o given in Figure 1 is very small compared to winding current. So, the current of this branch is ignored for the purpose of calculating the winding parameters. Hence, the branches which represent primary and secondary windings will become serial in simplified new circuit and their currents must be the same. This current can be obtained by taking average value of measured current values of each two branches as in eq. (17).

$$I^{ps} = \frac{(I^p + I^{s'})}{2} \tag{17}$$

The total values of winding resistances and leakage reactance are computed by using equations below. In these equations, the leakage reactance of windings are assumed to be equal and voltage drop equation between P and S' points are written in the new circuit.

$$U^p - U^{s'} = \left((R_p + R_s') + j \cdot (X_p + X_s')\right) \cdot I^{ps} = \left(R_t + j \cdot X_t\right) \cdot I^{ps} \tag{18}$$

$$R_t = \mathrm{Re}\left(\frac{U^p - U^{s'}}{I^{ps}}\right) \tag{19}$$

$$X_t = \mathrm{Im}\left(\frac{U^p - U^{s'}}{I^{ps}}\right) \tag{20}$$

3. EXPERİMENTAL WORKS

In this section, the results obtained from experiments on a single phased transformer are given. Experimental works are done for the purpose of determining the relationship between the voltages applied to the primary of the transformer and equivalent circuit parameters. Nominal values of the transformer are 5kVA, 380V/220V and N_p/N_s=150/90. Measurements are done by an energy analyzer working in 20 kHz sampling rate. Throughout the experiments, it has been taken care the temperature of windings and core to be remained constant. Also, each experiment has been done in a short time.

Open-circuit experiments were done by applying 33 different voltages to primary side of the transformer ranging from 20V to 410V. Throughout the experiments, core temperatures were measured about 22 ^{o}C and winding temperatures were measured about 23 ^{o}C. Values of magnetizing branch parameters were calculated by applying the data obtained from open-circuit experiment to the method explained in the previous section. Variations of computed values of parameters R_{fe} and X_m against the applied voltage are shown in Fig. 2.

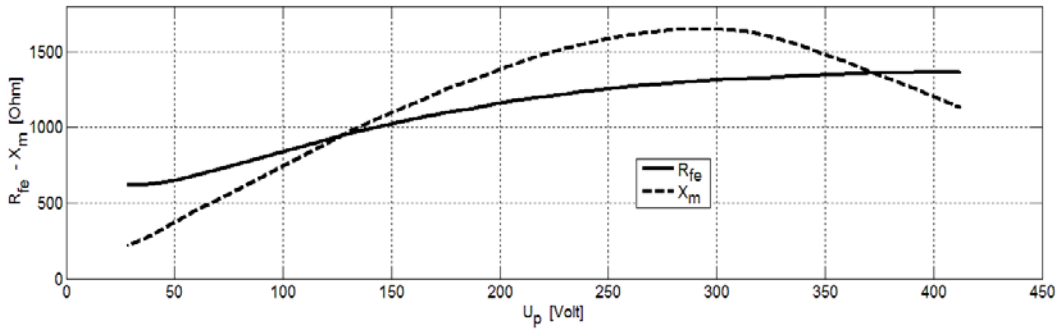

Figure 2. Variations of computed values of parameters R_{fe} and X_m against the applied voltages

On-load experiments were done by applying 33 different voltages to the primary side of the test transformer ranging from 30V to. In the each experiment, load current has been set to about 1A on the primary side of the transformer. Throughout the experiments, core and winding temperatures were measured about 23 ^oC and 25 ^oC respectively. Sum of the ohmic and inductive winding parameters ($R_t=R_p+R_s'$ and $X_t=X_p+X_s'$) were obtained by applying the data obtained from on-load experiments to the method explained in the previous section. In Fig. 3, computed values of parameters R_t and X_t against the applied voltage are given.

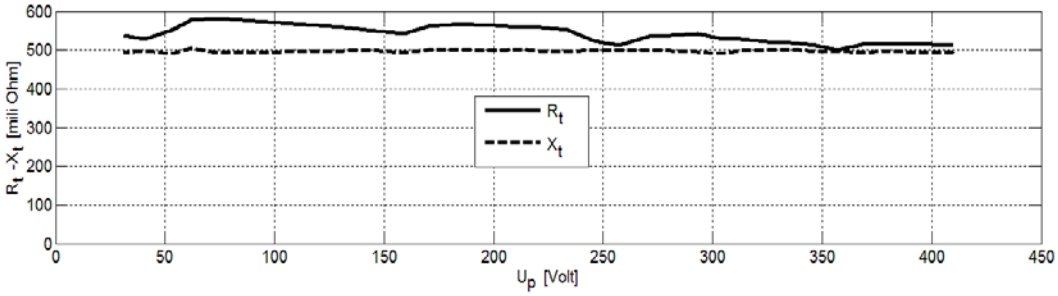

Figure 3. Values of ohmic and inductive winding parameters against the applied voltage

It can be seen from Fig. 2 that the parameters of magnetizing branch are closely related to the voltage applied to the transformer. Increasing the applied voltage also increases the value of resistance corresponding to iron loss (R_{fe}). This is actually an expected result due to the increase in hysteresis activity of iron. Because R_{fe} value of the test transformer shows small changes around nominal voltage (U_p=380V), it can be considered approximately constant. But, it cannot be said the same for magnetizing reactance (X_m). Magnetizing reactance shows more changes around nominal voltage. This means that voltage changes have significant effect to the values of magnetizing reactance, so this must be considered in experiments or studies on transformers.

Changes of winding parameters shown in Figure 3 indicate that generally voltage does not affect the leakage winding reactance and it has a small effect on the total winding resistance. It is thought that the reason of warped changes in calculated winding resistance from the data may be originated from measurement errors. It is also thought that winding leakage reactance has been remained almost constant due to the fact that values of inductive parameters depend only on the geometric structure of the windings and core of transformer.

CONCLUSIONS

In this paper, the relations between voltage applied to the transformer and its equivalent circuit parameters are investigated by using experimental works. Experiments were done by applying various level voltages to the test transformer in open-circuit and on-load experiments. The results indicate that the parameters of magnetizing branch are highly dependent to the applied voltage. Increase in voltage causes an increase in the resistance value representing the iron loss and also, magnetizing reactance increases to a maximum value as voltage rise, but after a specific value of voltage it decreases again. Values of winding resistances decrease in just a small amount along with the voltage increase and values of leakage reactance remain constant. It is thought that the reason of constant leakage reactance is the fact that values of inductive parameters depend only on the geometric structure of the windings and core of transformer. Change levels in the winding resistances are very small, therefore it can be ignored. In this study, it is generally shown that the values of voltage applied to the transformer change the values of equivalent circuit parameters. Therefore, this must be taken into account in theoretical and practical studies.

ACKNOWLEDGMENT

This work is supported by the Scientific Research Project Fund of Amasya University under the project number FMB-BAP 16-0180.

REFERENCES

[1]. H. Abniki, H. Afsharirad, A. Mohseni, F. Khoshkhati, H. Monsef, P. Shamsi, Effective on-line parameters for transformer monitoring and protection, *North American Power Symposium (NAPS)*, pp.1-5, 26-28 Sept. 2010.

[2]. X. Zhang, E. Gockenbach, Asset-Management of Transformers Based on Condition Monitoring and Standard Diagnosis, *IEEE Electrical Insulation Magazine*, vol.24, no.4, pp.26-40, July-Aug. 2008.

[3]. B. H. Ward, A survey of new techniques in insulation monitoring of power transformers, *IEEE Electrical Insulation Magazine*, vol.17, no.3, pp.16-23, May-June 2001.

[4]. Z. Zhang, N. Kang and M. J. Mousavi, Real-time transformer parameter estimation using terminal measurements, *2015 IEEE Power & Energy Society General Meeting*, Denver, CO, 2015, pp. 1-5.

[5]. S. N. Hettiwatte, Z. Wang and P. A. Crossley, Estimating transformer parameters for partial discharge location, *Power Engineering Conference (AUPEC)*, Australasian Universities, Perth, WA, , pp. 1-6, 2014.

[6]. Y. Li, G. Liu, L. Zhang, L. Zhang and Z. Lin, Transformer Winding Deformation Diagnosis Using Middle Band Frequency Response Analysis, *2007 IEEE International Conference on Solid Dielectrics*, Winchester, UK, pp. 677-680, 2007.

[7]. M. R. Feyzi, M. Sabahi, Online Dynamic Parameter Estimation of Transformer Equivalent Circuit, *IPEMC 2006, CES/IEEE 5th International Power Electronics and Motion Control Conference*, vol.2, no., pp.1-5, 14-16 Aug. 2006.

[8]. H. Dirik, C. Gezegin, M. Ozdemir, A Novel Parameter Identification Method for Single-Phase Transformers by Using Real-Time Data, *IEEE Transactions on Power Delivery*, vol.29, no.3, pp.1074-1082, June 2014.

[9]. C. P. Steinmetz, Theory and Calculation of Alternating Current Phenomena, First Edition Available Through Open Library McGraw,. Available: http://openlibrary.org, 1897

ICENS
INTERNATIONAL CONFERENCE ON ENGINEERING AND NATURAL SCIENCES
24-28 May 2016 /Sarajevo

Effect of TiCN Addition on the Microstructure and Mechanical Properties of PM Steels

Mehmet Akif Erden[1], Suleyman Gunduz[2], Halil Demir[2], Hasan Karabulut[1], Dogan Ozdemirler[3]

Abstract

In this work, the effects of TiCN additions on the microstructures and tensile behaviour of microalloyed powder metallurgy (PM) steels were investigated. The microstructure of the microalloyed PM steels was characterised by optical microscope, SEM and EDS. The results indicated that 0.2 wt. % TiCN added PM steel showed the highest values in yield strength (YS) and ultimate tensile strength (UTS). However, when the amount of TiCN content increased from 0.2 to 0.5 wt. %, yield strength and ultimate tensile strength decreased. Elongation also tended to increase with increasing TiCN content.

Keywords: *Powder metallurgy; powder metallurgy steels; TiCN; Microstructure.*

1. INTRODUCTION

The tendency to produce new materials for specific purposes has been increasing day by day because no simple material is able to meet the needs which has risen up in the last 20 years. [1] They are mixed whether to collect the best features of the materials, which are in the same or different groups and count two or more, or to bring about a new feature. Microalloyed steels are the steel group containing niobium, vanadium and titanium between 0.05% and 0.20% by wt., and have superior specifications like high strength, high toughness, low ductile-to-brittle transition temperature [2]. One of the features of the microalloyed elements is that they restrict grain size by formed carbide and nitrite during the austentizing or sintering process. TiCN are the microalloying precipitates which decrease the grain size and increase the toughness. Moreover, TiCN is resistant to high temperature and it is used commonly for precipitation strengthening and decreasing austenite grain sizes [3-5].

Powder metallurgy (P/M) paves the way for the economical production of high quality and relatively sophisticated tools. This production method turns the metal powders that are different in size, shape and packaging features into resistant, precise and high performance tools [6].

In this study, PM steel has been produced in the targeted compound by adding different proportions of TiCN into the Fe matrix with the powder metallurgy method and the resulting microstructural mechanical properties are going to be compared.

2. EXPERIMENTAL METHOD

In this study, the PM steel samples were produced in the desired compositions with the PM method. Having added in different proportions, the effect of the TiCN amount on microstructural and mechanical properties was examined. The samples were produced by way of mixing in the chemical compounds given in the Table 1. Tensile test was carried out on the produced samples after the microstructural characterisation. The results were compared. Before the mixing process, the powders were prepared in the proportions given in Table 1 by weighing on a digital precision scale of 0.0001 precision. The mixing process was conducted without ball using a Turbula T2F mixer for 1 hour. Having mixed homogeneously, the powders were pressed under 700 MPa unidirectionally with a Hidroliksan press of 96 ton pressure capacity. The samples of the tensile experiment were shaped into blocks by squeezing with the mould prepared according to ASTM (E 8M) standards of powder metal material tension test sample.

[1] *Karabük Üniversitesi, TOBB TB M.Y.O, Karabük, Türkiye, Tel 0370 433 82 00, makiferden@karabuk.edu.tr, hkarabulut@karabuk.edu.tr*
[2]*Karabük Üniversitesi, Teknoloji Fakültesi, İmalat Mühendisliği Bölümü, Karabük, Türkiye, Tel 0370 433 82 00, sgunduz@karabuk.edu.tr, hdemir@karabuk.edu.tr*
[3]*Karabük Üniversitesi, Fen Bilimleri Enstitüsü, Karabük, Türkiye, Tel 0370 4151689, dozdemirler@hotmail.com*

Table 1: Chemical compositions of powder metal steels.

Compound	C (%wt.)	TiCN (%wt.)	Fe (%wt.)
Fe +0.25 C (Alloy 1)	0.25	-	rest
Fe +0,25 C+ 0.1 TiCN (Alloy 2)	0.25	0.1	rest
Fe +0,25 C+ 0.2 TiCN (Alloy 3)	0.25	0.2	rest
Fe +0,25 C+ 0.5 TiCN (Alloy 4)	0.25	0.5	rest

The pressed samples were sintered in argon atmosphere at 1150 ºC for 1 hour. After sintering, density and pore values were measured. The sintered samples were subjected to standard metallographic procedures. Having sintered at 1150 ºC, the microstructures of the PM steel were examined under a Nikon Epiphot 200 optical microscope of X50-X1000 zoom capacity. Tensile test was carried out at 0.5 mm/min crosshead speed with a Shimadzu tensile testing device of 50 KN capacity. The yield strength (% 0.2), tensile strength and % (percentage) values of elongation of the tensile test samples were determined. Vickers hardness value was determined through applying 0.5 kg weight under a Shimadzu unit hardness device. The density of the samples was determined according to the principle of Archimedes. Likewise, the pearlite proportions of the powder metal steels were calculated using Gladman and Woodhead's metallographic point counting method [7]. Along with it, TiC, TiN and TiCN precipitates were detected with the help of the point and line EDS.

3. RESULTS AND DISCUSSION

3.1. Microstructure

The microstructural images of the samples are demonstrated in the Figure 1. As can be seen from the figure, the structure comprises of ferrite and pearlite phases in the whole alloys. When the images of the microstructure in the Figure 1 are examined, it is detected that there are pores in the grain borders. Although it is stated that porosity affect the strength of many materials negatively, it is reported that tiny and spherical pores do not reduce the strength [9]. It is inferred from the images of microstructure that as the proportion of the TiCN in the samples increases, the grains get smaller gradually. It is observed that the average grain size becomes bigger in the alloy that contains 0.5 % TiCN. For instance, the size of the grain decreased to 25.8 µm and 24.22 µm respectively with 0.1 and 0.2 percentage of weight increase in the amount of the TiCN while the average size of grain in the non-alloyed PM steel sample in the Fe+0.25C compound is 29.7 µm. It is observed to be 27.16 µm when the amount of TiCN is calculated 0.5 as weight percentage.

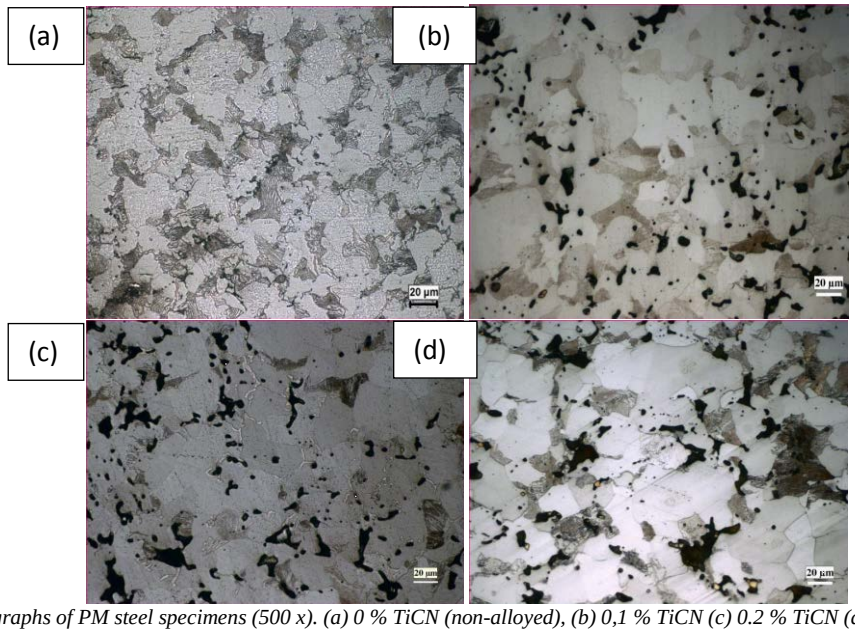

Figure 1. Micrographs of PM steel specimens (500 x). (a) 0 % TiCN (non-alloyed), (b) 0,1 % TiCN (c) 0.2 % TiCN (d) 0.5 % TiCN.

Table 2. Relative density, mean linear intercept grain sizes and volume fractions of ferrite and pearlite phases in sintered samples.

Alloy	Relative Density (%)	Porosity (%)	Ferrite (%)	Pearlite (%)	Grain Size (μm)
Alloy 1	92	8	79,4	21,6	29,7
Alloy 2	91,8	8,2	77,51	22,49	25,8
Alloy 3	90,2	9,8	76,98	23,02	24,22
Alloy 4	93	7	78,06	21,94	27,16

In the Table 2, it is seen that the average grain size decreases with a 0.2 % of increase in the proportion of the TiCN. This situation takes place when TiC, TiN and TiC(N) precipitates that formed during the sintering process prevent the austenite grains from getting bigger. One of the properties of microalloyed elements is that they restrict grain size by forming carbide and nitride in the austenitizing or sintering processes. Formation of small precipitates during the austenitizing process prevents austenite grains from growing and leads to the development of small ferrite grains [8-11].

It is observed that the average grain size increases slightly with an increase in TiCN amount from 0.2 % to 0.5 %. This can be attributed to formation of large precipitates within the grain boundaries [2-5]. These large precipitates lead to an increase in the average size of the grains as they cannot restrict grain size sufficiently.

3.2. Mechanical Properties

While Figure 2 shows the stress-strain diagrams of the sintered samples, Table 3 shows the yield strength, tensile strength, percentage elongation and hardness results. The yield and tensile strength with the percentage elongation and hardness values are observed to increase when TiCN proportion increases to %0.2. Being formed by the titanium, the carbide, nitride and carbonitride precipitates ensure the material to be small grained by way of restricting the size of the austenite grain and re-crystallisation of the austenite. The improvement of the resistance to dislocation movement is fulfilled thanks to the increasing grain boundaries in the small grained structure. The decrease of the grain size also contributes to the percentage elongation of the material. Along with these, the formed precipitates contributed to the increase in the yield and tensile strength via various strength increasing mechanisms like precipitates hardening and dispersion hardening [2-4;10-11].

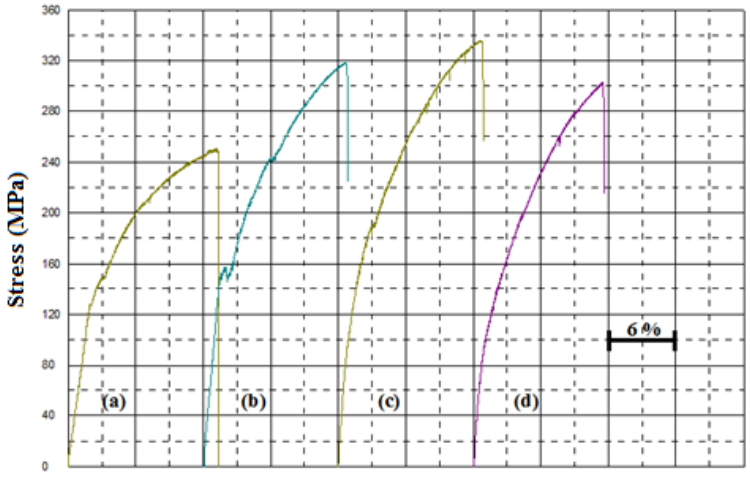

Figure 2. Variation of stress–strain curves of sintered samples in different percentages of TiCN content (a) Alloy 1, (b) Alloy 2, (c) Alloy 3, and (d) Alloy 4.

Table 3. Mechanical properties of the sintered samples.

Alloy	Yield Strength (MPa)	Ultimate Tensile Strength (MPa)	Elongation (%)	Hardness ($Hv_{0,5}$)
Alloy 1	144	252	13	68
Alloy 2	157	320	13	112
Alloy 3	193	337	13	125
Alloy 4	110	303	12	100

It is thought that TiC(N)-like precipitates lead to the development of small austenite grains by way of restricting the grain size during the sintering process, thereby improving the resistance of the materials. Similarly, Erden et al. [2] produced Ti microalloyed steel with PM method. They conducted the sintering process at 1150 °C for 60 minutes and determined an increase in the yield and tensile strength as the proportion of Ti (% 0,1-% 0,2) rises. The author demonstrates in their study that TiC(N)-like precipitates lead to the development of small austenite grains by restricting the grain size during sintering and as a result of this, the resistance of the materials improves. In the other studies [1;10-11], it is stated that the carbide and nitrite formed in the microalloyed steels lead to an increase in the toughness and strength. In the same study, it is pointed out that solid solution hardening remains at low percentage because of the precipitation of carbide and nitrite [3-7]. In addition, presence of TiCN in steel at a high proportion makes the material brittle and leads to the decrease of strength by causing over-hardening of the precipitate.

3.3. SEM-EDS Analysis

It is determined from the SEM image that the sample given in Figure 3 containing 0.2 % of TiCN results in different sizes of precipitates. In addition, the analysis results of the point EDS show that TiC(N) precipitates form because these precipitates contain titanium, carbon and nitrogen and that Fe3C precipitates form because they contain iron and carbon. It can be said that these formed precipitates restrict the growth of austenite grain size, re-crystallization and improve the strength of the material with precipitation hardening [10-12].

The effect of the microalloying elements in precipitates on the re-crystallization of the austenite is not much. The prevention of the grain boundary movement via the precipitated grains is more than that of the dissolved atoms [12].

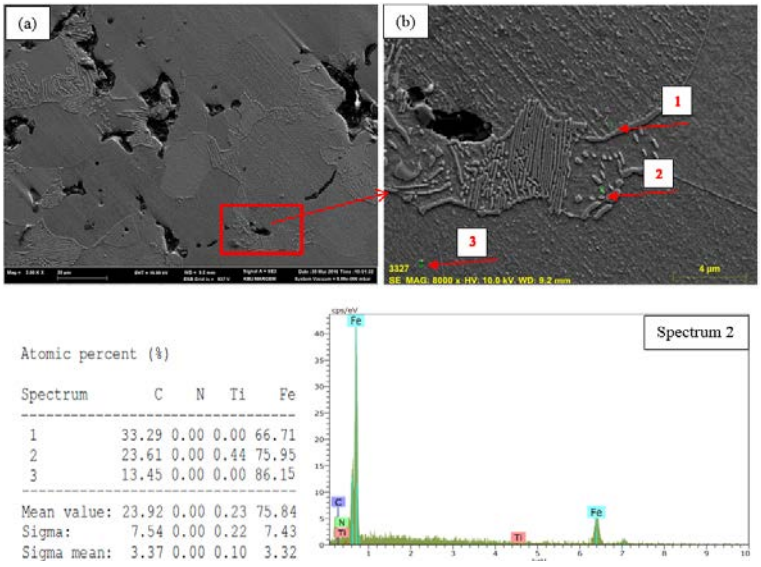

Figure 3. SEM micrograph Alloy 4 (a-2000X, b-8000X) and corresponding EDS of the indicated points.

Figure 4 shows the line EDS analysis results that were taken from the matrix and precipitates of the 0.2 % of TiCN including PM steel sample which was sintered at 1150 °C. When the results of the line EDS analysis of 0.2 % of TiCN including PM steel are examined, it is observed that there is a difference in the element type and amount along the stripe that cut the matrix and the precipitate. It is determined that matrix phase is iron-rich but round-shaped precipitate is titanium-rich. In addition, when the stripe which comes from the matrix cuts the sediment, there has been a sharp increase in the amount of titanium.

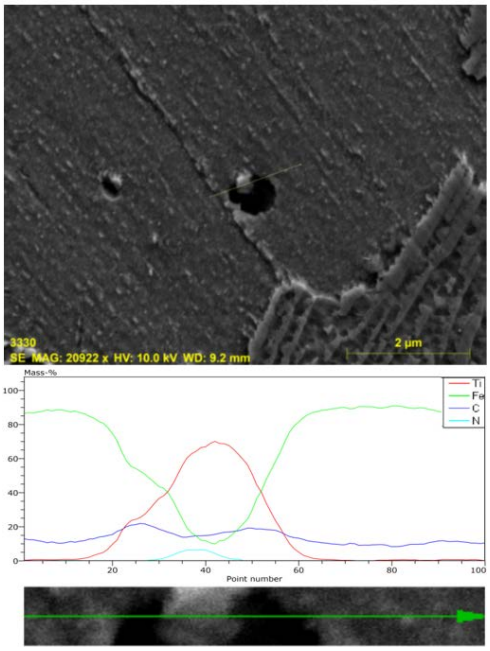

Figure 4. SEM micrograph for Alloy 3 sintered at 1350 °C and EDS lines scan of the indicated particle.

The results of the point and line EDS analysis that were obtained in this investigation demonstrates that the precipitates like TiC, TiN and TiC(N) develop in the titanium PM steels.

CONCLUSIONS

The non-alloyed and TiCN alloyed PM steel which has three different volume ratios (0.1 – 0.2 % and 0.5 %) is produced by cold pressing and sintering at the argon setting and the following results listed below are obtained from this study.

1. Composite materials which contain TiCN and Fe matrix can be produced with powder metallurgy. Solid solution hardening and precipitation hardening which arise during the sintering process or after-sintering cooling process increase the resistance of the steel.
2. Composite materials that are added 0.1 - 0.2 % and 0.5 % TiCN as weight compared to non-alloyed steels showed smaller grain structure. This situation stems from the restriction of grain size by the carbide and nitrite which alloy elements has created.
3. Usually, there has been an increase in the yield strength, tensile strength, percentage (%) elongation and hardness values of the compounds which have TiCN ratio by 0.2 % as the alloy ratio rises. This situation is a result of the development of the precipitates like TiCN during sintering process and after-sintering cooling process. These precipitates lead to the creation of small austenite grains by preventing grain size and thus improving the resistance of the materials.
4. After-sintering density of the nonalloy and TiCN added composite materials is observed to be generally at about 92 %. After-sintering density of the produced PM steels showed a little bit increase.

ACKNOWLEDGMENT

The author gratefully acknowledges financial support from Karabuk University Coordinatorship of Resarch Projects.

REFERENCES

[1]. Karaduman, "Production Of Titanium Carbide Reinforced Titanium Matrix Composites Via Conventional Powder Metallurgy Method" Thesis (M.Sc.), Institute of Science and Technology, İstanbul Technical University, İstanbul, Turkey, Feb. 2010.
[2]. Erden M. A., Gündüz S., Türkmen M., Karabulut H., "Microstructural characterization and mechanical properties of microalloyed powder metallurgy steels", *Materials Science and Engineering: A*, vol. 616, pp. 201-206, Agust. 2014.
[3]. Gladman, T., "The physical metallurgy of microalloyed steels", *The Institue of Materials*, England, 1997.
[4]. Sage A. M., "An overview of the use of mikroalloys in hsla steels with particular reference to vanadyum and titanium, processing, properties and applications", *Proceedings of the Second International Conference on HSLA Steels*, 11.05.92, p. 51.
[5]. Karabulut H., Gündüz S. "Effect of vanadium content on dynamic strain ageing in microalloyed medium carbon steel", *Materials and Design*, vol. 25, pp. 521–527, Jan. 2004.
[6]. Sarıtaş, S., Türker, M, Durlu, N. "Powder Metallurgy and Particulate Materials Processing", *Turkish Powder Metallurgy Association*, 2nd ed., Ankara, Türkiye, 2-34, 206-237, 379-410, 2007.
[7]. Gladman, T. and Woodhead, J. H., "The accuracy of point counting in metallographic investigations", *Journal of the Iron Steel*, vol. 194, pp.189, Jan. 1960.
[8]. Misra R. D. K., Tenneti K. K., Weatherly G. C., Tither G. "Microstructure and texture of hot rolled Cb-Ti and V-Cb microalloyed steels with differences in formability and toughness", *Metall. Mater. Trans. A*, vol. 34A, pp. 2341, 1 Oct. 2003.
[9]. Sarıtaş, S., Türker, M, Durlu, N. "Powder Metallurgy and Particulate Materials Processing", Turkish Powder Metallurgy Association, 2nd ed., Ankara, Türkiye, 5-33, 217-230, 2007.
[10]. Schade C, Murphy T, Lawley A, Doherty R., "Microstrucure and mechanical properties of microalloyed PM steels", *Int J of Powder Metall*. Vol. 48, pp. 51-59, Jan.2012.
[11]. Schade, C., Murphy, T., Lawley A., Doherty R., "Microstructure and mechanical properties of PM steels alloyed with silicon and vanadium *Int J of Powder Metall.* Vol. 48, pp. 41-48, Jan.2012.
[12]. Xiang-done H., Xin-ping M, Sheng-xia L. "Effect of annealing temperature on recrystallization behavior of cold rolled Ti-microalloyed steel", *J. of Iron and Steel Res Int.*, vol.20 (9) pp. 105-110, 13 Sept. 2013.

BIOGRAPHIES

Asist. Prof. Mehmet Akif ERDEN was born in Bursa, Turkey, 1986. He graduated from Karabük Üniversity in 2007 and took his MSc degree from Karabük University in 2011 and his Ph.D degree from Karabük University in 2015. He is Assist. Prof. in Karabük University, Vocational School, Department of Metallurgy.

Prof. Süleyman GÜNDÜZ was born in Bursa, Turkey, 1970. He graduated from Gazi Üniversity in 1992 and took his MSc degree in 1996 and his Ph.D degree in 2000 in the area of Metallurgy and Materials Engineering from Leeds University, UK. He is Professor in Department of Manufacturing Engineering at Technology Faculty of Karabuk University.

Prof. Halil DEMİR was born in Elazığ, Turkey, 1970. He graduated from Gazi Üniversity in 1992 and took his MSc degree in 1996 and his Ph.D degree in 2000 g from Gazi University. He is Professor in Department of Manufacturing Engineering at Technology Faculty of Karabuk University.

Asist. Prof. Hasan KARABULUT was born in İskendurun, Turkey, 1974. He graduated from Karabük Üniversity in 2000 and took his MSc degree from Karabük University in 2004 and his Ph.D degree from Gazi University in 2011. He is Assist. Prof. in Karabük University, Vocational School, Department of Metallurgy.

Doğan ÖZDEMİRLER was born in Karabük, Turkey, 1970. He graduated from Gazi Üniversity in 1992. He has been working on his MSc study at Karabük University since 2015.

ICENS
INTERNATIONAL CONFERENCE ON ENGINEERING AND NATURAL SCIENCES
24-28 May 2016 /Sarajevo

Microstructure and Mechanical Properties of AlC and TiCN Added PM Steels

Mehmet Akif Erden[1]

Abstract

In this work, microstructure and tensile behaviours of AlC and TiCN added PM steels were investigated. The microstructure of the PM steels was characterised by optic microscope, SEM and EDS. Results indicated that 0.2 wt. % (AlC-TiCN) added PM steel showed the highest values in yield strength (YS) and ultimate tensile strength (UTS). However, when the amount of (AlC-TiCN) content increased from 0.2 to 0.5 wt.%, yield strength, ultimate tensile strength and elongation decreased.

Keywords*: Powder metallurgy; powder metallurgy steels; AlC; TiCN; Microstructure.*

1. INTRODUCTION

Steels are the material group having superior properties such as; high strength and toughness, low ductile-to-brittle transition temperature, excellent weldability and corrosion resistance which are obtained by applying various hardening mechanisms and proper thermomechanical procedures. The main roles of microalloying elements are to refine the grain size, prevent recrystallization and facilitate precipitate hardening. The effect of microalloying elements on the grain boundary movement and recrystallization is a result of carbo-nitride precipitates. [1-5].

Powder metallurgy (P/M) paves the way for the economical production of high quality and sophisticated tools. This production method turns the metal powders that are different in size, shape and packaging features into resistant, precise and high performance tools [6].

In the present study, PM steel has been produced in the targeted compound by adding different proportions of TiCN and AlC into the Fe matrix with the powder metallurgy method and the output microstructural mechanical features have been compared.

2. EXPERIMENTAL METHOD

In this investigation, having been added in different proportions, the effect of the AlC and TiCN's amount on microstructural and mechanical properties is researched. Fe, TiCN and AlC powders by Aldrich were used.. Before the mixing process, powders were prepared in the proportions that had been given in Table 1 by weighing on a digital precision scale which has 0.0001 precision. The powders was mixed in an industrial conic mixer for 1 h. Graphite additions were 0.45 % to reach carbon concentration of 0.25 % in the test pieces after sintering. Additionally, Zn-stearate was used in all mixes as lubricant. Steel is produced by way of mixing in the chemical compounds given in the Table 1. Tensile test has been implemented on the produced samples after microstructural characterisation is performed. The results have been compared. Having been mixed homogeneously, the powders were pressurised under 700 MPa unidirectionally with Hidroliksan branded device which has 96 ton pressure capacity. Samples of the tensile experiment were turned into blocks by squeezing with the mould which had been prepared according to ASTM (E 8M) standards of powder metal material tension sample.

[1] *Karabük Üniversitesi, TOBB TB M.Y.O, Karabük, Türkiye, Tel 0370 433 82 00, makiferden@karabuk.edu.tr*

Table 1: Chemical compositions of powder metal steels.

Compound	C (%wt.)	AlC (%wt.)	TiCN (%wt.)	Fe (%wt.)
Fe +0.25 C (Alloy 1)	0.25	-	-	rest
Fe +0,25 C+ 0.05 AlC +0.05 TiCN (Alloy 2)	0.25	0.05	0.05	rest
Fe +0,25 C+ 0.1 AlC +0.1TiCN (Alloy 3)	0.25	0.1	0.1	rest
Fe +0,25 C+ 0.25 AlC +0.25TiCN (Alloy 4)	0.25	0.25	0.25	rest

The pressed samples were sintered in argon atmosphere at 1150 ºC for 1 hour. After sintering, density and pore values were measured. The sintered samples were subjected to standard metallographic procedures. Having sintered at 1150 ºC, the microstructures of the PM steel were examined under a Nikon Epiphot 200 optical microscope of X50-X1000 zoom capacity. Tensile test was carried out at 0.5 mm/min crosshead speed with a Shimadzu tensile testing device of 50 KN capacity. The yield strength (% 0.2), tensile strength and % (percentage) values of elongation of the tensile test samples were determined. Vickers hardness value was determined through applying 0.5 kg weight under a Shimadzu unit hardness device. The density of the samples was determined according to the principle of Archimedes. Likewise, the pearlite proportions of the powder metal steels were calculated using Gladman and Woodhead's metallographic point counting method [7]. Along with it, AlC, AlN, TiC, TiN and TiCN precipitates were detected with the help of the point and line EDS.

3. RESULTS AND DISCUSSION

3.1 Microstructure

The images of the microstructures of the samples are demonstrated in the Figure 1. As can be seen from the figure, the structure comprises of ferrite and pearlite phases in the whole alloys. When the images of the microstructure in the Figure 1 are examined, it is detected that there are partially uncovered pores on the borders of the grains. Although it is stated that porosity affect the strength of many welds negatively, it is reported that tiny and spherical pores do not reduce the strength [9]. It is inferred from the images of microstructure that as the proportion of the AlC and TiCN alloy in the composite samples increases, the size of the grain gets smaller gradually. It is observed that the average grain size gets bigger in the alloy that contains %5 AlC and TiCN. For instance; the size of the grain decreased to 26,7 µm and 25,3 µm respectively with 0,1 and 0,2 percentage of weight increase in the amount of the AlC +TiCN while the average size of grain in the nonalloyed PM steel sample in the Fe and 0,25C compound is 29,7 µm. It is observed as 28,5 µm when the amount of AlC and TiCN is calculated 0,5 as percentage weight.

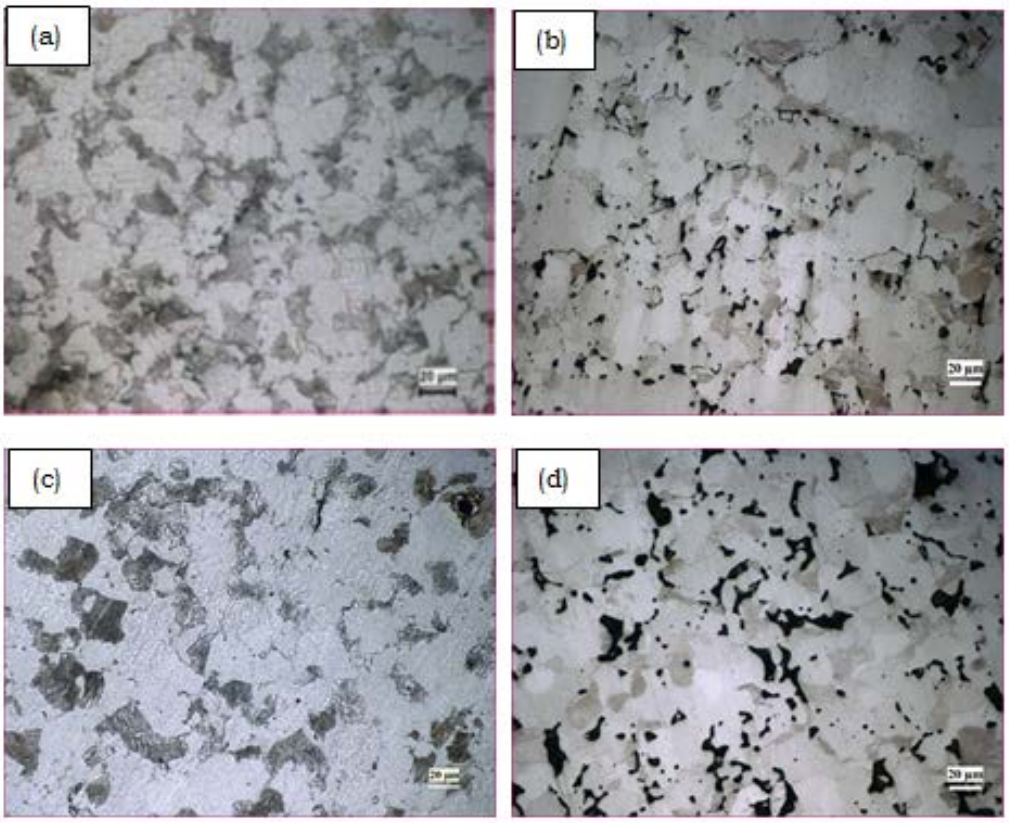

Figure 1. Micrographs of PM steel specimens (500 x). (a) 0 % AlC +TiCN (non-alloyed), (b) 0,1 % AlC +TiCN (c) 0.2 % AlC +TiCN (d) 0.5 % AlC +TiCN

Table 2. Relative density, mean linear intercept grain sizes and volume fractions of ferrite and pearlite phases in sintered samples.

Alloy	Relative Density (%)	Porosity (%)	Ferrite (%)	Pearlite (%)	Grain Size (µm)
Alloy 1	92	8	79.4	21.6	29.7
Alloy 2	91.8	8.2	80.3	19.7	26.7
Alloy 3	91.9	8.1	81	19	25.3
Alloy 4	91	9	80.1	20.9	28.5

In the Table 2, it is seen that the average size of grain decreases with a %0.2 of increase in the proportion of the AlC and TiCN. This situation emerges when AlC, AlN, TiC, TiN and TiC(N) precipitates that develop in the sintering process prevent the austenite grains from getting bigger. One of the features of microalloy elements is that they restrict grain size by creating carbide and nitride.in the austenitizing or sintering processes. Development of little sediments during the austenitizing process prevents austenite grains from growing and leads to the development of small ferrite grains [7-11].

It is observed that the average size of grain increases a little with an increase from %0.2 to %0.5 in the proportion of AlC and TiCN. As a reason for this, we might consider the development of big AlC and TiCN precipitates on the borders of the grains [2-5]. The big developed precipitates lead to an increase in the average size of the grains as they can not restrict grain size sufficiently.

3.2. Mechanical Properties

While Figure 2 shows the stress-strain diagrams of the sintered samples, Table 3 shows the yield strength, tensile strength, percentage elongation and hardness results. The yield and tensile strength with the percentage elongation and hardness values are observed to increase when AlC and TiCN proportion increases to %0.2. Being formed by the aluminum and titanium, the carbide, nitride and carbonitride precipitates ensure the material to be small grained by way of restricting the size of the austenite grain and re-crystallisation of the austenite. The improvement of the resistance to dislocation movement is fulfilled thanks to the increasing grain boundaries in the small grained structure. The decrease of the grain size also contributes to the percentage elongation of the material. Along with these, the formed precipitates contributed to the increase in the yield and tensile strength via various strength increasing mechanisms like precipitates hardening and dispersion hardening [2-4;10-11].

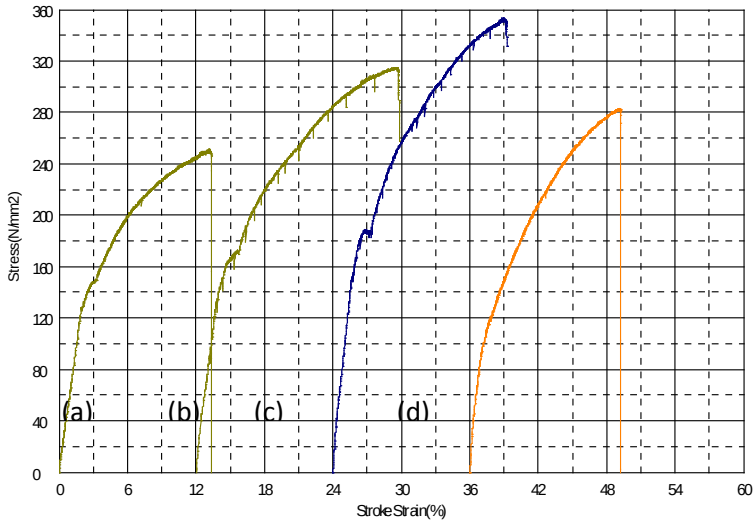

Figure 2. Variation of stress–strain curves of sintered samples in different percentages of AlC and TiCN content (a) Alloy 1, (b) Alloy 2, (c) Alloy 3, and (d) Alloy 4.

Table 3. Mechanical properties of the sintered samples.

Alloy	Yield Strength (MPa)	Ultimate Tensile Strength (MPa)	Elongation (%)	Hardness ($Hv_{0,5}$)
Alloy 1	144	252	13	68
Alloy 2	171	316	17	127
Alloy 3	189	355	15	153
Alloy 4	109	284	13	91

It is thought that AlN and TiC(N)-like precipitates lead to the development of small austenite grains by way of restricting the grain size during the sintering process, thereby improving the resistance of the materials. Similarly, Erden et al. [2] produced Ti microalloyed steel with PM method. They conducted the sintering process at 1150 °C for 60 minutes and determined an increase in the yield and tensile strength as the proportion of Ti (% 0,1-% 0,2) rises. The author demonstrates in their study that TiC(N)-like precipitates lead to the development of small austenite grains by restricting the grain size during sintering and as a result of this, the resistance of the materials improves. In the other studies [1;10-11], it is stated that the carbide and nitrite formed in the microalloyed steels lead to an increase in the toughness and strength. In the same study, it is pointed out that solid solution hardening remains at low percentage because of the precipitation of carbide and nitrite [3-7]. In addition, presence of AlC and TiCN in steel at a high proportion makes the material brittle and leads to the decrease of strength by causing over-hardening of the precipitate.

3.3. SEM-EDS Analysis

It is determined from the SEM image that the sample given in Figure 3 containing 0.1 % of AlC and TiCN results in different sizes of precipitates. In addition, the analysis results of the point EDS show that AlC precipitates form because these precipitates contain aluminum, carbon and that Fe_3C precipitates form because they contain iron and carbon. It can be said that these formed precipitates restrict the growth of austenite grain size, re-crystallization and improve the strength of the material with precipitation hardening [10-12].

The effect of the microalloying elements in precipitates on the re-crystallization of the austenite is not much. The prevention of the grain boundary movement via the precipitated grains is more than that of the dissolved atoms [12].

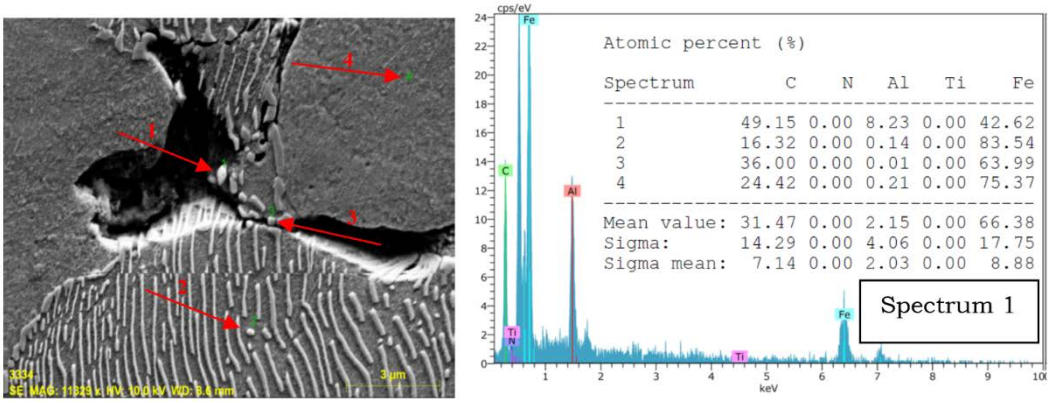

Figure 3. SEM micrograph Alloy 2 (11925X) and corresponding EDS of the indicated points.

Figure 4 shows the line EDS analysis results that were taken from the matrix and precipitates of the 0.2 % of AlC and TiCN including PM steel sample which was sintered at 1150 °C. When the results of the line EDS analysis of 0.2 % of TiCN including PM steel are examined, it is observed that there is a difference in the element type and amount along the stripe that cut the matrix and the precipitate. It is determined that matrix phase is iron-rich but round-shaped precipitate is titanium-rich. In addition, when the stripe which comes from the matrix cuts the precipitate, there has been a sharp increase in the amount of titanium.

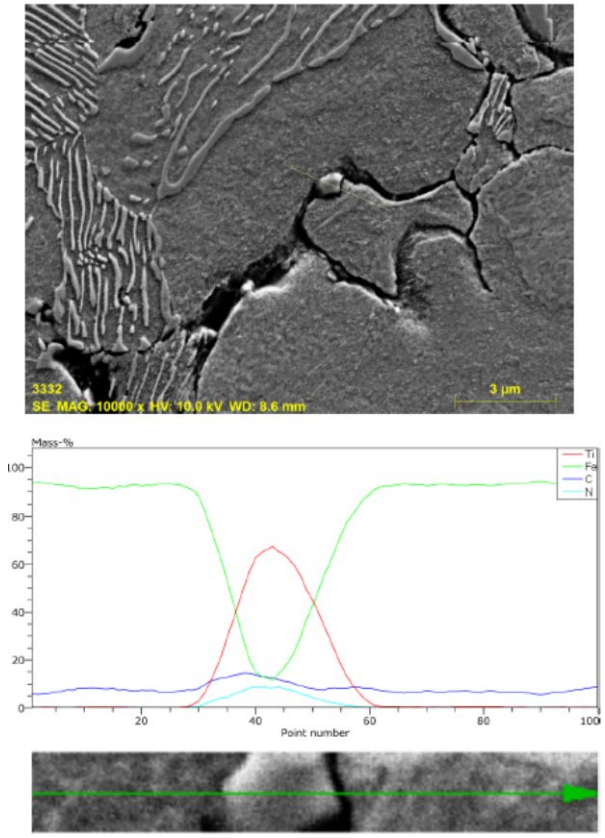

Figure 4. SEM micrograph for Alloy 3 sintered at 1150 °C and EDS lines scan of the indicated particle.

The results of the point and line EDS analysis that were obtained in this investigation demonstrates that the precipitates like AlN, TiC, TiN and TiC(N) develop in the AlC and TiCN alloyed PM steels.

CONCLUSIONS

The non-alloyed and AlC and TiCN alloyed PM steel which has three different volume ratios (0.1 – 0.2 % and 0.5 %) is produced by cold pressing and sintering at the argon setting and the following results listed below are obtained from this study.

1. Composite materials which contain AlC, TiCN and Fe matrix can be produced with powder metallurgy. Solid solution hardening and precipitation hardening which arise during the sintering process or after-sintering cooling process increase the resistance of the steel.
2. Composite materials that are added 0.1 - 0.2 % and 0.5 % AlC and TiCN as weight compared to non-alloyed steels showed smaller grain structure. This situation stems from the restriction of grain size by the carbide and nitrite which alloy elements has created.
3. Usually, there has been an increase in the yield strength, tensile strength, percentage (%) elongation and hardness values of the compounds which have AlC and TiCN ratio by 0.2 % as the alloy ratio rises. This situation is a result of the development of the precipitates like TiCN during sintering process and after-sintering cooling process. These precipitates lead to the creation of small austenite grains by preventing grain size and thus improving the resistance of the materials.
4. After-sintering density of the nonalloy and AlC and TiCN added composite materials is observed to be generally at about 91 %. After-sintering density of the produced PM steels showed a little bit increase.

ACKNOWLEDGMENT

The author gratefully acknowledges financial support from Karabuk University Coordinatorship of Resarch Projects.

REFERENCES

[1]. Karaduman, "Production Of Titanium Carbide Reinforced Titanium Matrix Composites Via Conventional Powder Metallurgy Method" Thesis (M.Sc.), Institute of Science and Technology, İstanbul Technical University, İstanbul, Turkey, Feb. 2010.
[2]. Erden M. A., Gündüz S., Türkmen M., Karabulut H., "Microstructural characterization and mechanical properties of microalloyed powder metallurgy steels", *Materials Science and Engineering: A*, vol. 616, pp. 201-206, Agust. 2014.

[3]. Gladman, T., "The physical metallurgy of microalloyed steels", *The Institue of Materials*, England, 1997.
[4]. Sage A. M., "An overview of the use of mikroalloys in hsla steels with particular reference to vanadyum and titanium, processing, properties and applications", *Proceedings of the Second International Conference on HSLA Steels*, 11.05.92, p. 51.
[5]. Karabulut H., Gündüz S. "Effect of vanadium content on dynamic strain ageing in microalloyed medium carbon steel", *Materials and Design*, vol. 25, pp. 521–527, Jan. 2004.
[6]. Sarıtaş, S., Türker, M, Durlu, N. "Powder Metallurgy and Particulate Materials Processing", *Turkish Powder Metallurgy Association*, 2nd ed., Ankara, Türkiye, 2-34, 206-237, 379-410, 2007.
[7]. Gladman, T. and Woodhead, J. H., "The accuracy of point counting in metallographic investigations", *Journal of the Iron Steel*, vol. 194, pp.189, Jan. 1960.
[8]. Misra R. D. K., Tenneti K. K., Weatherly G. C., Tither G. "Microstructure and texture of hot rolled Cb-Ti and V-Cb microalloyed steels with differences in formability and toughness", *Metall. Mater. Trans. A*, vol. 34A, pp. 2341, 1 Oct. 2003.
[9]. Sarıtaş, S., Türker, M, Durlu, N. "Powder Metallurgy and Particulate Materials Processing", Turkish Powder Metallurgy Association, 2nd ed., Ankara, Türkiye, 5-33, 217-230, 2007.
[10]. Schade C, Murphy T, Lawley A, Doherty R., "Microstrucure and mechanical properties of microalloyed PM steels", *Int J of Powder Metall*. Vol. 48, pp. 51-59, Jan.2012.
[11]. Schade, C., Murphy, T., Lawley A., Doherty R., "Microstructure and mechanical properties of PM steels alloyed with silicon and vanadium *Int J of Powder Metall.* Vol. 48, pp. 41-48, Jan.2012.
[12]. Xiang-done H., Xin-ping M, Sheng-xia L. "Effect of annealing temperature on recrystallization behavior of cold rolled Ti-microalloyed steel", *J. of Iron and Steel Res Int*., vol.20 (9) pp. 105-110, 13 Sept. 2013.

BIOGRAPHY

Asist. Prof. Mehmet Akif ERDEN was born in Bursa, Turkey, 1986. He graduated from Karabük Üniversity in 2007 and took his MSc degree from Karabük University in 2011 and his Ph.D degree from Karabük University in 2015. He is Assist. Prof. in Karabük University, Vocational School, Department of Metallurgy.

ICENS
INTERNATIONAL CONFERENCE ON ENGINEERING AND NATURAL SCIENCES
24-28 May 2016 /Sarajevo

Long Term Performance of a Pilot Anaerobic Digester Fed by Municipal Solid Waste and Effect of Trace Metal Addition

Duygu Karaalp Yavuzyilmaz[1], Kubra Arslan[2], Tugba Keskin Gundogdu[3], Nuri Azbar[4]

Abstract

In this study, anaerobic digestion of representative organic fraction of municipal solid waste was studied in the long run and the effect of trace element addition is also reported. A continual feeding of solid waste mixture with a dry matter of 5% for 200 days were carried out using a 100 L pilot scale CSTR type anaerobic digester under mesophilic operation conditions. Hydraulic retention time and organic loading rate were kept 30 days and 3.0 kg oDM/m^3.day, respectively. During the 160 days feeding period, daily and volumetric biogas production values were reported to be 30-146 L/day and 0.3-2.0 L/L/day, respectively. This corresponds to biogas production between 400 and 900 L/kg oDM, which means that between 40 and 100 m3 of biogas per wet ton of solid waste could be produced. As a follow up this study, trace element addition was also carried out after a batch Taguchi Statistical optimization method using BMP protocol. Bioreactor then was fed with this Taguchi recipe. Trace element addition resulted in unit biogas production varying 300 and 800 L/kg oDM, which did not provide any extra increase in biogas production but the main effect was the more stable operation of the bioreactor. In conclusion, there is tremendous amount of bio-methane production potential in Turkish solid wastes which could be exploited for environment friendly energy production either in the form of biofuel for public transportation or bioelectricity, which would provide great advantage for remedying the global warming impact of Turkey.

Keywords: *Bio-methane, municipal solid waste, trace element*

1. INTRODUCTION

Municipal solid waste generation exceeds 30 million tons per year in Turkey. Even though, most of the metropolitan cities in Turkey have landfills which is the main waste management option, the number of plants using either composting or anaerobic digestion techniques are quite limited in Turkey. Turkey is required to comply with EU 27 targets for landfilling of solid wastes and should gradually reduce the amount of solid waste landfilled. Turkish solid waste with more than 50% organic content is amenable for biotechnological processing either aerobically or anaerobically. Anaerobic digestion seems to be more attractive due to the high methane content of the solid waste, which is also beneficiary for Turkish renewable energy production targets in the frame of Kyoto protocol. Despite of current solid waste practices all over the world, there are still several MSW management problems in the world and the current technology is needed to be improved in order to increase the amount of generated energy as well as decreasing the amount of MSW to be landfilled. As in [1] reported a brief history of the legislative trends in Turkey for MSW management, primitive disposal methods in the form of open dumping and discharge into surface water had been used in various parts of Turkey although strict regulations on MSW management were in place. They also claimed that 70.57% of the total MSW was disposed of thereby [1]. The developments in environmental technology have been accelerated in Turkey over the last two decades in the frame of Turkey's 2023 vision and accession to EU. 30% of the demand of electricity in Turkey is planned to be met from renewable energy sources by 2023 [2]. The number of sanitary landfills which is 80 in 2013 in Turkey is planned to increase 130 at the end of 2017. According to Turkish Statistical Institute values, 59.9% of MSW was disposed in municipality sanitary landfills, 0.11% of MSW was combusted with incineration (2 incineration plants), 1.15% of MSW was disposed by using a recycling method, and 37.8% of MSW was accumulated by means of municipality dumps in Turkey by 2012. Landfills, which are most widely used disposal methods, naturally produce methane, however unintended losses from landfills [3] represent significant greenhouse gas (GHG) emissions with a global warming potential (GWP) 21–25 times that of carbon dioxide [4],[5]. In 2002, U.S. EPA, reported that landfill gas leakage was responsible for 3% of total U.S. GHG emissions. Furthermore, release of gas from landfills has been estimated at 8% of atmospheric methane [6]. Global warming and resultant climate change implications are widely recognized by the scientific community and significant decreases in carbon emissions are recommended [7]. IPPC reports indicates that in many countries, MSW management and energy system are closely linked in a way to exploit the economic and environmental benefits from this synergy. Moreover, a great part of the energy production from MSW is considered as a renewable energy source [8].

[1] *Ege University, Engineering Faculty, Bioengineering Department, İzmir, Turkey,* d_karaalp@hotmail.com

[2] *Ege University, Engineering Faculty, Bioengineering Department, İzmir, Turkey,* arslankubra03@gmail.com

[3] *Ege University, Engineering Faculty, Bioengineering Department, İzmir, Turkey,* keskin.tugba@gmail.com

[4] *Corresponding author: Ege University, Engineering Faculty, Bioengineering Department, 35100, Bornova-İzmir, Turkey,* nuri.azbar@ege.edu.tr

Amongst the solid waste management alternatives, biochemical conversion methods, either composting or preferably anaerobic digestion are considered to be more environment friendly in comparison to other methods such a landfilling or incineration. Especially, anaerobic digestion of the organic fraction of solid waste is much more advantageous due to the fact that both bioenergy (as methane) and organic fertilizer could simultaneously be produced while environment friendly management of MSW is carried out [9]. Furthermore, anaerobic digestion is a well-established and successfully used technology.

In this study, the long term performance of a pilot scale anaerobic digester is presented in a way to promote this technology as a solution for Municipalities.

2. MATERIALS & METHODS

2.1 Source of municipal solid waste (MSW)

MSW used in this study was kindly obtained from Izmir Metropolitan City, Solid Waste Management Department in Izmir, Turkey on a weekly basis. MSW was first grinded and diluted down to 5% DM (on the average) by adding water before use in digester. All MSW was stored in a refrigerator at +4°C until used.

2.2 Analytical methods

The parameters such as pH, DM%, oDM%, COD, TN, NO_2-N, NO_3-N, NH_4-N were measured according to "Standard Methods for the Examination of Water and Wastewater". All chemical solutions were prepared with deionized water (Milli-Q® Ultrapure Water Purification System, Millipore Corp.). Daily biogas productions were measured by Ritter Wet type gas meter. When needed, sample of known volume was extracted from each digester and analyzed for methane using a Gas Chromatograph with a flame ionization detector.

2.3 Experimental set-up

Anaerobic digestion of MSW was carried out in a pilot scale digester with a total volume of 100 L. This digester is equipped with automatic control system in which temperature and mixing are controlled. Biogas production was measured by Ritter wet type gas meter on a daily basis. MSW having 5% DM after grinding and diluting with fresh water was fed daily into the digester in a way to keep the hydraulic retention time (HRT) and organic loading rates (OLR) to be around 30 days and 3 kg oDM/m^3/day, respectively.

3 RESULTS AND DISCUSSIONS

Figure1 shows the OLR values used throughout the study for 200 days. As can be seen in Figure 1, OLR was adjusted according to performance of the digester and kept below 3 kg oDM/m^3/day.

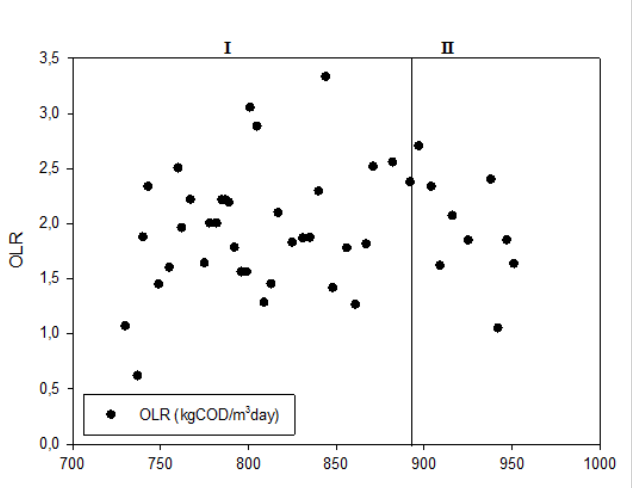

Figure 1. OLR values

Fig 2 shows the volumetric biogas productions, daily biogas productions and biogas production per oDM fed. This digester has been operation for more than 700 days with a feed of chicken manure and at 735th day, MSW with 5 DM% was started to be fed into the digester on a daily basis. Following the feed of MSW, daily biogas productions started to increase immediately. As can be seen in Fig 2, daily biogas production varied between 30-146 L/day corresponding to volumetric biogas production values of between 0.3-2.0 L/L/day. Considering the oDM of the feed, biogas per kg of oDM was calculated and plotted in Fig 2 which varied between 400-900 L/kg oDM. This indicates that 102 m^3 biogas per wet ton of MWS is possible. In order to test the effect of trace metal addition into the digester, at day 897, the digester was fed by MSW mixed with trace metal (TM) recipe determined by Taguchi statistical optimization method for the rest of the study. During this period of the study between

days of 897 and 950, the daily biogas production was varied between 60-140 L/day corresponding to 400-800 L/kg oDM volumetric biogas production. This results indicated that the addition of TM did not resulted in statistically meaningful difference in biogas production but it provided a more stable operational conditions and it was concluded that TM in MW is sufficient enough.

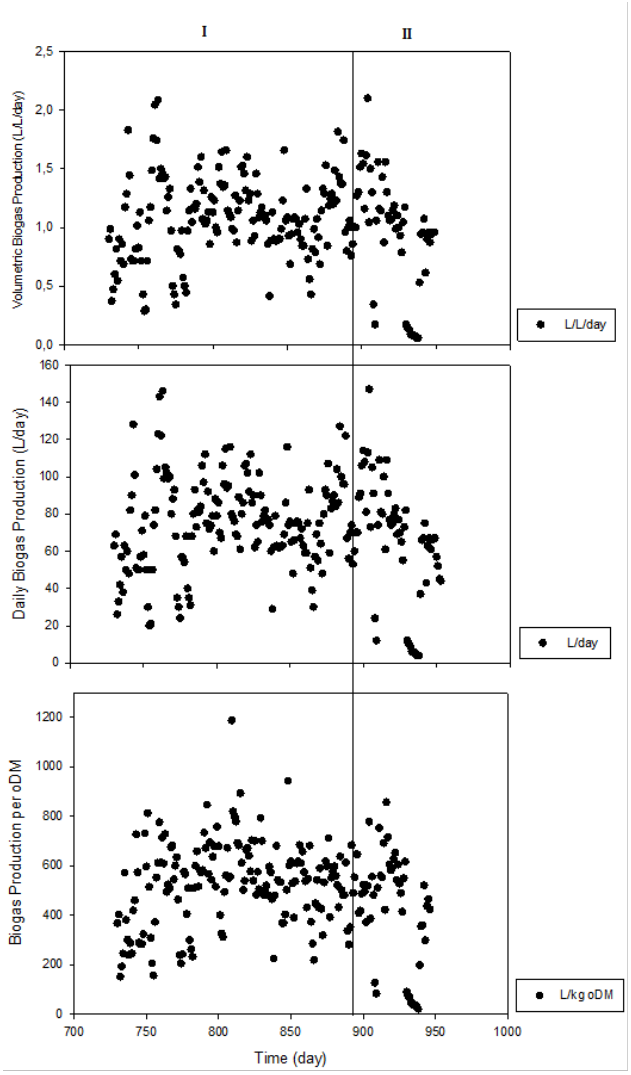

Figure 2. Biogas production performance of the digester

Fig 3 shows the operational parameters such as pH, DM%, oDM%, soluble and total COD in influent and effluent. It is seen in Fig 3 that pH is quite stable throughout the study and there was no need to provide an external alkalinity. Depending on the feed material, the initial DM% was varied between 3 and 9% (5% on the average). At 30 day of HRT condition, 60-75% removal of DM was realized resulting an effluent DM% varying between 1-2%. In regards to oDM removal, it was monitored that 42-94 % removal (79% on the average) in oDM% was carried out. TM addition did not again resulted in any difference in DM or oDM removal performance of the digester.

Total COD of the feed in the influent and the effluent was between 40-80 g/L and 6-20 g/L, respectively. These results indicated that on the average, 71% removal of TCOD was achieved. In regards to soluble COD values, it was monitored that influent and effluent SCOD values were 10-30 g/L and 2-6 g/L, respectively.

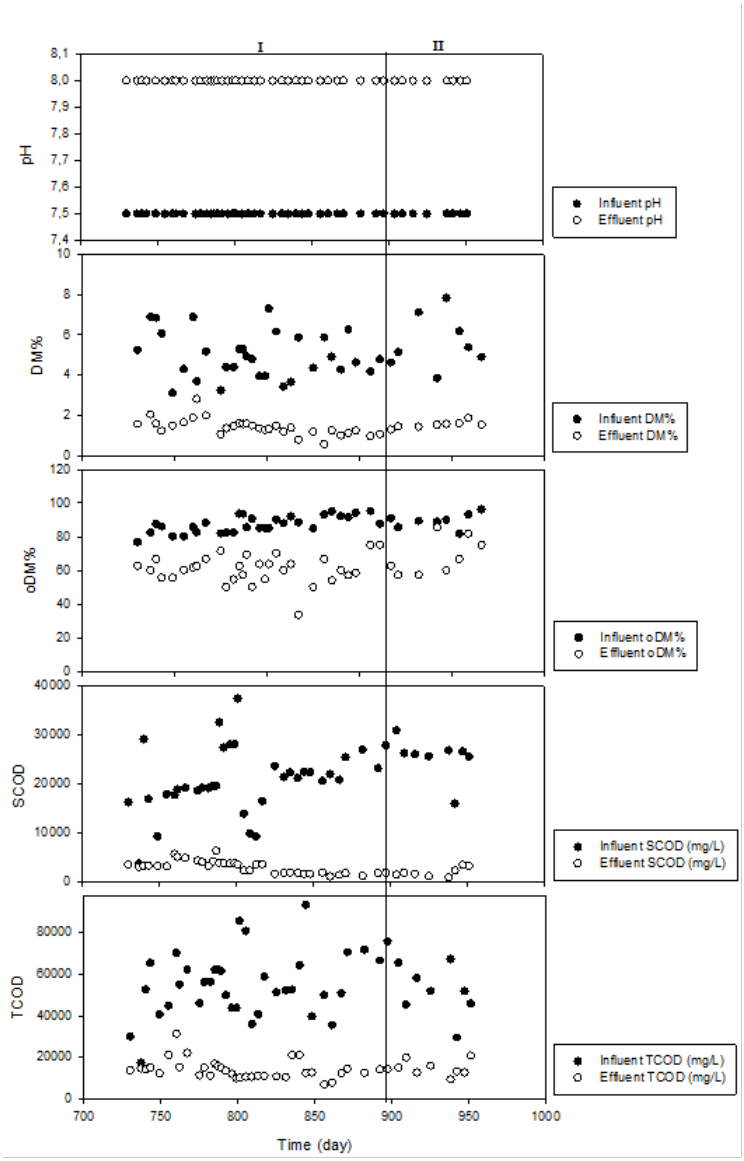

Figure 3. Operational parameters during the study period

Fig 4 shows the variation of nitrogen species throughout the study. According to these measurements;

For the first 90 days of operation, TN values varied between 3000-14000 mg/L with a decreasing trend which indicated that the digester has been washing out the residual nitrogen from previous study. TN values then stabilized at 500-1000 mg/L which is more representative for MSW feed.

Accordingly, NH_4-N values started to decrease from a value of 8000 mg/L and then stabilized at a value of 500 mg/L.

NH_3-N which is the most critical type of TN was initially quite higher than a toxic level reported in [10], but this value also started to decrease down to around 100 mg/L upon MSW feeding.

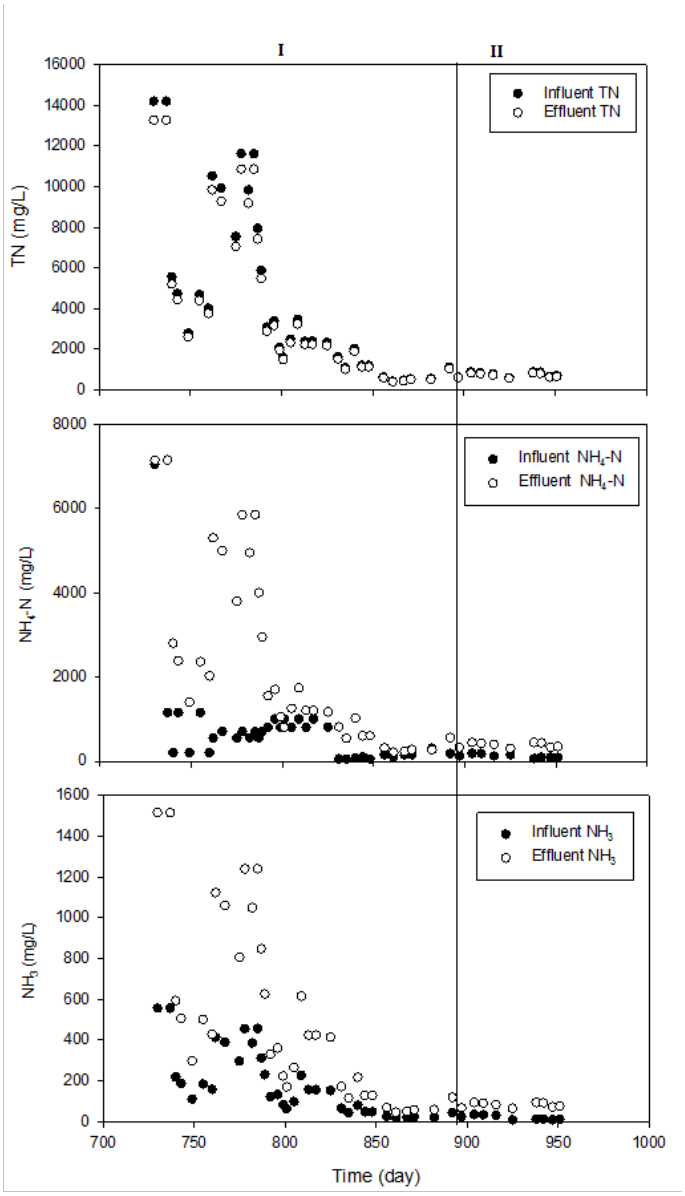

Figure 4. Nitrogen values in the digester

CONCLUSIONS

Anaerobic digestion of organic fraction of MSW is able to produce significant amount of biogas which has a great potential to be used as renewable and environment friendly energy alternative. The potential for Izmir city which could be a representative for a relatively big city is around 200.000 m^3 biogas per day corresponding to a 20 MW power generation. Thereby, let alone the prevention of uncontrolled emissions of CH_4, 73.000 tons of CO_2 emissions would be prevented each year.

ACKNOWLEDGMENT

The authors wish to thank TUBITAK-CAYDAG under the grant No 113Y534 and COST for the financial support of this study. The data presented in this article was produced within the project above, however it is only the authors of this article who are responsible for the results and discussions made herein. The authors would also thank to Izmir Metropolitan Municipality and General Directory of IZSU for their supports.

REFERENCES

[1]. N.G. Turan, S. Çoruh, A. Akdemir, O.N. Ergun,"Municipal solid waste management strategies in Turkey", *Waste Manag*, vol.29, pp. 465-469, 2009.
[2]. A.Tozlu, E. Özahi, A. Abuşoğlu,"Waste to energy technologies for municipal solid waste management in Gaziantep", *Renewable and Sustainable Energy Reviews*, vol. 54, pp. 809-815, 2016.
[3]. (2009) EPA website, [Online] Available: http://www.epa.gov/climatechange/emissions/usinventoryreport.html
[4]. P. Forster, *Climate Change 2007: The Physical Science Basis*, S. Solomon, D. Qin, M. R. Manning, Z. Chen, M. Marquis, K.B. Averyt, M. Tignor, H.L. Miller, eds., Cambridge, U.K., New York, Cambridge University Press, 2007
[5]. T. Houghton, L. G. Meiro Filho, B. A. Callander, N. Harris, A. Kattenburg and K. Maskell, Climate change 1995: The science of climate change, Cambridge University Press, Cambridge, U.K., 1996.
[6]. D.P. Chynoweth, *The Science of Global Change*, vol.483, chapter 17, pp.338-351,1992.
[7]. (2007) IPCC, Contribution of Working Group III to the Fourth Assessment Report of the Intergovernmental Panel on Climate Change, [Online] Available: https://www.ipcc.ch/publications_and_data/ar4/wg3/en/contents.html
[8]. (2012) IPCC, Renewable energy sources and climate change mitigation, [Online] Available: http://srren.ipcc-wg3.de/report
[9]. H. Rigby and S.R. Smith, "The nitrogen fertiliser value other agronomic benefits of industrial biowastes", *Nutr.Cycling.Agroecosyt.*, vol. 98, pp. 137-154, 2014.
[10]. P.L. McCarty and R.E. McKinney, "Salt toxicity in anaerobic digestion", *J. Water Pollut. Contr. Fed.*, vol. 33, pp. 399-415, 1961.

BIOGRAPHY

Dr. Nuri Azbar is full professor at Ege University, Bioengineering Department and he is also the direcyor of Center for Environmental Studies at Ege University. His main research interests is the production of value added chemicals (bioenergy, biopolymers etc) from organic wastes in a way to realize bio-refinery concept. He has many may papers and e-book chapters on Environmental Biotechnology.

ICENS
INTERNATIONAL CONFERENCE ON ENGINEERING AND NATURAL SCIENCES
24-28 May 2016 /Sarajevo

Investigation of Dry Deposition Fluxes of Atmospheric Particulate Matters in Denizli, Turkey by Bergerhoff Method

Sibel Cukurluoglu*

Abstract

In the scope of this study, particulate matters in ambient air were sampled at two different sites in Denizli, Turkey from April 2015 to May 2015. Bergerhoff Method was used for sampling. Dry deposition fluxes of particulate matters were calculated. The average dry deposition fluxes were calculated as 282.1±45.1 mg m^{-2} day^{-1} at Site 1 and 152.1±29.0 mg m^{-2} day^{-1} at Site 2. The minimum flux was determined as 115.4 mg m^{-2} day^{-1} at Site 2 on May 4-6, 2015 period, while the maximum flux was observed as 338.5 mg m^{-2} day^{-1} at Site 1 on April 27-29, 2015 and May 14-16, 2015 periods. It has been shown that the fluxes at Site 1 was approximately twice of the fluxes at Site 2. It can be said that Site 1 was exposed to more particulate matter pollution because this site was an area under the effect of traffic.

Keywords: *Bergerhoff method, particulate matter, dry deposition, flux, ambient air.*

1. INTRODUCTION

Natural and anthropogenic sources can cause to air pollution problems. The major anthropogenic sources of air pollution are industries (thermal power plants, steel plants, refineries, open cast mines, etc.), vehicular and domestic emissions [1]. Natural air pollution sources are volcanoes, dust, oceans, rivers and estuaries, sea salt, and forest fires.

Particulate matter (PM) is an important group among air pollutants. PM exists as a complex mixture of extremely small particles and liquid droplets including acids, metals, organic chemicals, etc. Surface area, shape, size, solubility, chemical composition and origin of particulate matters may affect grade of air pollution.

PM can be classified into $PM_{2.5}$ (PM with an aerodynamic diameter < 2.5 mm), PM_{10} (PM with an aerodynamic diameter < 10 mm), and total suspended particles (TSP) based on the aerodynamic diameter of particles [2].

Wet deposition and dry deposition are the ultimate paths by which particulate matters and trace gases are removed from the atmosphere. The relative importance of dry deposition, as compared with wet deposition, for removal of a particular species depends on the following factors [3]:

• Whether the substance is present in the gaseous or particulate form

• The solubility of the species in water

• The amount of precipitation in the region

• The terrain and type of surface cover

[1]*Corresponding author: Pamukkale University, Faculty of Engineering, Environmental Engineering Department, 20160, Kinikli/Denizli, Turkey. scukurluoglu@pau.edu.tr

Dry deposition is, broadly speaking, the transport of gaseous and particulate species from the atmosphere onto surfaces in the absence of precipitation. The factors that govern the dry deposition of a gaseous species or a particle are the level of atmospheric turbulence, the chemical properties of the depositing species, and the nature of the surface itself. The level of turbulence in the atmosphere, especially in the layer nearest the ground, governs the rate at which species are delivered down to the surface. For gases, solubility and chemical reactivity may affect uptake at the surface. For particles, size, density, and shape may determine whether capture by the surface occurs. The surface itself is a factor in dry deposition. A nonreactive surface may not permit absorption or adsorption of certain gases; a smooth surface may lead to particle bounce-off. Natural surfaces, such as vegetation, whereas highly variable and often difficult to describe theoretically, generally promote dry deposition [3].

The process of dry deposition of gases and particles is generally represented as consisting of three steps: (1) aerodynamic transport down through the atmospheric surface layer to a very thin layer of stagnant air just adjacent to the surface; (2) molecular (for gases) or Brownian (for particles) transport across this thin stagnant layer of air, called the *quasi-laminar sub layer*, to the surface itself; and (3) uptake at the surface. Each of these steps contributes to the value of the deposition velocity [3].

The study of PM pollution is a very important component of air quality management from many countries in the world [4]. Denizli has advanced industrialization, dense population and heavy traffic. Therefore air pollution problems can be experienced as well as the other environmental problems in Denizli.

In this study, dry deposition of particulate matters in ambient air was determined using Bergerhoff Method at two different sites in Denizli, Turkey from April 2015 to May 2015. The analyses of particulate matters were performed at the laboratory. Then dry deposition fluxes of particles were calculated. Finally the data of dry deposition of PM were evaluated according to the sampling sites and compared with PM_{10} values obtained from the Air Pollution Measurement Station, Republic of Turkey Ministry of Environment and Urbanization.

2. MATERIAL AND METHOD

2.1 Dry Deposition Sampling

Dry deposition samplings of particulate matters were performed at two different sites in Denizli, Turkey from April 2015 to May 2015. The one of the sampling sites was at the garden of the apartment under the heavy traffic effect at Kinikli, Denizli (Site 1). The other sampling area was at the garden of the opposite apartment at Pamukkale University, Kinikli Campus, Denizli (Site 2). Two samples in April and seven samples in May were collected at each sampling site as simultaneous.

The dry deposition sampling of particulate matters was performed using Bergerhoff Method. The dimensions of sampler were 13 cm of diameter and 26 cm of height. The sampler was transparent, polyethylene and cylindrical. The sampler was set at a stand approximately 0.5 m high from ground level. The samplers and laboratory materials were washed with 1:1 HNO_3 acid, then rinsed with tap water and deionized water and dried prior to use. The same procedure was replicate using 1:1 HCl acid [5].

Ultra-pure water of 500 mL was put to the sampler. The sampler was hold on throughout 2 days. At the end of the sampling, the dry deposition samples were transferred to cleaned sample storage containers and brought to the laboratory.

2.2. Analyses of Dry Deposition Samples

The analyses of particulate matters were made at the Environmental Engineering Research Laboratory, Environmental Engineering Department, Pamukkale University.

The volumes of the samples were measured. For analysis of suspended particles, the conditioned 0.45 µm cellulose acetate filters (Sartorius) were weighed with analytical balance. The deposition samples of 50 mL were filtered by filtration apparatus. The filter was put to oven at 103-105 ^{0}C for one hour. Then the filter was cooled at desiccator and weighed at analytical balance. The amount of suspended particulate matter (SPM) was calculated by the following formula:

$$SPM = \frac{A-B}{V} \times 1000 \quad (1)$$

A: Weight of filter + particulate matter (g)

B: Weight of empty filter (g)

V: Volume of sample (L)

The porcelain crucible was weighed by analytical balance for total particulate matter analysis. One hundred mL of deposition sample was taken to the porcelain crucible and put to oven at 103-105 ^{0}C for one hour. Then the crucible was cooled at desiccator and weighed at analytical balance. The amount of total particulate matter (TPM) was calculated as follows:

$$TPM = \frac{A-B}{V} \times 1000 \quad (2)$$

A: Weight of porcelain crucible + particulate matter (g)

B: Weight of empty porcelain crucible (g)

V: Volume of sample (L)

2.3. Calculation of Dry Deposition Fluxes

The dry deposition fluxes of the samples were calculated by the following formula:

$$F = \frac{C}{A \times T} \quad (3)$$

F: Flux (mg m^{-2} day^{-1})

C: Mass of particulate matter (mg)

A: Area (m^2)

T: Sampling time (day)

PM_{10} values obtained from the Air Pollution Measurement Station, Republic of Turkey Ministry of Environment and Urbanization were used for comment the levels of particulate matter. The temperature values were provided from Meteorology General Directorate.

2.4. Quality Control

Field and laboratory blanks were collected along with the dry deposition samples to determine the contaminants occurred during the sampling, handling, and filtration steps. The particulate matter analyses of these samples were also performed.

3. RESULTS

3.1 Dry Deposition Fluxes

The average dry deposition fluxes of particulate matters were determined as 282.1 ± 45.1 mg m^{-2} day^{-1} and 152.1 ± 29.0 mg m^{-2} day^{-1} at Sites 1 and 2 in Kinikli, Denizli, respectively. The minimum flux was observed as 115.4 mg m^{-2} day^{-1} in June 4, 2015 at Site 2. The maximum flux was determined as 338.5 mg m^{-2} day^{-1} in April 27, 2015 and May 27, 2015 at Site 1 (Figure 1).

The dry deposition fluxes at Site 1 were more than twice the value of the Site 2. It can be said that Site 1 more expose to pollution of particulate matter because of the heavy traffic effect.

The flux values at Uludag University, Bursa, Turkey by Bergerhoff Method were ranged from 300 to 7860 mg m^{-2} day^{-1} the period of April to June 2001. The daytime flux values (3078 ± 2412 mg m^{-2} day^{-1}) were more than six times the value for nighttime (524 ± 149 mg m^{-2} day^{-1}) [6].

Dust samples were collected at monthly intervals from three different sites (commercial, residential, and control) of the Jharia coal mining area, India by Rout et al. [1]. The yearly average dust fall was higher for the commercial site (15.5 t km^{-2} $month^{-1}$) than the residential site (10.7 t km^{-2} $month^{-1}$) of Jharia coal mining area. The dust deposition rate was highest during summer (March–June), followed by winter (October–February) and lowest in the monsoon season (July–September).

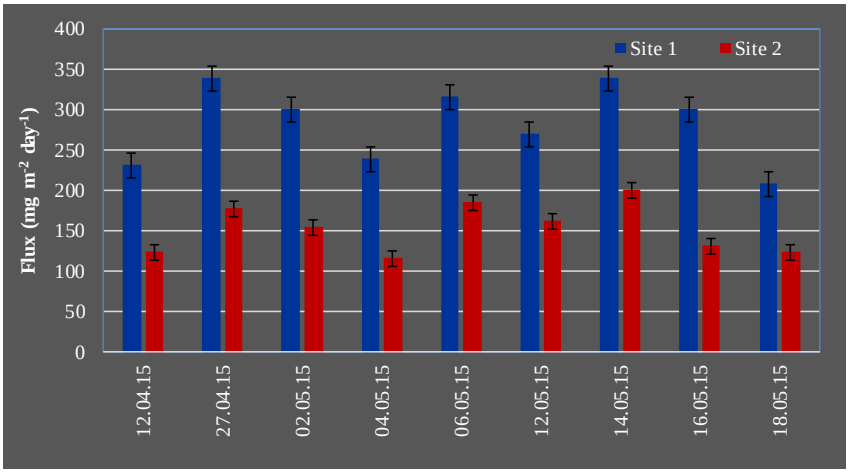

Figure 1. Dry deposition fluxes at sampling sites

Figure 2 shows that increase or decrease of each dry deposition fluxes at Sites 1 and 2 was seen same direction according to the sampling dates.

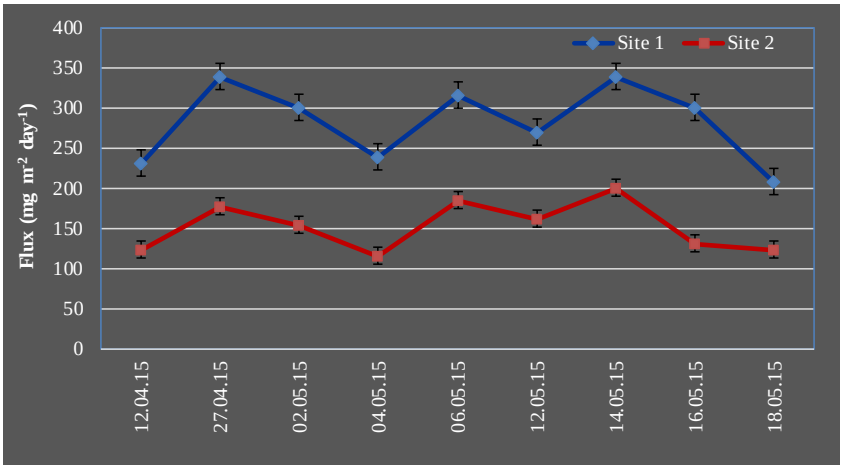

Figure 2. Variation of dry deposition fluxes at sampling sites

3.2 Dry Deposition Fluxes and PM_{10} Values

The PM_{10} concentrations were obtained from the Air Pollution Measurement Station, Republic of Turkey Ministry of Environment and Urbanization. The PM_{10} concentrations and daily dry deposition fluxes related to each sampling date were investigated in terms of interpretation the air particulate pollution level. It was seen that the minimum PM_{10} was observed as 59.7 µg m^{-3} in May 4, 2015 while the maximum PM_{10} concentration was determined as 94.3 µg m^{-3} in May 14, 2015. The minimum and maximum PM_{10} concentrations and the minimum-maximum dry deposition fluxes were observed at the same dates in general (Figure 3).

Antonel et al. [7] have measured the particulate matters in Bafoussam, Bamenda, and Yaoundé, Cameroon. Average concentrations in Bafoussam, Bamenda, and Yaoundé of $PM_{2.5}$ were 67 ± 14, 132 ± 64, and 49 ± 12 mg m^{-3} and PM_{10} are 105 ± 29, 141 ± 107, and 65 ± 21 mg m^{-3}, respectively. Daytime levels of $PM_{2.5}$ and PM_{10} were seen to be higher than nighttime levels in all cities except Bamenda where nighttime levels were higher for both PM sizes. $PM_{2.5}/PM_{10}$ mass ratios were 0.65 ± 0.05, 0.75 ± 0.05, and 0.78 ± 0.09 for Bafoussam, Bamenda, and Yaoundé, respectively. They have observed that $PM_{2.5}$ averages were highest during commercial meal preparation in Bafoussam (684 ± 546 mg m^{-3}), and on the road in Bamenda (417 ± 113 mg m^{-3}) and Yaoundé (110 ± 57 mg m^{-3}).

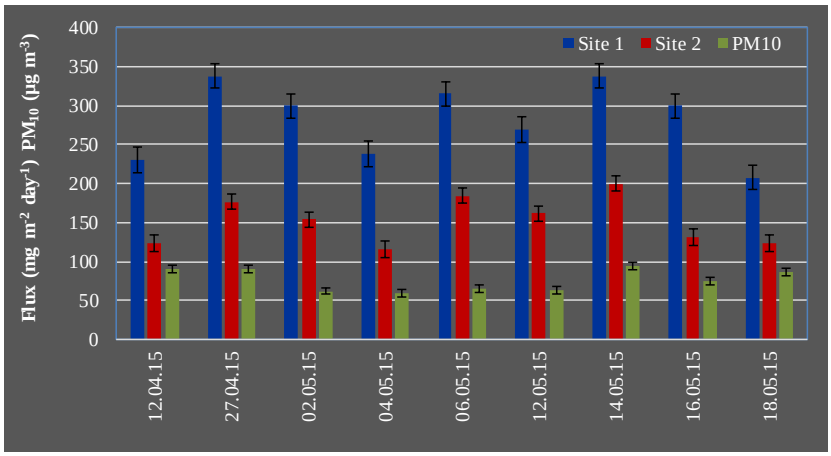

Figure 3. Dry deposition fluxes and PM_{10} values at the sampling sites

Ahmed et al. [4] have investigated the pollution status of particulate matter in ambient air based on the concentration data of three important PM fractions ($PM_{2.5}$, PM_{10}, and TSP) measured from a central area in Seoul, Korea during the period from 2004 to 2013. The mean concentrations of each fraction measured for the entire study period were found to be 26.6 ± 2.59, 54.0 ± 15.0, and 75.3 ± 16.6 mg m^{-3}, respectively. The seasonal mean of $PM_{2.5}$ varied in the range of 22.9 ± 7.10 (fall) to 30.2 ± 7.58 mg m^{-3} (winter). In contrast, PM_{10} and TSP showed a summer minimum (40.1 ± 12.6 and 55.6 ± 17.8 mg m^{-3}, respectively) and a spring maximum (67.1 ± 16.7 and 93.7 ± 21.1 mg m^{-3}, respectively). The contribution of regional or long-range transport to the observed PM levels in the study area was found to explain up to 72% of its input. The long term trend of PM indicated a gradual decreasing pattern over a 10 year period, although that of $PM_{2.5}$ was rather complicated to interpret in the recent years.

It was seen that the minimum temperature was observed as 18 ^{0}C in April 12, 2015 while the maximum temperature was determined as 32 ^{0}C in May 18, 2015. The statistical relation was not determined between the dry deposition fluxes at the sampling sites and the average air temperature values at the sampling dates.

ACKNOWLEDGEMENT

The author expresses her thanks to the Scientific Research Projects Fund of Pamukkale University for providing support in participation to the ICENS 2016. Also the students of Pamukkale University Environmental Engineering Department (Hatice Ince and Mehmet Koklu) are gratefully acknowledged for sampling and analytical help.

REFERENCES

[1]. T.K. Rout, R.E. Masto, P.K. Padhy, and J. George, “Dust Fall and elemental flux in a coal mining area,” Journal of Geochemical Exploration, vol. 144, pp. 443-455, 2014.

[2]. K.H. Kim, S.K. Pandey, H.T. Nguyen, S.Y. Chung, S.J. Cho, M.Y. Kim, J.M. Oh, and Y. Sunwoo, “Long-term behavior of particulate matters at urban roadside and background locations in Seoul, Korea,” Transp. Res. Part D Transp. Environ., vol. 15, pp. 168-174, 2010.

[3]. J.H. Seinfeld, and S.N. Pandis, Atmospheric Chemistry and Physics, from Air Pollution to Climate Change, 2nd ed., 900-931, New Jersey: John Wiley & Sons Inc., 2006.

[4]. E. Ahmed, K.H. Kim, Z.H. Shon, and S.K. Song, “Long-Term trend of airborne particulate matter in Seoul, Korea from 2004 to 2013,” Atmospheric Environment, vol. 101, pp. 125-133, 2015.

[5]. USEPA (U.S. Environmental Protection Agency), “Inorganic Analytes, EPA, Wastes, Hazardous Wastes, Test Methods, SW846”, Chapter 3, Revision 4, Washington, DC. Feb. 2007.

[6]. Y. Tasdemir, T. Erbaslar, and H. Gunez, “Measurement of dry deposition fluxes of atmospheric particulate matters: Application of Bergerhoff method,” Journal of Engineering and Natural Sciences, vol. 1, pp. 64-72, 2004.

[7]. J. Antonel, and Z. Chowdhury, “Measuring ambient particulate matter in three cities in Cameroon, Africa,” Atmospheric Environment, vol. 95, pp. 344-354, 2014.

BIOGRAPHY

Sibel Cukurluoglu is an Assistant Professor at Pamukkale University, Faculty of Engineering, Environmental Engineering Department, Denizli, Turkey. Her research interests include air quality management, air pollution control and air quality modeling.

ICENS
INTERNATIONAL CONFERENCE ON ENGINEERING AND NATURAL SCIENCES
24-28 May 2016 /Sarajevo

Wear Behavior of Cryogenically Treated TiN Coated Carbide Cutting Tool While Face Milling Inconel 718 Superalloy

Bilal Kursuncu[1], Halil Caliskan[2], Sevki Yilmaz Guven[3]

Abstract

Inconel 718 superalloy is one of the most-used superalloy due to its outstanding properties in aerospace industry. However, Inconel 718 is known to be a difficult-to-cut material due to the properties of this material such as high deformation hardening and low thermal conductivity and inclusions of hard carbide particles in its chemical composition. Nowadays, cryogenic treatment on carbide cutting tools is widely applied to extend the tool life. Therefore, in this study, for improving the wear resistance of TiN coated carbide cutting tools, cryogenic treatment was applied. The wear behaviors of cryogenically treated and un-treated TiN coated carbide cutting tools were investigated in face milling of Inconel 718 superalloy at dry conditions. In milling operations, surface roughness and wear depth were recorded in relation with cutting length. Wear mechanisms of the cutting tools were determined with scanning electron microscopy (SEM) and energy dispersive spectroscopy (EDS). Abrasive and adhesive wear mechanism was found as main failure mechanisms. Cryogenically treated TiN coated carbide cutting tool gave better wear resistance in milling operations, and thus provided around two times longer tool life than untreated one.

Keywords*: Tool wear, Coated Carbide cutting tool, Hard milling, Inconel 718, Cryogenic treatment*

1. INTRODUCTION

Inconel 718, one of the most-used nickel based superalloy used in turbine parts in aviation and nuclear plants [1], has unique properties like high oxidation and corrosion resistance and retains its high mechanical strength at elevated temperatures [2], [3]. However, Inconel 718 is known as a hard-to-cut material because of its physical properties like high tendency to work hardening, high affinity to cutting tool material and low thermal conductivity [4], [5]. In respect to this, the cutting speeds used in machining of this superalloy are kept at low values to prevent rapid tool wear [6], [7].

High performance machining is a designation of the machinability of a workpiece material. A workpiece material with high machinability is expected to have low cutting forces, high material removal rate, good surface integrity, accurate workpiece geometry and low tool wear [8]. Tool selection is very crucial in milling of Inconel 718 superalloy to provide high machining performance due to the fact that the superalloy includes Cr and Ni elements in its chemical composition [5], [9]. Carbide cutting tools are frequently used in milling operations of Inconel 718 superalloy. Although the carbide tools have high toughness, they suffer from their relatively low wear resistance. Therefore, wear resistance and tool life of carbide cutting tools are improved by using several methods such as deposition of a hard coating and/or cryogenic heat treatment.

Cryogenic treatment has made substantial improvement in wear resistance and tool life of cutting tools with microstructural changes in its chemical composition. In the course of cryogenic treatment, samples are cooled gradually (2 ^{o}C/min) to temperatures varying between -80 and -196 ^{o}C using gases such as nitrogen and helium. After a holding period, the samples are gradually brought back to the room temperature [10], [11]. Many studies report that the sintered carbide cutting tools' properties can be improved via cryogenic treatment. Ozbek et al. investigated the effects of cryogenic treatment on tool wear of uncoated carbide cutting tools in the turning of AISI 316 steel. The cryogenically treated carbide cutting tools exhibited outstanding wear performance than the uncoated one [12]. Yong et al. investigated the effect of carbide cutting tools in face milling of ASSAB 760 medium carbon steel. They found that cryogenically treated carbide cutting tool exhibited 40% longer tool life than the untreated one [13]. Thornton et al. investigated the effect of cryogenic treatment on carbide tools during the machining of AISI 1045 steel. The cryogenic treated carbide inserts were exhibited longer tool life than the untreated one [14].

In this study our aim is to show the effect of cryogenic treatment together with the TiN coating on wear behavior and tool life of sintered carbide cutting tools while machining Inconel 718 superalloy.

[1] *Corresponding author: Bartin University, Department of Mechanical Engineering, 74100, Bartin, Turkey.* bkursuncu@bartin.edu.tr

[2] *Bartin University, Department of Mechanical Engineering, 74100, Bartin, Turkey.* hcaliskan@bartin.edu.tr

[3] *Suleyman Demirel University, Department of Mechanical Engineering, 32100, Isparta, Turkey.* sevkiguven@sdu.edu.tr

2. MATERIALS AND METHODS

2.1 Workpiece Material

Inconel 718 was used as workpiece material in milling tests. The material has dimensions of 150×100×50 mm and the hardness of ~48 HRC. Chemical composition and some mechanical properties of the superalloy are presented in Table 1 and Table 2, respectively.

Table 1. Chemical composition of Inconel 718 (wt. %)

C	Si	Mn	S	P	Ni	Cr	Al	Ti	Nb	Mo	Cu
0.046	0.16	0.18	0.008	0.011	51.34	17.89	0.57	0.99	5.04	3.14	0.031

Table 2. Mechanical properties of Inconel 718

Yield Strength	Tensile Strength	Elongation (%)
1072 MPa	1032 MPa	0.14

2.2 Cutting Tools and Machine Tool

Uncoated sintered carbide cutting tools were used in milling tests. The tools were supplied from Sandvik Company (R390-11 T3 08M-KM H13A).The cutting tools were positioned on the tool holder (R390-025A25-11L) with a cutting diameter 25 mm. The tool holder has 2 teeth, but only single tooth was mounted on the tool holder during milling tests on the purpose to avoid the effect of run-out phenomenon and to maintain constant cutting conditions. The milling operations were carried out using a Falco VMC 855-B CNC three-axis vertical machining center (Figure 1).

2.3 Cutting Tests

The cutting parameters used in milling operations of the Inconel 718 superalloy are presented Table 3. A stereo zoom microscope aided with imaging software was used for evaluation of tool wear condition on the cutting tools. The wear depth of cutting tools was measured after several cutting distance. Wear images of cutting tools were taken from flank face. The dominant wear type on the tools during the used cutting length is observed as flank wear, therefore, a flank wear of 0.2 mm was stipulated as the criterion for tool life according to face milling standard (TS ISO 8688-1). Scanning electron microscopy (MAIA3 TESCAN) in combination with energy dispersive spectroscopy was used for analysis of wear mechanism of the cutting tools. Mitutoyo Surftest SJ-310 stylus-type instrument was used to measure the surface roughness of the machined surface of Inconel 718 superalloy.

Figure 1. Experimental set-up

Table 3. Cutting parameters

Cutting speed, V_c	20 m/min
Feed rate, f_z	0.05 mm/tooth
Axial depth of cut, a_p	0.2 mm
Radial depth of cut, a_e	15 mm
Workpiece material	Inconel 718
Lubricant	Dry cutting

3 RESULTS AND DISCUSSION

3.1 Tool Lifetime

Flank wear depth was measured in cutting tests due to the fact that treated and untreated carbide cutting tools were worn by flank wear while face milling Inconel 718 superalloy. Cryogenic treated and untreated carbide cutting tools' lifetime were presented in Figure 2. As seen from the figure, a swift increase in flank wear was observed with both cutting tools at the initial stage of tool life (cutting length of ~0.35 m). After this point, the cryogenically treated TiN coated tools had a steady state region, while the untreated tools reached to failure region. Due to the improved wear resistance of cryogenically treated TiN coated carbide tool, they gave around two times longer tool life than the untreated one.

3.2 Tool Wear Analysis

Optical microscope images of both worn tools are given in Figure 3. After milling tests of Inconel 718 superalloy, flank wear, notch wear and build-up edge formation are clearly seen on both treated and untreated carbide cutting tools. Abrasive wear mechanism was dominant failure mechanism because of hard carbide particles included in chemical composition of the superalloy [4], [15].

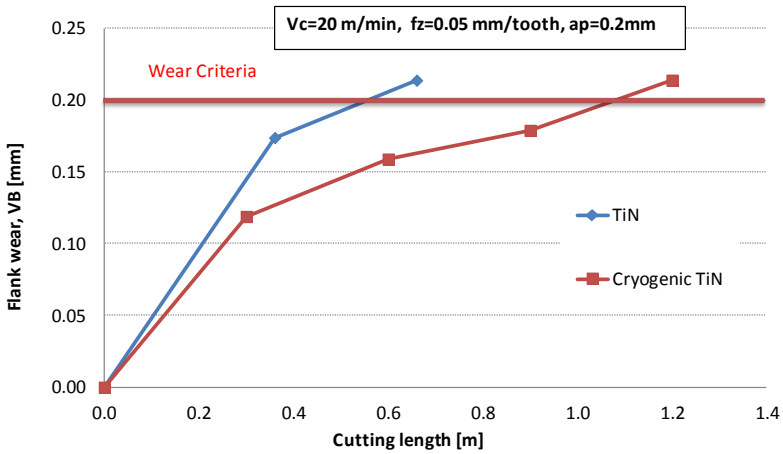

Figure 2. Comparison of cutting tool lifetime

Figure 3. Tools wear images of worn cutting tools

Scanning electron microscopy with EDS was used in order to perform a detailed investigation of wear mechanism on the cutting tools. SEM images of cryogenically treated and untreated TiN coated carbide tools are presented in Figures 4 and 5,

respectively. Flank wear is seen to be the dominant failure on the both tools, which is attributed to high temperatures at the cutting edge during machining of Inconel 718 superalloy. Notch wear, built-up formation and chipping were also observed at the cutting edge of both worn tools, which shows existence of a catastrophic failure. The diffusion and oxidation weaken the cutting edge and then the abrasive particles in the workpiece lead to abrasive wear at the weak edge. Chipping was observed on the both worn tools because of stress concentration during intermittent cutting process. The changing cutting forces lead to small fractures and in the ongoing process chipping is formed. The other wear type built-up edge formation is formed because of high cutting temperatures together with high forces at the cutting edge.

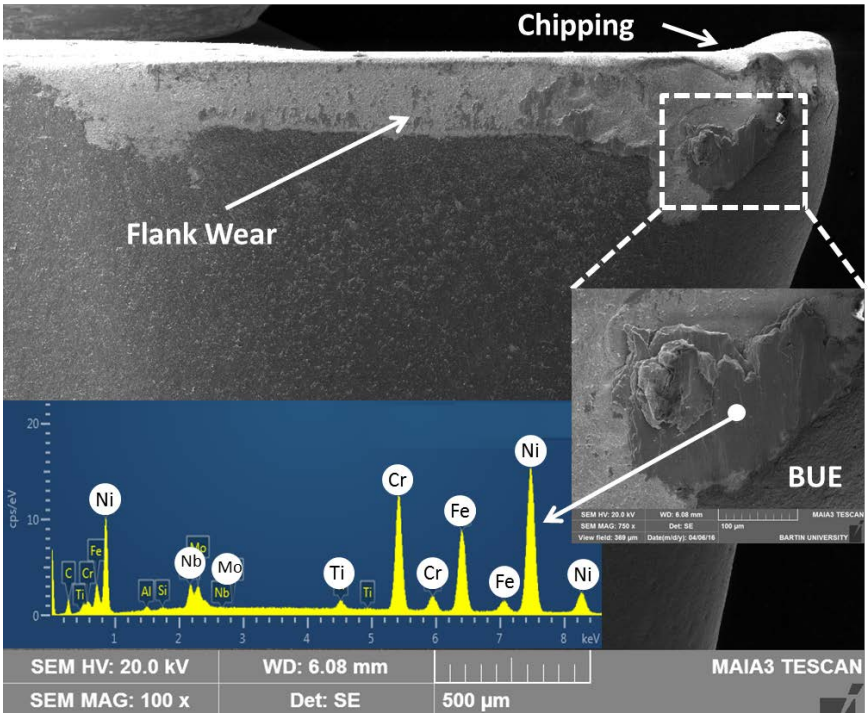

Figure 4. SEM image of the worn cryogenically treated TiN coated carbide cutting tool

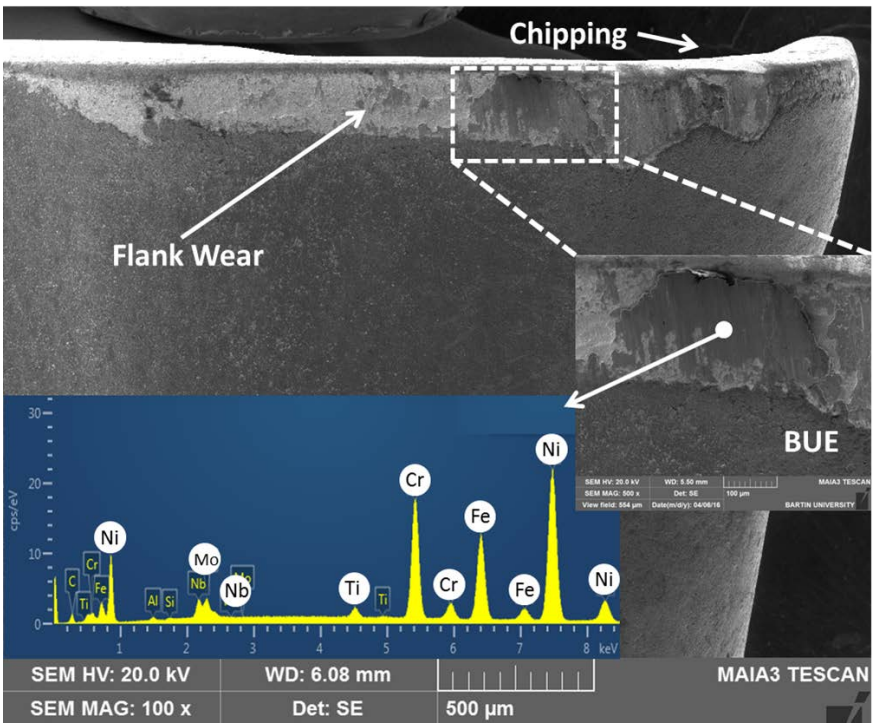

Figure 5. SEM image of the worn untreated TiN coated carbide cutting tool

3.3 Evaluation of Surface Roughness

Surface roughnesses of the workpiece material during machining with cryogenically treated and untreated carbide cutting tools were shown in Figure 6. A smoother surface was obtained with the cryogenically treated TiN coated carbide cutting tools than the untreated one. The increase of built-up edge formation and the damage of cutting edge in the untreated tools were thought to be resulted in a bigger surface roughness.

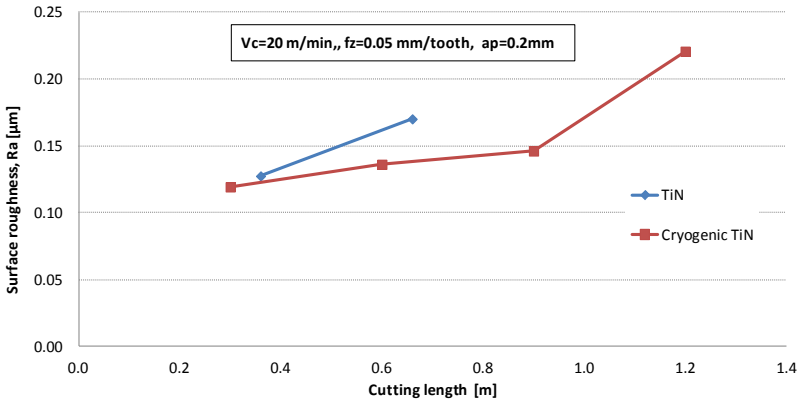

Figure 6 Surface roughness data on the machined Inconel 718

CONCLUSIONS

In this study, cryogenically treated TiN coated carbide cutting tools were compared with the untreated one for tool life and surface roughness in face milling of Inconel 718 superalloy. The main results can be summarized as follows:

- Cryogenically treated TiN coated carbide tool outperforms untreated one by ~100% in terms of tool life.
- A smoother surface is obtained with the cryogenically treated TiN coated carbide tool than the uncoated one.
- The main wear mechanisms on the both cutting tools are abrasion and adhesion. Tool failure modes are flank wear, notch wear, chipping and built-up edge.

As a result of superior properties of the cryogenically treated TiN coated tool in face milling tests, it is suggested to be applied on carbide tools in machining of Inconel 718.

ACKNOWLEDGEMENTS

The authors wish to place their sincere thanks to Suleyman Demirel University, Scientific Research Project Division for financial support for the Project No. 3563-D2-13.

REFERENCES

[1]. D. Zhu, X. Zhang, H. Ding, "Tool wear characteristics in machining of nickel-based superalloys," *International Journal of Machine Tools and Manufacture*., vol. 64, pp. 60-77, 2013.
[2]. T. Sugihara, T. Enomoto, "High Speed Machining of Inconel 718 Focusing on Tool Surface Topography of CBN Tool," *Procedia Manufacturing*., vol. 1, pp. 675-82, 2015.
[3]. T. Wakabayashi, Y. Maeda, K. Iwatsuka, T. Yazawa, editors. Tool Wear Characteristics for Near-Dry Cutting of Inconel 718. *Key Engineering Material*, 2014: Trans Tech Publ.
[4]. İ. Ucun, K. Aslantas, F. Bedir, "The Performance Of DLC-Coated And Uncoated Ultra-Fine Carbide Tools In Micromilling Of Inconel 718," *Precision Engineering*. vol., pp. 2015.
[5]. M. Zetek, I. Česáková, V. Švarc, "Increasing Cutting Tool Life when Machining Inconel 718," *Procedia Engineering*., vol. 69, pp. 1115-24, 2014.
[6]. A. Thakur, S. Gangopadhyay, "State-of-the-art in surface integrity in machining of nickel-based super alloys," *International Journal of Machine Tools and Manufacture*., vol. 100, pp. 25-54, 2016.
[7]. F. Pusavec, A. Deshpande, S. Yang, R. M'Saoubi, J. Kopac, O. W. Dillon Jr, et al., "Sustainable machining of high temperature Nickel alloy – Inconel 718: part 2 – chip breakability and optimization," *Journal of Cleaner Production*., vol. 87, pp. 941-52, 2015.
[8]. H. Çalışkan, C. Kurbanoğlu, P. Panjan, D. Kramar, "Investigation of the performance of carbide cutting tools with hard coatings in hard milling based on the response surface methodology," *Int J Adv Manuf Technol*., vol. 66, pp. 883-93, 2013.
[9]. A. Thomas, M. El-Wahabi, J. M. Cabrera, J. M. Prado, "High temperature deformation of Inconel 718," *Journal of Materials Processing Technology*., vol. 177, pp. 469-72, 2006.

[10]. W. Reitz, J. Pendray, "Cryoprocessing of materials: a review of current status," vol., pp. 2001.
[11]. S. S. Gill, H. Singh, R. Singh, J. Singh, "Cryoprocessing of cutting tool materials—a review," *Int J Adv Manuf Technol*., vol. 48, pp. 175-92, 2010.
[12]. N. A. Özbek, A. Çiçek, M. Gülesin, O. Özbek, "Effect of cutting conditions on wear performance of cryogenically treated tungsten carbide inserts in dry turning of stainless steel," *Tribology International*., vol. 94, pp. 223-33, 2016.
[13]. A. Y. L. Yong, K. H. W. Seah, M. Rahman, "Performance of cryogenically treated tungsten carbide tools in milling operations," *Int J Adv Manuf Technol*., vol. 32, pp. 638-43, 2007.
[14]. R. Thornton, T. Slatter, R. Lewis, "Effects of deep cryogenic treatment on the wear development of H13A tungsten carbide inserts when machining AISI 1045 steel," *Production Engineering*., vol. 8, pp. 355-64, 2014.
[15]. E. O. Ezugwu, Z. M. Wang, A. R. Machado, "The machinability of nickel-based alloys: a review," *Journal of Materials Processing Technology*., vol. 86, pp. 1-16, 1998.

ICENS
INTERNATIONAL CONFERENCE ON ENGINEERING AND NATURAL SCIENCES
24-28 May 2016 /Sarajevo

Effect of Different Treatment on Germination of Endemic *S. dichroantha* Stapf. in Turkey

Belgin Cosge Senkal [1], ***Cennet Yaman***[1], ***Ahmet Korkmaz*** [1]

Abstract

Turkey flora has 97 species of Salvia, which is found naturally. 51 of them are endemic, one of which is S. dichroantha Stapf located in LC categories of danger. Most of Salvia species have cutting propagation problem. Therefore, It was examined germination frequency of S. dichroantha. Seeds for germination application were/weren't waited 24 h at +4 ºC. Then, the seeds were taken to germination on filter paper conditions. The best germination frequency was observed to obtained from cold applications

Keywords:*S. dichroantha, in vitro, germination, cold application*

1 INTRODUCTION

Salvia, commonly known as sage, 97 Salvia species distributed naturally in Turkey, almost 50% of which are endemic ([1]). It has multiple uses such as folk medicine, aromatherapy and food. It has been used as folk medicine for their diuretic, antiseptic, haemostatic, antibacterial, spasmolitic, carminative and wound-healing effects ([2]). In aromatherapy, it is a good relaxant for stress, asthma and digestive and menstrual problems. It has multiple uses as food for condiment, food additive, seasoning, spice and herbal tea ([3]). In recent years, antitumor effects have been attributed to some diterpenoids obtained from Salvia species, and they are also used in the treatment of some heart failure ([4]).

An element of Irano-Turanian, *Salvia dichroantha* Stapf grown wildly is endemic of Turkey, in the provinces of Bolu, Kastamonu, Kütahya, Eskişehir, Konya, Niğde, Aksarayi Sivas, Muğla, Isparta, Antalya, Elağzı, widely distributed from 810 to 1800 m. It is a decorative plant of 25-55 cm, perennial. It flowers in July up to late September ([5]). *S. dichroantha* contains 0.04% essential oil and caryophyllene oxide (22.4%), hexadecanoic acid (18.3%), phytol (5.6%), and caryophyllenol II (5.5%) are found to the major constituents in the essential oil ([6]).

The aim of this study is to ascertain the seed germination characteristics of *Salvia dichroantha*, an economic asset to Turkey as an endemic plant, and to investigate the effects of cold application as well as germination on filter papers conditions.

2 MATERIALS AND METHODS

2.1 Plant material

S. dichroantha seeds are used as the materials in this study. The seeds were collected from Mudurnu/Bolu province at altitudes above 780 m (40º 29´ 0.93" N, 31º11´56.97" E) in August 2015 (Figure 1).

Figure 1. General appearance of *S. dichroantha* growing in the wild

2.2 Culture conditions

Each germination experiment comprised experimental series of 3x25 seeds. The experiments were carried out in four different media: 0, 250, 500, and 1000 ppm of GA_3 hormone. This research is carried out at 25±2 ºC, 16 h in light and 8 h in dark

[1] *Corresponding author: Bozok University, Department of Field Crops, 66200 Yozgat, Turkey.* belgin.senkal@bozok.edu.tr

environment to determine the effects of GA_3 hormone and pre-treatments (pre-cooling (+4 °C) and untreated). Filter-paper were used

2.3 Statistical analysis

Twenty five seeds were placed into each petri dish. Each treatment was replicated 3 times. After one weeks, Germination formed on seeds were counted. The percentage of germination was determined. The treatments were arranged in a completely randomized design.

3 RESULTS AND DISCUSSION

The highest germination rate (65.2% and 64.0%) was determined 500 ppm GA_3 concentrations. But pre-cooling was shown to lower than untreated. In general, the highest germination rate was found pre-cooling for a period of twenty four at a temperature of +4 ºC. The lowest germination rates (24.0%) was determined control group which had been untreated (Table 1).

Table 12. Effect of GA_3 hormone on pre-cooling and untreated

Media	Untreated Average± S.D (%)	Pre-cooling Average± S.D (%)
Control	24.0±2.6	32.0±1.7
250 ppm GA_3	38.8±2.3	46.8±2.1
500 ppm GA_3	65.2±2.1	64.0±2.0
1000 ppm GA_3	40.0±2.6	56.0±4.4

It is known that a cold/hot pre-treatment applied to seeds has an effect on germination, and, in particular, that cold pre-treatment stimulates it. In *Sideritis germanicopolitana ssp. germanicopolitana* seeds a five minute cold pre-treatment of -5ºC to -80ºC was stimulating to germination, while a hot pre-treatment inhibited it ([7]). For the *S. dichroantha* series subjected to a 24 h cold pre-treatment at +4 ºC, a high germination rate was ascertained.

CONCLUSIONS

There is dormancy in seeds of *Salvia* genus and their mucilage-like seed coats is an inhibiting factor for germination. But the seeds is shown that it have a little mucilage-like seed coats.

GA_3 is known to be a growth regulator and is used frequently in overcoming obstructions to germination. In this study, GA_3 was seen to be particularly effective on germination in *Salvia dicroantha.* It can be produced from seed.

REFERENCES

[1]. A. İpek and B. Gürbüz, "Türkiye Florasında Bulunan *Salvia* Türleri ve Tehlike Durumları, " *Tarla Bitkileri Merkez Araştırma Enstitüsü Dergisi*, " vol. 19(1-2), pp.30-35, 2010.
[2]. M.Öztürk and H. Özçelik, "Doğu Anadolu'nun Faydalı Bitkileri", *Semih Ofset Matbaacılık*, Ankara, 1991.
[3]. M. Er, O. Tugay, MM. Ozcan, D. Ulukus and F. Juhaimi, Biochemical properties of some Salvia L. Species," *Environ Monit Assess*, vol. 185, pp. 5193–5198, 2013.
[4]. G. Topçu and A. Ulubelen, "New diterpenoids from an endemic Salvia species," *Proceedings of the 9th Symposium on Plant Drugs*, Eskişehir, pp.61-71, 16-19may 1991.
[5]. P.H. Davis, R.R. Mill and K.Tan, "Flora of Turkey and the East Aegean Islands", 6, Edinburgh University press, Edinburgh, pp.402-434, 1988.
[6]. B., Kunduhoglu, M., Kurkcuoglu, M. E., Duru, K.H.C. Baser, "Antimicrobial and anticholinesterase activities of the essential oils isolated from Salvia dicroantha Stapf., Salvia verticillata L. subsp. amasiaca (Freyn and Bornm.) Bornm. and Salvia wiedemannii Boiss.," *J. Med. Plants Res.*, vol. 5(29), pp. 6484-6490, 2011.
[7]. E. Yücel, *"Sideritis germanicopolitana Bornm. ssp. germanicopolitana ve Sideritis germanicopolitanaBornm. ssp. viridis Hausskn. ex Bornm.'in Tohum Çimlenme Özellikleri Üzerine Bir Araştırma",* Anadolu Üniv. Fen Fakültesi Dergisi, vol. 2, pp. 61-73, 1996.

BIOGRAPHY

Name-Surname: **Cennet YAMAN**

Birth place: ÇORUM, TURKEY

Birth date: 01.03.1984

Address: Bozok University, Agriculture Faculty, 66100 YOZGAT, TURKEY

e-Mail: cennetyaman@gmail.com, cennet.yaman@bozok.edu.tr

Education:

Highschool: Polatlı Anatolian High School, 1999-2003, ANKARA- TURKEY

Licance: Selçuk University, Faculty of Science, Department of Biology, 2004-2008, KONYA- TURKEY

Selçuk University, Faculty of Agriculture, Department of Field Crop, 2006-2008, KONYA-TURKEY

MA: Selçuk University, Institute of Science, Department of Field Crop, 2008-2011, KONYA-TURKEY

PhD: Ankara University, Institute of Science, Department of Field Crop, (2012- Continue), ANKARA- TURKEY

Master of Science Thesis:

Thesis topic: The production of low-cost seed potato (Solanum tuberosum L.) with tissue culture (2008-2011)

Works:

2011- (Continue) Research Assistant, Bozok University, Faculty of Agriculture, YOZGAT - TURKEY

ICENS
INTERNATIONAL CONFERENCE ON ENGINEERING AND NATURAL SCIENCES
24-28 May 2016 /Sarajevo

Seed Germination Studies on Endemic *Salvia cryptantha* Montbret & Aucher ex Bentham in Turkey

Cennet Yaman [1], Guler Toprak [2], Belgin Cosge Senkal [1], Fatih Kose [1]

Abstract

Turkey flora has 97 species of Salvia genus belonging to Lamiaceae, which is found naturally. 51 of them are endemic, one of which is S. cryptantha Montbret & Aucher ex Bentham (synonym S. absconditiflora) located in LC categories of danger. To cultivated of S. cryptantha is the most important because it is endemic specie and also it have commercial properties. Most of Salvia species have problems of seed coat dormancy and cutting propagation. In this study, germination application was made both coated seeds and uncoated seeds of S. cryptantha. It was observed that most of Salvia species hadn't endosperm and embryo. Therefore, most of applications were carried out in vitro and seed coat removed. For germination application, agar, agar+2% sucrose, agar+2% sucrose+MS ve agar+GA_3 concentrations were used. The best germination frequency was observed in medium containing agar+500 ppm GA_3.

Key Word: *S. cryptantha, in vitro, germination, GA_3*

1. INTRODUCTION

Sage, which belongs to Lamiaceae (Labiatae) family and contains essential oils, is a typical Mediterranean plant. Being an important and one of the biggest species of this family, sage is said to be named being inspired by the word "Salveo" which means "saver" or "healer" in Latin ([1]). *Salvia* genus is represented by about 900 species on earth. There are 97 natural species of this genus, 51 of which are endemic in Turkey's flora ([2]).

S. cryptantha Montbret & Aucher ex Benth. (syn. *S. absconditiflora* (Montbret & Aucher ex Benth.) Greuter & Burdet) grown wildly is endemic (LC categories of danger) to the rocky lands and chalky hills of Turkey, widely distributed from 700 to 2500 m ([3]). *S. cryptantha* is a perennial bush branching in a disorderly fashion on the ground. Its older branches are brittle and rough while the younger ones are soft and covered by fine fuzz. It flowers in May up to late August. This species is generally propagated through cuttings ([4]). *S. cryptantha* contains 0.37% v/w essential oil and α-pinene, eucalyptol, camphor, camphene and borneol are found to be the major components in the essential oil ([5]).

There is dormancy in seeds of *Salvia* genus and their mucilage-like seed-coats are an inhibiting factor for germination. Seed germination studies of these species are of great importance in determining production strategies.

2. MATERIALS AND METHODS

2.1 Plant Material

Salvia cryptantha seeds are used as the materials in this study. The seeds were collected from Yozgat province at altitudes above 1.368 m (39º 47´ 25.23" N, 34º 47´8.63" E) in July 2015 (Figure 1).

2.2 Surface Sterilization of Seeds

Mature seeds were sterilized by immersion in 20% (v/v) NaOCl (ACE, Turkey commercial NaOCl was used as a stock in the sterilization process, 5% NaOCl) for 20 min, followed by rinsing 4-5 times in sterile distilled water and the seeds were incubated in sterile distilled water for 24 h under aseptic condition in laminar air hood.

[1] *Corresponding author: Bozok University, Department of Field Crops, 66200 Yozgat, Turkey. cennet.yaman@bozok.edu.tr*

[2] *Erciyes University, GENKÖK Research Center, 38039, Kayseri, Turkey.glrtoprak@gmail.com*

Figure 1. General appearance of *S. cryptantha* growing in the wild

2.3 Culture Conditions

Concentrations of 250, 500, and 1000 ppm of GA_3 hormone were added to the media after filter sterilization using a 0.25 µm filter. Coats of seeds were/weren't separated from the seeds under sterile conditions and inoculated on agar, agar+250 ppm GA_3, % agar+500 ppm GA_3, % agar+1000 ppm GA_3, % agar+ 2% sucrose, agar+MS ([6]) +2% sucrose. The experiments were carried out in climate chamber. In the climate chamber, *in vitro* media were used, a constant temperature (25±2 ºC) was maintained throughout the experiment and a photoperiod of 16 hours light (3000 lux) and 8 hours darkness was applied.

2.4 Statistical analysis

Twenty five seeds were placed into each petri dish. Each treatment was replicated 3 times. After 2 week, Germination formed on seeds was counted. The percentage of germination was determined. The treatments were arranged in a completely randomized design.

3 RESULTS AND DISCUSSION

Mucilage-like seed coats was appeared after seed incubated in sterile distilled water for 24 h under. It is known that mucilage is caused an inhibiting factor for germination. The seeds with coats weren't shown germination. It was shown germination in the seeds which was separated from their coats. But germination weren't shown on % agar+2% sucrose and agar+MS+2% sucrose. Other results are given in their entirety in Table 1.

Table 13. Effect of GA_3 hormone above seeds separated seed coat for germination in vitro condition

Media	**Average± S.D** (%)
Agar	66.4±0.6
Agar+250 ppm GA_3	73.2±1.2
Agar+500 ppm GA_3	86.4±1.2
Agar+1000 ppm GA_3	66.4±0.6

The highest germination was determined at Agar+500 ppm GA_3 concentrations, while agar and agar+1000 ppm GA_3 mediums were seen to inhibit germination.

CONCLUSIONS

There is dormancy in seeds of *Salvia* genus and their mucilage-like seed coats is an inhibiting factor for germination. Seed germination studies of these species are of great importance in determining production strategies.

GA_3 is known to be a growth regulator and is used frequently in overcoming obstructions to germination. In this study, GA_3 was seen to be particularly effective on germination in *Salvia cryptantha*.

S. cryptantha, as a decorative evergreen, perennial plant with its own special aromatic scent and bees take advantage of it. In addition, while it can becultivated for medicinal purposes, it can also be used as a principle plant in

erosion-control efforts. There was inhibitor on its germination process. Therefore, it is important to germination treatments. it can be produced from both seed and stem separation ([2,4].

REFERENCES

[1]. I.I. Özcan, O. Arabacı and N.G. Öğretmen, "*Bazı Adaçayı Türlerinde Farklı Tohum Çimlendirme Uygulamalarının Belirlenmesi*," Türk Tarım – Gıda Bilim ve Teknoloji Dergisi, vol. 2(5), pp. 203–207, may. 2014.
[2]. A. İpek and B. Gürbüz, "*Türkiye Florasında Bulunan Salvia Türleri ve Tehlike Durumları*," Tarla Bitkileri Merkez Araştırma Enstitüsü Dergisi, vol. 19(1-2), pp. 30–35, 2010.
[3]. P.H. Davis, R.R. Mill and K. Tan, *Flora of Turkey and the East Aegean Islands*, 7nd ed., Edinburgh University press, Edinburgh, pp.402-434, 1988.
[4]. A. İpek, B., Gürbüz, Ü. Bingöl, F. Geven, G. Akgül, K.A.P. Rezaeieh, and B. Coşge, "*Comparison of essential oil components of wild and field grown Salvia cryptantha Montbert & Aucher ex Benthan, in Turkey*", Turkish Journal of Agriculture & Forestry (ISI), pp 668-672, 2012.
[5]. B. Tepe, E. Dönmez and *et* all., *"Antimicrobial and antioxidative activities* of the *essential oils* and *methanol extracts* of *Salvia cryptantha* (*Montbret et Aucher ex Benth.*) and *Salvia multicaulis* (*Vahl*), *"* Food Chemistry, vol. 84 (4), p.p. 519–525, 2004.
[6]. T. Murashige, F. Skoog, *"A revised medium for rapid growth and bioassays with tobacco tissue cultures,"* Physiol. Plant, vol. 15, pp. 473-497, 1962.

BIOGRAPHY

Name-Surname: **Cennet YAMAN**

Birth place: ÇORUM, TURKEY

Birth date: 01.03.1984

Address: Bozok University, Agriculture Faculty, 66100 YOZGAT, TURKEY

e-Mail: cennetyaman@gmail.com, cennet.yaman@bozok.edu.tr

Education:

Highschool: Polatlı Anatolian High School, 1999-2003, ANKARA- TURKEY

Licance: Selçuk University, Faculty of Science, Department of Biology, 2004-2008, KONYA- TURKEY

Selçuk University, Faculty of Agriculture, Department of Field Crop, 2006-2008, KONYA-TURKEY

MA: Selçuk University, Institute of Science, Department of Field Crop, 2008-2011, KONYA-TURKEY

PhD: Ankara University, Institute of Science, Department of Field Crop, (2012- Continue), ANKARA- TURKEY

Master of Science Thesis:

Thesis topic: The production of low-cost seed potato (Solanum tuberosum L.) with tissue culture (2008-2011)

Works:

2011- (Continue) Research Assistant, Bozok University, Faculty of Agriculture, YOZGAT - TURKEY

ICENS
INTERNATIONAL CONFERENCE ON ENGINEERING AND NATURAL SCIENCES
24-28 May 2016 /Sarajevo

Rear Impact Whiplash Test Design by Using a Maxwell-Element Based Energy-Absorber

Selcuk Himmetoglu[1]

Abstract

This study presents a low-cost crash test system to evaluate whiplash risk in rear impacts encountered in road-traffic accidents. This whiplash test involves the deceleration of a seat-occupant system on a cart which impacts a Maxwell-element based energy-absorber fixed to a rigid wall. The energy-absorber is optimised to obtain crash pulses which mimic the medium severity crash pulse of the EuroNCAP whiplash test. In order to compare the obtained crash pulses with the EuroNCAP medium severity crash pulse, computational multi-body models of a generic car seat and a biofidelic 50th-percentile male human for rear impact are used. Two non-traditional anti-whiplash car-seat models are subjected to three crash pulses to evaluate the differences in seat and human model responses. The simulation results indicate that the crash pulses obtained by using a Maxwell-element based energy-absorber produce similar responses in comparison to those of the EuroNCAP medium severity crash pulse.

Keywords: car seat design, energy absorber, human body model, rear impact, whiplash test

1. INTRODUCTION

The term “whiplash” is used to describe neck injuries (or disorders) in which the sudden differential movement between the head and torso, leads to damage of soft tissue in the neck. The highest risk of sustaining whiplash injury has been found to occur in rear-end crashes [1], [2]. A common cause of whiplash is the formation of S-shape-like deformation in the neck due to retraction of the head relative to the upper torso, as shown in Figure 1 (a).

A head restraint with good stiffness and energy absorbing characteristics, positioned at the right height and with an appropriate (small) backset distance, can decrease whiplash risk in rear-end crashes. (Backset is the horizontal distance between the back of the head and the front surface of the head restraint). However, research has shown that seats with good static head-restraint geometry do not always offer good protection dynamically [3], [4]. The seat and the head restraint must work in unison to absorb the crash energy effectively so that neck internal motion and neck forces are reduced throughout the impact [4].

In consumer crash tests such as the European New Car Assessment Programme (EuroNCAP) whiplash test, car seats are tested on a sled which is accelerated in the $+x$ direction by using HyGe systems with the dummy facing the direction of motion as shown in Figure 1 (b). The acceleration of the sled versus time is called the crash pulse which is applied to the sled. In the EuroNCAP whiplash test [5], three different crash pulses are employed: a low-severity trapezoidal pulse (with ΔV=16 km/h, a_{mean}=4.5g, a_{peak}=5g), a medium-severity sinusoidal pulse (with ΔV=16 km/h, a_{mean}=5g, a_{peak}=10g) and a high-severity trapezoidal pulse (with ΔV=24 km/h, a_{mean}=6.5g, a_{peak}=7.5g). (The term ΔV is defined as the area under the acceleration-time curve of the struck vehicle over the course of the impact and g is the gravitational acceleration). EuroNCAP rates the car-seats as good, marginal and poor according to the total points they get from the scoring system.

In this study, a less expensive whiplash test system is proposed which involves the deceleration of a cart impacting a Maxwell-element based energy-absorber fixed to a rigid wall. The cart which involves the car seat and the dummy facing against the direction of motion, is accelerated to the impact speed by using a drop mass set-up. The designed energy-absorbers produce crash pulses similar to the EuroNCAP medium severity crash pulse.

2. A SEAT-OCCUPANT SYSTEM FOR REAR IMPACT SIMULATION

A biofidelic 50th-percentile male multi-body human model, as shown in Figure 1(b), was developed using MSC VisualNastran-4D with Matlab-Simulink; and validated using the responses of seven healthy 50th-percentile male volunteers from the Japan Automobile Research Institute (JARI) sled tests [6]. The human model is composed of rigid bodies connected by rotational springs and dampers. The initial configuration of the human model, as shown in Figure 1 (b), corresponds to the normal driving posture of a 50th-percentile male who is relaxed and unaware of the timing of the impact.

In validating the human model, the rigid-seat used in the JARI sled tests was modelled first and a contact model was developed to simulate the interaction of the human-body segments with the rigid seat surfaces [6]. Based on the JARI rigid-seat, a generic multi-body car-seat model was developed at the same time to implement various energy absorbing devices,

[1] *Corresponding author: Hacettepe University, Mechanical Engineering Department, 06800, Beytepe/Ankara, Turkey.*
s.himmetoglu@hacettepe.edu.tr

seatback, head restraint and recliner properties [4]. A typical head-restraint (HR), attached to the seatback as shown in Figure 1 (b), is also included in the seat-occupant system model. The seat model is able to simulate the mechanical function of a typical seatback foam and suspension. The developed seat-occupant system model helps to economically simulate different rear-impact scenarios.

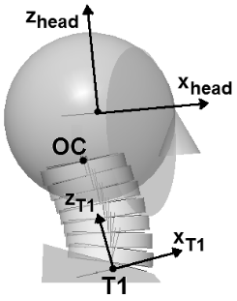

Figure 1. (a) S-shape-like deformation

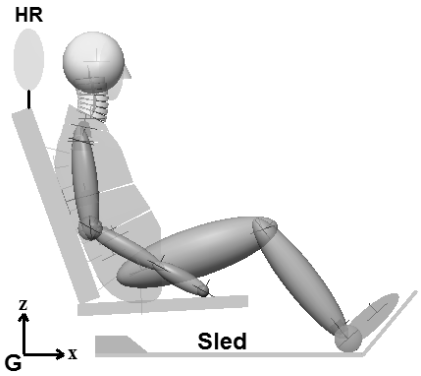

(b) The seat-occupant system model

3. WHIPLASH MITIGATING CAR-SEAT MODELS

A typical car-seat is composed of a head restraint (HR), a seatback, and a seat-pan, as shown in Figure 2. In a typical car-seat, the recliner attaches the seatback to the seat-pan. The recliner is a mechanism that remains locked during normal daily use. When a rear impact occurs, the structure of the recliner mechanism deforms and this causes the seatback to rotate backwards with respect to the seat-pan. The rotation of the seatback can be coupled with some translational deformation at the recliner and at the base of the seat-pan. However, the dominant or typical mode of deformation is the rotation of the seatback around the rotation-centre of the recliner mechanism.

Using the seat-occupant system model shown in Figure 1 (b), two different whiplash-mitigating car-seat models, namely WMS and RFWMS, were developed [4]. As shown in Figure 2, WMS and RFWMS are different than a typical car-seat as they employ anti-whiplash devices (AWDs) which control the relative motion between the structural members of the seat, to provide effective whiplash mitigation for a wide range of crash severity. Using these AWDs, a typical car-seat can be transformed into a seat which can offer improved protection in rear impacts. The AWDs, which are denoted by R, R*, R^+ and P, are passive energy-absorbing devices composed of nonlinear spring-and-damper units and they become operational, only when the corresponding breakaway forces and/or torques are exceeded.

In WMS, the rotational anti-whiplash denoted by R is positioned at the recliner and it enables the seatback to rotate with respect to the seat-pan. The translational anti-whiplash device denoted by P is placed under the seat-pan and it permits the whole seat to translate backwards a short distance during rear impact. The main difference between RFWMS and WMS is that in RFWMS, the seatback (which the torso directly interacts with) functions as an inner-frame and it is pivoted to the outer-seatback-frame (OF) using another rotational anti-whiplash denoted by R*. Besides, OF is connected to the seat-pan by the rotational anti-whiplash device R^+. When the breakaway torque at R* is overcome due to the pressure applied by the torso on the seatback, a rotation at R* occurs in the opposite direction to the rotation at R^+.

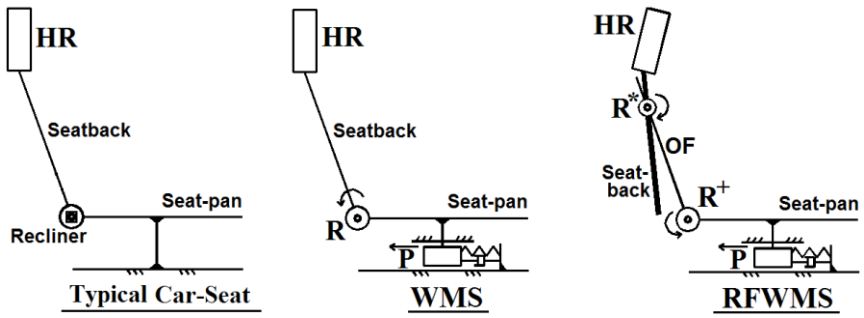

Figure 213. Schematic drawings of car-seat models

The mechanical properties of the AWDs were determined using a wide range of ΔV (between 4.5 and 35 km/h) and a variety of crash pulses [4]. The applied set of crash pulses also included the low, medium and high-severity crash pulses employed in the EuroNCAP whiplash test. As shown in Table 1, the AWDs become operational in succession, according to the severity of the rear impact. No AWD becomes operational for a ΔV value less than 7 km/h to prevent activation during normal daily use.

Table 14. Operational ranges of the anti-whiplash devices

	7 km/h ≤ Δ*V*< 10 km/h	**10 km/h ≤ Δ*V*≤ 13 km/h**	**Δ*V* > 13 km/h**
WMS	R	R , P	R , P
RFWMS	R^+	R^+ , P	R^+ , P , R*

Himmetoglu et al. [4] demonstrated that the whiplash-mitigating car-seat models (i.e. WMS and RFWMS) could successfully mitigate whiplash injuries for a wide range of crash severity (between 4.5 and 30 km/h of Δ*V*) through coordinated motion of seat components. For the highest severity considered, the seat-pan displacement and seatback rotational displacement were limited to 6.4 cm and 32 deg, respectively. This helped to limit the ramping of the unbelted occupant and the rearward displacement of the seat. RFWMS performed better than WMS at all severities, since the rotational AWD denoted by R* controls the rotation of the seatback more effectively and provides relatively earlier head-restraint contact. The performances of the whiplash-mitigating car-seat models were also compared with those of the typical car-seat models without any whiplash-mitigating feature. The numerical simulations indicated that both WMS and RFWMS represented a significant improvement over the typical-car-seat models although all of the seats had the same head restraint (HR) with the same static geometry (as shown in Figure 1 (b), with a backset distance of 60 mm) prior to impact. For example, for WMS and RFWMS, the neck shear-forces were about three times lower in comparison to the typical-car-seat models.

4. REAR IMPACT WHIPLASH TEST DESIGN

In this study, a rear impact whiplash test based on the deceleration of a cart is proposed as shown in Figure 3. The cart C which travels on four pneumatic tyres, is towed with the aid of cables and a drop mass M. The car seat is attached to the cart, and the dummy which is facing against the direction of motion, is placed on the car seat. The cart is towed to impact the energy-absorber EA fixed to the rigid wall W which is a reinforced concrete block. To reach the desired impact speed, the cart first needs to be accelerated by the drop mass M. When the cart reaches a speed around the desired impact speed, the drop mass M is stopped by an energy absorbing foam F. The cart is finally decelerated as it impacts the energy-absorber EA. This impact produces a crash pulse which is basically the deceleration-time curve of the cart. The cart should be gently accelerated to the impact speed in order to minimise pre-impact dummy movement, otherwise this would degrade test repeatability. The advantage of this whiplash test is that it is less expensive to produce and maintain.

Using the set-up shown in Figure 3, this study aims at designing an energy-absorber which can reproduce the EuroNCAP medium severity crash pulse (EMP) with a Δ*V* of 16 km/h (see Figure 4 (a)). Thus, the impact speed of the cart is selected as 16 km/h. The mass of the car seat is 15 kg. The dummy (or the human body model) is 50th-percentile male which weighs around 75 kg. The cart needs to have a robust structure since it should not deform under repeated testing. Considering that the trolleys used in EuroNCAP side impact tests have a mass around 1000 kg [7], the mass of the cart is taken as 860 kg. Hence the total mass of the cart, dummy and car seat system is 950 kg; this total mass value is used to determine the required drop mass. For impact tests which involve lighter (or heavier) car seats and dummies, the cart mass can be increased (or decreased) by adding (or removing) blocks of weights to (or from) the cart, thereby the design of the whiplash test system remains unaltered.

In the crash pulse EMP shown in Figure 4 (a), there is an initial sudden rise followed by a gradual descent in acceleration. This crash pulse is caused by the impact force acting on the vehicle, therefore the variation of the impact force must follow the shape of the crash pulse EMP. The Maxwell-element, as shown in Figure 4 (b), is found suitable to produce such a variation in impact force. The Maxwell-element which is composed of a spring (*k*) connected in series to a damper (*c*), can be used as the energy-absorber (EA) in Figure 3 to reproduce or mimic the crash pulse EMP. The governing differential equations for the Maxwell-element based energy-absorber are

$$m\ddot{x}_1 = k(x_2 - x_1) \quad (1)$$

$$-c\dot{x}_2 = k(x_2 - x_1) \quad (2)$$

where k is the stiffness of the spring, c is the viscous damping coefficient and m is the total mass of the cart, dummy and car seat system.

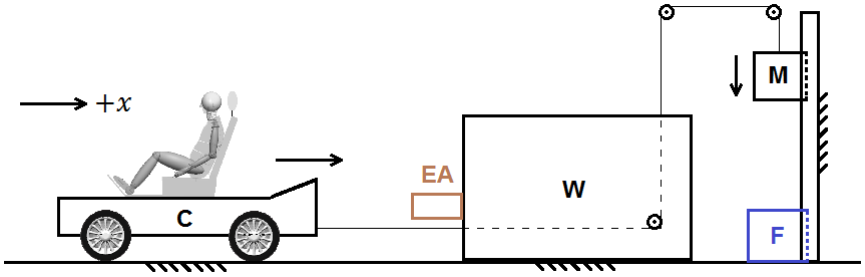

Figure 3. Rear impact whiplash test system

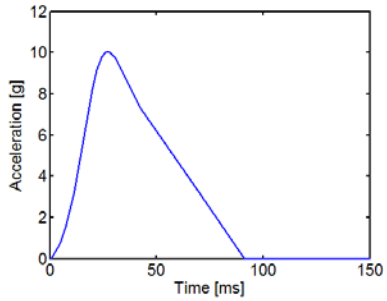

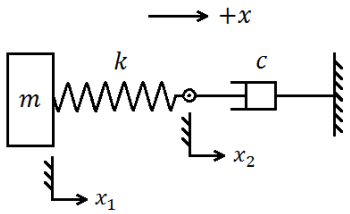

Figure 4. (a) EuroNCAP medium severity crash pulse (EMP) *(b) Maxwell element as an energy-absorber (m: mass)*

Using the initial conditions $x_1(0) = 0$ m, $\dot{x}_1(0) = 16/3.6$ m/s and $x_2(0) = 0$ m, Equations (1) and (2) were solved by trying various values for k and c so that $\ddot{x}_1$ mimics the shape of the crash pulse EMP. This optimisation process resulted in the crash pulse MAP1 which was obtained by using $k = 2500 \cdot 10^3$ N/m and $c = 30000$ Ns/m as shown in Figure 5 (a). The maximum deformation of the energy-absorber, i.e. $\max(x_1)$, turned out to be 14.33 cm. It can be seen that the crash pulse MAP1 has an earlier rise in acceleration when compared to the crash pulse EMP.

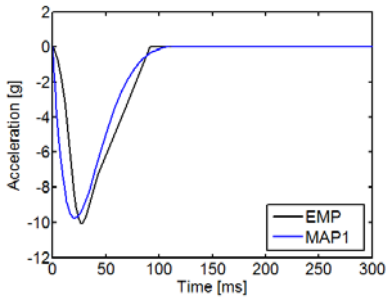

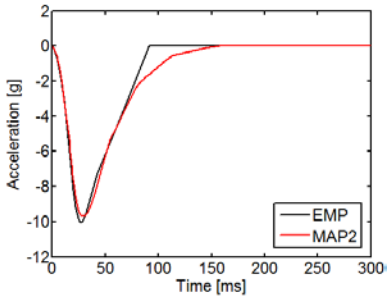

Figure 5. (a) Crash pulses EMP and MAP1 *(b) Crash pulses EMP and MAP2*

In order to correct this discrepancy between EMP and MAP1, nonlinear spring and nonlinear damping were used in the energy-absorber. After running several simulations, the properties of the spring and damper given in Figure 6 were obtained which produced the crash pulse MAP2 as shown in Figure 5 (b). MAP2 follows EMP quite accurately except the final stages of the pulses. With this selection of spring and damper, the maximum deformation of the energy-absorber became 18.16 cm. The force versus deformation behaviour of the nonlinear spring is given in Figure 6 (a). As shown in Figure 6 (b), the damper has a viscous damping coefficient which varies with the deformation of the damper.

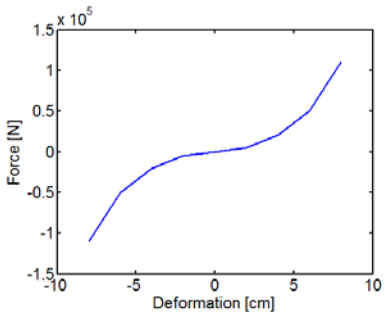

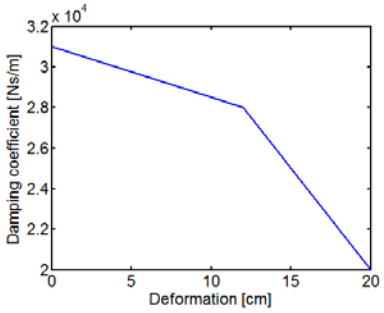

Figure 6. (a) Nonlinear spring to obtain crash pulse MAP2 *(b) Nonlinear damping to obtain crash pulse MAP2*

5. TEST PROCEDURE

The whiplash-mitigating car-seat models (WMS and RFWMS) were subjected to the crash pulses EMP, MAP1 and MAP2 to evaluate the differences in seat and human model responses. Prior to rear impact, the human model is positioned as shown in Figure 1 (b) to adopt a posture similar to the one practiced in dynamic whiplash sled-tests [8]. The initial seatback angle is set to 20 deg from the vertical and no seatbelt is used. The same head restraint (HR) is attached to both seats. The top of HR is level with the top of the head and the backset of HR is set to 60 mm; this pre-impact geometrical setting of HR is within the range of a good head-restraint geometry as specified by IIWPG [9].

As performed in the EuroNCAP whiplash test, the stationary seat-occupant system was first accelerated in the $+x$ direction (see Figure 1 (b)) by subjecting the sled to the crash pulse EMP given in Figure 4 (a). Then, in order to simulate the proposed whiplash test shown in Figure 3, the seat-occupant system (in Figure 1 (b)) which had an initial impact speed of 16 km/h, was decelerated by subjecting the sled to the crash pulses MAP1 and MAP2 shown in Figure 5.

In order to compare the responses of the seat-occupant system shown in Figure 1 (b) to the crash pulses EMP, MAP1 and MAP2, some of the assessment criteria of the EuroNCAP dynamic whiplash test are used which are *Fsh* (largest OC-shear-force), *Ftn* (maximum OC-tension-force), *NIC* (neck injury criterion), *HrCt* (head restraint contact time), $\Delta\theta_{SB}$ (maximum seatback rotational deflection) and N_{km}. OC is the occipital condyles which can be called as the junction between the head and the upper neck as shown in Figure 1 (a). *NIC* is associated with the formation of S-shape-like deformation in the neck and is based on the relative acceleration and velocity between the OC and the first thoracic vertebra T1 (see Figure 1 (a)). The proposed injury threshold value for *NIC* is 15 m^2/s^2 [10]. N_{km} is an injury criterion which uses a combination of the shear force and moment acting at the OC. The proposed injury threshold value for N_{km} is 1 [11]. In order to rate the OC forces, the IIWPG neck force classification, as shown in Figure 7, is used [9]. In addition to the assessment criteria of the EuroNCAP, the maximum rotation at R* (denoted by $\Delta\theta_{R*}$) and the maximum seat-pan displacement at P (denoted by Δx_{SP}) are also monitored (see Figure 2).

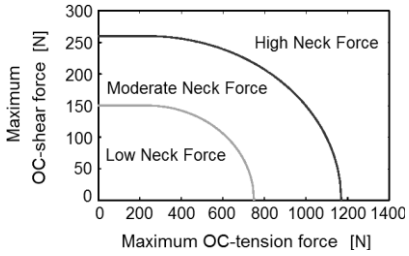

Figure 7. IIWPG neck force classification (adapted from [9])

6. RESULTS and DISCUSSION

The simulations have revealed that in comparison to the EuroNCAP crash pulse EMP, the crash pulses MAP1 and MAP2 cause small changes in seat and human model responses. The results are presented in Table 2. For each entry in Table 2 regarding the MAP1 and MAP2 results, the number in parenthesis indicates the percent change in the response relative to the crash pulse EMP. The ΔV values for the crash pulses MAP1 and MAP2 are 16.2 km/h and 17.45 km/h, respectively. In comparison to EMP, the ΔV value for MAP2 is higher due to the slowly decreasing deceleration in the late stages of this crash pulse as shown in Figure 5 (b).

Table 2. Seat and human model responses to the crash pulses

	Seat: WMS		
	EMP	MAP1	MAP2
Fsh [N]	167.6	164.8 (-1.67%)	175.5 (4.71%)
Ftn [N]	155.6	157.3 (1.09%)	135.7 (-12.8%)
NIC [m^2/s^2]	10.3	10.96 (6.41%)	10.72 (4.1%)
N_{km}	0.40	0.38 (-5%)	0.44 (10%)
HrCt [ms]	66	59 (-10.6%)	67 (1.51%)
ΔV [km/h]	16	16.2 (1.25%)	17.45 (9.06%)
$\Delta\theta_{SB}$ [deg]	9.44	9.72 (2.96%)	10.43 (10.5%)
Δx_{SP} [cm]	5.28	5.34 (1.14%)	5.48 (3.79%)
$\Delta\theta_{R^*}$ [deg]	NA*	NA*	NA*

	Seat: RFWMS		
	EMP	MAP1	MAP2
Fsh [N]	135.7	140.7 (3.68%)	140.6 (3.61%)
Ftn [N]	0	1.9 (-- %)	0 (0 %)
NIC [m^2/s^2]	11.1	11.74 (5.76%)	11.56 (4.14%)
N_{km}	0.42	0.38 (-9.52%)	0.42 (0%)
HrCt [ms]	58	52 (-10.3%)	60 (3.45%)
ΔV [km/h]	16	16.2 (1.25%)	17.45 (9.06%)
$\Delta\theta_{SB}$ [deg]	7.28	7.91 (8.65%)	8.90 (22.2%)
Δx_{SP} [cm]	5.22	5.34 (2.3%)	5.47 (4.79%)
$\Delta\theta_{R^*}$ [deg]	4.94	5.02 (1.62%)	5.18 (4.86%)

(*) : Not applicable ; ΔV : Change in velocity of the cart

6.1 Response of the Seat WMS

When the seat WMS is subjected to the crash pulse MAP1, the relative percent changes in the responses are below 10% on the whole. On the other hand, when the seat WMS is subjected to the crash pulse MAP2, the relative percent changes in the responses are slightly higher but below 12.8% on the whole. For MAP2, the upper-neck shear forces and moments (*Fsh*, N_{km}), and seat displacements ($\Delta\theta_{SB}$, Δx_{SP}) are higher since the cart experiences a higher change of velocity. Thus, MAP2 is slightly a stronger crash pulse than MAP1. In comparison to MAP2, MAP1 produces higher *NIC* and lower head-restraint contact time (*HrCt*) values because MAP1 has an earlier rise in the acceleration causing the head and upper torso to retract more quickly and contact the head restraint earlier. The peak acceleration occurs at 27 ms, 20 ms and 30 ms for the crash pulses EMP, MAP1 and MAP2, respectively. Compared to MAP2, MAP1 produces seat displacements closer to those of EMP. On the whole, MAP1 mimics EMP more closely.

6.2 Response of the Seat RFWMS

When the seat RFWMS is subjected to the crash pulse MAP1, the relative percent changes in the responses are below 10% on the whole. When the seat RFWMS is subjected to the crash pulse MAP2, the relative percent changes in the responses are below 10% except the seatback rotational deflection. Compared to MAP2, MAP1 produces higher *NIC* and lower head-restraint contact time (*HrCt*) values due to the earlier rise in the acceleration of MAP1. MAP2 results in larger seat-displacements ($\Delta\theta_{SB}$, Δx_{SP}, $\Delta\theta_{R^*}$) than MAP1 since the ΔV of MAP2 is slightly higher. For MAP2, the relative percent changes in the upper-neck forces and moments (*Fsh*, N_{km}, *Ftn*) are insignificant. In comparison to MAP2, MAP1 results in seat displacements closer to those of EMP. On the other hand, MAP2 mimics EMP more closely regarding the human model responses *Fsh*, N_{km}, *Ftn* and *NIC*.

The results indicate that either MAP1 or MAP2 can be used as a substitute for EMP.

CONCLUSIONS

In this paper, a rear impact whiplash test system is proposed which requires lower amounts of investment to build and operate. This impact test system utilises a Maxwell-element based energy-absorber to create the impact force required to decelerate the

seat-occupant system attached on a cart. The energy-absorber which comprises a spring connected in series to a damper, is designed to create a crash pulse that mimics the medium severity crash pulse of the EuroNCAP whiplash test. Two designs of the energy-absorber are presented involving linear and nonlinear stiffness and damping. These two energy-absorber designs produce two crash pulses MAP1 and MAP2 which are similar in shape to EuroNCAP's medium severity crash pulse EMP. Two whiplash-mitigating car-seat models (WMS and RFWMS) with a biofidelic 50th-percentile male human model were subjected to the crash pulses EMP, MAP1 and MAP2. The simulation results show that the crash pulses MAP1 and MAP2 successfully simulate the effects of the crash pulse EMP in terms of seat and human model responses. Therefore, the Maxwell-element based energy-absorber proposed in this study, can be used in a rear impact whiplash test to create a medium severity crash pulse very similar to that of EuroNCAP. The rear impact whiplash test system presented in this paper can be used to assess the dynamic performance of car seats in medium-severity rear impacts.

REFERENCES

[1]. V. Eis, P. Fay, and R. Sferco, "A detailed analysis of the characteristics of European rear impacts", in *Proc. 19th ESV*, 2005, paper 05-0385-O.
[2]. M. Avery, E. Giblen, A. M. Weekes, and D. S. Zuby, "Developments in dynamic whiplash assessment procedures", in *Proc. Int. Conf. on Neck Injuries in Road Traffic and Prevention Strategies*, 2007, paper 15.
[3]. M. Edwards, S. Smith, D. S. Zuby, and A. K. Lund, "Improved seat and head restraint evaluations", in *Proc. 19th ESV*, 2005, paper 05-0374-O.
[4]. S. Himmetoglu, M. Acar, K. Bouazza-Marouf, and A. J. Taylor, "Car-seat design to improve rear-impact protection", *Proc. IMechE Part D: Journal of Automobile Engineering*, vol.225, pp.441-459, 2011.
[5]. M. van Ratingen, J. Ellway, M. Avery, P. Gloyns, V. Sandner, and T. Versmissen, "The EuroNCAP whiplash test", in *Proc. 21st ESV*, 2009, paper 09-0231.
[6]. S. Himmetoglu, M. Acar, K. Bouazza-Marouf, and A. J. Taylor, "A multi-body human model for rear-impact simulation", *Proc. IMechE Part D: Journal of Automobile Engineering*, vol.223, pp.623-638, 2009.
[7]. *Side Impact Mobile Deformable Barrier Testing Protocol*, EuroNCAP, 2014.
[8]. *The Dynamic Assessment of Car Seats for Neck Injury Protection Testing Protocol*, EuroNCAP, 2014.
[9]. *RCAR-IIWPG Seat/Head Restraint Evaluation Protocol*, International Insurance Whiplash Prevention Group (IIWPG), 2008
[10]. O. Boström, M. Y. Svensson, B. Aldman, H. A. Hansson, Y. Håland, P. Lövsund, T. Seeman, A. Suneson, A. Säljö, and T. Örtengren, "A new neck injury criterion candidate-based on injury findings in the cervical spinal ganglia after experimental neck extension trauma', in *Proc. Int IRCOBI Conf*, 1996, pp.123-136.
[11]. K.-U. Schmitt, M. H. Muser, and P. Niederer, "A new neck injury criterion candidate for rear-end collisions taking into account shear forces and bending moments", in *Proc. 17th ESV*, 2001, paper 124.

BIOGRAPHY

Selçuk Himmetoğlu got his B.Sc. and M.Sc. degrees from the Mechanical Engineering Department of Middle East Technical University (METU) in Turkey and worked as a teaching assistant in the same department during his postgraduate studies. He got his PhD degree from the Mechanical and Manufacturing Engineering Department of Loughborough University in England. His research interests include multi-body and finite-element modelling of dynamic systems with a special emphasis on Automotive Safety, Injury Biomechanics, and Robotics.

A Review of Heavy Metal Removal in Constructed Wetlands and Most Widely Used Wetland Plant Varieties

Yasar Cirak Semra[1]

ABSTRACT

Heavy metals that interfere to the nature by industrial waste water are quite harmful for human and environment health. Heavy metals over the limit values in the human body causes several ailments and intoxication as cancer, central nervous system disorder, decrease of brain functions, high blood pressure, digestive system diseases, anemia, osteoporosis, allergy and loss of sense [14]. People usually intake heavy metals from air, water and vegetables grown by the water which includes heavy metal. Constructed wetlands are alternative removal systems for waste waters which is contaminated by heavy metals like Pb, Cr, Zn, Fe, Mn, Ni, Cu, etc. The aim of this study was to investigate the heavy metal removal capacity of constructed wetlands and most widely used wetland plant varieties in these systems. The studies that are reviewed in this paper showed that constructed wetlands have a capacity of heavy metal removal between 26% and 100%.

Keywords: *Constructed Wetlands, Heavy Metal Removal, Wetland Plants*

1. INTRODUCTION

Fast increase of the word population, high development levels of technology and industry, rapid production and consumption have led to a rapid increase in environmental pollution in all areas. This pollution has effected air, soil and most of water. The population growth has increased the amount of contaminated water and increase of industry meet human needs the amount of contamination by toxic substances in the water has increased. Many harmful substances to the environment and human health are confused to water. Those who have the most toxic effects of these substances are heavy metals encountered a lot particularly industrial waste waters. Mainly heavy metals are Lead (Pb), Cadmium (Cd), Mercury (Hg), Chromium (Cr), Zinc (Zn), Iron (Fe), Cobalt (Co), Manganese (Mn), Nickel (Ni), Copper (Cu), Arsenic (As), Selenium (Se), Vanadium (V), etc.The most common heavy metals and generally resources of environmental spread are shown in Table 1.

Table 1: Most common heavy metals and generally resources of environmental spread ([14], [30]).

Endustry	Cd	Cr	Cu	Hg	Pb	Ni	Sn	Zn
Paper	-	+	+	+	+	+	-	-
Petrochemistry	+	+	-	+	+	-	+	+
Chlor-Alkali	+	+	-	+	+	-	+	+
Fertilizer	+	+	+	+	+	+	-	+
Iron & Steel	+	+	+	+	+	+	+	+
Thermal Reactor	+	+	+	+	+	+	+	+
Electronics and Batteries	+	+	+	+	-	+	-	+

These heavy metals can't remove from water by biological treatments such as organic pollutants and so for water treatment it is necessary a removal process [26]. It is found that adsorption, one of physico-chemical treatment, is effective on remove of heavy metals from liquid solutions [2]. It's appropriate to remove metals in wetland areas, where the water discharged directly, with metal adsorbent plants than build a much cost facility. Constructed wetlands for the removal of heavy metals from wastewater (reed-beds), usage in recent years, has begun to be preferred because it requires both low-cost and low-tech [27]. Heavy metals in waste waters are removed in constructed wetlands by sedimentation, flocculation, adsorption, chemical precipitation, ion exchange, oxidation-reduction and plant's intake [19].

Aquatic plants are important components of wetlands. In addition to keeping the nutrients for their growth, physical, chemical and biological processes in the food transformation they have an effect in reducing food. In wetlands, they show resistance to

[1] *Kocaeli University, Department of Environmental Engineering, 41100, Kocaeli, Turkey* ozgur066@yahoo.com

water flow, improve waiting times and facilitate the settling of suspended solids. Many aquatic plants, realizes the transfer of oxygen to anaerobic layer in the soil. Thus they provide the precipitation of heavy metals and oxidation in the root zone ([31], [9]). In addition, constructed wetlands are used for the treatment of various types of waste waters as the ultimate source of sewage, acid drainage, agricultural waste, landfill leachate and non-point sources such as rain water flow [1].

Constructed wetlands are the systems that designed to simulate the phenomenon existing in wetlands and use the aquatic plants, among other tools, for free waste waters from contaminants, as soil and microorganisms [5]. Natural processes in natural systems includes more specific mechanisms such as photosynthesis, photo oxidation, vegetable intake ; together with many mechanical processes such as precipitation, filtration, gas transfer, adsorption, ion exchange, chemical precipitation, chemical oxidation and reduction, biological cycles and separation are used in wastewater treatment facilities. This process naturally speeds within a single ecosystem functioning reactor and tend to walk by itself in contrast to the sequential treatment facilities. These processes are interdependent in constructed wetlands [15].

Constructed wetlands can be designed in two ways, surface flow (Figure 1) and subsurface flow (Figure 2). In surface flow constructed wetlands, water surface in contact with air and according to plant varieties, the roots of plants, stem and leaf parts found in contact with water. Provided in contact with the air, generally aerobic microorganisms in the ambit play a role. In subsurface flow wetlands, water surface is usually in contact with, sand, gravel and plant roots and in the wetlands cycle anaerobic microorganisms are mostly active [7].

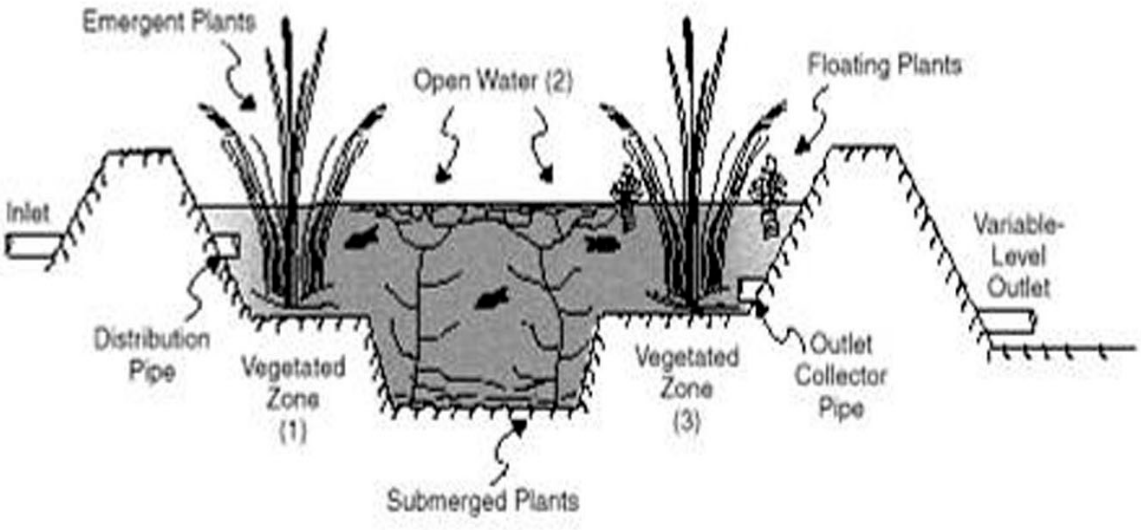

Figure 1: Surface flow constructed wetland [6].

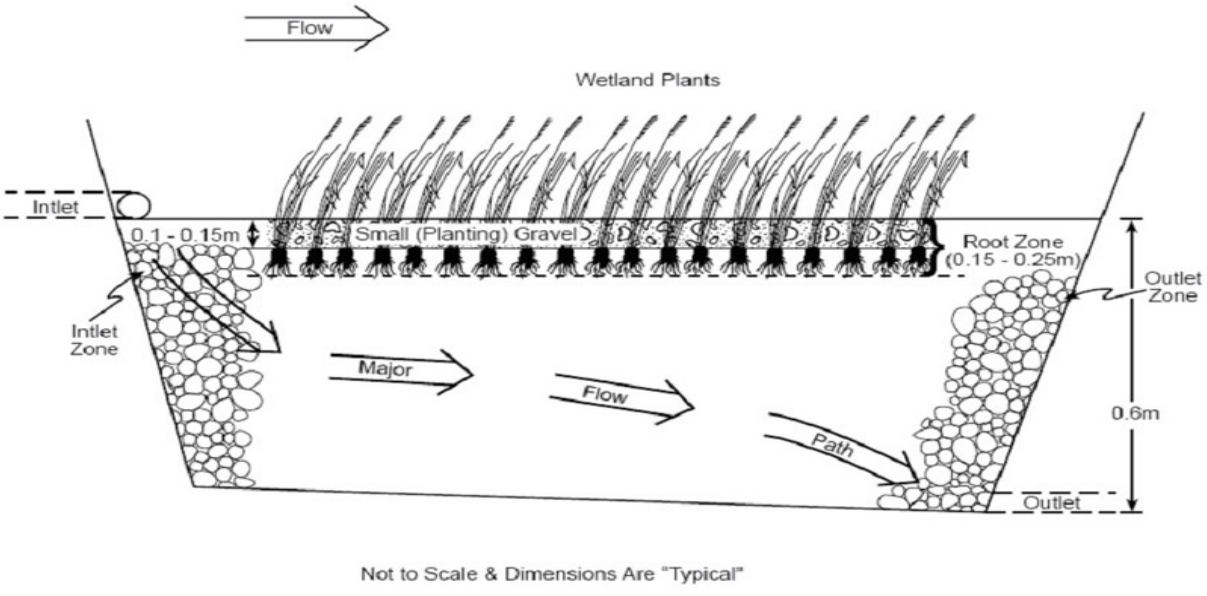

Figure2: Subsurface flow constructed wetland [6].

Studies showed that a high heavy metal removal capabilities of constructed wetlands and cadmium ratio of 75-99%, a rate of 40-96% copper, a rate of lead 0-86%, the rate of 49-88% nickel and zinc removal rate of 33-96% has provided [4]. Reference [13] indicated that they have succeeded to remove in constructed wetlands arsenic and zinc which are in industrial waste waters respectively removal rate of 33% and 99%. Reference [23] stated that in their study Phragmites australis (Common Reed) i plant is very effective in the removal of arsenic and zinc.

As Reference [4]'s report by some plants' taking pollutants successfully, water are hosted . For example *Brassica juncea (*Pb, Cd, Cu, Ni, Zn, Cr, Cs, Sr), *Myriophyllum spicatum* (Pb, Cd, Cu, Ni, Zn) and *Helianthus annuus (*Co, Cs, Sr, Cr, Mn, Cd, Ni, Cu, Pb, Zn), *Eichornia crassipes, Hydrocotyle umbellata* and *Lemna minor species have been very successfull in a short time against many pollution factors. Heavy metal accumulation trend in, research on plants Typha latifolia* and *Juncus effusus, was found to be in respectively roots, the rhizomes and the leaves* [29]. As seen in the wetlands plant species have an important effect of in heavy metal removal.

2. PREVIOUS STUDIES

Reference [17] reported that metal removal rate in wetlands depends upon the type of element (Hg>Mn>Fe=Cd>Pb=Cr>Zn=Cu>Al>Ni>As), the ionic structure, the concentration and selection of plants. In their research they have shown that treatments with *P. Australis, P. Canadensis, Potemogeton spp, Acorus spp., L. Salicaria, I. Pseudacorus, Schoenoplectus spp., E. Crassipes, H. Reticulatum , C. Demersum* and *P. Stratiotes* plants, metal removal rate is over 70%.

Reference [22] provided removal rate of 81.7- 91.8% Cu^{+2}, 75.8- 95.3% Pb^{+2} ve 82.8-90.4 % Zn^{+2} in constructed wetland which they have planted with *Typha latifolia , Phragmites australis , Schoenoplectus lacustris* and *Iris pseudacorus* plants.

Reference [8] reported that the wetland they created using water reed, removed the arsenic rate of 85-95%.

Reference [3] reported that, metal and nutrient removal treatment in wetland where Mangrove plant were used, they removed Cd^{+2}, Cr^{+2} and Cu^{+2} rate of 92%, Ni^{+2} and Zn^{+2} rate of 88%.

Reference [20] studied waste water which is contaminated with 32.4-47.4 mg/l Fe, 1.9-9.4 mg/l Mn, 10-40 mg/l Zn, 10-40 mg/l Cd, 2.0- 6.1 mg/l Pb in a *Scirpus cyperinus, Typha latifolia, Juncus effusus* plants situated constructed wetland and removed metals respectively rate of 97%, 47%, 33%, 100%, 26%.

Reference [16] has analyzed the remove capacity of Cd, Pb, Mn, Zn of Cu of the plants *Potomogetan pectinatus L* and *Potomogetan malaionus Miq.* which are feed by the water of the river Danghe polluted by the industrial waste in China. They used both of the plants together and as a result they observed that the plants are removing the heavy metals in the water by the ratio of 92%, 79%, 84%, 67% and 70% respectively.

Reference [28] has feed two separate constructed wetlands which they formed with *Typha latifolia* and *Phragmites australis* by the waste water insists of Cu and Zn that they gathered from a lumber plant. They had daily feed and exposed the plants to this waste water by 4 months. Consequently they found that the both of the plants provided removal of 83% Cu and 92% Zn.

Reference [27] has created 5 separate wetlands by using the plant of *Typha latifolia.* While watering the constructed wetland by the sewage they also added different concentrations of Cu, Ni and Zn to the both parts. They have enhanced the concentrations linearly in each adding and continued the process trough 10 weeks by feeding heavy metal solution once in two weeks. As a result they have found that the highest concentration of heavy metal solution feeding the highest removal. The removal ratios are found as Cu and Zn 100%, Ni 96%.

Reference [18] searched heavy metal removal at the constructed wetlands which they formed by using 19 types of plants. They used artifical waste water and added 2,0 mg/L Cu, 1,0 mg/L Cr and 2,0 mg/L Ni into it. The removal of Cu, Cr and Ni are evaluated according to the plant species' removed heavy metal concentration. In the research they used the plants; *1- Polygonum lapathifolium L., 2- Polygonum hydropiper L., 3- Eclipta prostrata L., 4- Aster subulatus Michx , 5- Cyperus iria L., 6- Cyperus difformis L., 7- Fimbristylis miliacea L. Vahl., 8- Aeschynomene indica L., 9- Monochoria vaginalis (Bumf.) Presl, 10-Alternanthera philoxeroides (Mart.) Griseb, 11- Echinochloa crus-galli L Beauv, 12- Echinochloa caudota Roshev, 13- Echinochloa oryzicola (Ard.) Fritsch, 14- Zizania latifolia (Griseb) Stapf, 15- Digitaria sanguinalis (l) Scop, 16- Eleusine İndica (L) Gaertn., 17- Phragmites communis Trin, 18- Isachne globosa (Thunb) Kuntze, 19- Oryza sotiva L.*

Consequently they found that about removal of Cu ;*Monochoria vaginalis (Bumf.) Presl, Alternanthera philoxeroides (Mert.) Griseb, Echinochloa crus-galli L Beauv, Zizonia latifolia Stapf, Digitoria sanguinalis (l) Scop* and *Isachne globosa (Thunb) Kuntze* plants are the most efficient ones by line, removal of Cr; *Aeschynomene indica L., Alternanthera philoxeroides (Mert.) Griseb, Echinochloa crus-galli L Beauv, Zizonia latifolia (Griseb) Stapf and Phragmites communis Trin* plants are the best, for Ni; *Polygonum hydropiper L., Alternanthera philoxeroides (Mert.) Griseb, Zizonia latifolia (Griseb) Stapf, Digitoria sanguinalis (l) Scop* and *Isachne globosa (Thunb) Kuntze* plants are the best ones.They ranked the best five plants about

removing the every three of heavy metals as*: Polygonum hydropiper L., Alternanthera philoxeroides (Mart.) Griseb, Echinochloa crus-galli L Beauv(Echinocloa colonum), Zizonia latifolia (Griseb) Stapf* , and *Isachne globosa (Thunb) Kuntze.* Totally they gathered heavy metal removal more than 97%.

Reference [12] feed the laboratory scale constructed wetland by two types of synthetic pollutian insists of Lead (Pb) and Zinc . In the system used four different wetland plants*: 1- Aneilema bracteatum, 2- Cyperus alternifolius, 3- Ludwigia hyssopifolia, 4- Veronica serpyllifolia*. They observed that the first three plants didn't created toxic symptoms in the low concentrations by Pb's 2,2-11 mg /kg and Zn's 30-157mg/kg but in the higher concentrations they saw that the plants created toxic symptoms. They determined 4. plant can rectify the high concentrations of Pb's 34 mg/kg and Zn's 261mg/kg.In the system 2. plant showed the lower and 4. plant showed the higher removal.

Reference [25] tried the removal in the constructed wetland of Pb, Cd, Fe, Ni, Cr and Cu which are in the industrial waste water of a factory in Pakistan by several factories. By the plants they used they gathered a removal ratio by order for Pb 50%,for Cd 91,9%, for Fe 74%, for Ni 40,9%, for Cr 89% and for Cu 48,3%. The plants they used are: *1-Typhia latifolia, 2- Scirpus cypernius , 3- Carex aquatilis, 4- Phragmites australis, 5- Juncus articulatus, 6- Ceratophylium demersum, 7- Lemna gibba L , 8- Echornia cressipes, 9- Polygonum Glabrum, 10- Alismaplantago – aquatica, 11- Pistia stratiotes.*

They ranked the plants have the best performance of remove according to the heavy metal type as: Pb is removed by all the plants but the best one is *Pistia stratiotes > Ceratophylium demersum,> Lemna gibba L* . For Cd all the plants could make remove but the first three are *Juncus articulatus > Pistia stratiotes > Carex aquatilis*.The most efficient three plants for Fe are *Carex aquatilis > Typhia latifolia > Ceratophylium demersum*. All the plants removed Ni and the first three are *Typhia latifolia > Lemna gibba L > Polygonum Glabrum*. The most efficient plant for Cr removal is *Alismaplantago – aquatica* .For Cu *Phragmites australis >Carex aquatilis > Typhia latifolia* are the best removing plants.By this study they showed that *Typhia latifolia, Pistia stratiotes, Phragmites australis, Carex aquatilis, Alismaplantago – aquatica* and *Juncus articulatus* plants can be used in the constructed wetlands to remove the heavy metals in the industrial waste water.

Reference [11] treated the water of river Schelde (Belgium and Netherlands) known as consists of heavy metal, by using 29 types of wetland plant, examined the removal of Cd, Cr, Cu, Fe, Mn, Ni, Pb and Zn in the water. They found that these eight heavy metals are removed by *S. Maritimus, T. Latifolia* and *P. australis* by the line of best.

Reference [10] reported that at the studies done before for the removal of heavy metals in the wetlands in 43 countries 150 type of plants are used. The most used macrophyte kinds are *Typha, Scirpus (Schoenoplectus), Pragmites, Juncus* and *Eleocharis* ; the most used macrophyte types are *Typha latifolia, Pragmites australis, Typha angustifolia, Juncus effusus, Scirpus lacustris, Scirpus colifornicus* and *Phalaris arundinacea*. Commonly seen growing land *T. Latifolia* is North America, *Cyperus papyrus* is Africa, *P. Australis* and *Typha domingensis* is South America, *Scirpus validus (S. Tabernaemantani)* is Oceania, *P. Australis* are Europe and Asia.

CONCLUSION

The studies proved that heavy metals like Pb, Cr, Cu, Cd, Ni, Zn, Mn, As exist in the industrial waste water can be removed about rate of 26% to 100% by the wetland plants in the constructed wetlands. Especially, it is showed by the researches that lots of the wetland plants like *Typha latifolia, Phrogmites australis,Ceratophylium demersum, Lemna minör, Eichornia crassipes, Pistia stratiotes, Schoenoplectus lacustris, Scirpus cyperus, Juncus effusus, Cyperus alternifolius, Potamogeton* species and *Carex aquatilis* are successful about removal of heavy metals. By the reasons of both low setup, operating cost and efficient heavy metal removal and including esthetical beauty where it is established, it is seen that constructed wetlands are the first choice removal systems about removing heavy metals from waste water.

REFERENCES

[1] A.K. Kivaisi, The *potential for constructed wetlands for wastewater treatment and reuse in developing countries: a review*, Ecol. Eng. 16 (2001) 545–560.

[2] Bailey, S.E., Olin, T.J., Bricka, R.M., Adrian, D.D., 1999. *A review of potentially low-cost sorbents for heavy metals.* Water Res. 33, 2469–2479.

[3] Chu H. Y., Chen N. C., Yeung M.C., Tam N. F.Y., and Wong Y. S., (1998). *Tide-tank system simulating mangrove wetland for removal of nutrients and heavy metals from wastewater*, Wat. Sci. Tech., Vol 38, s361-368.

[4] De Busk, William F. (1999a) Wastewater Treatment Wetlands: Contaminant Removal Processes. Soil and Water Science Department, University of Florida. SL155.

[5] D.P.L. Rousseau, E. Lesage, A. Story, P.A. Vanrolleghem, N.D. Pauw, *Constructed wetlands for water reclamation, Desalination* 218 (2008) 181–189.

[6] EPA, 2000 (Environmental Protection Agency), "*Introduction to Phytoremediation*", EPA/600/r-99/107, Cincinati, Ohio, U.S.A, p 72, http://www.clu-in.org

[7] EPA, 2001. "*Guilding Prenciples for Constructed Treatment Wetlands: Providing Water Quality and Wild Life Habitat.*"

[8] Esther ve ark. *Modelling of Arsenic retention in constructed wetlands.* Biosource Technology 147 (2013) 221-227

[9] Gopal, B., 1999. *Natural and Constructed Wetlands for Wastewater Treatment, Potentials and Problems.* Water Science Tech.

[10] Jan Vymazal. *Emengent Plants Used in Free Water Surface Constructed Wetlands: A Review*. Ecological Engineering In Press, Corrected Proof.

[11] Johannes Teuchies, Sander Jacobs, Lotte Oosterlee, Lievenn Bervoets, Patrick Meire. *Role of Plants in Metal Cycling in a Tidal Wetland: Implications for Phytoremediation.* Science of Total Environment 445-446 (2013) 146-154.

[12] Junxing Yang, Zuoluo Ma, Zhihang Ye, Xueyon Guo, Rangliang Qiu. *Heavy metal (Pb,Zn) uptake and chemical changes in mizosphere soils of four wetland plants with different rodial oxygen loss.* Journal of environmental Science 2010, 22(5) 696-702.

[13] Kadlec R. H., Wallace S.D. 2009 *Teatment Wetlands 2nd Ed*. CRC Press, Boca Rotan, FL.

[14] Kahvecioğlu Ö, Kartal G, Güven A, Timur S, 2009. *Metallerin Çevresel Etkileri-I*, Metalurji, 136.Sayı, http://www.metalurji.org.tr/dergi/dergi136/d136_4753.pdf

[15] Karul, C., Soyupak, S., Tuncer, A., Mukhallatatı, L., and Çilesiz, A. F., 1997. "*A Comprehensive Evaluation of Possible Eutrophication Control Methods for Keban Dam Reservoir with Special Emphasis on Pre-dam Construction.*" Fresenius Environmental Bulletin 6(5):284-289 ·

[16] Kejian Peng, Chunling Luo,Laiqing Luo, Xiangdong Li, Zhenguo Shen. *Bioaccumulation of heavy metals by aquatic plants Potamogeton pectinatus and Potamogeton malaionus Miq. And their potential us efor contamination indicators and in wastewater treatment.* Science of the total environment 392 (2008)22-29

[17] L. marchand, M. Mench, D.L. Jacob, M. L. Otte. *Metal and metalloid removal in constructed wetlands, with emphasison the importance of plants and standardized measurements: A review* Environmental pollution 158 (2010) 3447-3461

[18] Liu Jian-Guo, Li Guang-Hui, Shao Won-Chen, Xu Jia-Kuanand, WangDe-Ke. *Variations in Uptake and Translocation of Copper, Chromium and Nickel among Nineteen Wetland Plant Species.* Pedosphere 20(1):96-103,2010.

[19] Matagi, S. V., Swai D., ve Mugabe, R., 1998. *A Review of Heavy Metal Removal Mechanism In Wetlands.* Afr. J. Trop. Hydrobiol. Fish. (1998) 8: 23-35

[20] Mays P.A., and Edwards G.S., (2001). *Comparison of heavy metal accumulation in a natural wetland and constructed wetlands receiving acid mine drainage.* Ecological Engineering. Vol. 16, pp. 487-500.

[21] Miao, S.L., and W.F. Debusk. 1999. *Effects of P enrichment on struc ture and function of sawgrass and cattail communities in the Everglades.* p. 275–300 Lewis Publ., New York.

[22] Mungur, A.S., Shutes, R.B.E., Revitt D.M., and House M.A., (1997). *An assessment of metal removal by a laboratory scale wetland.* Water Science and Technology, Vol 35, No: 5 pp125-133.

[23] Paulo Arrayo, Gemma ansola, Luis E. Saenz de Miera. *Effect of substrate, vegetation and flow on arsenic and zinc removal and microbial diversity in constructed wetlands.* Ecological Engineering Volume 51, February 2013, Pages 95–103

[24] Reddy, K. R. Ve W. F. De Busk. 1985 *Nutrient removal potential of selected aquatic maqrophytes*. Journal of environmental quality 14 (4):459-462

[25] Sardar Khan, Irshad Ahmad, M. Tahir Shah, Shafiqur Rehman, Abdul Khaliq. *Use of Constructed Wetland fort the Removal of Heavy Metals from Industrial Wastewater*. Journal of Environmental Management 90 (2009) 3451-3457.

[26] Shuiping Cheng, Wolfgang Grosse, Friedhelm Karrenbrock, Manfred Thoennesse. Efficiency of constructed wetlands in decontamination of water polluted by heavy metals. Original Research Article Ecological Engineering, Volume 18, Issue 3, January 2002, Pages 317-325

[27] T. Manios , E.I. Stentiford , P. Millner. *Removal of heavy metals from a metaliferous water solution by Typha latifolia plants and sewage sludge compost* .Chemosphere 53 (2003) 487–494

[28] T.Y. Yeh, C. C. Chou, C. T. Pan. *Heavy metal removal within pilot scale constructed wetlands [1] receiving river water contaminated by confined swine operations*. Desalination 249 (2009) 368-373

[29] Taylor, G. J. and Crowder, A. A. 1983. "*Uptake and Accumulation of Heavy Metals By Typha latifolia in Wetlands of The Sudbury, Ontario Region.* Canadian Journal of Botany, 1983, 61(1): 63-73, 10.1139/b83-005

[30] Vanlı Ö. ve Yazgan M. *Ağır Metallerle Kirletilmiş Toprakların Temizlenmesinde Fitoremediasyon Tekniği* (2008) http://www.tarimsal.com/fitoremediasyon/fitoremediasyon.htm

[31] Vymazal, J., Brix, H., Cooper, P.F., Haberl, R., Perfler, R., ve Laber, J., 1998. *Removal Mechanisms and Types of Constructed Wetlands, In: Constructed Wetlands for Wastewater Treatment in Europe.* Backhuys Pub, Leiden, pp. 18–66.

ICENS
INTERNATIONAL CONFERENCE ON ENGINEERING AND NATURAL SCIENCES
24-28 May 2016 /Sarajevo

A web based complex network simulator with transition features between well-known network models

Ilker Turker[1], Gokhan Kutluana[2], Serhat Orkun Tan[3]

Abstract

Complex networks present a remarkable framework for understanding the evolution of real complex systems. Modeling complex networks helps capturing the generic properties taking role in most of these real systems. Well-known network models capture some of the real network properties but imitating a real network completely is only possible with real ingredients like node-aging, fitness, linking cost etc. On the other hand, defining transitions between the well-known models may generate these ingredients like small-world property that outlined by Watts-Strogatz model. Inspiring from this exploration, we developed a web based modeling framework providing transitions between three well-known models as regular, random and Barabasi-Albert networks. Beyond giving opportunity of educating these models online, this software also outlines the transitional properties between this models, providing the outputs of clustering coefficient, average separation and degree distribution metrics.

Keywords: *Complex networks, network modeling, scale free networks, random networks, regular networks.*

1. INTRODUCTION

Complex networks is a framework for understanding real complex systems across many fields [1], spanning the analysis of various systems like biological systems, neural networks, spatial games, genetic networks, food webs, scientific collaboration networks, social networks, actor networks, computer networks, power grid networks, linguistic networks and many other self-organizing systems [2-8]. Complex network science evaluated the components of these systems as nodes and the interconnections between these nodes as links [5]. The network approach to these systems help us understanding the behaviors of the whole system, by analyzing interconnections between numerous nodes and the evolving infrastructure also, leading a projection to realize how information spreads in a social network or how an epidemic spread through the links, and also which possible link may be established between nodes [9-11]. The traditional approaches that do not evaluate these systems as the interactions of existing nodes via links fail to understand the behaviors of the whole systems [12].

Most of the mentioned complex systems display some universal properties independent from what kind of system it is. These generic behaviors are termed as *"universality"*, indicating that they have similar organizing principles although they consist of dissimilar elements [13,14]. One of these generic properties is "small-world property" that indicates consisting of numerous nodes, these systems yield short paths from one node to another [4, 15, 16]. Another well-known property is high "clustering", yielding that the neighbors of a node are also neighbors of each other in a considerably high rate [17-19]. And the other striking ingredient of real networks is "scale-free property", stating out that the degree distribution of the network is power-law consistent, where the degree of a node is simply the number of nodes it is connected to [20, 21]. These type of degree distribution yields that the network consists of small number of hub nodes with numerous connections and large number of small-degree nodes, where the range between these extremities obey a linear decay in logarithmic scales. Further descriptions of these network parameters can be found in [2].

These well-known properties of complex real networks are also coupled by some other ingredients like modularity, assortative mixing, growth, aging etc. that are also subjects of various studies in this area. By the beginning of this century, scientists performed studies to tackle which ingredients take role in the organizing of real networks. These findings are then applied to the modeling studies, aiming to imitate these real systems successfully. Having derived numerous models with various ingredients, the complex network community is inspired by the basic network models known as Barabasi-Albert [20], Erdős-Rényi (also known as random network model) [22], and Watts-Strogatz models [4].

The last mentioned model (Watts-Strogatz) is an interpolation with the Erdős-Rényi model and a regular network. A regular network is a formation (preferably a mesh topology) that driven by the regular connections of neighbor nodes in a constant connection number. This study involves with a web based complex network simulator with transition features between three well-known network models: Erdős-Rényi, Barabasi-Albert and regular network models. Since it has transition support

[1] *Corresponding author: Karabuk University, Department of Computer Engineering, Karabuk, Turkey. iturker@karabuk.edu.tr*

[2] *Bartın University, Vocational School of Health Services, Bartin, Turkey. gkutluana@bartin.edu.tr*

[3] *Karabuk University, Vocational School, Karabuk, Turkey. serhatorkuntan@karabuk.edu.tr*

between these models, the Watts-Strogatz model is also the natural ingredient of this framework and a quick setup button is provided for this algorithm in the user interface.

1.1 Recent Software for Network Modeling and Analysis

By the end of the last century, the amount of data for networked systems revealed a steep increase. Current advances in data storage and processing favored the availability of various data sources and also analyzing them as well. The growing attention on complex systems as networks emerged the existence of some software for complex network modeling and analysis. As a result, there is a variety of software listed below each having some special utilities.

Gephi: Gephi is an open source software for the visual exploration of networks. Gephi users interact with the visualization in real-time to position the nodes in a two or three dimensional space using layout algorithms, or by manually moving nodes. It is built with Java SE 6 on top of the NetBeans Platform, which is software for creating applications [23]. It is a desktop application with the facilitation of calculating basic network parameters and distributions.

NetworkX: NetworkX is a Python language software package for the creation, manipulation, and study of the structure, dynamics, and functions of complex networks. Loading and storing networks in standard and nonstandard data formats, generating many types of random and classic networks, analyzing network structure, building network models, designing new network algorithms, drawing networks, and much more are possible using NetworkX. It is a desktop application with powerful facilities of the Phyton language package. User interface is through scripting in command-line provided by Python [24, 25].

CytoScape: Cytoscape is an open source software project for integrating biomolecular interaction networks with high-throughput expression data and other molecular states into a unified conceptual framework. Although Cytoscape was originally designed for biological research, now it is a general platform for complex network analysis and visualization. Cytoscape core distribution provides a basic set of features for data integration, analysis, and visualization [26]. It is a desktop application but the CytoScape community also provides a CytoScape.js file as a successor of HTML5 web applications of network visualizing, for the developers.

Similar desktop applications: Similar with the software mentioned above, there are some other desktop applications like iGraph, Pajek, NetMiner, GUESS etc. and toolboxes for Matlab and Mathematica [25].

Web based software: Beyond the well-known network analysis and visualization tools mentioned above, there are numerous software for both desktop and web medium [25]. Among these software, the web based applications get attention by providing a quick adaptation without installation. A big portion of these web based applications get an overview of the collaboration within and between groups such as geographical units, project teams, and business units, revealing how organizations really operate in day-to-day business. Some examples of these type applications are Maven7, Teamscom, KeyNetiQ, Sociliyzer, Polinode, SocioViz and Graph Commons [25]. These software work with internal or supplied data and they do not have modeling utilities. Another effective web based application is named Sigma.js, providing a JavaScript library dedicated to graph drawing. It allows developers to integrate network exploration in rich Web applications [27].

A web based model with basic modeling and analysis utilities is proposed by Shi et.al [28]. They provide on-line construction of basic network models with 2D presentation, in Japanese language. By the usage of the software, they aim to simplify the learning of basic network models.

Beyond the recent studies mentioned above, we propose a web based application including basic network models, with transition features with rewiring processes between these well-known network models. Another distinct feature of our application is providing 3D visualization by the usage of WebGL library. Before describing the software performed, the short definitions of the common network models will be worthwhile.

2. NETWORK MODELS

In this section we shortly describe the well-known network models that we implemented in our web based software.

2.1 The Regular Network Model

In a regular network, the nodes are arranged in a mesh or lattice order, where all the nodes are connected to k neighbors regularly, as in the left side of Fig.1. This network formation characteristically yields high clustering like real networks with local connections, while it lacks small-world and scale-free properties since having relatively long distances between node pairs, and also identical node degrees. The construction of a regular lattice is described in [4]. This network topology is not generated in the software as stand-alone, but contributes the mixing procedures that will be described below.

2.2 The Barabasi-Albert Model

This is the first model imitating the power-law consistent degree distribution of nodes forming a network, with two main ingredients: growth and preferential attachment. Starting with a small number of nodes (m_0), the network grows with the addition of a new node at every time step with connections to the $m \leq m_0$ existing nodes. The new nodes also prefer

connecting to the nodes having more connections rather than the newcomers. This mechanism is defined with a connection probability *Π(k)* that a new node will be connected to node *i* depending on the degree k_i of node *I* as follows [20]:

$$\Pi(k_i) = \frac{k_i}{\sum_j k_j} \quad (1)$$

The resulting state of the model displays a power-law degree distribution of nodes, as in the real networks. The model also successfully imitates the small-world property of the real networks, having small distances between the nodes. The only lacking property of the model is clustering, since it does not promote local connections between neighbors.

2.3 The Erdős-Rényi (Random Network) Model

Erdős and Rényi proposed the random graph concept, consisting of *N* nodes connected with *e* edges (connections) that are chosen randomly from the *N(N-1)/2* possible edges. The model also includes a *p* parameter that indicates the probability of establishing each *N(N-1)/2* possible edges. As a result, the network consists of an expected number of *pN(N-1)/2* edges.

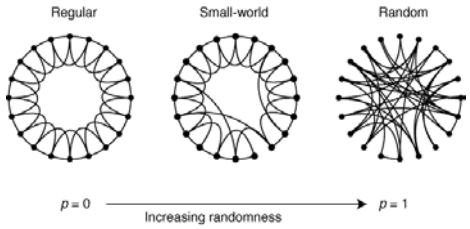

Fig.1. Small world model interpolating between regular and random models, proposed by Watts and Strogatz [4].

A common representation of a random graph is displayed in the right side of Fig.1. This type of networks have small-world property with small distances between nodes, but lack of clustering. Also, the expected degree distribution is Poisson that means a randomly chosen node is expected to have a degree close to the average degree of the whole network. The real networks were assumed to have random topology but the recent studies on complex network analysis stated out that real network are not random. They have both growth and preferential attachment ingredients resulting their tree-like topologies [20].

2.4 The Watts-Strogatz (small-world) model

Real networks display both small diameter (node distances) and high clustering. The former property is imitated by the random graphs, while the latter is observed in regular lattices. Inspiring from these two models, Watts and Strogatz proposed a model interpolating between these two graphs, named as small-world model. The started with a regular lattice and ran a rewiring procedure, breaking the regular links with a rewiring probability of p_{rewire}, and wired them to randomly chosen nodes in the whole network. This procedure illustrated in Fig.1 is detailed in ref. [4].

While p_{rewire} increases from 0 towards 1, average distances fall immediately while the clustering coefficient remains high for a longer period. This leads a small-world region that clustering is high while average path length (distance) is low.

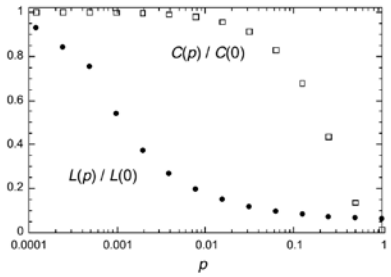

Fig.2. Evolution of average path length L(p) and clustering coefficient C(p) while p_{rewire} increases as in Fig.1. [4].

2.5 Defining rewiring procedures between the other models

Ispiring from the rewiring procedure in Watts-Strogatz model, we defined the similar rewiring procedures between the other network models as: (i) Random to Regular, (ii) Regular to Barabasi-Albert, (iii) Barabasi-Albert to Regular, (iv) Random to Barabasi-Albert, (v) Barabasi-Albert to Random, (vi) Random to Regular & Barabasi-Albert. We define the rewiring procedures as below:

2.5.1 Random to Regular

A random network can be expressed with two parameters: N (number of nodes) and L (number of links). The links are established with selecting source and target nodes as uniformly random numbers between 1 and N, avoiding the duplication of existing links and self-links [5].

Having constructed a random network, we run a rewiring procedure with rewiring probability p_{rewire}, which in turn breaks the target connections of all links in probability of p_{rewire} and wires them to new target nodes. For a network of N nodes and L edges, the expected value of number of rewired connections is (p_{rewire}, L). To regularize a random network, this procedure must evolve the target connections through the neighbor nodes of the source nodes. To achieve this goal, we selected the new target nodes by generating random numbers of Poisson distribution of Eq.2, where the source node's number is the median of the distribution, resulting to generate new target nodes close to the source node.

$$f(k,\lambda) = \frac{\lambda^k e^{-\lambda}}{k!} \tag{2}$$

2.5.2 Regular to Barabasi-Albert

Having constructed a regular network as described in section 1.1, we run a rewiring procedure with rewiring probability p_{rewire}, which in turn breaks the target connections of all links in probability of p_{rewire} and wires them to new target nodes. In the rewiring procedure, the source nodes of a rewired link remains static, while the new target node is selected with a "preferential attachment" principal that is described in section 1.2.

2.5.3 Barabasi-Albert to Regular

Having constructed a Barabasi-Albert network as described in section 1.2, we run a rewiring procedure as above by regularizing the target nodes with rewiring probability p_{rewire}. To construct "regular" links, the target are selected as described in section 1.5.1. as a characteristic property of Poisson distribution, the target nodes are likely to be selected close to the source node and therefore a more regular network is achieved.

2.5.4 Random to Barabasi-Albert

Having constructed a random network as described in section 1.3, we run a rewiring procedure as above by selecting the target nodes with a "preferential attachment" principal that is described in section 1.2. By the way, the random network gets Barabasi-Albert properties increasing with the probability p_{rewire}.

2.5.5 Barabasi-Albert to Random

Having constructed a Barabasi-Albert network as described in section 1.2, we run a rewiring procedure as above by randomly selecting the target nodes with uniform distribution that gives equal probability of selecting any node in the network. As a result, the Barabasi-Albert network is randomized with the rewiring probability p_{rewire}.

2.5.6 Random to Regular & Barabasi-Albert

The most interesting transition between the well-known network models is described in this section. The web application has the utility of running a rewiring procedure similar with the others, wiring the source node to a new target node by considering its physical closeness and also degree value. This means that while adding regularity to the random network and increasing neighborliness, it also promotes attaching to the "rich" neighbors by defining a complex wiring procedure described below.

While selecting a new target node to wire, we again run a Poisson procedure described in section 1.5.1, with a simple deviation that we do not select a node among the sequential node IDs, we select among the sequential and repeated node IDs. The repetition number of a node ID is affected by the node's degree. As a result, this rewiring procedure establishes new links to the nodes likely to be close to the source node, while the preferential attachment is also applied. By the way, the network gets more regular and more preferentially coupled with increasing rewiring probability p_{rewire}.

3. SOFTWARE UTILITIES

3.1 System Requirements

The high accessibility of this software is the main motivation of the study. That's why we developed a web based application that completely works in a web browser. The compatible browser list is : Chrome version 9+, Firefox version 4+, Safari version 6+, Opera version 11+, Internet Explorer version 11 and Microsoft Edge version 0.95+, all with WebGL capable graphic cards required. The software also works in mobile platforms which support WebGL, which is a JavaScript API for rendering interactive 3D computer graphics and 2D graphics within any compatible web browser without the use of plug-ins [29].

The project is available at the following URL: *http://www.ilkerturker.com/cnWebProject/*

3.2 Components

We aimed to design a cross-browser compatible application that works at standard browsers without any add-ons installed. On the other hand, to serve a rich user interface experience, we enriched the application with some external libraries for 3D presentation, zooming, moving and drawing graphs etc. The application is powered by 3 main libraries described as below:

jQuery and jQuery UI libraries: jQuery is a fast, small, and feature-rich JavaScript library. It makes things like HTML document traversal and manipulation, event handling, animation, and Ajax much simpler with an easy-to-use API that works across a multitude of browsers. jQuery UI is a curated set of user interface interactions, effects, widgets, and themes built on top of the jQuery JavaScript Library. For building highly interactive web applications, it facilitates adding commonly used components to the web page in a very simple and effective way [30]. We employed these libraries to design the tabbed input panels for each network model, including scroll-based input areas.

three.js for WebGL library: Three.js allows the creation of GPU-accelerated 3D animations using the JavaScript language as part of a website without relying on proprietary browser plugins. This is possible with the employment of WebGL in a HTML5 canvas object. High-level libraries such as Three.js make it possible to design complex 3D computer animations that display in the browser without the effort required for a traditional standalone application or a plugin [31]. We used three.js for 3D visualizations of the network models as well as for 3D animations and movements. For the 3D dragging, camera angle, zoom in and out actions, we used *trackballcontrols* actions of three.js library.

jqPlot library: jqPlot is a plotting and charting plugin for the jQuery Javascript framework. jqPlot produces well-designed line, bar and pie charts with many features. Computation and drawing of lines, axes, shadows even the grid itself is handled by pluggable "renderers". Not only are the plot elements customizable, plugins can expand functionality of the plot as well [32]. We employed jqPlot library for visualizing the degree distributions of the network models.

3.3 Features

The high accessibility of this software is the main motivation of the study. That's why we developed a web based application that no installation is needed and quick action to visualizing networks is provided. Beyond working on a browser, the software has two distinct properties that transitions between well-known network models and also 3D visualization with editable camera angles and closeness are provided. The logic behind the transitions are described in section 2.5. The visualization and analysis features will be detailed in this section.

3.3.1 Tabbed Adjustment Panel for Model Selection

In the upper left side of the user interface, a tabbed panel is provided for the selection of the network model that an instance will be generated. There are 9 choices consisting of 3 main models and 6 transition opportunities between these models plus regular network (RG) model. The first 3 models are Barabasi-Albert (BA), Erdos-Renyi (Random) and Watts-Strogatz (WS) models. The remaining 6 models including transitions described in section 2.5 are RN to RG (resulting an inverse WS model), RG to BA, BA to RG, RN to BA, RN to RG&BA, BA to RN models. While the tabs for the 3 main models include the basic initial parameters needed for the model, the tabs for the 6 transitive models include the initial parameters plus a rewiring probability p_{rewire} to be employed for the rewiring process defining the transition. A screenshot of the tabbed panel together with a basic BA network plot is provided in Fig.3.

3.3.2 2D visualization with 3D transformations

The user interface provides a "3D State" checkbox that enables 3D visualizing. While this box is unchecked, the network is plotted as 2D in a circular layout. But for a 2D drawing, 3D transformations like rotating, moving, zooming in and out are also available by using the left-right clicking, dragging and scrolling functions of the mouse. A 2D drawing with a modified camera-angle by left-dragging the mouse is shown in Fig.3.

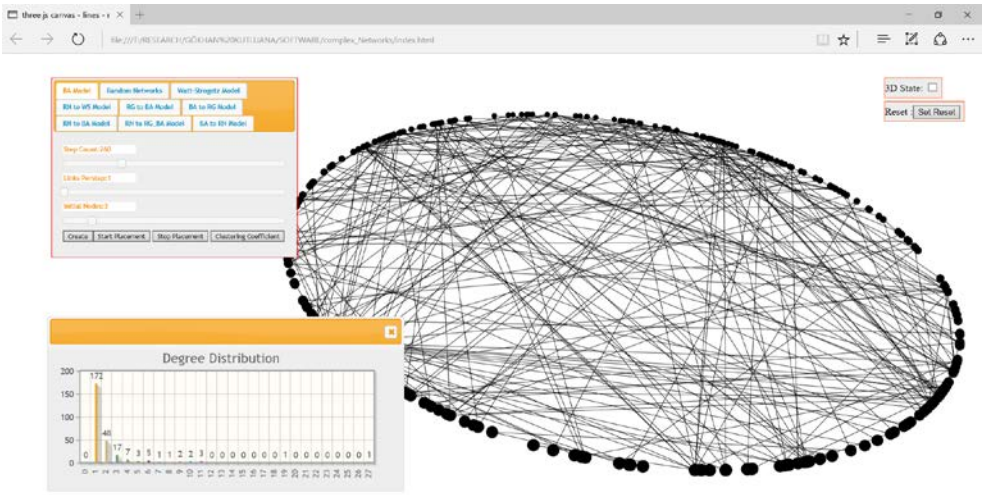

Fig.3. User interface of the web based application.

3.3.3 3D visualization with 3D transformations

If the "3D State" box is checked, the network is visualized as 3D with a spherical layout. For a 3D drawing, the transformations like rotating, moving, zooming in and out are also available as in 2D drawing. In Fig.4, a 3D visualization is presented with edited layout and camera angle options.

3.3.4 Mouse actions

Once a network is drawn, the user can zoom-in and out by mouse scrolling. By dragging with the left mouse button, the camera angle is changed resulting a rotation of the network around its center. Dragging with the right mouse button results the moving of the network to a desired position.

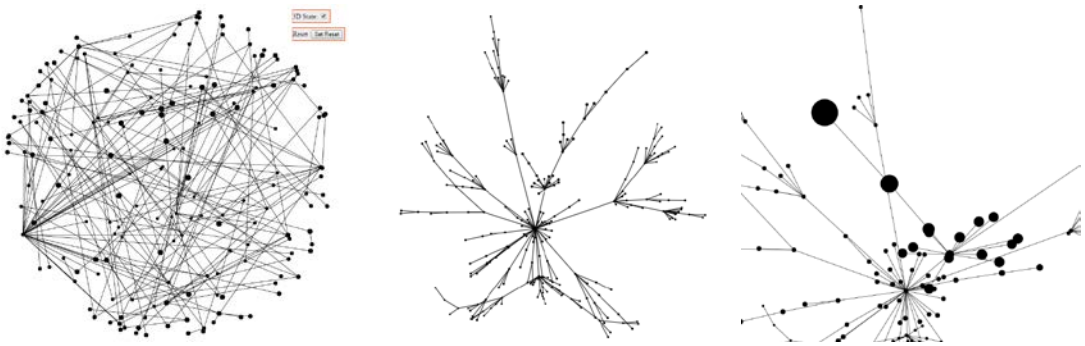

(a) (b) (c)

Fig.4. A 3D visualization (a) with a Fruchterman-Reingold layout applied in (b) and zoom-in and rotating applied in (c).

3.3.5 Changing the layout

While the initial drawing is performed as circular (for 2D) and spherical (for 3D), the start placement buttons provided in the tabbed panel runs a replacement procedure for the nodes according to the Fruchterman-Reingold algorithm [33]. This is the only layout algorithm other than the initial circular and spherical layouts. But successfully visualizes the network as a tree-like structure, providing a good understanding of the hierarchical network topology.

3.3.6 Degree distribution, clustering coefficient and average distance

Completing the drawing of a network model, the software immediately calculates and plots the degree distribution graph in an html layer as seen in Fig.3. The graph can be moved or closed by the user. The "Output Statistics" button in the tabbed panel calculates the *clustering coefficient* and *average distance* metrics and outputs these values in a message box.

4. DISCUSSION

Most web-like structures in nature have some generic organizing principles underlying their topologies [2]. Understanding these systems as a whole is possible with complex networks approach, which requires both theoretical and practical exercises. The various software applications provide opportunities of modeling, analyzing and in turn understanding complex networks. But only a small portion of these software are web-based, and as a result easy to use without installation.

Our web-based application is a lightweight and browser based software with a user friendly interface. It also provides 2D and 3D visualizing utilities, both having 3D transformation features. The user also has the opportunity of running a Fruchterman-Reingold layout routine to achieve a clear visualization. Beyond these visualization options the software provides the calculation of basic network metrics (average separation and clustering coefficient) along with the degree distribution plotting. By the way, to describe a basic network by visualizing it has been very practical, together with commenting about its separation and clustering values provided. We expect that the software will be useful for the education of complex networks with these features.

The rewiring properties between well-known network models are unique except for the Watts-Strogatz algorithm which interpolates between regular and random networks. Actually, the transition features between network models is mostly inspired by the rewiring processes defined in Watts-Strogatz network model. We expanded this approach to the other models successfully, providing another educative vision to network structures.

As a future study, we are studying the evolution of the network parameters under the transition conditions between these models, which will be the subject of an upcoming paper this year. The spreading analysis under the transition conditions mentioned in this paper is also a further challenge that we are planning to study.

ACKNOWLEDGEMENTS

This study has been funded by Scientific Research Project (BAP) Coordinatorship of Karabuk University with project code of KBU-BAP-16/1-YD-030.

REFERENCES

[1]. Strogatz, S.H., *Exploring complex networks.* Nature, 2001. **410**(6825): p. 268-276.
[2]. Albert, R. and A.L. Barabasi, *Statistical mechanics of complex networks.* Reviews of Modern Physics, 2002. **74**(1): p. 47-97.
[3]. Barabasi, A.L., et al., *Evolution of the social network of scientific collaborations.* Physica a-Statistical Mechanics and Its Applications, 2002. **311**(3-4): p. 590-614.
[4]. Watts, D.J. and S.H. Strogatz, *Collective dynamics of 'small-world' networks.* Nature, 1998. **393**(6684): p. 440-442.
[5]. Barabási, A.L., *Network Science*. 2016, Cambridge: Cambridge University Press.
[6]. Cavusoglu, A. and I. Turker, *Scientific collaboration network of Turkey.* Chaos Solitons & Fractals, 2013. **57**: p. 9-18.
[7]. Cavusoglu, A. and I. Turker, *Patterns of collaboration in four scientific disciplines of the Turkish collaboration network.* Physica a-Statistical Mechanics and Its Applications, 2014. **413**: p. 220-229.
[8]. Kim, J. and J. Diesner, *Coauthorship networks: A directed network approach considering the order and number of coauthors.* Journal of the Association for Information Science and Technology, 2015. **66**(12): p. 2685-2696.
[9]. Girvan, M. and M.E.J. Newman, *Community structure in social and biological networks.* Proceedings of the National Academy of Sciences of the United States of America, 2002. **99**(12): p. 7821-7826.
[10]. Newman, M.E.J., *Spread of epidemic disease on networks.* Physical Review E, 2002. **66**(1): p. 11.
[11]. Park, J. and M.E.J. Newman, *Statistical mechanics of networks.* Physical Review E, 2004. **70**(6): p. 13.
[12]. Newman, M.E.J., *The structure and function of complex networks.* Siam Review, 2003. **45**(2): p. 167-256.
[13]. Barabasi, A.L., R. Albert, and H. Jeong, *Scale-free characteristics of random networks: the topology of the World-Wide Web.* Physica A, 2000. **281**(1-4): p. 69-77.
[14]. Barzel, B. and A.L. Barabasi, *Universality in network dynamics.* Nature Physics, 2013. **9**(10): p. 673-681.
[15]. Milgram, S., *The small-world problem.* Psychology Today, 1967. **1**(1): p. 61-67.
[16]. Amaral, L.A.N., et al., *Classes of small-world networks.* Proceedings of the National Academy of Sciences of the United States of America, 2000. **97**(21): p. 11149-11152.
[17]. Newman, M.E.J., *The structure of scientific collaboration networks.* Proceedings of the National Academy of Sciences of the United States of America, 2001. **98**(2): p. 404-409.
[18]. Li, M.H., et al., *Evolving model of weighted networks inspired by scientific collaboration networks.* Physica a-Statistical Mechanics and Its Applications, 2007. **375**(1): p. 355-364.
[19]. Ferligoj, A., et al., *Scientific collaboration dynamics in a national scientific system.* Scientometrics, 2015. **104**(3): p. 985-1012.
[20]. Barabasi, A.L. and R. Albert, *Emergence of scaling in random networks.* Science, 1999. **286**(5439): p. 509-512.
[21]. Clauset, A., C.R. Shalizi, and M.E.J. Newman, *Power-Law Distributions in Empirical Data.* Siam Review, 2009. **51**(4): p. 661-703.
[22]. Erdős, P. and A. Rényi, *On random graphs. I.* Publicationes Mathematicae, 1959. **6**: p. 290-297.
[23]. Bastian, M., S. Heymann, and M. Jacomy, *Gephi: an open source software for exploring and manipulating networks*, in *International AAAI Conference on Weblogs and Social Media*. 2009: San Jose, California.
[24]. Schult, D.A. and P. Swart. *Exploring network structure, dynamics, and function using NetworkX*. in *Proceedings of the 7th Python in Science Conferences (SciPy 2008)*. 2008.
[25]. *Social network analysis software.* 2016; Available from: https://en.wikipedia.org/wiki/Social_network_analysis_software.
[26]. Shannon, P., et al., *Cytoscape: a software environment for integrated models of biomolecular interaction networks.* Genome research, 2003. **13**(11): p. 2498-2504.
[27]. *Sigma.js.* 2016; Available from: http://sigmajs.org/.
[28]. Shi, M., et al. *WEB Based Learning System for Complex Networks.* in *Information Technology Based Higher Education and Training, 2006. ITHET'06. 7th International Conference on*. 2006. IEEE.
[29]. Tavares, G. *WebGL Fundamentals.* 2012; Available from: http://www.html5rocks.com/en/tutorials/webgl/webgl_fundamentals/.
[30]. *jQuery, a JavaScript library*. Available from: https://jquery.com/.
[31]. *Three.js*. Available from: https://en.wikipedia.org/wiki/Three.js.
[32]. *jqPlot*. Available from: http://www.jqplot.com/.
[33]. Kobourov, S.G., *Spring embedders and force directed graph drawing algorithms.* arXiv preprint arXiv:1201.3011, 2012.

ICENS
INTERNATIONAL CONFERENCE ON ENGINEERING AND NATURAL SCIENCES
24-28 May 2016 /Sarajevo

Investigation of tensile-shear strength of automotive sheets in electrical resistance spot welding

Omer Savas[*1], *Faruk Varol*[2], *Salim Aslanlar*[3]

Abstract

In this study, effects of some parameters such as the welding current, electrode pressure, welding time and hold time on tensile-shear strength of welding joint in electrical resistance spot welding (ERSW) was investigated. Taguchi's experimental design has been used to examine the effects of the parameters using the L9(34) orthogonal array. Results showed that the most effective parameters on the tensile-shear (T-S) strength were found as welding current and welding time, whereas electrode pressure was less effective factors.

Keywords: *Resistance spot welding, Tensile shears strength, Taguchi method*

1. INTRODUCTION

Having low cost, high speed and suitability for automation, resistance spot welding (RSW) is the most popular joining technique to produce automobile body structure. This joining technique is based on the electrical resistance of which the components create a heat as a current is passed through them [1]. Proportion of the heat generated depends on the square of the current (I^2), the resistance of the components (R) and the time for which the current is passed (T). The heat generates (Q) according to the following Eq. (1) [2].

$$Q = I^2.R.t \qquad (1)$$

Where Q= heat generated, Joules (J); I= current, amperes (A), R= resistance of the components, ohms (Ω); t= time duration of current, seconds (s)

Due to fact that the expansion occurs during weld process, the metal parts are held together under pressure between two electrodes when the metal parts are heated and weld process take only few seconds (Fig. 1). It is required High current intensity (1A - 100 A) and low voltage (1-30 V) to obtain a local pool of molten metal in RSW process [3].

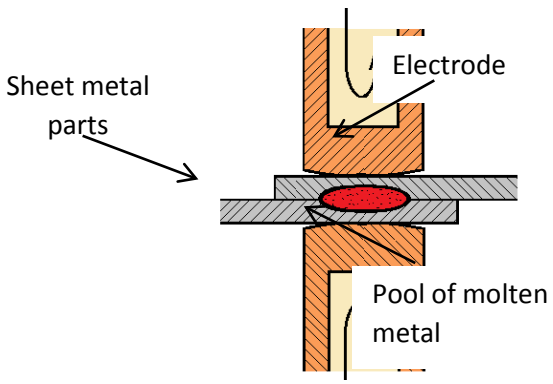

Figure 1 The Schematic representation of electrical resistance spot welding.

In previous studies, Taguchi method has been used to dentify an optimization of tensile shear (T-S) strength of galvanized steel metals welding. The results showed that the effective parameters on T-S strength were determined as welding current, electrode pressure, welding time, clamping time and holding time. The results also indicated that Taguchi approach was effectively used for optimization of welding parameters in RSW process [4-6].

In this work, Taguchi's experimental design has been used to obtain an optimal experimental prescription in order to determine max T-S strength of the welding joints. In order to provide some foundational information for improving tensile-shear strength properties of the welding joint of galvanized DP 600 steel sheets in electrical resistance spot welding, the availability of this method for galvanized DP 600 steel sheets welding and the effect of welding parameters (welding current, electrode pressure, welding time and hold time) on the characteristics of the joint were investigated.

2. MATERIALS AND METHOD

In this study. Galvanized DP 600 steel sheet was used, using widely in automobile body structure fabrication. The spectrometric analysis of them was given in Table 1. The workpieces are prepared as shown in Fig. 2 and cleaned ultrasonically.

Table 15. Chemical composition of workpiece materials

C	Si	Mn	Cr	Al	Cu	Mo	Balance
0.0544	0.158	1.840	0.0967	0.0277	0.0212	0.155	97.647

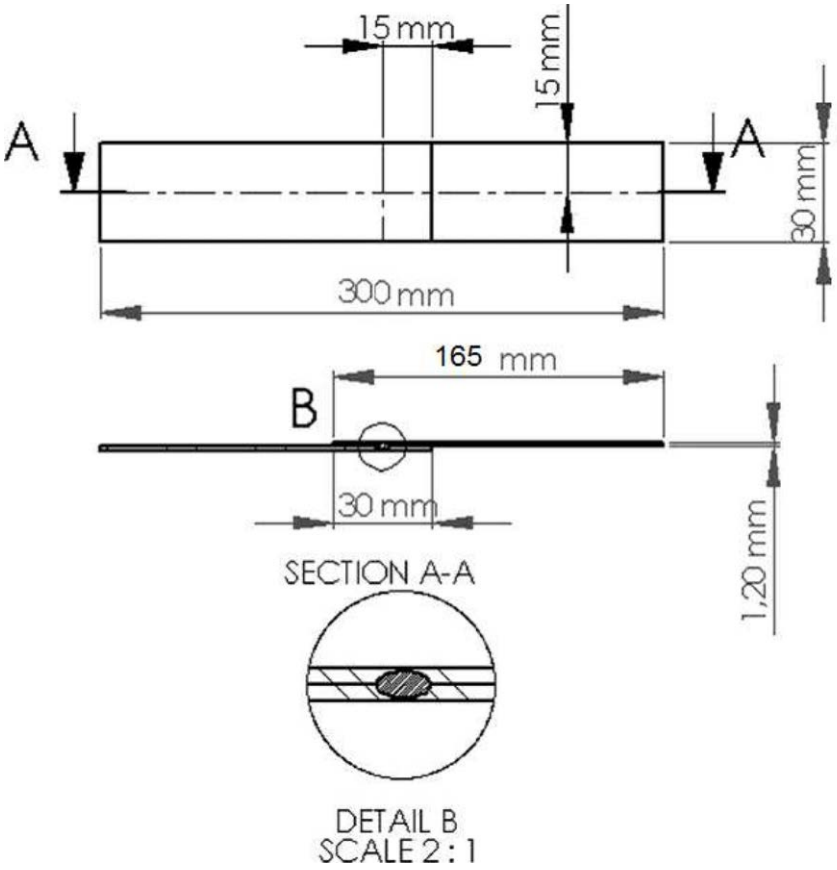

Figure. 2 The sizes of T-P test specimens

A current and timer controlled welding machine which has 120 kVA capacity and pneumatic application mechanism was used in experimental works. The workpieces were welded with changing electrode force, welding current, holding time and fixing electrode diameter at 12 mm sphere, and cooling water flow rate during experiments. The welding period applied was shown in Fig. 2 [7]

A current and timer controlled welding machine which has 120 kVA capacity and pneumatic application mechanism was used in experimental works. The workpieces were welded with changing electrode force, welding current, holding time and fixing electrode diameter at 12 mm sphere, and cooling water flow rate.

To determine the welding of strengths, the welded workpieces were performed to tensile-shear tests by in a 50kN computerized universal testing machine. The tensile speed was kept constant at a crosshead of 10 mm/min.

In this study, the welding process parameters include the welding current, electrode pressure, weld time and hold time. Each parameter has three levels as shown in Table 2. The welding experiments were designed to apply the Taguchi's methods to establish the effect of welding parameters on the optimum welding conditions to achieve max tensile strengths.

Table 2. Process parameters and their levels

Factors	Symbols	Level 1	Level 2	Level 3
Welding current, kA	A	6	10	14
Electrode pressure, kN	B	3	4	5
Welding times, period	C	10	15	20
Hold times, period	E	10	15	20

An $L_9(3^4)$ orthogonal array table has been employed in the design of the experiments which includes only 9 trials as seen Table 3. Using the average T-P strength values from the measurements, signal-to-noise (S/N) ratios were calculated by Eq. (2) and presented in relevant tables. The S/N ratio calculation is based on the "higher is better" approach as represented by Eq. (2).

$$S/N = -10\log\left(1/n\sum_{i=1}^{n}1/y^2\right) \quad (2)$$

Where n is the number of measurements in a trial and y is the value of measurement in a trial.

In order to determine the importance of the factors, analysis of variance statistical method (ANOVA) was prepared using the signal-to-noise (S/N) ratio values. ANOVA employs Eqs. (3)-(6) [9,10].

$$SS_T = \left[\sum_{I=1}^{N}(S/N)i^2\right] - \frac{T^2}{N} \quad (3)$$

$$SS_A = \left[\sum_{I=1}^{K_A}\left(\frac{Ai^2}{n_{A_i}}\right)\right] - \frac{T^2}{N} \quad (4)$$

$$v_{Total} = N - 1 \quad (5)$$

$$V_{Factor} = \frac{SS_{Factor}}{v_{Factor}} \quad (6)$$

$$F_{Factor} = \frac{V_{Factor}}{V_{Error}} \quad (7)$$

Where, N is the total number of experiments, SST is the sum of squares due to total variation, KA is the number of levels for factor A, SSA represents the sum of squares due to factor A. nAi is the number of samples for ith level of factor A., Ai stands for the sum of the total ith level of the factor A,. T is the sum of total (S/N) ratio of the experiments, vtotal is the degrees of freedom, SSfactor represents the sum of squares of the factor and Ffactor is the F ratio of the factor, Vfactor is the variance of the factors.

3. RESULTS AND DISCUSSION

The T-S strength values measured from each trial are given with the experiment prescriptions in Table 3. These values for each trial are also averaged as Tensile-shear strength and used for the calculation of S/N values as seen in Table 3. T-S strength values were varied between 336.7 MPa and 471.5 MPa as seen Table 4. The highest strength value was obtained from trial 5 and the lowest strength value tained from trials 2.

Table 3. $L_9(4^3)$ orthogonal design array, measured T-S strength and S/N ratios

Exp. No	Welding current, kA	Electrode pressure, kN	Welding times, period	Hold times, period	T-S strength, MPa	S/N ratio
	A	**B**	**C**	**D**		
1	6	4	10	10	355.0	51.00
2	6	3	15	20	336.7	50.54
3	6	5	20	15	370.0	51.36
4	9	4	15	15	415.0	52.36
5	9	3	20	10	471.5	53.47
6	9	5	10	20	400.9	52.06
7	13	4	20	20	431.8	52.71
8	13	3	10	15	396.0	51.95
9	13	5	15	10	403.3	52.11

The analysis of variance table (ANOVA) was prepared using Eq. (2)–(6). Table 4 shows the ANOVA table and the average values of S/N ratio for different levels of each trial. According to the ANOVA, the high contribution and variance of factors A and C indicate that the Welding current and the Welding time are significant at least 99% and 95% confidence, respectively. The Hold times (D) is the effective factor. Electrode pressure (B) has less influence factors on the Tensile-shear (P-S) strength. These results are also in good agreement with previous works reported by Aslanlar et al [11]. They are reported the welding current and welding time were significant factors on tesnsile strength of welding joints.

Table 4. Analysis of variance (ANOVA)

	Factors	Level (S/N)			Rank	Sum of squares (SS)	Degrees of freedom (v)	Variance (V)	F(factor)
		1	2	2					
A	($) Welding current	50.97	52.63	52.26	4.98	4.55	2	2.27	85.47
B	(e) Electrode pressure	51.99	52.02	51.85	0.53	0.05	2	0.03	1.00
C	($) Welding times	51.67	51.67	52.51	2.52	1.41	2	0.71	26.51
D	Hold times	52.20	51.89	51.77	1.28	0.29	2	0.14	5.39
	Total					6.25	6	1.04	
	Error (e)					0.05	2	0.03	

e pooling, $ At least 99% confidence (39.00), & At least 95% confidence (19.00), # At least 90% confidence (9.00).

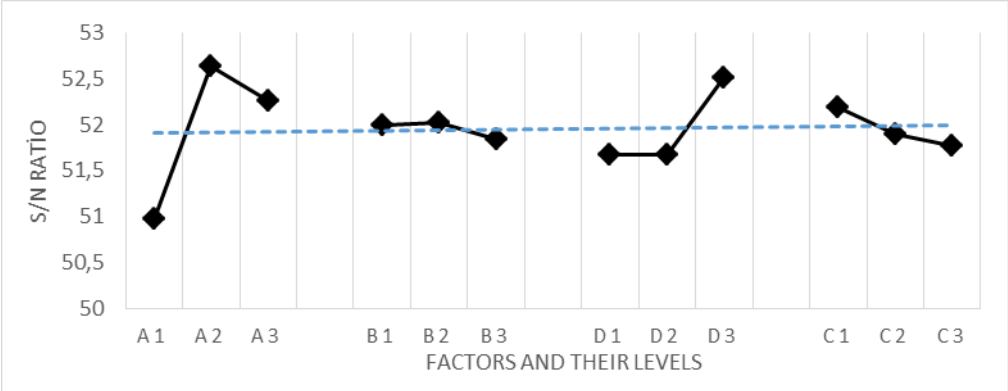

Figure 3 Factors response table

Using the average values of S/N ratio for different levels of each trial in Table 3, S/N response graph were derived as shown in Fig. 3. The study defines the high tensile-shear strength with a high S/N ratio according to the Taguchi method. Thus, Fig. 3 reveals the optimal combination of experimental parameters and the corresponding values of each factor. These are A_2, B_1, C_3 and D_1 for obtaining the highest the Tensile-shear strength.

It is absolutely required to perform an experiment for verification in order to compare the results with the expected conditions according to the principles. In this study, less influence factors (Electrode pressure) on the T-S strength were ignored. In order to obtain the confirmation experiment table the following Eq. (8)–(9) have been used [9,10].

$$\mu_{\text{Strength}} = \overline{A2} + \overline{C3} + \overline{D1} - 2\overline{T} \quad (8)$$

$$\mu \pm \sqrt{\frac{F_{(p)} V_e}{n}} \quad (9)$$

Where μ is estimated average S/N values, F(p) is F ratio, Ve is error variance, n is number of tests under given condition.

Table 5. Results from the verification experiment

Description	Shear strength, MPa
Optimum condition	A2B2C3D1
Pooled factors	B
Estimated average S/N ratio	53.43
Estimated S/N ratio range	53.02< μ <53.84
Exp. average S/N ratio	53.47
Estimated average value	469
Estimated value range	447< μ <492
Exp. average value	471

Table 5 show that estimated shear strength should be between 447 MPa and 492 MPa at the optimum condition (A2B1C3D2). The determined the optimum conditions have been included in the original set of trial 5 (see Table 3). So, an extra validation trial need not be carried out. According to the results, determined from trial 5, the average of the strength was 271 MPa which well lies within the calculated average of the strength range. This validates the confidence of this study.

CONCLUSION

This work has presented an investigation on the e ffects of T h in ERSW. Taguchi's method has been employed to examine the effects of four welding parameters namely, electrode pressure, welding current, welding time, Hold time on T-S strength. The conclusions from this study can be driven as follows;

1- According to the Taguchi method, the highest effective parameters on tensile-peel strength were determined as welding current and welding time, whereas Electrode pressure was less effective factors.

2- The results showed that welding current was about three times more important than the second effective factor (welding time) to obtain high tensile shear strength.

3- The highest tensile shear strength was average 471,5 MPa was obtained with the optimal combination of the factors as 10 kA welding current, 4 kN electrode pressure, 20 period welding time, and 10 period hold times.

REFERENCES

[1]. M. Vural, A. Akkus, Journal of Materials Processing Technology 153–154 (2004) 1–6, http://dx.doi.org/10.1016/j.jmatprotec.2004.04.063
[2]. Jenney, C.L. and Brien, A.O. (2001), Welding Handbook, (9th Ed.), Volume 1, American Welding Society.
[3]. J. Lantz, "Principles of Resistance Welding – Weld Heads, Electrodes and Quality", Trade Publication, Welding Design and Fabrication, 73(4) (2000 46 p.
[4]. U. Eşme, The Arabian Journal for Science and Engineering, Volume 34, Number 2B, October 2009. ISSN 1319-8025
[5]. Ö. Savaş, Steel and Composite Structures, An International Journal 18 (2015) 345-355, DOI: 10.12989/scs.2015.18.2.345
[6]. G. Thakur, T. E. Rao, M. S. Mukhedkar and V. M. Nandedkar, ARPN Journal of Engineering and Applied Sciences, Vol. 5, no. 11, November 2010, ISSN 1819-6608.
[7]. S. Aslanlar, A. Ogur, U. Ozsarac, E. Ilhan, Materials and Design 29 (2008) 1427–143, http://dx.doi.org/10.1016/j.matdes.2007.09.004
[8]. P. J. Ross, Taguchi techniques for quality engineering, loss function, orthogonal experiments, parameter and tolerance design, New York: McGraw-Hill Inc.; 1988. ISBN: 0-07-053866-2
[9]. R. H. Lochner, J. E. Matar, Designing For Quality "An Introduction to the Best of Taguchi and western methods of statistical experimental design, chapman and hall, London, Newyork, Tokyo, Melbourne, Madras, 1990. ISBN 10: 0527916331 / ISBN 13: 9780527916336
[10]. S. Aslanlar, A. Ogur, U. Ozsarac, E. Ilhan, Z. Demir, Mater Des, 28 (2007) 2–7. http://dx.doi.org/10.1016/j.matdes.2005.06.022